ISSN 0288-4534
CODEN: KPPJAD

# KONA Powder and Particle Journal

No.42 (2025)

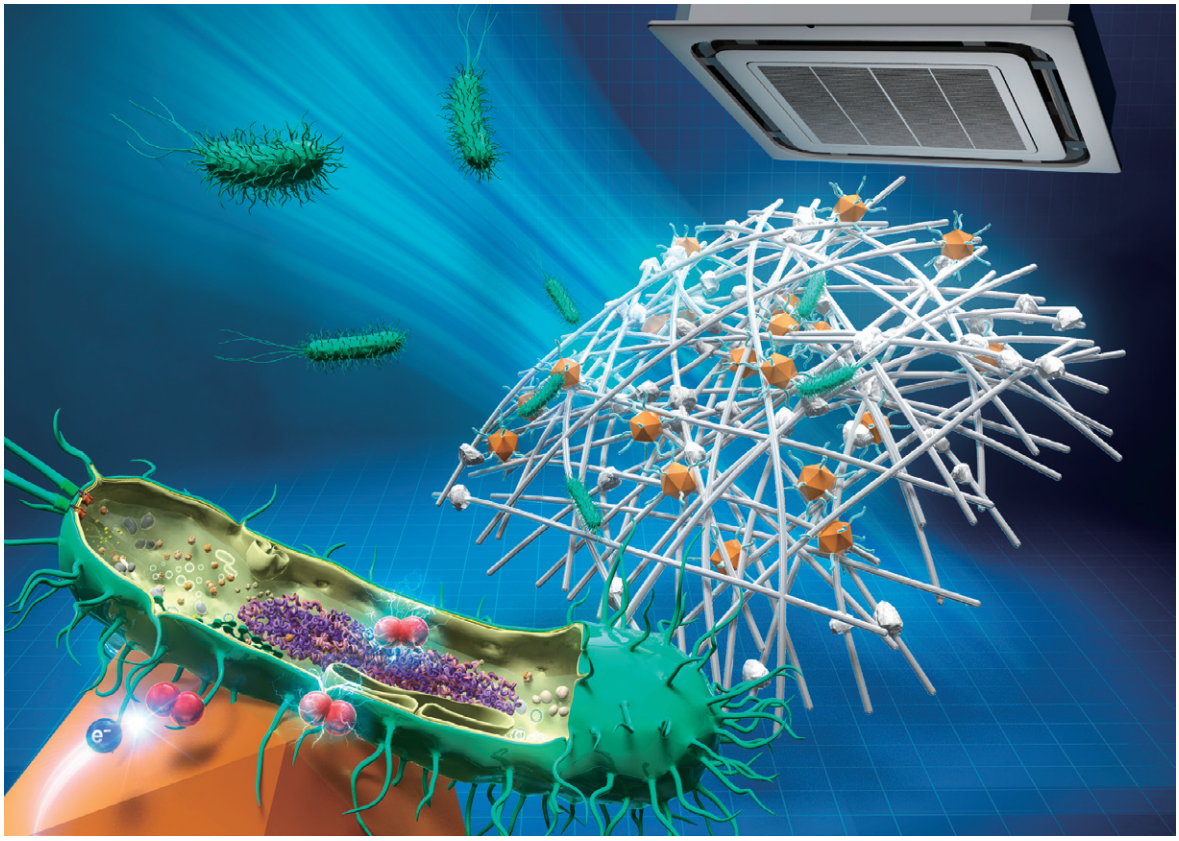

Hosokawa Powder Technology Foundation

available online-www.kona.or.jp

# About this Journal

KONA Powder and Particle Journal is an international, interdisciplinary, and Diamond Open-Access journal that focuses on publishing articles on powder and particle science and technology.

This journal is a refereed scientific journal with an annual publication history dating back to 1983. It is distributed free of charge to researchers, members of the scientific community, universities, and research libraries worldwide by the Hosokawa Powder Technology Foundation, established by the late Mr. Masuo Hosokawa in 1991.

The Chinese character "粉" featured on the cover of the journal is pronounced as "KONA" in Japanese and signifies "Powder." The calligraphy for this character is attributed to the late Mr. Eiichi Hosokawa, the founder of Hosokawa Micron Corporation.

KONA Powder and Particle Journal will cease publication with its issue in early 2026 (No. 43). Submissions close at the end of 2024. The articles published in this journal will remain available on J-STAGE.

## About the Cover

Airborne pathogens, including bacteria, viruses, and fungi, pose a significant threat to human health. Various mitigation strategies have been developed to combat this issue, such as air filtration, ventilation, UV irradiation, and photocatalytic oxidative disinfection (POD). The combination of passive air filtration and active POD techniques shows promise in effectively neutralizing airborne pathogens. However, the efficacy of POD is hindered by factors such as rapid charge recombination, limited understanding of pathogen-catalyst interactions, and short migration distances of reactive oxygen species (ROS). Therefore, it is essential to gain a cellular-level understanding of the fundamental principles and these limiting factors within POD systems. This knowledge will elucidate mechanistic pathways and guide the design of future catalyst particles aimed at improving air quality. This is discussed in detail on pp. 188–199.
<https://doi.org/10.14356/kona.2025013>

**Headquarters of Hosokawa Micron Corporation**

# Editorial Board




■ Publication Office

Hosokawa Powder Technology Foundation (www.kona.or.jp)
(in the headquarters building of Hosokawa Micron Corporation)
1-9, Shodaitajika, Hirakata-shi, Osaka 573-1132, Japan
E-mail: contact_zainq@hmc.hosokawa.com

■ Printing Office: Nakanishi Printing Co., Ltd., Japan

■ Publication Date: 10 January 2025

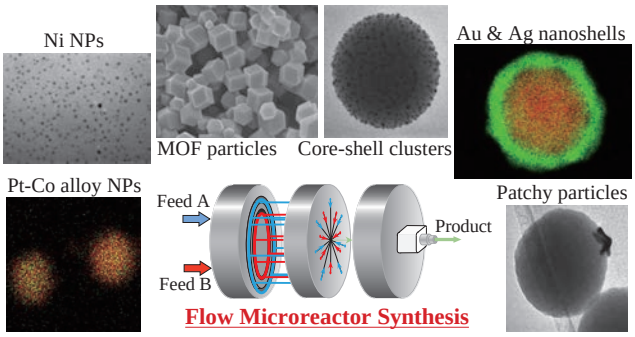




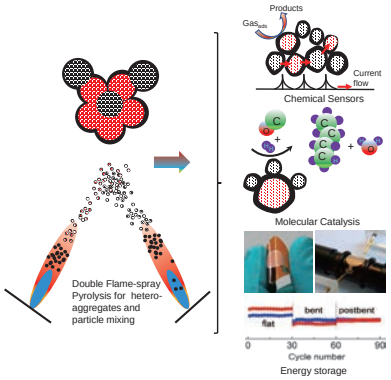




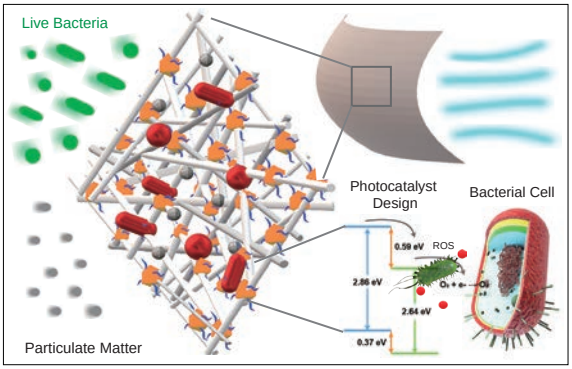




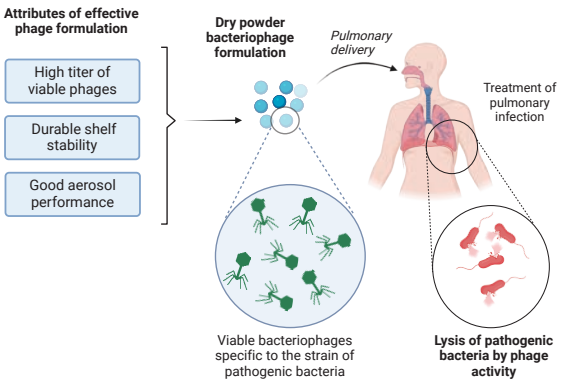

## <Original Research Papers>

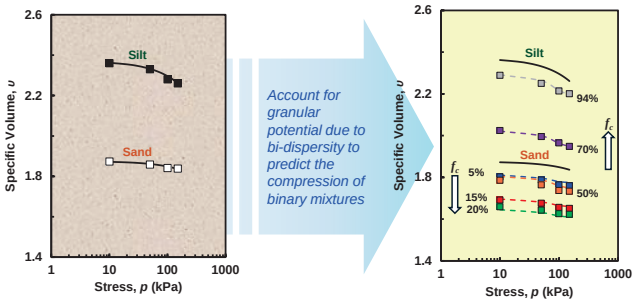




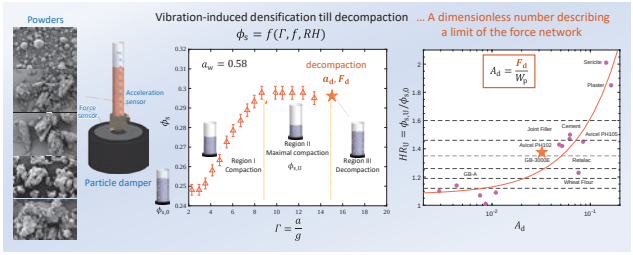


## <Information Articles>




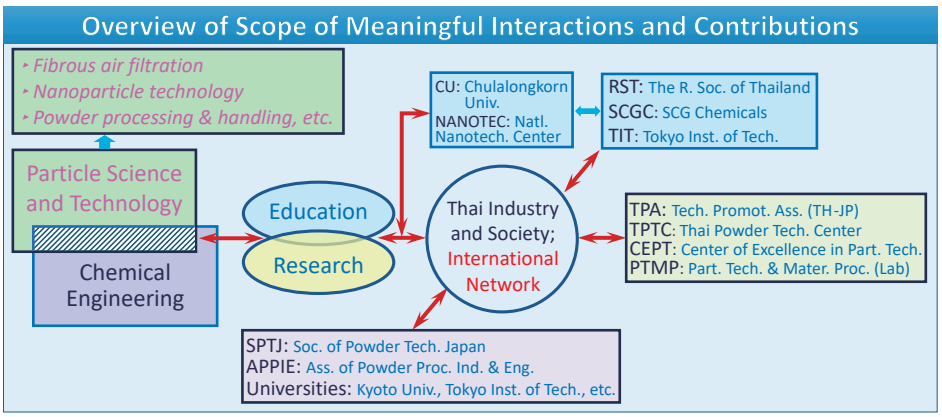


Selected research achievements for the KONA Award 2023 (Emeritus Prof. Wiwut Tanthapanichakoon): Contributions to the advancement of powder/particle and aerosol science and technology & promotion of bilateral collaboration between Thailand and Japan.

# Reviewer Appreciation

**Makio Naito, *Editor-in-Chief***

I would like to express my sincere gratitude to the reviewers for their hard work for the KONA Powder and Particle Journal. Thanks to the generous contributions of the volunteer reviewers as well as the interest of researchers in our journal, the number of submissions to this journal has been increasing since its registration on major international journal platforms, and its level has been further improving. Thanks to their strong support and effort, I am pleased to inform you that the 2023 Impact Factor (JCR) of the KONA Powder and Particle Journal has increased to 4.1, with the CiteScore 2023 of 8.4. Because of the limited space of this annual journal, the number of papers published here is regrettably rather restricted. Therefore, only the papers of good quality will be selected for the journal and further improved and refined by the reviewing process. Moreover, we have created a channel on J-STAGE Data, to enable authors to deposit, share and link to the data within their papers that will be or were published in this journal. J-STAGE Data, which is the data repository provided by the Japan Science and Technology Agency (JST), enables KONA authors to contribute to the promotion of Open Science with reviewers and editors.

The editorial team of the KONA Journal would like to take this opportunity to gratefully acknowledge the reviewers here and deeply appreciate their valuable time and professional contributions to the KONA Journal. We apologize to any reviewers who may have been inadvertently omitted from this list. We are sincerely grateful to all who have been of any assistance to the publication of this journal.

BISKOS, George
COPPENS, Marc-Olivier
FUJI, Masayoshi
HICKEY, Anthony
KAMIYA, Hidehiro
KWADE, Arno
MAINZA, Aubrey
MATSUSAKA, Shuji
MISRA, Anil
ROSATO, Anthony
SAKKA, Yoshio
TAVARES, Luis Marcelo
TUAN, Wei-Hsing
WANG, Wei-Ning
YOKOYAMA, Toyokazu

Makio Naito
Professor Emeritus, Osaka University
October 2024

# Editor's Preface

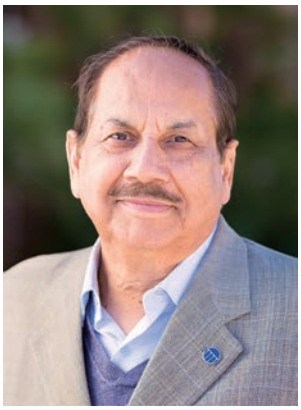

**Brij M. Moudgil**
***Chairman of American Editorial Board***
*University of Florida, USA*

As Chair of the American Editorial Board, I am pleased to introduce the KONA Powder & Particle Journal No. 42. Consistent with our tradition, this issue contains 13 high-quality reviews and 4 original papers.

It is no secret that with the explosive growth of artificial intelligence/machine learning (AI/ML) modalities, we are witnessing a unique opportunity to not only realize phenomenal growth in practical applications of particulate systems, but also to overcome certain long-standing challenges that have impeded particle technologists over the ages. Through judicious integration of AI, particle technologists can reduce the cost of production and accelerate the development of customized functionalities that might not otherwise be feasible by traditional methods.

Particle technologies continue to play a vital role in advancing useful developments in a wide variety of industries, from food to pharmaceuticals and mining to microelectronics, and beyond. The use of tailored powders in additive manufacturing is growing, particularly in industries like aerospace, automotive, and healthcare. Particle technologies offer the potential for the development of novel materials with improved mechanical properties and complex geometries. Nanoparticles with specific functionalities (e.g., magnetic, optical, electronic, or catalytic properties) can be used in applications such as imaging, sensors, and energy harvesting. These particles enable the creation of new products and technologies with enhanced performance across various sectors, including healthcare and electronics. Particle technologies are being explored for enhancing bioavailability of nutrients, and in precision agriculture for controlled release of fertilizers and pesticides. These advancements could lead to more sustainable food production and improved nutritional quality. In energy production, particle technologies are important for applications like solar panels, fuel cells, and batteries. Enhanced energy efficiency and the development of sustainable, renewable energy solutions can be achieved through the optimization of particle-based systems.

Collaborative approaches between academic researchers in particle technology and AI/ML, and contract manufacturers (CMOs) and research organizations that specialize in scaling up particle-mediated processes provide a unique opportunity to develop robust system specific scale up protocols.

Where there are opportunities, challenges are to be expected. The production and handling of nanoparticles and fine particulates can pose health risks, including respiratory issues or toxicity, as well as environmental contamination. The toxicity of nanoparticles is highly dependent on their specific characteristics, such as size, shape, composition, and surface properties. While some nanoparticles have shown toxic effects, particularly in high doses, many nanoparticles and nanostructures have been successfully designed to minimize risk and maximize therapeutic or functional benefits. Ongoing research is beginning to address these challenges, but the rapidly evolving field of nanotechnology requires constant updates in both research and policy to ensure safe use.

AI will be transformational for the field of nanotechnology. Models can simulate complex particle interactions in

various media (liquids, gases, biofluids etc.), predicting agglomeration, sedimentation, or dispersion properties. This can help optimize the use of particles in applications such as functional coatings, advanced composites, healthcare, and pharmaceuticals.

High throughput particulate mediated experimentation is still under development. However, AI has the potential to expedite reliable data acquisition by automating the experimentation process. At the same time, robotic systems equipped with AI may enable rapid testing of different particle formulations and conditions.

Although numerous applications of AI/ML systems for on-demand commercial production of nanoparticles and nanostructures have been proposed, practical applications of AI are not without challenges. For example, ongoing collaborative efforts have revealed that the scarcity of high-quality, standardized data is a critical barrier to developing robust and reliable nano-QSAR models. One of the primary issues is the lack of availability of sufficient number of uniform datasets, since different experimental groups have employed different assays, and different biological systems. This makes it challenging to develop computational models that are universally applicable, since minor changes in nanoparticle composition can lead to vastly different toxicological outcomes. Additionally, validating these models is challenging due to the limited availability of comprehensive external datasets and the difficulty in defining the applicability domain—i.e., the range of nanoparticle properties for which the model predictions are dependable. Integrating these models into regulatory frameworks is further complicated by the need for standardized guidelines and protocols, which require coordination among researchers, regulatory bodies, and industry stakeholders to ensure these computational tools are effectively and appropriately used in nano-safety assessments.

It is interesting to note that despite the myriad AI/ML challenges, a recently published paper has illustrated the potential of using ChatGPT-4 and LLM (Large Language Models) to write an original pharmaceutics manuscript. Although the results generated appeared plausible, the authors strongly advise that human interpretation and validation are necessary to enhance AI capabilities in generating robust data that may be suitable for practical applications.

On the educational front, artificial intelligence has wide-ranging potential. For example, AI-powered platforms are already offering personalized tutoring. For educators, AI can help tailor instruction to meet individual student needs and predict which students may require additional support for understanding a specific topic.

Overall, I believe harnessing the application of AI/ML and advanced computational tools has the potential of stimulating both the instruction and applications of particle and powder technology for continued societal benefit. However, the need for domain expertise is going to be ever more critical to make proper use of AI/ML tools, which otherwise may lead to highly risky developments. Regarding our collaborative efforts to ensure KONA's continued relevance and reputation as a foundational source of particle and powder technology knowledge, more review papers authored/coauthored by current and past industry researchers and practioners are highly desired to further enrich KONA's literature and library. Mini reviews on emerging topics by younger professionals is another opportunity to present breaking developments to KONA readers.

I would like to close by thanking all the authors and reviewers who have contributed to the "KONA Powder and Particle Journal" Issue No. 42. Their research, contribution and partnership have been instrumental in making this edition a success and ensuring that we all have an eye on the future of KONA and the technologies on the horizon with respect to which our expertise will be sought.

Brij M. Moudgil, Chair
American Editorial Board
September 2, 2024

KONA Powder and Particle Journal

KONA Powder and Particle Journal No. 42 (2025) 3–14/https://doi.org/10.14356/kona.2025010 Review Paper

# Fine and Nanoparticle Adhesion and Aggregation Behaviour Characterisation and Control†

**Hidehiro Kamiya**

*Institute of Engineering, Tokyo University of Agriculture and Technology, Japan*

The control of adhesion and aggregation behaviour in gases, liquids, and solids is important for the application of inorganic nano- and fine particles in various fields, such as functional materials and devices, pharmaceuticals, cosmetics, and pigments. We have developed original methods for the characterisation of interfacial molecular- and nanometre-scale structures and interactions between particles and substrate materials. The surface molecular-structure design by an organic surfactant, commonly called a "ligand," was investigated with different molecular structures for nanoparticle-dispersion stability control in various organic solvents and polymer solid materials. First, we introduce various approaches for controlling the interfacial molecular structure of nanoparticles to disperse nanoparticles in various liquids. Next, aggregation- and adhesion-behaviour characterisation methods, such as colloid probe atomic force microscopy and the control of fine powders and microcapsules in the ceramic and pharmaceutical fields, are reviewed. Finally, the characterisation and control of the adhesion behaviour of fine ash particles at high temperatures in energy generation and environmental systems are investigated. Original characterisation devices and a model of an ash-particle preparation method from pure silica were developed by adding small amounts of elements, such as alkali metals and phosphates, to analyse the increase mechanism of the ash-adhesion force at high temperatures. Based on the results of the analysis, the adhesion behaviour can be controlled by the addition of various materials.

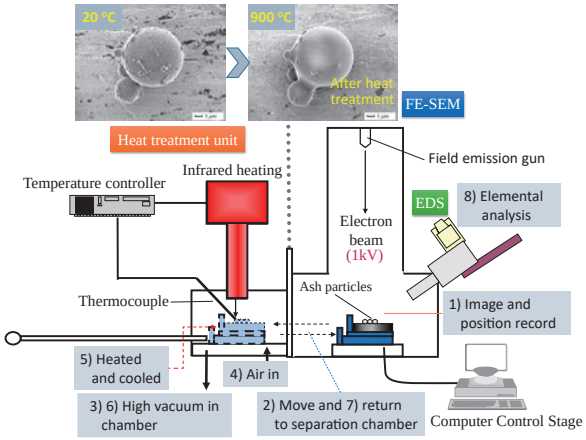


**Keywords:** particle surface interaction, interface structure design, ligand and dispersant, dispersion/aggregation control, high temperature effect

## 1. Introduction

Nanoparticles, which are smaller than 100 nm in diameter, have various functional properties such as quantum, optical, electromagnetic, and chemical catalytic properties. Recently, mass-production processes for nanoparticles and nanomaterials have been developed, and cost reduction is progressing. For example, the mass production of carbon nanotubes has been developed at the commercial level using a fluidised bed process (Li et al., 2021) and a new reactor design (Yoko et al., 2020). Technologies for controlling the size, shape, composition, and crystallinity of various nanoparticles and materials in gas and liquid phases have also been developed (Park et al., 2004). However, the aggregation- and adhesion-behaviour control of fine and nanoscale particles remains important for the application of nanoparticles in functional material processing, pharmaceuticals, cosmetics, and pigments. For example, when hydrophilic nanoparticles such as metal oxides are dispersed in a nonpolar solvent, a surfactant or ligand comprising a hydrophobic organic chain and an adsorbent group or coupling agent is adsorbed or reacts on the surface of the nanoparticles. The theory required to obtain the optimum molecular size and structure of the ligand and coupling agent for nanoparticle aggregation control in various solvents has not yet been completed. For nanoparticle dispersion, a ligand that is not too large compared with the polymer is typically used. In contrast, for fine particles and microcapsules, which are larger than 100 nm in diameter, a polymer dispersant with a size of approximately 10,000 g/mol is typically adsorbed on the particles for dispersion (Kamiya et al., 1999). In the gas phase, a nanometre-scale surface treatment was developed to reduce the adhesion force of fine particles. In particular, at high temperatures, the increase in ash adhesion causes various problems in power generation using coal and in environmental plants for biomass and waste combustion. The control of adhesion and aggregation behaviours in air is also an important subject.

This paper discusses the fundamentals of fine and nanoscale particle behaviours such as the reason for the difference in surface activity and structure, focusing on the

† Received 2 August 2023; Accepted 18 October 2023
J-STAGE Advance published online 29 June 2024
Add: 2-24-16 Naka-cho, Koganei, Tokyo 184-8588, Japan
E-mail: kamiya@cc.tuat.ac.jp
TEL/FAX: +81-42-388-7068

dispersion and aggregation control of nanoparticles in various solvents. The combination of the materials, size, shape, and surface structure of nanoparticles with solvent properties is an important factor in the selection of a molecular design structure for nanoparticles. Two approaches are proposed to disperse nanoparticles: one is the development of ligands with universal dispersibility in different solvents, and the other is ligand-exchange technology for particle synthesis and dispersion control in the final desired solvent. Next, we focus on fine-particle and microcapsule aggregation- and adhesion-behaviour characterisation and control in liquid. By Ducker et al. (1992), the surface interactions between fine particles were determined using colloidal probe atomic force microscopy, AFM and other characterisation methods. Based on the characterisation results, the optimum polymer and surface molecular structure required to control the surface interaction and dense suspension behaviour is determined. Finally, some original characterisation methods for fine-ash particle-adhesion behaviour at high temperatures have been developed. Based on the characterisation results of the surface interaction, the mechanism of the adhesion-increasing behaviour is investigated, and new methods for controlling ash adhesion at high temperatures have been also developed and introduced in this paper.

## 2. Interface-structure design of nanoparticles for aggregation-behaviour control in liquid

### 2.1 Interface structure and behaviour of nanoparticles

Nanoparticles have large specific surface areas and high surface energies. To discuss the effect of the particle size on the surface energy and structure, a simple crystal structure was assumed as in a simple cubic and one-atom basis. The relationship between the surface atom ratio, $R_i$, and the particle size, which is determined by the number of atoms per side, $i$, is calculated using the following equation (see **Fig. 1(a)**):

$$R_i = \frac{i^3-(i-2)^3}{i^3} = 1-\left(\frac{i-2}{i}\right)^3 \quad (1)$$

When $i = 1$ or 2, all atoms exist on the surface; when $i = 3$, only one atom exists inside, and the surface atom ratio is 8/9, which is approximately 90 %. With an increase in $i$, the surface atom ratio $R_i$ decreases; however, for $i < 10$, the surface atom ratio and surface energy are still high, as shown in **Fig. 1(b)**, which displays the relationship between $i$ and $R_i$. The particle size was calculated; because the atomic radius is 0.124 nm, the particle is not stable, and is formed as a cluster. When particle growth reaches $i > 10$, the surface atom ratio is smaller than 50 %, cubic particle-surface energy is reduced, and the cubic particle is "stable" as a nanoparticle.

Another example of the effect of the particle diameter on the surface molecular structure is shown in the surface silanol structure of alkoxide-derived silica particles, which was determined using FT-IR, as shown in **Fig. 2(a)** (Kamiya et al., 2000). The spectrum peak of free silanol at 3750 $cm^{-1}$ decreased with increasing particle diameter and disappeared, and almost all the silanol was hydrogen-bonded when the particle size reached 260 nm. This change in the silanol group structure may be related to the distance between the neighbouring silanol groups, as shown in **Fig. 2(b)**.

The estimated distance between the O and H atoms of the neighbouring silanol groups increased with decreasing

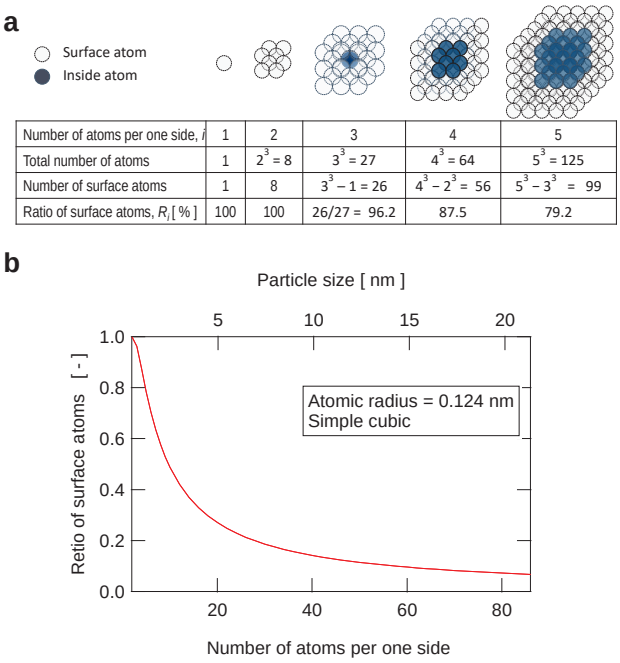


| Number of atoms per one side, $i$ | 1 | 2 | 3 | 4 | 5 |
|---|---|---|---|---|---|
| Total number of atoms | 1 | $2^3 = 8$ | $3^3 = 27$ | $4^3 = 64$ | $5^3 = 125$ |
| Number of surface atoms | 1 | 8 | $3^3 - 1 = 26$ | $4^3 - 2^3 = 56$ | $5^3 - 3^3 = 99$ |
| Ratio of surface atoms, $R_i$ [ % ] | 100 | 100 | 26/27 = 96.2 | 87.5 | 79.2 |

**Fig. 1** Estimated effect of simple cubic particle size on surface atom ratio. **(a)** Conceptual diagram and table for calculation of surface atom ratio. **(b)** Relationship between number of atoms per one side and surface atom ratio estimated by **Eqn. (1)**.

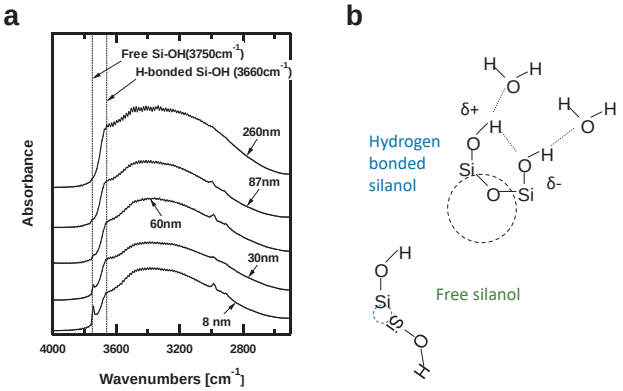


**Fig. 2** Effect of silica particle diameter on surface silanol structure. **(a)** FT-IR diagram of silica with different diameter. **(b)** Estimated surface silanol structure. Adapted with permission from Ref. (Kamiya et al., 2000). Copyright (2000) Wiley.

particle diameter. This difference in the surface molecular structure affects the reaction density of the silane coupling agent on the silica surface. Because of the large distance between the O and H atoms and the low surface silanol density of the nanoparticles, the amount of chemisorbed silane coupling agent per unit surface area on the nanoparticles (30 nm in diameter) was lower than that on the fine particles (200 nm in diameter), as shown in **Fig. 3** (Iijima et al., 2007).

## 2.2 Simultaneous design of nanoparticle synthesis and dispersion in nonpolar solvent

Using a metal oleate complex as the raw material, oleyl-group surface-modified nanoparticles were synthesised in a nonpolar solvent under high temperature and pressure conditions. The synthesised nanoparticles were dispersed and stabilised in a nonpolar solvent and self-assembled to form a close-packed structure via the coating and drying process using the nanoparticle suspension by Park et al. (2004). The size and shape of nanoparticles could be controlled by varying the synthesis conditions. In the normal hydrothermal synthesis process, oleic-group surface-modified nanoparticles were synthesised by adding an organic surfactant with an oleic chain. For example, the particle size and morphology of titanium oxide (Dinh et al., 2009) and iron oxide (Cara et al., 2015) nanoparticles were controlled by adding different ratios of oleic acid and oleic amine in the hydrothermal process. The synthesis of nanoparticles in the presence of oleic acid and amine enabled control of the particle structure and functional behaviours of metal, metal oxide, and sulphide nanoparticles. This method has been detailed in review articles by Mourdikoudis et al. (2022).

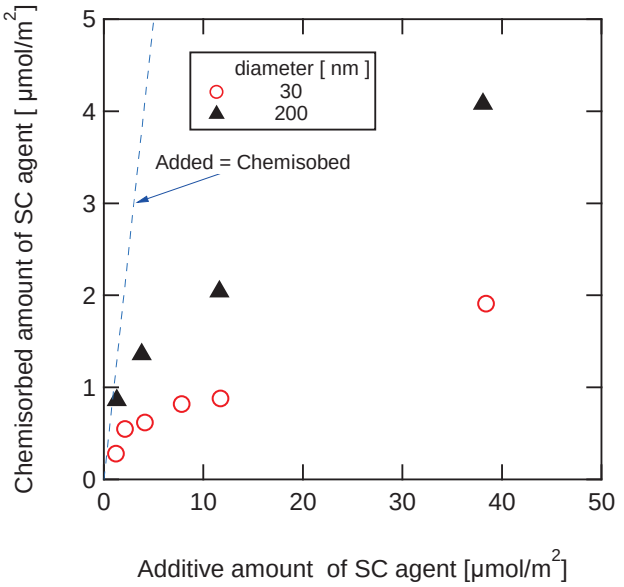


**Fig. 3** Chemisorbed amount of silane coupling agent on silica particles measured using an organic element analyzer. Adapted with permission from Ref. (Iijima et al., 2007). Copyright (2007) Elsevier B.V.

Oleic-group modified nanoparticles are effective for dispersion stability in nonpolar solvents such as toluene. However, if the solution properties are changed by a small amount of a hydrophilic solvent, such as methanol, the dispersion stability decreases and nanoparticle aggregation is promoted. To obtain nanoparticles dispersed in a polymer composite, a hydrophilic polymer resin monomer was added to nanoparticles dispersed in a nonpolar solvent. Because of the change in solvent polarity, white turbidity due to nanoparticle aggregation was observed. If the solvent, solution, or matrix solid selected for application cannot maintain dispersion stability with oleic-group modified nanoparticles, the following two approaches may be used:

1) Development of ligand molecular-structure design for dispersion in various solvent and solid materials.
2) Ligand exchange to change in surface-modified molecular structure from the synthesis process used to obtain the optimum surface organic structure for dispersion in different solvents and solid matrix.

The details of each approach will be introduced in the following sections.

## 2.3 Development of ligand-structure design for dispersion of nanoparticles in various solvents

To select organic ligands to disperse nanoparticles in the target solvent, the optimum organic chain in the ligand should be selected and synthesised; however, the theory for optimum ligand selection has not yet been completed. To disperse nanoparticles in various organic solvents, various commercial ligands and surfactants with different molecular structures, including hydrophilic and hydrophobic groups in one molecule, were added to the nanoparticle suspension. Iijima et al. (2009) discovered the optimum surfactant by examining the stability of each dispersion, as shown in **Fig. 4(a)**. This surfactant included PEG and a hydrocarbon chain in the molecule. Titanium-oxide nanoparticles modified with this surfactant were dispersed in various solvents, ranging from methanol to toluene. Furthermore, ligand-modified $TiO_2$ nanoparticles were dispersed in a PMMA resin, and this polymer composite exhibited shape-memory properties against temperature changes.

Because this ligand has an anionic phosphonic group for adsorption on nanoparticles, metal-oxide nanoparticles, such as titanium and aluminium oxide, can be dispersed in various solvents by the adsorption of this ligand. However, noble-metal nanoparticles, such as gold and silver, as well as silica nanoparticles, cannot disperse in solvents without the adsorption of these ligands. A two-step adsorption method was developed in which a polymer dispersant with amine groups, such as polyethyleneimine, is first adsorbed, followed by ligand adsorption (Iijima and Kamiya, 2010). Because amine polymer dispersants have multiple cationic

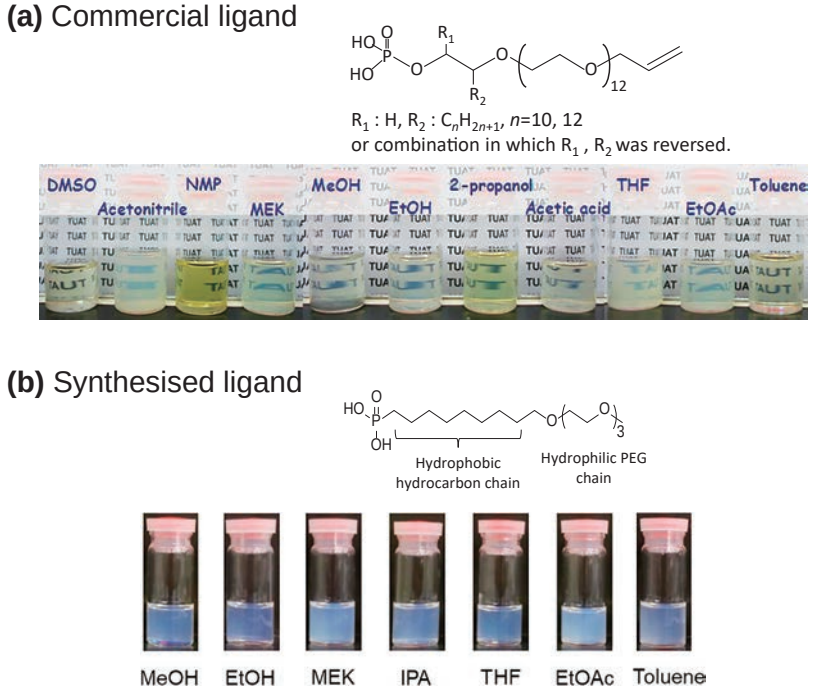


**Fig. 4** Ligand molecular structure and photo of transparent suspension, **(a)** Commercial ligand, adapted with permission from Ref. (Iijima et al., 2009). Copyright (2009) American Chemical Society. **(b)** Synthesised ligand, adapted with permission from Ref. (Okada et al., 2018a). Copyright (2018) Wiley.

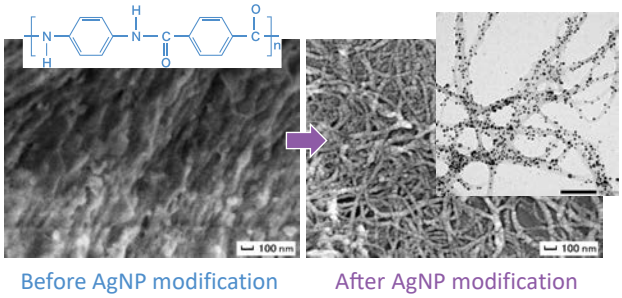


**Fig. 5** SEM and TEM observation of aramid nanofiber before and after surface modification of silver nanoparticle, AgNP, with surface treatment. Adapted with permission from Ref. (Iijima and Kamiya, 2015). Copyright (2015) Elsevier B.V.

amino groups in one molecule, the nanoparticle surface is positively charged, and the anionic ligand can be adsorbed. Using the two-step adsorption process, gold, silver, and silica nanoparticles were universally dispersed in various solvents. For application in conductive and antistatic polymers, surface-modified silver nanoparticles using this process were attached and distributed on aramid nanofibers (ANFs). Because the ANFs formed aggregates, surface-modified silver nanoparticles promoted the uniform dispersion of ANFs, as shown in **Fig. 5** (Iijima and Kamiya, 2015). The surface-modified silver nanoparticles coated with ANFs were uniformly distributed in the epoxy resin.

The number of organic molecules on the surface increased owing to multilayer adsorption, and the final concentration of organic compounds in the inorganic nanoparticles reached approximately 10–30 wt% because of the high specific surface area of the nanoparticles. Furthermore, the dispersed suspension and composite turned yellow because the commercial ligand contained impurities.

To reduce the concentration of organic compounds in the surface-modified nanoparticles as well as impurities in the ligand, Iijima et al. (2009) synthesised various ligands based on the clarification of which structure in the commercial ligand, shown in **Fig. 4(a)**, contributes to universal dispersibility in various solvents. Finally, they discovered the serial structure of simple alkyl and PEG chains for the universal dispersibility of nanoparticles in various solvents, as shown in **Fig. 4(b)** (Okada et al., 2018a). By purifying each ligand-synthesis process, the yellow colour disappeared. For silica and noble-metal nanoparticles that could not be adsorbed by phosphonic groups, ligands with amino groups as the adsorbing group were synthesised and adsorbed on each nanoparticle (Maeta et al., 2018). Using the characterisation method for adsorption strength described later, the adsorbed group was selected for different nanoparticle materials, and the optimum ligand for dispersion in various solvents was synthesised.

## 2.4 Ligand exchange for various applications

Because the adsorbed strength of the exchanged ligand must be higher than that of the ligand during the synthesis process, characterisation of the adsorbed strength of the ligand for the nanoparticle materials is important (Zeininger et al., 2016). Examples of adsorption groups for inorganic

nanoparticles are shown in **Fig. 6**. By combining one adsorptive group with a modified organic chain structure, a designed ligand is synthesised for the dispersion of nanoparticles. The optimal modified organic chain structure for the final dispersion in solvents and solids should be combined with the strongest adsorption group.

One characterisation method for the adsorption strength is a simple visual method, and the other is an instrumental method using NMR. A visual observation method was applied by utilising the properties of a mixed solvent of cyclohexane and methanol, which were separated at room temperature and uniformly mixed at temperatures higher than 40 °C. For example, as shown in **Fig. 7**, the first ligands combined with a hydrophilic organic chain with a PEG group and catechol were adsorbed onto iron-oxide nanoparticles (Okada et al., 2018b). The two phases were separated, and the surface-modified iron-oxide nanoparticles were dispersed in methanol. Upon heating to 40 °C, the two solvents were mixed uniformly and a second ligand with an oleyl chain and phosphite group was added to the suspension. Finally, the suspension was cooled to room temperature for 3 h, and the two solvents were separated. Because oleic ligands with phosphite groups were exchanged on the surface of iron oxide, the nanoparticles were dispersed into the upper phase, a hydrophobic solvent. Based on this result, we determined that the phosphite group had a higher adsorption strength compared with catechol for the iron-oxide nanoparticles. This method was applied to different combinations of organic chains and adsorbed groups, and the ranking of adsorption strength was determined for each nanoparticle material.

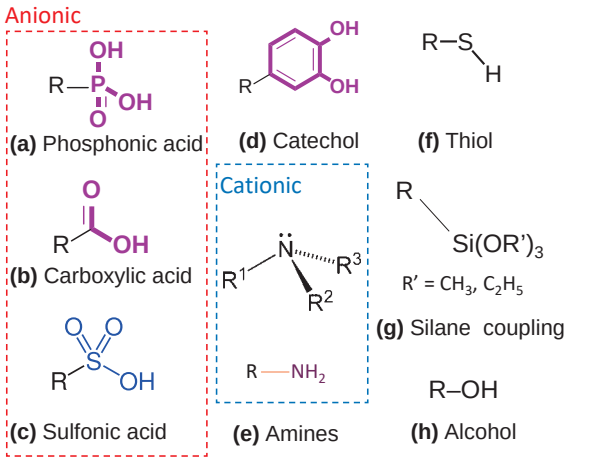


**Fig. 6** Examples of adsorption groups.

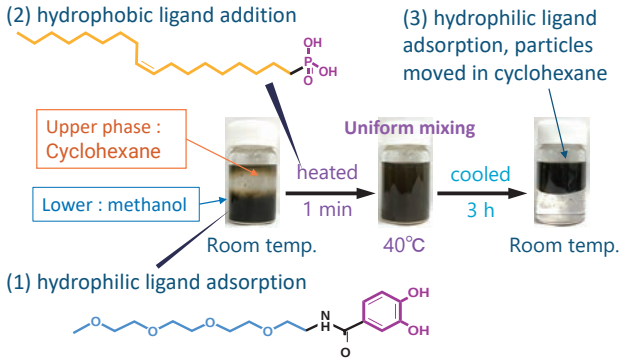


**Fig. 7** Direct observation to determine for the adsorption strength on iron-oxide nanoparticles, adapted with permission from Ref. (Okada et al., 2018b). Copyright (2018) Wiley.

The second method using NMR is also a popular method for observing ligand exchanges. Compared to the NMR signal of the free dissolved ligand in the solvent, the NMR peak of the adsorbed ligand on the nanoparticles was broadened (Aiello et al., 2021; Hens et al., 2013; Schechtel et al., 2019; Yamashita et al., 2021). Different ligands were added to the suspension, and the ligands with broadened peaks exhibited higher adsorption strengths. This method required the synthesis of high-purity ligands with uniform molecular structures.

Recently, crown ether-associated ligands with different salts led to the stripping of oleic acid on $Fe_3O_4$ nanoparticles, which were used during the nanoparticle-synthesis process, and different ligands could be re-grafted onto the nanoparticles (Shirmardi Shaghasemi et al., 2017). If crown ethers have the same function for stripping different ligands from nanoparticles, this approach may be applied to ligand exchange on various nanoparticles.

## 2.5 Analysis of dispersion mechanism and advanced behaviours of surface-modified nanoparticles

The detailed mechanism describing why the above-described oleyl, alkyl-PEG chain structures exhibited dispersion stability of nanoparticles in nonpolar or various solvents are not clear. Various approaches, such as a thermodynamic analysis of the effect of the organic chain structure (branched or linear) and a molecular-dynamics simulation of the adsorbed ligand structure on the nanoparticle surface, have been proposed (Elimelech et al., 2022; Saito et al., 2021; Yang et al., 2016). The action mechanisms of each ligand were elucidated by combining various analyses and simulation methods. Yamashita et al. (2022) discovered an attracting phenomenon, which was the temperature dependence of the dispersion behaviour of surface-modified nanoparticles in solvents. This phenomenon was similar to the solubility of the molecules in the solvent, and the dispersibility of the nanoparticles increased with increasing temperature. The boundary temperature between aggregation and dispersion depended on the molecular-chain length and ligand structure. For a simple straight alkyl chain in the ligand, the optimum chain length for maintaining dispersion over a wide temperature range is shown in **Fig. 8**. The range of optimum chain lengths for dispersion over a wide temperature range appeared to depend on the particle diameter and material.

Challenges arise in promoting the application of surface-modified nanoparticles in liquids, some of which are summarised in **Table 1**. First, the critical particle-solid concentration in suspensions with high fluidity is considerably lower than that in submicron-particle suspensions. In the field of fine-ceramic processing, the critical solid fraction of submicron-particle suspensions is higher than 60 vol%; however, the critical concentration of nanoparticle suspensions is approximately 30 vol%.

Another problem is that the surface-modified organic ligand mass fraction is approximately 20–30 % of that of the nanoparticles to ensure complete coverage of the nanoparticle surface, owing to the high specific surface area. Ligand molecules are similar in size to the nanoparticles. From a different perspective, surface-modified inorganic nanoparticles are almost considered organic–inorganic composite materials. After coating silicon oligomer on silica nanoparticles in an aqueous suspension, additional silicon oligomer was added to the suspension, which was polymerised, and coated on the base; thus, silicone sheets with dispersed silica nanoparticles were prepared by Iijima et al. (2013). This composite sheet was considerably more flexible than a silicone sheet without a silica-nanoparticle dispersion, and adding other functional nanoparticles is simple. New applications for silicon with optical and electrical functional properties are expected.

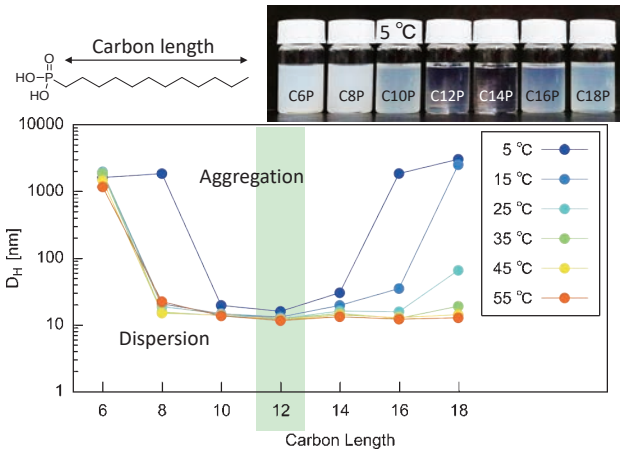


**Fig. 8** Relationship between mean particle diameter determined by DLS and carbon length in ligand at temperature ranging from 5 to 55 °C. Adapted with permission from Ref. (Yamashita et al., 2022). Copyright (2022) Wiley.

## 3. Characterisation of aggregation and adhesion behaviour and control of submicron-sized fine particles in liquid and gas phases

Submicron fine particles and microcapsules with diameters larger than 100 nm have been used as raw materials and products in various fields, such as ceramics, batteries, pigments, pharmaceuticals, and cosmetics. The characterisation of the aggregation and adhesion behaviour of these particles and their control in the liquid and gas phases are also important for the development of each application field. In the energy generation and environmental fields, ash adhesion and growth phenomena at high temperatures are important for the stable operation of coal, biomass and waste combustion, and gasification processes. Direct characterisation methods for the surface interactions between particles and materials have been developed using various original methods in the gas and liquid phases. Surface-modification and structure-design methods have also been developed for the control of surface interactions based on the characterisation and analysis of surface interactions. In this section, the characterisation and analysis methods for surface interactions in the liquid and gas phases are reviewed.

### 3.1 Characterisation of surface interactions between particles, microcapsules, and various substrates in the liquid phase using colloid probe AFM

#### 3.1.1 Ceramics processing

In the fine-ceramic preparation process, the raw materials of fine particles are dispersed in water or organic solvents, and a suspension with high fluidity and solid concentrations higher than 50 vol% is prepared. Foamed powder bodies are obtained via a shaping process, such as coating and drying, or drying/granulation followed by dry pressing the powder into a mould and applying cold isostatic pressing. The final ceramic materials are then prepared by sintering. To obtain a high-fluidity suspension with a high solid content, the surface interaction between fine particles is generally controlled using a polymer dispersant. The particles are larger than 100 nm in diameter, and the van der Waals forces start to act at a surface distance of several nanometres. This surface distance

**Table 1** Summary of key challenges for nanoparticle applications.

| Subject | Main application fields | Example of solutions, approaches |
|---|---|---|
| Low solid content in fluid suspension | Advanced ceramics, polymer composite for functional materials | Small molecules for surface modification |
| High organic content caused by high surface area | Polymer composite, ceramics and functional sensor | Pre-coating by monomer or oligomer of polymer source, decreasing before sintering |
| High surface reaction activity | Composite, catalyst, DDS | Surface coating and treatment |

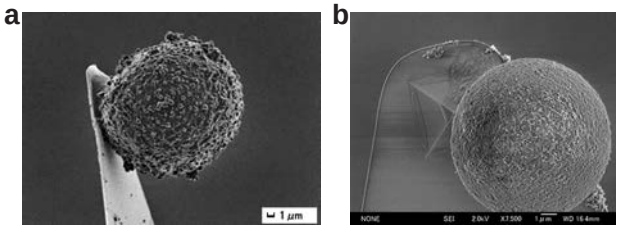


**Fig. 9** SEM observation of colloid probe prepared by different methods. **(a)** Spray dried and sintered granule probe, adapted with permission from Ref. (Iijima et al., 2007). Copyright (2007) Elsevier B.V. **(b)** Carbon nanoparticle coating on spherical resin particle by mechanical process, adapted with permission from Ref. (Hanada et al., 2013). Copyright (2013) Elsevier B.V.

decreases with decreasing particle size. For the dispersion of submicron particles, the molecular weight of the polymer dispersant is approximately 10,000 g/mol, which is larger than that of the ligand for the nanoparticles (Kamiya et al., 1999).

Colloid probe AFM has been applied to characterise the change in interaction owing to various surface modifications to analyse the action mechanism and determine the optimum condition of the polymer dispersant structure and surface modification, such as silane coupling agents or thiols. An example of a colloid probe is shown in **Fig. 9**, where a fine spherical particle attached to the top of a commercially available tip was prepared for AFM. A system combining a high-resolution optical video system and micromanipulator was also developed for probe fabrication by Kamiya et al. (2006). Preparing a fine particle probe with a size smaller than 1 μm by optical microscope is difficult; therefore, a spherical particle of several micrometres was prepared using spray drying granulation and sintering (**Fig. 9(a)**, Iijima et al., 2007) or coating nanoparticles on spherical resin particles via a mechanical compounding method (Hanada et al., 2013). By using colloidal probes with different materials, the effect of the polymer structure and silane coupling surface-modification conditions on the surface interaction between particles and dispersion behaviour in suspensions has been discussed for aqueous solutions and organic solvents (Mori et al., 2016).

Polymer dispersants are generally used to increase the fluidity of slurries by dispersing fine-particle aggregates. In the case of cast moulding of slurries, shape-retention agents are used to provide strength to the formed bodies. Recently, a new functional polymer was discovered, which acts as a dispersant during slurry preparation, followed by time-dependent gelation to maintain the shape of the formed bodies (Yang et al., 2013). The action mechanism of this polymer over time was discussed using the colloidal probe AFM method (Yamamoto et al., 2019).

### 3.1.2 Pharmaceutical application

To characterise the interfacial structure and properties of microcapsules for drug-delivery systems, a colloid probe or substrate was prepared from a granule of microcapsules, and surface interactions were measured via probe AFM in aqueous solutions with different pH conditions. For example, microcapsules with modified pH-sensitive gel surfaces have been used in oral-delivery medicine. Under the acidic conditions in the stomach, the pH-sensitive surface gel shrank and protected the incorporated peptide drug. Under the neutral pH conditions in the small intestine, the pH-sensitive gel swelled and released the peptide drug. Using the colloidal probe AFM method (Iijima et al., 2008), the surface interaction between the microcapsule and mucin-layer substrate was determined under different aqueous pH conditions. The mucin layer that formed on the mica surface mimicked the mucosa of the small intestine and stomach. A long-range adhesive force was measured at neutral pH owing to the swollen surface of the pH-sensitive gel, and the microcapsule remained in the small intestine. Under low-acidic pH conditions, a short-range attractive force was detected because the surface gel layer shrank and had a rigid structure. Furthermore, using carbon-nanotube probe AFM, the interaction between chitosan-modified liposome capsules and the mucin layer under different pH conditions was investigated (Yamamoto et al., 2018).

### 3.1.3 Surface-nanostructure control for toner and cosmetic applications

To improve the image quality of electronic copying, a mechanical surface-treatment technology for a surface-modified silica nanoparticle-coated toner was developed, and the adhesion force was determined using colloid probe AFM (Tanaka et al., 2008a). The surface structure was characterised by the fractal dimension, and the relationship between the adhesion force of the toner and the fractal dimension was determined using colloid probe AFM (Tanaka et al., 2008b). Experiments confirmed that the inclusion of the silica nanoparticles increased the fractal dimension and reduced the adhesion force.

The effect of surface-adhered nanoparticles and nanoporous structures on particle–particle interactions was investigated using colloid probe AFM for cosmetic applications. The adhered nanoparticles decreased cosmetic particle–particle interactions. With the nanoporous structure, the formation of liquid bridges was enhanced; thus, the adhesion force did not increase with humidity (Kani et al., 2007).

## 3.2 Fine-particle adhesion-behaviour characterisation under high-temperature conditions

For the inorganic-compound properties in the pulverised-coal combustion process, the target temperature range was higher than 1500 °C because the viscosity of molten ash is important. However, because ash deposition

occurred on the surface of the superheater and heat exchanger, and dust was collected by a ceramic filter, the target temperature was lower than 1000 °C. Thus, it was necessary to characterise the adhesion properties of solid ash particles.

Two methods have been developed to characterise the adhesion force at high temperatures of up to 1000 °C. One method is the measurement of a direct single-particle adhesion force, which uses the same method as the AFM force curve. Another method is the powder-bed strength method. The main targets were ash particles generated during coal, biomass and waste combustion, and gasification processes.

### 3.2.1 Interaction-measurement system between a single ash particle and substrate

A schematic of the adhesion-force measurement system is shown in **Fig. 10** (Gao et al., 2020). A single ash particle that adhered to the top of a pure alumina rod was pressed onto a substrate prepared from a superheater material on a high-purity quartz glass leaf spring. A small area of the ash particles and substrate was heated to 900 °C using an infrared condensing heater. The compression force was measured by the displacement at the top of the leaf spring. As it reached the maximum compression value, a single ash turned and reduced the compression force, as shown in **Fig. 10**. The movement of the alumina rod was controlled by a high-resolution linear motor. If an adhesion force acted between the ash and substrate, the leaf spring warped to the tension side. When the tensile force of the leaf spring balanced the adhesion force between the ash particle and the substrate, the ash particle separated from the substrate surface. The maximum tensile force was determined to be the adhesion force.

The adhesion force was measured at different high temperatures and maximum compression forces, and the results of the relationship between the maximum compression and adhesion force at different temperatures is shown in **Fig. 11**. When the temperature increased to 900 °C, the adhesion force increased with an increase in the maximum compression force. At 750 °C and 850 °C, the adhesion force was similar for different maximum compression forces. It appears that plastic deformation at the contact point increased the adhesion force at 900 °C; this was analysed using Hertz's deformation theory at the contact point. A fitting line was obtained using this theory, as shown in **Fig. 11**.

### 3.2.2 Powder-bed method

Using the principle of a room-temperature measuring device, a split-type tensile-strength tester of powder beds for high temperatures was developed, and the schematic of the measurement device is shown in **Fig. 12(a)** (Kamiya et al., 2002a). Fused silica glass with a low thermal-expansion coefficient was used as the material for the suspended cell for measurements at high temperatures. Because the metal cell has a higher thermal-expansion coefficient than that of an inorganic powder bed, the powder bed breaks owing to the thermal expansion of the cell at elevated temperatures. The tensile strengths of the ashes, coal, biomass, and waste increased sharply at a particular temperature, depending on the ash. An increase in the

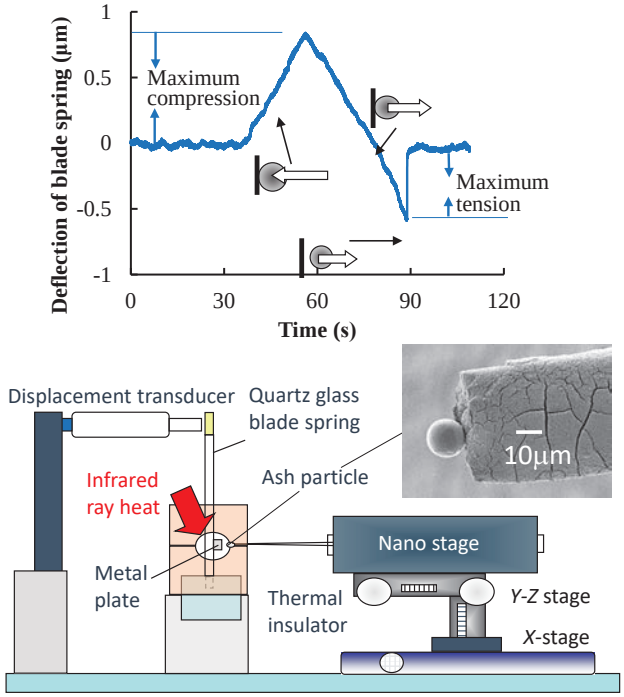


**Fig. 10** Measurement system for adhesion force between single particle and metal substrate at high temperature, adapted with permission from Ref. (Gao et al., 2020). Copyright (2020) American Chemical Society.

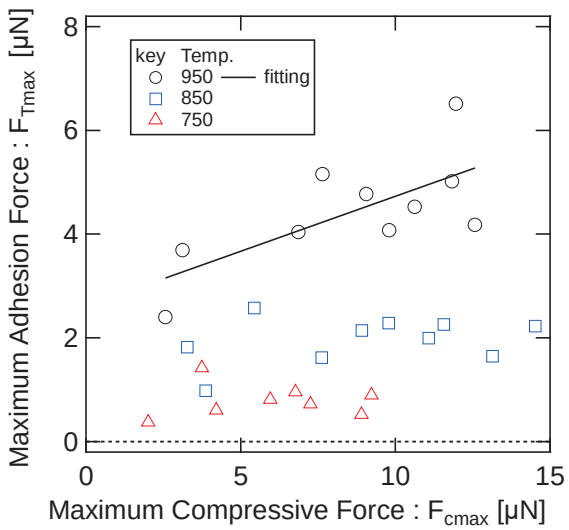


**Fig. 11** Example of relationship between maximum compression compressive force and adhesion force at different temperatures, adapted with permission from Ref. (Gao et al., 2020). Copyright (2020) American Chemical Society.

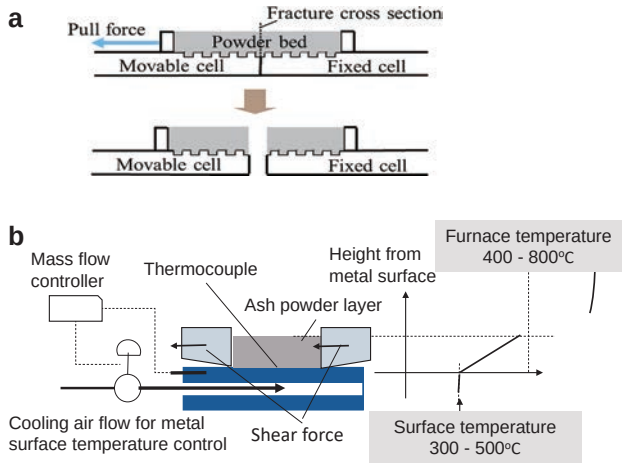


**Fig. 12** Principle of measurement system for tensile and shear strength of powder bed. **(a)** Tensile strength tester of powder bed, adapted with permission from Ref. (Kamiya et al., 2002a). Copyright (2002) American Chemical Society. **(b)** Shear strength test at interface between powder bed and metal, adapted with permission from Ref. (Aoki et al.,2020). Copyright (2020) American Chemical Society.

adhesion force at high temperatures has been shown to cause various problems in different plants.

Tensile stress was applied to the ash layer on the substrate metal surface to measure the surface interaction between the ash powder bed and the surface of the superheater and/or heat-transfer tube (Liu et al., 2023). However, measuring strength by creating a fracture surface between the metal surface and ash powder layer is difficult. As the fluid flows inside the superheater and heat exchanger, the temperature from the inside to the surface changes in a complex manner, as shown in **Fig. 12(b)** (Aoki et al., 2020; 2022). The temperature distribution was reproduced by air at a controlled flow rate under a metal plate. The shear strength between the ash layer and metal surface and the corrosion behaviour of the metal surface by the ash layer at high temperatures were also observed under different temperature distributions.

### 3.2.3 Analysis and control of ash adhesion behaviour at high temperatures

The increase in the adhesion force at high temperatures has been attributed to the formation of a small amount of liquid phase from low-melting-point eutectic compounds. To observe liquid-phase formation, the ash particles were observed at the high-temperature heating stage using a field emission scanning electron microscope (FE-SEM). However, because the generated liquid phase was volatilised under high-vacuum conditions in the FE-SEM, analysing the elements in the generated liquid phase was difficult. Therefore, after recording the observation image and ash-sample coordinates under a high vacuum, the ash samples were moved to a separate chamber under high-vacuum conditions and crossed the threshold to the FE-SEM, as

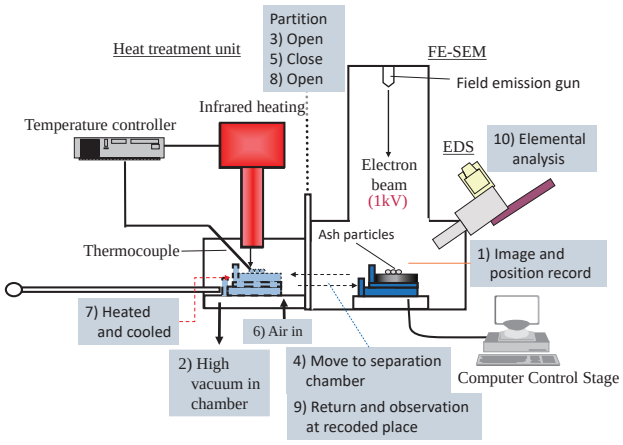


**Fig. 13** FE-SEM observation system of fine particles before and after heat treatment. Adapted with permission from Ref. (Tsukada et al., 2003). Copyright (2003) Elsevier B.V.

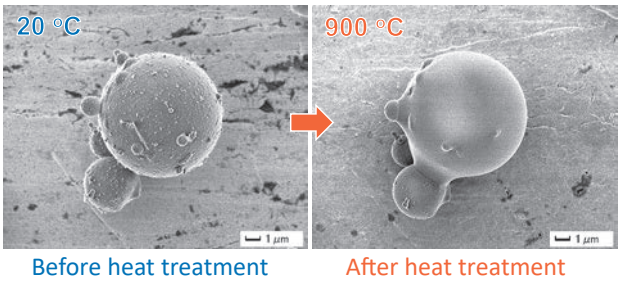


**Fig. 14** FE-SEM observation of ash particles before and after heat treatment at 900 °C. Adapted with permission from Ref. (Horiguchi et al., 2018). Copyright (2018) American Chemical Society.

shown in **Fig. 13** (Tsukada et al., 2003). Air was introduced into the chamber to raise the pressure to a normal value, and the ash samples were heated in an infrared condensing furnace to a predetermined temperature. After being cooled to room temperature under high-vacuum conditions in the chamber, the ash samples were returned to the FE-SEM, and the morphology change was observed before and after the heat treatment. As an example, **Fig. 14** shows the results of the observations of the pulverised coal combustion ash (Horiguchi et al., 2018). Before and after the heat treatment, morphological changes due to liquid-phase formation were observed in some parts. Using energy-dispersive X-ray spectroscopy at the deformed parts, a high content of alkali metal and aluminium was confirmed, and low-temperature melting based on thermodynamic calculations was discussed. In the case of sewage slag ash, the phosphate content in the morphologically changed part was higher than that in the other unchanged parts, and the phosphate generated a low-melting-point eutectic phase with other elements.

### 3.2.4 Model of ash preparation from pure fine particles and discussion on adhesion-increase mechanism

Combustion ash includes many types of elemental components; therefore, analysing the increase mechanism of the ash adhesion force at high temperatures is difficult. With the development of the abovementioned devices for measurement and analysis, a model of an ash synthesis method from fine pure silica particles was developed by adding the estimated elements to increase the adhesion force at high temperatures. First, for pulverised coal combustion ash, a small amount of alkali metal, sodium or potassium, and oxalate aqueous solution were added to fine pure silica particles, followed by a heat treatment, grinding, and the classification of the modelled ash (Kamiya et al., 2002b). The tensile strength of the modelled ash beds was determined at different temperatures, ranging from room temperature to 900 °C. The increase in tensile strength of a real combustion ash bed was almost reproduced by the modelled ash, as shown in **Fig. 15**. The low-melting-point eutectic phase of silica and alkali metal was responsible for the increase in high-temperature adhesion. Based on this result, a similar method was applied to synthesise the modelled ash from waste- and biomass-combustion ash, such as sewage sludge, in which phosphorus was added to pure silica particles (Gao and Kamiya, 2020; Horiguchi et al., 2021a).

### 3.2.5 Ash adhesion-behaviour control at high temperatures

To solve the ash-adhesion problem and problems with the superheater and heat exchanger, various additives, such as kaolinite and dolomite for coal and biomass combustion (Duchesne et al., 2017), and iron oxide for sewage-sludge combustion, have been investigated to prevent ash deposition and reduce ash-layer growth in combustion plants (Horiguchi et al., 2021a). The changes in the liquid- and slag-phase formation temperature owing to composition were discussed using thermodynamic calculations to analyse the adhesion-behaviour control mechanism via the addition of various materials. The scientific selection of optimum additives to control ash behaviour has progressed with the development of characterisation and analysis methods.

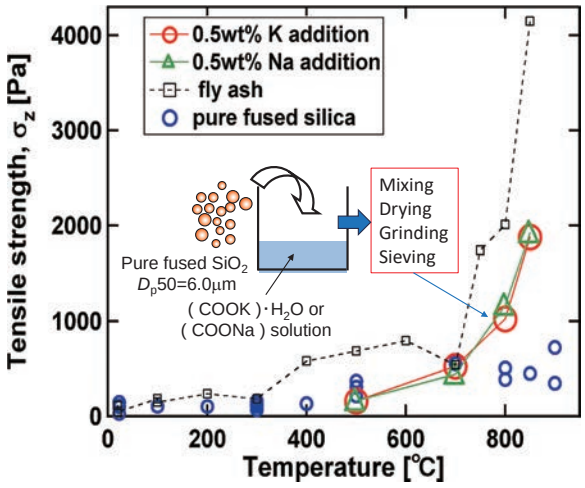


**Fig. 15** Effect of temperature on tensile strength of real fly ash and model synthesised ash powder bed. Adapted with permission from Ref. (Kamiya et al., 2002b). Copyright (2002) American Chemical Society.

Recent reports have shown that the addition of alumina nanoparticles effectively reduced the tensile strength of the ash powder layer (Gao et al., 2019; Horiguchi et al., 2018, 2022). All cases of the real and modified model of coal, biomass and waste combustion ash showed that the addition of alumina nanoparticles controlled the tensile strength of the particle layer at high temperatures. Because alumina nanoparticles have high reactivity, the addition of nanoparticles chemically suppressed the formation of a low-melting-point eutectic phase. Furthermore, nanoparticle addition increased the porosity ratio of the ash-particle layer by forming porous aggregates between the ash particles. By increasing the liquid-phase formation temperature using chemical reactions and the physical suppression of the packing behaviour of the ash layer, the addition of nanoparticles controlled the tensile strength of the ash layer at high temperatures.

The increase mechanism of ash adhesion at high temperatures was estimated using liquid- and slag-phase formation and the liquid-bridge force of the small amount of generated slag. However, the adhesion increase at relatively lower temperatures (below 500 °C) was observed using pure calcium carbonate fine particles. In this temperature range, liquid- and slag-phase formation and sintering with volume changes were not observed (Horiguchi et al., 2021b). Therefore, investigating the mechanism of the adhesion force and developing adhesion-behaviour control technology are necessary.

## 4. Conclusion

Molecular and nanometre-scale surface-structure designs of particles were reviewed from the perspective of controlling the adhesion and aggregation of nanoscale and fine particles in gas and liquid. These control methods are indispensable for realising the various functions of nanoparticles and fine particles. However, real situations were implemented based on empirical knowledge; thus, developing scientific approaches for controlling adhesion and aggregation is necessary. With the recent development of mass production and cost reduction for various nanoparticles, the interface structure design of nanoparticles has also been developed. This is expected to establish a systematic interface-structure design method that can handle various combinations of particle characteristics, such as size, shape, materials, surface structure, and the matrix of the

solid and solvent that disperse the nanoparticles. There are many challenges related to the practical use of functional nanoparticles, such as increasing the solid content in solution and reducing the number of adsorbed ligands. However, the development of fundamental research for interface-structure design will overcome these barriers. The control of fine-particle behaviour, such as high-temperature adhesion and the interaction between organic/inorganic solid particles, microcapsules, and biomolecules, is also important for applying powder technology in various industrial fields, such as energy generation, environmental systems, and medical and health industries.

## Acknowledgments

This work was supported by a JSPS KAKENHI Grant Number (20K20358, 16H02413, 23246132, 20360346), and the Proposal-Based R&D Program of NEDO Project No. 99Ea10-006-1, the Hosokawa Powder Technology Foundation, and the Information Center of Particle Technology, Japan.

## References

Aiello F., Masi S., The contribution of NMR spectroscopy in understanding perovskite stabilization phenomena, Nanomaterials, 11 (2021) 2024. https://doi.org/10.3390/nano11082024

Aoki N., Okada Y., Kamiya H., Direct measurement of the shear strength of fly ash powder beds, ACS Sustainable Chemistry & Engineering, 8 (2020) 18864–18868. https://doi.org/10.1021/acssuschemeng.0c05280

Aoki N., Horiguchi G., Kamiya H., Okada Y., Shear strength testing of synthetic ash: the role of surface vs interparticle adhesions, Industrial & Engineering Chemistry Research, 61 (2022) 3358–3364. https://doi.org/10.1021/acs.iecr.1c04308

Cara C., Musinu A., Mameli V., Ardu A., Niznansky D., Bursik J., Scorciapino M.A., Manzo G., Cannas C., Dialkylamide as both capping agent and surfactant in a direct solvothermal synthesis of magnetite and titania nanoparticles, Crystal Growth & Design, 15 (2015) 2364–2372. https://doi.org/10.1021/acs.cgd.5b00160

Dinh C.-T., Nguyen T.-D., Kleitz F., Do T.-O., Shape-controlled synthesis of highly crystalline titania nanocrystals, ACS Nano, 3 (2009) 3737–3743. https://doi.org/10.1021/nn900940p

Duchesne M.A., Hughes R.W., Slag density and surface tension measurements by the constrained sessile drop method, Fuel, 188 (2017) 173–181. http://dx.doi.org/10.1016/j.fuel.2016.10.023

Ducker W.A., Senden T.J., Pashley R.M., Measurement of forces in liquids using a force microscope, Langmuir, 8 (1992) 1831–1836. https://doi.org/10.1021/la00043a024

Elimelech O., Aviv O., Oded M., Peng X., Harries D., Banin U., Entropy of branching out: linear versus branched alkylthiols ligands on CdSe nanocrystals, ACS Nano, 16 (2022) 4308–4321. https://doi.org/10.1021/acsnano.1c10430

Gao J., Aozasa T., Tsukada M., Matsuda H., Makino H., Kamiya H., Direct measurement of single-particle adhesion behaviors on metal surfaces at high temperatures using model and modified pulverized coal combustion ash, Energy & Fuels, 34 (2020) 6338–6345. https://dx.doi.org/10.1021/acs.energyfuels.0c00262

Gao J., Kamiya H., Modification of phosphorus-rich sewage sludge combustion ash using pure source materials for analysis of ash adhesion behavior at high temperature, Energy & Fuels, 34 (2020) 3797–3804. https://doi.org/10.1021/acs.energyfuels.9b04379

Gao J., Matsushita M., Horiguchi G., Fujii R., Tsukada M., Okada Y., Kamiya H., Toward stable operation of sewage sludge incineration plants: the use of alumina nanoparticles to suppress adhesion of fly ash, Energy & Fuels, 33 (2019) 9363–9366. https://doi.org/10.1021/acs.energyfuels.9b02305

Hanada Y., Masuda S., Iijima M., Kamiya H., Analysis of dispersion and aggregation behavior of carbon black particles in aqueous suspension by colloid probe AFM method, Advanced Powder Technology, 24 (2013) 844–851. http://dx.doi.org/10.1016/j.apt.2013.02.010

Hens Z., Martins J.C., A solution NMR toolbox for characterizing the surface chemistry of colloidal nanocrystals, Chemistry of Materials, 25 (2013) 1211–1221. https://doi.org/10.1021/cm303361s.

Horiguchi G., Fujii R., Yamauchi Y., Okabe H., Tsukada M., Okada Y., Kamiya H., Toward stable operation of coal combustion plants: the use of alumina nanoparticles to prevent adhesion of fly ash, Energy & Fuels, 32 (2018) 13015–13020. https://doi.org/10.1021/acs.energyfuels.8b03043

Horiguchi G., Ito M., Ito A., Kamiya H., Okada Y., Role of phosphorus and iron in particle adhesiveness at high temperatures using synthetic ashes, ACS Sustainable Chemistry & Engineering, 9 (2021a) 15315–15321. https://doi.org/10.1021/acssuschemeng.1c05676

Horiguchi G., Ito M., Ito A., Kamiya H., Okada Y., Controlling particle adhesion of synthetic and sewage sludge ashes in high temperature combustion using metal oxide nanoparticles, Fuel, 321 (2022) 124110. https://doi.org/10.1016/j.fuel.2022.124110

Horiguchi G., Kamiya H., García-Triñanes P., Evaluation and control of the adhesiveness of cohesive calcium carbonate particles at high temperatures, Advanced Powder Technology, 32 (2021b) 283–289. https://doi.org/10.1016/j.apt.2020.12.009

Iijima M., Tsukada M., Kamiya H., Effect of particle size on surface modification of silica nanoparticles by using silane coupling agents and their dispersion stability in methylethylketone, Journal of Colloid and Interface Science, 307 (2007) 418–424. https://doi.org/10.1016/j.jcis.2006.11.044

Iijima M., Kobayakawa M., Yamazaki M., Ohta Y., Kamiya H., Anionic surfactant with hydrophobic and hydrophilic chains for nanoparticle dispersion and shape memory polymer nanocomposites, Journal of the American Chemical Society, 131 (2009) 16342–16343. https://doi.org/10.1021/ja906655r

Iijima M., Kamiya H., Layer-by-layer surface modification of functional nanoparticles for dispersion in organic solvents, Langmuir, 26 (2010) 17943–17948. https://doi.org/10.1021/la1030747

Iijima M., Kamiya H., Non-aqueous colloidal processing route for fabrication of highly dispersed aramid nanofibers attached with Ag nanoparticles and their stability in epoxy matrixes, Colloids and Surfaces A: Physicochemical and Engineering Aspects, 482 (2015) 195–202. https://doi.org/10.1016/j.colsurfa.2015.05.007

Iijima M., Omori S., Hirano K., Kamiya H., Free-standing, roll-able, and transparent silicone polymer film prepared by using nanoparticles as cross-linking agents, Advanced Powder Technology, 24 (2013) 625–631. https://doi.org/10.1016/j.apt.2012.11.011

Iijima M., Tsukada M., Kamiya H., Effect of surface interaction of silica nanoparticles modified by silane coupling agents on viscosity of methylethylketone suspension, Journal of Colloid and Interface Science, 305 (2007) 315–323. https://doi.org/10.1016/j.jcis.2006.10.005

Iijima M., Yoshimura M., Tsuchiya T., Tsukada M., Ichikawa H., Fukumori Y., Kamiya H., Direct measurement of interactions between stimulation-responsive drug delivery vehicles and artificial mucin layers by colloid probe atomic force microscopy, Langmuir, 24 (2008) 3987–3992. https://doi.org/10.1021/la7038043

Kamiya H., Fukuda Y., Suzuki Y., Tsukada M., Kakui T., Naito M., Effect of polymer dispersant structure on electrosteric interaction and dense alumina suspension behavior, Journal of the American Ceramic Society, 82 (1999) 3407–3412. https://doi.org/10.1111/j.1151-2916.1999.tb02258.x

Kamiya H., Mitsui M., Takano H., Miyazawa S., Influence of particle diameter on surface silanol structure, hydration forces, and aggregation behavior of alkoxide-derived silica particles, Journal of the American Ceramic Society, 83 (2000) 287–293. https://doi.org/10.1111/j.1151-2916.2000.tb01187.x

Kamiya H., Matsui S., Kakui T., Analysis of action mechanism of anionic polymer dispersant with different molecular structure in dense silicon nitride suspension by using colloidal probe AFM, Ceramic

Transactions, 152 (2006) 83–92. https://doi.org/10.1002/9781118406861.ch9
Kamiya H., Kimura A., Yokoyama T., Naito M., Jimbo G., Development of a split-type tensile-strength tester and analysis of mechanism of increase of adhesion behavior of inorganic fine powder bed at high-temperature conditions, Powder Technology, 127 (2002a) 239–245. https://doi.org/10.1016/S0032-5910(02)00117-1
Kamiya H., Kimura A., Tsukada M., Naito M., Analysis of the high-temperature cohesion behavior of ash particles using pure silica powders coated with alkali metals, Energy & Fuels, 16 (2002b) 457–461. https://doi.org/10.1021/ef010208l
Kani T., Suzuki T., Tsukada M., Kamiya H., Influence of surface-adhered nanoparticles and nanoporous structure on bulk flowability of silica, Powder Technology, 176 (2007) 108–113. https://doi.org/10.1016/j.powtec.2007.02.005
Li M., Hachiya S., Chen Z., Osawa T., Sugime H., Noda S., Fluidized-bed production of 0.3 mm-long single-wall carbon nanotubes at 28 % carbon yield with 0.1 mass% catalyst impurities using ethylene and carbon dioxide, Carbon, 182 (2021) 23–31. https://doi.org/10.1016/j.carbon.2021.05.035
Liu Z., Jin J., Zheng L., Zhang R., Dong B., Liang G., Zhai Z., Adhesion strength of straw biomass ash: effect of dolomite additive, Energy, 262 (2023) 125320. https://doi.org/10.1016/j.energy.2022.125320
Maeta N., Kamiya H., Okada Y., Direct monitoring of molecular events at the surface: one-step access to flexibly stable colloidal Ag nanoparticles, Langmuir, 34 (2018) 5495–5504. https://doi.org/10.1021/acs.langmuir.7b03870
Mori T., Okada Y., Kamiya H., Effect of surface modification of silica particles on interaction forces and dispersibility in suspension, Advanced Powder Technology, 27 (2016) 830–838. https://doi.org/10.1016/j.apt.2015.10.020
Mourdikoudis S., Menelaou M., Fiuza-Maneiro N., Zheng G., Wei S., Pérez-Juste J., Polavarapu L., Sofer Z., Oleic acid/oleylamine ligand pair: a versatile combination in the synthesis of colloidal nanoparticles, Nanoscale Horizons, 7 (2022) 941–1015. https://doi.org/10.1039/d2nh00111j
Okada Y., Ishikawa K., Maeta N., Kamiya H., Understanding the colloidal stability of nanoparticle–ligand complexes: design, synthesis, and structure–function relationship studies of amphiphilic small-molecule ligands, Chemistry – A European Journal, 24 (2018a) 1853–1858. https://doi.org/10.1002/chem.201704306
Okada Y., Asama H., Koike N., Yamashita S., Maeta N., Uesaka A., Kamiya H., Direct ordering of anchoring events at the surface of iron oxide nanoparticles enabled by a stepwise phase-transfer strategy, ChemistrySelect, 3 (2018b) 8458–8461. https://doi.org/10.1002/slct.201801416
Park J., An K., Hwang Y., Park J.-G., Noh H.-J., Kim J.-Y., Park J.-H., Hwang N.-M., Hyeon T., Ultra-large-scale syntheses of monodisperse nanocrystals, Nature Materials, 3 (2004) 891–895. https://doi.org/10.1038/nmat1251
Saito T., Shoji E., Kubo M., Tsukada T., Kikugawa G., Surblys D., Evaluation of the work of adhesion at the interface between a surface-modified metal oxide and an organic solvent using molecular dynamics simulations, The Journal of Chemical Physics, 154 (2021) 114703. https://doi.org/10.1063/5.0040900
Schechtel E., Dören R., Frerichs H., Panthöfer M., Mondeshki M., Tremel W., Mixed ligand shell formation upon catechol ligand adsorption on hydrophobic $TiO_2$ nanoparticles, Langmuir, 35 (2019) 12518–12531. https://doi.org/10.1021/acs.langmuir.9b02496
Shirmardi Shaghasemi B., Dehghani E.S., Benetti E.M., Reimhult E., Host–guest driven ligand replacement on monodisperse inorganic nanoparticles, Nanoscale, 9 (2017) 8925–8929. https://doi.org/10.1039/c7nr02199b
Tanaka M., Komagata M., Tsukada M., Kamiya H., Evaluation of the particle–particle interactions in a toner by colloid probe AFM, Powder Technology, 183 (2008a) 273–281. https://doi.org/10.1016/j.powtec.2007.07.039
Tanaka M., Komagata M., Tsukada M., Kamiya H., Fractal analysis of the influence of surface roughness of toner particles on their flow properties and adhesion behavior, Powder Technology, 186 (2008b) 1–8. https://doi.org/10.1016/j.powtec.2007.10.030
Tsukada M., Yamada H., Kamiya H., Analysis of biomass combustion ash behavior at elevated temperatures, Advanced Powder Technology, 14 (2003) 707–717. https://doi.org/10.1163/15685520360731990
Yamamoto M., Shimai S., Oguma K., Wang S., Kamiya H., Alumina particle surface interaction in copolymer of isobutylene and maleic anhydride aqueous solution characterized by colloidal probe atomic force microscopy, Powder Technology, 354 (2019) 369–376. https://doi.org/10.1016/j.powtec.2019.06.014
Yamamoto M., Tsuchiya T., Iijima M., Takeuchi H., Kamiya H., Characterization of surface interaction between chitosan-modified liposomes and mucin layer by using CNT probe AFM method, YAKUGAKU ZASSHI, 138 (2018) 1191–1199. https://doi.org/10.1248/yakushi.18-00015
Yamashita S., Sudo T., Kamiya H., Okada Y., Ligand exchange reactions between phosphonic acids at $TiO_2$ nanoparticle surfaces, ChemistrySelect, 6 (2021) 2923–2927. https://doi.org/10.1002/slct.202100541
Yamashita S., Sudo T., Kamiya H., Okada Y., Colloidal stability of $TiO_2$ nanoparticles: the roles of phosphonate ligand length and solution temperature, Chemistry – A European Journal, 28 (2022) e202201560. https://doi.org/10.1002/chem.202201560
Yang Y., Qin H., Peng X., Intramolecular entropy and size-dependent solution properties of nanocrystal–ligands complexes, Nano Letters, 16 (2016) 2127–2132. https://doi.org/10.1021/acs.nanolett.6b00737
Yang Y., Shimai S., Wang S., Room-temperature gelcasting of alumina with a water-soluble copolymer, Journal of Materials Research, 28 (2013) 1512–1516. https://doi.org/10.1557/jmr.2013.132
Yoko A., Seong G., Tomai T., Adschiri T., Continuous flow synthesis of nanoparticles using supercritical water: process design, surface control, and nanohybrid materials, KONA Powder and Particle Journal, 37 (2020) 28–41. https://doi.org/10.14356/kona.2020002
Zeininger L., Portilla L., Halik M., Hirsch A., Quantitative determination and comparison of the surface binding of phosphonic acid, carboxylic acid, and catechol ligands on $TiO_2$ nanoparticles, Chemistry – A European Journal, 22 (2016) 13506–13512. https://doi.org/10.1002/chem.201601920

## Author's Short Biography

**Dr. Hidehiro Kamiya** was the Vice President, Trustee, Tokyo University of Agriculture and Technology, Japan from April 2020 to March 2024. He was Dean of the Graduate School of Bio-Applications and Systems Engineering (2013–2019), and Dean of the Global Innovation Research Institute (2017–2020). He has been an editorial board member of "Powder Technology" from 2002. He received his B.C. degree (1981) and PhD (1986) from the Department of Chemical Engineering at Nagoya University, Japan. He has published over 250 papers on fine and nanoparticles, as well as powder science and technology, applied across various fields such as energy and environment, ceramics, surfactants, power generation, and waste treatment. He has received various awards including the SCEJ Award (2022), and the KONA Award (2022). Currently a Professor at Waseda University.

KONA Powder and Particle Journal

KONA Powder and Particle Journal No. 42 (2025) 15–36/https://doi.org/10.14356/kona.2025007 Review Paper

# Numerical Modelling and Imaging of Industrial-Scale Particulate Systems: A Review of Contemporary Challenges and Solutions†

**C. R. Kit Windows-Yule[1]*, Sofiane Benyahia[2], Peter Toson[3], Hanqiao Che[1] and A. Leonard Nicuşan[1]**

[1] *School of Chemical Engineering, the University of Birmingham, UK*
[2] *National Energy Technology Laboratory, US*
[3] *Research Center Pharmaceutical Engineering, Austria*

Numerical modelling offers the opportunity to better understand, predict, and optimise the behaviours of industrial systems, and thus provides a powerful means of improving efficiency, productivity and sustainability. However, the accurate modelling of industrial-scale particulate and particle–fluid systems is, due to the complex nature of such systems, highly challenging. This challenge arises primarily from three factors: the lack of a universally accepted continuum model for particulate media; the computational expense of discrete particle simulations; and the difficulty of imaging industrial-scale systems to obtain validation data. In recent years, however, advances in software, hardware, theoretical understanding, and imaging technology have all combined to the point where, in many cases, these challenges are now surmountable—though some distance remains to be travelled. In this review paper, we provide an overview of the most promising solutions to the issues highlighted above, discussing also the major strengths and limitations of each.

**Keywords:** discrete element method, two fluid model, kinetic theory of granular flows, coarse graining, particle tracking, tomography

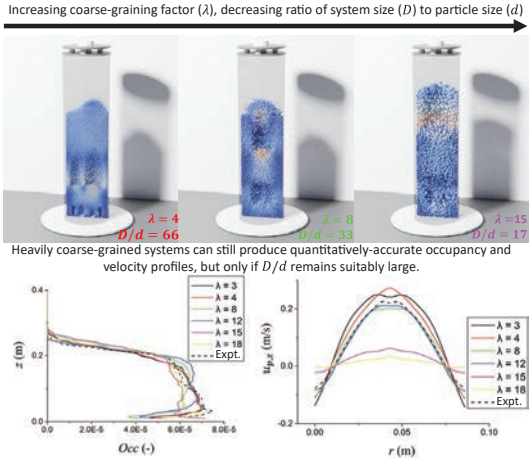


## 1. Introduction

The handling and processing of particulate solids is of central importance to myriad processes in diverse industries, including (but by no means limited to) the chemical, defense, food, green energy, and pharmaceutical sectors (Seville et al., 2012). Indeed, particulate media are involved in the production of more than 50 % of all goods sold worldwide (Blais et al., 2019). Despite their ubiquity, however, the mechanics of particulate solids remain poorly understood compared to 'classical' solids, liquids and gases. This lack of understanding manifests itself in industry in many negative manners, spanning numerous unit operations, be it the woeful energy-efficiency of processes such as milling (Holmberg et al., 2017), the tendency of hoppers and feeders to become 'jammed' (Schulze, 2014), or the highly unpredictable nature of mixing and segregation between non-identical species of particles (Windows-Yule et al., 2015). If we wish to reduce waste, increase efficiency, and in general develop more robust and sustainable manufacturing methods, we must improve our understanding of particulate media. In industrial processes involving *fluids*, a digital, 'Industry 4.0' approach to the optimisation of industrial equipment has already been widely adopted thanks to the wide availability of user-friendly computational fluid dynamics (CFD) software, and the ability of CFD to efficiently numerically model the flow dynamics of large, pilot/industrial-scale systems. The adoption of such digital approaches has been significantly slower for particulate media, however. There are several reasons underlying this slow adoption, but most can be traced back to the complexity of particulate materials, meaning that—to date—there does not exist a universally accepted particulate equivalent to the Navier–Stokes equations, and thus few commercially available, generalisable, "plug and play" CFD equivalents capable of (accurately) modelling industrial scale systems.

There are currently two main approaches to the modelling of industrial particle-handling systems: the discrete element method (DEM), which models all particles within a system as individual, discrete objects, and the kinetic theory of granular flows (KTGF), which takes a continuum approach similar to CFD, but solves equations that have

† Received 15 May 2023; Accepted 1 August 2023
J-STAGE Advance published online 23 March 2024
* Corresponding author: C. R. Kit Windows-Yule;
Add: Edgbaston, Birmingham, B15 2TT, UK
E-mail: c.r.windows-yule@bham.ac.uk
TEL: +44-798-947-2953

been modified to represent particulate or multiphase flows[1]. A brief overview of each technique is provided in **Sections 2 and 3**. Each of these techniques suffers from its own distinct limitations. DEM has been widely shown to facilitate the quantitatively accurate simulation of particulate systems (Coetzee, 2017), but in its standard form is highly computationally demanding (Golshan et al., 2023). KTGF simulations are significantly more efficient, but the modelling assumptions required to describe a discrete, particulate system as a continuous medium make calibration and (thus) quantitative accuracy much more challenging to achieve.

Nonetheless, in recent years, improvements in hardware, software, and the development of new theoretical models mean that the tractable, accurate modelling of industrial systems is achievable—albeit with some limitations and caveats. In this review article, we provide an overview of the most promising contemporary methods for modelling industrial-scale particulate systems, highlighting their individual strengths and weaknesses, and summarising important recent developments.

## 2. Discrete methods

### 2.1 Overview of the discrete element method (DEM)

The discrete element method is currently the most common method for the numerical modelling of particulate systems. Though its efficient implementation can be highly challenging, the underlying concept of DEM is exceedingly simple: each individual particle within a given system is modelled as a distinct computational object, and assigned all the relevant properties of a 'real' particle—i.e. a position in space, a mass, a size, a friction coefficient etc. Each simulated particle within a DEM simulation is also subject to the relevant forces one may expect in a 'real' system, most notably gravity, and relevant 'contact forces' experienced during collisions with other objects. By coupling DEM with CFD, drag and other fluid forces may also be simulated (El Geitani et al., 2023). The sum of these forces may be used to predict the net force acting on a given particle at a given point in time (see **Fig. 1**), and from this and the particle's known mass, the instantaneous acceleration acting upon it. This, in turn, may be used to predict the velocity, and thus position, of the particle at some future point in time (assuming that the 'timestep' between this future point and the present point in time is small enough that the particle experiences no significant change in acceleration).

By repeating the above process again and again—effectively stepping through time in pseudo-infinitesimal increments—one may thus simulate the motion of a system of particles. By tuning the relevant parameters (friction coefficients, restitution coefficients, cohesive properties...) used to represent the interactions between particles, this simulated motion can be brought into quantitative alignment with the dynamics of the real system being modelled (Windows-Yule et al., 2016; Windows-Yule and Neveu, 2022)[2]. A significant shortcoming of the discrete element method, however, is its computational expense. Unlike CFD, each individual particle within a system must be individually modelled, meaning that the time required to run a simulation increases sharply with the number, $N$, of particles being simulated. Indeed, even with a highly optimised DEM engine, computation time can be expected to scale as $N \log N$ (Thompson et al., 2022). This shortcoming typically hampers efforts to simulate industrial-scale systems. In the following sections, we discuss some of the main ways in which this issue may be circumvented. It should be noted that the above provides only a rather crude overview of DEM. A more detailed yet still accessible introduction to the discrete element method can be found in Chapter 4 of reference (Rosato and Windows-Yule, 2020), and a deeper dive in reference (Luding, 2008).

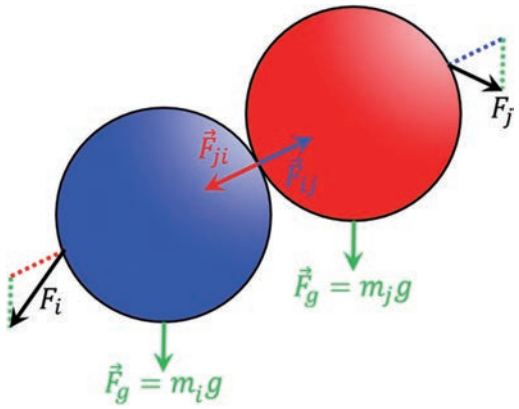


**Fig. 1** A schematic illustration of two interacting DEM particles. Particle $i$ is subject to a gravitational force $\vec{F}_g$ proportional to its mass $m_i$, and a contact force $F_{ji}$ due to contact with a second particle $j$. The net force $F_i$ acting on the particle is used to predict its position and velocity at the next point in time. Reproduced with permission from (Rosato and Windows-Yule, 2020).

### 2.2 Parallelisation and GPU acceleration

As discussed in the preceding section, the computational expense of a simulation—that is to say, the required number of CPU (central processing unit) operations required to simulate a system—increases monotonically with the number of particles, $N$, simulated. As each operation takes a finite time to perform, this means that, for simulations run on a single CPU core, the time required to run a simulation

[1] While these are certainly not the only available methods, they are decidedly the most commonly-applied, and thus will form the focus of this review.

[2] The calibration of numerical simulations is a complex field in its own right, and has been the subject of several recent review articles (Ketterhagen and Wassgren, 2022; Windows-Yule and Neveu, 2022) and as such will not be discussed in detail here.

increases with time. One of the simplest methods through which to reduce the time required is thus simply to split this effort across multiple CPUs—a process known as 'parallelisation' (Sawley and Cleary, 1999). Like DEM itself, the implementation of a parallelisation strategy may be complex, but the strategy itself is conceptually very simple: the computational volume is subdivided into two or more distinct regions (see e.g. **Fig. 2**) and each region is assigned its own CPU, which only performs operations for particles falling within said region. Thus, for a perfectly implemented parallelisation strategy, a simulation using two CPU cores might be expected to run in half the time of an equivalent 'serial' simulation, a simulation parallelised across 4 cores in a quarter of the time, and so on. With access to a suitable high-performance computing (HPC) system, one may hypothetically speed up a simulation hundreds or even thousands of times, and thus simulate numbers of particles which would be simply unfeasible using a single CPU.

In reality, however, such 'linear' speed-up is not easy (or, in absolute terms, possible) to achieve for several reasons. Firstly, to achieve linear speed-up, the computational load must be balanced equally across all processors, meaning that the individual domains into which the computational volume is divided must be sensibly chosen. For example, in **Fig. 2**, the division shown in the top-most panel (which exploits the uniformity of the system along the axial direction) is significantly more efficient than that shown in the middle panel, where the lower domain contains many more particles than the upper domain. In the bottom panel, we see that one of the processors is entirely unused, making this an exceedingly inefficient configuration—yet one that is often accidentally used by DEM practitioners who leave their parallelisation schemes on default settings! In recent years, however, the use of 'dynamic load balancing' algorithms—which, as their name suggests, automatically optimise the spread of computational load across processors—have become increasingly common (Golshan and Blais, 2021; Yan and Regueiro, 2018). As such, in the future, this particular problem is likely to be less frequently encountered. Dynamic load balancing schemes, unlike 'manual' methods, also allow the distribution of processor power to be adjusted *during simulation*, allowing for even greater efficiency savings.

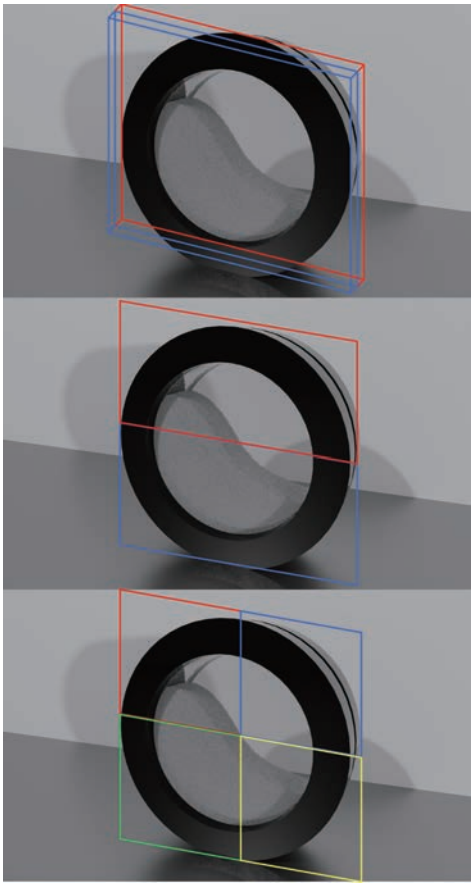

**Fig. 2** Examples of possible parallelisation schemes for a simulated rotating drum (Herald et al., 2022).

The second major issue to consider when parallelizing DEM is that a finite 'overlap' or 'communication region' must exist between all adjacent domains[3] allowing information (e.g. contacts between particles) from one domain to be passed to another. It is this restriction which ultimately provides an upper bound on the degree of speed-up which may be achieved through parallelisation: if a simulation is 'sliced too thinly'—for example if the width of a domain is smaller than the width of a particle—then no speed-up can be achieved (indeed the simulation may even become slower due to the increased overheads of such a scheme (Eibl and Rüde, 2019)).

In addition to CPU processing, the past decade has seen a considerable rise in interest in the use of GPU (graphics processing unit) computation in DEM (Fang et al., 2021; Govender et al., 2014; Lisjak et al., 2018; Lu, 2022; Spellings et al., 2017; Steuben et al., 2016; Wang et al., 2021). Though the development of GPUs has been largely driven by the desire for improved 3D graphics in the gaming and film industries (Das and Deka, 2016), their innate capability to efficiently perform highly-parallelised computations makes them well suited to the speed-up of DEM simulations (Govender et al., 2014).

The advent of GPU computing has not only helped to increase the number of particles that can realistically be simulated on a single PC (as opposed to the HPC clusters required for large-scale parallel CPU computations), but has also played a role in overcoming another major limitation of DEM—the difficulty of (efficiently) modelling aspherical particles (Govender et al., 2014; Spellings et al., 2017; Wang et al., 2021), which are all but ubiquitous in industry. The computational complexity of detecting

[3] It is for this reason that perfectly linear scaling is never fully possible in the parallelisation of DEM simulations, though for well-chosen schemes may come very close (Markauskas and Kačeniauskas, 2015).

collisions between simulated particles is significantly higher for aspherical particles than for simple spheres, meaning that historically a majority of DEM practitioners have preferentially used the latter, even when attempting to model the former. While under certain conditions the modelling of aspherical particles as spheres can produce quantitatively accurate results (Che et al., 2023a), this is not always the case, especially when considering denser packings and/or more elongated, 'needle-like' particles (Rhodes, 2008). Recently developed GPU-accelerated codes capable of modelling particles with arbitrary polyhedral geometries (Govender et al., 2014; 2015) thus represent a significant step toward the simulation of truly representative industrial systems.

It is important to note that, even with recent advances in both DEM software and computer hardware, DEM simulations are still typically limited to billions of particles (Kosaku et al., 2021), whereas in industrial systems the required numbers may easily reach the trillions or quadrillions. As such, the methods described here are often used in conjunction with other methods, notably the coarse-graining technique introduced in the next section.

For example, the MFIX-Exa Exascale Computing Project (ECP) (Musser et al., 2022) is currently developing a CFD–DEM architecture for future "exascale" supercomputers—i.e. capable of executing $10^{18}$ operations per second—for high-fidelity simulations of multiphase systems specifically targeted at carbon capture and storage. MFIX-Exa is based on the AMReX (Zhang et al., 2021b) software framework, which provides the data structures and iterators to enable massively parallel simulation, and allows simulations to be run using Nvidia, AMD, and Intel hardware. Using MFIX-Exa, a simulation of a pilot-scale 50 kW chemical looping reactor involving 5 billion particles and 2.5 billion fluid cells has been run on the Frontier supercomputer on 62,000 GPUs, with each GPU processing 14,080 stream processors and 128 GB of memory.

### 2.2.1 Pros and cons

The most notable benefit of accelerating DEM simulations through hardware and parallelisation alone is that—unlike for the coarse-graining method discussed in **Section 2.3** and the continuum methods described in **Section 3**—the system is still simulated at full resolution (i.e. all particles are directly, individually modelled). As such, this technique does not require the introduction of additional modelling assumptions, and in most cases the calibration parameters used to develop the system have real, physical meaning.

A major drawback to these methods is that significant speed-up requires access to significant computational resources. The inherent costs associated with acquiring and maintaining the necessary hardware are thus likely to price many smaller companies out of the market. That said, the rise of on-demand cloud computing platforms such as AWS, Microsoft Azure, Google Cloud Platform etc. has, to an extent, lowered this barrier, and will likely continue to do so over the coming years and decades.

A second issue with fully resolved DEM simulations is that, with current hardware, we can still 'only' simulate of the order of billions of particles, yet in industry one may easily reach the trillions or even quadrillions. While, in the long term, these numbers will inevitably improve in lockstep with the advancement of computer hardware, in the shorter term, if we wish to simulate such systems, then parallelisation and GPU acceleration can only form part of the solution, and must be used in combination with some of the other techniques discussed below.

## 2.3 Coarse-grained DEM (CG or CDEM)

As discussed in the preceding sections, the time—or, more specifically, the processor time—required to perform a given simulation increases monotonically with the number of particles to be simulated. As such, if we are able to represent multiple particles with a single 'pseudo-particle' then the computational expense of said simulation will naturally decrease. This is the underlying principle of the coarse-graining technique which lumps several distinct particles into a single 'coarse grain' or 'computational particle' (Patankar and Joseph, 2001).

All CG techniques available in the literature consider particles within a parcel to have the same properties and velocities—i.e. there can be no gradients within a parcel. In this way, CG is somewhat similar to continuum methods such as the two-fluid model (discussed in **Section 3**), where no gradients of particle properties (velocity, temperature et.) are allowed within a cell. Due to this similarity, the term 'coarse graining' is also widely employed to describe the post-processing of DEM data to represent continuum fields (Goldhirsch, 2010; Weinhart et al., 2012), or the smoothing of discrete data to be transferred to CFD for the calculation drag correlations in coupled CFD–DEM simulations (Che et al., 2021; Labra et al., 2013). As can be seen from **Fig. 3**, in recent years there has been a seemingly exponential increase in the number of papers published concerning coarse-graining, which is likely related to an increased interest in the use of DEM to simulate industrial systems (Di Renzo et al., 2021).

A coarse-grained pseudo-particle is typically characterised by the number, $W$, of particles represented by each cluster, and the coarse-graining ratio, $\lambda = d_{cg}/d$, where $d$ is the (linear) size of a 'normal' particle and $d_{cg}$ is that of a coarse-grained parcel of such particles, where $\lambda^3 = W$. It is typically assumed that the mass and volume of a coarse grain are equal to the sum of the masses and volumes of the constituent particles. Even in a publication where the parcel is assumed to have a non-zero void fraction for dilute flows (Lu et al., 2014), this void fraction is considered to

tend to zero at packing. Though the assumption of a particle packing with zero void fraction is obviously unphysical for all except a very small subset of particle geometries and system conditions, said assumption allows the user to keep the same initial bed weight and height in coarse-grained DEM (CDEM) that would be expected in conventional DEM.

As one may intuitively expect, the physical properties of a coarse-grained pseudo particle do not necessarily have a one-to-one mapping to those of their constituent particles. Notably, one must typically lower the restitution coefficient as energy dissipation in a particulate system is a function of particle number density, which by definition decreased when the size of particles is increased (Benyahia and Galvin, 2010; Lu et al., 2014). There exist numerous scaling laws through which authors have attempted to relate the properties of individual particles to their CG equivalents. Perhaps the most commonly used is that of Sakai (Sakai, 2016) in which all forces are scaled by $\lambda^3$, thus providing the same overlap for the parcel and real particle, as well as the same spring constant, restitution coefficient, and friction coefficients. Where the Sakai method ensures a constant *absolute* overlap between parcel and particle, the approach of Queteschiner et al. (2018b) instead ensures the same *relative* overlap by scaling the spring constant by $\lambda$. There exist also a number of other scaling approaches, see for example (Che et al., 2023b; de Munck et al., 2023; Kishida et al., 2021; Kushimoto et al., 2021; Nasato et al., 2015; Sakai, 2016; Zhang et al., 2021a), including approaches for modelling cohesive particles (Chen and Elliott, 2020; Nasato et al., 2015; Sakai et al., 2012), systems in which liquid bridges are present (Chan and Washino, 2018; Zhang et al., 2021a), aspherical particles (Zhou et al., 2022) and even heat and mass transfer (Lu et al., 2017b)—matters of considerable importance in many industrial processes. Interestingly, recent comparative studies have found a surprising lack of differentiation between simulations employing different coarse-graining models (Che et al., 2023b; de Munck et al., 2023); however, both studies used fluidised beds as their benchmarking systems. Since, in these systems, particle dynamics are largely dominated by drag effects as opposed to particle–particle interactions, it is unclear whether the same degree of similarity could be expected in denser systems, and in particular single-phase particulate systems.

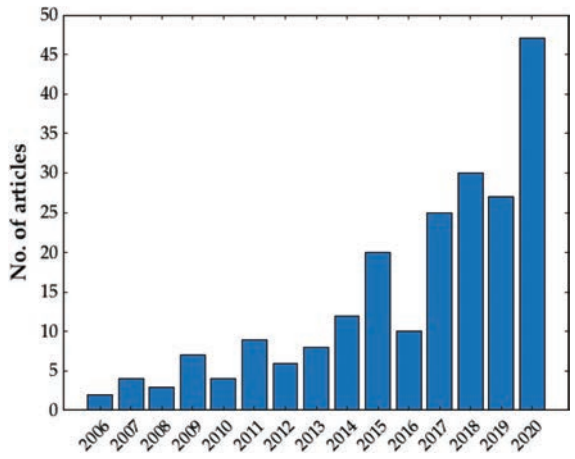


**Fig. 3** Number of indexed articles published per year concerning coarse-grained DEM. Image reproduced from reference (Di Renzo et al., 2021).

As alluded to at the start of this section, all particles forming a CG parcel must possess the same properties

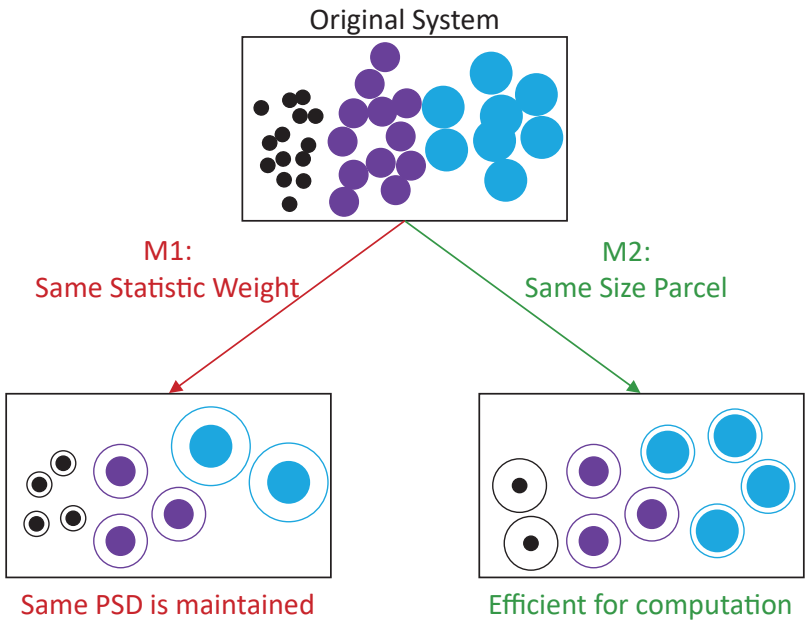


**Fig. 4** Simple schematic depicting the two methods for the coarse-graining of polydisperse systems described in the main text. Adapted with permission from Ref. (Lu et al., 2018). Copyright: (2018) Elsevier Ltd.

—including particle size. As such, when coarse-graining highly polydisperse systems (as are commonly found in industry) one must determine a suitable manner in which to represent the particle size distribution (PSD). There are two main ways to do so: the same statistical weight (SSW) method, in which the same number of particles are included in parcels corresponding to each size fraction, and the same size parcel (SSP) method in which (as the name implies) the size of the particles is instead kept constant. These methods are depicted schematically in **Fig. 4**. While the latter method is naturally more efficient, it is arguable that the former provides a more 'realistic' representation of the original PSD, and in some cases produces greater accuracy (Lu et al., 2018).

A notable limitation of the CG method is that in certain systems with heterogeneous geometries (e.g. hoppers (Coetzee, 2019)), coarsening cannot be conducted in the whole geometry due to flow restrictions. In such cases, it has been shown possible to locally refine CDEM back to DEM, or simply to a lower level of coarse-graining (De et al., 2022; Queteschiner et al., 2018a, 2018b).

Due to the different assumptions in CDEM, it is important to validate this method against data obtained with both finer DEM methods and experiments (discussed in further detail in **Section 4**). One can envision a series of validation studies by first comparing the simulation results of CDEM and DEM. Differences between the two simulation results can be quantified as uncertainties (UQ) due to the coarse-graining assumption. The UQ analysis can be extended to DEM simulation data through comparison with resolved DEM and/or DNS (dependent on the nature of the system studied) to quantify errors due to the assumed forms of fluid–particle interaction terms. Finally, the resolved DEM/DNS data can be compared with small-scale well-instrumented experimental setups where the experimental errors are carefully quantified. There exist limited examples of such a 'cascading series' of UQ missing in the literature due to the inherent complexity of conducting such numerical simulations and experiments for many different scenarios. Nevertheless, many attempts to validate CDEM with both finer DEM and experimental data are available in the literature.

Mori et al. (2019) compared bed height and pressure drop in a small-scale experimental dense fluidised bed of 0.05 m diameter using a factor $\lambda$ of between 5 and 10.

Oyedeji et al. (2022) validated CDEM for biomass (corn) pyrolysis reactions in a small-scale reactor of 0.15 m diameter with a coarsening factor $W = 10$ and 20, and at this low level of coarsening (real particles were already coarse), the results showed simulation data within a few percent of experimental pyrolysis reaction yields.

Zhou and Zhao (2021) conducted CDEM simulations of a small-scale fluidised bed with an immersed tube with $\lambda$ up to 3 which resulted in up to two orders of magnitude simulation speed-up for the discrete phase (the fluid solver required significant CPU effort and is not included in this comparison). Obvious agreement of bed expansion height and pressure drop reported as these are roughly equal to the weight of the bed, however noticeable disagreement was observed for the velocity profiles for different coarsening levels as compared with finer DEM results.

Wang and Shen (2022) studied biomass gasification in a small-scale dense fluidised bed reactor of 0.05 m diameter. CDEM results were validated against both finer DEM simulations and experimental data for CG ratios $\lambda = 2$, 3, with an order of magnitude speed-up of obtained by using CDEM.

A study of a small-scale gas-particle cyclone separator for monodisperse particles of 0.5 mm diameter using $\lambda = 4$ was conducted recently by Napolitano et al. (2022). The numerical results were observed to degrade with increasing $\lambda$, likely due to the small number of parcels used.

Sakai et al. (2014) validated CDEM in a small-scale fluidised bed where good agreement of bed height and pressure drop were obtained with for $\lambda = 5$. This study and many others in the literature compared only the bed height and pressure drop, commonly measured experimentally, indicating a good agreement because the weight of the bed and the drag laws are usually sufficiently accurate for fluidised beds. Less accuracy is usually observed for quantities that are affected by collisions, such as particle velocity and granular energy.

Lungu et al. (2022) conducted a validation study of CDEM in a small-scale fluidised bed containing large 3 mm particles with values of $\lambda$ up to 2. Their results showed little sensitivity of simulation time to $\lambda$ due to the small number of parcels used, which is usually an indication that the fluid solver is taking most of the CPU time. In fact, many cases in the literature that compare CDEM to finer DEM results use a small system with a relatively small number of particles so that a DEM simulation can be conducted. These simulations are not able to validate CDEM for a large parcel-to-particle ratio. Such results provide a useful cautionary tale for researchers—it is important to know whether the computational costs of your simulation are dominated by the particle phase or the fluid phase. If the latter, the application of coarse-graining may degrade one's results whilst not achieving any significant speed-up!

Takabatake et al. (2018) compared CDEM and DEM results in a small-scale spouted bed using $\lambda$ values of 2 and 3, achieving respectively a factor of 8- and 30-times speed-up, while maintaining similar mixing patterns to those obtained in resolved DEM simulations.

Coetzee (2017) found that while $\lambda$ values of up to 9 can be used to accurately model dynamic angles of repose in a medium-scale rotating drum as long as the drum-to-particle diameter ratio is above 25, hoppers showed a much

stronger dependence on the scaling factor, with hopper discharge only being reasonably predicted for $\lambda$ values up to 1.3. However, $\lambda = 1.3$ still provided a decrease in computational time by a factor of 3.2, showing both the usefulness and care required in using CDEM.

Cai and Zhao (2020) conducted a validation study of CDEM in a small-scale drum and conical mixer with $\lambda = 3$ and obtained reasonable agreements for mixing time and power consumption whilst achieving a speed-up of almost two orders of magnitude.

Other small-scale CDEM simulations have demonstrated the validity of this technique in powder die-filling using $\lambda = 3$ (Widartiningsih et al., 2020), and for a dry powder inhaler where only fine particles were coarsened (Liu et al., 2021).

Most recently, Che et al. (2023b) applied values of $\lambda$ up to 30 to a laboratory-scale fluidised bed of Geldart group B particles, providing detailed comparison both to lower degrees of coarse graining (due to the number of particles in the system, fully resolved DEM was not computationally tractable) as well as experimental data obtained using positron emission particle tracking (Windows-Yule et al., 2020; 2022a). It was found that values of $\lambda$ up to ~20 still produced good agreement with experimental data, despite the comparatively small size of the system and the rigorous validation methods implemented.

As is evident from the above-discussed studies, the majority of existing studies have focused on smaller laboratory-scale systems, as opposed to larger-scale flow systems of greater interest to industry. One reason underlying the lack of industrial-scale studies may be the difficulty in obtaining accurate experimental data in large systems, which makes such data less available in the literature. This issue—and potential solutions to it—are discussed in **Section 4**. Nevertheless, some such studies do exist. Work by Lu et al. (2017a) and Lu and Benyahia (2018a) has included the simulation of pilot-scale catalytic crackers and regenerators, methanol to olefin reactors, and rare-earth elements solid-liquid extractors, none of which could feasibly have been simulated using resolved (non-coarse-grained) DEM.

Stroh et al. (2018) studied a pilot-scale circulating fluidised bed carbonator of approximately 0.6 m diameter and 9 m height during stable operation by CDEM, using a coarsening factor $\lambda = 60$. Reasonable comparison between simulation and the available experimental data of pressure drop and $CO_2$ absorption rate was obtained. The same group later studied a smaller (0.2 m diameter, 3 m height) cold-flow circulating fluidised bed, this time instrumenting the system with a capacitance probe to allow more detailed experimental validation.

Nikolopoulos et al. (2017) compared the performance of CDEM and two-fluid model (TFM—see **Section 3**) approaches for a 1 MWth pilot-scale fluidised bed carbonator of 0.6 m diameter and 8.7 m height. The CDEM approach compared well with experimental pressure-drop data, whilst also achieving a reasonable computation time, similar to the TFM simulation.

Hu et al. (2019) conducted CDEM simulations of a medium-scale (0.22 m width by 2 m height) fluidised bed coal gasifier in the bubbling regime with $\lambda = 5$. Their results were compared to both previously published TFM and experimental results, demonstrating a good degree of accuracy.

In 2019, a medium-scale biomass gasification reactor of 1.3 m height with a diameter varying from 0.08 to 0.2 m CDEM study was pursued by Ostermeier et al. (2019b) who also provided a nice summary of the different CFD approaches to model biomass gasification in fluidised bed reactors. Large values of $\lambda$ up to 50 were used to represent the finest particles due to consideration of the wide PSD of sand and biomass particles. This level of coarsening allowed the authors to validate the technique over a long range of operating hours, and found good agreement with available experimental data of bed pressure and temperature as well as chemical products of the gasification reactions.

Prior authors have already conducted CDEM simulations of industrial-scale gas–particle cyclone separators (Chu et al., 2016, 2022; Ji et al., 2018). In the 2022 work of Chu et al. (2022), the models used could accurately predict the cyclone efficiency and the formation of ribbons of particles in the cyclone.

## 2.4 Pros and cons

In summary, the past two decades of research have demonstrated the ability of CDEM to tackle complex, industrially relevant problems in chemical engineering. CDEM can provide solutions with almost any computer resources available to the engineer, ranging from a desktop computer to the most powerful supercomputers, and still produce a good representation of the systems being modelled. The main challenge at present regarding CDEM is the lack of consensus regarding the mapping of the properties of ‘true’ particles to those of coarse-grained ‘meso-particles’. More research is also necessary to evaluate the uncertainties associated with the coarsening assumption keeping in mind that DEM solutions are available for UQ analysis (Lu and Benyahia, 2018b).

## 2.5 Mapping-based extrapolation

Perhaps the most recent development in the speed-up of discrete particle simulations is the ‘mapping-based extrapolation’ technique, originally developed by Bednarek et al. (2019). Mapping-based extrapolation techniques exploit the pseudo-periodic behaviour of processes. The periodic time is a process-inherent variable and does not depend on any DEM parameters. The period is several orders of magnitude larger than the DEM integration time steps.

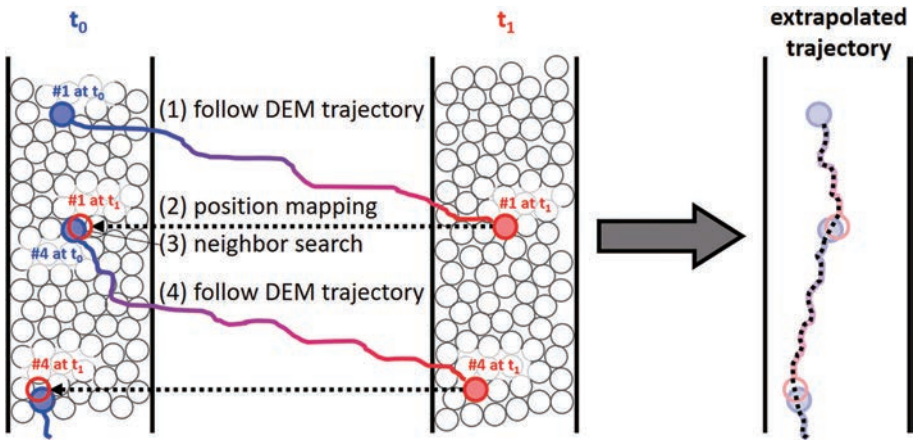


**Fig. 5** Schematic overview of a mapping-based extrapolation algorithm. Image reproduced from Ref. (Siegmann et al., 2021). Copyright: (2021) Elsevier B.V.

Examples of a process period could be one rotation of mixing blade, or the time between refills of a twin-screw feeder.

The method uses two simulation states taken at time points $t_0$ and $t_1$. These two points represent, respectively, the start and end points of the periodic time (or an integer multiple of periods). **Fig. 5** shows a sketch of the mapping-based extrapolation. The numbers in the figure pertain to the following key steps of the algorithm:

1. The trajectory of particle #1 from $t_0$ to $t_1$ is known from the simulation states. However, the particle did not leave the system at $t_1$ (continuous process) or the process has not ended at $t_1$ (batch process).
2. Although the exact trajectory of particle #1 after $t_1$ is not known, it makes intuitive sense that it will be very similar to a particle that started at a similar position at $t_0$.
3. A neighbour search finds that particle #4 has a similar starting position where particle #1 ended.
4. The extrapolated trajectory of particle #1 uses the data for particle #4. This process is repeated until the particle leaves the system (continuous process) or the process duration has been reached (batch process).

The exact mapping procedure depends on the application. If the goal is to only extrapolate the trajectories of a subset of particles (e.g. tracer particles for a virtual spike experiment to characterise the residence time distribution), the mapping procedure is a nearest-neighbour search (Siegmann et al., 2021). However, if the goal is to extrapolate all particle positions, it makes sense to invest computational time in a bijective[4] mapping function that minimises the average mapping error (i.e. the distance between the particles at $t_1$ and their mapping partners at $t_0$).

As a relatively young technique, mapping-based extrapolation does not have the same extensive back catalogue of example applications as coarse-graining, but nonetheless has demonstrated some success in the limited number of papers produced to date, accelerating DEM models of conical screw mixers (Jadidi et al., 2022), continuous blenders (Moreno-Benito et al., 2022), and tablet press feed frames (Forgber et al., 2022). The applications are not limited to DEM simulations, but can also be extended to other particle-based methods such as smoothed particle hydrodynamics (SPH), for example, in the accelerated modelling of twin screw extrusion processes (Bauer and Khinast, 2022; Bauer et al., 2022; Matić et al., 2023).

One hard requirement for mapping-based extrapolation is the existence of pseudo-periodic process behaviour. For example, the discharge of a twin-screw feeder from maximum to minimum fill level is an inherently transient process and will never reach some kind of pseudo-periodicity: the fill level in the hopper of the feeder is constantly decreasing and causes constantly changing flow patterns (Toson and Khinast, 2019). Thus, mapping-based extrapolation is not able to speed up the prediction of the discharge process. However, if periodic refills at the same fill level are considered, mapping-based extrapolation can predict, for example, the washout of old material over multiple refills (Toson and Khinast, 2019).

A soft requirement for the successful application of the technique is the presence of dense flows in the process, as such flows offer multiple (good) mapping partners for each particle. The mapping error is then in the order of one particle radius (Siegmann et al., 2021). It is speculated that mapping-based extrapolation could be applied to more dilute flows at the expense of accuracy (Bednarek et al., 2019), though there are currently no examples in literature to either support or disprove this. In addition, if the dilute particle flow is caused by interaction with air (e.g. in fluidised beds), it is generally a better idea to use the air flow field for extrapolation (Lichtenegger, 2020; Lichtenegger and Miethlinger, 2020; Lichtenegger and Pirker, 2020).

[4] Bijective mapping means that each particle in time step $t_1$ has exactly one mapping target at $t_0$, and that each particle at $t_0$ is referenced by exactly one particle from $t_1$. This optimised mapping function can then be used for all mapping steps and does not need ad-hoc neighbor searches in each mapping step.

### 2.5.1 Pros and cons

The main benefit of the mapping-based extrapolation method is that it allows significant speed-up yet, unlike coarse-graining methods, is still 'fully resolved'—i.e. particles can be modelled at their true size, and calibrated using their 'real' properties. As such, for processes involving dense particle flows, the technique has been shown to facilitate high-accuracy simulations. It can also be applied to other particle-based methods such as SPH, thus allowing the acceleration of fluid simulations in a similar manner. The main drawbacks of the technique are that it is not suitable for transient (i.e. non-periodically-repeating) processes and is currently untested for more dilute flows.

### 2.5.2 Recurrence CFD

It is worth, at the end of this section, briefly mentioning the existence of another technique—recurrence CFD (rCFD)—which provides another approach not dissimilar to the technique discussed above, though for fluid-phase (as opposed to particle) simulations. As the main focus of this work is on the particulate phase, we will not discuss rCFD in detail here, but rather point the reviewer to some useful references, namely (Lichtenegger et al., 2017; Lichtenegger and Pirker, 2016).

## 3. Continuum methods

As has been made abundantly clear in the preceding sections, the main limitation of discrete methods for the simulation of industrial-scale particulate systems is the computational expense of modelling each distinct particle individually. This problem can be overcome by instead modelling particulate media as continua, much as CFD does not consider the individual molecules forming a fluid. There are two crucial differences between particulate media and 'classical' fluids, however, that make the construction of a continuum formulation more complex:

I. Particulate media do not possess a reference equilibrium state.
II. Their temporal and spatial scales are not well separated—that is to say the scales of the dynamics of the individual particles are comparable to those of the bulk medium.

As put succinctly by the great Isaac Goldhirsch at the turn of the millennium, "*the notion of a hydrodynamic or macroscopic description of granular materials is based on unsafe grounds and it requires further study*" (Goldhirsch, 1999). Since then, much 'further study' has indeed been conducted, to the point that accurate continuum models of diverse industrial systems can be found in the literature.

While continuum models exist for both pure particulate systems and multiphase particle–fluid systems, the vast majority of (successful) industrial-scale studies have been performed with the latter, and as such for the present review we focus on the two-phase case.

The Eulerian–Eulerian Two-Fluid Model (TFM) treats both the liquid and solid phases as continua that can fully interpenetrate one another. When it comes to simulating the flow of particulate media, the remaining challenge is to develop closure laws for determining solid flow parameters, such as dynamic/bulk viscosities, particle pressure, and interfacial momentum transfer in multi-sized systems. The Kinetic Theory of Granular Flow (KTGF) has been developed for this purpose. TFM has a lower computational cost compared to (CFD–)DEM and other frequently used approaches for granular flow modeling and, as a result, are better suited for simulating industrial-scale applications.

It is worth prefacing the remainder of this section with the warning that the TFM and the KTGF are unavoidably mathematical, and as such any description thereof which does not include the relevant equations is inevitably somewhat vague and 'hand-waving'. That said, a full understanding of the methods themselves is not necessary to the purposes of the present review article. As such, for brevity (and so as not to be off-putting to the casual reader) we will provide in the main text only the 'hand-waving' explanation, but include as supplementary material a more complete, mathematical description.

Key publications introducing the theories of TFM and KTGF can be found in references (Anderson and Jackson, 1967; Bishop, 1975; Ding and Gidaspow, 1990; Karlsson et al., 2009; Liu et al., 2017; Zhou et al., 2010) and (Brilliantov et al., 2004; Ding and Gidaspow, 1990; Iddir and Arastoopour, 2005; Jenkins and Savage, 1983; Karlsson et al., 2009; Lun et al., 1984; Rao et al., 2008; Savage and Jeffrey, 1981; Schaeffer, 1987), respectively. Although these theories are well-established, there are numerous variations in the formulations, taking into account factors such as elasticity (Lun et al., 1984), particle size distribution (Liu et al., 2022), and particle types (Iddir and Arastoopour, 2005), among others. Consequently, the descriptions of TFM and KTGF are not unique.

The role of the KTGF is to formulate the stresses associated with particulate-phase flow. It is an extension of the classical kinetic theory of gases (Fowler, 1939) adapted for dense particulate flows. Initially, the kinetic theory was developed by Chapman and Cowling (Fowler, 1939) for gases to predict the behaviour of mass point molecules with conserved interaction energies. About three decades ago, this theory was extended to particulate flow, where interactions between particles are not conserved. Savage and Jeffrey (1981) were among the first to apply the kinetic theory to rapidly deforming materials in the (relatively simple) form of smooth, hard, spherical particles. In this theory, the fluctuation energy of particles is described by introducing the concept of a 'granular temperature', analogous to thermodynamic temperature for gases. Though different researchers consider different definitions of the

granular temperature (Goldhirsch, 2008), in the current context we adopt the most common (and indeed literal) definition as the ensemble average of the square of particles' fluctuating velocities. Having introduced a granular analogue for temperature, one must also develop expressions for granular pressure, bulk viscosity, shear viscosity, frictional shear viscosity, and diverse other terms (Lun et al., 1984; Johnson and Jackson, 1987; Schaeffer, 1987). Examples of these expressions can be found in the Supplementary Material.

The granular pressure represents the particle phase normal force caused by the particle–particle interactions. Its description, based on the kinetic theory of granular flow, was developed by Jenkins and Savage (1983) and Lun et al. (1984). The bulk viscosity is a measure for the resistance of a fluid against compression. It is obvious that the importance of the bulk viscosity depends strongly on the velocity gradients. In a fluidised bed, the bulk viscosity and the shear viscosity are of the same order of magnitude, and hence the bulk viscosity should not be neglected, as can be done when simulating Newtonian fluids. While the granular pressure and bulk viscosity describe normal forces, the shear viscosity accounts for the tangential forces. It was shown by Lun et al. (1984) that it is possible to combine different inter-particle forces and use a momentum balance similar to that of a true continuous fluid. In similarity to the particle pressure, a particle shear viscosity can also be derived from the kinetic theory.

While continuum models have been shown capable of simulating various particulate systems, including rotating drums (Schlick et al., 2015) and free-surface flows (Chassagne et al., 2020), the majority of industry-relevant studies have concerned two-phase flows, and in particular fluidised beds—including circulating fluidised beds (Liu et al., 2021), tapered fluidised beds (Khodabandehlou et al., 2018; Liu H. et al., 2017; Liu X. et al., 2019), spray coaters (Shuyan et al., 2010; Srčič et al., 2013), spouted beds (Gryczka et al., 2009; Moliner et al., 2019) and bubbling beds (Lungu et al., 2021; Nikolopoulos et al., 2017; Ostermeier et al., 2019a; Xi et al., 2021), as well as being used to study jet behaviour (Chen and Wang, 2014).

A number of recent studies have also focused specifically on the comparison of CFD–DEM and TFM models (Chen and Wang, 2014; Moliner et al., 2019; Lungu et al., 2021; Ostermeier et al., 2019a). While in general—as one may expect—CFD–DEM models are generally found to provide stronger agreement with experimental baseline data than TFM, TFM models are found in many (though not all) cases to provide reasonable agreement with experiment. Perhaps surprisingly, some specific aspects of system behaviour are, in some cases, *better* captured by TFM than CFD–DEM (Chen and Wang, 2014; Lungu et al., 2021), though overall agreement in the cited cases remains stronger for CFD–DEM.

### 3.1 Pros and cons

TFM is typically—though (dependent on system size and other factors) not always (Moliner et al., 2019)—the most computationally efficient of all the methods discussed thus far. However, as is evident from the preceding section, TFM simulations are typically less accurate than equivalent CFD–DEM simulations, though in many cases can still provide reasonable agreement with experimental data. As is also evident from the above, the models require a significantly larger number of modelling assumptions than either fully resolved or coarse-grained DEM simulations, and the existence of many competing theories makes the choice of the correct model somewhat challenging.

## 4. Validation of models via industrial-scale imaging

As touched upon above, one of the most significant (and often-overlooked) problems with the application of numerical models of particulate systems is the lack of rigorous calibration and validation (Windows-Yule et al., 2016). While the matter of calibration has been addressed in detail in recent reviews (Ketterhagen and Wassgren, 2022; Windows-Yule and Neveu, 2022), the matter of validation—and in particular the validation of simulations concerning industrial-scale systems—has received less attention.

The most rigorous validation of particulate systems is typically performed through comparison with experimental imaging data. At the laboratory scale, simulation models can be rigorously and (relatively) easily validated through comparison with comparatively cheap and readily available, optical methods such as particle imaging velocimetry (PIV) and particle tracking velocimetry (PTV) (Marigo and Stitt, 2015; Shirsath et al., 2015; Weber et al., 2019; 2021), see e.g. **Fig. 6**. At the industrial scale, however, this becomes still more challenging due to the fact that in most cases industrial systems are a) large and b) optically opaque.

The issue of opacity can be overcome by a variety of techniques, including X-ray tomography (CT) (Wang et al., 2004; 2007), radioactive particle tracking (RPT) (Roy, 2017), positron emission particle tracking (PEPT) (Windows-Yule et al., 2020), magnetic resonance imaging (MRI) (Gladden and Alexander, 1996), electrical capacitance, impedance or resistivity tomography (ECT/EIT/ERT[5]) (Wang, 2015), or magnetic particle tracking (MPT) (Neuwirth et al., 2013). An introductory summary of each of these techniques can be found in Chapter 4 of (Windows-Yule et al., 2022b). However, of these imaging techniques, many are still not suitable for industrial imaging. The small bore size of MRI systems, for example,

[5] For the sake of this article, where the focus is not a deep analysis of the techniques discussed, we will refer to this group of techniques simply as 'EXT'.

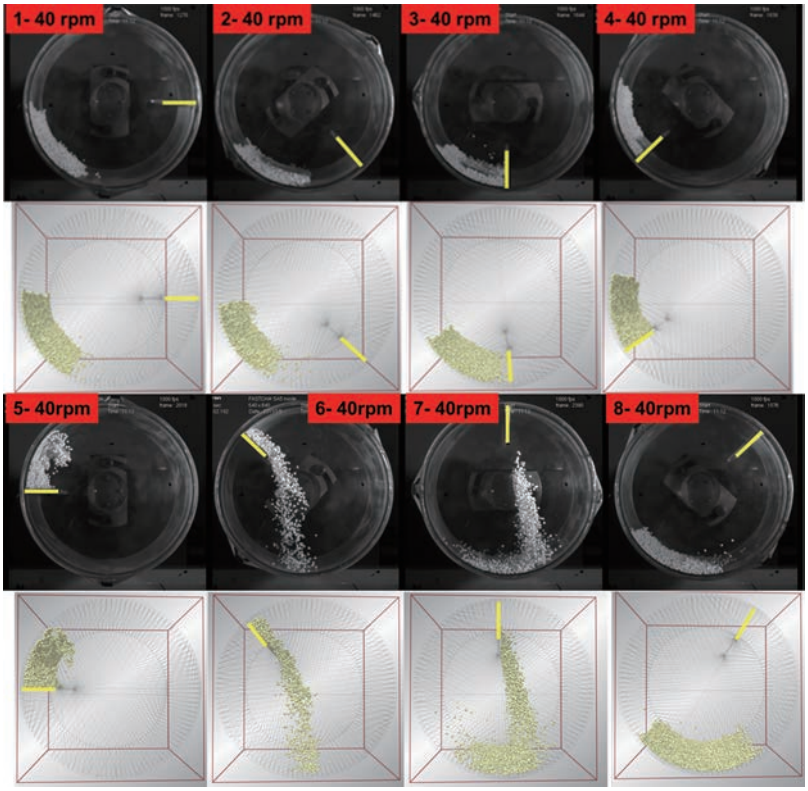


**Fig. 6** An example of the use of optical data for the validation of DEM simulations for a laboratory-scale rotating drum. Image reproduced from Ref. (Marigo and Stitt, 2015) under the terms of the CC-BY 4.0 license. Copyright: (2015) The Authors, published by Hosokawa Powder Technology Foundation.

combined with the fact that most industrial systems are metal-clad, makes this technique largely unsuitable (Elkins and Alley, 2007).

The requirement of MPT for strongly magnetic tracer particles (Buist et al., 2014) again means that it cannot be realistically used in systems containing (or constructed from) ferrous or other magnetic materials, thus again limiting its industrial value. Even in nonmagnetic systems, the tracers used for imaging are typically of millimetre size, making them unsuitable for representing a wide variety of industry-relevant particles, which (in the chemical and pharmaceutical sectors in particular) tend to be closer to the micron scale.

X-ray CT is widely used in industrial applications (De Chiffre et al., 2014) and, as commercially available systems become able to use higher-energy X-rays (Sun et al., 2022), it can be used to image increasingly thick, dense targets. However, its primary use in industry is for metrology, and the imaging of individual parts (Sun et al., 2012), as opposed to imaging the dynamics of active industrial systems—though that is not to say that it has not found certain valuable applications, for example studying fluid flow in porous media (Bultreys et al., 2016), or studying morphological changes in batteries (Finegan et al., 2016). However, despite significant recent improvements in the acquisition rate of X-ray CT systems (Withers et al., 2021), and in particular the very impressive capabilities of synchrotron systems (Dewanckele et al., 2020) and lab-scale systems (Maire and Withers, 2014), the temporal resolution offered by current, commercially-available industrial scanners still remains too low to meaningfully capture the rapid flows exhibited by many industrial particle-handling systems (Zwanenburg et al., 2021). The requirement for X-ray CT systems to be entirely shielded also means that their use for the in situ imaging of real industrial processes remains challenging.

Following from the above, we are left with three techniques which can realistically be applied to the in situ imaging of a reasonably wide range of industrial particle handling systems: EXT, RPT, and PEPT. All three techniques carry the advantages of being able to penetrate metal-walled systems, image comparatively large systems, and having suitably high temporal resolution to capture the dynamics of rapid granular flows. All three techniques can also be applied using a modular array of detector devices (Wang, 2015), allowing the imaging of large systems with complex geometries. Each technique, however, also carries its own distinct strengths and weaknesses. In the following paragraphs, we will briefly summarise these strengths and weaknesses in the specific context of industrial imaging and the validation of numerical models, provide an overview of the types of systems which can (and cannot) be successfully imaged, and highlight recent developments in the relevant fields.

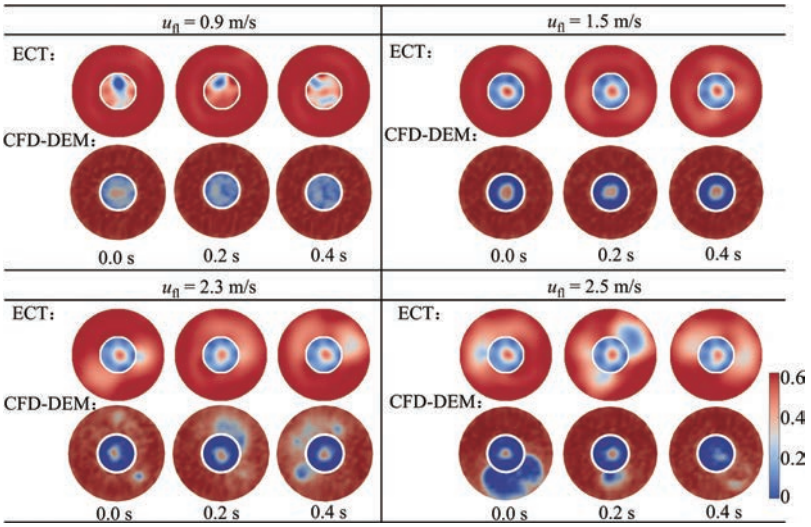


**Fig. 7** Example of the use of ECT data in the validation of a CFD–DEM model of a Wurster coater. Reproduced with permission from Ref. (Che et al., 2020). Copyright: (2020) Elsevier B.V.

## 4.1 Electrical tomography

EXT techniques operate, in simple terms, by transmitting an electrical signal through a given system of interest, which is then received by an array of detectors (electrodes) placed strategically around the system. By analysing the intensity of the signals received by each part of the sensor array, various system properties can be back-computed (Scott and McCann, 2005). A previous KONA review paper providing an more detailed yet still accessible introduction to electrical tomography techniques can be found in reference (Rasteiro et al., 2011). EXT is already widely used for the imaging of a wide range of industrial systems and unit operations, including pipes (Dong et al., 2003), storage vessels (Kowalski et al., 2010), mixers (Holden et al., 1998), reactors (Bolton and Primrose, 2005), cyclones (Meng et al., 2008). Indeed, EXT methods can realistically be applied to almost any system physically resembling a pipe or tank (Rasteiro et al., 2011; Sharifi and Young, 2013).

Key metrics which can potentially be used to validate numerical simulations include the flow rates and velocity distributions, the distributions of different materials and (thus) various mixing and mixing rate metrics, solids concentration, and solids hold-up (Sharifi and Young, 2013). **Fig. 7** shows an example in which ECT-derived cross-sectional images of solid distributions are used to validate CFD–DEM simulations of a Wurster coater (Che et al., 2020). This set of images, as well as those shown in **Fig. 8**, clearly illustrate the advantage gained in terms of the thoroughness and rigour when using two/three-dimensional imaging techniques (as opposed to simpler, lower-dimensional data such as pressure drop measurements) when validating simulations.

In terms of the relative advantages and disadvantages of the ECT technique, two particularly significant benefits for industrial applications are the low cost and easy installation of the technique (Eda et al., 2013). Compared to nuclear imaging techniques such as PEPT and RPT (which we discuss next), it also carries the advantage of not using ionising radiation, thus providing non-trivial benefits in terms of ease of use, as no permits etc. are required for its implementation. Electrical tomography systems can also be used as on-line, in-line sensors, offering access to real-time data from a system.

In terms of drawbacks, EXT techniques offer comparatively poor spatial resolution—typically of the order of 10 % of the diameter of the vessel being imaged when used in practice in industrial systems (Xie et al., 1995). While of course these figures fall well below what is hypothetically achievable with more carefully controlled conditions and cutting-edge algorithms, it is nonetheless well accepted that spatial resolution remains an Achilles heel of EXT techniques (Rymarczyk et al., 2019; York, 2001). Another disadvantage of electrical tomography compared to methods such as RPT and PEPT is that it provides only Eulerian information—that is, it can provide information regarding the bulk motion of a particulate medium (velocity distributions, solids distributions...), but provides no particle-level information (e.g. circulation time, dispersion rate, etc.).

## 4.2 Positron emission particle tracking

Positron emission particle tracking, as its name implies, tracks the motion of a 'tracer particle'[6] which is 'labelled' with a positron-emitting radioisotope.

When the positrons produced by said isotope annihilate with electrons within the tracer particle, they produce a pair

[6] PEPT may also be conducted using multiple such tracers (Nicuşan and Windows-Yule, 2020; Yang et al., 2006), but for the sake of simplicity in the present explanation of the technique we will only consider the case of a single tracer.

of 511 keV gamma photons whose trajectories are collinear and antiparallel, thus effectively 'drawing a straight line' (known as a line of response or LoR) through the tracer's position. If multiple such LoRs are detected by suitably-placed detectors surrounding a given system of interest, they can be used to triangulate the position of the tracer. For current detector systems and algorithms, tracers can be located with micron-scale spatial resolution and microsecond-scale temporal resolution (Windows-Yule et al., 2022b). Through suitable temporal averaging, the dynamics of the tracked particle(s) may be used to build up a picture of the full, three-dimensional dynamics of the system of interest. PEPT's use of high-energy gamma radiation means that it can be used to probe the interior dynamics of large, dense, optically-opaque, three-dimensional systems, making it well-suited to industrial imaging. The tracers used are also typically physically identical to those belonging to the system of interest, meaning that the technique is also non-invasive. A more complete but still accessible introduction to the PEPT technique can be found in reference (Windows-Yule et al., 2020), and a deeper dive into the algorithms used to track particles in reference (Windows-Yule et al., 2022a).

Like ECT, PEPT has been applied to the study of a wide range of industry-relevant processes and unit operations, including pipe flow (Fairhurst et al., 2001), diverse types of mixers (Jones and Bridgwater, 1998; Marigo et al., 2013; Mihailova et al., 2015), stirred tank reactors (Fangary et al., 2000), fluidized beds (Leadbeater et al., 2023), spouted beds (Al-Shemmeri et al., 2021), and vibrated beds (Windows-Yule et al., 2014), cyclones (Chan et al., 2009), drum roasters (Al-Shemmeri et al., 2023), mills (Conway-Baker et al., 2002), froth flotation devices (Cole et al., 2022), extruders (Diemer et al., 2011), and even household appliances such as washing machines, dishwashers and tumble dryers (Jones et al., 2022; Pérez-Mohedano et al., 2015).

Due to the rich, high-resolution, three-dimensional data provided by PEPT, the technique is also widely used in the validation of numerical models of particulate and particle-fluid systems, including industry-relevant systems. **Fig. 8** shows a comparison of PEPT and CFD–DEM data for a

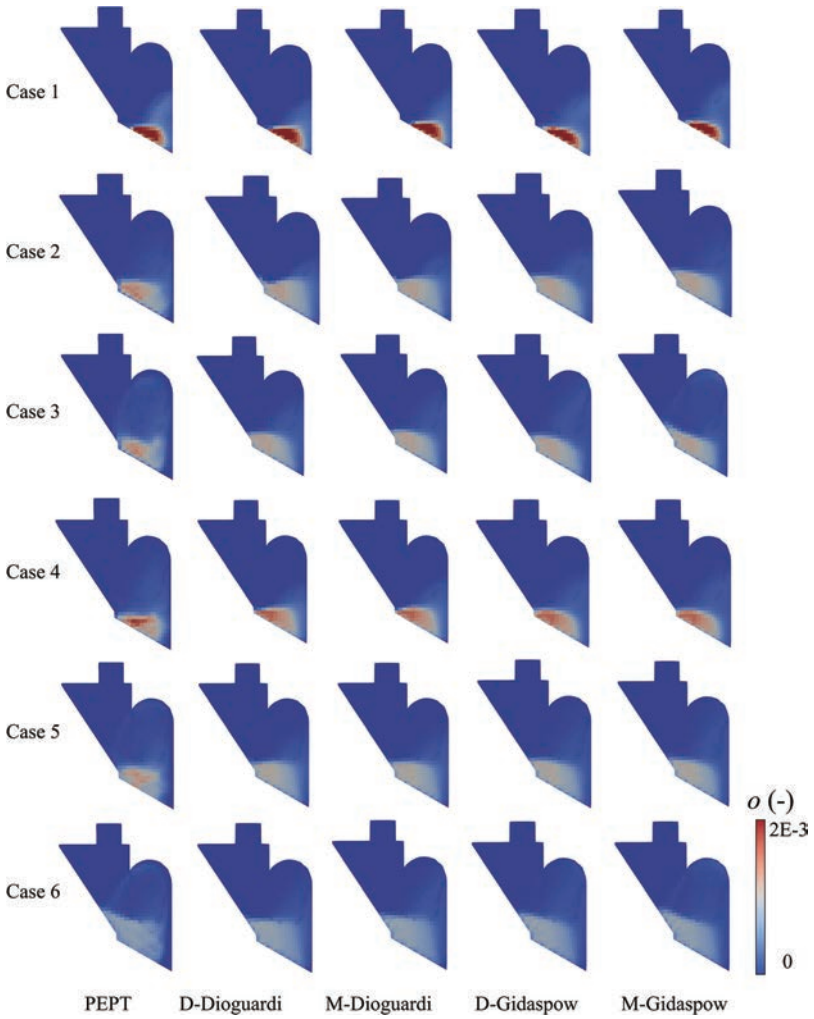


**Fig. 8** Comparison of PEPT and CFD–DEM derived solid occupancy distributions for a variety of different system conditions (rows) and drag models (columns). Reproduced with permission from Ref. (Che et al., 2023a). Copyright: (2023) Elsevier B.V.

NEUHAUS NEOTEC spouted-bed coffee roaster (Che et al., 2023a). By post-processing both PEPT and CFD–DEM data on the same Eulerian grid, it is possible to conduct a cell-by-cell comparison of experimental and numerical data for a variety of physical fields, and thus provide a fully quantitative assessment of the degree of accuracy exhibited by a given simulation. Full details of the process through which this may be achieved may be found in reference (Che et al., 2023a).

To date, however, while PEPT has been used to image a number of 'real' industrial systems, including pilot-scale systems, in the laboratory (Windows-Yule et al., 2022b), its use for the in situ imaging on active industrial sites has been comparatively limited as compared to techniques such as EXT.

In 2007, using a portable, modular detector system developed at the University of Birmingham, PEPT was successfully used to extract information from a large (750 mm diameter) fluidised bed at BP's site in Hull, operating at pressure and under industry-relevant conditions (Ingram et al., 2007). Data obtained included velocity vector fields indicating the flow regime of the system, and circulation rate data, both providing valuable insight into mass transport within the system and the variation thereof with changes to key system parameters.

In 2022, an upgraded modular camera system (Herald et al., 2023; Parker et al., 2022) was used to image particle motion within an active fluidised-bed pyrolysis reactor used for the chemical recycling of waste plastics (Ingenia, 2022). In this instance, not only were particles corresponding to the bed material used to image the flow dynamics of the system, radioactively labelled plastic pellets were also used to assess crucial aspects of system performance including the residence time of the particle (i.e. the time required for its complete volatilisation), as well as indicating whether or not the plastics injected into the system were subject to adequate mass transport to ensure temperature uniformity (and thus product quality).

The lack (to date) of PEPT's wider use in on-site imaging can likely be ascribed to one (or both) of two major factors: firstly, the current lack of widespread availability of the relevant expertise or equipment (there presently only exists one portable, modular PEPT camera). Secondly, the fact of the use of ionising radiation means there exists a considerable amount of 'red tape' as compared to techniques such as ECT. However, there do not exist any specific *technological* barriers to the wider adoption of industrial PEPT.

The above represents perhaps the most significant 'con' regarding the industrial application of PEPT imaging. Another notable drawback, however, is that while PEPT can provide real-time information regarding the motion of individual particles, the requirement of the time-averaging of multiple tracer passes to produce full, Eulerian data means that, unlike EXT, PEPT cannot provide direct information regarding transient bulk phenomena (e.g. bubble dynamics in fluidised beds)—though some indirect and/or statistical information regarding such processes can still be obtained (Windows-Yule et al., 2022b).

In terms of PEPT's advantages, as noted above, it facilitates the extraction of both Lagrangian and Eulerian data, providing a depth of information that can be extremely valuable for the rigorous calibration and validation of numerical models, as forms the focus of this section. It also offers the highest spatial resolution of all techniques discussed which can be crucial, for example, when investigating the mixing of micron-scale particles in the pharmaceutical industry.

### 4.3 Radioactive particle tracking

The fundamental approach of radioactive particle tracking (RPT)[7] is not dissimilar to that of PEPT, in that a single[8] radioactively-labelled tracer particle is followed through a given system of interest, and the time-averaged dynamics thereof are used to provide three-dimensional Eulerian information. Unlike PEPT, however, RPT does not require the use of positron-emitting tracers (though such tracers can be used for RPT if desired), but can feasibly be applied using any gamma-emitting radioisotope. Rather than finding the intersection of multiple LoRs produced by back-to-back gamma rays, in RPT the location of the tracer is determined by measuring the relative intensity of the radiation emitted by the tracer across a series of detectors placed around the system. In an entirely homogeneous system, the intensity received by a given detector will be proportional to the square of its distance from the tracer. As such, with multiple such detectors placed strategically around the system of interest, one could hypothetically determine the position of the tracer through triangulation. In reality, however, since the vast majority of particulate systems are heterogeneous to some degree, correction factors must be applied to account for the differing degrees of attenuation experienced by gamma rays taking different paths through the system. For this reason, unlike PEPT, RPT must be specifically calibrated for each new system and set of materials to which it is applied (Roy et al., 2002). The fact that local densities (and thus their ability to attenuate gamma rays) may, in many systems, undergo non-negligible fluctuations means that RPT measurements are typically subject to a larger degree of uncertainty than PEPT measurements, and thus correspondingly offer lower temporal resolution.

Like PEPT, RPT has been applied to a diverse range of

[7] RPT is also commonly referred to as *computer aided* radioactive particle tracking (CARPT). The two terms can, at least in the context of the present work, be used interchangeably.

[8] As with PEPT, RPT may also be conducted using multiple such tracers (Rasouli et al., 2015), but for the sake of simplicity in the present explanation of the technique we will only consider the case of a single tracer.

industry-relevant systems and applications including fluidised beds (Fraguío et al., 2007), packed beds (Chen et al., 2001), stirred tanks (Rammohan et al., 2001), bubble columns (Devanathan et al., 1990), and rotating drums (Rasouli et al., 2016). The advantages and disadvantages of RPT compared to ECT are also largely similar to those of PEPT, and as such will not be repeated here. Of greater interest in the current section are RPT's strengths and weaknesses compared to PEPT. One of the most notable differences between PEPT and RPT—as indeed has been explicitly noted by one of the most prominent practitioners of the RPT technique (Roy et al., 2002)—PEPT can in many ways be considered an 'off-the-shelf' or 'plug-and-play' technique, whereas for RPT "*a laborious trial and error experimental procedure has to be undergone before a good experimental run can be implemented*" (Roy et al., 2002). As alluded to above, the assumptions required for the calibration of RPT systems also mean that the spatial resolution achievable with this technique is typically lower than that achievable with PEPT—though sub-millimetre accuracy is still possible to achieve under suitable conditions.

In the context of industrial imaging, however, RPT does offer one significant advantage: PEPT's requirement for the use of back-to-back gamma rays produced by positron-electron annihilation events inherently fixes the energy of usable gamma rays at 511 keV. As RPT is free of such restrictions, radioisotopes producing higher energy gamma rays may be used, thus—due to their increased characteristic penetration lengths—allowing the imaging of larger systems.

### 4.4 Summary

**Table 1** provides a brief summary of the relative strengths and weaknesses of the techniques discussed in the previous sections. Though perhaps the weakest of the three in terms of its actual imaging capabilities, considering the reduced red tape, lower costs, and fewer health and safety concerns associated with electrical tomography techniques, it is perhaps unsurprising that, in the general context of commercial, industrial imaging, it remains by far the most popular technique. However, in the specific context of the calibration and validation of numerical models, it can be argued that the depth of data which can be extracted from PEPT and RPT (and the precision of said data) makes them more suitable choices: the calibration and validation of simulation models can (and, in the authors' view, should) be seen as a numerical optimisation problem, with a number of free parameters equal to the number of tunable variables in the simulation (Windows-Yule and Neveu, 2022). Even a simple, single-phase, one material simulation has in excess of 10 such free parameters, and a simulation involving a fluid phase and/or multiple distinct materials many more still. If we wish to provide closures for each of these parameters, then a greater range of data (as is available from the aforementioned particle tracking methods) is required.

**Table 1** Summary of the comparative strengths and weaknesses of electrical tomography (EXT), positron emission particle tracking (PEPT) and radioactive particle tracking (RPT) techniques.

| | EXT | PEPT | RPT |
|---|---|---|---|
| Spatial resolution | × | ✓ | ✓ |
| Capable of imaging large systems | ✓ | ✓ | ✓✓ |
| Cost | ✓ | × | × |
| Eulerian information | ✓ | ✓ | ✓ |
| Lagrangian information | × | ✓ | ✓ |
| Transient information | ✓ | × | × |
| Plug-and-play | × | ✓ | × |
| Non-ionising radiation | ✓ | × | × |

In the 'factory of the future', then, one might imagine that there exists an important role for both electrical tomography *and* particle tracking methods, the latter being used more occasionally for the development of new models (i.e. digital twins of process equipment), and the former for regular, day-to-day process monitoring, and informing the models created.

## 5. Summary and conclusion

In this review, we have provided an overview of several leading techniques for the numerical modelling of industrial-scale particulate and particle-fluid systems, as well as the experimental imaging techniques which may be used for the validation thereof. In both cases, it is evident that, with currently available technologies, there does not exist 'one technique to rule them all'; rather, different techniques are more suitable for different systems and situations, with clear tradeoffs to be considered. In terms of simulation models, the trade-off is typically between accuracy, ease of calibration/implementation, and computational cost. In terms of experimental imaging, the tradeoff is typically between accuracy, ease of calibration/implementation, and financial cost.

In keeping with the title of the review, it is perhaps of value to end by providing a brief summary of the main challenges associated with the methods discussed, and the potential solutions thereto. The main challenges can be broadly distilled down as follows:

(i) The use of fully resolved DEM can provide quantitatively accurate numerical models of experimental systems, created with relatively few simplifying assumptions, but even with state-of-the-art hardware and parallelisation techniques, is currently limited to the simulation of billions of particles, whereas industrial systems may contain trillions or even

quadrillions.

(ii) Coarse-grained DEM models can seemingly facilitate the meaningful simulation of systems containing arbitrarily large numbers of particles, but there is at present no consensus on the mapping of individual particle properties to meso-particle properties.

(iii) Mapping-based extrapolation methods also allow further acceleration of DEM simulations, but unlike CG methods remain fully resolved, thus allowing direct calibration; however, these methods are unsuitable for transient processes, and may not be viable for dilute systems.

(iv) Simulations based on the kinetic theory of granular flow are potentially (though not necessarily) capable of increasing simulation speed further still, but introduce still more extreme simplifying assumptions than CG, most notably by treating discrete systems as continuous.

(v) Experimental methods such as electrical tomography, radioactive particle tracking and positron emission particle tracking are capable of imaging industrial-scale systems, and thus providing validation data for numerical simulations, yet those techniques which offer greatest accuracy often involve the highest financial costs and most red tape, and vice versa.

In terms of a solution, the most effective route—and one increasingly being adopted by researchers—is not to use any one method in isolation, but to take a 'multi-scale' or 'bootstrapping' approach involving several (if not all) of the above-described methodologies. For example, one may begin by considering the largest (e.g. pilot scale) model of the system of interest that can both a) be simulated using fully resolved (CFD-)DEM, and b) be imaged with a desired imaging method (the ultimate size of the system being determined by whichever of a) and b) is the limiting factor). Once fully calibrated and validated against suitable experimental data, this resolved model may be used either to develop suitable closure relations for a KTGF/TFM model, or to determine suitable coarse-grained DEM properties. Since the models developed should be dependent only on the materials involved, one may reasonably expect—if they have been suitably rigorously calibrated—that they may then be used to efficiently model larger-scale systems[9]. Though convoluted, this process—as evidenced by the literature discussed in the preceding sections—provides a viable route to the accurate simulation of industrial-scale systems.

[9] The results of these full-scale simulations may then be pseudo-validated using more crude methods applicable to larger systems than may be imaged using EXT, PEPT or RPT (e.g. measurements of pressure fluctuations for a bubbling fluidised bed, or torque measurements for a bladed mixer).

## Supplementary Information

The online version contains supplementary material available at https://doi.org/10.14356/kona.2025007.

## References


Al-Shemmeri M., Windows-Yule K., Lopez-Quiroga E., Fryer P.J., Coffee bean particle motion in a spouted bed measured using Positron Emission Particle Tracking (PEPT), Journal of Food Engineering, 311 (2021) 110709. https://doi.org/10.1016/j.jfoodeng.2021.110709

Al-Shemmeri M., Windows-Yule K., Lopez-Quiroga E., Fryer P.J., Coffee bean particle motion in a rotating drum measured using positron emission particle tracking (PEPT), Food Research International, 163 (2023) 112253. https://doi.org/10.1016/j.foodres.2022.112253

Anderson T.B., Jackson R., Fluid mechanical description of fluidized beds. Equations of motion, Industrial & Engineering Chemistry Fundamentals, 6 (1967) 527–539. https://doi.org/10.1021/i160024a007

Bauer H., Khinast J., Detecting mixing barriers in Twin-Screw extruder elements via Lagrangian Coherent Structures, Chemical Engineering Science, 263 (2022) 118069. https://doi.org/10.1016/j.ces.2022.118069

Bauer H., Matić J., Evans R.C., Gryczke A., Ketterhagen W., Sinha K., Khinast J., Determining local residence time distributions in twin-screw extruder elements via smoothed particle hydrodynamics, Chemical Engineering Science, 247 (2022) 117029. https://doi.org/10.1016/j.ces.2021.117029

Bednarek X., Martin S., Ndiaye A., Peres V., Bonnefoy O., Extrapolation of DEM simulations to large time scale. Application to the mixing of powder in a conical screw mixer, Chemical Engineering Science, 197 (2019) 223–234. https://doi.org/10.1016/j.ces.2018.12.022

Benyahia S., Galvin J.E., Estimation of numerical errors related to some basic assumptions in discrete particle methods, Industrial & Engineering Chemistry Research, 49 (2010) 10588–10605. https://doi.org/10.1021/ie100662z

Bishop R.F., Thermo-fluid dynamic theory of two-phase flow, Physics Bulletin, 26 (1975) 544. https://doi.org/10.1088/0031-9112/26/12/034

Blais B., Vidal D., Bertrand F., Patience G.S., Chaouki J., Experimental methods in chemical engineering: discrete element method—DEM, The Canadian Journal of Chemical Engineering, 97 (2019) 1964–1973. https://doi.org/10.1002/cjce.23501

Bolton G.T., Primrose K.M., An overview of electrical tomographic measurements in pharmaceutical and related application areas, AAPS PharmSciTech, 6 (2005) 21. https://doi.org/10.1208/pt060221

Brilliantov N., Salueña C., Schwager T., Pöschel T., Transient structures in a granular gas, Physical Review Letters, 93 (2004) 134301. https://doi.org/10.1103/physrevlett.93.134301

Buist K.A., van der Gaag A.C., Deen N.G., Kuipers J.A.M., Improved magnetic particle tracking technique in dense gas fluidized beds, AIChE Journal, 60 (2014) 3133–3142. https://doi.org/10.1002/aic.14512

Bultreys T., Boone M.A., Boone M.N., De Schryver T., Masschaele B., Van Hoorebeke L., Cnudde V., Fast laboratory-based micro-computed tomography for pore-scale research: Illustrative experiments and perspectives on the future, Advances in Water Resources, 95 (2016) 341–351. https://doi.org/10.1016/j.advwatres.2015.05.012

Cai R., Zhao Y., An experimentally validated coarse-grain DEM study of monodisperse granular mixing, Powder Technology, 361 (2020) 99–111. https://doi.org/10.1016/j.powtec.2019.10.023

Chan C.W., Seville J.P.K., Fan X., Baeyens J., Particle motion in CFB cyclones as observed by positron emission particle tracking, Industrial & Engineering Chemistry Research, 48 (2009) 253–261. https://doi.org/10.1021/ie800213g

Chan E.L., Washino K., Coarse grain model for DEM simulation of dense and dynamic particle flow with liquid bridge forces, Chemical Engineering Research and Design, 132 (2018) 1060–1069. https://doi.org/10.1016/j.cherd.2017.12.033

Chassagne R., Chauchat J., Frey P., Gray J.M.N.T., Maurin R., Discrete

and continuum modelling of grain size segregation during bedload transport, Journal of Fluid Mechanics, 895 (2020) A30. https://doi.org/10.1017/jfm.2020.274

Che H., Al-Shemmeri M., Fryer P.J., Lopez-Quiroga E., Kokalova Wheldon T., Windows-Yule K., PEPT validated CFD-DEM model of aspherical particle motion in a spouted bed, Chemical Engineering Journal, 453 (2023a) 139689. https://doi.org/10.1016/j.cej.2022.139689

Che H., Liu D., Tian W.B., Gao S., Sun J.T., Xu L.J., CFD-DEM study of gas-solid flow regimes in a Wurster type fluidized bed with experimental validation by electrical capacitance tomography, Chemical Engineering Journal, 389 (2020) 124280. https://doi.org/10.1016/j.cej.2020.124280

Che H., O'Sullivan C., Sufian A., Smith E.R., A novel CFD-DEM coarse-graining method based on the Voronoi tessellation, Powder Technology, 384 (2021) 479–493. https://doi.org/10.1016/j.powtec.2021.02.025

Che H., Werner D., Seville J., Wheldon T.K., Windows-Yule K., Evaluation of coarse-grained CFD-DEM models with the validation of PEPT measurements, Particuology, 82 (2023b) 48–63. https://doi.org/10.1016/j.partic.2022.12.018

Chen J., Rados N., Al-Dahhan M.H., Duduković M.P., Nguyen D., Parimi K., Particle motion in packed/ebullated beds by CT and CARPT, AIChE Journal, 47 (2001) 994–1004. https://doi.org/10.1002/aic.690470506

Chen X., Elliott J.A., On the scaling law of JKR contact model for coarse-grained cohesive particles, Chemical Engineering Science, 227 (2020) 115906. https://doi.org/10.1016/j.ces.2020.115906

Chen X., Wang J., A comparison of two-fluid model, dense discrete particle model and CFD-DEM method for modeling impinging gas–solid flows, Powder Technology, 254 (2014) 94–102. https://doi.org/10.1016/j.powtec.2013.12.056

Chu K., Chen J., Yu A., Applicability of a coarse-grained CFD–DEM model on dense medium cyclone, Minerals Engineering, 90 (2016) 43–54. https://doi.org/10.1016/j.mineng.2016.01.020

Chu K., Chen Y., Ji L., Zhou Z., Yu A., Chen J., Coarse-grained CFD-DEM study of gas-solid flow in gas cyclone, Chemical Engineering Science, 260 (2022) 117906. https://doi.org/10.1016/j.ces.2022.117906

Coetzee C.J., Review: Calibration of the discrete element method, Powder Technology, 310 (2017) 104–142. https://doi.org/10.1016/j.powtec.2017.01.015

Coetzee C.J., Particle upscaling: calibration and validation of the discrete element method, Powder Technology, 344 (2019) 487–503. https://doi.org/10.1016/j.powtec.2018.12.022

Cole K., Barker D.J., Brito-Parada P.R., Buffler A., Hadler K., Mackay I., Mesa D., Morrison A.J., Neethling S., Norori-McCormac A., Shean B., Cilliers J., Standard method for performing positron emission particle tracking (PEPT) measurements of froth flotation at PEPT Cape Town, Methods X, 9 (2022) 101680. https://doi.org/10.1016/j.mex.2022.101680

Conway-Baker J., Barley R.W., Williams R.A., Jia X., Kostuch J., McLoughlin B., Parker D.J., Measurement of the motion of grinding media in a vertically stirred mill using positron emission particle tracking (PEPT), Minerals Engineering, 15 (2002) 53–59. https://doi.org/10.1016/s0892-6875(01)00199-6

Das P.K., Deka G.C., History and evolution of GPU architecture, in: Deka G.C., Siddesh G.M., Srinivasa K.G., Patnaik L.M. (Eds.), Emerging Research Surrounding Power Consumption and Performance Issues in Utility Computing, IGI Global, Hershey, PA, USA, 2016, pp. 109–135, ISBN: 9781466688537. https://doi.org/10.4018/978-1-4666-8853-7.ch006

De T., Chakraborty J., Kumar J., Tripathi A., Sen M., Ketterhagen W., A particle location based multi-level coarse-graining technique for discrete element method (DEM) simulation, Powder Technology, 398 (2022) 117058. https://doi.org/10.1016/j.powtec.2021.117058

De Chiffre L., Carmignato S., Kruth J.P., Schmitt R., Weckenmann A., Industrial applications of computed tomography, CIRP Annals, 63 (2014) 655–677. https://doi.org/10.1016/j.cirp.2014.05.011

de Munck M.J.A., van Gelder J.B., Peters E.A.J.F., Kuipers J.A.M., A detailed gas-solid fluidized bed comparison study on CFD-DEM coarse-graining techniques, Chemical Engineering Science, 269 (2023) 118441. https://doi.org/10.1016/j.ces.2022.118441

Devanathan N., Moslemian D., Dudukovic M.P., Flow mapping in bubble columns using CARPT, Chemical Engineering Science, 45 (1990) 2285–2291. https://doi.org/10.1016/0009-2509(90)80107-p

Dewanckele J., Boone M.A., Coppens F., Van Loo D., Merkle A.P., Innovations in laboratory-based dynamic micro-CT to accelerate in situ research, Journal of Microscopy, 277 (2020) 197–209. https://doi.org/10.1111/jmi.12879

Di Renzo A., Napolitano E.S., Di Maio F.P., Coarse-grain DEM modelling in fluidized bed simulation: a review, Processes, 9 (2021) 279. https://doi.org/10.3390/pr9020279

Diemer J., Chilles C., Colbert J., Miri T., Ingram A., David P., Fard A.S., Anderson P.D., Flow visualisation in co-rotating twin screw extruders: positron emission particle tracking and numerical particle trajectories, International Polymer Processing, 26 (2011) 540–550. https://doi.org/10.3139/217.2475

Ding J., Gidaspow D., A bubbling fluidization model using kinetic theory of granular flow, AIChE Journal, 36 (1990) 523–538. https://doi.org/10.1002/aic.690360404

Dong F., Jiang Z.X., Qiao X.T., Xu L.A., Application of electrical resistance tomography to two-phase pipe flow parameters measurement, Flow Measurement and Instrumentation, 14 (2003) 183–192. https://doi.org/10.1016/s0955-5986(03)00024-4

Eda T., Sapkota A., Haruta J., Nishio M., Takei M., Experimental study on liquid spread and maldistribution in the trickle bed reactor using electrical resistance tomography, Journal of Power and Energy Systems, 7 (2013) 94–105. https://doi.org/10.1299/jpes.7.94

Eibl S., Rüde U., A systematic comparison of runtime load balancing algorithms for massively parallel rigid particle dynamics, Computer Physics Communications, 244 (2019) 76–85. https://doi.org/10.1016/j.cpc.2019.06.020

El Geitani T., Golshan S., Blais B., Toward high-order CFD-DEM: development and validation, Industrial & Engineering Chemistry Research, 62 (2023) 1141–1159. https://doi.org/10.1021/acs.iecr.2c03546

Elkins C.J., Alley M.T., Magnetic resonance velocimetry: applications of magnetic resonance imaging in the measurement of fluid motion, Experiments in Fluids, 43 (2007) 823–8858. https://doi.org/10.1007/s00348-007-0383-2

Fairhurst P.G., Barigou M., Fryer P.J., Pain J.P., Parker D.J., Using positron emission particle tracking (PEPT) to study nearly neutrally buoyant particles in high solid fraction pipe flow, International Journal of Multiphase Flow, 27 (2001) 1881–1901. https://doi.org/10.1016/s0301-9322(01)00038-6

Fang L., Zhang R., Vanden Heuvel C., Serban R., Negrut D., Chrono::GPU: an open-source simulation package for granular dynamics using the discrete element method, Processes, 9 (2021) 1813. https://doi.org/10.3390/pr9101813

Fangary Y.S., Barigou M., Seville J.P.K., Parker D.J., Fluid trajectories in a stirred vessel of non-Newtonian liquid using positron emission particle tracking, Chemical Engineering Science, 55 (2000) 5969–5979. https://doi.org/10.1016/s0009-2509(00)00176-7

Finegan D.P., Tudisco E., Scheel M., Robinson J.B., Taiwo O.O., Eastwood D.S., Lee P.D., Di Michiel M., Bay B., Hall S.A., Hinds G., Brett D.J.L., Shearing P.R., Quantifying bulk electrode strain and material displacement within lithium batteries via high-speed operando tomography and digital volume correlation, Advanced Science, 3 (2016) 1500332. https://doi.org/10.1002/advs.201500332

Forgber T., Rehrl J., Matic M., Sibanc R., Sivanesapillai R., Khinast J.G., Experimental and numerical investigations of the RTD in a GEA ConsiGma CTL25 tablet press, Powder Technology, 405 (2022) 117507. https://doi.org/10.1016/j.powtec.2022.117507

Fowler R.H., The mathematical theory of non-uniform gases, Nature, 144 (1939) 993–995. https://doi.org/10.1038/144993a0

Fraguío M.S., Cassanello M.C., Larachi F., Limtrakul S., Dudukovic M., Classifying flow regimes in three-phase fluidized beds from CARPT experiments, Chemical Engineering Science, 62 (2007) 7523–7529. https://doi.org/10.1016/j.ces.2007.08.039

Gladden L.F., Alexander P., Applications of nuclear magnetic resonance imaging in process engineering, Measurement Science and Technology, 7 (1996) 423. https://doi.org/10.1088/0957-0233/7/3/026

Goldhirsch I., Scales and kinetics of granular flows, Chaos: An Interdisciplinary Journal of Nonlinear Science, 9 (1999) 659–672. https://doi.org/10.1063/1.166440

Goldhirsch I., Introduction to granular temperature, Powder Technology, 182 (2008) 130–136. https://doi.org/10.1016/j.powtec.2007.12.002

Goldhirsch I., Stress, stress asymmetry and couple stress: from discrete particles to continuous fields, Granular Matter, 12 (2010) 239–252. https://doi.org/10.1007/s10035-010-0181-z

Golshan S., Blais B., Load-balancing strategies in discrete element method simulations, Processes, 10 (2022) 79. https://doi.org/10.3390/pr10010079

Golshan S., Munch P., Gassmöller R., Kronbichler M., Blais B., LetheDEM: an open-source parallel discrete element solver with load balancing, Computational Particle Mechanics, 10 (2023) 77–96. https://doi.org/10.1007/s40571-022-00478-6

Govender N., Wilke D.N., Kok S., Collision detection of convex polyhedra on the NVIDIA GPU architecture for the discrete element method, Applied Mathematics and Computation, 267 (2015) 810–829. https://doi.org/10.1016/j.amc.2014.10.013

Govender N., Wilke D.N., Kok S., Els R., Development of a convex polyhedral discrete element simulation framework for NVIDIA Kepler based GPUs, Journal of Computational and Applied Mathematics, 270 (2014) 386–400. https://doi.org/10.1016/j.cam.2013.12.032

Gryczka O., Heinrich S., Deen N.G., van Sint Annaland M., Kuipers J.A.M., Jacob M., Mörl L., Characterization and CFD-modeling of the hydrodynamics of a prismatic spouted bed apparatus, Chemical Engineering Science, 64 (2009) 3352–3375. https://doi.org/10.1016/j.ces.2009.04.020

Herald M., Hampel D., Wheldon T.K., Seville J., Windows-Yule C., Monte Carlo model of the large modular array for positron emission particle tracking, IEEE Access, 11 (2023) 25982–25990. https://doi.org/10.1109/access.2023.3255505

Herald M.T., Sykes J.A., Werner D., Seville J.P.K., Windows-Yule C.R.K., DEM2GATE: combining discrete element method simulation with virtual positron emission particle tracking experiments, Powder Technology, 401 (2022) 117302. https://doi.org/10.1016/j.powtec.2022.117302

Holden P.J., Wang M., Mann R., Dickin F.J., Edwards R.B., Imaging stirred-vessel macromixing using electrical resistance tomography, AIChE Journal, 44 (1998) 780–790. https://doi.org/10.1002/aic.690440403

Holmberg K., Kivikytö-Reponen P., Härkisaari P., Valtonen K., Erdemir A., Global energy consumption due to friction and wear in the mining industry, Tribology International, 115 (2017) 116–139. https://doi.org/10.1016/j.triboint.2017.05.010

Hu C., Luo K., Wang S., Sun L., Fan J., Influences of operating parameters on the fluidized bed coal gasification process: a coarse-grained CFD-DEM study, Chemical Engineering Science, 195 (2019) 693–706. https://doi.org/10.1016/j.ces.2018.10.015

Iddir H., Arastoopour H., Modeling of multitype particle flow using the kinetic theory approach, AIChE Journal, 51 (2005) 1620–1632. https://doi.org/10.1002/aic.10429

Ingenia, Imaging the plastic recycling process, Ingenia Magazine, 92 (2022). <https://www.ingenia.org.uk/articles/imaging-the-plastic-recycling-process/> accessed05022024.

Ingram A., Hausard M., Fan X., Parker D., Seville J., Finn N., Evans M., Portable positron emission particle tracking (PEPT) for industrial use, The 12th International Conference on Fluidization, (2007) 497–504.

Jadidi B., Ebrahimi M., Ein-Mozaffari F., Lohi A., A comprehensive review of the application of DEM in the investigation of batch solid mixers, Reviews in Chemical Engineering, 39 (2023) 729–764. https://doi.org/10.1515/revce-2021-0049

Jenkins J.T., Savage S.B., A theory for the rapid flow of identical, smooth, nearly elastic, spherical particles, Journal of Fluid Mechanics, 130 (2006) 187–202. https://doi.org/10.1017/s0022112083001044

Ji L., Chu K., Kuang S., Chen J., Yu A., Modeling the multiphase flow in hydrocyclones using the coarse-grained volume of fluid—discrete element method and mixture-discrete element method approaches, Industrial & Engineering Chemistry Research, 57 (2018) 9641–9655. https://doi.org/10.1021/acs.iecr.8b01699

Jackson R., Johnson P.C., Frictional–collisional constitutive relations for granular materials, with application to plane shearing, Journal of Fluid Mechanics, 176 (2006) 67–93. https://doi.org/10.1017/s0022112087000570

Jones C.R., Corona A., Amador C., Fryer P.J., Dynamics of fabric and dryer sheet motion in domestic clothes dryers, Drying Technology, 40 (2022) 2087–2104. https://doi.org/10.1080/07373937.2021.1918706

Jones J.R., Bridgwater J., A case study of particle mixing in a ploughshare mixer using positron emission particle tracking, International Journal of Mineral Processing, 53 (1998) 29–38. https://doi.org/10.1016/s0301-7516(97)00054-9

Karlsson S., Rasmuson A., van Wachem B., Björn I.N., CFD modeling of the Wurster bed coater, AIChE Journal, 55 (2009) 2578–2590. https://doi.org/10.1002/aic.11847

Ketterhagen W., Wassgren C., A perspective on calibration and application of DEM models for simulation of industrial bulk powder processes, Powder Technology, 402 (2022) 117301. https://doi.org/10.1016/j.powtec.2022.117301

Khodabandehlou R., Askaripour H., Molaei Dehkordi A., Numerical investigation of gas bubble behavior in tapered fluidized beds, Particuology, 38 (2018) 152–164. https://doi.org/10.1016/j.partic.2017.05.013

Kishida N., Nakamura H., Takimoto H., Ohsaki S., Watano S., Coarse-grained discrete element simulation of particle flow and mixing in a vertical high-shear mixer, Powder Technology, 390 (2021) 1–10. https://doi.org/10.1016/j.powtec.2021.05.028

Kosaku Y., Tsunazawa Y., Tokoro C., Investigating the upper limit for applying the coarse grain model in a discrete element method examining mixing processes in a rolling drum, Advanced Powder Technology, 32 (2021) 3980–3989. https://doi.org/10.1016/j.apt.2021.08.039

Kowalski A., Davidson J., Flanagan M., York T., Electrical resistance tomography for characterisation of physical stability in liquid compositions, Chemical Engineering Journal, 158 (2010) 69–77. https://doi.org/10.1016/j.cej.2009.10.054

Kushimoto K., Suzuki K., Ishihara S., Soda R., Ozaki K., Kano J., Development of simpler coarse-grain model for analyzing behavior of particles in fluid flow, Processes, 9 (2021) 1098. https://doi.org/10.3390/pr9071098

Labra C., Ooi J.Y., Sun J., Spatial and temporal coarse-graining for DEM analysis, AIP Conference Proceedings, 1542 (2013) 1258–1261. https://doi.org/10.1063/1.4812167

Leadbeater T.W., Seville J.P.K., Parker D.J., On trajectory and velocity measurements in fluidized beds using positron emission particle tracking (PEPT), The Canadian Journal of Chemical Engineering, 101 (2023) 269–282. https://doi.org/10.1002/cjce.24622

Lichtenegger T., Fast Eulerian-Lagrangian simulations of moving particle beds under pseudo-steady-state conditions, Powder Technology, 362 (2020) 474–485. https://doi.org/10.1016/j.powtec.2019.10.113

Lichtenegger T., Miethlinger T., On the connection between Lagrangian and Eulerian metrics for recurrent particulate flows, Physics of Fluids, 32 (2020) 113308. https://doi.org/10.1063/5.0025597

Lichtenegger T., Peters E.A.J.F., Kuipers J.A.M., Pirker S., A recurrence CFD study of heat transfer in a fluidized bed, Chemical Engineering Science, 172 (2017) 310–322. https://doi.org/10.1016/j.ces.2017.06.022

Lichtenegger T., Pirker S., Recurrence CFD – A novel approach to simulate multiphase flows with strongly separated time scales, Chemical Engineering Science, 153 (2016) 394–410. https://doi.org/10.1016/j.ces.2016.07.036

Lichtenegger T., Pirker S., Toward data-assisted particle-fluid simulations of heat transfer in blast furnaces, Steel Research International, 91 (2020) 2000132. https://doi.org/10.1002/srin.202000132

Lisjak A., Mahabadi O.K., He L., Tatone B.S.A., Kaifosh P., Haque S.A., Grasselli G., Acceleration of a 2D/3D finite-discrete element code for

geomechanical simulations using General Purpose GPU computing, Computers and Geotechnics, 100 (2018) 84–96. https://doi.org/10.1016/j.compgeo.2018.04.011

Liu H., Yoon S., Li M., Three-dimensional computational fluid dynamics (CFD) study of the gas–particle circulation pattern within a fluidized bed granulator: by full factorial design of fluidization velocity and particle size, Drying Technology, 35 (2017) 1043–1058. https://doi.org/10.1080/07373937.2016.1230628

Liu X., Sulaiman M., Kolehmainen J., Ozel A., Sundaresan S., Particle-based coarse-grained approach for simulating dry powder inhaler, International Journal of Pharmaceutics, 606 (2021) 120821. https://doi.org/10.1016/j.ijpharm.2021.120821

Liu X., Zhao M., Hu S., Ge W., Three-dimensional CFD simulation of tapered gas-solid risers by coupling the improved EMMS drag, Powder Technology, 352 (2019) 305–313. https://doi.org/10.1016/j.powtec.2019.04.070

Liu Y., Wang H., Song Y., Qi H., Numerical study on key issues in the Eulerian-Eulerian simulation of fluidization with wide particle size distributions, International Journal of Chemical Reactor Engineering, 20 (2022) 357–372. https://doi.org/10.1515/ijcre-2021-0194

Lu L., GPU accelerated MFiX-DEM simulations of granular and multiphase flows, Particuology, 62 (2022) 14–24. https://doi.org/10.1016/j.partic.2021.08.001

Lu L., Benyahia S., Chapter two - advances in coarse discrete particle methods with industrial applications, in: Parente A., De Wilde J. (Eds.), Advances in Chemical Engineering, Academic Press, 2018a, pp. 53–151, ISBN: 0065-2377. https://doi.org/10.1016/bs.ache.2017.12.001

Lu L., Benyahia S., Method to estimate uncertainty associated with parcel size in coarse discrete particle simulation, AIChE Journal, 64 (2018) 2340–2350. https://doi.org/10.1002/aic.16100

Lu L., Gao X., Li T., Benyahia S., Numerical investigation of the ability of salt tracers to represent the residence time distribution of fluidized catalytic cracking particles, Industrial & Engineering Chemistry Research, 56 (2017a) 13642–13653. https://doi.org/10.1021/acs.iecr.7b03773

Lu L., Morris A., Li T., Benyahia S., Extension of a coarse grained particle method to simulate heat transfer in fluidized beds, International Journal of Heat and Mass Transfer, 111 (2017b) 723–735. https://doi.org/10.1016/j.ijheatmasstransfer.2017.04.040

Lu L., Xu J., Ge W., Yue Y., Liu X., Li J., EMMS-based discrete particle method (EMMS–DPM) for simulation of gas–solid flows, Chemical Engineering Science, 120 (2014) 67–87. https://doi.org/10.1016/j.ces.2014.08.004

Lu L., Xu Y., Li T., Benyahia S., Assessment of different coarse graining strategies to simulate polydisperse gas-solids flow, Chemical Engineering Science, 179 (2018) 53–63. https://doi.org/10.1016/j.ces.2018.01.003

Luding S., Introduction to discrete element methods, European Journal of Environmental and Civil Engineering, 12 (2008) 785–826. https://doi.org/10.1080/19648189.2008.9693050

Chepurniy N., Jeffrey D.J., Lun C.K.K., Savage S.B., Kinetic theories for granular flow: inelastic particles in Couette flow and slightly inelastic particles in a general flowfield, Journal of Fluid Mechanics, 140 (2006) 223–256. https://doi.org/10.1017/s0022112084000586

Lungu M., Siame J., Mukosha L., Comparison of CFD-DEM and TFM approaches for the simulation of the small scale challenge problem 1, Powder Technology, 378 (2021) 85–103. https://doi.org/10.1016/j.powtec.2020.09.071

Lungu M., Siame J., Mukosha L., Coarse-grained CFD-DEM simulations of fluidization with large particles, Powder Technology, 402 (2022) 117344. https://doi.org/10.1016/j.powtec.2022.117344

Maire E., Withers P.J., Quantitative X-ray tomography, International Materials Reviews, 59 (2014) 1–43. https://doi.org/10.1179/1743280413y.0000000023

Marigo M., Davies M., Leadbeater T., Cairns D.L., Ingram A., Stitt E.H., Application of positron emission particle tracking (PEPT) to validate a discrete element method (DEM) model of granular flow and mixing in the Turbula mixer, International Journal of Pharmaceutics, 446 (2013) 46–58. https://doi.org/10.1016/j.ijpharm.2013.01.030

Marigo M., Stitt E.H., Discrete element method (DEM) for industrial applications: comments on calibration and validation for the modelling of cylindrical pellets, KONA Powder and Particle Journal, 32 (2015) 236–252. https://doi.org/10.14356/kona.2015016

Markauskas D., Kačeniauskas A., The comparison of two domain repartitioning methods used for parallel discrete element computations of the hopper discharge, Advances in Engineering Software, 84 (2015) 68–76. https://doi.org/10.1016/j.advengsoft.2014.12.002

Matić J., Stanković-Brandl M., Bauer H., Lovey J., Martel S., Herkenne C., Paudel A., Khinast J., Pharmaceutical hot melt extrusion process development using QbD and digital twins, International Journal of Pharmaceutics, 631 (2023) 122469. https://doi.org/10.1016/j.ijpharm.2022.122469

Sun M., Liu S., Li Z., Lei J., Application of electrical capacitance tomography to the concentration measurement in a cyclone dipleg, Chinese Journal of Chemical Engineering, 16 (2008) 635–639. https://doi.org/10.1016/s1004-9541(08)60133-0

Mihailova O., Lim V., McCarthy M.J., McCarthy K.L., Bakalis S., Laminar mixing in a SMX static mixer evaluated by positron emission particle tracking (PEPT) and magnetic resonance imaging (MRI), Chemical Engineering Science, 137 (2015) 1014–1023. https://doi.org/10.1016/j.ces.2015.07.015

Moliner C., Marchelli F., Spanachi N., Martinez-Felipe A., Bosio B., Arato E., CFD simulation of a spouted bed: comparison between the Discrete Element Method (DEM) and the Two Fluid Model (TFM), Chemical Engineering Journal, 377 (2019) 120466. https://doi.org/10.1016/j.cej.2018.11.164

Moreno-Benito M., Lee K.T., Kaydanov D., Verrier H.M., Blackwood D.O., Doshi P., Digital twin of a continuous direct compression line for drug product and process design using a hybrid flowsheet modelling approach, International Journal of Pharmaceutics, 628 (2022) 122336. https://doi.org/10.1016/j.ijpharm.2022.122336

Mori Y., Wu C.-Y., Sakai M., Validation study on a scaling law model of the DEM in industrial gas-solid flows, Powder Technology, 343 (2019) 101–112. https://doi.org/10.1016/j.powtec.2018.11.015

Musser J., Almgren A.S., Fullmer W.D., Antepara O., Bell J.B., Blaschke J., Gott K., Myers A., Porcu R., Rangarajan D., Rosso M., Zhang W., Syamlal M., MFIX-Exa: a path toward exascale CFD-DEM simulations, The International Journal of High Performance Computing Applications, 36 (2022) 40–58. https://doi.org/10.1177/10943420211009293

Napolitano E.S., Di Renzo A., Di Maio F.P., Coarse-grain DEM-CFD modelling of dense particle flow in gas–solid cyclone, Separation and Purification Technology, 287 (2022) 120591. https://doi.org/10.1016/j.seppur.2022.120591

Nasato D.S., Goniva C., Pirker S., Kloss C., Coarse graining for large-scale DEM simulations of particle flow – an investigation on contact and cohesion models, Procedia Engineering, 102 (2015) 1484–1490. https://doi.org/10.1016/j.proeng.2015.01.282

Neuwirth J., Antonyuk S., Heinrich S., Particle dynamics in the fluidized bed: magnetic particle tracking and discrete particle modelling, AIP Conference Proceedings, 1542 (2013) 1098–1101. https://doi.org/10.1063/1.4812127

Nicuşan A.L., Windows-Yule C.R.K., Positron emission particle tracking using machine learning, Review of Scientific Instruments, 91 (2020) 013329. https://doi.org/10.1063/1.5129251

Nikolopoulos A., Stroh A., Zeneli M., Alobaid F., Nikolopoulos N., Ströhle J., Karellas S., Epple B., Grammelis P., Numerical investigation and comparison of coarse grain CFD – DEM and TFM in the case of a 1MWth fluidized bed carbonator simulation, Chemical Engineering Science, 163 (2017) 189–205. https://doi.org/10.1016/j.ces.2017.01.052

Ostermeier P., DeYoung S., Vandersickel A., Gleis S., Spliethoff H., Comprehensive investigation and comparison of TFM, DenseDPM and CFD-DEM for dense fluidized beds, Chemical Engineering Science, 196 (2019a) 291–309. https://doi.org/10.1016/j.ces.2018.11.007

Ostermeier P., Fischer F., Fendt S., DeYoung S., Spliethoff H., Coarse-grained CFD-DEM simulation of biomass gasification in a fluidized bed reactor, Fuel, 255 (2019b) 115790.

https://doi.org/10.1016/j.fuel.2019.115790
Oyedeji O.A., Brennan Pecha M., Finney C.E.A., Peterson C.A., Smith R.G., Mills Z.G., Gao X., Shahnam M., Rogers W.A., Ciesielski P.N., Brown R.C., Parks Ii J.E., CFD–DEM modeling of autothermal pyrolysis of corn stover with a coupled particle- and reactor-scale framework, Chemical Engineering Journal, 446 (2022) 136920. https://doi.org/10.1016/j.cej.2022.136920
Parker D.J., Hampel D.M., Kokalova Wheldon T., Performance evaluation of the current Birmingham PEPT cameras, Applied Sciences, 12 (2022) 6833. https://doi.org/10.3390/app12146833
Patankar N.A., Joseph D.D., Modeling and numerical simulation of particulate flows by the Eulerian–Lagrangian approach, International Journal of Multiphase Flow, 27 (2001) 1659–1684. https://doi.org/10.1016/s0301-9322(01)00021-0
Pérez-Mohedano R., Letzelter N., Amador C., VanderRoest C.T., Bakalis S., Positron emission particle tracking (PEPT) for the analysis of water motion in a domestic dishwasher, Chemical Engineering Journal, 259 (2015) 724–736. https://doi.org/10.1016/j.cej.2014.08.033
Queteschiner D., Lichtenegger T., Pirker S., Schneiderbauer S., Multi-level coarse-grain model of the DEM, Powder Technology, 338 (2018a) 614–624. https://doi.org/10.1016/j.powtec.2018.07.033
Queteschiner D., Lichtenegger T., Schneiderbauer S., Pirker S., Coupling resolved and coarse-grain DEM models, Particulate Science and Technology, 36 (2018b) 517–522. https://doi.org/10.1080/02726351.2017.1402836
Rammohan A.R., Kemoun A., Al-Dahhan M.H., Dudukovic M.P., A Lagrangian description of flows in stirred tanks via computer-automated radioactive particle tracking (CARPT), Chemical Engineering Science, 56 (2001) 2629–2639. https://doi.org/10.1016/s0009-2509(00)00537-6
Rao K.K., Nott P.R., An Introduction to Granular Flow, Cambridge University Press, Cambridge, 2008, ISBN: 9780521571661. https://doi.org/10.1017/cbo9780511611513
Rasouli M., Bertrand F., Chaouki J., A multiple radioactive particle tracking technique to investigate particulate flows, AIChE Journal, 61 (2015) 384–394. https://doi.org/10.1002/aic.14644
Rasouli M., Dubé O., Bertrand F., Chaouki J., Investigating the dynamics of cylindrical particles in a rotating drum using multiple radioactive particle tracking, AIChE Journal, 62 (2016) 2622–2634. https://doi.org/10.1002/aic.15235
Rasteiro M.G., Silva R.C.C., Garcia F.A.P., Faia P.M., Electrical tomography: a review of configurations and applications to particulate processes, KONA Powder and Particle Journal, 29 (2011) 67–80. https://doi.org/10.14356/kona.2011010
Rhodes M.J., Introduction to Particle Technology. John Wiley & Sons, 2008, ISBN: 978-0470014288.
Rosato A., Windows-Yule K., Segregation in Vibrated Granular Systems, Academic Press, 2020, ISBN: 978-0128141991. https://doi.org/10.1016/c2017-0-00407-x
Roy S., Radiotracer and particle tracking methods, modeling and scale-up, AIChE Journal, 63 (2017) 314–326. https://doi.org/10.1002/aic.15559
Roy S., Larachi F., Al-Dahhan M.H., Duduković M.P., Optimal design of radioactive particle tracking experiments for flow mapping in opaque multiphase reactors, Applied Radiation and Isotopes, 56 (2002) 485–503. https://doi.org/10.1016/s0969-8043(01)00142-7
Rymarczyk T., Kłosowski G., Kozłowski E., Tchórzewski P., Comparison of selected machine learning algorithms for industrial electrical tomography, Sensors, 19 (2019) 1521. https://doi.org/10.3390/s19071521
Sakai M., How should the discrete element method be applied in industrial systems?: a review, KONA Powder and Particle Journal, 33 (2016) 169–178. https://doi.org/10.14356/kona.2016023
Sakai M., Abe M., Shigeto Y., Mizutani S., Takahashi H., Viré A., Percival J.R., Xiang J., Pain C.C., Verification and validation of a coarse grain model of the DEM in a bubbling fluidized bed, Chemical Engineering Journal, 244 (2014) 33–43. https://doi.org/10.1016/j.cej.2014.01.029
Sakai M., Takahashi H., Pain C.C., Latham J.-P., Xiang J., Study on a large-scale discrete element model for fine particles in a fluidized bed, Advanced Powder Technology, 23 (2012) 673–681. https://doi.org/10.1016/j.apt.2011.08.006
Savage S.B., Jeffrey D.J., The stress tensor in a granular flow at high shear rates, Journal of Fluid Mechanics, 110 (2006) 255–272. https://doi.org/10.1017/s0022112081000736
Sawley M.L., Cleary P.W., A parallel discrete element method for industrial granular flow simulations, EPFL Supercomputing Review, 11 (1999) 23–29.
Schaeffer D.G., Instability in the evolution equations describing incompressible granular flow, Journal of Differential Equations, 66 (1987) 19–50. https://doi.org/10.1016/0022-0396(87)90038-6
Schlick C.P., Fan Y., Ottino J.M., Umbanhowar P.B., Lueptow R.M., Granular segregation in circular tumblers: theoretical model and scaling laws, Journal of Fluid Mechanics, 765 (2015) 632–652. https://doi.org/10.1017/jfm.2015.4
Schulze D., Powders and Bulk Solids: Behavior, Characterization, Storage and Flow, Springer-Verlag, Berlin, 2008, ISBN:978-3540737674. https://doi.org/10.1007/978-3-540-73768-1
Scott D.M., McCann H., Process Imaging For Automatic Control, 1st ed., CRC Press, 2005, ISBN9781315220895. https://doi.org/10.1201/9781420028195
Seville J.P., Tüzün U., Clift R., Processing of Particulate Solids, Springer Netherlands, 2012, ISBN: 9789400914599.
Sharifi M., Young B., Electrical resistance tomography (ERT) applications to chemical engineering, Chemical Engineering Research and Design, 91 (2013) 1625–1645. https://doi.org/10.1016/j.cherd.2013.05.026
Shirsath S.S., Padding J.T., Clercx H.J.H., Kuipers J.A.M., Cross-validation of 3D particle tracking velocimetry for the study of granular flows down rotating chutes, Chemical Engineering Science, 134 (2015) 312–323. https://doi.org/10.1016/j.ces.2015.05.005
Shuyan W., Zhenghua H., Dan S., Yikun L., Lixin W., Shuai W., Hydrodynamic simulations of gas–solid spouted bed with a draft tube, Chemical Engineering Science, 65 (2010) 1322–1333. https://doi.org/10.1016/j.ces.2009.09.060
Siegmann E., Enzinger S., Toson P., Doshi P., Khinast J., Jajcevic D., Massively speeding up DEM simulations of continuous processes using a DEM extrapolation, Powder Technology, 390 (2021) 442–455. https://doi.org/10.1016/j.powtec.2021.05.067
Spellings M., Marson R.L., Anderson J.A., Glotzer S.C., GPU accelerated discrete element method (DEM) molecular dynamics for conservative, faceted particle simulations, Journal of Computational Physics, 334 (2017) 460–467. https://doi.org/10.1016/j.jcp.2017.01.014
Šibanc R., Srčič S., Dreu R., Numerical simulation of two-phase flow in a Wurster coating chamber and comparison with experimental results, Chemical Engineering Science, 99 (2013) 225–237. https://doi.org/10.1016/j.ces.2013.05.057
Steuben J., Mustoe G., Turner C., Massively parallel discrete element method simulations on graphics processing units, Journal of Computing and Information Science in Engineering, 16 (2016) 031001. https://doi.org/10.1115/1.4033724
Stroh A., Alobaid F., von Bohnstein M., Ströhle J., Epple B., Numerical CFD simulation of 1 MWth circulating fluidized bed using the coarse grain discrete element method with homogenous drag models and particle size distribution, Fuel Processing Technology, 169 (2018) 84–93. https://doi.org/10.1016/j.fuproc.2017.09.014
Sun W., Brown S., Leach R., An overview of industrial X-ray computed tomography, National Measurement System (NPL), NPL REPORT ENG 32, 2012. http://eprintspublications.npl.co.uk/id/eprint/5385
Sun W., Symes D.R., Brenner C.M., Böhnel M., Brown S., Mavrogordato M.N., Sinclair I., Salamon M., Review of high energy X-ray computed tomography for non-destructive dimensional metrology of large metallic advanced manufactured components, Reports on Progress in Physics, 85 (2022) 016102. https://doi.org/10.1088/1361-6633/ac43f6
Takabatake K., Mori Y., Khinast J.G., Sakai M., Numerical investigation of a coarse-grain discrete element method in solid mixing in a spouted bed, Chemical Engineering Journal, 346 (2018) 416–426. https://doi.org/10.1016/j.cej.2018.04.015
Thompson A.P., Aktulga H.M., Berger R., Bolintineanu D.S., Brown

W.M., Crozier P.S., in't Veld P.J., Kohlmeyer A., Moore S.G., Nguyen T.D., Shan R., Stevens M.J., Tranchida J., Trott C., Plimpton S.J., LAMMPS—a flexible simulation tool for particle-based materials modeling at the atomic, meso, and continuum scales, Computer Physics Communications, 271 (2022) 108171. https://doi.org/10.1016/j.cpc.2021.108171

Toson P., Khinast J.G., Particle-level residence time data in a twin-screw feeder, Data in Brief, 27 (2019) 104672. https://doi.org/10.1016/j.dib.2019.104672

Wang L.B., Frost J.D., Lai J.S., Three-dimensional digital representation of granular material microstructure from X-Ray tomography imaging, Journal of Computing in Civil Engineering, 18 (2004) 28–35. https://doi.org/10.1061/(asce)0887-3801(2004)18:1(28)

Wang L., Park J.-Y., Fu Y., Representation of real particles for DEM simulation using X-ray tomography, Construction and Building Materials, 21 (2007) 338–346. https://doi.org/10.1016/j.conbuildmat.2005.08.013

Wang M., Industrial Tomography: Systems And Applications, 1st edition, Elsevier, 2015, ISBN: 9781782421184. https://doi.org/10.1016/c2013-0-16466-5

Wang S., Shen Y., Coarse-grained CFD-DEM modelling of dense gas-solid reacting flow, International Journal of Heat and Mass Transfer, 184 (2022) 122302. https://doi.org/10.1016/j.ijheatmasstransfer.2021.122302

Wang S., Zhang Q., Ji S., GPU-based parallel algorithm for super-quadric discrete element method and its applications for non-spherical granular flows, Advances in Engineering Software, 151 (2021) 102931. https://doi.org/10.1016/j.advengsoft.2020.102931

Weber J., Bobek M., Rowan S., Yang J., Breault R., Tracker: an open-source particle tracking velocimetry (PTV) application applied to multiphase flow reactors, Proceedings of the ASME-JSME-KSME 2019 8th Joint Fluids Engineering Conference, 5 (2019) V005T05A032. https://doi.org/10.1115/ajkfluids2019-5181

Weber J., Higham J.E., Musser J., Fullmer W.D., Critical analysis of velocimetry methods for particulate flows from synthetic data, Chemical Engineering Journal, 415 (2021) 129032. https://doi.org/10.1016/j.cej.2021.129032

Weinhart T., Thornton A.R., Luding S., Bokhove O., From discrete particles to continuum fields near a boundary, Granular Matter, 14 (2012) 289–294. https://doi.org/10.1007/s10035-012-0317-4

Widartiningsih P.M., Mori Y., Takabatake K., Wu C.-Y., Yokoi K., Yamaguchi A., Sakai M., Coarse graining DEM simulations of a powder die-filling system, Powder Technology, 371 (2020) 83–95. https://doi.org/10.1016/j.powtec.2020.05.063

Windows-Yule C.R.K., Douglas G.J.M., Parker D.J., Competition between geometrically induced and density-driven segregation mechanisms in vibrofluidized granular systems, Physical Review E, 91 (2015) 032205. https://doi.org/10.1103/physreve.91.032205

Windows-Yule C.R.K., Herald M.T., Nicuşan A.L., Wiggins C.S., Pratx G., Manger S., Odo A.E., Leadbeater T., Pellico J., de Rosales R.T.M., Renaud A., Govender I., Carasik L.B., Ruggles A.E., Kokalova-Wheldon T., et al., Recent advances in positron emission particle tracking: a comparative review, Reports on Progress in Physics, 85 (2022a) 016101. https://doi.org/10.1088/1361-6633/ac3c4c

Windows-Yule C., Neveu A., Calibration of DEM simulations for dynamic particulate systems, Papers in Physics, 14 (2022) 140010. https://doi.org/10.4279/pip.140010

Windows-Yule C.R.K., Seville J.P.K., Ingram A., Parker D.J., Positron emission particle tracking of granular flows, Annual Review of Chemical and Biomolecular Engineering, 11 (2020) 367–396. https://doi.org/10.1146/annurev-chembioeng-011620-120633

Windows-Yule C.R.K., Tunuguntla D.R., Parker D.J., Numerical modelling of granular flows: a reality check, Computational Particle Mechanics, 3 (2016) 311–332. https://doi.org/10.1007/s40571-015-0083-2

Windows-Yule C.R.K., Weinhart T., Parker D.J., Thornton A.R., Effects of packing density on the segregative behaviors of granular systems, Physical Review Letters, 112 (2014) 098001. https://doi.org/10.1103/physrevlett.112.098001

Windows-Yule K., Nicuşan L., Herald M.T., Manger S., Parker D., Positron Emission Particle Tracking, IOP Publishing, 2022b, ISBN: 9780750330718. https://doi.org/10.1088/978-0-7503-3071-8

Withers P.J., Bouman C., Carmignato S., Cnudde V., Grimaldi D., Hagen C.K., Maire E., Manley M., Du Plessis A., Stock S.R., X-ray computed tomography, Nature Reviews Methods Primers, 1 (2021) 18. https://doi.org/10.1038/s43586-021-00015-4

Xi K., Guo Q., Boyce C.M., Comparison of CFD-DEM and TFM simulations of single bubble injection in 3D gas-fluidized beds with MRI results, Chemical Engineering Science, 243 (2021) 116738. https://doi.org/10.1016/j.ces.2021.116738

Xie C.G., Reinecke N., Beck M.S., Mewes D., Williams R.A., Electrical tomography techniques for process engineering applications, The Chemical Engineering Journal and the Biochemical Engineering Journal, 56 (1995) 127–133. https://doi.org/10.1016/0923-0467(94)02907-5

Yan B., Regueiro R.A., A comprehensive study of MPI parallelism in three-dimensional discrete element method (DEM) simulation of complex-shaped granular particles, Computational Particle Mechanics, 5 (2018) 553–577. https://doi.org/10.1007/s40571-018-0190-y

Yang Z., Parker D.J., Fryer P.J., Bakalis S., Fan X., Multiple-particle tracking—an improvement for positron particle tracking, Nuclear Instruments and Methods in Physics Research Section A: Accelerators, Spectrometers, Detectors and Associated Equipment, 564 (2006) 332–338. https://doi.org/10.1016/j.nima.2006.04.054

York T., Status of electrical tomography in industrial applications, Journal of Electronic Imaging, 10 (2001) 608–619. https://doi.org/10.1117/1.1377308

Zhang B., Huang Y., Zhao T., Comparison of coarse graining DEM models based on exact scaling laws, Computer Modeling in Engineering & Sciences, 127 (2021a) 1133–1150. https://doi.org/10.32604/cmes.2021.016018

Zhang W., Myers A., Gott K., Almgren A., Bell J., AMReX: block-structured adaptive mesh refinement for multiphysics applications, The International Journal of High Performance Computing Applications, 35 (2021b) 508–526. https://doi.org/10.1177/10943420211022811

Zhou L., Ma H., Liu Z., Zhao Y., Development and verification of coarse-grain CFD-DEM for nonspherical particles in a gas–solid fluidized bed, AIChE Journal, 68 (2022) e17876. https://doi.org/10.1002/aic.17876

Zhou L., Zhao Y., CFD-DEM simulation of fluidized bed with an immersed tube using a coarse-grain model, Chemical Engineering Science, 231 (2021) 116290. https://doi.org/10.1016/j.ces.2020.116290

Zhou Z.Y., Kuang S.B., Chu K.W., Yu A.B., Discrete particle simulation of particle–fluid flow: model formulations and their applicability, Journal of Fluid Mechanics, 661 (2010) 482–510. https://doi.org/10.1017/s002211201000306x

Zwanenburg E.A., Williams M.A., Warnett J.M., Review of high-speed imaging with lab-based X-ray computed tomography, Measurement Science and Technology, 33 (2022) 012003. https://doi.org/10.1088/1361-6501/ac354a

## Authors' Short Biographies

**Dr. Kit Windows-Yule** is a Turing Fellow, a two-time Royal Academy of Engineering Industrial Fellow, Associate Professor of Chemical Engineering at the University of Birmingham. His research concerns the imaging and modelling of particulate and multiphase systems, employing diverse techniques, notably DEM modelling, and Positron Emission Particle Tracking. Current projects include work, funded by EPSRC, the Royal Academy of Engineering and the Royal Society, developing novel plastic recycling methods, work funded by the British Heart Foundation aiming to develop novel methods of blood-flow imaging, and diverse industry-funded projects with partners spanning the aerospace, chemical, defense, food, pharmaceutical, and green energy sectors.

**Dr. Sofiane Benyahia** currently works as a research engineer at the National Energy Technology Laboratory in Albany, Oregon. Dr. Benyahia has more than 20 years' experience conducting computational fluid dynamics (CFD) simulations of multiphase flows resulting in more than 40 peer-reviewed publications. He focuses on developing computationally efficient and physically accurate numerical tools to better understand, predict, and troubleshoot fluidized bed systems at the heart of most energy and chemical industries. Dr. Benyahia earned a bachelor's in chemical engineering from Polytechnic School in Algiers (Algeria) and a doctorate in chemical engineering from Illinois Institute of Technology in Chicago.

**Dr. Peter Toson** studied computer science and physics and received his PhD from the Vienna University of Technology in 2015. From 2016 to 2023, he worked at the Research Center Pharmaceutical Engineering in Graz as a principal scientist. His research focused on the discrete element method, modeling the flow of cohesive powders in pharmaceutical production equipment, especially the unit operations present in continuous direct compression.

**Dr. Hanqiao Che** holds a PhD from the Institute of Engineering Thermophysics, Chinese Academy of Sciences (2018). He was a Research Fellow at the University of Birmingham, specializing in multi-phase flow mechanics, particularly experimental measurement and numerical simulation of gas-solid fluidization. He has co-authored 16+ peer-reviewed papers in renowned journals.

**Dr. Andrei Leonard Nicusan** is a researcher at the University of Birmingham focusing on data-driven engineering across scales. He published featured articles and Scientific Highlights on machine learning-based positron emission particle tracking algorithms. His work on evolutionary algorithms for simulation calibration, optimisation and physics discovery has raised more than £260,000 from research and industrial funding bodies. His frameworks are actively being used in projects with Johnson Matthey, GranuTools, Jacobs Douwe Egberts and Unilever.

KONA Powder and Particle Journal

KONA Powder and Particle Journal No. 42 (2025) 37–56/https://doi.org/10.14356/kona.2025017 Review Paper

# Towards 3D Shape Estimation from 2D Particle Images: A State-of-the-Art Review and Demonstration †

**Priya Tripathi [1], Seung Jae Lee [1]*, Chang Hoon Lee [2] and Moochul Shin [2]**

[1] *Department of Civil & Environmental Engineering, Florida International University, USA*
[2] *Department of Civil & Environmental Engineering, Western New England University, USA*

Particle shape plays a critical role in governing the properties and behavior of granular materials. Despite advances in capturing and analyzing 3D particle shapes, these remain more demanding than 2D shape analysis due to the high computational costs and time-consuming nature of 3D imaging processes. Consequently, there is a growing interest in exploring potential correlations between 3D and 2D shapes, as this approach could potentially enable a reasonable estimation of a 3D shape from a 2D particle image, or at most, a couple of images. In response to this research interest, this study provides a thorough review of previous studies that have attempted to establish a correlation between 3D and 2D shape measures. A key finding from the extensive review is the high correlation between 2D perimeter circularity ($c_p$) and Wadell's true sphericity ($S$) defined in 3D, suggesting that a 3D shape can be estimated from the $c_p$ value in terms of $S$. To further substantiate the correlation between $c_p$ and $S$, this study analyzes approximately 400 mineral particle geometries available from an open-access data repository in both 3D and 2D. The analysis reveals a strong linear relationship between $S$ and $c_p$ compared with other 2D shape descriptors broadly used in the research community. Furthermore, the limited variance in $c_p$ values indicates that $c_p$ is insensitive to changes in viewpoint, which indicates that fewer 2D images are needed. This finding offers a promising avenue for cost-effective and reliable 3D shape estimation using 2D particle images.

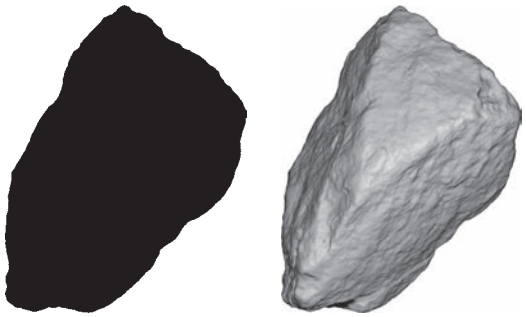


**Keywords:** particle shape, shape descriptor, 3D shape analysis, 2D shape analysis, true sphericity, perimeter circularity

## 1. Introduction

Particle shape significantly influences the macroscopic properties and behavior of granular materials (Cho et al., 2006; Cook et al., 2017; Lee et al., 2017; Payan et al., 2016; Shin and Santamarina, 2013; Stark et al., 2014). For example, track ballast, which is a granular material essential for railroad infrastructure, plays a vital role in facilitating drainage around the tracks and distributing the load from the train traffic, thereby stabilizing the railway track system. The geometry of the ballast particle is a key parameter that affects drainage and significantly affects track performance, including strength, track modulus, and permanent deformation. In the granular materials research community, the influence of particle shape has been studied experimentally (Cho et al., 2006; Lee et al., 2019) and numerically (e.g., using the Discrete Element Method (DEM)) by explicitly modeling particle geometries (Lee, 2014; Lee et al., 2010, 2012, 2021; Lee and Hashash, 2015; Qian et al., 2013; Tutumluer et al., 2018). More recently, 3D-printed synthetic particles have been employed for the investigations. These particles were first digitally represented and then 3D printed for experimental studies to investigate the effect of particle shape (Hanaor et al., 2016; Landauer et al., 2020; Su et al., 2017, 2020b).

Particle shape characterization has been conducted through either 3D or 2D analysis, each with its own distinct methodologies and inherent trade-offs. In 3D analysis, geometric attributes such as the three principal dimensions (such as length, width, and thickness), volume, and surface area are measured using advanced imaging tools, including 3D laser scanning and X-ray microcomputed tomography (μCT). The obtained geometric information is then used to describe the shape, e.g., elongation, flatness, and sphericity. These methods enable us to capture the 3D geometry of particles with greater accuracy, making them increasingly popular in the granular materials research community. Nevertheless, 3D analysis is generally time-consuming, computationally expensive, and labor-intensive. It requires significant effort in the pre- and post-processing of data, as well as in scanning particles whether individually or collectively. In contrast, 2D analysis evaluates planar geometric attributes such as the projected area and perimeter, which are derived from projected 2D particle images. This method, being more traditional with a longer history than

† Received 30 May 2024; Accepted 12 July 2024
J-STAGE Advance published online 31 August 2024
* Corresponding author: Seung Jae Lee;
Add: 10555 W Flagler Street, EC 3603, Miami, FL 33174, USA
E-mail: sjlee@fiu.edu
TEL: +1-305-348-1086 FAX: +1-305-348-2802

3D analysis methods, offers simplicity and speed, making it suitable for rapid assessment of particle shapes. However, it fails to provide a comprehensive understanding of 3D particle geometry. In addition, 2D analysis can be sensitive to changes in viewpoint, which can skew the analysis results.

Given the distinct strengths and limitations of 3D and 2D analysis methods, there is increasing interest in bridging the gap between these two approaches, aiming to ultimately estimate 3D shape properties from a 2D particle image or images. Many review papers have examined various 3D and 2D shape descriptors (Anusree and Latha, 2023; Blott and Pye, 2007; Jia and Garboczi, 2016; Rodriguez et al., 2012). However, there appears to be a lack of comprehensive reviews specifically focusing on the correlation between 3D and 2D shape measures with the goal of estimating 3D shape from 2D particle images.

This review paper aims to examine existing research to identify effective correlations between 3D and 2D shape measures. This review is particularly timely given the recent advances in 3D imaging techniques that facilitate the creation of digitally representable 3D particles and enable more accurate correlations across the different spatial dimensions. The comparative study of 3D and 2D shapes has relevance across disciplines, including applications for general objects in computer graphics fields (Petre et al., 2010). However, this review narrows the focus to mineral particles, ensuring that the findings are relevant and applicable to the field of granular materials research.

We begin by reviewing various 3D and 2D shape analysis methods that have been adopted by the research community, highlighting their benefits and drawbacks. These are discussed in **Sections 2** and **3**. The salient conclusion from the comprehensive reviews (as described in **Section 4**) is that there is a good correlation between Wadell's 3D *true sphericity* ($S$) and 2D *perimeter circularity* ($c_p$), which is attributable to the inherent relevance of their definitions. To further substantiate the findings, this paper includes a study using a dataset of 3D digital particles from the NSF DesignSafe-CI, an open-access data repository (Tripathi et al., 2023). The study analyzes 382 granite and limestone particle geometries in the dataset. The analysis compares the five broadly used 2D circularities, including $c_p$, with the 3D true sphericity ($S$), which is elaborated in **Section 5**. For clarity, the upper-case symbols denote 3D geometric properties, while the lower-case symbols are used to indicate 2D properties throughout this paper. For example, $A$ indicates a particle's surface area in 3D, while $a$ represents the projection area of a particle in 2D.

## 2. 3D shape analysis

### 2.1 3D shape descriptors

Particle shape has been traditionally characterized on three different scales: (i) *form*, (ii) *roundness*, and (iii) *surface texture*, as shown in **Fig. 1**. Form identifies the shape on the scale of particle diameter $D$. Three principal dimensions are commonly used to describe the form of a particle contained in a hypothetical tight box: length ($D_1$), width ($D_2$), and thickness ($D_3$). These dimensions are perpendicular to each other and represent the long, intermediate, and short dimensions, respectively. Ratios derived from these three dimensions are used as form factors to quantify the shape. For example, the $D_2/D_1$ ratio has been traditionally used to indicate *elongation*, and the $D_3/D_1$ ratio has been adopted for *flatness*. Various form classification diagrams have been developed based on this approach, most notably by Zingg (1935), Krumbein (1941), and Sneed and Folk (1958). The lineage of efforts to define the particle form based on three principal dimensions also includes contributions from Wentworth (1923), Corey (1949), Aschenbrenner (1956), Janke (1966), Dobkins and Folk (1970), among others. Interested readers can refer to Blott and Pye (2007), which provides a comprehensive summary of the various form factors. Roundness is defined at an intermediate scale, describing the sharpness of local corners and edges, which is one order of magnitude smaller than the particle diameter scale, i.e., $D/10$ (Cho et al., 2006; Jerves et al., 2016). The diameters of the curvature at the corners are commonly used as major parameters to quantify roundness. Surface texture, which relates to surface roughness at the micro-to-nano scale, requires high-resolution optical characterization (Alshibli et al., 2015). Unlike form and roundness that are characterized optically, surface texture has frequently been characterized mechanically, e.g., through measurements of the interparticle friction angle (Lee and Seed, 1967; Rowe, 1962; Terzaghi et al., 1996). This mechanical characterization is also driven by the fact that intrinsic mineralogy primarily determines surface texture (Terzaghi et al., 1996).

*Sphericity* is another aspect of 3D particle shape and is a measure of how closely the shape of a particle resembles that of a sphere. Wadell (1932) developed the concept of *true sphericity* ($S$) to quantify sphericity. This measure compares the particle's surface area $A$ to the surface area of a sphere with the same volume as the particle $A_s$, as defined in **Eqn. (1)**. He added that sphericity was best measured by

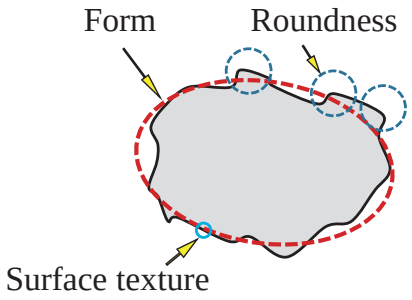


**Fig. 1** Particle shape defined on three different scales Ref. (Mitchell and Soga, 2005).

the true sphericity (Wadell, 1933).

$$S = A_s / A \quad (1)$$

Later, Wadell (1934) introduced an alternative measure of sphericity, denoted as $\Psi$, as defined in **Eqn. (2)**, because of the challenges in measuring surface area. In this definition, $V$ is the volume of a particle, and $V_{cs}$ is the volume of the smallest circumscribed sphere.

$$\Psi = (V / V_{cs})^{1/3} \quad (2)$$

Krumbein (1941) showed that $\Psi$ can be effectively represented by **Eqn. (3)**, where $D'$, $D''$, and $D'''$ are the three principal diameters of an ellipsoid. These diameters, ordered such that $D' > D'' > D'''$, define an ellipsoid with the same volume as the particle. He termed this measure *intercept sphericity*. This approach uses the same definition as the alternative sphericity in **Eqn. (2)** while simplifying the measurement to three principal dimensions.

$$\Psi = (D'' \times D''' / D'^2)^{1/3} \quad (3)$$

There has been some confusion within the granular materials research community regarding whether sphericity is a form factor or a fourth aspect of shape. Sphericity has often been considered a form factor because it can be measured using three principal dimensions, as shown in **Eqn. (3)**. However, many studies have suggested that sphericity is a distinct aspect that is separate from particle form. This view is supported by the fact that Wadell's true sphericity ($S$) is influenced by both form and roundness, highlighting the need to treat sphericity as a distinct characteristic (Barrett, 1980; Blott and Pye, 2007; Zhu and Zhao, 2021). Particle form is defined by particle's three principal dimensions; thus, it is independent of local shape features, such as roundness. However, true sphericity quantifies a comprehensive aspect of shape by measuring equidimensionality in all directions; thus, it is not completely independent of roundness. For example, a cube and a regular dodecahedron are considered 'equant' across the three principal dimensions; thus, they are evaluated as having the same form. However, the regular dodecahedron, which is close to the shape of a perfect sphere, exhibits higher true sphericity. A form described as 'equant' needs only be equidimensional in three directions, whereas a true sphere is equidimensional in all directions; thus, equant shapes are not equally spherical from the perspective of true sphericity. For this reason, it is appropriate to discuss 'sphericity measures' such as $\Psi$ as a form factor, while treating 'true sphericity' $S$ as a distinct fourth aspect of shape, even though $S$ was originally proposed as a shape descriptor to measure sphericity.

Larger-scale properties such as particle form and true sphericity are more critical for understanding 3D shape characteristics than local scale properties like roundness and surface texture. Specifically, the 3D form is defined by three principal dimensions, and true sphericity is measured based on the 3D surface area of the particle. Therefore, these measurements are inherently limited when estimated from 2D projection images. However, since roundness and surface texture are defined at a more localized level, 2D analysis may not result in significant loss of information compared with 3D analysis. This perspective aligns with Wadell's observation: "*while sphericity is essentially a three-dimensional conception, roundness is obtained by measurements in one plane only*" (Wadell, 1932). The minimal emphasis on roundness analysis in 3D may explain why Wadell never proposed a concept of 3D roundness despite his extensive studies on 3D sphericity. Given that surface texture operates at an even smaller scale, the importance of understanding the 3D surface texture may not be as significant. Therefore, the correlation between 3D and 2D shape analyses may provide a more practical value for characterizing form and true sphericity. Therefore, this paper focuses on larger-scale shape properties rather than roundness and surface texture.

## 2.2 Advances and challenges in 3D shape analysis

When the concept of 3D shape description was first conceptualized in the 1920s and later, 3D shape analysis relied on measuring three principal dimensions to quantify form and sphericity. Today, 3D shape analysis is primarily conducted using 3D digital imaging techniques. These methods enable the capture of full particle geometries with unprecedented accuracy, including particle volume and surface area, and facilitate measurements such as true sphericity. The 3D digital imaging techniques adopted within the granular materials research community can be broadly categorized into four approaches: (i) using a set of projection images, (ii) employing general-purpose handheld or desktop 3D scanners that utilize laser or structured light, (iii) applying X-ray micro-computed tomography (μCT), and (iv) utilizing other methods, including various microscopes. Zhang et al. (2019) similarly classified modern 3D shape analysis methods as involving charge-coupled device image processing, laser scanning, or μCT.

(i) 3D shape analysis based on a set of projection images: Early approaches to image-based 3D shape analysis attempted to reconstruct a particle's geometry by combining multiple 2D images from different viewpoints, commonly using three orthogonal projection images. The early efforts include Kuo et al. (1996), Lee et al. (2005), and Cavarretta et al. (2009). Later, researchers at the University of Illinois developed the Enhanced University of Illinois Aggregate Image Analyzer (E-UIAIA), a 3D shape analysis system specifically developed for coarse aggregates, as shown in **Fig. 2**. The proposed system creates a polyhedral digital representation of a 3D particle by combining three orthogonal particle images (Huang and Tutumluer, 2014; Moaveni et al., 2013; Qian et al., 2013). However, using only three

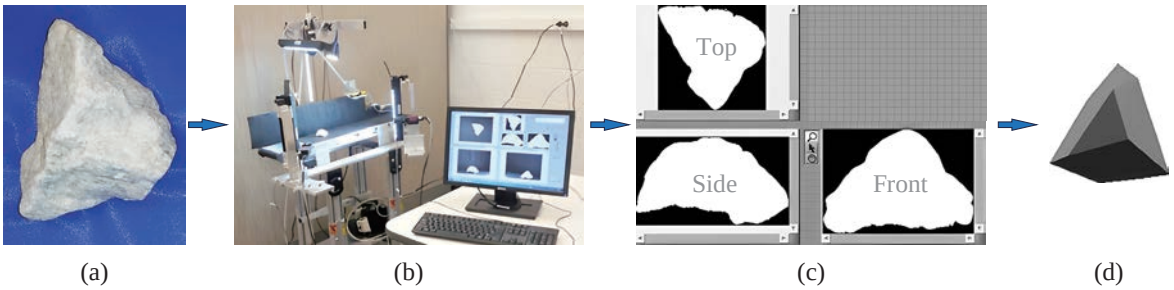


**Fig. 2** E-UIAIA 3D shape analysis system (modified from Qian et al. (2013)): **(a)** mineral particle for analysis; **(b)** particle placed on the E-UIAIA system; **(c)** three orthogonal images of the particle; **(d)** polyhedral representation of the particle, which is subsequently used for 3D shape analysis, e.g., elongation, flatness, and sphericity; image reused with written permission from the publisher.

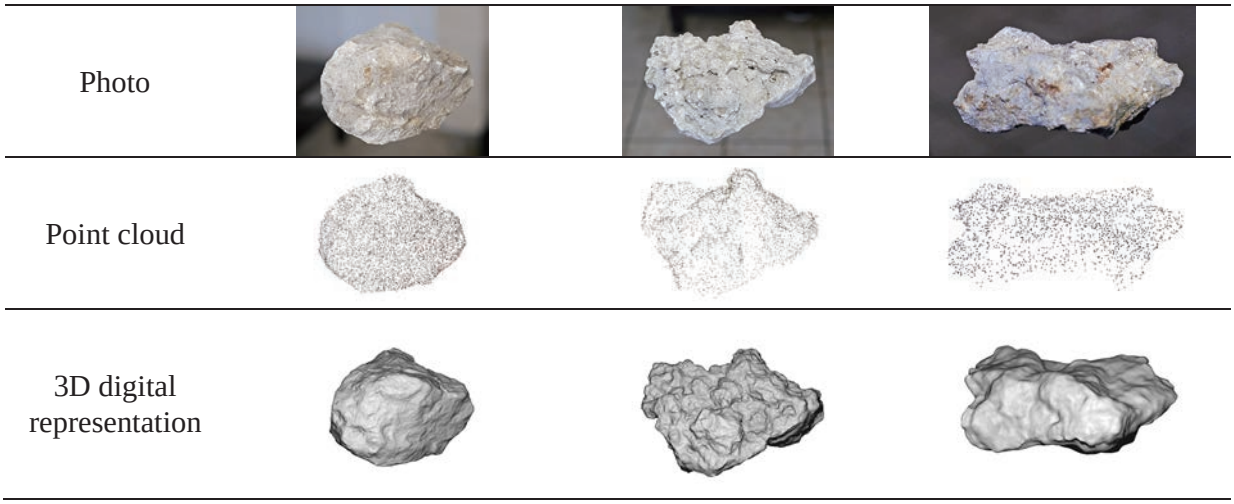


**Fig. 3** Digital representation of 3D particles obtained using structure-from-motion (SfM) photogrammetry (Zhang et al., 2016); image reused with written permission from the publisher.

projections limits its ability to accurately represent detailed particle shapes, such as surface concavities, as depicted in **Fig. 2(d)**. More recent methodologies, such as 3D Dynamic Image Analysis (DIA), extract features from a greater number of projections of a particle, ranging from 8 to 12 (Li Linzhu et al., 2023; Li and Iskander, 2021). Structure-from-motion (SfM) photogrammetry, which is extensively used in the computer vision field, has also been adopted by the granular materials research community. This method facilitates digital representation of 3D particle geometry from multiple photographs taken at random viewpoints with standard or cellphone cameras (Ozturk and Rashidzade, 2020; Paixão et al., 2018; Tunwal and Lim, 2023; Zhang et al., 2016; Zhao et al., 2021). **Fig. 3** shows an example of SfM-based imaging applied to mineral particles. Although this approach enables a more accurate representation of particle shape, capturing detailed geometries requires extensive photographic efforts.

(ii) General-purpose handheld or desktop 3D scanners using laser or structured light: This approach employs laser or structured light (SL), differentiating it from the above-described photo-based approach. A study by Lee et al. (2005) can be considered an early attempt in this category. Their system captured one side of a particle on a conveyor belt, employing a customized setup that combined two cameras and a uniform line laser. While the effect of scanning resolution needs to be further studied, the approach to capture 3D particle geometries employing laser or SL is becoming increasingly popular in the granular materials research community because many commercial tools are available (Bhattacharya et al., 2020; Hu et al., 2023; Latham et al., 2008; Lee C.H. et al., 2022; Lee S.J. et al., 2022; Li et al., 2021; Sun et al., 2014; Tripathi et al., 2023, 2024; Xiao et al., 2020; Yang et al., 2023). **Fig. 4** shows the setup of a 3D SL scanning system applied to mineral particles. **Fig. 5** shows a digitally represented particle obtained by SL scanning.

(iii) X-ray micro-computed tomography (μCT): This technique utilizes an X-ray beam to generate cross-sectional images of a specimen, which are then combined to reconstruct its 3D digital representation. Unlike the other methods that use the selective 'projection' images, this μCT approach employs 'slice' images which are compiled into a 3D digital image. This non-destructive technique allows for detailed visualization of the intricate particle contacts that compose the internal structure of a specimen,

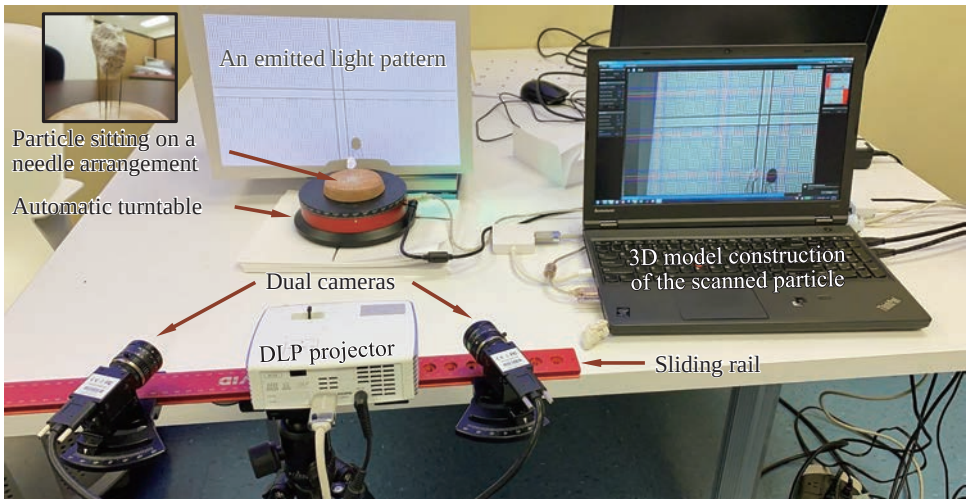


**Fig. 4** 3D structured light (SL) scanning system to capture 3D particle geometry (Bhattacharya et al., 2020); image reused with written permission from the publisher.


**Fig. 5** Captured 3D particle geometry using 3D SL scanning: **(a)** original particle; and **(b)** digitally represented particle (Bhattacharya et al., 2020); image reused with written permission from the publisher.

such as soil fabric. The μCT imaging system is often integrated with conventional laboratory experiments, such as triaxial compression, for *in situ* tomography. Therefore, this setup facilitates the simultaneous loading and scanning of specimen inside a triaxial cell, allowing the observation of changes in the internal structure. Consequently, many studies have adopted μCT to capture changes in soil fabric along with the evolution of particle geometries within soil samples (Al-Raoush, 2007; Alshibli et al., 2015; Bagheri et al., 2015; Bloom et al., 2010; Druckrey et al., 2016; Erdogan et al., 2006; Fei et al., 2019; Fonseca et al., 2012; Fu et al., 2006; Kutay et al., 2010; Li Linzhu et al., 2023; Maroof et al., 2020; Masad et al., 2005; Nie et al., 2020; Su and Yan, 2018a; Vlahinić et al., 2014; Wu et al., 2018; Yang et al., 2017; Zhou et al., 2015; Zhou and Wang, 2017). **Fig. 6** presents a schematic and experimental setup for in situ tomography using μCT. In general, 3D particle geometry characterization using μCT can be categorized into three approaches (Zhao and Wang, 2016): (a) voxel assembly in images (Alshibli et al., 2015; Fonseca et al., 2012; Lin and Miller, 2005; Ueda, 2020; Yang et al., 2017), (b) reconstructed surface mesh (Lin and Miller, 2005), and (c) calculations based on surfaces formed through 3D spherical harmonic (SH) analysis (Cepuritis et al., 2017; Erdogan et al., 2006; Kutay et al., 2011; Masad et al., 2005; Nie et al., 2020; Su and Yan, 2018a; Wei et al., 2022; Zhou et al., 2015; Zhou and Wang, 2017).

(iv) Other 3D analysis methods: These approaches include, but are not limited to, the following: using digital microscopes (Fang et al., 2022), optical tomography systems composed of an inverted microscope and a digital camera (Bloom et al., 2010), confocal microscopes

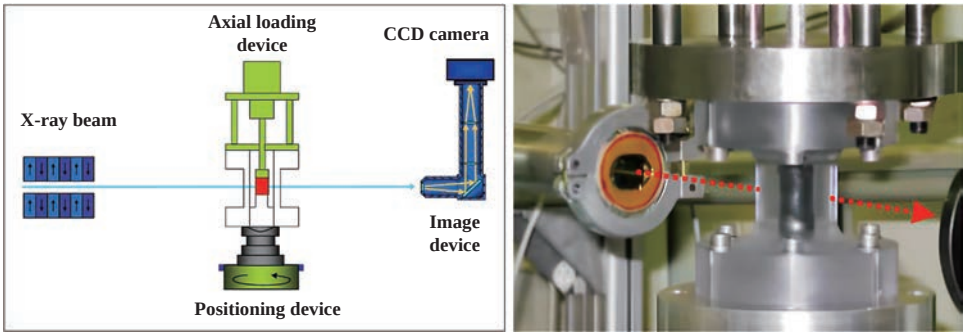


**Fig. 6** X-ray micro-computed tomography (μCT) setup for in-situ tomography: schematic and experimental setup (Bésuelle et al., 2006); image reused with written permission from the publisher.

(McCormick and Gee, 2005), and optoelectronic analysis (Krawczykowski et al., 2022). An approach worth mentioning is the study by Yeong and Torquato (1998), which involved probabilistic reconstruction of mesoscale 3D particulate media from a 2D slice image. This technique has gained interest owing to its ability to extrapolate three-dimensional structures from two-dimensional data, particularly due to the limited access to μCT and computing resources available at the time. Subsequent research has applied this technique to reproduce mesoscale 3D heterogeneous rocks from 2D cross-section images for discrete element simulation (Wei et al., 2023). However, it remains uncertain whether these probabilistically generated 3D particles accurately reflect actual 3D shapes. Additionally, high-fidelity 3D reconstruction is computationally expensive. In their article, it was highlighted that using the exhaustive method to calculate the two-point probability function requires enumerating hundreds of millions of particle pairs, which can easily exceed the memory capacity of a standard personal computer, necessitating the use of Monte Carlo simulations. Consequently, further research is required to determine whether the reconstructed 3D medium truly represents the actual geometries of the particles.

Recent approaches have also adopted Artificial Intelligence and Machine Learning (AI/ML) technologies. Wang et al. (2023) utilized a deep learning-based approach to capture 2D randomly projected images from a vibration screen machine. Zubić and Liò (2021) demonstrated an application within the computer graphics domain to reconstruct 3D models from a 2D image of general objects such as cars and birds. Xiao et al. (2020) introduced an AI/ML-based method for statistically reconstructing 3D particle geometries using trained datasets. There have been attempts to use SfM for field analysis of particles, such as stockpiles, by creating a 3D point cloud directly from images taken on site and then segmenting the point cloud into individual particles. A major challenge arises from the occlusion problem, where only a few particles are fully visible on the surface. To address this issue, Huang et al. (2022) adopted an AI/ML approach to reconstruct the occluded sides of partially visible particles.

A 3D shape analysis is generally considered time-consuming, labor-intensive, and computationally costly. When particles are individually scanned for 3D shape analysis, such as with a desktop 3D scanner: (a) each particle requires multiple scans for full 3D geometry characterization, necessitating the use of a rotating table and flipping particles upside down to capture all sides (Bhattacharya et al., 2020); and (b) a significant number of particles need to be scanned to ensure statistical significance for representing the shapes of the bulk. While scanning a few particles using a handheld or desktop scanner is feasible, scaling up to hundreds or thousands of particles is practically challenging, which limits statistical significance in the analysis. On the other hand, X-ray μCT allows the simultaneous capture of 3D geometries of all particles within a sample, eliminating the need to scan each particle individually (Wu et al., 2018). However, this method is also time-consuming and computationally expensive due to the processes required for sample preparation, operation, and data post-processing (Anusree and Latha, 2023; Bloom et al., 2010; Guida et al., 2020; Roslin et al., 2022). Moreover, μCT equipment is less accessible due to its high initial costs and setup requirements. Radiation safety is another concern with its use. Lastly, irrespective of whether the particles are scanned individually or collectively, the process of creating 3D digital representations of particles for shape analysis typically results in large computer files to preserve detail, sometimes exceeding hundreds of megabytes or even gigabytes per particle. For example, the 382 publicly available 3D particle files in the NSF DesignSafe-CI repository comprise 188 gigabytes, with an average of approximately 500 megabytes per file (Tripathi et al., 2023).

A 3D shape analysis is also costly due to the algorithmic complexities involved in quantifying a shape stemming from the intricacies of 3D analysis (Hu et al., 2023; Lee et al., 2005). Digitally captured 3D particle geometries have been modeled in various ways, including as sphere clumps (Zhao et al., 2021), polyhedrons (Chen et al., 2018; Huang and Tutumluer, 2014), and 3D spherical harmonic (SH) representations (Jia and Garboczi, 2016; Su and Yan, 2018a; Zhou et al., 2015), among others. These methods necessitate additional mathematical operations compared with their 2D counterparts, such as circle clumps, polygons, and 2D Fourier-based models. For a state-of-the-art review of these modeling strategies, please refer to the discussions by Augarde et al. (2021) and Zhao et al. (2023).

## 3. 2D shape analysis

### 3.1 2D shape descriptors

The history of 2D shape analysis based on projected particle images dates back nearly a century to pioneering work by Wentworth (1923), Cox (1927), Tickell (1931), Wadell (1932, 1935), and others. Tickell (1931) introduced a shape descriptor known as *area circularity* ($c_a$), which compares two areas, as detailed in **Eqn. (4)**. Wadell (1933) introduced a measure, then termed *degree of circularity* ($c_p$), which is now commonly referred to as *perimeter circularity* (to distinguish it from various circularities introduced since then in the research community), which compares two perimeters, as shown in **Eqn. (5)**. Wadell (1933, 1935) introduced another descriptor ($c_d$), referred to as *diameter circularity*, which is defined based on two diameters, as shown in **Eqn. (6)**. While $c_d$ is computed based on diameter, it requires calculating the area of the projected particle to determine the diameter of a circle with the same area. Therefore, the adoption of these methods was limited due to the need to manually determine the area and perim-

eter of the projected particle. Although these measurements could be performed using tools such as a planimeter or an opisometer, their widespread use was hindered by the time-consuming nature of the measurement process. Inspired by $c_d$, Riley (1941) proposed the *inscribed circle circularity* ($c_c$), as shown in **Eqn. (7)**. Unlike $c_a$, $c_p$, or $c_d$, the shape descriptor $c_c$ does not require measurement of the area or perimeter, eliminating the need for a planimeter or opisometer; thus, it has been favored in practice due to its simplicity of measurement and ability to deliver results similar to those of $c_d$ (Blott and Pye, 2007). Another traditional circularity is $c_{wl}$ in **Eqn. (8)**, known as *width-to-length ratio circularity*, which quantifies a particle shape by comparing two principal dimensions. A schematic of the 2D shape analysis is shown in **Fig. 7**, where the raw projection image is binarized to capture the outline and geometric parameters are then applied to evaluate the circularity. It is worth noting that in the original publications, some of these metrics are referred to as sphericities, not circularities. However, to emphasize their 2D nature and avoid confusion with 3D sphericities, we refer to them as circularity in this review.

$$c_a = a / a_{cc} \quad (4)$$
$$c_p = p_c / p \quad (5)$$
$$c_d = d_c / d_{cc} \quad (6)$$
$$c_c = (d_{ci} / d_{cc})^{1/2} \quad (7)$$
$$c_{wl} = d_2 / d_1 \quad (8)$$

In **Eqns. (4)** to **(8)**, the variables are defined as follows:
$a$ is the projection area of a particle.
$a_{cc}$ is the area of the smallest circle circumscribing a particle.
$p_c$ is the perimeter of a circle with the same area as the projected particle.
$p$ is the perimeter of the projected particle.
$d_c$ is the diameter of a circle with the same area as the projected particle.
$d_{cc}$ is the diameter of the smallest circumscribing circle.
$d_{ci}$ is the diameter of the largest inscribed circle.
$d_1$ is the largest dimension of the particle.
$d_2$ is the width of a particle, orthogonal to $d_1$.

The $c_{wl}$ is evaluated based on two principal dimensions; thus, it can be perceived as a measure of 2D form. Pye and Pye (1943) analytically derived that $c_d$ is essentially the square root of $c_{wl}$, indicating that $c_d$ is also a 2D form factor. They showed that $d_c$ can be expressed as the square root of the product of two principal dimensions of an ellipse with the same area, i.e., $d_c = (d'd'')^{1/2}$ , where $d' > d''$. Subsequently, by substituting $a = \pi(d_c / 2)^2$ and $a_{cc} = \pi(d' / 2)^2$ into **Eqn. (4)**, it becomes evident that $c_a$ essentially acts as a 2D form factor. Given the equivalence between $c_d$ and $c_c$, as discussed by Riley (1941), $c_c$ can be considered a measure of the 2D form. Therefore, except for $c_p$, the other circularities essentially serve as 2D form factors.

There are variations indicating circularity. For instance, many studies, including Bagheri et al. (2015), introduced *Cox circularity* ($c_{cox}$) after Cox (1927). However, note that $c_{cox}$ is essentially the same as $c_p$. The definition of $c_{cox}$ is provided in **Eqn. (9)**, where $a$ and $p$ follow the definitions given in **Eqns. (4)** and **(5)**. Given that $a = \pi(d_c / 2)^2$, it follows that $4\pi a = p_c^2$. Therefore, $c_{cox}$ is the square of $c_p$. Kuo and Freeman (2000) also discussed this equivalency. Additionally, some articles introduced a different version of $c_c$. Originally presented in the square root format as shown in **Eqn. (7)**, the version without the square root is also used and is referred to as *circle ratio sphericity* (Zheng and Hryciw, 2015).

$$c_{cox} = 4\pi a / p^2 = c_p^2 \quad (9)$$

The five circularities from **Eqns. (4)** to **(8)** are the most commonly used circularities in the granular materials research community for measuring 2D shapes (Mitchell and Soga, 2005; Zheng and Hryciw, 2015). An additional series of 2D shape descriptors have been developed in the research community, expanding on traditional descriptors. These include shape measures using radial segments (Sukumaran and Ashmawy, 2001), Fourier descriptors

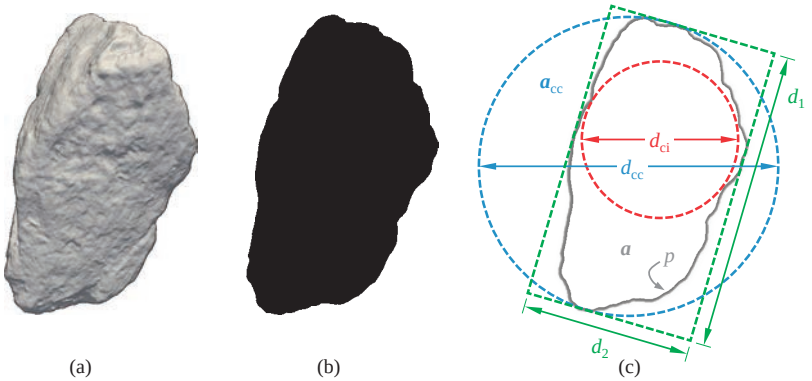


**Fig. 7** Schematic of 2D shape analysis: **(a)** raw projection image; **(b)** binary image derived from captured image for 2D shape analysis; and **(c)** geometric parameters used to assess circularities.

(Bowman et al., 2001; Chen et al., 2022; Su and Yan, 2018b; Wang et al., 2005), and fractal analysis (Bouzeboudja et al., 2022; Guida et al., 2020). A comprehensive review of broadly used 2D circularities and form factors is provided in other review papers, including those by Blott and Pye (2007) and Rodriguez et al. (2012).

### 3.2 Advances and challenges in 2D shape analysis

Modern digital imaging technology has enabled rapid analysis of shape and size based on 2D particle images (Hryciw et al., 2014). Early initiatives, such as those by Kwan et al. (1999), used digital particle image processing to analyze the shape characteristics of coarse aggregates. Notably, WipFrag, a commercial image-based particle geometry analyzer, has been available since the 1990s, primarily for size analysis (Maerz et al., 1996; WipWare, 2023). Subsequent developments include the Aggregate Image Measurement System (AIMS) (Chandan et al., 2004; Masad et al., 2005; Masad, 2005) and its successor, AIMS2 (Gates et al., 2011), which were specifically designed to characterize aggregate geometries. Bloom et al. (2010) employed an optical microscopic system consisting of a Nikon TS100 microscope and a Coolpix950 2-megapixel digital camera for 2D particle geometry characterization. With the advent of scanning electron microscopy (SEM) techniques, capturing the 2D shapes of fine particles has become more straightforward (Kodicherla, 2023).

Recently, dynamic image analysis (DIA) systems have gained popularity in the research community. These systems allow particles to fall through a vertical chute, where high-resolution, high-speed cameras optically capture them for further geometric analysis. Several commercial products such as QICPIC (Sympatec GmbH, 2022) have been used in research (Cavarretta et al., 2009; Krawczykowski et al., 2022; Li and Iskander, 2020; Zhou and Wang, 2017). Although this method provides rapid characterization, researchers have noted issues associated with its somewhat limited resolution. Cepuritis et al. (2017) highlighted the limitation of accurately characterizing particles smaller than approximately 40 μm due to the relatively large pixel size of the DIA system. Li and Iskander (2021) also noted similar resolution limitations in their discussion of 2D DIA measurements.

Attempts have also been made to estimate the 3D geometry of particle shapes from a single image by augmenting 2D imaging. Montenegro Ríos et al. (2013) employed a light source alongside a digital camera system to estimate the third dimension based on projected shadows. Additionally, Zheng and Hryciw (2017) introduced a stereophotography approach for estimating the third dimension of particles.

An advantage of 2D analysis includes its potential to conveniently analyze shapes from field photographs, such as those taken from stockpiles, making it useful for field inspections and on-site geometry quantification (Moaveni et al., 2013; Tutumluer et al., 2017). The process involves an image segmentation phase to identify individual particles in the photo, followed by 2D shape analysis to quantify the geometry. Various image segmentation algorithms and software are available, including the watershed segmentation algorithm (Vincent and Soille, 1991), which effectively isolates individual particles in an image. With recent advances in AI/ML techniques, image segmentation has become more convenient, as demonstrated by tools such as Meta AI's Segment Anything (Meta, 2023). **Fig. 8** shows an example in which different colors indicate the segmented particles. Nevertheless, perfecting this process for analyzing particle geometry in the field is ongoing, with limited success. Challenges such as inaccuracies caused by shadows and occlusion, where particles are partially obscured by nearer particles in the images, require further investigation in future. Consequently, 2D shape analysis is still predominantly conducted in a laboratory environment.

The major disadvantage of 2D shape analysis is its susceptibility to changes in viewpoint and sensitivity, resulting in analysis outcomes that depend on how a particle is projected (Alshibli et al., 2015; C.H. Lee et al., 2022; Li Lianghui et al., 2023; Zheng et al., 2021). This limitation can be addressed by capturing a sufficient number of 2D images for each particle and repeating this process for a large number of particles to achieve statistical significance (Cepuritis et al., 2017); however, this approach compromises the primary advantages of 2D analysis—speed, simplicity, and convenience. Given the uncertainties regarding the required number of 2D samples per particle, researchers have made different and often contradicting suggestions. Xie et al. (2020) suggested using three orthogonal projections, although they acknowledged the practical difficulties in field applications and therefore recommended using three maximum-area and three minimum-area projections as alternatives. Li Linzhu et al. (2023) employed Digital Image Analysis (DIA) with 8 to 12 projections per

**Fig. 8** Image segmentation performed on a photo using the Segment Anything code. The raw photo was taken from DepositPhotos (2014) and used under its standard license.

particle, but they argued that this number may not sufficiently capture the 3D geometry of particles. Zhao et al. (2021) reported that even 50 2D projection images may not faithfully represent 3D particle geometry. Attempts have also been made to optimize the number of particle projections required for effective and efficient 2D characterization (Křupka and Říha, 2015). In general, 2D shape analysis compromises accuracy and a comprehensive understanding of 3D particle geometry, in favor of speed and convenience.

## 4. Correlation between 3D and 2D shape measures

### 4.1 Approaches and challenges in estimating 3D shape from 2D images

There has been a growing interest within the research community in bridging the gap between 3D and 2D shape analyses due to their distinct strengths and limitations. This interest stems from the vision to leverage the speed and simplicity of 2D analysis while obtaining the accuracy of 3D analysis. Efforts to achieve this integration include the development of a 2D-to-3D conversion database via particle sampling. This process begins by conducting 3D imaging to digitally represent the 3D particle geometry, followed by creating a series of 2D projections to generate a set of 2D digital images. These images were then analyzed to develop a conversion database that could later be used to estimate 3D geometry from 2D images (Ueda, 2020; Ueda et al., 2019; Wang et al., 2019). However, opinions vary regarding the efficacy of this approach. Studies investigating this relationship have reported a range of conclusions, from limited effectiveness to highly promising results, indicating a complex and evolving understanding of the potential for integrating 2D and 3D shape analyses.

Many studies have concluded that using 2D shape parameters, obtained from projected particle images, to estimate 3D shape properties is inherently limited, as capturing the full complexity of a 3D shape by a 2D particle image, or even a set of 2D images, cannot adequately represent all dimensions (Alshibli et al., 2015; Bouzeboudja et al., 2022; Fonseca et al., 2012; Hu et al., 2023; Jia and Garboczi, 2016; C.H. Lee et al., 2022; Li Lianghui et al., 2023; Li Linzhu et al., 2023; Li and Iskander, 2021; Maroof et al., 2020; Su et al., 2019; Sun et al., 2014; Zheng et al., 2021). The 2D shape analysis captures only the planar geometry attributes of a particle, thereby missing critical information about its 3D geometry. Additionally, 2D descriptions are dependent on viewpoint, which can compromise the reliability of shape characterization.

Nevertheless, many other studies have demonstrated the significant potential of using 2D particle images to estimate 3D shapes, often reporting a strong correlation between 3D and 2D shape analysis results. This suggests that the relationship between 3D and 2D geometry measures could be leveraged in a 2D-to-3D approach, indicating a viable pathway for reasonably deriving 3D shape properties from 2D data (Cavarretta et al., 2009; Cepuritis et al., 2017; Han et al., 2023; Kaviani-Hamedani et al., 2024; Krawczykowski et al., 2022; Kutay et al., 2011; Lu et al., 2022; Masad et al., 2005; Ozturk and Rashidzade, 2020; Sandeep et al., 2023; Suh et al., 2017; Xie et al., 2020; Zhao et al., 2021; Zheng et al., 2019).

The granular materials research community has developed a diverse array of shape descriptors (Alshibli et al., 2015; Chandan et al., 2004; Fang et al., 2022; Hu et al., 2023; Kong and Fonseca, 2018; S.J. Lee et al., 2022; Su et al., 2020a; Sun et al., 2014; Xiao et al., 2020). The large number of currently available descriptors can be overwhelming and can even lead to confusion (Cavarretta et al., 2009; Maroof et al., 2020). As a result, the correlation between 3D and 2D shape measures, whether strong or weak, often hinges on the specific shape descriptors selected from the available array. For instance, Ozturk and Rashidzade (2020) noted a good correlation between 3D sphericity and 2D circularity measures they selected for their study. However, they found no significant correlation with the form factors, demonstrating that the effectiveness of using 2D data to estimate 3D shapes varies depending on the descriptor employed.

For a successful 2D-to-3D approach, the ‘mean’ value of 2D shape measures obtained from a set of 2D images should have a strong relationship with the 3D shape measure. For example, by capturing ten 2D projection images of a particle from various viewpoints and evaluating the 2D shape using a circularity descriptor, one should find that the mean value of these circularity measurements strongly correlates with the 3D shape measurement across all sample particles. This indicates a robust correlation between 2D circularity and 3D shape measure, fulfilling a necessary condition for the 2D-to-3D approach. At the same time, it is equally important that the 2D shape measures exhibit a low ‘variance’ and remain insensitive to changes in viewpoints. Even if 2D shape measures show a strong mean relationship with 3D measures, high variance caused by differing viewpoints requires capturing many 2D images to estimate a 3D shape accurately and reliably. Such requirement could limit the practicality and efficiency of the 2D-to-3D approach because the need for more images complicates the process and reduces its overall feasibility. For instance, Zheng et al. (2021) reported that the variation in the data obtained from random-projection tests was too substantial to reliably infer 3D particle shapes. This problem is inherently an ill-posed problem because the variance arises solely from 2D images despite the corresponding 3D descriptor exhibiting zero variance. Consequently, this variability has led some researchers to view the 2D-to-3D approach skeptically due to significant data scatter, despite the strong correlation between the mean values of 2D and

3D shape measures.

Therefore, to establish a reliable 2D-to-3D relationship for 3D shape estimation from a 2D particle image, or at most a couple of images, it is essential to identify a set of 2D and 3D shape descriptors that address both criteria regarding 'mean' and 'variance'. Specifically: (i) when multiple 2D projection images are available, the mean value of the 2D shape measures should exhibit a strong relationship with the measures from the 3D shape descriptor, and (ii) the 2D shape measures must be minimally sensitive to variations in viewpoint to ensure consistent results, although determination of the satisfactory tolerance may depend on the cases. The achievement of a relatively low variance in 2D shape measures is critical for minimizing discrepancies in quantifying a shape, thereby enhancing the reliability of 3D shape estimation. If such a set of 2D and 3D shape descriptors can be identified, it will be possible to confidently use a smaller number of 2D particle images, ideally even a single random 2D image, for accurate 3D shape estimation.

### 4.2 Correlation between 3D true sphericity and 2D perimeter circularity

As discussed in **Section 3.1**, $c_a$, $c_d$, $c_c$, and $c_{wl}$ function as 2D form factors. According to our comprehensive review, no meaningful correlation has been identified between these circularities and a 3D form factor. The 3D form is characterized using three principal dimensions to measure equidimensionality in three directions, whereas the 2D form relies on only two principal dimensions from the projected particle image. Thus, this inherent limitation restricts the accuracy of estimating 3D form from 2D form measurements.

On the other hand, a number of studies have observed a modest-to-good correlation between 2D perimeter circularity ($c_p$) and 3D true sphericity ($S$), commonly showing that the mean values of $c_p$ correlate well with $S$ (Cavarretta et al., 2009; Han et al., 2023; Rorato et al., 2019; Sandeep et al., 2023; Su and Yan, 2020; Xie et al., 2020; Zheng et al., 2019). For example, Sandeep et al. (2023) demonstrated that $S$ was more closely related to $c_p$ than to other circularities. The higher correlation likely stems from the equivalence of their definitions across the different spatial dimensions. In 2D space, the projected area captures the object's footprint, and the perimeter defines its boundary. In parallel, in 3D space, the volume captures the full extent of an object, and the surface area defines its boundary. Accordingly, the definition of $c_p$, as presented in **Eqn. (5)** serves as the 2D counterpart of $S$ in **Eqn. (1)**. Wadell (1933) indeed introduced both 3D true sphericity ($S$) and 2D perimeter circularity ($c_p$) using similar notations, implying that $c_p$ was developed as a 2D version of $S$ (see pages 317 and 321 to compare the definitions in the article). Rorato et al. (2019) also noted that perimeter circularity is the 2D descriptor that best correlates with true sphericity, reflecting the equivalence of their definitions in 2D and 3D. Therefore, among the traditional circularities discussed in **Section 3.1**, $c_p$ is unique in that it serves as a 2D version of true sphericity.

If the mean of $c_p$ demonstrates good correlation with $S$, then it is essential to assess how sensitive $c_p$ is to random projections. A recent study by Lee et al. (2022) reported that $c_p$ showed the smallest variance compared with other classical 2D shape descriptors, indicating its relatively low sensitivity to how a particle is projected. This indicates that $c_p$ can be reliably used to estimate 3D shape from 2D images, highlighting its potential for robust 3D shape analysis based on random 2D projections. Bagheri et al. (2015) is another study that confirmed a strong correlation between the mean values of $c_p$ and $S$, while emphasizing that the standard deviation of $c_p$ data is notably low. (They analyzed $c_{cox}$, which is the square of $c_p$.) The study suggested that if $c_p$ is employed, the use of a minimum number of projection images—specifically two projections, including minimum and maximum projections, or three perpendicular projections—can achieve an optimal balance between efficiency and accuracy. This approach was found to limit the maximum error to less than 10 %, even when compared to scenarios utilizing up to 1000 projections, demonstrating that $c_p$ maintains a relatively invariant nature regardless of how a particle is projected. This consistency implies that a limited number of 2D projection images can effectively estimate a 3D shape using $c_p$ due to its low variance and strong correlation with $S$.

Wadell originally developed 2D circularities, $c_p$ and $c_d$, to address the practical challenges associated with measuring 3D surface areas for quantifying particle shapes as defined by true sphericity $S$ (Hayakawa and Oguchi, 2005; Howarth, 2017). With 3D imaging tools, it is now possible to evaluate 3D particle geometry in terms of $S$ with high accuracy. These techniques present an opportunity to re-examine the correlation between 2D circularity and 3D sphericity, particularly between $c_p$ and $S$, given their definitional equivalency. Establishing a strong correlation between these shape measures will significantly enhance the accuracy of estimating 3D shape from random projection 2D particle images.

## 5. Demonstration

To further substantiate the findings from the literature review, a series of shape analyses is conducted to determine (i) whether there is a strong correlation between 3D true sphericity ($S$) and the mean of 2D perimeter circularity ($c_p$), among others, and (ii) whether the variance of $c_p$ is minimal compared to those of other 2D shape measures, thereby making it a more reliable predictor of 3D shape from any 2D projection image.

### 5.1 3D and 2D shape analyses

This study analyzes an extensive dataset of 382 mineral particles sourced from Florida and Virginia. All particles from Florida in this dataset are limestone, while all particles from Virginia are freshly crushed granite sourced from a quarry in Richmond, Virginia. The Florida limestone (FL) particles are composed of three groups: FL-A, FL-B, and FL-C. The FL-A group consists of 100 limestone particles selected from a batch provided by the Florida Department of Transportation (FDOT) from District Four and Six regions in South Florida. The FL-B and FL-C groups, supplied by Titan America LLC, each comprises 50 particles sourced from the same limestone quarry and processed using different crushers. The Virginia granite (VG) particles, also provided by Titan America LLC, are composed of two groups: VG-A and VG-B. The VG-A group includes 100 randomly selected granite particles, while group VG-B consists of 82 particles containing crushed particles from the same granite batch. Therefore, the dataset comprises five distinct groups of 382 particles.

#### 5.1.1 3D shape analysis procedure

Each particle is individually scanned to digitally represent the 3D geometry using a Polyga C504 structured light (SL) 3D scanner. This scanner is capable of scanning objects ranging from 5 to 30 mm in size with high resolution and accuracy, down to 6 microns (Polyga, 2021). The scanning setup is shown in **Fig. 9**. Each particle is placed on a small clump of putty to scan one side of its surface at a time (**Fig. 9a**). The particle is rotated while the 3D scanner, which is positioned directly above, captures its geometry from all corners to ensure comprehensive coverage (**Fig. 9b**). The particle is turned upside down, and scanning continues to ensure that all sides are captured thoroughly. Approximately 15 to 20 scans are performed per particle to complete the process. The scanned partial geometries are merged to create a 3D digital particle that realistically represents the original particle (**Fig. 9c**), for which the companion software FlexScan3D is employed. The 3D digital particle is created in the Wavefront .obj file format. The 3D particle geometry attributes, including surface area ($A$) and volume ($V$), are measured using the 3D print toolbox in Blender (2022), an open-source 3D computer graphics software. An advantage of SL scanning is that it performs 3D scanning at a 1-to-1 scale, which means that the captured 3D digital particle is the exact size of the original particle (Lansdown, 2019). As a result, the particle surface area and volume can be directly obtained from 3D digital particles without the need for re-scaling. These values are then used to compute the true sphericity ($S$) per **Eqn. (1)**. Listing the 3D geometry information obtained for all 382 particles is extensive, but readers can directly refer to the dataset, which is publicly available in the NSF DesignSafe-CI data repository (Tripathi et al., 2023).

#### 5.1.2 2D shape analysis procedure

Ten 2D projection images are captured from random viewpoints for each particle using ParaView (Kitware Inc., 2022), as illustrated in the first row of **Fig. 10**. A custom Python script is developed to automate this random projection process in batch mode. Subsequently, each 2D image is converted into a binary format with the background in white and the foreground (particle) in black to capture the outline geometry, as depicted in the second row of **Fig. 10**. OpenCV (2023) is used for this binary conversion. This process generates 3820 2D projection images. These 2D binary images are then used to analyze the 2D shape in terms of five commonly used circularities, $c_a$, $c_p$, $c_d$, $c_c$, and $c_{wl}$, as shown in **Eqns. (4)** to **(8)**. The 2D analysis uses MATLAB code developed by Zheng and Hryciw (2016),

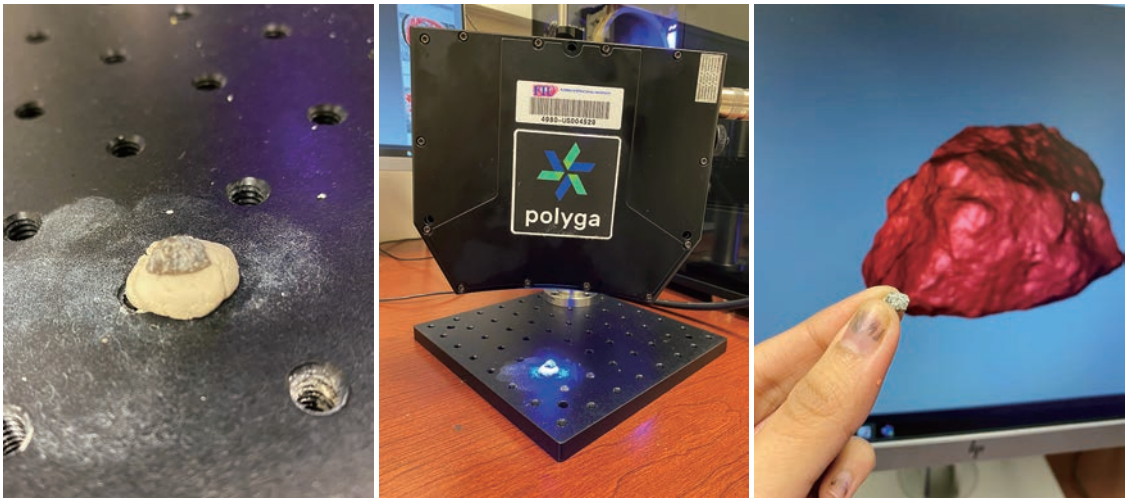


(a) (b) (c)

**Fig. 9** 3D scanning of a particle: **(a)** particle placed on putty; **(b)** 3D scan conducted using Polyga C504 SL 3D scanner; and **(c)** digitally represented 3D particle (shown on the screen); image source: Tripathi et al. (2023), available under the Open Data Commons Attribution License.

originally developed as a companion code to their earlier work (Zheng and Hryciw, 2015). The circularity measure $c_c$ computed by this code differs from the original definition by Riley (1941) as per **Eqn. (7)**. Therefore, the code is modified to align with Riley's original formulation. The mean and standard deviation of the circularity measures are then computed for each particle.

## 5.2 Analysis results

The analysis results for the five particle groups, FL-A, FL-B, FL-C, VG-A, and VG-B, are presented in **Figs. 11–15**. Each data point in the figures represents the shape analysis result for a particle. **Fig. 16** aggregates the data for all five particle groups. In the figures, the *x*-coordinate of the data point represents the mean ($\mu$) of circularities evaluated from ten 2D projection images of each particle. These are assessed using five circularity measures: $c_a$, $c_p$, $c_d$, $c_c$, and $c_{wl}$, as shown in the figures. In the first-row figures, the *y*-coordinate represents the evaluated true sphericity ($S$), comparing the mean circularity values with $S$. The blue line in the figure indicates the regression line for the data points, and the coefficient of determination ($R^2$) indicates the data's coherence with the regression line. In the second-row figures, the *y*-coordinate represents the standard deviation ($\sigma$) of circularities, evaluated from the ten 2D projection images of each particle. This comparison highlights how standard deviations relate to mean values.

From all first-row figures in **Figs. 11–16**, it is apparent that the mean of $c_p$ values, $\mu(c_p)$, demonstrates a relatively strong linear relationship with $S$, with the data points clustered coherently along the regression line. Compared with the other circularity measures, $c_p$ consistently exhibits the highest $R^2$ value across all five particle groups. This indicates the reliability of using $c_p$ as a predictive measure, as evidenced by prior studies. Furthermore, from all second-row figures, it is evident that the distributed values of the standard deviation of $c_p$, $\sigma(c_p)$, are significantly lower than those of other circularity measures. This indicates that a random 2D projection image yields a comparable $c_p$ value, demonstrating its insensitivity to viewpoint changes around a particle. However, the other circularities, $c_a$, $c_d$, $c_c$, and $c_{wl}$, do not exhibit a strong linear relationship with $S$ as compared with $c_p$, as indicated by the low $R^2$ values and high data scatter. This lack of correlation may be explained by the fact that $c_a$, $c_d$, $c_c$, and $c_{wl}$ function as 2D form factors, whereas $c_p$ acts as the 2D analog of true sphericity,

**Fig. 10** Ten 2D projection images of a VG-A particle.

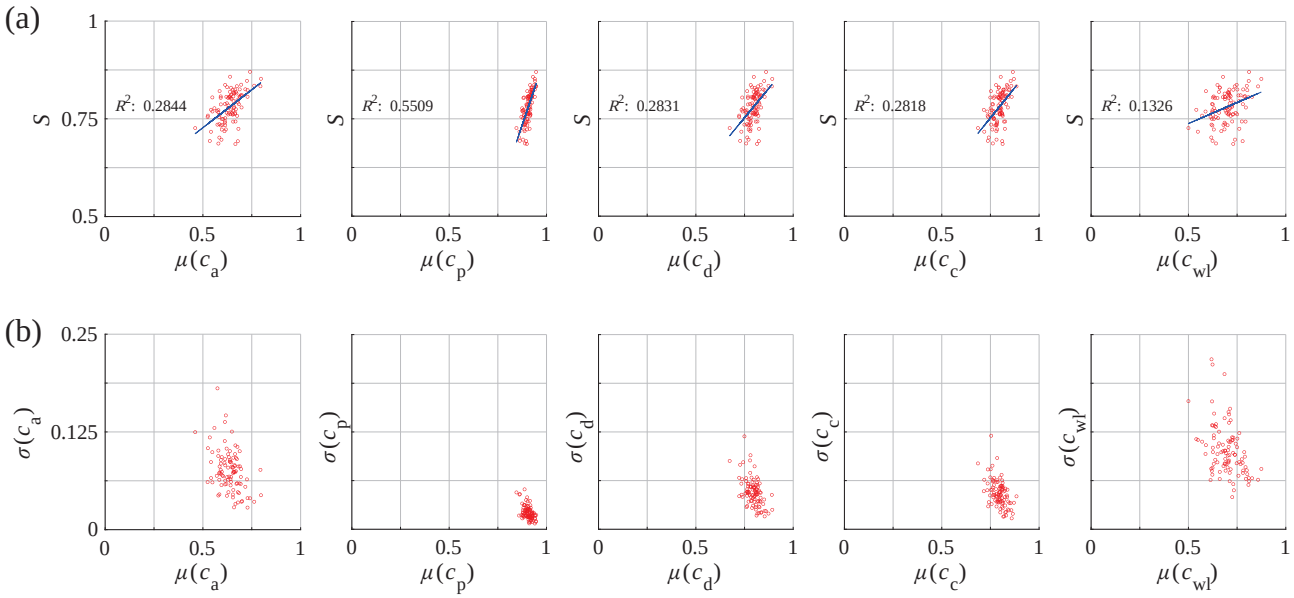


**Fig. 11** 2D and 3D shape analysis results for FL-A particles. **(a)** Mean ($\mu$) of 2D circularities vs. 3D true sphericity $S$, **(b)** mean ($\mu$) vs. standard deviation ($\sigma$) of 2D circularities.

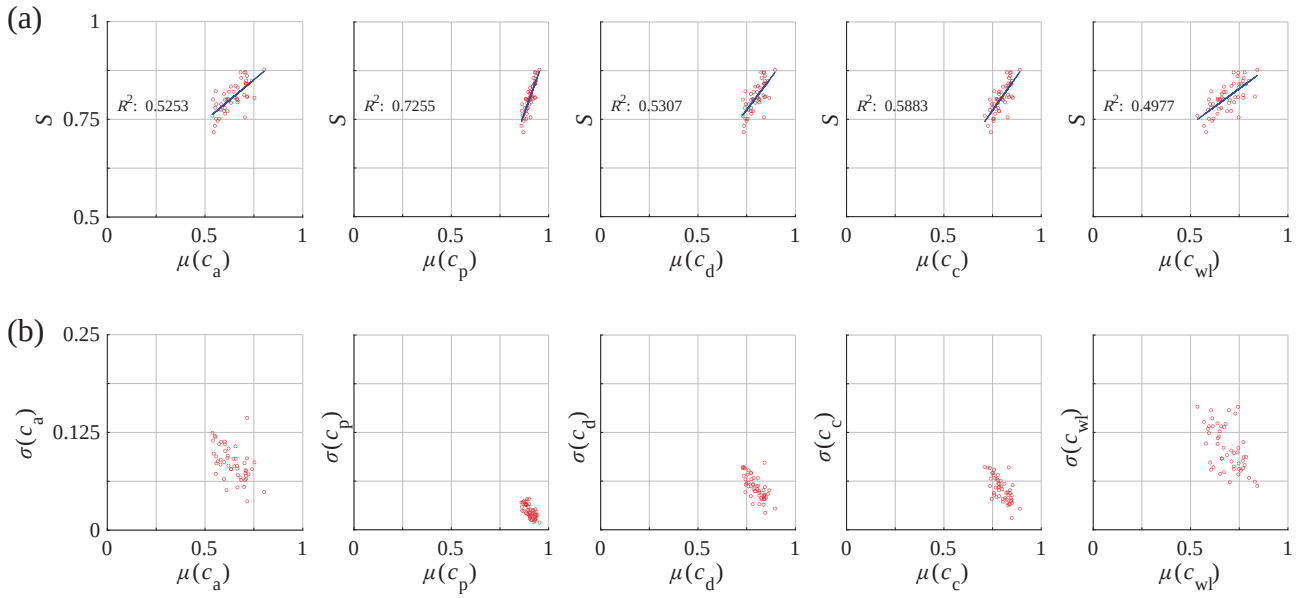


**Fig. 12** 2D and 3D shape analysis results for FL-B particles. **(a)** Mean ($\mu$) of 2D circularities vs. 3D true sphericity $S$, **(b)** mean ($\mu$) vs. standard deviation ($\sigma$) of 2D circularities.

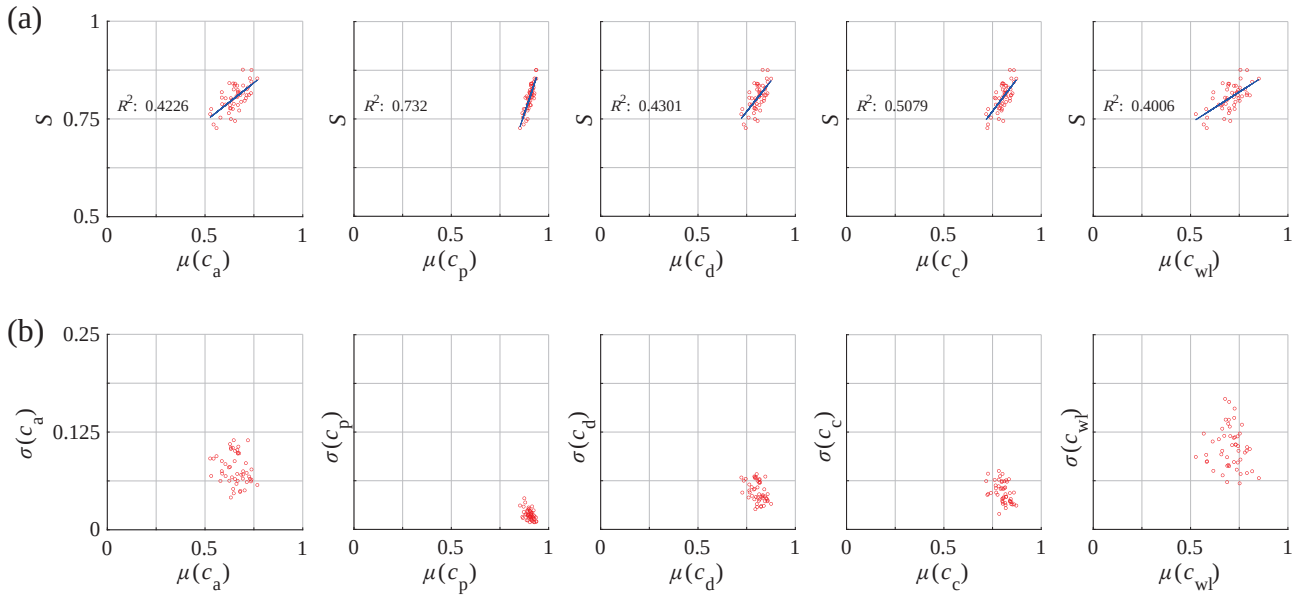


**Fig. 13** 2D and 3D shape analysis results for FL-C particles. **(a)** Mean ($\mu$) of 2D circularities vs. 3D true sphericity $S$, **(b)** mean ($\mu$) vs. standard deviation ($\sigma$) of 2D circularities.

supporting why $c_p$ correlates well with $S$. The standard deviations of $c_a$, $c_d$, $c_c$, and $c_{wl}$ are also significantly higher than $\sigma(c_p)$, because these measures rely on two principal dimensions from the projected particle image, leading to high variability depending on the viewpoint.

In summary, the low $\sigma(c_p)$ indicates that a small number of 2D projection images can effectively estimate $c_p$ that closely approximates $\mu(c_p)$ for each particle, thus eliminating the need to evaluate many 2D projection images to get $\mu(c_p)$. The strong linear relationship between $\mu(c_p)$ and $S$, accompanied by limited data scatter along the regression line, supports the feasibility of high-fidelity estimation of $S$ from $c_p$. For example, the regression line for FL-A in **Fig. 11(a)** can be expressed as $S = 1.48 \times \mu(c_p) - 0.56$. Given the low $\sigma(c_p)$, this can be approximated as $S \sim 1.48 \times c_p - 0.56$. This approach provides a fast and reliable method for estimating a 3D shape in terms of $S$ from the 2D perimeter circularity, $c_p$, obtained from a 2D particle image.

## 6. Concluding remarks

Particle shape significantly influences the behavior and properties of granular materials, highlighting the importance of shape characterization. This characterization has been conducted through either 3D or 2D analysis, each

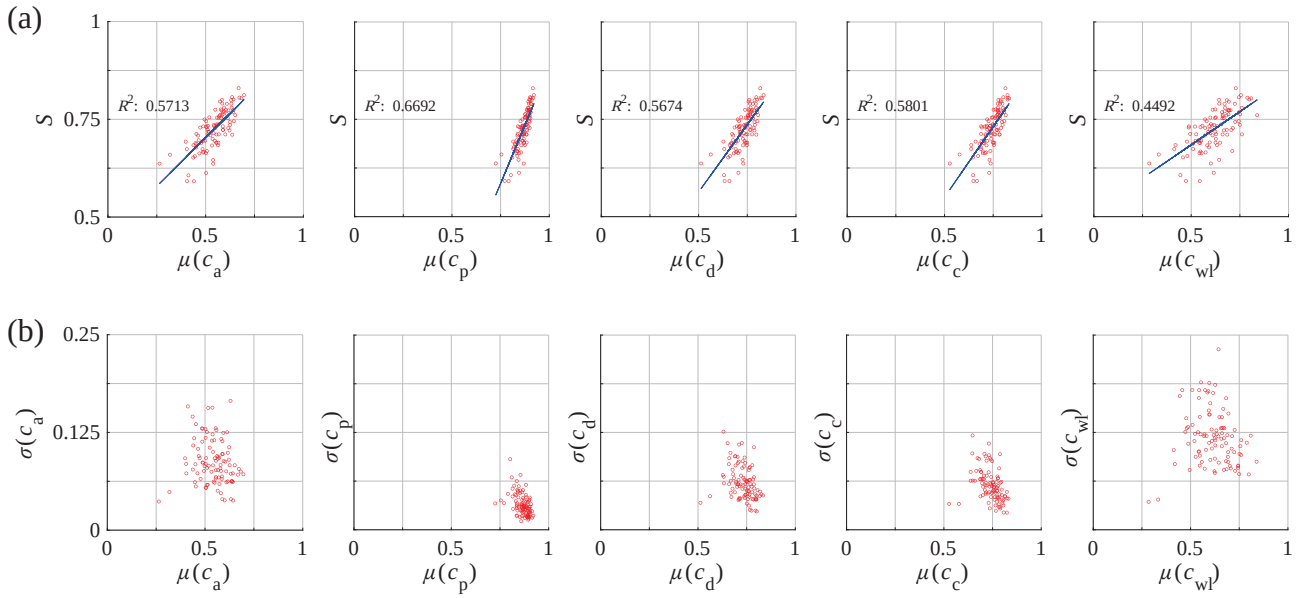


**Fig. 14** 2D and 3D shape analysis results for VG-A particles. **(a)** Mean ($\mu$) of 2D circularities vs. 3D true sphericity $S$, **(b)** mean ($\mu$) vs. standard deviation ($\sigma$) of 2D circularities.

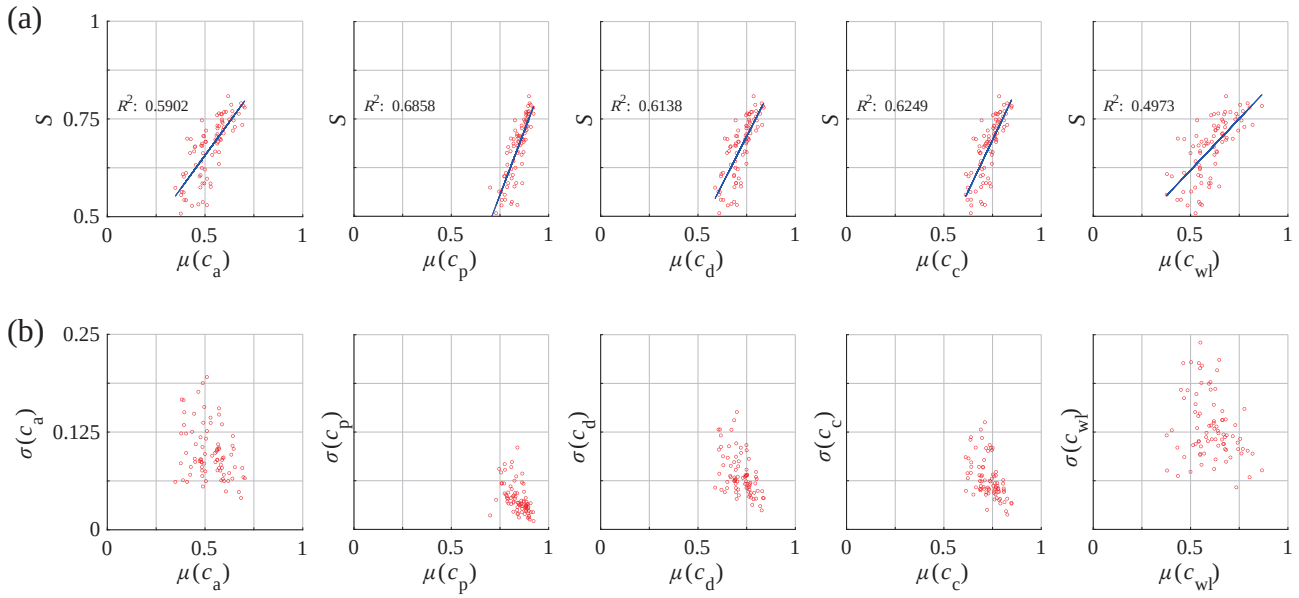


**Fig. 15** 2D and 3D shape analysis results for VG-B particles. **(a)** Mean ($\mu$) of 2D circularities vs. 3D true sphericity $S$, **(b)** mean ($\mu$) vs. standard deviation ($\sigma$) of 2D circularities.

offering distinct methodologies and associated trade-offs. Although 3D analysis provides greater accuracy by capturing the complete geometry of particles, it is more time-consuming and computationally expensive. In contrast, 2D analysis is simpler and faster, suitable for rapid assessment but less effective for providing a comprehensive understanding of 3D geometry. These distinct strengths and limitations have ignited interest within the granular materials research community to explore the correlation between 3D and 2D shapes, potentially enabling more efficient estimation of 3D shape from a 2D particle image or images. In response to this research interest, this paper comprehensively reviews previous studies to identify a set of 3D and 2D shape measures that best correlate with each other, aiming to bridge the gap between these two approaches.

Particle shapes are commonly characterized by large-scale properties such as form and true sphericity and local scale properties such as roundness and surface texture. This review focuses on larger scale shape properties, as they are more critical for understanding 3D shape characteristics. The literature review reveals a lack of meaningful correlation between 3D and 2D form factors, primarily because the 2D form is measured using only two principal dimensions from the projected particle image, while the 3D form

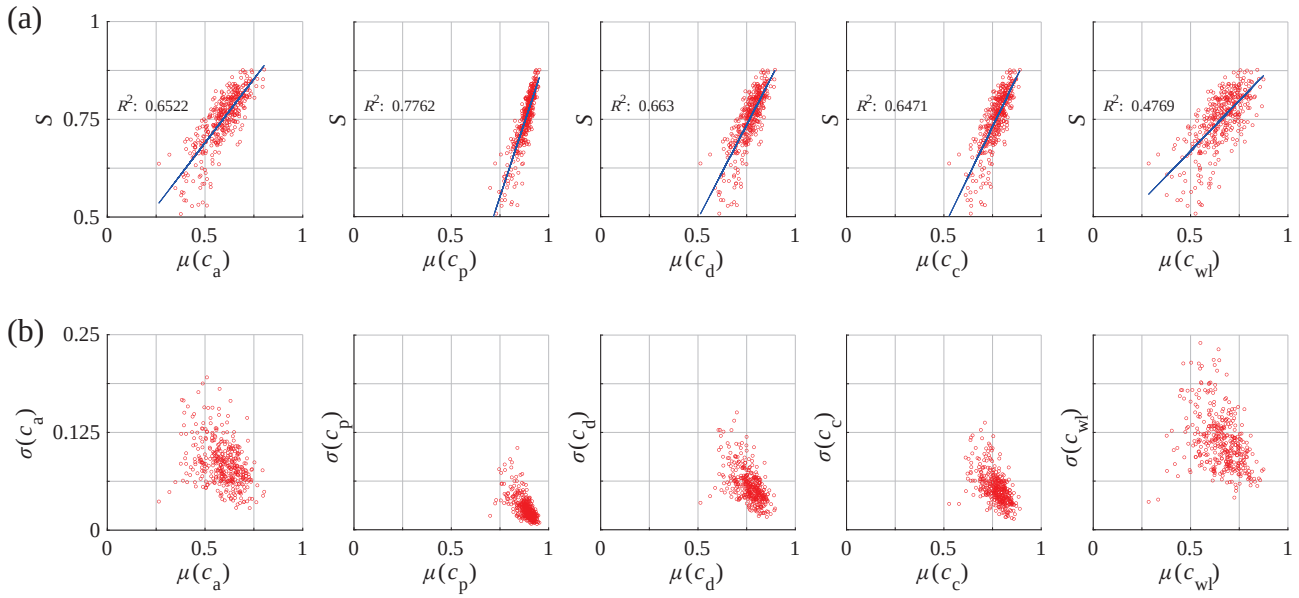


**Fig. 16** 2D and 3D shape analysis results for all 382 particles. **(a)** Mean ($\mu$) of 2D circularities vs. 3D true sphericity $S$, **(b)** mean ($\mu$) vs. standard deviation ($\sigma$) of 2D circularities.

is defined using aspect ratios based on three principal dimensions. This limitation restricts the accuracy of estimating 3D form from 2D random projection images. On the other hand, true sphericity measures how closely a particle's shape approximates that of a perfect sphere. From the comprehensive literature review, this study finds that previous research has reported a good correlation between true sphericity ($S$) and perimeter circularity ($c_p$). This correlation exists because $c_p$ acts as the 2D analog of $S$; true sphericity ($S$) is calculated based on the particle's surface area, whereas $c_p$ is derived using a similar definition, employing the perimeter of the projected particle to mirror the role of surface area in $S$. Therefore, these definitions create a natural equivalence across the different spatial dimensions. Furthermore, $S$ quantifies a comprehensive aspect of shape by measuring equidimensionality in all directions, unlike form measurements that are limited to only three directions. The 2D image retains geometric characteristics that facilitate partial evaluation of equidimensionality in all directions, which supports the strong correlation between true sphericity and perimeter circularity.

It is also worth noting that true sphericity ($S$) should be distinguished from other sphericity measures such as intercept sphericity ($\Psi$), even though $S$ was originally proposed as a shape descriptor to measure sphericity. Conventional sphericity measures are often considered form factors because they can be calculated using the three principal dimensions, independent of local shape features such as roundness. However, true sphericity is influenced by both form and roundness because it evaluates a more comprehensive aspect of shape by measuring equidimensionality in all directions. This highlights the need to treat true sphericity as a distinct fourth aspect of shape. This differentiation extends to 2D circularities: commonly used circularities such as $c_a$, $c_d$, $c_c$, and $c_{wl}$ function as 2D form factors because they can be defined using two principal dimensions from a projected particle image. In contrast, $c_p$ and $c_{cox}$ (essentially $c_p$ squared) serve as 2D analogs of true sphericity.

This study further validates the correlation between $S$ and $c_p$ by analyzing approximately 400 mineral particles. A robust linear relationship is evident between the mean of $c_p$ values and $S$, which is characterized by high $R^2$ values and limited data scatter. In addition, the standard deviations of $c_p$ are significantly lower than those of other circularities, indicating its insensitivity to viewpoint changes around a particle. This finding underscores the potential of using some 2D particle images to effectively and efficiently estimate 3D particle shape based on the 2D-to-3D relationship between $c_p$ and $S$. This approach combines the speed and simplicity of 2D analysis with the accuracy of 3D analysis. We encourage the granular materials research community to further investigate the implications of the findings presented in this paper.

## Data Availability Statement

The complete dataset of the digital particles analyzed in this study is available in the NSF DesignSafe-CI repository (Tripathi et al., 2023) at the following link: https://doi.org/10.17603/ds2-p634-pg95. The dataset is available under the Open Data Commons Attribution License.

## Acknowledgments

This work was supported in part by the US National Science Foundation (NSF) under the awards CMMI #1938431 and #1938285. The authors extend their

appreciation to the Florida Department of Transportation (FDOT) District Four & Six Materials Office and Titan America LLC for providing the particles analyzed in this study. The authors greatly appreciate these supports. The authors extend their appreciation to the anonymous reviewers for their valuable comments, which enhanced the paper. The opinions, findings, conclusions, or recommendations expressed in this article are solely those of the authors and do not necessarily reflect the views of the sponsors.

## Conflicts of Interest

The authors declare no conflicts of interest.

## References

Al-Raoush R., Microstructure characterization of granular materials, Physica A: Statistical Mechanics and its Applications, 377 (2007) 545–558. https://doi.org/10.1016/j.physa.2006.11.090

Alshibli K.A., Druckrey A.M., Al-Raoush R.I., Weiskittel T., Lavrik N.V, Quantifying morphology of sands using 3D imaging, Journal of Materials in Civil Engineering, 27 (2015) 04014275. https://doi.org/10.1061/(ASCE)MT.1943-5533.0001246

Anusree K., Latha G.M., Characterization of sand particle morphology: state-of-the-art, Bulletin of Engineering Geology and the Environment, 82 (2023) 269. https://doi.org/10.1007/s10064-023-03309-x

Aschenbrenner B.C., A new method of expressing particle sphericity, Journal of Sedimentary Research, 26 (1956) 15–31. https://doi.org/10.1306/74D704A7-2B21-11D7-8648000102C1865D

Augarde C.E., Lee S.J., Loukidis D., Numerical modelling of large deformation problems in geotechnical engineering: a state-of-the-art review, Soils and Foundations, 61 (2021) 1718–1735. https://doi.org/10.1016/j.sandf.2021.08.007

Bagheri G.H., Bonadonna C., Manzella I., Vonlanthen P., On the characterization of size and shape of irregular particles, Powder Technology, 270 (2015) 141–153. https://doi.org/10.1016/j.powtec.2014.10.015

Barrett P.J., The shape of rock particles, a critical review, Sedimentology, 27 (1980) 291–303. https://doi.org/10.1111/j.1365-3091.1980.tb01179.x

Bésuelle P., Viggiani G., Lenoir N., Desrues J., Bornert M., X-ray micro CT for studying strain localization in clay rocks under triaxial compression, in: Desrues Jacques, Viggiani Gioacchino, Bésuelle Pierre (Eds.), Advances in X-ray Tomography for Geomaterials, Wiley, 2006, pp. 35–53. https://doi.org/10.1002/9780470612187.ch2

Bhattacharya S., Subedi S., Lee S.J., Pradhananga N., Estimation of 3D sphericity by volume measurement – application to coarse aggregates, Transportation Geotechnics, 23 (2020) 100344. https://doi.org/10.1016/j.trgeo.2020.100344

Blender, Blender Foundation, 2022 <https://www.blender.org/> accessed 25072024.

Bloom M., Corriveau J., Giordano P., Lecakes G.D., Mandayam S., Sukumaran B., Imaging systems and algorithms for the numerical characterization of three-dimensional shapes of granular particles, IEEE Transactions on Instrumentation and Measurement, 59 (2010) 2365–2375. https://doi.org/10.1109/TIM.2009.2034579

Blott S.J., Pye K., Particle shape: a review and new methods of characterization and classification, Sedimentology, 55 (2007) 31–63. https://doi.org/10.1111/j.1365-3091.2007.00892.x

Bouzeboudja H., Melbouci B., Bouzeboudja A., Experimental study of crushed granular materials by the notion of fractal dimension in 2D and 3D, Geotechnical and Geological Engineering, 40 (2022) 2009–2031. https://doi.org/10.1007/s10706-021-02007-3

Bowman E.T., Soga K., Drummond W., Particle shape characterisation using Fourier descriptor analysis, Géotechnique, 51 (2001) 545–554. https://doi.org/10.1680/geot.2001.51.6.545

Cavarretta I., O'Sullivan C., Coop M.R., Applying 2D shape analysis techniques to granular materials with 3D particle geometries, in: AIP Conference Proceedings, AIP, 2009a, pp. 833–836. https://doi.org/10.1063/1.3180057

Cepuritis R., Garboczi E.J., Jacobsen S., Snyder K.A., Comparison of 2-D and 3-D shape analysis of concrete aggregate fines from VSI crushing, Powder Technology, 309 (2017) 110–125. https://doi.org/10.1016/j.powtec.2016.12.037

Chandan C., Sivakumar K., Masad E., Fletcher T., Application of imaging techniques to geometry analysis of aggregate particles, Journal of Computing in Civil Engineering, 18 (2004) 75–82. https://doi.org/10.1061/(ASCE)0887-3801(2004)18:1(75)

Chen J., Li R., Mo P.-Q., Zhou G., Cai S., Chen D., A modified method for morphology quantification and generation of 2D granular particles, Granular Matter, 24 (2022) 16. https://doi.org/10.1007/s10035-021-01149-8

Chen J., Wang H., Dan H., Xie Y., Random modeling of three-dimensional heterogeneous microstructure of asphalt concrete for mechanical analysis, Journal of Engineering Mechanics, 144 (2018) 04018083. https://doi.org/10.1061/(ASCE)EM.1943-7889.0001505

Cho G.-C., Dodds J., Santamarina J.C., Particle shape effects on packing density, stiffness, and strength: natural and crushed sands, Journal of Geotechnical and Geoenvironmental Engineering, 132 (2006) 591–602. https://doi.org/10.1061/(ASCE)1090-0241(2006)132:5(591)

Cook C.S., Tanyu B.F., Yavuz A.B., Effect of particle shape on durability and performance of unbound aggregate base, Journal of Materials in Civil Engineering, 29 (2017) 04016221. https://doi.org/10.1061/(ASCE)MT.1943-5533.0001752

Corey A.T., Influence of shape on the fall velocity of sand grains, master's thesis, Colorado A & M College, 1949.

Cox E.P., A method of assigning numerical and percentage values to the degree of roundness of sand grains, Journal of Paleontology, 1 (1927) 179–183. <https://www.jstor.org/stable/1298056> accessed 18 July 2024.

DepositPhotos, Stone wall with randomtiled pattern, <https://depositphotos.com/photo.html>, 2014.

Dobkins J.E., Folk R.L., Shape development on Tahiti-Nui, SEPM Journal of Sedimentary Research, 40 (1970) 1167–1203. https://doi.org/10.1306/74D72162-2B21-11D7-8648000102C1865D

Druckrey A.M., Alshibli K.A., Al-Raoush R.I., 3D characterization of sand particle-to-particle contact and morphology, Computers and Geotechnics, 74 (2016) 26–35. https://doi.org/10.1016/j.compgeo.2015.12.014

Erdogan S.T., Quiroga P.N., Fowler D.W., Saleh H.A., Livingston R.A., Garboczi E.J., Ketcham P.M., Hagedorn J.G., Satterfield S.G., Three-dimensional shape analysis of coarse aggregates: new techniques for and preliminary results on several different coarse aggregates and reference rocks, Cement and Concrete Research, 36 (2006) 1619–1627. https://doi.org/10.1016/j.cemconres.2006.04.003

Fang H., Zhu H., Yang J., Huang X., Hu X., Three-dimensional angularity characterization of coarse aggregates based on experimental comparison of selected methods, Particulate Science and Technology, 40 (2022) 1–9. https://doi.org/10.1080/02726351.2021.1879979

Fei W., Narsilio G.A., Disfani M.M., Impact of three-dimensional sphericity and roundness on heat transfer in granular materials, Powder Technology, 355 (2019) 770–781. https://doi.org/10.1016/j.powtec.2019.07.094

Fonseca J., O'Sullivan C., Coop M.R., Lee P.D., Non-invasive characterization of particle morphology of natural sands, Soils and Foundations, 52 (2012) 712–722. https://doi.org/10.1016/j.sandf.2012.07.011

Fu X., Elliott J.A., Bentham A.C., Hancock B.C., Cameron R.E., Application of X-ray microtomography and image processing to the investigation of a compacted granular system, Particle & Particle Systems Characterization, 23 (2006) 229–236. https://doi.org/10.1002/ppsc.200601054

Gates L., Masad E., Pyle R., Bushee D., Aggregate image measurement system 2 (AIMS2): final report, 2011. <https://rosap.ntl.bts.gov/view/dot/54171> accessed 18072024.

Guida G., Viggiani G.M.B., Casini F., Multi-scale morphological descriptors from the fractal analysis of particle contour, Acta Geotechnica, 15 (2020) 1067–1080. https://doi.org/10.1007/s11440-019-00772-3

Han S., Wang C., Liu X., Li B., Gao R., Li S., A random algorithm for 3D modeling of solid particles considering elongation, flatness, sphericity, and convexity, Computational Particle Mechanics, 10 (2023) 19–44. https://doi.org/10.1007/s40571-022-00475-9

Hanaor D.A.H., Gan Y., Revay M., Airey D.W., Einav I., 3D printable geomaterials, Géotechnique, 66 (2016) 323–332. https://doi.org/10.1680/jgeot.15.P.034

Hayakawa Y., Oguchi T., Evaluation of gravel sphericity and roundness based on surface-area measurement with a laser scanner, Computers & Geosciences, 31 (2005) 735–741. https://doi.org/10.1016/j.cageo.2005.01.004

Howarth R.J., W, in: Dictionary of Mathematical Geosciences, Springer International Publishing, Cham, 2017, pp. 653–665, ISBN:978-3-319-57314-4. https://doi.org/10.1007/978-3-319-57315-1_23

Hryciw R.D., Zheng J., Ohm H.-S., Li J., Innovations in optical geocharacterization, in: Geo-Congress 2014 Keynote Lectures: Geo-Characterization and Modeling for Sustainability, 2014, pp. 97–116. https://doi.org/10.1061/9780784413289.005

Hu Q., Gao R., Chen J., Yuan Z., Ballast deterioration inspection and quantification with 3D form method based on particle inscribed ellipsoid, Granular Matter, 25 (2023) 54. https://doi.org/10.1007/s10035-023-01348-5

Huang H., Tutumluer E., Image-aided element shape generation method in discrete-element modeling for railroad ballast, Journal of Materials in Civil Engineering, 26 (2014) 527–535. https://doi.org/10.1061/(ASCE)MT.1943-5533.0000839

Huang H., Tutumluer E., Luo J., Ding K., Qamhia I., Hart J., 3D image analysis using deep learning for size and shape characterization of stockpile riprap aggregates—phase 2, Rantoul, 2022. https://doi.org/10.36501/0197-9191/22-017

Janke N.C., Effect of shape upon the settling vellocity of regular convex geometric particles, Journal of Sedimentary Research, 36 (1966) 370–376. https://doi.org/10.1306/74D714C4-2B21-11D7-8648000102C1865D

Jerves A.X., Kawamoto R.Y., Andrade J.E., Effects of grain morphology on critical state: a computational analysis, Acta Geotechnica, 11 (2016) 493–503. https://doi.org/10.1007/s11440-015-0422-8

Jia X., Garboczi E.J., Advances in shape measurement in the digital world, Particuology, 26 (2016) 19–31. https://doi.org/10.1016/j.partic.2015.12.005

Kaviani-Hamedani F., Esmailzade M., Adineh K., Shafiei M., Shirkavand D., Quantifying three-dimensional sphericity indices of irregular fine particles from 2D images through sequential sieving tests, Granular Matter, 26 (2024) 13. https://doi.org/10.1007/s10035-023-01376-1

Kitware Inc., Paraview, <https://www.paraview.org/>.

Kodicherla S.P.K., Discrete element modelling of granular materials incorporating realistic particle shapes, International Journal of Geo-Engineering, 14 (2023) 15. https://doi.org/10.1186/s40703-023-00193-y

Kong D., Fonseca J., Quantification of the morphology of shelly carbonate sands using 3D images, Géotechnique, 68 (2018) 249–261. https://doi.org/10.1680/jgeot.16.P.278

Krawczykowski D., Krawczykowska A., Gawenda T., Comparison of geometric properties of regular and irregular mineral grains by dynamic image analysis (2D) and optoelectronic analysis (3D) methods, Minerals, 12 (2022) 540. https://doi.org/10.3390/min12050540

Krumbein W.C., Measurement and geological significance of shape and roundness of sedimentary particles, Journal of Sedimentary Petrology, 11 (1941) 64–72.

Křupka A., Říha K., Minimal prerequisites for measuring two-dimensional contour roundness in a particle classification context, Powder Technology, 284 (2015) 486–495. https://doi.org/10.1016/j.powtec.2015.07.018

Kuo C.-Y., Freeman R.B., Imaging indices for quantification of shape, angularity, and surface texture of aggregates, Transportation Research Record: Journal of the Transportation Research Board, 1721 (2000) 57–65. https://doi.org/10.3141/1721-07

Kuo C.-Y., Frost J.D., Lai J.S., Wang L.B., Three-dimensional image analysis of aggregate particles from orthogonal projections, Transportation Research Record: Journal of the Transportation Research Board, 1526 (1996) 98–103. https://doi.org/10.1177/0361198196152600112

Kutay M.E., Arambula E., Gibson N., Youtcheff J., Three-dimensional image processing methods to identify and characterise aggregates in compacted asphalt mixtures, International Journal of Pavement Engineering, 11 (2010) 511–528. https://doi.org/10.1080/10298431003749725

Kutay M.E., Ozturk H.I., Abbas A.R., Hu C., Comparison of 2D and 3D image-based aggregate morphological indices, International Journal of Pavement Engineering, 12 (2011) 421–431. https://doi.org/10.1080/10298436.2011.575137

Kwan A.K., Mora C., Chan H., Particle shape analysis of coarse aggregate using digital image processing, Cement and Concrete Research, 29 (1999) 1403–1410. https://doi.org/10.1016/S0008-8846(99)00105-2

Landauer J., Kuhn M., Nasato D.S., Foerst P., Briesen H., Particle shape matters – using 3D printed particles to investigate fundamental particle and packing properties, Powder Technology, 361 (2020) 711–718. https://doi.org/10.1016/j.powtec.2019.11.051

Lansdown H., Digital Modelmaking: Laser Cutting, 3D Printing and Reverse Engineering, Crowood Press, 2019, ISBN: 9781785005862.

Latham J.-P., Munjiza A., Garcia X., Xiang J., Guises R., Three-dimensional particle shape acquisition and use of shape library for DEM and FEM/DEM simulation, Minerals Engineering, 21 (2008) 797–805. https://doi.org/10.1016/j.mineng.2008.05.015

Lee C., Suh H.S., Yoon B., Yun T.S., Particle shape effect on thermal conductivity and shear wave velocity in sands, Acta Geotechnica, (2017) 1–11. https://doi.org/10.1007/s11440-017-0524-6

Lee C.H., Lee S.J., Shin M., Characterization of variability in 2-dimensional particle geometry via 3D structured light scanning, Transportation Geotechnics, 34 (2022) 100760. https://doi.org/10.1016/j.trgeo.2022.100760

Lee J.R.J., Smith M.L., Smith L.N., Midha P.S., A mathematical morphology approach to image based 3D particle shape analysis, Machine Vision and Applications, 16 (2005) 282–288. https://doi.org/10.1007/s00138-005-0181-x

Lee K.L., Seed H.B., Drained strength characteristics of sands, Journal of the Soil Mechanics and Foundations Division, 93 (1967) 117–141. https://doi.org/10.1061/JSFEAQ.0001048

Lee S.J., Developments in large scale discrete element simulations with polyhedral particles, University of Illinois at Urbana-Champaign, Urbana, 2014. https://hdl.handle.net/2142/50542

Lee S.J., Hashash Y.M.A., iDEM: An impulse-based discrete element method for fast granular dynamics, International Journal for Numerical Methods in Engineering, 104 (2015) 79–103. https://doi.org/10.1002/nme.4923

Lee S.J., Hashash Y.M.A., Nezami E.G., Simulation of triaxial compression tests with polyhedral discrete elements, Computers and Geotechnics, 43 (2012) 92–100. https://doi.org/10.1016/j.compgeo.2012.02.011

Lee S.J., Hashash Y.M.A., Wilkinson R.A., Agui J.H., Simulation of experimental tests on the JSC-1A lunar soil simulant with polyhedral discrete elements, in: Earth and Space 2010, American Society of Civil Engineers, Reston, VA, 2010, pp. 208–216. https://doi.org/10.1061/41096(366)22

Lee S.J., Lee C.H., Shin M., Bhattacharya S., Su Y.F., Influence of coarse aggregate angularity on the mechanical performance of cement-based materials, Construction and Building Materials, 204 (2019) 184–192. https://doi.org/10.1016/j.conbuildmat.2019.01.135

Lee S.J., Lee C.H., Shin M., Tripathi P., The “signature” of particle geometry - DEM modelling perspective, 7th edition of the International Conference on Particle-based Methods, (2021) 7. https://doi.org/10.23967/particles.2021.033

Lee S.J., Shin M., Lee C.H., Tripathi P., Phenotypic trait of particle geometries, Granular Matter, 24 (2022) 79. https://doi.org/10.1007/s10035-022-01240-8

Li L., Iskander M., Evaluation of dynamic image analysis for characterizing granular soils, Geotechnical Testing Journal, 43 (2020) 1149–1173. https://doi.org/10.1520/GTJ20190137

Li L., Iskander M., Comparison of 2D and 3D dynamic image analysis for

characterization of natural sands, Engineering Geology, 290 (2021) 106052. https://doi.org/10.1016/j.enggeo.2021.106052

Li Linzhu, Sun Q., Iskander M., Efficacy of 3D dynamic image analysis for characterising the morphology of natural sands, Géotechnique, 73 (2023) 586–599. https://doi.org/10.1680/jgeot.21.00128

Li Lianghui, Wang J., Yang S., Klein B., Wang Z., Liu F., Estimate of three-dimensional Wadell roundness of irregular particles using image processing and topographic analysis, Construction and Building Materials, 396 (2023) 132273. https://doi.org/10.1016/j.conbuildmat.2023.132273

Li R., Lu W., Chen M., Wang G., Xia W., Yan P., Quantitative analysis of shapes and specific surface area of blasted fragments using image analysis and three-dimensional laser scanning, International Journal of Rock Mechanics and Mining Sciences, 141 (2021) 104710. https://doi.org/10.1016/j.ijrmms.2021.104710

Lin C.L., Miller J.D., 3D characterization and analysis of particle shape using X-ray microtomography (XMT), Powder Technology, 154 (2005) 61–69. https://doi.org/10.1016/j.powtec.2005.04.031

Lu R., Luo Q., Wang T., Zhao C., Comparison of clumps and rigid blocks in three-dimensional DEM simulations: curvature-based shape characterization, Computers and Geotechnics, 151 (2022) 104991. https://doi.org/10.1016/j.compgeo.2022.104991

Maerz N.H., Palangio T.C., Franklin J. a, WipFrag image based granulometry system, in: In B. Mohanty (Ed.), 5th International Symposium on Rock Fragmentation by Blasting, Workshop on Measurement of Blast Fragmentation, 1996, pp. 91–99.

Maroof M.A., Mahboubi A., Noorzad A., Safi Y., A new approach to particle shape classification of granular materials, Transportation Geotechnics, 22 (2020) 100296. https://doi.org/10.1016/j.trgeo.2019.100296

Masad E., Saadeh S., Al-Rousan T., Garboczi E., Little D., Computations of particle surface characteristics using optical and X-ray CT images, Computational Materials Science, 34 (2005) 406–424. https://doi.org/10.1016/j.commatsci.2005.01.010

Masad E.A., Aggregate imaging system (AIMS): basics and applications, National Technical Reports Library, PB2006107471, 2005. <https://static.tti.tamu.edu/tti.tamu.edu/documents/5-1707-01-1.pdf> accessed 2507024.

McCormick N.J., Gee M.G., The measurement of the shape of abrasive particles with confocal optical microscopy, National Physical Laboratory Report, DEPC MPE 010, 2005. <https://eprintspublications.npl.co.uk/3162/1/DEPC_MPE10.pdf> accessed 2507024.

Meta AI (Facebook Research), Segment Anything, 2023. <https://segment-anything.com/> accessed 2507024.

Mitchell J.K., Soga K., Fundamentals of Soil Behavior, John Wiley & Sons, 3rd edition, 2005, ISBN: 978-0471463023.

Moaveni M., Wang S., Hart J.M., Tutumluer E., Ahuja N., Evaluation of aggregate size and shape by means of segmentation techniques and aggregate image processing algorithms, Transportation Research Record: Journal of the Transportation Research Board, 2335 (2013) 50–59. https://doi.org/10.3141/2335-06

Montenegro Ríos A., Sarocchi D., Nahmad-Molinari Y., Borselli L., Form from projected shadow (FFPS): an algorithm for 3D shape analysis of sedimentary particles, Computers & Geosciences, 60 (2013) 98–108. https://doi.org/10.1016/j.cageo.2013.07.008

Riley N.A., Projection sphericity, Journal of Sedimentary Research, 11 (1941) 94–95. https://doi.org/10.1306/d426910c-2b26-11d7-8648000102c1865d

Nie J.-Y., Li D.-Q., Cao Z.-J., Zhou B., Zhang A.-J., Probabilistic characterization and simulation of realistic particle shape based on sphere harmonic representation and Nataf transformation, Powder Technology, 360 (2020) 209–220. https://doi.org/10.1016/j.powtec.2019.10.007

OpenCV, Open Source Computer Vision Library, 2023. <https://opencv.org/> accessed 25072024.

Ozturk H.I., Rashidzade I., A photogrammetry based method for determination of 3D morphological indices of coarse aggregates, Construction and Building Materials, 262 (2020) 120794. https://doi.org/10.1016/j.conbuildmat.2020.120794

Paixão A., Resende R., Fortunato E., Photogrammetry for digital reconstruction of railway ballast particles – A cost-efficient method, Construction and Building Materials, 191 (2018) 963–976. https://doi.org/10.1016/j.conbuildmat.2018.10.048

Payan M., Senetakis K., Khoshghalb A., Khalili N., Effect of gradation and particle shape on small-strain Young's modulus and Poisson's ratio of sands, International Journal of Geomechanics, 17 (2016) 04016120. https://doi.org/10.1061/(ASCE)GM.1943-5622.0000811

Petre R.-D., Zaharia T., Prêteux F., An overview of view-based 2D/3D indexing methods, in: Proceedings Volume 7799, Mathematics of Data/Image Coding, Compression, and Encryption with Applications XII, Society of Photo-Optical Instrumentation Engineers (SPIE), San Diego, CA, USA, 2010, p. 779904. https://doi.org/10.1117/12.861542

Polyga, Polyga Compact C504, <polyga.com> 2021.

Pye W.D., Pye M.H., Sphericity determinations of pebbles and sand grains, Journal of Sedimentary Research, 13 (1943) 28–34. https://doi.org/10.1306/D4269184-2B26-11D7-8648000102C1865D

Qian Y., Lee S.J., Tutumluer E., Hashash Y.M.A., Mishra D., Ghaboussi J., Simulating ballast shear strength from large-scale triaxial tests, Transportation Research Record: Journal of the Transportation Research Board, 2374 (2013) 126–135. https://doi.org/10.3141/2374-15

Rodriguez J., Johansson J., Edeskär T., Particle shape determination by two-dimensional image analysis in geotechnical engineering, in: Proceedings Of Nordic Conference On Soil Mechanics And Geotechnical NGM, Danish Geotechnical Society, Copenhagen, Denmark, 2012, pp. 207–218. <https://www.diva-portal.org/smash/get/diva2:1008311/FULLTEXT01.pdf> accessed 25072024.

Rorato R., Arroyo M., Andò E., Gens A., Sphericity measures of sand grains, Engineering Geology, 254 (2019) 43–53. https://doi.org/10.1016/j.enggeo.2019.04.006

Roslin A., Marsh M., Piché N., Provencher B., Mitchell T.R., Onederra I.A., Leonardi C.R., Processing of micro-CT images of granodiorite rock samples using convolutional neural networks (CNN), Part I: Super-resolution enhancement using a 3D CNN, Minerals Engineering, 188 (2022) 107748. https://doi.org/10.1016/j.mineng.2022.107748

Rowe P.W., The stress-dilatancy relation for static equilibrium of an assembly of particles in contact, Proceedings of the Royal Society A: Mathematical, Physical and Engineering Sciences, 269 (1962) 500–527. https://doi.org/10.1098/rspa.1962.0193

Sandeep C.S., Hernandez A., Stangeland K., Evans T.M., Shape characteristics of granular materials through realistic particle avatars, Computers and Geotechnics, 157 (2023) 105352. https://doi.org/10.1016/j.compgeo.2023.105352

Shin H., Santamarina J.C., Role of particle angularity on the mechanical behavior of granular mixtures, Journal of Geotechnical and Geoenvironmental Engineering, 139 (2013) 353–355. https://doi.org/10.1061/(ASCE)GT.1943-5606.0000768

Sneed E.D., Folk R.L., Pebbles in the lower Colorado River, Texas a study in particle morphogenesis, The Journal of Geology, 66 (1958) 114–150. https://doi.org/10.1086/626490

Stark N., Hay A.E., Cheel R., Lake C.B., The impact of particle shape on the angle of internal friction and the implications for sediment dynamics at a steep, mixed sand–gravel beach, Earth Surface Dynamics, 2 (2014) 469–480. https://doi.org/10.5194/esurf-2-469-2014

Su D., Wang X., Yang H.-W., Hong C., Roughness analysis of general-shape particles, from 2D closed outlines to 3D closed surfaces, Powder Technology, 356 (2019) 423–438. https://doi.org/10.1016/j.powtec.2019.08.042

Su D., Yan W.M., 3D characterization of general-shape sand particles using microfocus X-ray computed tomography and spherical harmonic functions, and particle regeneration using multivariate random vector, Powder Technology, 323 (2018a) 8–23. https://doi.org/10.1016/j.powtec.2017.09.030

Su D., Yan W.M., Quantification of angularity of general-shape particles by using Fourier series and a gradient-based approach, Construction and Building Materials, 161 (2018b) 547–554. https://doi.org/10.1016/j.conbuildmat.2017.12.004

Su D., Yan W.M., Prediction of 3D size and shape descriptors of irregular

granular particles from projected 2D images, Acta Geotechnica, 15 (2020) 1533–1555. https://doi.org/10.1007/s11440-019-00845-3
Su Y.-F., Zhang B., Lee S.J., Sukumaran B., Parametric sensitivity study of particle shape effect through 3D printing, in: Li X., Feng Y., Mustoe G. (Eds.), DEM 2016: Proceedings of the 7th International Conference on Discrete Element Methods, Springer, 2017, pp. 593–600. https://doi.org/10.1007/978-981-10-1926-5_61
Su Y.F., Bhattacharya S., Lee S.J., Lee C.H., Shin M., A new interpretation of three-dimensional particle geometry: M-A-V-L, Transportation Geotechnics, 23 (2020a) 100328. https://doi.org/10.1016/j.trgeo.2020.100328
Su Y.F., Lee S.J., Sukumaran B., Influence of particle morphology simplification on the simulation of granular material behavior, Granular Matter, 22 (2020b) 19. https://doi.org/10.1007/s10035-019-0987-2
Suh H.S., Kim K.Y., Lee J., Yun T.S., Quantification of bulk form and angularity of particle with correlation of shear strength and packing density in sands, Engineering Geology, 220 (2017) 256–265. https://doi.org/10.1016/j.enggeo.2017.02.015
Sukumaran B., Ashmawy A.K., Quantitative characterisation of the geometry of discrete particles, Géotechnique, 51 (2001) 619–627. https://doi.org/10.1680/geot.2001.51.7.619
Sun Y., Indraratna B., Nimbalkar S., Three-dimensional characterisation of particle size and shape for ballast, Géotechnique Letters, 4 (2014) 197–202. https://doi.org/10.1680/geolett.14.00036
Sympatec GmbH, QICPIC.<https://www.sympatec.com/en/particle-measurement/sensors/dynamic-image-analysis/qicpic/> accessed 25072024.
Terzaghi K., Peck R.B., Mesri G., Soil Mechanics in Engineering Practice, 3rd edition, Wiley, 1996, ISBN: 978-0471086581.
Tickell F.G., The Examination of Fragmental Rocks, Stanford University Press, Stanford, CA, 1931.
Tripathi P., Lee S.J., Shin M., Lee C.H., Replication data: 3D geometry characterization of Florida and Virginia mineral particles, US National Science Foundation (NSF) Designsafe-CI, (2023). https://doi.org/10.17603/Ds2-P634-Pg95
Tripathi P., Lee S.J., Shin M., Lee C.H., A new paradigm integrating the concepts of particle abrasion and breakage, in: Geo-Congress 2024, American Society of Civil Engineers, Reston, VA, 2024, pp. 272–281. https://doi.org/10.1061/9780784485309.028
Tunwal M., Lim A., A low-cost, repeatable method for 3D particle analysis with SfM photogrammetry, Geosciences, 13 (2023) 190. https://doi.org/10.3390/geosciences13070190
Tutumluer E., Ahuja N., Hart J.M., Moaveni M., Huang H., Zhao Z., Shah S., Field evaluation of ballast fouling conditions using machine vision, Transportation Research Board, 2017. <https://www.trb.org/Main/Blurbs/176825.aspx> accessed 25072024.
Tutumluer E., Hashash Y.M.A., Ghaboussi J., Qian Y., Lee S.J., Huang H., Discrete element modeling of railroad ballast behavior, Federal Railroad Administration, 2018. <https://railroads.dot.gov/elibrary/discrete-element-modeling-railroad-ballast-behavior> accessed.
Ueda T., Experimental validation of a 2D–3D conversion method for estimation of multiple 3D characteristics of discrete elements, Microscopy, 69 (2020) 37–43. https://doi.org/10.1093/jmicro/dfz112
Ueda T., Oki T., Koyanaka S., 2D-3D conversion method for assessment of multiple characteristics of particle shape and size, Powder Technology, 343 (2019) 287–295. https://doi.org/10.1016/j.powtec.2018.11.019
Vincent L., Soille P., Watersheds in digital spaces: an efficient algorithm based on immersion simulations, IEEE Transactions on Pattern Analysis and Machine Intelligence, 13 (1991) 583–598. https://doi.org/10.1109/34.87344
Vlahinić I., Andò E., Viggiani G., Andrade J.E., Towards a more accurate characterization of granular media: extracting quantitative descriptors from tomographic images, Granular Matter, 16 (2014) 9–21. https://doi.org/10.1007/s10035-013-0460-6
Wadell H., Volume, shape, and roundness of rock particles, The Journal of Geology, 40 (1932) 443–451.
Wadell H., Sphericity and roundness of rock particles, The Journal of Geology, 41 (1933) 310–331.
Wadell H., Shape determinations of large sedimental rock fragments, Pan-American Geologist, 61 (1934) 187–220.
Wadell H., Volume, shape, and roundness of quartz particles, The Journal of Geology, 43 (1935) 250–280.
Wang L., Wang X., Mohammad L., Abadie C., Unified method to quantify aggregate shape angularity and texture using Fourier analysis, Journal of Materials in Civil Engineering, 17 (2005) 498–504. https://doi.org/10.1061/(ASCE)0899-1561(2005)17:5(498)
Wang X., Tian K., Su D., Zhao J., Superellipsoid-based study on reproducing 3D particle geometry from 2D projections, Computers and Geotechnics, 114 (2019) 103131. https://doi.org/10.1016/j.compgeo.2019.103131
Wang X., Zhang H., Yin Z.-Y., Su D., Liu Z., Deep-learning-enhanced model reconstruction of realistic 3D rock particles by intelligent video tracking of 2D random particle projections, Acta Geotechnica, 18 (2023) 1407–1430. https://doi.org/10.1007/s11440-022-01616-3
Wei D., Zhao B., Gan Y., Surface reconstruction with spherical harmonics and its application for single particle crushing simulations, Journal of Rock Mechanics and Geotechnical Engineering, 14 (2022) 232–239. https://doi.org/10.1016/j.jrmge.2021.07.016
Wei X., Deng Z., Li Q., Huang Y., Zhao G., A 3D grain-based reconstruction method from a 2D surface image for the Distinct Lattice Spring Model, International Journal for Numerical and Analytical Methods in Geomechanics, 47 (2023) 2027–2048. https://doi.org/10.1002/nag.3549
Wentworth C.K., The shapes of beach pebbles, USGS Publications Warehouse, 1923. https://doi.org/10.3133/pp131C
WipWare, WipFrag iOS with GIS capabilities, 2023. <https://wipware.com/> accessed 25072024.
Wu J., Wang L., Hou Y., Xiong H., Lu Y., Zhang L., A digital image analysis of gravel aggregate using CT scanning technique, International Journal of Pavement Research and Technology, 11 (2018) 160–167. https://doi.org/10.1016/j.ijprt.2017.08.002
Xiao J., Zhang X., Zhang D., Xue L., Sun S., Stránský J., Wang Y., Morphological reconstruction method of irregular shaped ballast particles and application in numerical simulation of ballasted track, Transportation Geotechnics, 24 (2020) 100374. https://doi.org/10.1016/j.trgeo.2020.100374
Xie W.-Q., Zhang X.-P., Yang X.-M., Liu Q.-S., Tang S.-H., Tu X.-B., 3D size and shape characterization of natural sand particles using 2D image analysis, Engineering Geology, 279 (2020) 105915. https://doi.org/10.1016/j.enggeo.2020.105915
Yang D., Tang J., Hu N., Xia Y., Yu Y., Huang Q., The shape parameters of coal and gangue particles derived from 3D scanning, Scientific Data, 10 (2023) 107. https://doi.org/10.1038/s41597-023-02019-z
Yang X., Chen S., You Z., 3D voxel-based approach to quantify aggregate angularity and surface texture, Journal of Materials in Civil Engineering, 29 (2017). https://doi.org/10.1061/(ASCE)MT.1943-5533.0001872
Yeong C.L.Y., Torquato S., Reconstructing random media. II. Three-dimensional media from two-dimensional cuts, Physical Review E, 58 (1998) 224–233. https://doi.org/10.1103/PhysRevE.58.224
Zhang B., Lee S.J., Qian Y., Tutumluer E., Bhattacharya S., A smartphone-based image analysis technique for ballast aggregates, in: International Conference on Transportation and Development 2016, American Society of Civil Engineers, 2016, pp. 623–630. https://doi.org/10.1061/9780784479926.057
Zhang S., Li R., Pei J., Evaluation methods and indexes of morphological characteristics of coarse aggregates for road materials: a comprehensive review, Journal of Traffic and Transportation Engineering (English Edition), 6 (2019) 256–272. https://doi.org/10.1016/j.jtte.2019.01.003
Zhao B., Wang J., 3D quantitative shape analysis on form, roundness, and compactness with μCT, Powder Technology, 291 (2016) 262–275. https://doi.org/10.1016/j.powtec.2015.12.029
Zhao J., Zhao S., Luding S., The role of particle shape in computational modelling of granular matter, Nature Reviews Physics, 5 (2023) 505–525. https://doi.org/10.1038/s42254-023-00617-9
Zhao L., Zhang S., Deng M., Wang X., Statistical analysis and comparative study of multi-scale 2D and 3D shape features for unbound granular geomaterials, Transportation Geotechnics, 26 (2021)

100377. https://doi.org/10.1016/j.trgeo.2020.100377
Zheng J., He H., Alimohammadi H., Three-dimensional Wadell roundness for particle angularity characterization of granular soils, Acta Geotechnica, 16 (2021) 133–149. https://doi.org/10.1007/s11440-020-01004-9
Zheng J., Hryciw R.D., Traditional soil particle sphericity, roundness and surface roughness by computational geometry, Géotechnique, 65 (2015) 494–506. https://doi.org/10.1680/geot.14.P.192
Zheng J., Hryciw R.D., Soil particle size and shape distributions by stereophotography and image analysis, Geotechnical Testing Journal, 40 (2017) 317–328. https://doi.org/10.1520/GTJ20160165
Zheng J., Hryciw R.D., Particle Roundness and Sphericity Computation Code, 2016. <https://www.mathworks.com/matlabcentral/fileexchange/60651-particle-roundness-and-sphericity-computation> accessed 25072024.
Zheng W., Hu X., Tannant D.D., Zhang K., Xu C., Characterization of two- and three-dimensional morphological properties of fragmented sand grains, Engineering Geology, 263 (2019) 105358. https://doi.org/10.1016/j.enggeo.2019.105358
Zhou B., Wang J., Generation of a realistic 3D sand assembly using X-ray micro-computed tomography and spherical harmonic-based principal component analysis, International Journal for Numerical and Analytical Methods in Geomechanics, 41 (2017) 93–109. https://doi.org/10.1002/nag.2548
Zhou B., Wang J., Zhao B., Micromorphology characterization and reconstruction of sand particles using micro X-ray tomography and spherical harmonics, Engineering Geology, 184 (2015) 126–137. https://doi.org/10.1016/j.enggeo.2014.11.009
Zhu F., Zhao J., Interplays between particle shape and particle breakage in confined continuous crushing of granular media, Powder Technology, 378 (2021) 455–467. https://doi.org/10.1016/j.powtec.2020.10.020
Zingg T., Beitrag zur Schotteranalyse, Doctoral dissertation, ETH Zurich, 1935. https://doi.org/10.3929/ethz-a-000103455
Zubić N., Liò P., An effective loss function for generating 3D models from single 2D image without rendering, in: Artificial Intelligence Applications and Innovations, 2021, pp. 309–322. https://doi.org/10.1007/978-3-030-79150-6_25

## Authors' Short Biographies

**Priya Tripathi** is currently pursuing a doctoral degree in Civil Engineering at Florida International University (FIU) in Miami, Florida, USA. She also completed her master's degree at FIU after finishing her undergraduate studies in civil engineering at Mumbai University, India. Her research is focused on the characterization of 3D particle shapes and the development of a comprehensive framework for describing 3D particle geometry. Her work is particularly relevant in fields requiring precise particle shape analysis and has contributed significantly to advances in geotechnical and construction engineering.

**Dr. Seung Jae Lee** is an Associate Professor in the Department of Civil and Environmental Engineering at Florida International University, Miami, Florida, USA. His expertise lies in computational mechanics at the interfaces of geotechnical, structural, and computational engineering. His research focuses on understanding the fundamental mechanisms encoded at the micro- and grain-scales behind the complex macroscopic behaviors of discrete systems and materials. His contributions include expanding the length and time scale limits in discrete mechanical simulations by two orders of magnitude, and coining the new concept of 'particle geometry space.' This innovative approach enabled integrated characterization of particle shape, surface area, volume, specific surface, and size distribution within a single framework. He has received multiple awards from various research communities, including the ASCE Engineering Mechanics Institute.

**Dr. Chang Hoon Lee** is an Associate Professor in the Department of Civil and Environmental Engineering at Western New England University, Springfield, Massachusetts, USA. His research interests include developing multi-functional construction materials, sensor technology, and probabilistic modeling of physical-chemical property transitions. Furthermore, his current research integrates the chemistry of the corrosion process with mechanical damage across multiple length scales. He has been a member of the American Concrete Institute since 2016.

**Dr. Moochul Shin** is currently working as an Associate Professor in the Department of Civil and Environmental Engineering at Western New England University, Springfield, Massachusetts, USA. He has served as the institutional lead of the University of Transportation Center in the New England Region since 2018. His research interests are primarily in the structural applications of smart and innovative materials, advanced modeling, earthquake engineering, and prestressed concrete structures.

KONA Powder and Particle Journal

KONA Powder and Particle Journal No. 42 (2025) 57–78/https://doi.org/10.14356/kona.2025014 Review Paper

# Integrating Flow Testing and Particle Imaging: Advances in Characterising Granular Flows†

**Zohreh Farmani[1,2], Jan A. Wieringa[3], John van Duynhoven[3,4] and Joshua A. Dijksman[1,2*]**

[1] *Van der Waals-Zeeman Institute, Institute of Physics, University of Amsterdam, The Netherlands*
[2] *Dept. of Physical Chemistry and Soft Matter, Wageningen University, The Netherlands*
[3] *Unilever Foods Innovation Centre, The Netherlands*
[4] *Laboratory of Biophysics, Wageningen University, The Netherlands*

In this study, we explore the intersection of mechanical testing and particle imaging techniques, offering a new perspective on granular material science. We examine a range of flow testers, such as the Schulze shear tester, FT4 powder flow tester, and split-bottom tester, each of which provides valuable insights into how materials respond to compression and shear forces. Simultaneously, we discuss imaging techniques such as refractive index matching, MRI, and X-ray imaging, revealing their capacity to capture the intricate behaviours of particles and flow dynamics at a microscopic level. This combination of macroscopic flow testing and microscopic imaging promises to unlock unprecedented insights into granular materials and complex fluids. Furthermore, we discuss the current challenges in imaging granular flows and recent advances in coupling flow tests with particle imaging.

**Keywords:** flow tester, particle imaging, flow dynamics, granular materials, material science

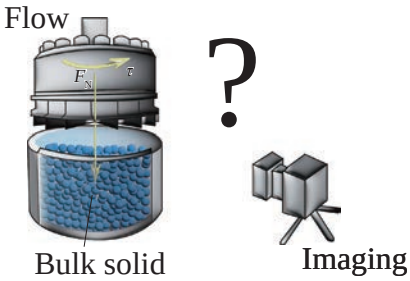


## 1. Introduction

Powders and granular materials are integral components in the production of everyday products, playing a pivotal role across various industrial sectors, spanning from the food industry (Cataldo et al., 2009), pharmaceuticals (Wang et al., 2016), ceramics (Curran et al., 1993), battery assembly (Gaitonde, 2016), and glue production (Duran, 2012). In these applications, the handling, flow, and compaction properties of powders and granular materials is of paramount importance. A profound understanding of their behaviour under shear and compression is indispensable for optimising industrial processes, ensuring product quality, and enhancing overall efficiency (Mesri and Vardhanabhuti, 2009). To gain such insights, one can rely on a diverse array of techniques and instruments, enabling researchers to probe the mechanical response and structural characteristics of granular materials.

In addition, particle imaging techniques have emerged as indispensable tools for understanding the dynamic behaviour of granular materials (Clarke et al., 2023), particularly due to the inhomogeneous and anisotropic flow properties exhibited by these materials. These techniques encompass a range of methodologies, including digital image correlation, particle tracking velocimetry, and X-ray tomography (Vego et al., 2022). They provide researchers with the capability to visualise and track individual particles within granular assemblies, allowing for the direct observation of important variables such as particle motion, packing density, packing structures, and flow patterns. Particle imaging techniques are particularly valuable in the context of granular material flow because they offer insights into phenomena such as particle rearrangements (Chen et al., 2021), shear banding (Wang et al., 2022a), and interparticle interactions (Wiebicke et al., 2020). By integrating mechanical testing with particle imaging, we can bridge the gap between macroscopic and microscopic observations, leading to a more comprehensive understanding of how granular materials respond to external forces.

The primary objective of flow testing is to characterise the flow behaviour of powders and granular materials—an essential facet of powder properties that requires comprehensive understanding. Flow testing involves the measurement of stress in multiple directions or planes, along with strain and flow rates. It allows for the manipulation of various experimental variables, including boundary conditions (e.g., slip, no slip, partial slip, fluidity) and rigidity (e.g., constant pressure vs. constant volume). However, selecting an appropriate flow tester presents a significant challenge because the choice depends on the specific experimental conditions, including the size constraints of the shear cell relative to the particle sizes used. Size effects also play a

† Received 17 February 2024; Accepted 15 April 2024
J-STAGE Advance published online 10 August 2024
* Corresponding author: Joshua. A Dijksman;
[1] Science Park 904, 1098 XH Amsterdam The Netherlands
[2] Helix Building, 6708 WK Wageningen, The Netherlands
E-mail: j.a.dijksman@uva.nl
TEL: +31-20-525-6311

crucial role in many flow properties; however, for very small particle sizes, the container size's impact is minimal. Nonetheless, the issue of size effects merits thorough discussion and consideration. Therefore, it is imperative to classify the various types of shear and compression testers available. Additionally, flow testers tend to become known in a particular sub-field of science and engineering, limiting the reach of the results obtained from such work.

This review paper provides a comprehensive examination of two key aspects in the study of granular materials: flow testing methodologies and particle imaging techniques. By categorising, explaining, and critically assessing these methods from a range of different fields, we aim to offer a valuable resource for researchers and engineers working in the field of granular materials. We also address the typical challenges that one might encounter in the imaging of granular materials, offering insights into how to navigate and overcome these hurdles effectively. Finally, we provide a comprehensive overview of the recent advances in imaging particulate systems. These include the following: 1) X-ray rheography, which enables the study of continuous granular flows; 2) the utilisation of multiple imaging methods, combining various techniques to align with specific research goals; 3) ultrafast electron beam X-rays, allowing for time-resolved imaging of dynamic processes; and 4) rheo-MRI, a method that has recently attracted significant attention due to its capacity to provide detailed insights into the rheological properties of a system while simultaneously offering dynamic imaging capabilities.

## 2. Confined flow testers

As illustrated in **Fig. 1**, flow testers can generally be categorised into two main groups: direct and indirect approaches. In direct shear testers, the direction of applied stress is not fixed, whereas in indirect methods, the applied stress remains constant, allowing for the control and direct measurement of principal stresses and deformations. The subgroups of direct methods are further divided into translational and rotational categories. In translational shear testers, relative displacement occurs in a straight-line motion, as typified by the Jenike shear tester (Jenike, 1964).

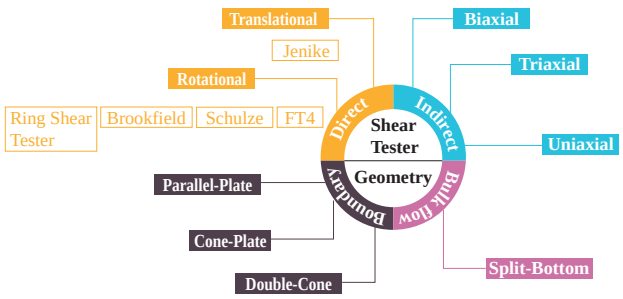


**Fig. 1** Overview of existing flow testers, including direct and indirect testers and bulk and boundary flow testers.

On the other hand, rotational shear testers feature the top part of the cell rotating relative to the bottom part, and these can be further divided into torsional (Orband and Geldart, 1997) and ring shear testers (Schulze, 2011). Torsional testers involve shear deformation by rotating particles around the vertical axis, whereas ring shear testers have annular shapes that promote more homogeneous deformation (Sun, 2016). In the indirect group, testers like uniaxial, triaxial, and biaxial testers play a crucial role in studying the deformation properties of granular materials.

To study granular flows while maintaining reasonable control over boundary conditions and achieving quasi-two-dimensional flow profiles, one can turn to classical rheological geometries. Examples include parallel-plate (PP) (Lu et al., 2007), cone-plate (CP), and double-cone (DC) geometries (Tsai et al., 2020). These geometries allow for the control of shear and normal stresses on the bottom and top walls, with the imposed strain rate being independent of the radial position. Consequently, the induced flow profiles exhibit radial symmetry, at least in steady-state conditions, and even an up–down symmetry in the case of double-cone geometry when gravity can be neglected. These profiles can be accurately and relatively easily measured over a wide range of flow rates (Boyer et al., 2011; Tsai et al., 2020). Another example of such flow tests is a hopper flow tester. Extensive research has been conducted on both 2D (Wang et al., 2021) and 3D (Stannarius et al., 2019b) hopper configurations to investigate the influence of various parameters. These parameters include the hopper's height (Tsai et al., 2020), which affects the gravitational forces and pressure on the materials, and the angle of the hopper walls (Guo et al., 2023), which influences flow dynamics, the presence of an obstacle (Wang et al., 2022b), which affects the stress gradient in the packing, and the inherent characteristics of the granular material itself, such as particle size and shape (Pongó et al., 2022), friction, and stiffness (Stannarius et al., 2019a). All of these factors can significantly impact the rate and behaviour of the material as it flows through the hopper. Hoppers are also used to prepare bulk powder (e.g. in an angle of repose test). Nevertheless, we are not aware of (standardised) hopper-flow-based testers that directly quantify flow properties.

Probing the flow dynamics of granular materials presents a challenge, especially in the context of slow and fast flow limits, as defined by inertial or viscous inertial numbers (Boyer et al., 2011; Dijksman et al., 2010). For slow flows, one typically employs boundary motion, slowly shifting a container's boundary containing grains. Stress and flow profiles become independent of the flow rate, often resulting in localised shear bands near the moving boundaries. Geometries like the split-bottom Couette geometry or its variants (Dijksman and van Hecke, 2010) allow the imposition of specific flow boundary conditions

that induce wide shear zones away from boundaries. However, these flow profiles are fully three-dimensional and intricate, making it challenging to impose stress conditions. In more industrial contexts, testers designed by Jenike, Schulze, and others exhibit narrow shear zones and well-controlled stress boundary conditions (Schulze, 2008).

For faster flow limits, inclined planes (MiDi, 2004), avalanche flows (Tegzes et al., 2002), hopper flows, or impact tests (Faug, 2020) are employed. Although these setups offer access to bulk flow behaviour, they provide limited control over flow profiles and boundary conditions. Finally, rotating drum experiments, while offering good control over the overall flow rate, often exhibit intricate flow behaviour, ranging from stick-slip to highly heterogeneous flow, particularly in cohesive particle systems.

Francia et al. (2021) explored innovative techniques for characterising granular flow transitions and noted challenges in standardisation. In another review, Ogata (2019) reviewed advancements in assessing cohesive powder flowability across various handling processes.

## 2.1 Jenike shear tester

The Jenike shear tester is one of the earliest and most widely used powder flow characterisation techniques, originally developed around 1960 by Jenike for applications in hoppers and silos (Jenike, 1964). This shear tester simulates the flow within a hopper or silo by applying specific pressures that induce shear and consolidation of the powders.

A schematic of the Jenike tester is shown in **Fig. 2**. It consists of a fixed base part with a horizontally movable ring and a shear lid. Particles, covered with the shear lid, are placed inside the ring and the base. The testing process begins by applying a normal load to the shear lid and the particles using a weight hanger. To measure the shear force, the shear ring and lid are moved horizontally through a stem connected to a drive system. The bracket, shear lid, and shear ring transfer the measured shear force through a force transducer to the particles. Pre-consolidation is a crucial preparatory step in Jenike shear testing to establish a consistent and controlled initial state for the powders. Pre-consolidation involves subjecting the powder to a specific level of compaction or consolidation pressure before the actual shear test. This ensures that the limited shear displacement available in the tester is effectively utilised to study the material's shear behaviour without interference from inconsistent initial packing.

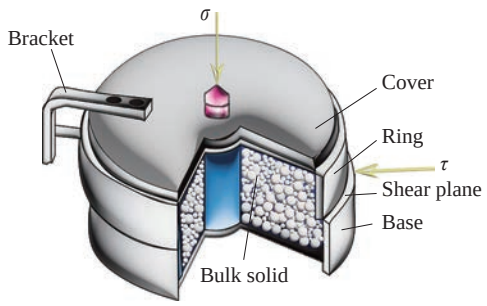


**Fig. 2** Illustration of the Jenike shear tester, comprising a bracket, a stationary base section with a horizontally adjustable ring, and a shear lid by which you can impose a certain shear stress $\tau$. The test starts by applying a normal load $\sigma$ to the shear lid using a weight hanger.

**Fig. 3** illustrates the stages of shear testing in the Jenike shear tester. Initially, there is a sharp increase in shear stress as time passes during the pre-shear stage. However, the curve gradually flattens until it reaches a plateau, indicating a steady-state condition. After achieving a steady state, the stem reverses, reducing the shear stress to zero. Subsequently, the stem moves forward, causing the shear stress to increase until it reaches a maximum peak. At this point, the particles begin to move and deform, leading to failure, after which the shear stress decreases.

The Jenike tester allows the measurement of parameters such as failure strength, internal friction, and wall friction (Grima et al., 2010; Han, 2011). Despite its simplicity, robustness, versatility, suitability for cohesive powders, and ability to measure wall friction, it has some limitations. The primary limitations of the Jenike shear tester are particle size (<2 mm), shear displacement (typically 6–8 mm), and small normal loads (<7 kPa) (Bilgili et al., 2004). To address these limitations, annular-shaped testers, such as the

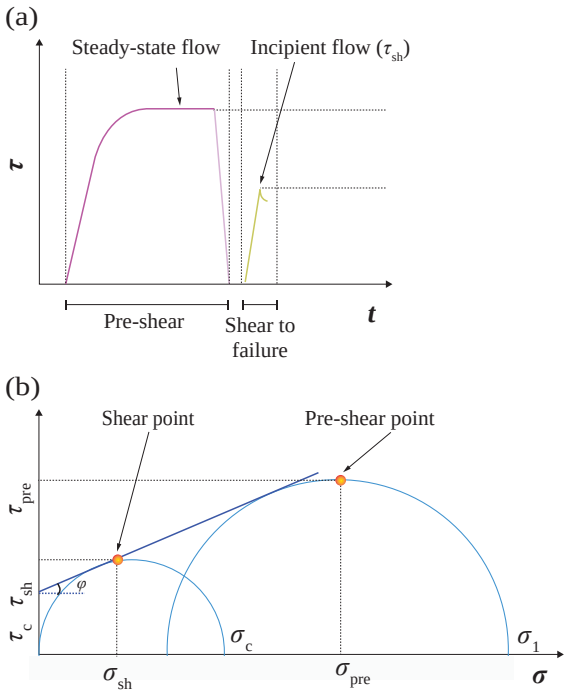


**Fig. 3** **(a)** Various stages of shear testing in a Jenike shear tester, from the pre-shear phase to shear initiation and eventual failure. **(b)** Mohr circle representation, illustrating the corresponding shear point ($\tau_{sh}$, $\sigma_{sh}$), pre-shear point ($\tau_{pre}$, $\sigma_{pre}$), compressive strength or unconfined yield strength $\sigma_c$, consolidation stress $\sigma_1$, and angle of internal friction $\phi$.

Schulze shear tester, have been introduced (Schulze, 2008). These testers offer improved capabilities for studying powders under specific conditions and have become valuable tools in powder flow research.

## 2.2 Schulze shear tester

The Schulze shear tester, depicted in **Fig. 4**, features an annular design in which particles are placed within an annular bottom ring of the shear cell. An annular lid attached to a crossbeam covers the particles from above. To measure the shear force, two parallel tie rods are connected to a load beam, allowing for the measurement of forces acting on the tie rods. The shearing test starts by rotating the bottom ring in a specific direction, with the tie rods preventing any rotation in the crossbeam and lid. Similar to the Jenike tester, a normal load is applied using a weight hanger attached to the crossbeam. Unlike the Jenike tester, where preconsolidation is required (due to limited shear displacement), the Schulze shear tester eliminates this need. After inserting the weight hanger, counterweight system, and tie rods on the crossbeam, the cell is ready for the shearing test. The steps involved in conducting the experiments are illustrated in **Fig. 5**. During the pre-shearing phase, the shear stress increases with time until it reaches a maximum value. Subsequently, in the steady state, the rotation direction is reversed until the shear stress drops to zero. The next shearing step continues until another maximum shear stress, indicating particle flow (failure), is achieved. Testing can proceed further by repeating the pre-shearing and shearing stages until another failure point is reached.

Two versions of the Schulze tester are currently available: the shear cell XS with a specimen volume of 30 cm$^3$ (RST-XS) and the shear cell M with a specimen volume of 900 cm$^3$ (RST-M). In 2008, a "round robin" project was initiated to investigate ring shear testers (Schulze, 2011). The primary objective of this round robin project was to establish a range of results for specified bulk solid, specifically limestone powder CRM-116. This initiative aimed to create a reference range of results, similar to what had been accomplished with the Jenike shear tester (Akers, 1992). This reference range serves as a benchmark, enabling users to assess whether their testing equipment can yield results that align with the established reference values. The round robin study also provides recommendations for the operational conditions of the Schulze tester.

The Schulze shear tester has been widely used in various research works focussed on powders and granular materials. Researchers have employed Discrete Element Method (DEM) simulations to replicate powder flow in this tester (Guo et al., 2019). These simulations, conducted with spherical and elongated particles, serve to calibrate the parameters influencing shear flow. Key parameters, including particle shape, particle stiffness (Coetzee and Els, 2009), shear cell size (Aigner et al., 2013), shear rate, Poisson's ratio, and coefficient of restitution (Wang et al., 2020), and particle–wall friction coefficient (Simons et al., 2015) were evaluated through shear tester simulations.

The Schulze shear tester offers several advantages over the Jenike shear tester, such as low and negative normal forces (<100 Pa), delicate materials, adjustable lid (more uniform shear distribution), lightweight design, unlimited shear displacement and strain, and particle size (up to

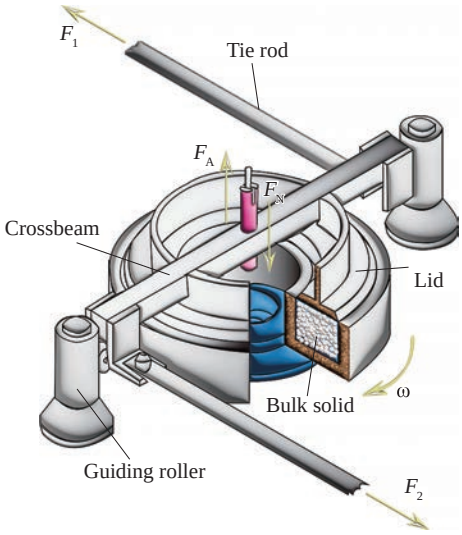


**Fig. 4** Illustration of the Schulze shear tester, comprising an annular bottom ring, annular lid, crossbeam, two parallel tie rods (measuring two acting forces $F_1$ and $F_2$), load beam, and guiding rollers. Shear force $\tau$ is equal to $F_1 + F_2$. A normal load $\sigma$ is applied using a weight hanger attached to the crossbeam.

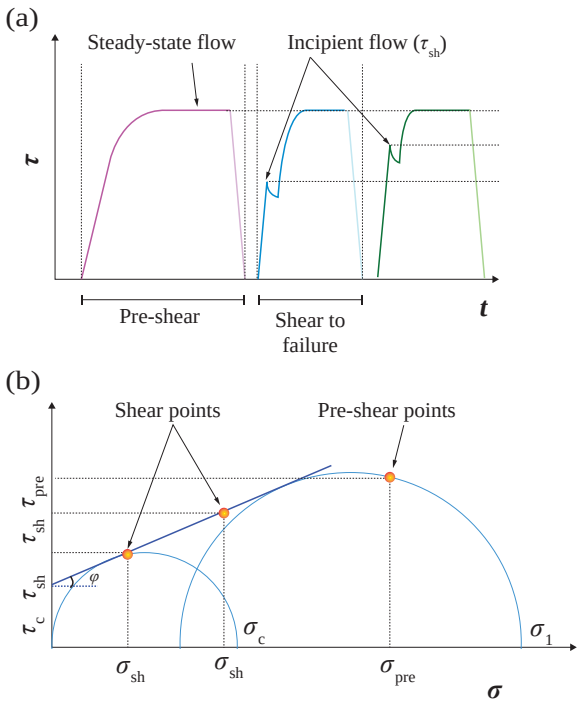


**Fig. 5** Various stages of shear testing in a Schulze ring shear tester. **(b)** Mohr circle representation.

5 mm). For very fine or very coarse materials, alternative testing methods may be required.

Although the Schulze shear tester is versatile, it may not be ideal for all types of materials. It is particularly well suited to bulk solids and dry powders. Materials with unique properties, such as highly-cohesive particles, may pose challenges in the testing and interpretation of results. Similar to many other testing methods, the Schulze shear tester may be sensitive to temperature and moisture levels. Variations in environmental conditions, such as temperature and moisture level can impact material behaviour during testing.

## 2.3 FT4 shear tester

In 2003, Freeman Technology, a company based in Tewkesbury, UK, introduced the FT4 powder tester (Freeman, 2004). Originally intended for characterising the rheological properties of powders, this tester has evolved to cover a broad spectrum of applications. Over time, it has incorporated various accessories and methodologies, categorising it into bulk (density, compressibility, and permeability), dynamic flow (flowability, aeration, consolidation, flow rate, and specific energy), shear (shear cell, and wall friction), and process (segregation, attrition, caking, electrostatics, moisture, and agglomeration) testing capabilities. This versatility has resulted in a substantial body of work employing this shear tester (Hare et al., 2015; Khala et al., 2021).

The FT4 tester combines rotational and translational testing principles. It features a twisted blade that rotates and moves vertically downward and upward through the powder bed. A schematic of the FT4 tester is shown in **Fig. 6**. The testing procedure involves four key steps: conditioning, consolidation, pre-shearing, and shearing, which closely mirror the procedures of other shear testers. Upon filling the glass cell, the blade initially descends to compress the powder bed. It then ascends to remove excess powder from the surface, creating a homogeneous layer—a process similar to that of the Schulze tester. Notably, the FT4 tester incorporates an automated conditioning mode, distinguishing it from other testers that require manual intervention with a spatula.

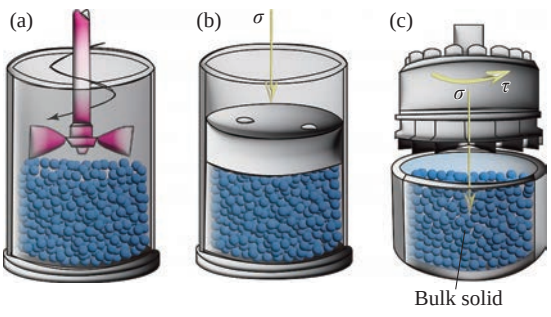


**Fig. 6** Schematic of the FT4 shear tester. **(a)** A twisted blade rotates vertically downward and upward (torque and force can be measured), **(b)** a vented piston can consolidate the powder under a controlled normal stress $\sigma$, and **(c)** an automated rotational shear cell accessory that can go inside the packing and rotate.

During the testing procedure of the FT4 tester, after the conditioning step, a specific normal stress $\sigma$ is applied during the consolidation step. Subsequently, the pre-shearing and shearing steps follow, analogous to the procedure illustrated in **Fig. 5** for the Schulze tester. This entire sequence can be repeated multiple times (typically 3 to 5) to enhance the accuracy and reliability of the results.

The FT4 shear tester is a versatile and comprehensive powder tester that covers a broad range of testing methodologies and parameters, including powder flowability, air flow (Nan et al., 2017b), particle shape (Nan et al., 2017a), dynamic flow behaviour (Hare et al., 2015; 2017), shear characteristics (Hare and Ghadiri, 2017), and various process-related attributes. In addition to the extensive volume of powder rheometry experiments conducted with FT4, a body of numerical research complements the experimental work (Khala et al., 2021; Nan and Gu, 2020).

The FT4 tester typically operates within a maximum consolidation normal stress of 3–7 kPa, maximum torque of 900 mN·m, and maximum rotational and axial speeds of 120 rpm and 30 mm/s. The FT4 tester may not be suitable for powders with large particle sizes. Its maximum particle size capability is around 1 mm, which is smaller than that of some other shear testers like the Schulze tester (up to 5 mm). This limitation may affect its applicability to coarser materials (Cordts and Steckel, 2012). In comparison with certain other shear testers, the FT4 tester measures a moderate range of shear stresses. This limitation means that it may not be an ideal choice for materials requiring very high shear stresses for characterisation.

## 2.4 Brookfield powder flow tester

In 2009, a powder flow tester emerged through collaborative efforts between the Wolfson Centre for Bulk Solids Handling Technology at the University of Greenwich and certain private food manufacturers. The tester garnered attention for its ease of use and broad applicability (Berry et al., 2015). While this tester's design principles align with those of the Jenike tester, their primary distinction lies in their intended purpose, which is to tailor it for quality control applications. Numerous studies in the literature (Salehi et al., 2017) have now showcased industrial trial results and affirmed the applicability and utility of the Brookfield powder flow tester.

**Fig. 7** illustrates the Brookfield setup, including the flow function lid and trough filling accessories. Notably, the Brookfield tester incorporates an annular shear cell, similar to the Schulze tester. However, it is different in its design, where the lid attaches to the compression plate, facilitating powder filling and load application with minimal operator involvement. The simplicity of conducting powder

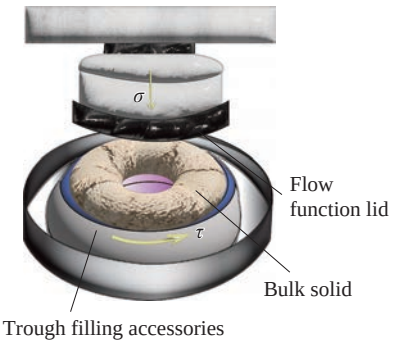


**Fig. 7** Schematic of the Brookfield shear tester including the annular shear cell, flow function lid, and trough filling accessories.

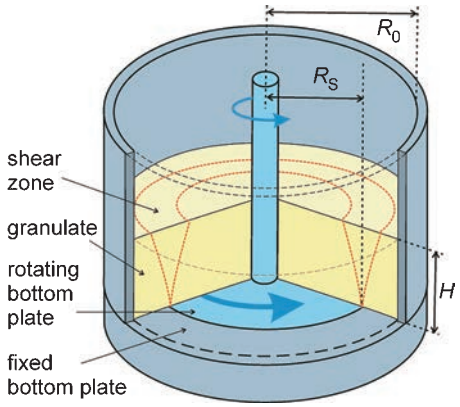


**Fig. 8** A schematic of the split-bottom shear cell, with $R_s$ the radius of the inner cylinder, $R_0$ the radius of the outer cylinder, and $H$ the thickness of the particle layer. (Reprinted from Ref. (Wang et al., 2022a) under the terms of the CC-BY 4.0 license. Copyright: (2022) The Authors, published by Springer Nature.

rheology tests with Brookfield equipment has recently made it a popular choice (Leaper, 2021; Navar et al., 2022).

The Brookfield tester facilitates the measurement of several key parameters, including flow function, unconfined failure strength, time consolidation, internal friction angle, cohesion, wall friction, bulk density, and compressibility. In terms of the shear stress they measure, a comparison reveals that the Brookfield tester measures moderate shear stresses compared to the Jenike and Schulze testers, where Jenike < Brookfield < Schulze.

However, like its counterparts, the Brookfield tester is not without limitations. Its primary constraint pertains to the maximum consolidation normal stress (4.8–13 kPa), which is much lower than that of the Schulze shear tester (50 kPa). Regarding the particle size that it can accommodate, one can consider Brookfield < Jenike < Schulze. This implies that the Brookfield tester is most suitable for materials with particle sizes up to approximately 1 mm, which is considerably smaller than the maximum particle sizes accommodated by the Jenike (2 mm) and Schulze (5 mm) testers.

## 3. Unconfined flow testers

### 3.1 Split-bottom shear tester

In granular flow, the tendency towards localisation in narrow shear bands is a common phenomenon (Szabó et al., 2014; Unger et al., 2004), but there are instances, particularly in slow granular flows, where wider shear zones can be observed (Dijksman and van Hecke, 2010; Fenistein and van Hecke, 2003). To generate slow flows with distinct shear bands, researchers have proposed the use of split-bottom geometry (Fenistein et al., 2004; Wang et al., 2022a). This configuration involves splitting the bottom part of a concentric cylinder system into two sections that can slide past each other, offering greater stability to the shear bands at fixed positions.

**Fig. 8** presents a schematic of the split-bottom geometry. By rotating the inner part, a shear zone is observed to propagate upward and inward from the slip position. The split-bottom cell's unique geometry allows for investigating various factors beyond flow transitions in slow granular flows. These factors include suspension and granular flows (Shaebani et al., 2021; Singh et al., 2014; Wang et al., 2022a), segregation mechanisms (Gillemot et al., 2017), fluid depletion (Mani et al., 2012), non-local flows (Henann and Kamrin, 2013), and faster flows (Luo et al., 2017).

In addition to the experimental investigations, the split-bottom shear cell is often used in numerical simulations, particularly either in Finite Element Method (FEM) simulations (Henann and Kamrin, 2013) or Discrete Element Method (DEM) simulations (Luding, 2007). The geometry of the split-bottom shear cell provides a well-defined boundary condition and initial configuration for FEM and DEM simulations, making it an excellent choice for calibration.

Despite the above-mentioned advantages of the split-bottom geometry, there are some limitations. The limitations of a split-bottom shear cell include constraints related to particle size compatibility (100 μm to a few mm), the range of applicable confining stresses (0.1–2 kPa), and the absence of features for precise temperature or environmental control. Thus far, the flow geometry has not been used in any commercially available or standardised testing machine.

### 3.2 Rotating drum

In addition to traditional shear testers, a rotating drum is another valuable tool for studying the behaviour of granular materials. This dynamic testing system, originally introduced by Yuri Oyama (1940) in 1940, has gained significant attention from researchers interested in granular material dynamics. It has proven to be an effective method for investigating mixing and segregation, which are fundamental processes in various industrial applications.

Researchers have conducted numerous experiments (Huang et al., 2021; Li et al., 2021) and theoretical (Li et

al., 2021; Xiu et al., 2021) studies using rotating drums, exploring various parameters that affect granular material behaviour. These parameters include particle shape (Preud'homme et al., 2021), drum geometry (Fiedor and Ottino, 2003), filling ratio (Inagaki and Yoshikawa, 2010), and segregation mechanisms (Chen et al., 2010).

A typical rotating drum setup, depicted in **Fig. 9**, consists of a cylindrical vessel with specific dimensions that can rotate at an angular velocity $\omega$. The drum is partially filled with particles, although fully filled drums have been studied under specific conditions (Inagaki and Yoshikawa, 2010).

The testing procedure for rotating drum involves partially filling the drum with particles. The drum is then rotated at a controlled angular velocity $\omega$. As the drum rotates, various flow regimes are observed (Yang et al., 2008), depending on the rotational speed, including slipping at low $\omega$, slumping, rolling, cascading at intermediate $\omega$, and cataracting and centrifuging at high $\omega$. Researchers typically focus on rolling regimes, which are relevant to many industrial processes. Throughout the experiment, parameters such as particle motion, segregation, mixing behaviour, and the angle of repose, which defines the maximum angle at which a granular material remains stable on a surface, were closely monitored and analysed.

Rotating drum allows for the visualisation of the flow regime transitions, segregation, and mixing efficiency (Beaulieu et al., 2022). The velocity profiles of particles in the drum can be measured to gain insights into the distribution of particle speeds during mixing. Moreover, one can measure a (dynamic) "angle of repose" that provides information about its flowability and internal friction. Parameters like the flowability index ($\frac{\rho_{Tapped}-\rho_{Bulk}}{\rho_{Tapped}}$) or the Hausner ratio ($\rho_{Tapped}/\rho_{Bulk}$) can be determined to assess the flow properties of granular materials. The drum can also be used to study how particle shape influences segregation, mixing, and flow patterns (Cunez et al., 2023; He et al., 2023).

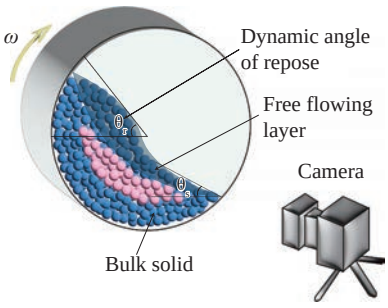


**Fig. 9** Schematic of a rotating drum consisting of a cylindrical vessel rotating at an angular velocity $\omega$. The drum is partially filled with particles. By visualising the particle motion through a camera, one can measure the dynamic angle of repose $\theta$.

## 4. Compression testing techniques

### 4.1 Uniaxial compression tester

A schematic of the uniaxial compression cell is depicted in **Fig. 10**. The uniaxial compression test procedure is similar to that of the Jenike shear tester (Parrella et al., 2008). A sample is filled into a cylinder with frictionless walls and is consolidated under a normal stress $\sigma_1$ (consolidation stress), leading to an increase in bulk density $\rho_b$ (Cavarretta and O'Sullivan, 2012). This consolidation step is the same as the pre-shear step in shear testers. After removing the cylinder, the sample is loaded vertically with an increasing normal stress up to the point of failure, where the sample will experience a break or failure at a certain stress $\sigma_2$. The stress at failure is the unconfined yield strength. Contrary to the results of the shear tests, steady-state flow cannot be reached during consolidation. By reaching the failure point, the sample begins to flow. Uniaxial compression tests can be conducted at different consolidation stresses, allowing us to plot the unconfined yield strength against the consolidation stress. This produces a flow function curve, as illustrated in **Fig. 11**, which aids in assessing the sample's flowability. In order to characterise the flowability, the term $ff_c$ is defined as the ratio of consolidation stress $\sigma_1$ to

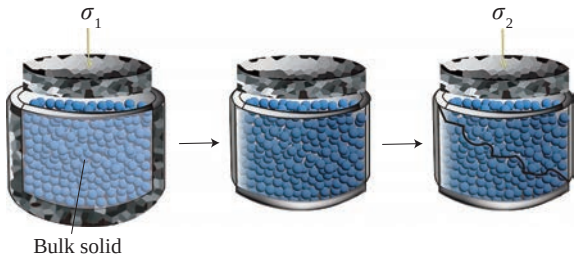


**Fig. 10** Steps of the uniaxial compression test. The first step **(left)** is the consolidation of particles inside the cylinder under a normal stress $\sigma_1$. In the next step, we remove the cylinder. At the final step **(right)**, the particles will experience a failure at a certain stress $\sigma_2$ called unconfined yield strength.

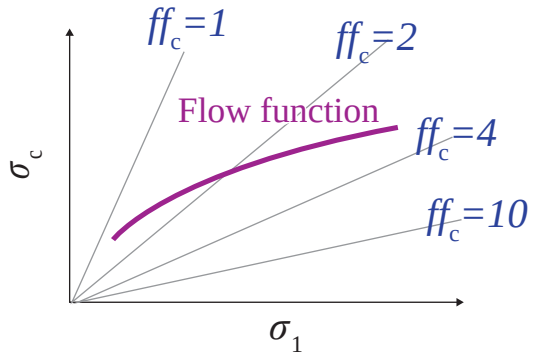


**Fig. 11** Flowability curve: unconfined yield strength $\sigma_c$ versus consolidation stress $\sigma_1$. The term $ff_c = \sigma_1/\sigma_c$, characterises the flowability of particles. The larger the $ff_c$ is, the better the particle flow. There are five regions in the flowability curve: no flowing ($ff_c < 1$), very cohesive ($1 < ff_c < 2$), cohesive ($2 < ff_c < 4$), easy-flowing ($4 < ff_c < 10$), and free-flowing ($ff_c > 10$).

unconfined yield strength $\sigma_2$. The larger the $ff_c$ is, the better the particle flow. In **Fig. 11**, you can find a flowability classification close to the Jenike classification, which specifies that under higher consolidation stress, a particle can flow better.

## 4.2 Biaxial compression tester

The biaxial tester can be considered as a translational tester because it consists of two movement in *x* and *y* directions. As can be observed from **Fig. 12**, there is a loading plate, loading rod, and guide rod by which the test can be performed. In the first step after filling the cell with particles, the loading plate, which is placed on top of the base cell, moves through *x* direction until the favourable consolidation stress $\sigma$ is gained. By moving this plate, the particles are consolidated. In order to obtain a constant consolidation stress and reach a steady-state flow, the loading plate can be pushed further in *x* direction and at the same time, the guide rod will move backward in *y* direction. After the steady-state step, there is an unloading step in both *x* and *y* directions. To measure the unconfined yield strength, the guide rod should first be removed, and then the loading plate moves again in *x* direction until failure occurs. The unconfined yield strength can be calculated from the force acting on the loading rod at failure. The similarity between uniaxial and biaxial tests is in the application of consolidation stress and measurement of the unconfined yield strength (Satone et al., 2017).

## 4.3 Triaxial compression tester

This tester is the standard shear tester in soil mechanics (Balla, 1960; Oda, 1972), and is mostly applicable for the measurement of shear strength, cohesion, permeability, and stiffness (Schnaid et al., 2001; Shinohara et al., 2000). For testing, the sample must be placed in a cell that can be pressurised and sealed with a rubber membrane along its walls. The rubber membrane must be pre-stressed; therefore, the tester in its standard form is not applicable to the low-stress region of interest in powder technology. After filling the cell with particles, the particles are usually, but not always, saturated, consolidated, and sheared. During the shearing step, the particles are loaded axially, which can be by compression or extension. Based on the schematic of the triaxial setup shown in **Fig. 13**, the triaxial cell is placed inside a pressure vessel. By pressing the fluid surrounding the cell, the confining pressure $\sigma$ is applied. The triaxial cell is placed between a loading platform from the bottom, which can move upward, and a loading cell on the top. There is also a hydraulic unit to control the cell pressure. Vacuum is used to hold the particles inside the cell until the confining pressure is applied. The entire setup is connected to a computer system to record the transducer data of displacement, pressure, and force.

Within the domain of granular materials, researchers frequently employ triaxial tests to examine a diverse array of mechanical properties and behaviours exhibited by these materials under carefully controlled conditions. Triaxial tests also have substantial utility in the field of experimental granular physics, where they serve as valuable tools for delving into the fundamental (anisotropic) mechanical characteristics and behaviours inherent to granular materials. Such investigations provide valuable insights into intriguing phenomena, including jamming (Peshkov and Teitel, 2022), shear localisation, and the dynamics of granular flow (Nadimi et al., 2020). Additionally, noteworthy studies have explored the application of triaxial tests to the rheology of soft particles (Nezamabadi et al., 2021; Vu et al., 2021), further expanding the scope of research in this area.

Note that beyond the aforementioned flow testers, the capillary flow tester has been employed to optimise manufacturing processes and ensure product quality of particles

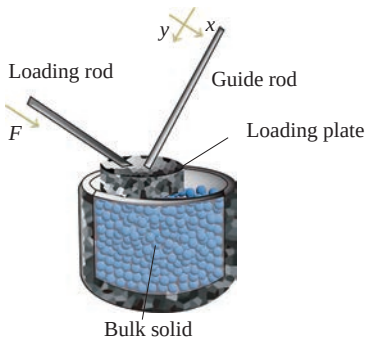


**Fig. 12** Schematic of biaxial tester including a loading plate, loading rod, and guide rod. By moving the loading plate until a certain consolidation stress $\sigma$, the particles are consolidated. The unconfined yield strength can be calculated from the force *F* acting on the loading rod at failure.

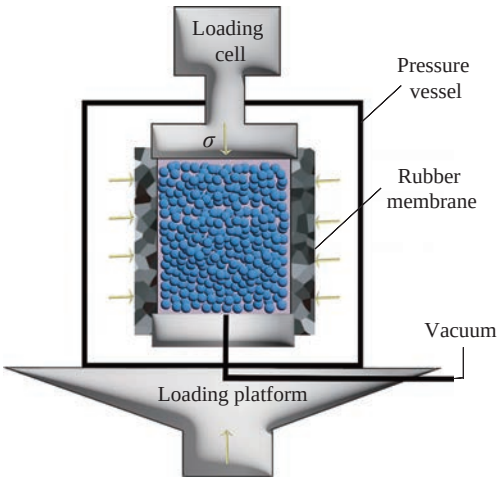


**Fig. 13** Schematic of triaxial tester including the loading cell, loading platform, pressure vessel, rubber membrane, and vacuum. The triaxial cell is placed between a loading platform from the bottom and a loading cell on the top. A hydraulic unit controls the cell pressure, while vacuum holds particles until confining pressure $\sigma$ is applied.

in industrial processes, albeit at limited scale so far for particles or particle-fluid mixtures. The capillary flow tester focuses on the fluid or ductile material's behaviour as it flows into and within a capillary. Typically, the pressure difference along the capillary is measured in relation to the material flow rate, allowing the extraction of specific rheological information from this data (Mackley and Rutgers, 1998), especially at elevated pressures. Utilising a capillary flow tester, or capillary rheometry, offers the advantage of efficiently accessing high shear rate flow properties and flow instabilities relevant to industrial processing. Capillary rheometry has found application in simulating polymer extrusion processes (Couch and Binding, 2000; Laun, 2004), food processing (Zhang et al., 2022), coatings production (Luo et al., 2021), and pellet manufacturing (Bastiaansen et al., 2023).

## 5. Comparison of confined and unconfined flow testers

We have summarised the advantages, limitations, and applications of the various powder testers in **Tables 1** and **2**. Extensive research has been conducted to compare the functionality and applicability of these powder rheometry methods. These studies encompass comparative analyses of flow properties in cohesive powders (Du et al., 2023; Koynov et al., 2015; Leturia et al., 2014; Salehi et al., 2017; Shi et al., 2018; Zafar et al., 2019), pharmaceutical powders (Deng et al., 2022; Leaper, 2021; Shah et al., 2008; Tay et al., 2017), steel powders (Marchetti and Hulme-Smith, 2021), and food powders (Juliano and Barbosa-Cánovas, 2010).

## 6. Particle imaging methods

Imaging of particle systems is highly valuable because it provides visual insights into the behaviour and interactions of individual particles within a larger assembly. This enables researchers to observe microscopic details, analyse flow dynamics, track changes over time, and bridge micro (particle) and macro (constitutive modelling) levels. Imaging techniques have been combined with rheometry or particle flow measurements in various systems to gain a comprehensive understanding of the material behaviour (Amon et al., 2017). In the study of granular materials, imaging techniques such as high-speed cameras, X-ray imaging, and laser-based imaging methods have been integrated with rheometers to perform rotational shear and compression measurements. This combination allows simultaneous measurement of the rheological properties of the particles under shear or compression and visualise the particle flow and interactions in real time. In addition to granular materials, the combination of imaging with flow measurements has been used in complex fluids, such as emulsions (Paredes et al., 2011), suspensions (Graziano et al., 2021; Moud et al., 2022), and foams (Verma et al.,

**Table 1** Comparison of different shear and compression testers.

| Tester | Advantages | Limitations | Typical applications |
|---|---|---|---|
| Jenike (Jenike, 1961) | Simplicity and robustness; Historical significance. | Limited shear displacement (6–8 mm); Normal loads (>7 kPa); Particle size <2 mm; Stress homogeneity. | Design of silos for flow (Schwedes, 2003); measurement of failure strength and wall friction (Han, 2011). |
| Schulze (Schulze, 2008) | Unlimited shear displacement; Low or negative normal forces possible (<100 Pa); Uniform shear distribution. | Particle size <5 mm; Not suitable for highly cohesive and highly elastic powders. | Measuring shear strength, flow function $ff_c$, angle of internal friction $\phi$, wall friction, bulk density $\rho_b$ (Schulze, 2021; Wang C. et al., 2022). |
| FT4 (Freeman, 2004; 2007) | Originally designed for rheology; Versatile and comprehensive; Addresses diverse needs in research and industry. | Limited maximum consolidation normal stress (3–7 kPa); Particle size <1 mm; Not suitable for extremely elastic/coarse powders. | Bulk (density, compressibility, and permeability) (Nkurikiye et al., 2023); Dynamic flow (flowability, aeration, consolidation, flow rate, and specific energy) (Divya and Ganesh, 2019); Shear (shear cell, and wall friction) (Hare and Ghadiri, 2017) ; Process (segregation, attrition, caking, electrostatics, moisture, and agglomeration) (Mitra et al., 2017). |
| Brookfield (Berry and Bradley, 2010) | Fast, economical, and easy to use; product improvement and quality control. | Limited maximum consolidation normal stress (4.8–13 kPa); Particle size <1 mm, Not for extremely elastic bulk solids. | Measuring flow function, unconfined failure strength, time consolidation, angle of internal friction $\phi$, wall friction, bulk density $\rho_b$, compressibility (Navar et al., 2022). |

**Table 2** Comparison of different shear and compression tests.

| Tester | Advantages | Limitations | Typical applications |
|---|---|---|---|
| Split-Bottom (Fenistein et al., 2004; Fenistein and van Hecke, 2003). | Robust shear bands; Can be easily coupled with 3D imaging techniques. | Limited control over complex industrial flow conditions; Not suitable for powders due to split geometry; Only for quasi-static flows. | Dense suspensions and slow granular flows (Wang et al., 2022a), segregation (Gillemot et al., 2017); fluid depletion (Mani et al., 2012), non-local flows (Henann and Kamrin, 2013); faster flow (Luo et al., 2017). |
| Rotating Drum (Oyama, 1940) | Studying mixing and segregation; Visualisation of flow regime transition. | Limited control over complex industrial flow conditions. | Fundamental research on granular materials; Measuring dynamic angle of repose, flowability, and internal friction (Huang et al., 2021; Li et al., 2021). |
| Uniaxial | Measures compressive strength under 1D compression; Simple and widely used. | Limited to 1D compression tests and fine-grained/cohesive powders; Cannot measure internal or wall friction. | Basic assessment of compressive behaviour in granular materials (Cheng and Wang, 2022; Le, 2022) and flowability. |
| Biaxial | Measures compressive strength under confined conditions. | Limited to confined compression tests. | Study of confined compression behaviour in granular materials (Satone et al., 2017). |
| Triaxial | Measures compressive strength under controlled confining pressure. | Requires complex testing equipment. | Soil mechanics (Oda, 1972) (measurement of shear strength, cohesion, permeability and stiffness (Schnaid et al., 2001)). |

2018). For example, particle tracking velocimetry (PTV) or particle image velocimetry (PIV) techniques combined with rheological measurements provide insights into the microstructure, particle dynamics, and flow behaviour of these complex fluid systems.

We review several common approaches that stretch the limits of particle imaging-based techniques. These techniques provide insights into the behaviour, properties, and dynamics of granular systems. They allow us to unravel the fundamental principles governing the behaviour of granular materials, such as their flow patterns, packing structures, particle rearrangements, and interparticle interactions. Furthermore, these methods extend their reach beyond granular materials alone.

## 6.1 Optical techniques

### 6.1.1 Optical microscopy

Optical microscopy (OM) is a widely used technique for studying particle flow fields (Wang et al., 2022b). **Fig. 14** shows a schematic representation of the optical microscope. OM involves the use of visible light to observe and analyse the behaviour, properties, and dynamics of particles. It requires a light source, typically a lamp or laser, to provide illumination. Light passes through or reflects off the particles of interest. Proper sample preparation, including mounting and positioning, ensures adequate interaction of the light with the particles. The light transmitted or reflected by the particles is collected by an objective lens, which focuses on the light onto an image plane or an eyepiece. The lens system provides magnification, allowing for detailed visualisation of the particles and their interactions. The focussed light forms an image of the particles on a detector, which can be a camera or the human eye. The captured images are then analysed using various techniques, such as image processing, particle tracking

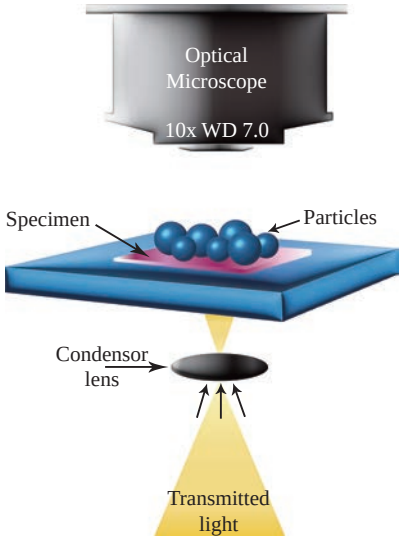


**Fig. 14** Schematic of optical microscopy (OM) including a light source and a condenser lens.

algorithms, and manual measurements, to extract relevant information about particle size, shape, packing arrangements, and flow behaviour.

### 6.1.2 Confocal microscopy

Confocal microscopy (CM) is a powerful imaging technique used to study colloidal suspensions (Hooiveld et al., 2023; Rathee et al., 2020), Pickering emulsions (Benyaya et al., 2023), fluid flow and particle dynamics in microfluidic devices (Lochab et al., 2019), inkjet printing (Shi et al., 2021) and more. It provides high-resolution three-dimensional imaging by selectively focussing on a specific plane within the sample while rejecting out-of-focus light. **Fig. 15** shows a schematic of the confocal microscope. CM uses a laser as the light source. The laser beam is directed onto the sample, and the light emitted from the particles is collected. A pinhole aperture is placed in front of the detector to block out-of-focus light. This pinhole allows only the light emitted from the focal plane to pass through, ensuring that only in-focus information is captured. The laser beam is scanned across the sample using a scanning system such as a galvanometer mirror or acousto-optic deflector. This scanning mechanism rapidly moves the focal point of the laser through the sample in a predefined pattern. The emitted light passes through the pinhole and is detected by a sensitive photodetector, such as a photomultiplier tube or avalanche photodiode. The detected signal is then used to reconstruct a two-dimensional or three-dimensional image of the sample.

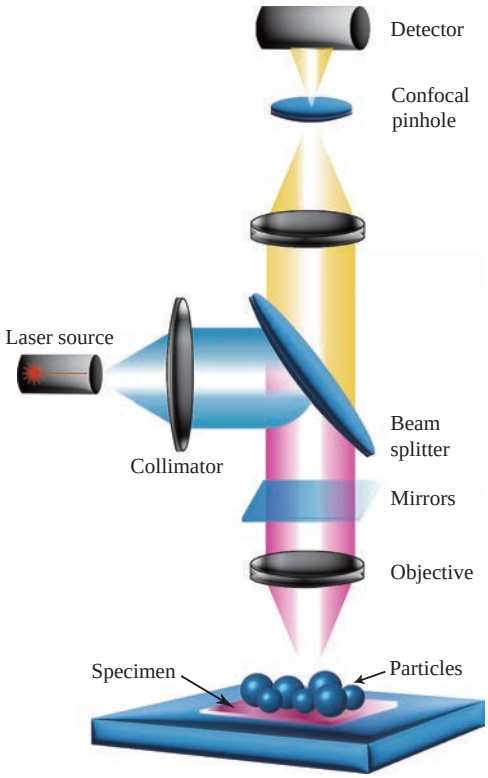


**Fig. 15** Schematic of confocal microscopy (CM) including a laser, detector, pinhole, galvanometer mirrors, objective lenses, and beam splitter.

## 6.2 Refractive index matched scanning (RIMS)

Refractive index matched scanning (RIMS) is a technique used in particle flow field studies to improve the visibility of particles in transparent or translucent media (Dijksman et al., 2013; 2017). It involves the use of a matching fluid or medium with a refractive index similar to that of the particles or surrounding medium. This paper (Dijksman et al., 2012) provides a comprehensive review of the use of RIMS to study densely packed granular materials and suspensions.

**Fig. 16** represents a schematic of the RIMS. To initiate RIMS, the first step involves selecting a refractive index matching fluid that aligns with either the refractive index of the particles or that of the surrounding medium. This fluid is usually a transparent liquid, such as a mixture of glycerol and water or silicone oil, with carefully controlled optical properties. When the refractive index of the matching fluid closely matches that of the particles or surrounding medium, it reduces the refractive index mismatch between the particles and the fluid. This minimises the light scattering and refraction at the particle-fluid interface, resulting in improved particle visibility. The experimental setup involves immersing the particles in a refractive index-matching fluid. The fluid fills the gaps between the particles, effectively matching the refractive indices of the particles and the fluid. This allows for clearer observation and imaging of particle positions, trajectories, and interactions (Barés et al., 2020; Dijksman et al., 2010).

RIMS is employed across a range of scientific domains to study particle flows (Barés et al., 2020) and suspensions (Ojeda-Mendoza et al., 2018). RIMS also finds applications in multiphase flows (Poelma, 2020), biological systems (Khan et al., 2021), chemical engineering processes

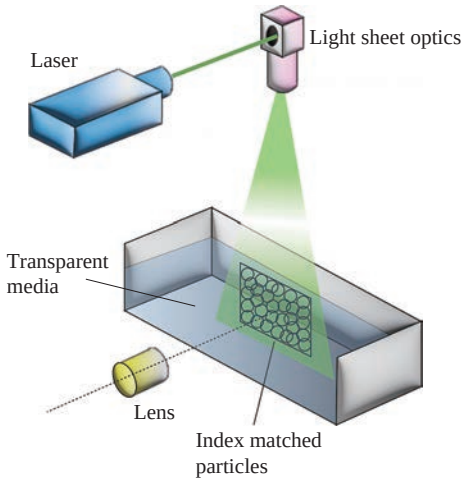


**Fig. 16** The setup comprises a laser sheet, a refractive index matching fluid, and particles with matched refractive indices.

(Häfeli et al., 2016), geological and environmental studies (Sather et al., 2023), material characterisation (Butscher et al., 2012), and fluidised beds (Reddy et al., 2013).

## 6.3 Magnetic resonance imaging (MRI)

Over the past few decades, various types of MRI systems have emerged, ranging from compact benchtop setups to large (pre-)clinical scanners. All these systems have basic components in common, including a magnet providing a magnetic field, gradient coils, and radiofrequency (RF) transmit and receive coils. A detailed explanation of the different types of MRI scanners is well described in a recent review article (Clarke et al., 2023). MRI relies on nuclear magnetic resonance (NMR) principles. When a material, like water with NMR-active hydrogens encounters a strong magnetic field, its nuclear spins will align. Transmit coils send RF pulses, causing nuclear spins to briefly absorb and emit energy. Gradient coils create spatial field variations for precise signal localisation. By manipulating gradients and RF pulses, MRI systems can create detailed images based on nuclear spin properties like density and relaxation times (Dale et al., 2015). In MRI imaging, two crucial parameters are relaxation times, known as $T_1$ (spin–lattice relaxation time) and $T_2$ (spin–spin relaxation time). $T_1$ and $T_2$ relaxation times determine how quickly the nuclear spins return to equilibrium or lose phase coherence. These times depend on various factors, including the material type being imaged and the properties of the MRI system itself. These factors are essential for creating contrast in images and providing information about material characteristics. Meanwhile, receive coils capture the emitted RF signals, which are then processed to produce the final images, providing invaluable insights into the structure and composition of materials without ionising radiation. MRI can also measure displacements over time, and thus quantify both self-diffusion behaviour as well as net displacements. The latter is the basis of the velocimetric assessment of flow, which can provide insights into the non-Newtonian behaviour of complex fluids.

While MRI is primarily known for its medical applications, it can also be adapted for material studies, including granular systems (Stannarius, 2017). **Fig. 17** shows a schematic of a (pre-)clinical MRI setup used for particle flow measurements. In the context of particle flow fields, MRI can provide insights into the internal structure, porosity, and flow patterns of granular materials. It can track the motion and distribution of fluids or particles within the system (Wang et al., 2022a). Using suitable contrast agents, one can differentiate between different phases or components within the granular system, enabling the visualisation and quantification of particle flows.

## 6.4 X-ray imaging

X-ray imaging is a valuable technique for studying particle flow fields in granular materials (Chen et al., 2021). **Fig. 18** depicts a schematic of X-ray imaging. It utilises X-rays, which are a form of electromagnetic radiation, to penetrate the material and generate images that reveal the internal structure, particle arrangements, and flow behaviour. X-rays have high energy and short wavelengths, allowing them to penetrate solid or dense materials, including most non-metallic granular systems. As X-rays pass through the material, they interact with the particles and undergo attenuation, which means that their intensity decreases based on the density and composition of the material (Hermanek et al., 2018).

### 6.4.1 Radiographic imaging

In X-ray radiography, a beam of X-rays is directed towards the material, and a detector captures the X-rays that pass through. The detected X-rays are converted into an image representing the attenuation of the X-rays within the material. This image provides information about the distribution of particles, their packing density, and the presence

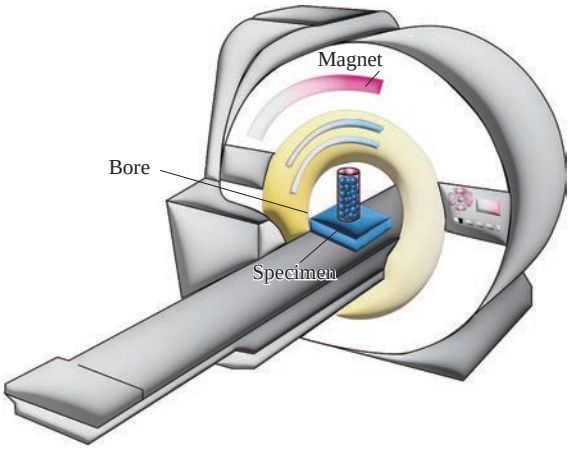


**Fig. 17** Schematic of a (pre-)clinical MRI machine. This allows for the placement of a container filled with particles on the specimen, enabling the imaging of static particle arrangements.

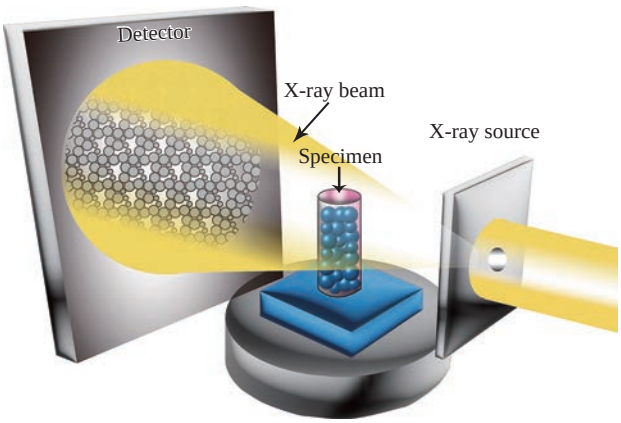


**Fig. 18** Schematic of the X-ray imaging setup. The setup consists of an X-ray source, a detector, and a specimen or rotating table where you place a container filled with particles.

of voids or channels within the granular system (Guillard et al., 2017).

### 6.4.2 X-ray computed tomography (CT)

CT is a more advanced technique that combines multiple X-ray radiographic images taken from different angles to reconstruct a detailed three-dimensional image of the material (Withers et al., 2021). By capturing X-ray projections at various angles, CT can provide volumetric information, enabling the visualisation of particle flow patterns and internal structures in greater detail (Lyu et al., 2023; Mohsin Thakur et al., 2020).

### 6.4.3 Ultrafast electron beam X-ray computed tomography

Ultrafast electron beam X-ray computed tomography (CT) is an advanced imaging technique that combines ultrafast electron beams and CT. It aims to provide high-speed, high-resolution imaging of dynamic processes, such as multiphase flow in vertical pipes (Fischer and Hampel, 2010), in a gas-solid fluidised bed, dynamic quality control of agricultural products, particle flow fields, and within granular materials (Bieberle et al., 2012).

**Fig. 19** shows a schematic of the high-performance ROFEX (ROssendorf Fast Electron beam X-ray tomography) imaging method, designed for non-invasive exploration of dynamic processes. This technique boasts an impressive capability of capturing up to 8,000 cross-sectional images per second, providing a spatial resolution of approximately 1 mm. ROFEX employs an ultrafast electron beam as the imaging source. This beam is generated using an electron gun and accelerated to high energies. The electrons act as a source of X-rays through a process called "braking radiation", in which the electron beam interacts with a target material and produces X-ray photons. When an ultrafast electron beam strikes a target material, such as a metal, it produces a broad spectrum of X-ray photons due to the deceleration of the electrons. The X-ray spectrum contains a range of energies that can be tuned and selected depending on the desired imaging characteristics (Frust et al., 2017).

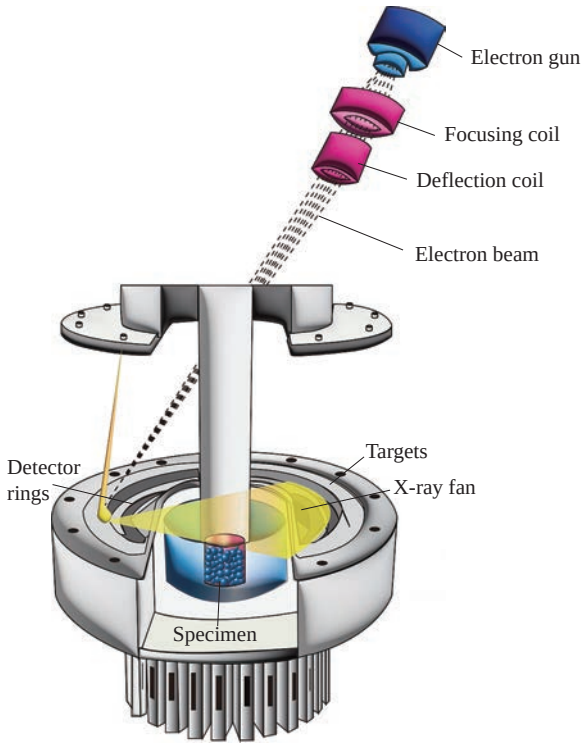


**Fig. 19** Schematic of the high-performance ROFEX (ROssendorf Fast Electron beam X-ray tomography) imaging method at Helmholtz-Zentrum Dresden-Rossendorf. ROFEX consists of an electron beam that is generated using an electron gun, focussing coil, deflection coil, X-ray fan, detector rings, and a specimen.

The usefulness of ROFEX in the field of granular materials lies in its ability to provide time-resolved imaging of dynamic processes (Stannarius et al., 2019a). ROFEX can capture fast flow phenomena, particle interactions, and granular rearrangements on a timescale that may not be achievable with other imaging techniques. The reconstructed three-dimensional images obtained through ROFEX can be analysed quantitatively to extract important parameters, such as particle velocities, trajectories, packing densities, and flow rates. Moreover, ROFEX can study multiphase systems (Bieberle and Hampel, 2015), where different components or phases have distinct X-ray attenuation properties.

## 6.5 Comparative analysis

**Table 3** summarises the applicability ranges of various imaging techniques for capturing particle properties. In addition, we compared the advantages, limitations, and

**Table 3** Summary of the imaging techniques' applicability ranges for capturing particle properties.

| Technique | Particle size | Particle type | Spatial resolution |
|---|---|---|---|
| MRI | µm | Solid particles, liquid droplets, and soft materials | 10–100 µm |
| XRT | sub-µm to mm | Dense- and low-density particles | sub-µm to µm |
| CM | sub-µm to µm | Fluorescent or highly scattering particles | 500 nm to µm |
| OM | sub-µm to mm | Biological particles, colloids, and solid particles | sub-µm to µm |
| RIMS | µm to mm | Transparent or translucent particles and fluids | sub-µm to µm |

**Table 4** Summary and comparison of the advantages, limitations, and typical applications of various particle imaging techniques reviewed in this paper.

| Technique | Advantages | Limitations | Typical applications |
|---|---|---|---|
| OM | Versatility and accessibility; morphological properties; real-time observation. | Limited depth of field; particle behaviour analysis; particle tracking limitations; limited to visible light spectrum; size and resolution limitations [a]. | Particle behaviour analysis; flow field visualisation; particle size and shape determination. |
| CM | High spatial resolution 3D imaging; optical sectioning [b]. Rejects out-of-focus light; suitable for transparent samples. | Limited imaging depth; slow imaging speed; limited to relatively thin samples; limited field of view. | Thick or densely packed granular samples; nondynamic particle flow fields; small-scale or microscopic particle flow fields. |
| RIMS | Enhanced particle visibility; reduced optical distortions; increased imaging depth. | Selection of matching fluid; refractive index sensitivity; experimental constraints [c]. | Particle tracking in transparent or translucent media; optically complex or dense systems; void and channel analysis. |
| MRI | Non-invasive; 3D; multi-phase imaging [d]. | Time-consuming and costly; trade-off between spatial and temporal resolution to be set by experts; signal loss and artifacts [e]. | Multi-phase interactions; internal flow patterns. |
| XRT | Non-destructive; high penetration depth; quantitative analysis [f]; high spatial resolution. | Radiation safety; contrast and sensitivity [g]; limited temporal resolution [h]; costly. | Particle distribution in granular materials; internal structure analysis; multi-phase systems. |

[a] OM has limitations in resolving particles below the diffraction limit of light.
[b] The ability to selectively focus on a specific plane within the sample enables optical sectioning.
[c] It may introduce additional complexities, such as changes in particle behaviour due to interactions with the matching fluid.
[d] MRI can differentiate between different phases within the granular material, such as solid particles and fluid phases.
[e] Granular materials, especially those with high density or metallic components, can cause signal loss and susceptibility artefacts in MRI images.
[f] XRT can provide quantitative information on particle distributions, void fractions, and packing densities within granular materials.
[g] XRT may face challenges in differentiating materials with similar X-ray attenuation coefficients. Contrast agents can be used to enhance sensitivity.
[h] Slower acquisition times.

typical applications of the various particle imaging techniques reviewed in this paper in **Table 4**.

## 7. Challenges in imaging of granular flows

Combining imaging with flow testing is pursued to gain a deeper understanding of material behaviour and fluid dynamics. It enables the visualisation of individual particle dynamics (Aliseda and Heindel, 2021), microscale phenomena (Milatz et al., 2021), and complex interactions within materials (L. Li and Iskander, 2022), providing insights that traditional flow testing alone cannot offer. This integration is valuable for validating models (Larsson et al., 2021), optimising industrial processes, characterising materials, and studying fluid dynamics in biological (Moosavi et al., 2014) and geotechnical contexts (Dai et al., 2023). By bridging the macroscopic and microscopic domains, we can enhance our ability to analyse and manipulate materials and fluids, facilitating advancements in various fields and applications. While combining flow tests with particle imaging techniques has opened new frontiers in the study of granular flows, several challenges still persist, presenting opportunities for further research and innovation. In this section, we discuss some current challenges faced in the imaging of granular flows.

### 7.1 Real-time analysis

Real-time analysis of imaging data is crucial for gaining immediate insights into granular flow behaviours. However, processing large datasets generated during experiments can be computationally intensive and time-consuming. Streamlining and automating real-time data analysis (Munir et al., 2018) to provide researchers with actionable information during experiments is an ongoing challenge.

One can observe and interpret data as it is generated, allowing them to make adjustments to the experiment in real time. This immediate feedback is valuable for optimising experimental conditions, making critical decisions, and ensuring data quality. Real-time analysis enables the identification of key events or phenomena as they occur within the granular flow. It allows for quality control by promptly identifying issues with data acquisition or imaging

equipment. One can address problems such as sensor malfunctions or calibration errors in real time.

### 7.2 Particle tracking in complex flows

Accurate tracking of individual particles within complex flow fields is essential for understanding granular flow dynamics. However, in real-world scenarios, particles can experience a wide range of interactions, including collision, adhesion, and fragmentation. Developing robust tracking algorithms capable of handling such complexities and uncertainties is an ongoing research challenge (Liang et al., 2021).

Accurately tracking the motion of individual particles involves monitoring the trajectories, velocities, and interactions of particles as they move within the flow. This tracking provides critical data for characterising flow behaviour, identifying flow regimes, and studying phenomena like particle collisions and adhesion.

Various methods and techniques can be employed to address the challenges of particle tracking in granular flows (Mallery et al., 2020; Wang et al., 2019). Particle Tracking Velocimetry (PTV) methods involve tracking individual particles in successive frames of imaging data to calculate particle trajectories and velocities (Mäkiharju et al., 2022). This approach can capture complex particle interactions and flow dynamics. Particle Image Velocimetry (PIV) techniques use the displacement of particle patterns in successive images to calculate flow velocities. Although not particle-specific, PIV is valuable for analysing bulk flow behaviour (Molina et al., 2021; Sarno et al., 2019). Advanced algorithms, often based on machine learning, are employed to automate and improve particle tracking accuracy, especially in complex and noisy flows (Duarte and Vlimant, 2022).

### 7.3 Integration of multimodal imaging

Combining multiple imaging modalities, such as Neutron and X-ray imaging (Sleiman et al., 2021; Vego et al., 2023b), offers the potential for richer data. However, the seamless integration of these techniques to provide complementary information poses technical challenges. Ensuring compatibility and synchronisation between different imaging systems is an area that requires further attention. While the integration of flow tests with particle imaging techniques has propelled our understanding of granular flows, addressing these current challenges will be crucial for pushing the boundaries of knowledge in this field.

## 8. Recent advances in coupling flow testing and particle imaging in granular flows

In recent years, significant strides have been made in the field of granular and particulate systems through the integration of dynamic flow measurements with particle imaging techniques.

### 8.1 X-ray rheography

In this context, Baker et al. (2018) introduced a novel X-ray rheography technique (**Fig. 20**) for studying the flow of granular materials, addressing the limitations of traditional methods that require model materials or intermittent motion stoppage. The authors used correlation analysis of high-speed X-ray radiographs from three directions to directly reconstruct three-dimensional velocities, enabling the study of continuous granular flows. Surprisingly, in a steady granular system, they discovered a compressible flow field with planar streamlines, despite the presence of non-planar confining boundaries. This finding contrasts with the behaviour of Newtonian fluids. The paper also discusses the impact of particle shape on flow and suggests future applications of the technique in the study of various soft matter systems, including biological tissues, geomaterials, and foams.

### 8.2 Multiple imaging methods

The integration of multiple imaging methods has enabled multiscale analysis, allowing researchers to gain insights into particle behaviour that spans the microscale to the macroscale (**Fig. 21**) (Vego et al., 2023a). This approach has proven particularly beneficial when studying complex and heterogeneous particle systems, such as those found in food products.

### 8.3 Rheo-MRI

In addition to the recent advances in the use of X-ray tomography techniques, the combination of rheology and

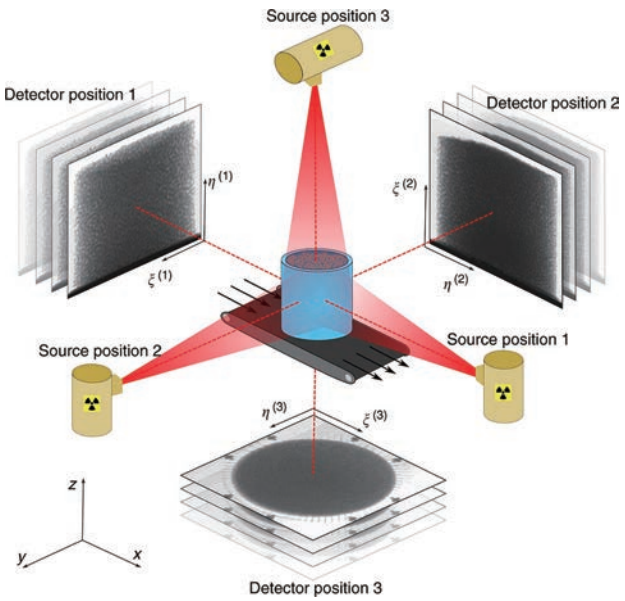


**Fig. 20** Experimental configuration for rheography. The particles within the blue cylinder are subject to shearing from below. The diagram highlights the three X-ray source locations in yellow. Reprinted from Ref. (Baker et al., 2018) under the terms of the CC-BY 4.0 license. Copyright: (2018) The Authors, published by Springer Nature.

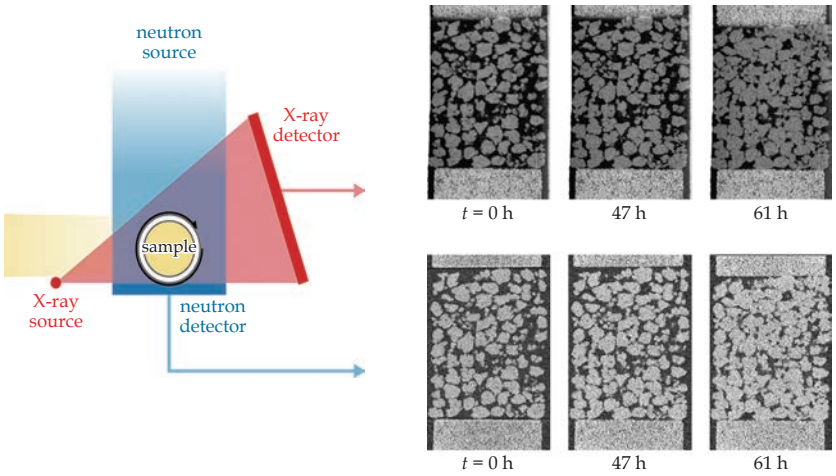


**Fig. 21** Neutron and X-ray tomographic scans. The **top row** displays vertical sections from X-ray tomography, whereas the **bottom row** shows equivalent slices from neutron tomography. Reprinted from Ref. (Vego et al., 2023b) under the terms of the CC-BY 4.0 license. Copyright: (2023) The Authors, published by Springer Nature.

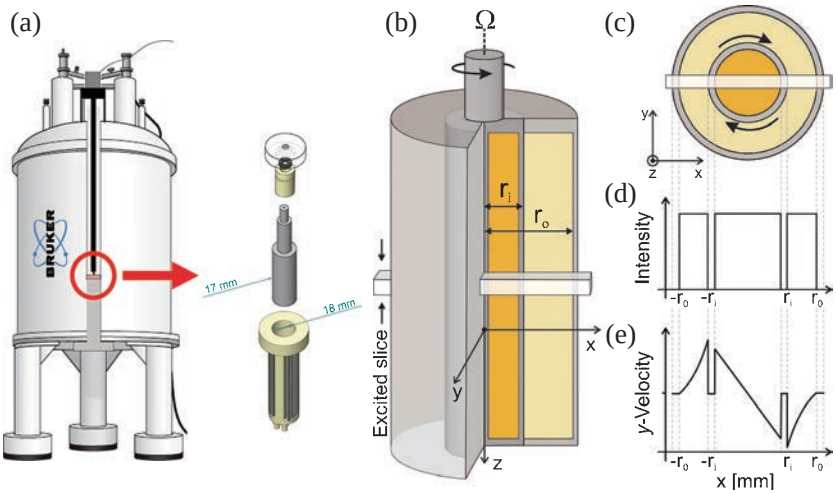


**Fig. 22** **(a)** Schematic of a Rheo-MRI setup, **(b)** experimental Couette cell geometry, **(c)** top-down view of the cell, **(d)** one-dimensional concentration and **(e)** *y*-velocity within the excited slice. This figure is taken with permission from Refs. (Milc et al., 2022; Serial et al., 2019).

MRI is a powerful technique used in various systems to study the mechanical properties and flow behaviour of complex fluids and soft materials (Serial et al., 2021; 2022). A rheo-cell, typically with a Couette or Cone-Plate geometry, is placed in an MRI system, allowing velocimetric measurements. By combining this with *in situ* or *ex situ* measurement of torque, local rheological properties such as viscosity, shear stress, and shear rate can be measured (**Fig. 22**). This combination provides insights into the relationship between the material's rheological response and its microstructure during flow (Coussot, 2020; Milc et al., 2022). Rheo-MRI is typically used in velocimetric mode, meanwhile relaxometric behaviour can give insights in structure formation/degradation. Maps of material density can provide insights into shear-induced migration.

## 9. Critical review and future directions

The integration of flow tests with particle imaging techniques has undeniably advanced our understanding of granular materials and complex fluids. These combined approaches have enabled researchers to uncover critical information about particle behaviour and interactions at the microscale, offering insights that were previously elusive. Shear testers such as the Schulze shear tester and FT4 powder flow tester have provided valuable data on bulk flow properties, while imaging techniques such as MRI, X-ray imaging, and confocal microscopy have facilitated the visualisation of particle dynamics. However, challenges persist, particularly in the integration of flow tests with imaging, which often involves complex experimental set-ups and resource-intensive data processing.

To overcome these challenges, it is natural to suggest the development of more simple, small-scale flow testers designed to align with selected 3D imaging techniques, specifically tailored to the material being investigated. A straightforward flow tester can take the form of a basic tube

or container equipped with motors and sensors for flow analysis. In addition, maintaining a database containing information about the studied material, flow geometry, and raw images could prove highly beneficial and time-saving for researchers seeking to replicate similar studies. Another crucial ongoing improvement involves integrating advanced processing techniques and conducting real-time flow analysis. This enhancement can significantly increase the efficiency of the testing procedure, while also addressing the cost considerations associated with 3D imaging facilities.

The future of this integration holds promise in the development of high-speed, high-resolution imaging methods, such as X-ray rheography and high-speed X-ray imaging (such as ROFEX), providing detailed insights into dynamic processes within granular materials. Artificial intelligence further contributes by enabling real-time image analysis to manage the overwhelming volume of data generated. Moreover, the integration of computational simulations, such as Discrete Element Method (DEM) or Molecular Dynamic (MD) simulations, with experimental flow tests and imaging offers a comprehensive understanding of complex systems, allowing validation and calibration of theoretical models against empirical observations.

## 10. Conclusion

We explored mechanical testers and particle imaging techniques and highlighted their combined potential. By merging these fields, we can gain unparalleled insights into the dynamics of granular materials and complex fluids, deepening our understanding of bulk flow behaviours. We have explored various shear testers, from the Schulze shear tester to the FT4 powder flow tester, each of which provides valuable insights into the macroscopic properties of materials under shear. Simultaneously, refractive index matching, MRI, and X-ray imaging have emerged as powerful tools for capturing microscale particle interactions and flow patterns. We also highlighted the need for technological advancements in imaging methods, especially ultrafast imaging and advanced data analysis techniques, to meet the growing demands for particle-level analysis.

## Acknowledgments

This project received funding from the European Union's Horizon 2020 research and innovation program under the Marie Skłodowska-Curie grant agreement No 812638. We acknowledge the valuable discussions with Cino Viggiani, Ralf Stannarius, and Frans Leermakers.

## Nomenclature

| | |
|---|---|
| CP | Cone–plate geometry |
| DC | Double-cone geometry |
| DEM | Discrete Element Method |
| FEM | Finite Element Modelling |
| PIV | Particle Image Velocimetry |
| PP | Plate–plate geometry |
| PTV | Particle Tracking Velocimetry |
| RF | Radio frequent |
| RST-M | Ring Shear Tester with size medium |
| RST-XS | Ring Shear Tester with size x-small |
| $T_1$ | Spin–lattice relaxation time (s) |
| $T_2$ | Spin–spin relaxation time (s) |
| $ff_c$ | Flowability index (-) |
| $F$ | Force (N) |
| $H$ | Thickness of the particle layer (mm) |
| $r_i$ | Radius of the inner cylinder (mm) |
| $r_o$ | Radius of the outer cylinder (mm) |
| $R_s$ | Radius of the inner cylinder or split radius in the split-bottom shear cell (mm) |
| $R_o$ | Radius of the outer cylinder in the split-bottom shear cell (mm) |
| $\tau$ | Shear stress (Pa) |
| $\tau_{sh}$ | Shear stress at the shear point (Pa) |
| $\tau_{pre}$ | Shear stress at pre-shear (Pa) |
| $\sigma_{1,2}$ | Consolidation stress (Pa) |
| $\sigma_c$ | Compressive strength or unconfined yield strength (Pa) |
| $\omega$ | Rotation speed or angular velocity (rpm) |
| $\theta$ | Dynamic angle of repose (-) |
| $\phi$ | Angle of internal friction (-) |
| $\rho_b$ or $\rho_{bulk}$ | Bulk density (kg·m$^{-3}$) |
| $\rho_{Tapped}$ | Tapped density (kg·m$^{-3}$) |

## References

Aigner A., Schneiderbauer S., Kloss C., Pirker S., Determining the coefficient of friction by shear tester simulation, PARTICLES III: Proceedings of the III International Conference on Particle-Based Methods: Fundamentals and Applications, (2013) 335–342. <http://hdl.handle.net/2117/188464> accessed 24052024.

Akers R.J., The certification of a limestone powder for Jenike shear testing, EUR14022, (1992).

Aliseda A., Heindel T.J., X-ray flow visualization in multiphase flows, Annual Review of Fluid Mechanics, 53 (2021) 543–567. https://doi.org/10.1146/annurev-fluid-010719-060201

Amon A., Born P., Daniels K.E., Dijksman J.A., Huang K., Parker D., Schröter M., Stannarius R., Wierschem A., Preface: focus on imaging methods in granular physics, Review of Scientific Instruments, 88(5) (2017) 051701. https://doi.org/10.1063/1.4983052

Baker J., Guillard F., Marks B., Einav I., X-ray rheography uncovers planar granular flows despite non-planar walls, Nature Communications, 9(1) (2018) 5119. https://doi.org/10.1038/s41467-018-07628-6

Balla A., Stress conditions in triaxial compression, Journal of the Soil Mechanics and Foundations Division, 86(6) (1960) 57–84. https://doi.org/10.1061/JSFEAQ.0000312

Barés J., Brodu N., Zheng H., Dijksman J.A., Transparent experiments: releasing data from mechanical tests on three dimensional hydrogel sphere packings, Granular Matter, 22 (2020) 1–7. https://doi.org/10.1007/s10035-019-0985-4

Bastiaansen T.M.M., Benders R.T., de Vries S., Hendriks W.H., Thomas M., Bosch G., Dijksman J.A., Capillary rheometry as a model methodology for obtaining insight in feed mash behaviour at conditions approximating pellet manufacturing, Animal Feed Science and Technology, 303 (2023) 115693. https://doi.org/10.1016/j.anifeedsci.2023.115693

Beaulieu C., Vidal D., Niyonkuru C., Wachs A., Chaouki J., Bertrand F., Effect of particle angularity on flow regime transitions and segregation of bidisperse blends in a rotating drum, Computational Particle Mechanics, 9 (2022) 443–463. https://doi.org/10.1007/s40571-021-00421-1

Benyaya M., Bolzinger M.-A., Chevalier Y., Ensenat S., Bordes C.,

Pickering emulsions stabilized with differently charged particles, Soft Matter, 19(25) (2023) 4780–4793. https://doi.org/10.1039/D3SM00305A

Berry R.J., Bradley M.S.A., Development of the Brookfield powder flow tester. Proceedings of the School of Engineering, Wolfson Centre for Bulk Solids Handling Technology, 2010. <http://gala.gre.ac.uk/id/eprint/7163> accessed 24052024.

Berry R.J., Bradley M.S.A., McGregor R.G., Brookfield powder flow tester–Results of round robin tests with CRM-116 limestone powder, Proceedings of the Institution of Mechanical Engineers, Part E: Journal of Process Mechanical Engineering, 229(3) (2015) 215–230. https://doi.org/10.1177/0954408914525387

Bieberle M., Barthel F., Hoppe D., Banowski M., Wagner M., Lucas D., Stürzel T., Hampel U., Ultrafast electron beam X-ray computed tomography for 2D and 3D two-phase flow imaging, 2012 IEEE International Conference on Imaging Systems and Techniques Proceedings, (2012) 605–610. https://doi.org/10.1109/IST.2012.6295548

Bieberle M., Hampel U., Level-set reconstruction algorithm for ultrafast limited-angle X-ray computed tomography of two-phase flows, Philosophical Transactions of the Royal Society A: Mathematical, Physical and Engineering Sciences, 373(2043) (2015) 20140395. https://doi.org/10.1098/rsta.2014.0395

Bilgili E., Yepes J., Stephenson L., Johanson K., Scarlett B., Stress inhomogeneity in powder specimens tested in the Jenike shear cell: myth or fact?, Particle & Particle Systems Characterization, 21(4) (2004) 293–302. https://doi.org/10.1002/ppsc.200400942

Boyer F., Guazzelli É., Pouliquen O., Unifying suspension and granular rheology, Physical Review Letters, 107(18) (2011) 188301. https://doi.org/10.1103/PhysRevLett.107.188301

Butscher D., Hutter C., Kuhn S., von Rohr P., Particle image velocimetry in a foam-like porous structure using refractive index matching: a method to characterize the hydrodynamic performance of porous structures, Experiments in Fluids, 53 (2012) 1123–1132. https://doi.org/10.1007/s00348-012-1346-9

Cataldo A., Vallone M., Tarricone L., Cannazza G., Cipressa M., TDR moisture estimation for granular materials: an application in agro-food industrial monitoring, IEEE Transactions on Instrumentation and Measurement, 58(8) (2009) 2597–2605. https://doi.org/10.1109/TIM.2009.2015636

Cavarretta I., O'Sullivan C., The mechanics of rigid irregular particles subject to uniaxial compression, Géotechnique, 62(8) (2012) 681–692. https://doi.org/10.1680/geot.10.P.102

Chen P., Ottino J.M., Lueptow R.M., Onset mechanism for granular axial band formation in rotating tumblers, Physical Review Letters, 104(18) (2010) 188002. https://doi.org/10.1103/PhysRevLett.104.188002

Chen Y., Ma G., Zhou W., Wei D., Zhao Q., Zou Y., Grasselli G., An enhanced tool for probing the microscopic behavior of granular materials based on X-ray micro-CT and FDEM, Computers and Geotechnics, 132 (2021) 103974. https://doi.org/10.1016/j.compgeo.2020.103974

Cheng Z., Wang J., Estimation of contact forces of granular materials under uniaxial compression based on a machine learning model, Granular Matter, 24 (2022) 1–14. https://doi.org/10.1007/s10035-021-01160-z

Clarke D., Hogendoorn W., Penn A., Serial R., Magnetic resonance imaging in granular flows: an overview of recent advances, Particuology, (2023). https://doi.org/10.1016/j.partic.2023.08.007

Coetzee C.J., Els D.N.J., Calibration of discrete element parameters and the modelling of silo discharge and bucket filling, Computers and Electronics in Agriculture, 65(2) (2009) 198–212. https://doi.org/10.1016/j.compag.2008.10.002

Cordts E., Steckel H., Capabilities and limitations of using powder rheology and permeability to predict dry powder inhaler performance, European Journal of Pharmaceutics and Biopharmaceutics, 82(2) (2012) 417–423. https://doi.org/10.1016/j.ejpb.2012.07.018

Couch M.A., Binding D.M., High pressure capillary rheometry of polymeric fluids, Polymer, 41(16) (2000) 6323–6334. https://doi.org/10.1016/S0032-3861(99)00865-4

Coussot P., Progress in rheology and hydrodynamics allowed by NMR or MRI techniques, Experiments in Fluids, 61 (2020) 1–20. https://doi.org/10.1007/s00348-020-03037-y

Cunez F.D., Patel D., Glade R., How particle shape affects granular segregation in industrial and geophysical flows, Proceedings of the National Academy of Sciences, 121 (6) (2023) e2307061121. https://doi.org/10.1073/pnas.2307061121

Curran D.R., Seaman L., Cooper T., Shockey D.A., Micromechanical model for comminution and granular flow of brittle material under high strain rate application to penetration of ceramic targets, International Journal of Impact Engineering, 13(1) (1993) 53–83. https://doi.org/10.1016/0734-743X(93)90108-J

Dai X., He L., Wu W., Chen J., Visualization experiment technology based on transparent geotechnical materials and its engineering application, Journal of Visualization, 26(1) (2023) 145–159. https://doi.org/10.1007/s12650-022-00863-6

Dale B.M., Brown M.A., Semelka R.C., MRI: Basic Principles and Applications, John Wiley & Sons, 2015, ISBN: 9781119013051. https://doi.org/10.1002/9781119013068

Deng T., Garg V., Diaz L.P., Markl D., Brown C., Florence A., Bradley M.S.A., Comparative studies of powder flow predictions using milligrams of powder for identifying powder flow issues, International Journal of Pharmaceutics, 628 (2022) 122309. https://doi.org/10.1016/j.ijpharm.2022.122309

Dijksman J.A., Brodu N., Behringer R.P., Refractive index matched scanning and detection of soft particles, Review of Scientific Instruments, 88(5) (2017) 51807. https://doi.org/10.1063/1.4983047

Dijksman J.A., Rietz F., Lőrincz K.A., Van Hecke M., Losert W., Invited article: refractive index matched scanning of dense granular materials, Review of Scientific Instruments, 83(1) (2012) 011301. https://doi.org/10.1063/1.3674173

Dijksman J.A., van Hecke M., Granular flows in split-bottom geometries, Soft Matter, 6 (2010) 2901–2907. https://doi.org/10.1039/B925110C

Dijksman J.A., Wandersman E., Slotterback S., Berardi C.R., Updegraff W.D., van Hecke M., Losert W., From frictional to viscous behavior: three-dimensional imaging and rheology of gravitational suspensions, Physical Review E, 82(6) (2010) 60301. https://doi.org/10.1103/PhysRevE.82.060301

Dijksman J.A., Zheng H., Behringer R.P., Imaging soft sphere packings in a novel triaxial shear setup, AIP Conference Proceedings, 1542 (2013) 457–460. https://doi.org/10.1063/1.4811966

Divya S., Ganesh G.N.K., Characterization of powder flowability using FT4–powder rheometer, Journal of Pharmaceutical Sciences and Research, 11(1) (2019) 25–29. <https://www.jpsr.pharmainfo.in/Documents/Volumes/vol11Issue01/jpsr11011906.pdf> accessed 11062024.

Du H., Lu H., Tang J., Liu H., Characterization of powder flow properties from micron to nanoscale using FT4 powder rheometer and PT-X powder tester, Particuology, 75 (2023) 1–10. https://doi.org/10.1016/j.partic.2022.05.014

Duarte J., Vlimant J.-R., Graph neural networks for particle tracking and reconstruction, in: Calafiura P., Rousseau D., Terao K. (Eds.), Artificial Intelligence for High Energy Physics, 2022, pp. 387–436, ISBN: 9789811234026. https://doi.org/10.1142/9789811234033_0012

Duran J., Sands, Powders, and Grains: An Introduction to the Physics of Granular Materials, Springer Science & Business Media, 2012, ISBN: 9780387986562. https://doi.org/10.1007/978-1-4612-0499-2

Faug T., Impact force of granular flows on walls normal to the bottom: slow versus fast impact dynamics, Canadian Geotechnical Journal, 58(1) (2020) 114–124. https://doi.org/10.1139/cgj-2019-0399

Fenistein D., van Hecke M., Wide shear zones in granular bulk flow, Nature, 425 (2003) 256. https://doi.org/10.1038/425256a

Fenistein D., van de Meent J.-W., van Hecke M., Universal and wide shear zones in granular bulk flow, Physical Review Letters, 92 (2004) 94301. https://doi.org/10.1103/PhysRevLett.92.094301

Fiedor S.J., Ottino J.M., Dynamics of axial segregation and coarsening of dry granular materials and slurries in circular and square tubes, Physical Review Letters, 91(24) (2003) 244301. https://doi.org/10.1103/PhysRevLett.91.244301

Fischer F., Hampel U., Ultra-fast electron beam X-ray computed tomography for two-phase flow measurement, Nuclear Engineering and

Design, 240(9) (2010) 2254–2259. https://doi.org/10.1016/j.nucengdes.2009.11.016
Francia V., Yahia L.A.A., Ocone R., Ozel A., From quasi-static to intermediate regimes in shear cell devices: theory and characterisation, KONA Powder and Particle Journal, 38 (2021) 3–25. https://doi.org/10.14356/kona.2021018
Freeman R., The importance of air content on the rheology of powders: an empirical study, American Laboratory, 36(23) (2004) 8–10.
Freeman R., Measuring the flow properties of consolidated, conditioned and aerated powders—a comparative study using a powder rheometer and a rotational shear cell, Powder Technology, 174(1–2) (2007) 25–33. https://doi.org/10.1016/j.powtec.2006.10.016
Frust T., Wagner M., Stephan J., Juckeland G., Bieberle A., Rapid data processing for ultrafast X-ray computed tomography using scalable and modular CUDA based pipelines, Computer Physics Communications, 219 (2017) 353–360. https://doi.org/10.1016/j.cpc.2017.05.025
Gaitonde A.J.U., Thermal transport in lithium ion batteries: an experimental investigation of interfaces and granular materials, Master's thesis, Purdue University, (2016). https://docs.lib.purdue.edu/open_access_theses/850
Gillemot K.A., Somfai E., Börzsönyi T., Shear-driven segregation of dry granular materials with different friction coefficients, Soft Matter, 13(2) (2017) 415–420. https://doi.org/10.1039/C6SM01946C
Graziano R., Preziosi V., Uva D., Tomaiuolo G., Mohebbi B., Claussen J., Guido S., The microstructure of Carbopol in water under static and flow conditions and its effect on the yield stress, Journal of Colloid and Interface Science, 582 (2021) 1067–1074. https://doi.org/10.1016/j.jcis.2020.09.003
Grima A., Mills B.P., Wypych P.W., Investigation of measuring wall friction on a large scale wall friction tester and the Jenike direct shear tester, University of Wollongong Research Online, (2010). https://ro.uow.edu.au/engpapers/2671
Guillard F., Marks B., Einav I., Dynamic X-ray radiography reveals particle size and shape orientation fields during granular flow, Scientific Reports, 7(1) (2017) 8155. https://doi.org/10.1038/s41598-017-08573-y
Guo C., Ye K., Xu Y., Dai X., Zheng J., Ya M., Discharge characteristics of conical and hyperbolic hoppers based on discharge time distribution, Powder Technology, 426 (2023) 118665. https://doi.org/10.1016/j.powtec.2023.118665
Guo Y., Buettner K., Lane V., Wassgren C., Ketterhagen W., Hancock B., Curtis J., Computational and experimental studies of flexible fiber flows in a normal-stress-fixed shear cell, AIChE Journal, 65(1) (2019) 64–74. https://doi.org/10.1002/aic.16397
Häfeli R., Rüegg O., Altheimer M., von Rohr P.R., Investigation of emulsification in static mixers by optical measurement techniques using refractive index matching, Chemical Engineering Science, 143 (2016) 86–98. https://doi.org/10.1016/j.ces.2015.12.022
Han T., Comparison of wall friction measurements by Jenike shear tester and ring shear tester, KONA Powder and Particle Journal, 29 (2011) 118–124. https://doi.org/10.14356/kona.2011014
Hare C., Ghadiri M., Stress and strain rate analysis of the FT4 powder rheometer, EPJ Web of Conferences, 140 (2017) 3034. https://doi.org/10.1051/epjconf/201714003034
Hare C., Zafar U., Ghadiri M., Freeman T., Clayton J., Murtagh M.J., Analysis of the dynamics of the FT4 powder rheometer, Powder Technology, 285 (2015) 123–127. https://doi.org/10.1016/j.powtec.2015.04.039
Hare C., Zafar U., Ghadiri M., Freeman T., Clayton J., Murtagh M.J.. Correction to "Analysis of the dynamics of the FT4 powder rheometer" [Powder Technol. 285 (2015) 123–127], Powder Technology, 315 (2017) 37–38. https://doi.org/10.1016/j.powtec.2017.02.061
He S., Wang Y., Zhou Z., Gan J., Yu A., Pinson D., Size-induced axial segregation of ellipsoids in a rotating drum, Powder Technology, 422 (2023) 118490. https://doi.org/10.1016/j.powtec.2023.118490
Henann D.L., Kamrin K., A predictive, size-dependent continuum model for dense granular flows, Proceedings of the National Academy of Sciences, 110(17) (2013) 6730–6735. https://doi.org/10.1073/pnas.1219153110
Hermanek P., Rathore J.S., Aloisi V., Carmignato S., Principles of X-ray computed tomography, Industrial X-Ray Computed Tomography, (2018) 25–67. https://doi.org/10.1007/978-3-319-59573-3_2
Hooiveld E., van der Kooij H.M., Kisters M., Kodger T.E., Sprakel J., van der Gucht J., In-situ and quantitative imaging of evaporation-induced stratification in binary suspensions, Journal of Colloid and Interface Science, 630 (2023) 666–675. https://doi.org/10.1016/j.jcis.2022.10.103
Huang P., Miao Q., Ding Y., Sang G., Jia M., Research on surface segregation and overall segregation of particles in a rotating drum based on stacked image, Powder Technology, 382 (2021) 162–172. https://doi.org/10.1016/j.powtec.2020.12.063
Inagaki S., Yoshikawa K., Traveling wave of segregation in a highly filled rotating drum, Physical Review Letters, 105(11) (2010) 118001. https://doi.org/10.1103/PhysRevLett.105.118001
Jenike A.W., Gravity flow of bulk solids. Bulletin No. 108, Utah Engineering Experiment Station, University of Utah, (1961).
Jenike A.W., Storage and flow of solids. Bulletin No. 123, Utah State University, (1964). <https://digital.library.unt.edu/ark:/67531/metadc1067072/m2/1/high_res_d/5240257.pdf> accessed 24052024.
Juliano P., Barbosa-Cánovas G.V., Food powders flowability characterization: theory, methods, and applications, Annual Review of Food Science and Technology, 1 (2010) 211–239. https://doi.org/10.1146/annurev.food.102308.124155
Khala M.J., Hare C., Wu C.-Y., Venugopal N., Murtagh M.J., Freeman T., Density and size-induced mixing and segregation in the FT4 powder rheometer: an experimental and numerical investigation, Powder Technology, 390 (2021) 126–142. https://doi.org/10.1016/j.powtec.2021.05.027
Khan R., Gul B., Khan S., Nisar H., Ahmad I., Refractive index of biological tissues: review, measurement techniques, and applications, Photodiagnosis and Photodynamic Therapy, 33 (2021) 102192. https://doi.org/10.1016/j.pdpdt.2021.102192
Koynov S., Glasser B., Muzzio F., Comparison of three rotational shear cell testers: powder flowability and bulk density, Powder Technology, 283 (2015) 103–112. https://doi.org/10.1016/j.powtec.2015.04.027
Larsson S., Rodríguez Prieto J.M., Gustafsson G., Häggblad H.-Å., Jonsén P., The particle finite element method for transient granular material flow: modelling and validation, Computational Particle Mechanics, 8 (2021) 135–155. https://doi.org/10.1007/s40571-020-00317-6
Laun H.M., Capillary rheometry for polymer melts revisited, Rheologica Acta, 43 (2004) 509–528. https://doi.org/10.1007/s00397-004-0387-2
Le T.-T., Investigation of force transmission, critical breakage force and relationship between micro-macroscopic behaviors of agricultural granular material in a uniaxial compaction test using discrete element method, Particulate Science and Technology, 40(5) (2022) 620–637. https://doi.org/10.1080/02726351.2021.1983904
Leaper M.C., Measuring the flow functions of pharmaceutical powders using the Brookfield powder flow tester and Freeman FT4, Processes, 9(11) (2021) 2032. https://doi.org/10.3390/pr9112032
Leturia M., Benali M., Lagarde S., Ronga I., Saleh K., Characterization of flow properties of cohesive powders: a comparative study of traditional and new testing methods, Powder Technology, 253 (2014) 406–423. https://doi.org/10.1016/j.powtec.2013.11.045
Li L., Iskander M., Visualization of interstitial pore fluid flow, Journal of Imaging, 8(2) (2022) 32. https://doi.org/10.3390/jimaging8020032
Li R., Xiu W., Liu B., Zheng G., Yang H., Velocity distribution of rice particles in a rotating drum, Powder Technology, 386 (2021) 394–398. https://doi.org/10.1016/j.powtec.2021.03.050
Liang J., Cai S., Xu C., Chen T., Chu J., DeepPTV: particle tracking velocimetry for complex flow motion via deep neural networks, IEEE Transactions on Instrumentation and Measurement, 71 (2021) 1–16. https://doi.org/10.1109/TIM.2021.3120127
Lochab V., Yee A., Yoda M., Conlisk A.T., Prakash S., Dynamics of colloidal particles in microchannels under combined pressure and electric potential gradients, Microfluidics and Nanofluidics, 23 (2019) 1–13. https://doi.org/10.1007/s10404-019-2304-0
Lu K., Brodsky E.E., Kavehpour H.P., Shear-weakening of the transitional

regime for granular flow, Journal of Fluid Mechanics, 587 (2007) 347–372. https://doi.org/10.1017/S0022112007007331
Luding S., The effect of friction on wide shear bands, Particulate Science and Technology, 26(1) (2007) 33–42. https://doi.org/10.1080/02726350701759167
Luo Q., Zheng Q.J., Yu A.B., Finite element investigation of granular dynamics in a split-bottom shear cell, Powder Technology, 314 (2017) 121–128. https://doi.org/10.1016/j.powtec.2016.09.069
Luo S., Weinell C.E., Okkels F., Østergård A.L., Kiil S., On-line, non-Newtonian capillary rheometry for continuous and in-line coatings production, Journal of Coatings Technology and Research, 18 (2021) 611–626. https://doi.org/10.1007/s11998-020-00447-9
Lyu Q., Chen A., Jia J., Singh A., Dai P., Fluids flow in granular aggregate packings reconstructed by high-energy X-ray computed tomography and lattice Boltzmann method, Computers & Fluids, 253 (2023) 105787. https://doi.org/10.1016/j.compfluid.2023.105787
Mackley M.R., Rutgers R.P.G., Capillary rheometry, in: Collyer A.A., Clegg D.W. (Eds.), Rheological Measurement, 1998, pp. 167–189, ISBN: 978-0-412-72030-7. https://doi.org/10.1007/978-94-011-4934-1_5
Mäkiharju S.A., Dewanckele J., Boone M., Wagner C., Griesser A. Tomographic X-ray particle tracking velocimetry: proof-of-concept in a creeping flow, Experiments in Fluids, 63 (2022) 1–12. https://doi.org/10.1007/s00348-021-03362-w
Mallery K., Shao S., Hong J., Dense particle tracking using a learned predictive model, Experiments in Fluids, 61 (2020) 1–14. https://doi.org/10.1007/s00348-020-03061-y
Mani R., Kadau D., Or D., Herrmann H.J., Fluid depletion in shear bands, Physical Review Letters, 109(24) (2012) 248001. https://doi.org/10.1103/PhysRevLett.109.248001
Marchetti L., Hulme-Smith C., Flowability of steel and tool steel powders: a comparison between testing methods, Powder Technology, 384 (2021) 402–413. https://doi.org/10.1016/j.powtec.2021.01.074
Mesri G., Vardhanabhuti B., Compression of granular materials, Canadian Geotechnical Journal, 46(4) (2009) 369–392. https://doi.org/10.1139/T08-123
MiDi G.D.R., On dense granular flows. The European Physical Journal E, 14(4) (2004) 341–365. https://doi.org/10.1140/epje/i2003-10153-0
Milatz M., Hüsener N., Andò E., Viggiani G., Grabe J., Quantitative 3D imaging of partially saturated granular materials under uniaxial compression, Acta Geotechnica, 16(11) (2021) 3573–3600. https://doi.org/10.1007/s11440-021-01315-5
Milc K.W., Serial M.R., Philippi J., Dijksman J.A., van Duynhoven J.P.M., Terenzi C., Validation of temperature-controlled rheo-MRI measurements in a submillimeter-gap Couette geometry, Magnetic Resonance in Chemistry, 60(7) (2022) 606–614. https://doi.org/10.1002/mrc.5157
Mitra H., Pushpadass H.A., Franklin M.E.E., Ambrose R.P.K., Ghoroi C., Battula S.N., Influence of moisture content on the flow properties of basundi mix, Powder Technology, 312 (2017) 133–143. https://doi.org/10.1016/j.powtec.2017.02.039
Mohsin Thakur M., Penumadu D., Bauer C., Capillary suction measurements in granular materials and direct numerical simulations using X-ray computed tomography microstructure, Journal of Geotechnical and Geoenvironmental Engineering, 146(1) (2020) 4019121. https://doi.org/10.1061/(ASCE)GT.1943-5606.0002194
Molina R., Gonzalez V., Benito J., Marsi S., Ramponi G., Petrino R., Implementation of particle image velocimetry for silo discharge and food industry seeds, Applications in Electronics Pervading Industry, Environment and Society, 2021, pp. 3–11, ISBN: 9783030667283. https://doi.org/10.1007/978-3-030-66729-0_1
Moosavi M.-H., Fatouraee N., Katoozian H., Pashaei A., Camara O., Frangi A.F., Numerical simulation of blood flow in the left ventricle and aortic sinus using magnetic resonance imaging and computational fluid dynamics, Computer Methods in Biomechanics and Biomedical Engineering, 17(7) (2014) 740–749. https://doi.org/10.1080/10255842.2012.715638
Moud A.A., Kamkar M., Sanati-Nezhad A., Hejazi S.H., Suspensions and hydrogels of cellulose nanocrystals (CNCs): characterization using microscopy and rheology, Cellulose, 29(7) (2022) 3621–3653. https://doi.org/10.1007/s10570-022-04514-9
Munir M., Baumbach S., Gu Y., Dengel A., Ahmed S., Data analytics: industrial perspective & solutions for streaming data, in: Last M., Bunke H., Kandel A. (Eds.), Data Mining in Time Series and Streaming Databases, World Scientific, 2018, pp. 144–168, ISBN: 9789813228030. https://doi.org/10.1142/9789813228047_0007
Nadimi S., Fonseca J., Andò E., Viggiani G., A micro finite-element model for soil behaviour: experimental evaluation for sand under triaxial compression, Géotechnique, 70(10) (2020) 931–936. https://doi.org/10.1680/jgeot.18.T.030
Nan W., Ghadiri M., Wang Y., Analysis of powder rheometry of FT4: effect of particle shape, Chemical Engineering Science, 173 (2017a) 374–383. https://doi.org/10.1016/j.ces.2017.08.004
Nan W., Gu Y., Stress analysis of blade rheometry by DEM simulations, Powder Technology, 376 (2020) 332–341. https://doi.org/10.1016/j.powtec.2020.08.026
Nan W., Vivacqua V., Ghadiri M., Wang Y., Numerical analysis of air effect on the powder flow dynamics in the FT4 powder rheometer, EPJ Web of Conferences, 140 (2017b) 3036. https://doi.org/10.1051/epjconf/201714003036
Navar R., Leal J.H., Davis B.L., Semelsberger T.A., Rheological effects of moisture content on the anatomical fractions of loblolly pine (Pinus taeda), Powder Technology, 412 (2022) 118031. https://doi.org/10.1016/j.powtec.2022.118031
Nezamabadi S., Radjai F., Mora S., Delenne J.-Y., Ghadiri M. Rheology of soft granular materials: uniaxial compression, EPJ Web of Conferences, 249 (2021) 5008. https://doi.org/10.1051/epjconf/202124905008
Nkurikiye E., Pulivarthi M.K., Bhatt A., Siliveru K., Li Y., Bulk and flow characteristics of pulse flours: a comparative study of yellow pea, lentil, and chickpea flours of varying particle sizes, Journal of Food Engineering, 357 (2023) 111647. https://doi.org/10.1016/j.jfoodeng.2023.111647
Oda M., Deformation mechanism of sand in triaxial compression tests, Soils and Foundations, 12(4) (1972) 45–63. https://doi.org/10.3208/sandf1972.12.4_45
Ogata K., A review: recent progress on evaluation of flowability and floodability of powder, KONA Powder and Particle Journal, 36 (2019) 33–49. https://doi.org/10.14356/kona.2019002
Ojeda-Mendoza G.J., Contreras-Tello H., Rojas-Ochoa L.F., Refractive index matching of large polydisperse silica spheres in aqueous suspensions, Colloids and Surfaces A: Physicochemical and Engineering Aspects, 538 (2018) 320–326. https://doi.org/10.1016/j.colsurfa.2017.10.088
Orband J.L.R., Geldart D., Direct measurement of powder cohesion using a torsional device, Powder Technology, 92(1) (1997) 25–33. https://doi.org/10.1016/S0032-5910(97)03212-9
Oyama Y., Studies on mixing of binary system of two size by ball mill motion, Scientific Papers of the Institute of Physical and Chemical Research, 951 (1940) 17–29.
Paredes J., Shahidzadeh-Bonn N., Bonn D., Shear banding in thixotropic and normal emulsions, Journal of Physics: Condensed Matter, 23(28) (2011) 284116. https://doi.org/10.1088/0953-8984/23/28/284116
Parrella L., Barletta D., Boerefijn R., Poletto M., Comparison between a uniaxial compaction tester and a shear tester for the characterization of powder flowability, KONA Powder and Particle Journal, 26 (2008) 178–189. https://doi.org/10.14356/kona.2008016
Peshkov A., Teitel S., Universality of stress-anisotropic and stress-isotropic jamming of frictionless spheres in three dimensions: uniaxial versus isotropic compression, Physical Review E, 105(2) (2022) 24902. https://doi.org/10.1103/PhysRevE.105.024902
Poelma C., Measurement in opaque flows: a review of measurement techniques for dispersed multiphase flows, Acta Mechanica, 231(6) (2020) 2089–2111. https://doi.org/10.1007/s00707-020-02683-x
Pongó T., Fan B., Hernández-Delfin D., Török J., Stannarius R., Hidalgo R.C., Börzsönyi T., The role of the particle aspect ratio in the discharge of a narrow silo, New Journal of Physics, 24(10) (2022) 103036. https://doi.org/10.1088/1367-2630/ac9923
Preud'homme N., Opsomer E., Vandewalle N., Lumay G., Effect of grain shape on the dynamics of granular materials in 2D rotating drum,

EPJ Web of Conferences, 249 (2021) 6002. https://doi.org/10.1051/epjconf/202124906002
Rathee V., Arora S., Blair D.L., Urbach J.S., Sood A.K., Ganapathy R., Role of particle orientational order during shear thickening in suspensions of colloidal rods, Physical Review E, 101(4) (2020) 40601. https://doi.org/10.1103/PhysRevE.101.040601
Reddy R.K., Sathe M.J., Joshi J.B., Nandakumar K., Evans G.M., Recent developments in experimental (PIV) and numerical (DNS) investigation of solid–liquid fluidized beds, Chemical Engineering Science, 92 (2013) 1–12. https://doi.org/10.1016/j.ces.2012.11.017
Salehi H., Barletta D., Poletto M., A comparison between powder flow property testers, Particuology, 32 (2017) 10–20. https://doi.org/10.1016/j.partic.2016.08.003
Sarno L., Tai Y.-C., Carravetta A., Martino R., Papa M.N., Kuo C.-Y., Challenges and improvements in applying a particle image velocimetry (PIV) approach to granular flows, Journal of Physics: Conference Series, 1249 (2019) 12011. https://doi.org/10.1088/1742-6596/1249/1/012011
Sather L.J., Roth E.J., Neupauer R.M., Crimaldi J.P., Mays D.C., Experiments and simulations on plume spreading by engineered injection and extraction in refractive index matched porous media, Water Resources Research, 59(2) (2023) e2022WR032943. https://doi.org/10.1029/2022WR032943
Satone H., Iimura K., Teraoka T., Hanafusa T., Hisatani S., Nishiwaki M., Suzuki M., Analysis of granule fracture under biaxial compression, Ceramics International, 43(18) (2017) 16835–16842. https://doi.org/10.1016/j.ceramint.2017.09.081
Schnaid F., Prietto P.D.M., Consoli N.C., Characterization of cemented sand in triaxial compression, Journal of Geotechnical and Geoenvironmental Engineering, 127(10) (2001) 857–868. https://doi.org/10.1061/(ASCE)1090-0241(2001)127:10(857)
Schulze D., Powders and Bulk Solids: Behaviour, Characterization, Storage and Flow, Springer, 2008, ISBN: 9783540737674. https://doi.org/10.1007/978-3-540-73768-1
Schulze D., Round robin test on ring shear testers, Advanced Powder Technology, 22(2) (2011) 197–202. https://doi.org/10.1016/j.apt.2010.10.015
Schulze D., Discussion of testers and test procedures, in: Schulze D. (Ed.), Powders and Bulk Solids: Behavior, Characterization, Storage and Flow, 2021, pp. 187–234, ISBN: 9783030767198. https://doi.org/10.1007/978-3-030-76720-4_6
Schwedes J., Review on testers for measuring flow properties of bulk solids, Granular Matter, 5 (2003) 1–43. https://doi.org/10.1007/s10035-002-0124-4
Serial M.R., Arnaudov L.N., Stoyanov S., Dijksman J.A., Terenzi C., van Duynhoven J.P.M., Non-invasive rheo-MRI study of egg yolk-stabilized emulsions: yield stress decay and protein release, Molecules, 27(10) (2022) 3070. https://doi.org/10.3390/molecules27103070
Serial M.R., Bonn D., Huppertz T., Dijksman J.A., van der Gucht J., Van Duynhoven J.P.M., Terenzi C., Nonlocal effects in the shear banding of a thixotropic yield stress fluid, Physical Review Fluids, 6(11) (2021) 113301. https://doi.org/10.1103/PhysRevFluids.6.113301
Serial M.R., Nikolaeva T., Vergeldt F.J., Van Duynhoven J.P.M., Van As H., Selective oil-phase rheo-MRI velocity profiles to monitor heterogeneous flow behavior of oil/water food emulsions, Magnetic Resonance in Chemistry, 57 (2019) 766–770. https://doi.org/10.1002/mrc.4811
Shaebani M.R., Török J., Maleki M., Madani M., Harrington M., Rice A., Losert W., Gravity governs shear localization in confined dense granular flows, Physical Review Letters, 127(27) (2021) 278003. https://doi.org/10.1103/PhysRevLett.127.278003
Shah R.B., Tawakkul M.A., Khan M.A., Comparative evaluation of flow for pharmaceutical powders and granules, AAPS PharmSciTech, 9 (2008) 250–258. https://doi.org/10.1208/s12249-008-9046-8
Shi H., Mohanty R., Chakravarty S., Cabiscol R., Morgeneyer M., Zetzener H., Ooi J.Y., Kwade A., Luding S., Magnanimo V., Effect of particle size and cohesion on powder yielding and flow, KONA Powder and Particle Journal, 35 (2018) 226–250. https://doi.org/10.14356/kona.2018014
Shi S., Bai W., Xuan T., Zhou T., Dong G., Xie R.-J., In situ inkjet printing patterned lead halide perovskite quantum dot color conversion films by using cheap and eco-friendly aqueous inks, Small Methods, 5(3) (2021) 2000889. https://doi.org/10.1002/smtd.202000889
Shinohara K., Oida M., Golman B., Effect of particle shape on angle of internal friction by triaxial compression test, Powder Technology, 107(1–2) (2000) 131–136. https://doi.org/10.1016/S0032-5910(99)00179-5
Simons T.A.H., Weiler R., Strege S., Bensmann S., Schilling M., Kwade A., A ring shear tester as calibration experiment for DEM simulations in agitated mixers–a sensitivity study, Procedia Engineering, 102 (2015) 741–748. https://doi.org/10.1016/j.proeng.2015.01.178
Singh A., Magnanimo V., Saitoh K., Luding S., Effect of cohesion on shear banding in quasistatic granular materials, Physical Review E, 90(2) (2014) 22202. https://doi.org/10.1103/PhysRevE.90.022202
Sleiman H.C., Tengattini A., Briffaut M., Huet B., Dal Pont S., Simultaneous X-ray and neutron 4D tomographic study of drying-driven hydro-mechanical behavior of cement-based materials at moderate temperatures, Cement and Concrete Research, 147 (2021) 106503. https://doi.org/10.1016/j.cemconres.2021.106503
Stannarius R., Magnetic resonance imaging of granular materials, Review of Scientific Instruments, 88(5) (2017) 51806. https://doi.org/10.1063/1.4983135
Stannarius R., Martinez D.S., Börzsönyi T., Bieberle M., Barthel F., Hampel U., High-speed X-ray tomography of silo discharge, New Journal of Physics, 21(11) (2019a) 113054. https://doi.org/10.1088/1367-2630/ab5893
Stannarius R., Sancho Martinez D., Finger T., Somfai E., Börzsönyi T., Packing and flow profiles of soft grains in 3D silos reconstructed with X-ray computed tomography, Granular Matter, 21 (2019b) 1–10. https://doi.org/10.1007/s10035-019-0910-x
Sun C.C., Quantifying effects of moisture content on flow properties of microcrystalline cellulose using a ring shear tester, Powder Technology, 289 (2016) 104–108. https://doi.org/10.1016/j.powtec.2015.11.044
Szabó B., Török J., Somfai E., Wegner S., Stannarius R., Böse A., Rose G., Angenstein F., Börzsönyi T., Evolution of shear zones in granular materials, Physical Review E, 90 (2014) 32205. https://doi.org/10.1103/PhysRevE.90.032205
Tay J.Y.S., Liew C.V., Heng P.W.S., Powder flow testing: judicious choice of test methods, AAPS PharmSciTech, 18 (2017) 1843–1854. https://doi.org/10.1208/s12249-016-0655-3
Tegzes P., Vicsek T., Schiffer P., Avalanche dynamics in wet granular materials, Physical Review Letters, 89(9) (2002) 94301. https://doi.org/10.1103/PhysRevLett.89.094301
Tsai J.-C., Chou M.-R., Huang P.-C., Fei H.-T., Huang J.-R., Soft granular particles sheared at a controlled volume: rate-dependent dynamics and the solid–fluid transition, Soft Matter, 16(32) (2020) 7535–7543. https://doi.org/10.1039/D0SM00405G
Unger T., Török J., Kertész J., Wolf D.E., Shear band formation in granular media as a variational problem, Physical Review Letters, 92(21) (2004) 214301. https://doi.org/10.1103/PhysRevLett.92.214301
Vego I., Benders R.T., Tengattini A., Vergeldt F.J., Dijksman J.A., van Duynhoven J.P.M., Heterogeneous swelling of couscous particles exposed to a high relative humidity air, as revealed by TD-NMR and X-ray tomography, Food Structure, (2023a) 100330. https://doi.org/10.1016/j.foostr.2023.100330
Vego I., Tengattini A., Andò E., Lenoir N., Viggiani G., The effect of high relative humidity on a network of water-sensitive particles (couscous) as revealed by in situ X-ray tomography, Soft Matter, 18(25) (2022) 4747–4755. https://doi.org/10.1039/D2SM00322H
Vego I., Tengattini A., Lenoir N., Viggiani G., The influence of water sorption on the microstructure of a hydro-sensitive granular material (couscous) deduced from simultaneous neutron and X-ray tomography, Granular Matter, 25(4) (2023b) 1–14. https://doi.org/10.1007/s10035-023-01356-5
Verma A., Chauhan G., Baruah P.P., Ojha K., Morphology, rheology, and kinetics of nanosilica stabilized gelled foam fluid for hydraulic fracturing application, Industrial & Engineering Chemistry Research, 57(40) (2018) 13449–13462. https://doi.org/10.1021/acs.iecr.8b04044

Vu T.-L., Nezamabadi S., Mora S., Effects of particle compressibility on structural and mechanical properties of compressed soft granular materials, Journal of the Mechanics and Physics of Solids, 146 (2021) 104201. https://doi.org/10.1016/j.jmps.2020.104201

Wang B.-D., Song J., Li R., Han R., Zheng G., Yang H. A novel particle tracking velocimetry method for complex granular flow field, Chinese Physics B, 29(1) (2019) 14207. https://doi.org/10.1088/1674-1056/ab5936

Wang C., Song S., Gunawardana C.A., Sun D.J., Sun C.C. Effects of shear cell size on flowability of powders measured using a ring shear tester, Powder Technology, 396 (2022) 555–564. https://doi.org/10.1016/j.powtec.2021.11.015

Wang J., Fan B., Pongó T., Harth K., Trittel T., Stannarius R., Illig M., Börzsönyi T., Hidalgo R.C., Silo discharge of mixtures of soft and rigid grains, Soft Matter, 17(16) (2021) 4282–4295. https://doi.org/10.1039/D0SM01887B

Wang J., Farmani Z., Dijksman J.A., Lübeck C., Speck O., Stannarius R., Characterization of shear zones in soft granular beds by means of a novel magnetic resonance imaging technique, Granular Matter, 24(4) (2022a) 103. https://doi.org/10.1007/s10035-022-01271-1

Wang J., Harth K., Puzyrev D., Stannarius R., The effect of obstacles near a silo outlet on the discharge of soft spheres, New Journal of Physics, 24(9) (2022b) 93010. https://doi.org/10.1088/1367-2630/ac8bea

Wang L., Zheng Z., Yu Y., Liu T., Zhang Z., Determination of the energetic coefficient of restitution of maize grain based on laboratory experiments and DEM simulations, Powder Technology, 362 (2020) 645–658. https://doi.org/10.1016/j.powtec.2019.12.024

Wang Y., Snee R.D., Meng W., Muzzio F.J., Predicting flow behavior of pharmaceutical blends using shear cell methodology: a quality by design approach, Powder Technology, 294 (2016) 22–29. https://doi.org/10.1016/j.powtec.2016.01.019

Wiebicke M., Andò E., Viggiani G., Herle I. Measuring the evolution of contact fabric in shear bands with X-ray tomography, Acta Geotechnica, 15(1) (2020) 79–93. https://doi.org/10.1007/s11440-019-00869-9

Withers P.J., Bouman C., Carmignato S., Cnudde V., Grimaldi D., Hagen C.K., Maire E., Manley M., Du Plessis A., Stock S.R., X-ray computed tomography, Nature Reviews Methods Primers, 1 (2021) 18. https://doi.org/10.1038/s43586-021-00015-4

Xiu W.Z., Li R., Chen Q., Sun Q.C., Zivkovic V., Yang H., Binary-size granules segregation from core pattern to streak pattern in a rotating drum, Powder Technology, 380 (2021) 518–525. https://doi.org/10.1016/j.powtec.2020.11.035

Yang R.Y., Yu A.B., McElroy L., Bao J., Numerical simulation of particle dynamics in different flow regimes in a rotating drum, Powder Technology, 188(2) (2008) 170–177. https://doi.org/10.1016/j.powtec.2008.04.081

Zafar U., Vivacqua V., Hassanpour A., Raso G., Marigo M., Applications and case studies, in: A Hassanpour, C Hare, M Pasha (Eds.), Powder Flow: Theory, Characterisation and Application, 2019, pp. 177–208, ISBN: 9781788012249. https://doi.org/10.1039/9781788016100-00177

Zhang W., Zhao D., Dong Z., Li J., Zhang B., Yu W., The consistency factor and the viscosity exponent of soybean-protein-isolate/wheat-gluten/corn-starch blends by using a capillary rheometry, Molecules, 27(19) (2022) 6693. https://doi.org/10.3390/molecules27196693

## Authors' Short Biographies

**Zohreh Farmani** is a PhD candidate in the Soft Matter group at the University of Amsterdam, Institute of Physics since December 2022, having previously conducted three years of research at Wageningen University (NL). Her research focuses on granular material rheology, designing experiments to understand their flow behavior. Her aim is to utilize 3D imaging to calibrate numerical methods and link microscopic details to collective mechanical behavior. She holds an MSc and BSc in Chemical and Petroleum Engineering from Persian Gulf and Shiraz Universities in Iran, with a focus on fluid dynamics in porous media.

**Dr. Jan Wieringa** obtained his PhD in Physics from Delft University of Technology. Since then, he mostly worked at Unilever in several R&D functions, mostly for food applications. His expertise area is primarily process science and the interaction between process and product properties.

**Prof. Dr. John van Duynhoven** obtained his PhD in Biophysical Chemistry and then worked as Assistant Professor and NMR facility manager at Twente University. He later switched to Unilever R&D (The Netherlands), where he led the Spectroscopy and Imaging expertise team. In his industrial career he has been involved in a wide range of industrial food research and technology projects, being responsible for development and deployment of advanced measurement techniques. In this area he also managed a wide range of academic-industrial research collaborations. Since 2010 he has held a Part-time Professorship at Wageningen University, supervising PhD students in development and application of advanced analytical methods in food and nutritional sciences.

**Dr. Joshua Dijksman** obtained his PhD in Physics from Leiden University and worked at Duke University (USA) as postdoctoral scholar. He held assistant and associate professor positions in the Physical Chemistry and Soft Matter group at Wageningen University. Since 2022, he is Associate Professor at the University of Amsterdam, in the Soft Matter group of the Van der Waals-Zeeman Institute, at the Institute of Physics.

KONA Powder and Particle Journal

KONA Powder and Particle Journal No. 42 (2025) 79–99/https://doi.org/10.14356/kona.2025001 Review Paper

# Engineering $SiO_2$ Nanoparticles: A Perspective on Chemical Mechanical Planarization Slurry for Advanced Semiconductor Processing†

**Ganggyu Lee[1$], Kangchun Lee[2$], Seho Sun[3$], Taeseup Song[1*] and Ungyu Paik[1*]**

[1] *Department of Energy Engineering, Hanyang University, Republic of Korea*
[2] *Department of Electronic Engineering, Kyonggi University, Republic of Korea*
[3] *School of Chemical Engineering, Yeungnam University, Republic of Korea*

Chemical mechanical polishing (CMP) is a process that uses mechanical abrasive particles and chemical interaction in slurry to remove materials from the surface of films. With advancements in semiconductor device technology applying various materials and structures, $SiO_2$ (silica) nanoparticles are the most chosen abrasives in CMP slurries. Therefore, understanding and developing silica nanoparticles are crucial for achieving CMP performance, such as removal rates, selectivity, decreasing defects, and high uniformity and flatness. However, despite the abundance of reviews on silica nanoparticles, there is a notable gap in the literature addressing their role as abrasives in CMP slurries. This review offers an in-depth exploration of silica nanoparticle synthesis and modification methods detailing their impact on nanoparticle characteristics and CMP performance. Further, we also address the unique properties of silica nanoparticles, such as hardness, size distribution, and surface properties, and the significant contribution of silica nanoparticles to CMP results. This review is expected to interest researchers and practitioners in semiconductor manufacturing and materials science.

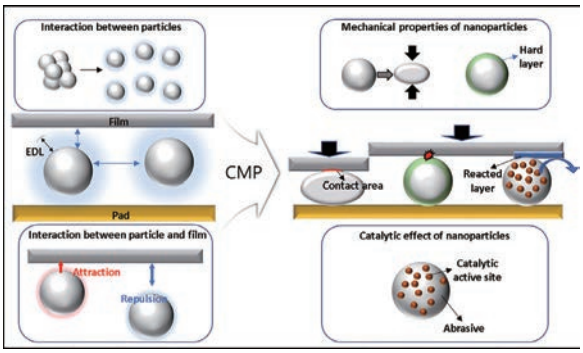


**Keywords:** CMP (Chemical mechanical polishing), silica nanoparticles, synthesis, modification, surface functionalization, core-shell structure

## 1. Introduction

Chemical mechanical polishing (CMP) is a technique employed in the semiconductor fabrication process to remove material from the surface of films during integrated circuit (IC) manufacturing (Lee et al., 2022; Paik U. and Park J.-G., 2009). The process involves a chemical slurry and mechanical polishing by abrasive nanoparticles to achieve high planarity and smoothness on the film surface (Ein-Eli and Starosvetsky, 2007; Lee et al., 2016). IBM first developed and commercialized CMP in the late 1980s to planarize layers of silicon dioxide ($SiO_2$) during the fabrication of microelectronics (Beyer, 2015; Fury, 1997). CMP has attracted attention as a key step in manufacturing integrated circuits, including microprocessors, memory, and logic devices, due to growing demand for higher integration densities and smaller device sizes, which require greater control over surface topography (Zwicker, 2022).

**Fig. 1** illustrates the CMP process and the role of nanoparticles in CMP slurry (Mikhaylichenko, 2018; Seo, 2021). A multiple platen design offers flexibility in pad materials, slurries, and conditioning processes, enabling high throughput and optimized polishing. Wafers are cleaned after CMP and transferred back to their boxes by a robotic arm. A slurry is applied to the polishing pad, and the wafer rotates on a custom CMP table, where mechanical and chemical actions remove imperfections. After several steps, the wafer becomes ultra-smooth and ready for subsequent fabrication stages (Srinivasan et al., 2015).

The slurry consists of stable suspensions of abrasive nanomaterials, such as $Al_2O_3$ (alumina), $SiO_2$ (silica), and $CeO_2$ (ceria), dispersed in water with prescribed chemicals (Armini et al., 2008; Feng et al., 2006; Parker, 2004). The choice of abrasive nanoparticles depends on the type of polishing required. Silica is an abundant, representative, and versatile particle that minimizes defects and scratches, improves planarity and uniformity, and increases removal rates and selectivity (Lee et al., 2015).

Interactions between particles in suspended media are related to dispersion stability of the particles. Agglomerated

† Received 31 May 2023; Accepted 2 August 2023
J-STAGE Advance published online 28 December 2023
$ Authors contributed equally to this publication
* Corresponding author: Taeseup Song; Ungyu Paik;
Add: 222 Wangsimni-ro, Seoul 04763, Republic of Korea
E-mail: tssong@hanyang.ac.kr (T.S.); upaik@hanyang.ac.kr (U.P.)
TEL: +82-2-2220-0502

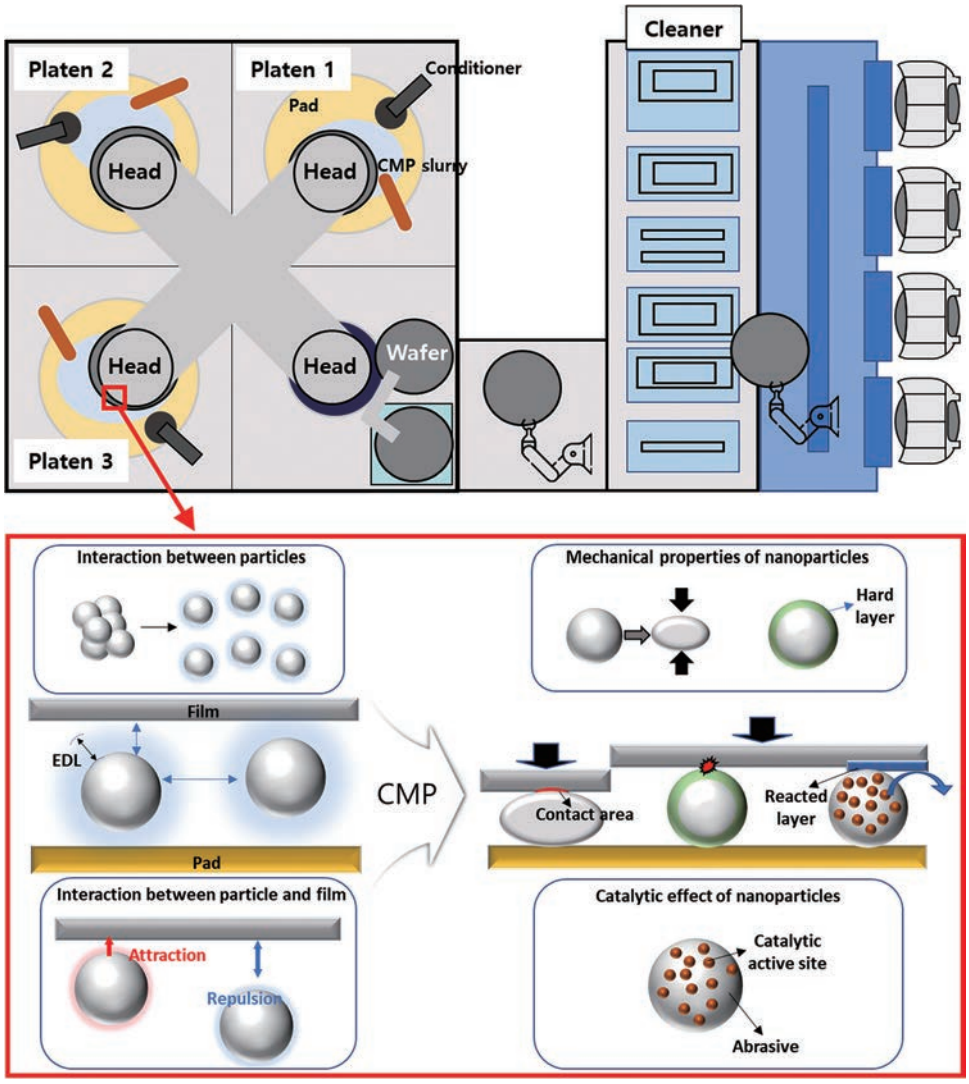


**Fig. 1** Schematic illustrations of a standard CMP tool highlighting the influence of nanoparticle properties in the slurry on the CMP process. Key factors, such as the dispersion stability of nanoparticle abrasives in the slurry, interactions between particles and the film, the nanoparticle's elastic modulus and hardness, as well as their catalytic effects, are illustrated. These factors are crucial in determining the overall outcomes of CMP.

particles in CMP slurry can cause surface defects, reduce the CMP removal rate, and damage neighboring patterns, resulting in lower selection ratio. In particular, aggregate particles larger than 1 μm in diameter are a leading cause of scratch defects on films (Armini et al., 2008; Lu et al., 2013; Seipenbusch et al., 2010; Shin et al., 2019). Van der Waals and electrostatic forces are critical factors influencing the cohesion and stability of particles in suspended media. Van der Waals forces always act as an attractive force between particles, and a system dominated by van der Waals forces results in particle agglomeration. The electrostatic force that acts as a repulsive force between two particles is the electrostatic force. In the aqueous system, the adsorbed ions on the nanoparticles determine the repulsive force between the particles. Ions distributed around the nanoparticle form an electric double layer (EDL) (Hayashi et al., 1995). The Coulomb force produced by an EDL is an electrostatic and repulsive force between particles of the same material; the thicker the EDL, the stronger the repulsive force between the particles and the weaker the agglomeration (Gun'ko et al., 1998). These forces can be controlled by adjusting the slurry chemistry, and nanoparticle engineering can help maintain a stable slurry, prevent particle agglomeration, and ensure a successful polishing process.

Material removal occurs when abrasive particles and the substrate surface are in direct contact (Luo and Dornfeld, 2003). Contact between abrasive particles and films also occurs when van der Waals and electrostatic forces dominate the attraction, resulting in higher removal rates. Controlling the attraction or repulsion between abrasive particles and the film surface is critical for improving removal rates and selectivity. A model based on the contact mechanism has been proposed to explain the mechanical aspects of the material removal mechanism (Seo et al., 2016b). According to the model, the greater the total

contact area between the particle and the film, the greater the removal rate. Assuming all particles participate in material removal, the particle-film surface contact area is calculated as $A \propto C^{1/3} \cdot d^{-1/3}$, where C is the concentration of abrasive particles, and $d$ is the abrasive diameter (Basim et al., 2000). However, only abrasive particles larger than the gap between the polishing pad and the film surface (active particles) can contribute to material removal (Seo, 2021).

Another key property of nanoparticles can affect CMP performance. First, the catalytic effect of nanoparticles can improve the removal rate during metal CMP by enhancing the oxidation reaction (Lei et al., 2012; Wang et al., 2016). Second, the mechanical properties of the particles. The ability to control the elastic modulus can increase the removal rate by enlarging the contact area with the film and reducing scratches and roughness (Chen et al., 2019; Mu and Fu, 2012). Moreover, improving the abrasive surface hardness is advantageous for achieving higher removal rates, especially when working with films with relatively high hardness and chemical stability, such as alumina, silicon carbide (SiC), and tungsten (Dai et al., 2020). Therefore, careful selection and use of nanoparticles with these desirable properties can significantly impact the efficiency of CMP.

As the materials for the next generation of semiconductor devices become more diverse and the device structures more complex, the performance requirements for CMPs are becoming increasingly stringent. Silica nanoparticle abrasives, which can reduce defects and scratches, improve flatness and uniformity, and increase removal rates and selectivity, are among the most popular materials. This review of silica nanoparticles as CMP abrasives is organized in the following order: properties of nanoparticles that affect CMP, silica particle synthesis methods and their properties, and finally, silica nanoparticle modifications such as surface functionalization, coating or doping with other materials, and core-shell structure formation to overcome the limitations of conventional synthesis methods.

## 2. Nanoparticle properties and their impact on CMP

Nanoparticle abrasives in slurries can affect CMP results due to their dispersion stability, interactions between particles and film, elastic modulus and hardness, and catalytic effects (**Fig. 1**). Dispersion stability is closely related to interactions between nanoparticles (Kawaguchi, 2020). When there is a sufficient repulsive force between nanoparticles, dispersion stability increases. A slurry with high dispersion stability prevents scratch defects caused by agglomerated particles and contributes to improved planarity through uniform removal on the film surface and increased removal rates by enlarging the contact area (Choi et al., 2004). Interactions between particles and films affect the number of active particles (Wang et al., 2022). Increasing the force between particles and films increases both the number of active particles and removal rate (Hwang et al., 2008). This is also important for selectivity control in patterned wafers (Seo et al., 2014). The elastic modulus and hardness of the particles are related to the removal rate and defects. Depending on the target film, particle design should consider whether the main issue is high defects or low removal rate (Kwon et al., 2013; Saka et al., 2008). The last catalytic effect refers to the effect of particles on the promotion of chemical reactions on the film surface (Wang et al., 2021). To improve the performance of CMP, it is necessary to understand and control these nanoparticle properties.

### 2.1 Interactions between nanoparticles in suspension

Between 1945 and 1948, two research teams, one led by Derjaguin and Landau in the Soviet Union and the other by Verwey and Overbeek in the Netherlands, independently proposed a theory regarding repulsion between charged particles in water (Ninham, 1999). This is now commonly referred to as the DLVO theory, after the initials of the four scientists involved (van Oss, 2008).

The DLVO theory suggests that the stability of a particle in solution depends on its total potential energy function ($V_T$). The primary potential energy between two particles arises from the attractive van der Waals force ($V_A$) and the electrostatic force ($V_R$) from the electrical double layer. An extended DLVO theory, which incorporates the steric force ($V_S$) due to adsorbed layers of polymers or surfactants, has been proposed to better explain the stabilization of colloidal systems (van Oss, 2008). This can be represented by the equation:

$$V_T = V_A + V_R + V_S \tag{1}$$

The van der Waals force is the attraction resulting from the instantaneous dipoles formed by temporary polarization of atoms and the induced dipoles caused by these instantaneous dipoles (**Fig. 2(a)**) (Margenau, 1939). This force is always present in nanoparticles within a dispersion and becomes significantly stronger when the distance between particles decreases. The van der Waals force is a major reason for particle agglomeration. The equation for the van der Waals force between two spherical particles (Hamaker, 1937) can be expressed as

$$V_A(s) = -\frac{A}{3}\left[\frac{R^2}{s(s+4R)} + \frac{R^2}{(s+2R)^2} + \frac{1}{2}\ln\left(1-\frac{4R^2}{(s+2R)^2}\right)\right] \tag{2}$$

$$V_A(s) = -\frac{AR}{12s} \quad (s \ll R) \tag{3}$$

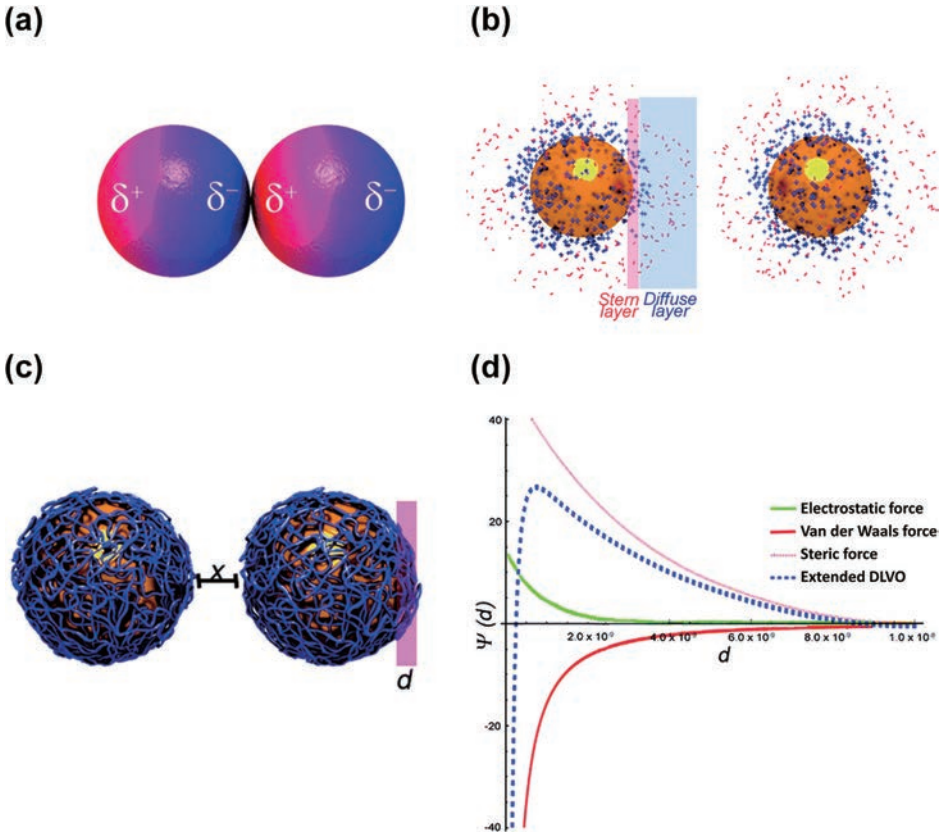


**Fig. 2** Interactions between nanoparticles in CMP slurry according to DLVO theory: **(a)** van der Waals force, **(b)** electrostatic force, **(c)** steric force and **(d)** the potential as a function of the distance between two particles derived from their net potential. Reproduced from Ref. (Moore et al., 2015) with permission from the Royal Society of Chemistry.

where $A$ is the Hamaker constant, $s$ is the distance between the two particles, and $R$ is the radius of the spherical particle. When the distance between two particles is small enough, as in **Eqn. (3)**, the expression can be approximated. According to this equation, the larger are the particles, the shorter is the distance; and the higher is the Hamaker constant, the stronger is the van der Waals force. The Hamaker constant is determined by the dielectric constant and refractive index of the nanoparticles and the dispersion medium (Bergström, 1997). The Hamaker constant is difficult to manipulate once the materials of nanoparticles and medium are determined. Much research into increasing dispersion stability has been directed toward increasing the repulsive forces rather than reducing van der Waals forces (Tolias, 2018).

Charges on particle surfaces can influence electrostatic forces. In an aqueous system, nanoparticles acquire charges based on pH (Serrano-Lotina et al., 2023). In acidic conditions, they carry a positive charge, which gradually weakens as the pH increases, and they carry a negative charge in alkaline conditions. A surface charge occurs because protons adsorb and bind to a particle surface under acidic conditions, generating a positive charge. A negative charge arises as the pH increases and hydroxide ions become more prevalent. In other words, the degree of surface charge depends on the reactivity with protons or hydroxide ions.

When a particle acquires a surface charge by binding with a proton or hydroxide ion, counter ions are adsorbed to the exterior, forming an EDL, which consists of a Stern layer (the first layer strongly bound to the particle surface) and a diffusion layer outside of which ions are distributed (**Fig. 2(b)**). The two layers differ because the potential linearly decreases with distance in the Stern layer, where the particles are strongly bound (Lunardi et al., 2021). In contrast, in the diffusion layer, the effects of surface charge and thermal motion are considered together, resulting in parabolic potential behavior.

Each material has a pH at which the charge becomes zero, called the isoelectric point (IEP) (Seo et al., 2016a). The IEP varies by material, and it is important to understand the IEP of each material and to select a pH that maintains sufficient electrostatic repulsive force. For example, pure silica typically has an IEP of 2 to 3, and alumina has an IEP of 9 (Kosmulski, 2009). The IEP is inversely proportional to the electronegativity of the metal composing the oxide, with a higher electronegativity leading to a lower IEP (Bebieet al., 1998). Factors affecting IEP also include particle functional group and crystal facet number and impurity.

The steric force between particles is caused by the adsorption of polymers (**Fig. 2(c)**). Steric forces can be largely divided into the force for volume restriction ($\Delta G^{VR}$)

and the force by mixing energy ($\Delta G^M$). The former represents the repulsive force caused by the volume of the polymer, while the latter is caused by osmotic pressure due to the affinity between the solvent and the polymer as the polymer layers approach each other (Sedev and Exerowa, 1999). When the adsorbed particles of the two polymers are separated by less than the distance between the polymer layers, a force due to $\Delta G^M$ is generated. At this point, the relationship between the polymer and the solvent is important. In an effective solvent with a strong affinity between the polymer and the solvent, the solvent penetrates by osmotic pressure and causes a repulsive force (Babchinand Schramm, 2012). When the two particles approach each other, a repulsive force is generated by $\Delta G^{VR}$.

The interaction between two particles, depicted in **Fig. 2(d)**, is determined by the combined forces of van der Waals forces, the electrostatic force due to the EDL, and steric forces. If this value is positive, repulsive forces dominate, resulting in higher dispersion stability. If it is negative, attractive forces dominate, and the particles agglomerate (Moore et al., 2015).

## 2.2 Interactions between nanoparticles and film during CMP

When nanoparticles and film substrates interact in an aqueous system, the adhesion between them is influenced by van der Waals, electrostatic, and steric forces. These forces can either attract or repel particles from the surface, affecting the rate of removal. Measuring these forces directly can be difficult, but atomic force microscopy (AFM) can now gauge the net force between the particles and substrate (Kappl and Butt, 2002). AFM is a powerful tool in various research fields, including powder technology. It uses a probe with a sharp tip to scan the surface of a sample and detect the reflected laser beam to create an image (Shluger et al., 1994). An AFM instrument has a basic configuration, consisting of a micro-machined cantilever with a sharp tip, a piezoelectric scanner, and a photodiode detector (**Fig. 3(a)**). AFM can also be performed in liquid environments using a fluid cell (Dorobantu et al., 2009).

To apply AFM to force measurement, the probe or sample substrate is moved vertically (z-direction) to change the distance between the probe and the surface (Kappl and Butt, 2002). By attaching a colloidal nanoparticle at the end

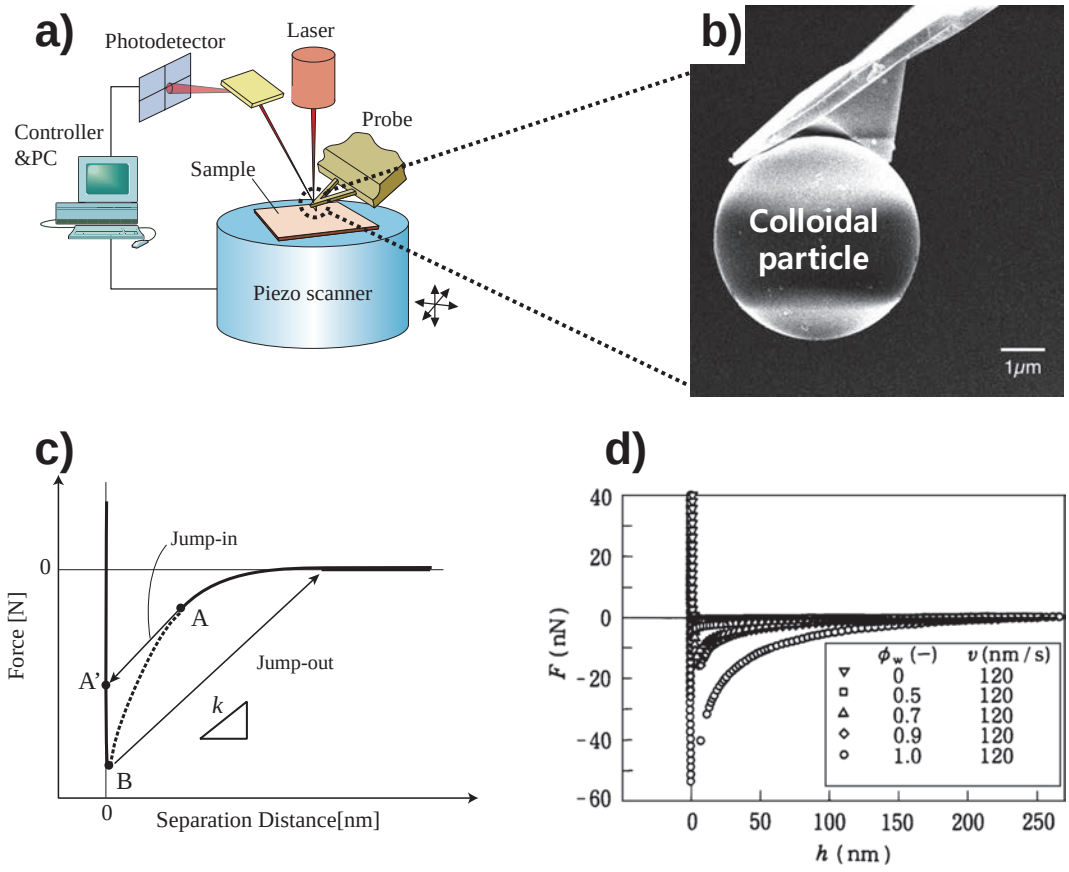


**Fig. 3** Analysis of particle-film interactions through force-distance curve measurements by AFM: **(a)** schematic of AFM equipment, **(b)** an AFM cantilever with colloidal particles attached, **(c)** force-distance curve measurement results using an AFM cantilever with colloidal particles attached, and **(d)** surface charge variation with the ratio of water and IPA and corresponding force distance curve variation. Reusing with permission from Ref. (Ishida and Craig, 2019) under the terms of the CC-BY 4.0 license. Copyright: (2019) The Authors, published by Hosokawa Powder Technology Foundation.

of the pointed tip, the force-displacement curve between the particle and substrate can be obtained. For colloidal probes (**Fig. 3(b)**), spherical particles between 2 μm and 40 μm in diameter are typically attached to the probe with an epoxy adhesive or hot-melt epoxy resin (Ralston et al., 2005).

For the force in **Fig. 3(c)**, the attraction between the surfaces is sensed. When the surfaces are in contact, the change in cantilever deflection is equal to the change in displacement, often represented by a linear region called the constant compliance region (Ishida and Craig, 2019). It is necessary to focus on the shape of the curve, which suddenly decreases or increases before re-entering the constant compliance region (**Fig. 3(d)**). When attraction is a strong function of separation, the instability of the cantilever often causes the surfaces to "jump in" to a contact (denoted by A and A' in **Fig. 3(c)**). This occurs when the gradient of the interaction force with separation distance exceeds the spring constant of the cantilever. As the surfaces separate, adhesion may appear between them. In this case, the cantilever typically "jumps out" with zero interaction force, as represented by point B in the figure. This is the opposite effect of jumping in. If the system were applied to a repulsive force, the curve would instead bend to a positive value first before reaching the compliance region.

## 2.3 Mechanical properties of nanoparticles

AFM nano-indentation is an effective method to determine the elastic behavior of samples by analyzing force-displacement curves and nano-indentation data. Passeri et al. (2011) used AFM to measure the elastic modulus ($E$) and hardness of polyaniline films on glass substrates. Nowatzki et al. (2008) computed the $E$ values of thin films using the thin-film Hertzian model. Song et al. (2008) assessed the E values of PS, polymethylmethacrylate (PMMA) spheres, and PMMA/silica composites by applying an AFM force-volume technique and Hertz's theory of contact mechanics (**Table 1**) (Chen et al., 2015a).

In AFM indentation tests, the shape of the indenter (cantilever tip) significantly influenced the calculated results. Indenters can be modeled in two geometries: spherical or conical (depicted in **Fig. 4(a)** and **(b)**). **Eqns. (4)** and **(5)**, which are related to force, indentation, and Young's modulus, were utilized to compute the results, where $F$ represents the indentation force, $\delta$ denotes the indentation depth, $R$ is the tip radius, and $\alpha$ is the half-opening angle of the conical tip. The reduced modulus of elasticity ($E^*$) can be calculated using $E$ and $v$ for the sample and $E_t$ and $v_t$ for the AFM tip, as shown in **Eqn. (6)**. If the elastic modulus of the indenter is much greater than that of the sample, $E^*$ can be simplified, as shown in **Eqn. (7)** (Chen et al., 2015a).

$$F_{\text{Sphere}} = \frac{4}{3} \cdot E^* \cdot \delta^{3/2} \cdot R^{1/2} \tag{4}$$

$$F_{\text{Cone}} = \frac{2}{\pi} \cdot E^* \cdot \delta^2 \cdot \tan(\alpha) \tag{5}$$

**Table 1** Core shell structure mechanical properties by the composition of particles. Reprinted with permission (Chen et al., 2015a). Copyright: (2015) Elsevier B.V.

| Samples | Core size [nm] | Shell thickness [nm] | $E$ [GPa] |
|---|---|---|---|
| PS | 200 | — | 2.01 ± 0.70 |
| PS/$SiO_2$ | 200 | 10 | 4.42 ± 0.27 |
| PS/$SiO_2$ | 200 | 15 | 5.88 ± 0.48 |
| PS/$SiO_2$ | 200 | 20 | 9.07 ± 0.94 |
| PS | 120 | — | 2.80 |
| PS/$CeO_2$ | 120 | 8 | 7.93 |
| PS | 120 | 12 | 8.25 |
| PS | 120 | 16 | 10.67 |
| PMMA | 367 | — | 4.3 ± 0.7 |
| PMMA/$SiO_2$ | 367 | 15 | 4.5 ± 0.7 |
| PMMA/$SiO_2$ | 367 | 30 | 10.3 ± 1.5 |
| PP | 200–500 | — | 1.3–2.8 |
| Bulk PP | — | — | 1.5–2.0 |
| Bulk PS | — | — | 2–5 |
| Bulk $SiO_2$ | — | — | 75, 72 |
| Bulk $CeO_2$ | — | — | 264.1 |

$$\frac{1}{E^*}=\frac{1-\nu^2}{E}+\frac{1-\nu_t{}^2}{E_t} \tag{6}$$

$$\frac{1}{E^*}\approx\frac{1-\nu^2}{E} \tag{7}$$

Chen et al. (2015a) conducted experiments by depositing particles through spin coating on the substrate (**Fig. 4(c)**). They measured the modulus of the particles by contacting the tip at the location where the particle was located and measuring the $F$ value according to the depth of indentation. **Fig. 4(d)** shows the force-distance curve of a spin-coated deposit of nanoparticles on a substrate. Retract curve was fitted using the Hertzian model (using a spherical indenter), and as shown in this figure, the fitted curve was mainly consistent with the force-distance curve. This fitting allowed us to measure the elastic modulus of the nanoparticle using the force-distance curve.

There are several possible sources of error in calculating the elastic modulus, such as uncertainty in contact point determination and errors in $k_c$ measurement of AFM cantilevers, surface and probe roughness, scanner and sample creep, and AFM photodetectors. Chen et al. (2015a) found that the substrate can also influence the measured mechanical properties, causing some error in the results. Despite these sources of error, it is possible to measure the relative change in modulus for each particle under the same measurement conditions.

## 2.4 Catalytic effect of nanoparticles

Kauffman proposed a model for CMP of tungsten and similar metals, in which the surface is oxidized to form a weak interface between the metal oxide and the metal (Lim et al., 2013; Tamboli et al., 1999). The abrasive attacks the weak interface to remove material. This model has been applied not only to tungsten, but also to metals such as copper, cobalt, and molybdenum, as well as materials with high hardness, including sapphire and SiC, to secure an adequate removal rate during polishing (Krishnan et al., 2010).

To promote oxidation reactions on the surface of the material being polished, catalysts and oxidizing agents are essential. Metals (Ag, Fe) and metal oxides such as copper oxide (CuO, $Cu_2O$), silver oxide ($Ag_2O$), and iron oxide ($Fe_2O_3$, $Fe_3O_4$) can act as catalysts in the reaction that decomposes the most commonly used CMP oxidizing agent, $H_2O_2$, to produce hydroxyl (OH) radicals (Kanungo, 1979; Xu et al., 2014). However, these particles do not ensure

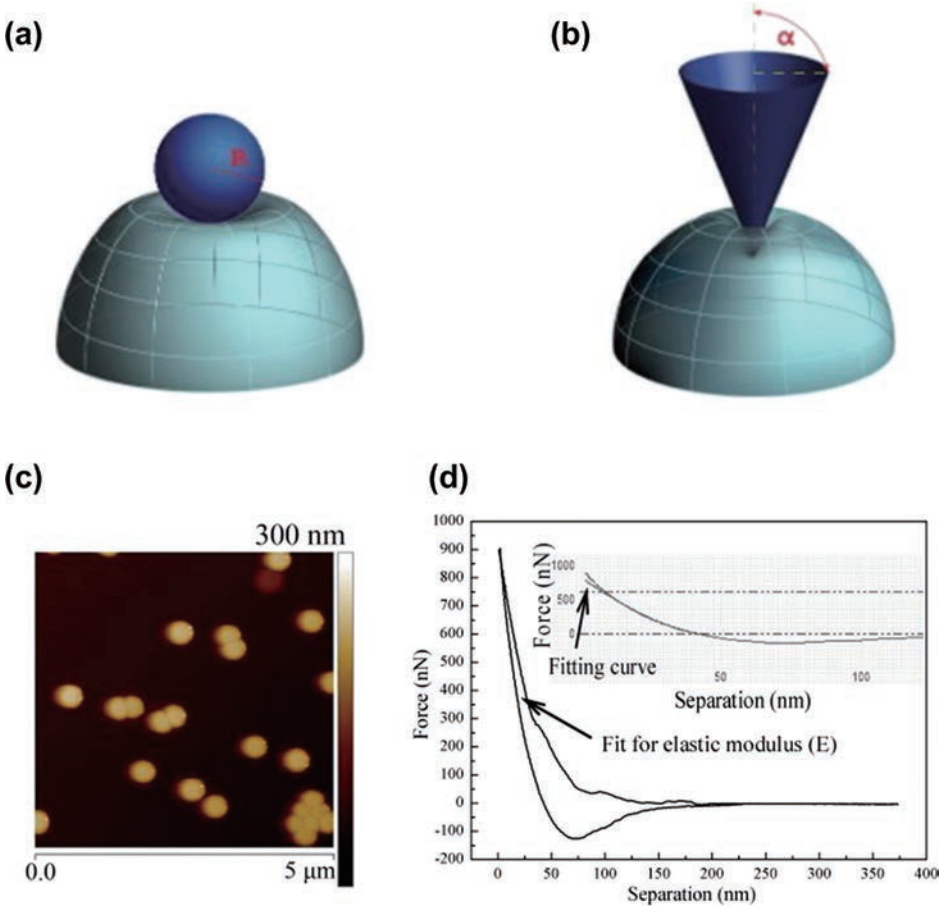


**Fig. 4** Measurement of mechanical properties through force-distance curve measurements by AFM: Tip-particle surface contact models: **(a)** spherical indenter and **(b)** conical indenter. **(c)** AFM 2D image of nanoparticles deposited on the substrate. **(d)** Force separation curves and fitting curves obtained from nanoparticles. Reprinted with permission from Ref. (Chen et al., 2015a). Copyright: (2015) Elsevier B.V.

dispersion stability or achieve desirable polishing rates from a mechanical perspective (Guedes et al., 2009; Xu et al., 1998). Commonly used CMP abrasives such as silica, alumina, and ceria do not have any catalytic effects on oxidation reactions. Research on the use of composites of catalyst-containing particles and abrasives in CMP will be discussed in detail later.

## 3. Synthesis strategy for silica nanoparticles to improve CMP

The choice of abrasive plays a crucial role in the performance of a CMP slurry, as slurry properties can vary widely depending on the synthesis method. Silica particles, which are a common component of CMP slurries, can be classified into two types: fumed silica, which is synthesized through a gas phase process, and Stöber (or colloidal) silica, which is synthesized through a liquid phase process (Hyde et al., 2016). **Table 2** outlines the advantages and disadvantages of each type. Fumed silica offers a large surface area and an amorphous structure, but its irregular shape and wide particle-size distribution can lead to surface defects during polishing (Khan et al., 2004). By comparison, Stöber silica with uniform particle size and shape can result in more predictable polishing and fewer surface defects (Ahn et al., 2004). However, its lower removal rate compared to fumed silica is still an issue that needs to be overcome (Kim et al., 2021). Ultimately, the choice between fumed and Stöber silica depends on the specific requirements of the CMP, which may include desired material removal rate, selectivity, surface finish, and slurry stability.

### 3.1 Gas phase synthesis: fumed silica

Flame hydrolysis is a large-scale industrial process that generates silica with large surface area. **Fig. 5(a)** illustrates the flame hydrolysis setup for producing fumed silica. The synthesis reaction equations follow (Garrett, 2017; Hyde et al., 2016);

$$2H_2 + O_2 \rightarrow 2H_2O \quad (8)$$

$$SiCl_4 + 2H_2O \rightarrow SiO_2 + 4HCl \quad (9)$$

$$2H_2 + O_2 + SiCl_4 \rightarrow SiO_2 + 4HCl \quad (10)$$

Fumed silica is synthesized by combusting silicon tetrachloride ($SiCl_4$) or other silicon-containing precursors in a hydrogen-oxygen flame (Khavryutchenko et al., 2001). The heat from combustion vaporizes the $SiCl_4$, which then reacts with water vapor to form silica nanoparticles.

These primary particles coagulate through intergrowth in the flame and agglomerate due to cohesive forces during and after cooling. Silica is separated from the off-gas containing hydrogen chloride (HCl) using filters or cyclones. The high-temperature residence time, along with the interplay of surface growth, coagulation, and sintering, determines the characteristics of the particles. These nanoparticles aggregate into chains and ultimately form a three-dimensional network structure, resulting in fumed silica (**Fig. 5(b)**) (Jin et al., 2019; Meled, 2011).

Fumed silica nanoparticles are an anhydrous material synthesized using gas-based dry processes, resulting in low concentration of surface silanol (Si–OH) groups. When silica nanoparticles are dispersed in aqueous solutions, the silanol groups on their surface can form hydrogen bonds with water molecules and develop a surface charge through reactions with $H^+$ or $OH^-$ ions, which are potential determining ions. These reactions are the driving force for the good dispersion of nanoparticles. However, fumed silica can be challenging to disperse in water, and the rheological properties of the dispersion exhibit shear thinning behavior (Barthel et al., 2005; Kim et al., 2021; Liu and Maciel, 1996). In static condition, the silanol groups on the surface interact weakly with fluids through hydrogen bonding, increasing the viscosity of the fluid. In dynamic environment, even mild shear deformation can break the connection between fluid molecules and silica due to the relatively small number of silanol groups available for hydrogen bonding. This is a characteristic observed in fumed silica dispersions due to shear thinning, a decrease in viscosity under shear stress.

**Table 3** lists the results of CMP on $SiO_2$ layer using fumed silica-based slurry. The data indicate that the removal rate increased as the particle size grew from 80.2 to 138 nm (Kim et al., 2021). The increase in removal rate is due to the more frequent and direct interaction of the larger particles with the film surface and the larger penetration

**Table 2** Comparing the advantages and disadvantages of fumed silica and Stöber silica aspect to the CMP process.

| | Fumed silica | Stöber silica |
|---|---|---|
| Advantages | • Easy for mass production<br>• High purity<br>• Large surface area to volume<br>• High removal rate | • Monodisperse size distribution<br>• Regular and spherical particle shape<br>• High dispersion stability<br>• Lower surface defects and scratches |
| Disadvantages | • Wide size distribution<br>• Irregular shape of the particle<br>• Difficult to control secondary particle size and dispersion stability<br>• Causing surface defects and scratches | • Expensive precursor price<br>• Alcohol by-product<br>• Low removal rate<br>• Small surface area to volume |

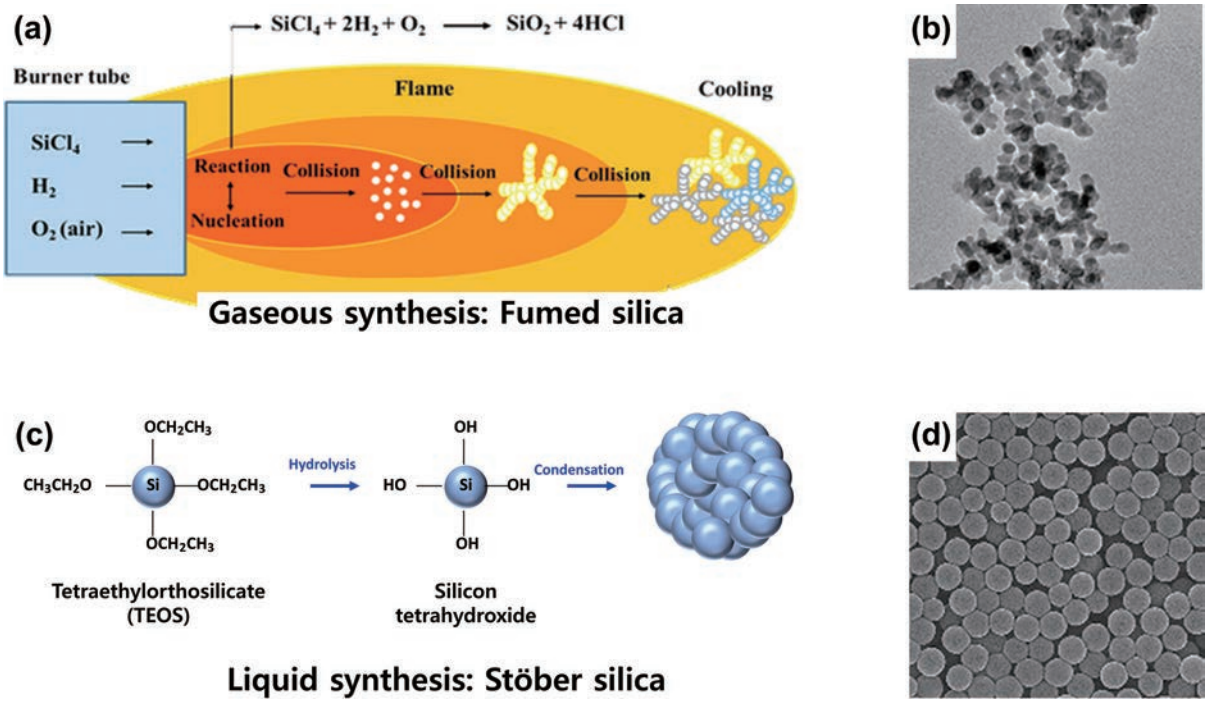


**Fig. 5** **(a)** Schematic illustrations of fumed silica nanoparticle synthesis through gas-phase reaction for CMP slurry. Reprinted with permission (Hyde et al., 2016). Copyright: (2016) American Chemical Society. **(b)** TEM images displaying the morphologies of the fumed silica nanoparticles. Reprinted with permission from (Chen et al., 2022). Copyright: (2022) American Chemical Society. **(c)** Schematic illustrations of Stöber silica nanoparticle synthesis through liquid-phase reaction for CMP slurry. **(d)** TEM images displaying the morphologies of Stöber silica nanoparticles. Reprinted from Ref. (Sui et al., 2016) under the terms of the CC-BY 4.0 license. Copyright: (2016) The Authors, published by Springer Nature.

**Table 3** CMP results using fumed silica-based slurry.

| Size [nm] | Solid loading [%] | pH (Adjustor) | CMP pad | Applied pressure [psi] | Removal rate [Å/min] | Roughness [nm] | Reference |
|---|---|---|---|---|---|---|---|
| 140.9 | 12 | 10.5 ($NH_4OH$) | IC1000/subaIV | 4 | 2600 | Ra 0.29 | (Kim et al., 2021) |
| 138.8 | 12 | 10.5 ($NH_4OH$) | IC1000/subaIV | 4 | 2850 | Ra 0.31 | (Kim et al., 2021) |
| 99.4 | 12 | 10.5 ($NH_4OH$) | IC1000/subaIV | 4 | 1500 | Ra 0.17 | (Kim et al., 2021) |
| 80.2 | 12 | 10.5 ($NH_4OH$) | IC1000/subaIV | 4 | 1200 | Ra 0.14 | (Kim et al., 2021) |
| 156 | 10 | 10.5 ($NH_4OH$) | IC1400 | 4 | 1680 | RMS 0.25 | (Haba et al., 2003) |
| 220 | 15 | 10.1 (KOH) | IC1000/subaIV | 3 | 620 | — | (Estel et al., 2010) |
| 220 | 15 | 4.1 (HCl) | IC1000/subaIV | 3 | 80 | — | (Estel et al., 2010) |
| 220 | 15 | 3.0 (HCl) | IC1000/subaIV | 3 | 10 | — | (Estel et al., 2010) |

volume. However, as the particle size exceeded 138 nm, the contact area decreased, gradually decreasing the removal rate (Haba et al., 2003). That means the contact area becomes more dominant in the removal rate above a specific particle size than the penetration volume. Whether penetration volume or contact area is the dominant factor in the removal rate depends on the film and particle being polished and the process conditions (Basim et al., 2000). As shown in **Table 3**, for CMP of $SiO_2$ layer with fumed silica, the contact area or penetration volume becomes the more important factor starting from 138 nm. Below 138 nm, the effect of the penetration volume is more dominant on the

removal rate change, and above 138 nm, the contact area is more dominant. However, CMP with particles penetrating the film can cause many defects in the post-CMP film, which is why the roughness increases with increasing size up to 138 nm.

Fumed silica needs adequate electrostatic repulsive force for effective dispersion (Estel et al., 2010). Due to its low ion impurity content, the IEP of fumed silica falls between pH 2 and 3. As a result, fumed silica demonstrated high dispersion stability at pH 10, where the surface charge is high, but poor dispersion stability near its IEP at pH 3. This led to a high removal rate at pH 10, which can be attributed to the greater contact area between particles and the film substrate. In contrast, a low removal rate was observed at pH 4 due to the reduced dispersion stability.

Fumed silica offers several advantages, such as the ability to be synthesized in large-scale processes to high purity levels due to its nearly complete absence of ionic impurities, as well as the high hardness of the primary particles with few pores. In the early days of implementing CMP in semiconductor manufacturing processes, fumed silica-based CMP slurries were widely used, particularly for interlayer dielectric CMP, to remove the $SiO_2$ layer (Li et al., 2010). However, excessive energy requirements and harsh reaction conditions, which produce toxic gases such as hydrogen chloride (HCl), reduced its usefulness in efficiency-minded and environmentally conscious societies (Croissant et al., 2020). Moreover, as semiconductor devices become ever smaller, the standards for defects and scratches are becoming more stringent. In conclusion, the shift from fumed silica to Stöber silica in CMP slurries for semiconductor manufacturing reflects the industry's increasing focus on environmental sustainability, energy efficiency, and the need for high-quality materials with better control over particle size, shape, and dispersion stability to meet the demands of ever-shrinking electronic devices.

### 3.2 Liquid phase synthesis: Stöber silica

The Stöber method named after Werner Stöber, is a sol-gel process for synthesizing monodisperse spherical silica nanoparticles (Ibrahim et al., 2010). The method involves hydrolyzing and condensing alkoxysilane precursors such as tetraethyl orthosilicate (TEOS) or tetramethyl orthosilicate (TMOS) in the presence of water and alcohol solvents, usually under basic conditions. In 1968, Stöber et al. reported the synthesis of spherical monodisperse silica nanoparticles using TEOS as the silicon alkoxide and an aqueous ethanol solution of ammonia and water (Stöber et al., 1968).

**Fig. 5(c)** is an illustration of particle synthesis mechanism. Silica particles are made into nanoparticles through a two-step reaction: hydrolysis and condensation (Ghimire and Jaroniec, 2021). In hydrolysis the–OR around the silicon in alkoxysilane is changed to –OH, with an alcohol in the form of ROH as a byproduct. The alcohol byproduct is determined by the alkyl group of alkoxysilane. After the hydration reaction with $Si(OH)_4$, condensation proceeds as water escapes (Selvarajan et al., 2020). The size and distribution of the particles are affected by the reaction kinetics of the hydrolysis and condensation reactions, which are strongly influenced by the type of alkyl group of the alcohol and silicon alkoxide, the amount of base catalyst, and the temperature (Costa et al., 2003; Fernandes et al., 2019; Green et al., 2003; Plumeré et al., 2012). The technique allowed for the production of nanoparticles between 50 nm and 1 μm in diameter with a narrow distribution of spherical shapes (**Fig. 5(d)**). Silica synthesized with the Stöber method has inspired many research areas, including CMP slurries.

When synthesizing Stöber silica, the choice of alkoxysilane precursor (e.g., TEOS or TMOS) can affect the reactivity and overall properties of the synthesized nanoparticles. The alkyl in alkoxysilane acts as a leaving group during hydrolysis. The larger the molecular weight of the alkyl group serving as the leaving group, the slower the reaction rate (Costa et al., 2003). The hydrolysis reaction therefore proceeds in the order of methyl > ethyl > propyl. A slower hydrolysis reaction results in smaller particle size with a narrow size distribution, which helps create monodispersed particles. However, particles with slow reaction rate may lengthen the synthesis time and reduce reaction yields. In contrast, TMOS, which has higher reaction rate, leads to larger particles with a broader distribution. Due to its balanced properties, TEOS is the most commonly used alkoxysilane for silica synthesis.

The high cost of TEOS has been a persistent issue with Stöber silica. Soh et al. (1999) developed a process for synthesizing TMOS at a significantly lower unit cost by reacting silicon and methanol under copper catalyst. As a result, research on synthesizing monodisperse silica with reduced manufacturing costs has been reported. One method involves controlling the molar ratio of water to TMOS (Anderson and Carroll, 2011). A higher water-to-TMOS ratio accelerates hydrolysis and condensation reactions, producing smaller particles with a narrow size distribution. Temperature also plays a role in particle size and distribution. Higher temperatures accelerate hydrolysis and condensation, leading to smaller particles with a narrow size distribution. Conversely, lower temperatures decelerate reactions, resulting in larger particles with a broader size distribution.

The type and concentration of catalyst (acidic or basic) used in the Stöber process can significantly affect hydrolysis and condensation reaction rates and, therefore the size and morphology of silica nanoparticles. Acidic catalysts (e.g., HCl) tend to produce smaller particles, while basic catalysts (e.g., ammonia) often result in larger particles (Ghimire and Jaroniec, 2021). Adjusting the catalyst

concentration allows control of reaction kinetics and tuning of particle size.

In summary, the chemical composition variables of the Stöber method, such as alkoxysilane precursor, catalyst, solvent, water-to-precursor ratio, temperature, and reaction time, can significantly affect the synthesis results. By controlling these variables, researchers can tailor the size, shape, and properties of silica nanoparticles for various applications.

Stöber silica is synthesized in liquid phase reaction, has Newtonian behavior in its hydrophilic and rheological behavior due to the multiple silanol groups on its surface, and is highly dispersible. The IEP of silica synthesized using the sol–gel method can be affected by the washing process. Washing is used to remove residual reactants and impurities such as unreacted precursors, alcohols, and counter ions (Ibrahim et al., 2010). The IEP of silica is closely related to the presence of silanol groups on the surface and the adsorption of counterions (De Keizer et al., 1998; Srinivasan et al., 1994; Szekeres et al., 2002; Wells et al., 2000). During the cleaning process, these counterions can be removed, changing the surface charge of silica particles and consequently the IEP. For example, if an ammonia catalyst remains on a silica particle, the IEP will shift to pH 4. This is because the positively charged ammonium ions remain inside the silica, making the surface charge positive.

**Fig. 6** shows the results of CMP of $SiO_2$ film as a function of pH using silica dispersion according to particle synthesis method. In the case of fumed silica slurry, the removal rate occurs at strong base conditions above pH 10, and the removal rate decreases as it approaches pH 3. This is because fumed silica with low dispersion stability is prone to agglomeration if sufficient electrostatic attraction is not maintained, and active particles are reduced due to small contact area. Compared with Stöber silica, fumed silica is harder from a mechanical point of view due to fewer pores and a higher surface area, and therefore has a higher removal rate compared with Stöber silica when it is highly dispersible (Estel et al., 2010). In the case of Stöber silica, the removal rate is also higher in acidic region, resulting from the higher dispersion stability of Stöber silica compared to fumed silica. However, at high pH, the contact area decreases because the zeta potential of the film is as high as that of Stöber silica.

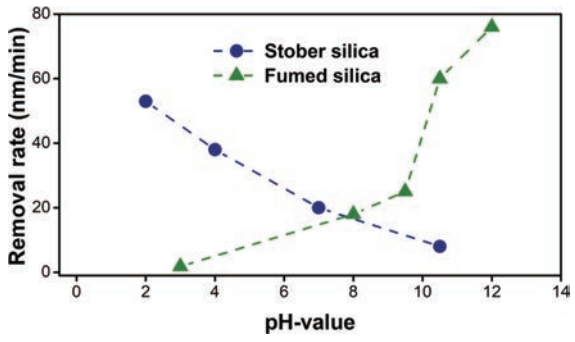


**Fig. 6** $SiO_2$ film removal rate as a function of pH in an abrasive-based slurry according to a silica synthesis method. Reprinted with permission from Ref. (Estel et al., 2010). Copyright: (2010) Springer Nature.

## 4. Modification of silica nanoparticles

Stöber silica is also utilized in metal CMP of tungsten and copper films, in addition to $SiO_2$ films, due to its high acidity and ability to reduce scratches and defects. The slurry in which Stöber silica is dispersed contains chemical additives such as passivation agents, dispersants, inhibitors, and removal-rate enhancers to improve the zeta potential of silica in acidic conditions or increase selectivity and removal rates (Lee et al., 2016). However, predicting and controlling reactions in a slurry system can be challenging, as these additives act simultaneously on the film and abrasive silica nanoparticles. Consequently, ongoing research aims to improve CMP performance by modifying existing silica particles and enhancing their surface properties.

As illustrated in **Fig. 7**, several strategies to improve CMP performance are available for modifying silica. One is to reduce scratches and roughness by coating the surface of silica on a relatively soft core, creating a core–shell structure (**Fig. 7(a)**) (Chen et al., 2015b). Another is to enhance the removal rate by coating a harder shell on the silica core (**Fig. 7(b)**) (Ma et al., 2018). Some particles exhibit improved reactivity by embedding particles with a chemically catalytic effect on the silica surface (**Fig. 7(c)**) (Sun et al., 2022). Other particles have a controlled zeta potential or improved chemical reactivity through the doping of other metals (**Fig. 7(d)**) (Bykov et al., 2021). Finally, the zeta potential of particles can be controlled by substituting surface functional groups or reducing friction force by adjusting the hydrophilicity or hydrophobicity (**Fig. 7(e)**) (Björkegren et al., 2017). These strategies are designed to optimize the properties of silica particles for CMP applications, leading to superior performance in semiconductor manufacturing.

### 4.1 Core–shell structure: silica shell

Films made of copper or $SiO_2$, which are relatively soft, are susceptible to mechanical damage (Paik and Park, 2009). The use of hard and large particles during polishing can increase defect density, surface roughness, and scratches (Guo et al., 2013). To address this issue, composite materials made of polymers and silica are being explored as an alternative to traditional silica nanoparticles. These composites have relatively low hardness, which makes them less likely to cause mechanical damage during polishing. To reduce defects while maintaining removal rates, researchers have been investigating using organic/inorganic core–shell composites (polymers as the core material, with a silica coating on the surface) (Debnath and

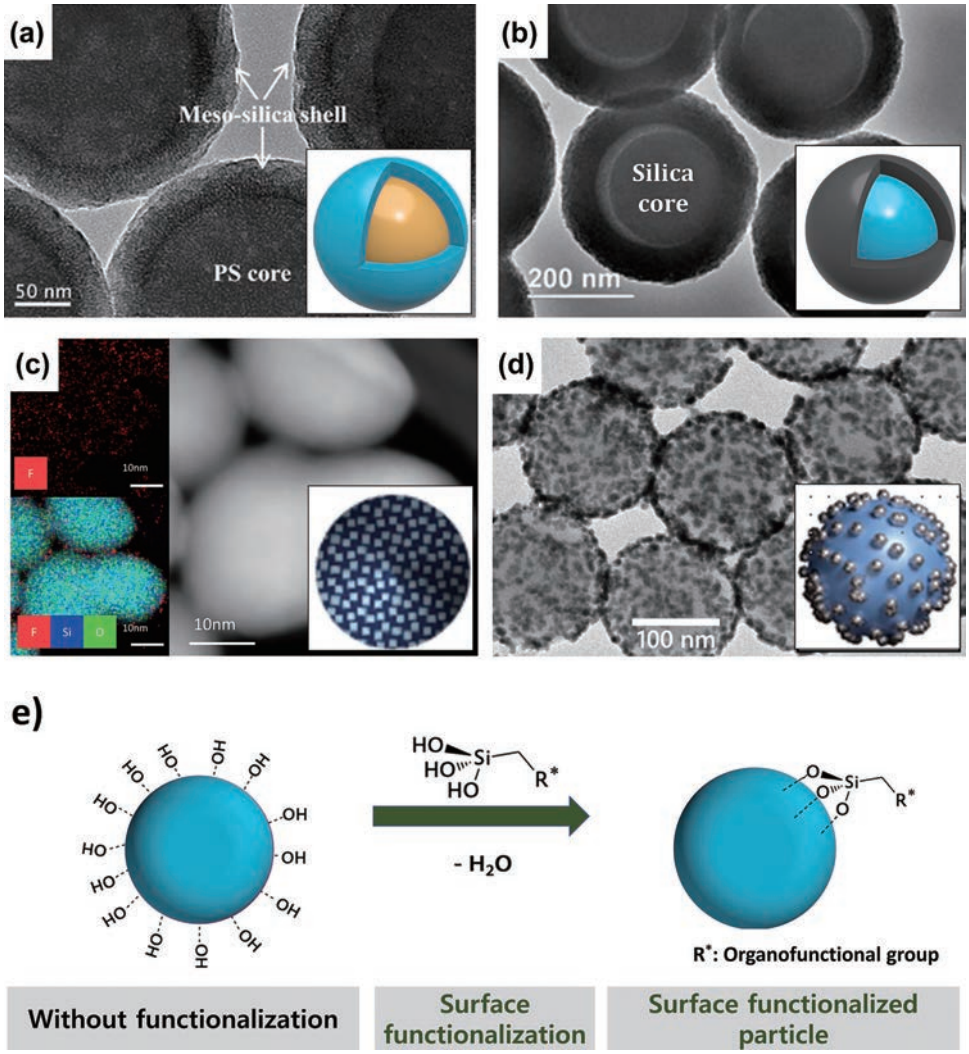


**Fig. 7** Classifying silica abrasive surface modifications to improve CMP properties. **(a)** Core-shell structure of silica shell. Reprinted with permission from Ref. (Chen et al., 2015b). Copyright: (2015) Springer Nature. **(b)** Core-shell structure of silica core. Reprinted with permission from Ref. (Ma et al., 2018). Copyright: (2018) Elsevier. **(c)** Silica doped with other elements. Reprinted permission from Ref. (Sun et al., 2022). Copyright: (2022) Elsevier. **(d)** Silica dot-coated with other materials. Reprinted with permission from Ref. (Bykov et al., 2021) under the terms of the CC-BY 4.0 license. Copyright: (2021) The Authors, published by De Gruyter. **(e)** Surface functional group substituted silica. Reprinted with permission from Ref. (Björkegren et al., 2017). Copyright: (2017) Elsevier.

Khatua, 2011). This approach has shown promise in reducing defects while maintaining the desired level of material removal. Overall, the development of new composite materials for CMP films can improve the efficiency and quality of polishing processes while reducing the risk of damage to the finished materials.

When organic–inorganic composites are used as abrasives in CMP, polystyrene (PS) and PMMA are mainly used as core materials. PS and PMMA offer controllable properties, as they can produce particles of various sizes and shapes depending on the conditions required in CMP (Lee, 2000). Using PS and PMMA is relatively inexpensive, and both are widely available polymeric materials, helping reduce process costs. PS and PMMA are chemically and thermally stable, making them suitable for most process environments, and this stability contributes to high yields and quality in CMP processes. When organic materials such as PS and PMMA are combined with inorganic materials, the interaction between abrasive particles increases, and the flexibility of the organic material improves, resulting in enhanced abrasive effects (Chen et al., 2016).

Chen et al., (2014) experimented with measuring modulus of PS/silica core–shell nanocomposites using AFM. They functionalized the surface of a 450 nm PS particle with azodiisobutyramidine dihydrochloride and allowed it to react with TEOS to coat a 10 nm $SiO_2$ shell. As a result, the Young's modulus of the PS particle, originally 2.85 GPa, increased by a factor of approximately 1.8, to 5.1 GPa, when it became a composite. Considering that the Young's modulus of bulk $SiO_2$ is approximately 70 GPa, the PS/silica composite is clearly a relatively soft abrasive. Zhang et al. (2019) reported that the value of the Young's modulus increased as the thickness of the $SiO_2$ shell increased. When performing CMP on $SiO_2$ films with core–shell

particles, the root mean squared value decreased from 0.48 nm to 0.37 nm compared with silica particles of the same size. This reduction can be attributed to the lower Young's modulus of the nanoparticles compared to that of the silica particles, resulting in a decreased volume indented during CMP and improved contact area.

Chen et al. (2017) compared solid silica and mesoporous silica coatings on PS surfaces. When coating approximately 200 nm PS particles with 30 nm silica shell, the mesoporous silica shell exhibited similar roughness of 0.22 nm and 0.25 nm, respectively, compared with the solid silica shell. The removal rate was 123 nm/min for mesoporous silica shell and 47 nm/min for solid silica shell, which can be explained by the higher contact area offered with mesoporous silica compared to solid silica.

### 4.2 Core-shell structure: silica core

Compared with silica, using silica nanoparticles in CMP for materials with high hardness can be challenging, as an adequate removal rate may be difficult to achieve. However, harder particles also tend to have reduced dispersion stability and can be damaged by scratches (Lei and Zhang, 2007). As a result, researchers have been attempting to create particles with both good dispersion stability and acceptable removal rate by coating a silica core with other materials with greater hardness (Dai et al., 2020; Lei and Zhang, 2007). This approach combine the advantages of both components, resulting in an improved abrasive for CMP applications involving harder materials. **Table 4** summarizes the CMP results for composite particles with different core-shell structures using silica as core material.

Dai et al. (2020) coated SiC on a silica surface and applied a core-shell composite for CMP of a sapphire film with a high Mohs hardness of 9.0. SiC has Mohs hardness of 9 to 9.5, which enhances the mechanical properties of silica. Moreover, silica's high zeta potential under basic conditions gives it superior dispersion stability compared with SiC particles. In their experiments, SiC had a zeta potential of –44.6 mV at pH 10, while the silica-SiC composite had a zeta potential of –68.8 mV. Consequently, the removal rate was approximately double that of silica and 1.8 times that of SiC, and the respective roughness values were 1.9 nm and 1.97 nm for silica and SiC. The core–shell composite achieved a roughness of 1.52 nm.

Lei and Zhang (2007) coated alumina on silica surface to increase the polishing rate and flatness of nickel phosphorus (NiP). Alumina particles had a zeta potential of –40.8 mV, whereas silica–alumina composite achieved greater dispersion stability at –60.1 mV. In this experiment, while the polishing rate was lower for the core-shell composite compared with alumina, the roughness decreased by approximately 33 %.

Ding et al. (2022) employed a silica-diamond composite for $ZrO_2$ CMP. In this case, a core-shell composite using silica as the core had a higher zeta potential compared with a nanodiamond, ranging from –35 mV to –55 mV, leading to improvements in both removal rate and roughness, as confirmed by CMP results.

Although the same silica material was used in other core–shell composites, one study compared solid silica and core–shell particles coated with mesoporous silica on solid silica (Chen et al., 2018). Mesoporous silica has larger contact area than solid silica but mechanically weaker. To enhance the mechanical strength and increase the contact area, core–shell structure was adopted, which resulted in an improved removal rate.

### 4.3 Metal doped silica nanoparticles

Increasing the absolute value of zeta potential of silica can further enhance its dispersion stability. Metal-doped silica modification can maintain the spherical shape of silica while shifting its IEP. Silica is a material in which $Si^{4+}$ ions form covalent bonds with oxygen (Tao et al., 2010). Doping or substituting the $Si^{4+}$ site with metal ions carrying a 3+ charge increases the negative zeta potential of silica and shifts the IEP toward the acidic range, or even gives it a negative charge throughout the entire pH range. This allows for high dispersion stability in the challenging pH 2–3 range of silica's IEP, making it suitable for use in CMP slurries. The conditions for metals used in silica doping require the metal ions to be similar in size to silicon ions and carry a charge lower than 4+.

Doping with $Sm^{3+}$, $Nb^{3+}$, $Al^{3+}$, $Fe^{3+}$, and $Co^{3+}$ ions, which meet these criteria has been reported (Lei et al., 2019; Liu and Lei, 2017; Ma et al., 2015; Sun et al., 2022). Silica doped with these ions maintains smooth surface and has higher zeta potential than un-doped silica, resulting in higher dispersion stability. While it is theoretically possible to dope with ions carrying a charge higher than $Si^{4+}$ to achieve positive charge, there are no reports of this being accomplished. The size of ions carrying 5+ charge is presumably not suitable for silica doping.

In a report on silica doped with $Fe^{3+}$ ions, Sun et al. (2022) clarified the conditions and mechanism for synthesizing doped silica. Silica dissolves as tetrahedral $Si(OH)_4$ in highly alkaline conditions at high temperatures (Niibori et al., 2000). At the same time, metal hydroxides with similar tetrahedral structure can replace vacant $Si(OH)_4$ sites. According to Sun et al. (2022), the synthesis of pH is crucial in this reaction and proceeds under conditions in which $Si(OH)_4$ can dissolve. **Fig. 8** illustrates $Fe^{3+}$ ion doping and coating as a function of pH. At pH 11, the silica surface dissolves as $Si(OH)_4$, and $Fe^{3+}$ exists as $Fe(OH)_4^-$, allowing the doping reaction to proceed. In contrast, at pH 5, $Si(OH)_4$ dissolution rarely occurred, and iron hydroxide coated the silica surface.

Using such reactions, researchers synthesized silica particles with various metal-ion doping and high dispersion

**Table 4** CMP results using core-shell composite abrasive.

| Core | Shell | pH | CMP equipment | CMP pad | Substrate | Removal rate | Roughness | Reference |
|---|---|---|---|---|---|---|---|---|
| Silica | — | 10 | UNIPOL-1502 (Kejing Co. Ltd.) | Polyurethane pad (DOW Chemical) | Sapphire | 0.15 μm/h | Ra: 1.90 nm | (Dai et al., 2020) |
| SiC | — | 10.5 | UNIPOL-1502 (Kejing Co. Ltd.) | Polyurethane pad (DOW Chemical) | Sapphire | 0.17 μm/h | Ra: 1.97 nm | (Dai et al., 2020) |
| SiC | Silica | 10.5 | UNIPOL-1502 (Kejing Co. Ltd.) | Polyurethane pad (DOW Chemical) | Sapphire | 0.31 μm/h | Ra: 1.52 nm | (Dai et al., 2020) |
| Alumina | — | 9–10 | SPEED-FAM-16B-4M (SPEEDFAM Co. Ltd.) | Rodel porous polyurethane pad (DOW Chemical) | NiP | 540 nm/min | Ra: 0.7 nm | (Lei and Zhang, 2007) |
| Alumina | Silica | 9–10 | SPEED-FAM-16B-4M (SPEEDFAM Co. Ltd.) | Rodel porous polyurethane pad (DOW Chemical) | NiP | 440 nm/min | Ra: 0.45 nm | (Lei and Zhang, 2007) |
| Silica | — | 10 | UNIPOL-1000S (Kejing Co. Ltd.) | Rodel porous polyurethane pad (DOW Chemical) | $ZrO_2$ | 0.142 μm/h | Ra: 2.49 nm | (Ding et al., 2022) |
| Nano diamond | — | 10 | UNIPOL-1000S (Kejing Co. Ltd.) | Rodel porous polyurethane pad (DOW Chemical) | $ZrO_2$ | 0.91 μm/h | Ra: 9.92 nm | (Ding et al., 2022) |
| Nano diamond | Silica | 10 | UNIPOL-1000S (Kejing Co. Ltd.) | Rodel porous polyurethane pad (DOW Chemical) | $ZrO_2$ | 1.062 μm/h | Ra: 2.26 nm | (Ding et al., 2022) |
| Silica (solid) | — | 8 | TegraForce-1/ TrgraPol-15 (Struers) | Porous polyurethane pad (MD-Chem) | $SiO_2$ | 137 μm/min | RMS: 0.343 nm | (Chen et al., 2018) |
| Silica (solid) | Mesoporous silica | 8 | TegraForce-1/ TrgraPol-15 (Struers) | Porous polyurethane pad (MD-Chem) | $SiO_2$ | 269 nm/min | RMS: 0.203 nm | (Chen et al., 2018) |

stability. These particles were applied in CMP to achieve higher removal rates and planarity. This method modifies silica properties without significantly altering its mechanical properties.

### 4.4 Metal compound dot-coated silica nanoparticles

Silica nanoparticles are chemically unreactive, and it is unrealistic to expect a catalytic effect from silica alone in CMP (Eppler et al., 2000). However, silica can serve as template for highly reactive catalysts. In other words, by coating the surface of silica particles with highly reactive catalysts, it is possible to synthesize abrasives with catalytic effects and apply them to CMP (Giraldo et al., 2007; Janaun and Ellis, 2011).

Zhang et al. (2017) investigated the use of an $Ag_2O$–silica composite to enhance the removal rate of sapphire CMP. $Ag^+$ in $Ag_2O$ acts as a catalyst to react $Al_2O_3$ with $SiO_2$, forming aluminum silicon oxide ($Al_xSi_yO$). The relatively weak $Al_xSi_yO$ on the sapphire surface can be easily removed by silica abrasive, ensuring a high removal rate in the hard sapphire CMP. Yin et al. applied MgO-doped silica as a more affordable alternative to expensive $Ag_2O$ to improve the removal rate of sapphire CMP. Adding MgO under alkaline conditions causes the Al–O–Al chemical bonds to break more easily, and the formed softening layer is more easily removed from the surface. At the same time, reactions of MgO with the sapphire substrate surface produced $MgAl_2O_4$. The reaction products of $H_2O$, MgO, $SiO_2$, and $Al_2O_3$, such as $Al_2Si_2O_7$–$2H_2O$, $MgAl_2O_4$, and the softening layer of $Al_2SiO_5$, can be easily removed by mechanical action.

Kang et al. (2010) studied silica-containing iron metal for CMP of tungsten. In this process, $H_2O_2$ was added to form $WO_3$ on the tungsten surface. The metal catalyst decomposed $H_2O_2$ through Fenton reaction, generating highly reactive OH radicals. The iron metal on silica surface acted as a catalyst for decomposing $H_2O_2$. Kang et al. reported achieving the same level of CMP performance by comparing two cases: one in which iron ion was added as an

additive, and another where iron metal–silica composite was applied. To address the issue of poor dispersion stability of silica in the acidic region of pH 2, where iron metal-silica is typically applied, Kim et al. (2017) proposed a CuO–silica composite that can be utilized at pH 6. CuO can decompose $H_2O_2$ through Fenton-like reaction, which also occurs in neutral regions. They reported the successful use of silica particles with CuO catalyst.

## 4.5 Functionalization of surfaces on silica nanoparticles

Surface functionalization of silica nanoparticles involves altering the particle surface properties of silica by attaching specific functional groups or molecules. This process is crucial in enhancing the attributes of silica nanoparticles for a range of applications, such as drug delivery, sensors, catalysis, and environmental remediation (Nayl et al., 2022). CMP is often employed to enhance surface charge, control adsorption to passivation agents or films, and manage friction (Seo, 2021).

Silane coupling agents such as organosilanes are commonly used to functionalize silica nanoparticle surfaces (Karnati et al., 2020). These molecules possess a reactive silicon-containing group (e.g., alkoxysilane or chlorosilane)

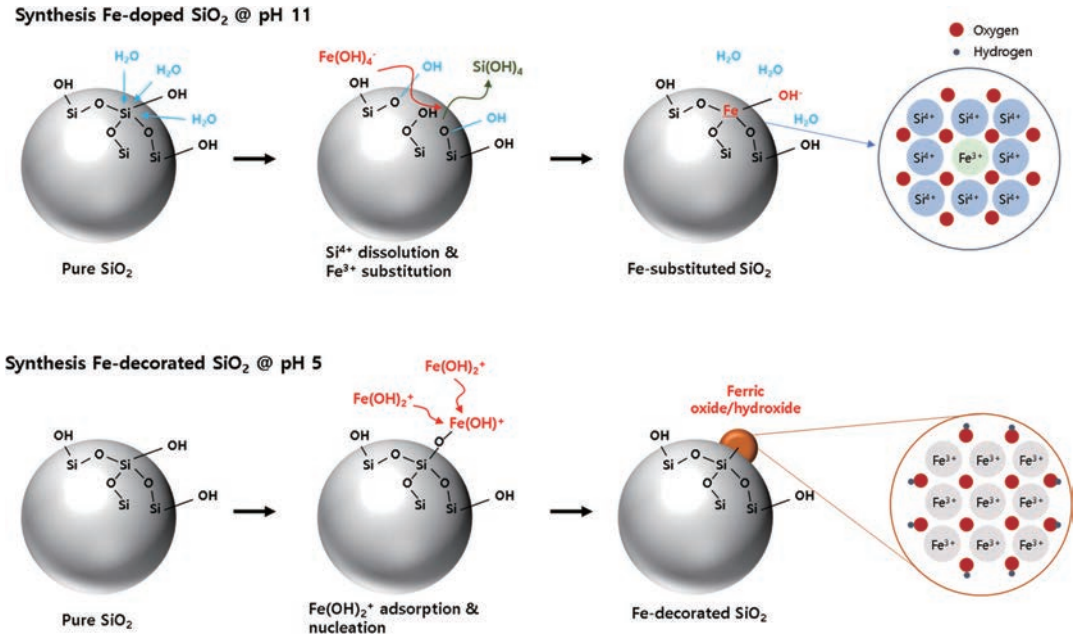


**Fig. 8** Schematic from mechanistic perspective of pH-dependent doping and coating of Fe on silica surfaces. Reprinted with permission from Ref. (Sun et al., 2022). Copyright: (2022) Elsevier B.V.

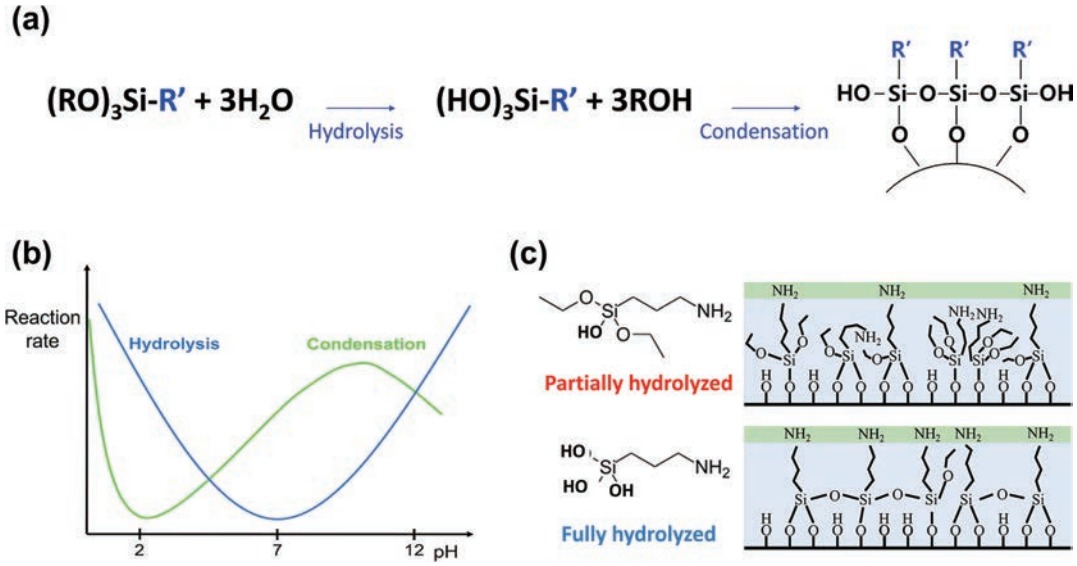


**Fig. 9** **(a)** Reaction mechanism for the surface modification of silica nanoparticles using silane coupling agent. **(b)** Effect of pH on hydrolysis and condensation rates. Reprinted with permission from Ref. (Gutiérrez-Climente et al., 2021). Copyright: (2021) The Royal Society of Chemistry. **(c)** The structure of silica surface functional groups upon partially or fully hydrolyzed organosilane (APTES).

**Table 5** Organosilane coupling agents for improving properties of silica nanoparticles.

| Classification | Chemical name | Molecular structure | Properties | Reference |
|---|---|---|---|---|
| Amino silanes | (N,N-Dimethyl-3-aminopropyl)trimethoxysilane | 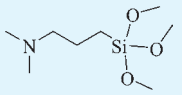 | Increased interaction with surfactants | (Wang et al., 2019) |
| | 3-aminopropylsilane | 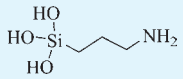 | IEP shift (Increasing positive charge) | (Wang et al., 2019) |
| Epoxy silanes | 3-Glycidoxypropylmethyldimethoxysilane | 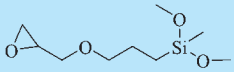 | Improving adhesion to film | (Pan et al., 2016) |
| | 2-(3,4-Epoxycyclohexyl)ethyl]trimethoxysilane | 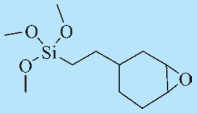 | Improving adhesion to film | (Pan et al., 2016) |
| Acryl silanes | 3-Acetoxypropyltrimethoxysilane | 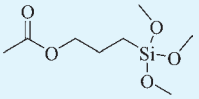 | Supplying electrophilic reaction sites | (Göppert et al., 2023) |
| | 3-Methacryloxypropylmethyldiethoxysilane | 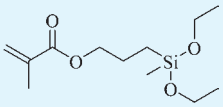 | | (Göppert et al., 2023) |
| Vinyl silanes | Vinyltrimethoxysilane | 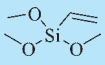 | Supplying nucleophilic reaction sites | (Nasab and Kiasat, 2016) |
| | Triethoxyvinylsilane | 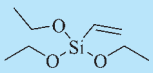 | | (Nasab and Kiasat, 2016) |
| | Vinyl tris(2-methoxyethoxy) silane | 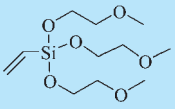 | | (Nasab and Kiasat, 2016) |
| Phenyl silanes | Diphenyldimethoxysilane | 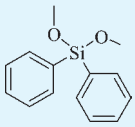 | Increased interaction with surfactants | (Chen et al., 2004) |
| | Phenylmethyldimethoxysilane | 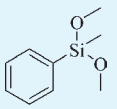 | | (Chen et al., 2004) |
| Alkyl silanes | Isobutyltriethoxysilane | 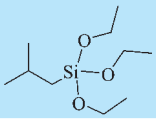 | Improving hydrophobic properties Decreasing friction force | (Wang and Zhang, 2020) |
| | *n*-Hexadecyltrimethoxysilane | 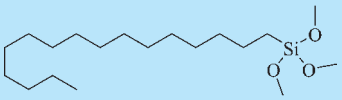 | | (Wang and Zhang, 2020) |
| | Dodecyltrimethoxysilane | 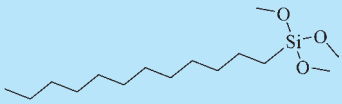 | | (Wang and Zhang, 2020) |
| | Triethoxyoctylsilane | 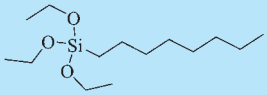 | | (Wang and Zhang, 2020) |

that can bind to the silanol groups present on the silica surface, and an organic functional group (e.g., an amine, thiol, or carboxyl) capable of reacting with other molecules or biomolecules (Franz and Wilson, 2013). By selecting appropriate silane-coupling agent, various functional groups can be introduced onto the silica surface. **Fig. 9(a)** depicts the reaction between organosilane and silanol groups on the surface of silica nanoparticle. Initially, the organosilane reacts with water and undergoes hydrolysis to form hydroxyl groups, and then the functional groups of the organosilane are exposed on the silica surface as the hydroxyl groups condense on the silanol groups on the silica surface (Li et al., 2021).

For successful functionalization, it is crucial to ensure that no particles form due to condensation between organosilanes. **Fig. 9(b)** depicts the rate of hydrolysis and condensation reactions depending on pH (Gutiérrez-Climente et al., 2021; Chiriac et al., 2010). In highly acidic or basic conditions, in which both reaction rates are high, organosilanes react primarily with each other, leading to particle formation (Argekar et al., 2013). However, at a neutral pH of 7, the reaction rate is too slow, resulting in partial hydrolysis (**Fig. 9(c)**), with bridging between methoxy groups. The functionalization reaction is therefore typically carried out in a slightly acidic environment of pH 4–6. **Table 5** categorizes organosilanes and summarizes the properties of silica during functionalization. For complete hydrolysis through functionalization reaction of each organosilane, it is essential to control the concentration of organosilanes and temperature, taking into account the number of silanol groups on the silica nanoparticles.

## 5. Conclusion

Silica nanoparticles are used extensively in CMP, and their performance can be improved through modification techniques such as surface functionalization, core–shell structure formation, coating or doping with other metal atoms. These particles reduce defects and scratches, improve flatness and uniformity, and increase the removal rate and selectivity. The careful selection and utilization of nanoparticles with these properties therefore has significant impact on the efficiency of CMP. This review offers valuable information on how to improve the quality of products and reduce costs in the semiconductor industry. The development of silica nanoparticles is currently an important area of research. Different synthesis methods were applied to CMP slurries and their properties were investigated. Further study of their properties and synthesis methods will be of great help in creating better products in semiconductor industry.

## Acknowledgments

G. Lee, K. Lee and S. Sun. contributed equally to this work. T. Song and U. Paik reviewed and revised the manuscript. This work was supported by the Energy Technology Human Resource Development Project (202300000000101) of the Ministry of Trade, Industry and Energy (KITIE) and the Samsung Electronics University R&D Program (202200000630003). All authors have given approval to the final version of the manuscript.

## Conflict of Interest

The authors declare no conflicts of interest.

## References

Ahn Y., Yoon J.-Y., Baek C.-W., Kim Y.-K., Chemical mechanical polishing by colloidal silica-based slurry for micro-scratch reduction, Wear, 257 (2004) 785–789. https://doi.org/10.1016/j.wear.2004.03.020

Anderson A.M., Carroll M.K., Hydrophobic silica aerogels: review of synthesis, properties and applications, Aerogels Handbook, (2011) 47–77. https://doi.org/10.1007/978-1-4419-7589-8_3

Argekar S.U., Kirley T.L., Schaefer D.W., Determination of structure-property relationships for 3-aminopropyltriethoxysilane films using X-ray reflectivity, Journal of Materials Research, 28 (2013) 1118–1128. https://doi.org/10.1557/jmr.2013.54

Armini S., De Messemaeker J., Whelan C., Moinpour M., Maex K., Composite polymer core–ceria shell abrasive particles during oxide CMP: a defectivity study, Journal of the Electrochemical Society, 155 (2008) H653. https://doi.org/10.1149/1.2949085

Babchin A.J., Schramm L.L., Osmotic repulsion force due to adsorbed surfactants, Colloids and Surfaces B: Biointerfaces, 91 (2012) 137–143. https://doi.org/10.1016/j.colsurfb.2011.10.050

Barthel H., Rösch L., Weis J., Chapter 91, Fumed silica-production, properties, and applications, in: Auner N. and Weis J. (Eds.), Organosilicon Chemistry Set: From Molecules to Materials, ISBN: 9783527292547, 2005, pp. 761–778. https://doi.org/10.1002/9783527619894.ch91

Basim G., Adler J., Mahajan U., Singh R., Moudgil B., Effect of particle size of chemical mechanical polishing slurries for enhanced polishing with minimal defects, Journal of the Electrochemical Society, 147 (2000) 3523. https://doi.org/10.1149/1.1393931

Bebie J., Schoonen M.A., Fuhrmann M., Strongin D.R., Surface charge development on transition metal sulfides: an electrokinetic study, Geochimica et Cosmochimica Acta, 62 (1998) 633–642. https://doi.org/10.1016/s0016-7037(98)00058-1

Bergström L., Hamaker constants of inorganic materials, Advances in Colloid and Interface Science, 70 (1997) 125–169. https://doi.org/10.1016/S0001-8686(97)00003-1

Beyer K., The dynamics of the CMP discovery for device applications in IBM, 2015 International Conference on Planarization/CMP Technology (ICPT), IEEE, (2015). https://doi.org/10.11470/OUBUTSU.90.2_119

Björkegren S., Nordstierna L., Törncrona A., Palmqvist A., Hydrophilic and hydrophobic modifications of colloidal silica particles for Pickering emulsions, Journal of Colloid and Interface Science, 487 (2017) 250–257. https://doi.org/10.1016/j.jcis.2016.10.031

Bykov A.Y., Roth D.J., Sartorello G., Salmón-Gamboa J.U., Zayats A.V., Dynamics of hot carriers in plasmonic heterostructures, Nanophotonics, 10 (2021) 2929–2938. https://doi.org/10.1515/nanoph-2021-0278

Chen A., Chen Y., Zhao X., Wang Y., Core/shell structured PS/m$SiO_2$ hybrid particles: controlled preparation, mechanical property, and their size-dependent CMP performance, Journal of Alloys and Compounds, 779 (2019) 511–520. https://doi.org/10.1016/j.jallcom.2018.11.314

Chen A., Mu W., Chen Y., Compressive elastic moduli and polishing performance of non-rigid core/shell structured PS/$SiO_2$ composite abrasives evaluated by AFM, Applied Surface Science, 290 (2014) 433–439. https://doi.org/10.1016/j.apsusc.2013.11.100

Chen X., Huang Q., Hao W., Ding C., Wang Y., Zeng H., Controlling of fumed silica particle size uniform production process based on

burner fluid dynamic simulation, Industrial & Engineering Chemistry Research, 61 (2022) 7235–7244. https://doi.org/10.1021/acs.iecr.2c00606

Chen Y.-C., Lin H.-C., Lee Y.-D., The effects of phenyltrimethoxysilane coupling agents on the properties of PTFE/silica composites, Journal of Polymer Research, 11 (2004) 1–7. https://doi.org/10.1023/B:JPOL.0000021757.94577.a3

Chen Y., Chen A., Qin J., Polystyrene core–silica shell composite particles: effect of mesoporous shell structures on oxide CMP and mechanical stability, RSC Advances, 7 (2017) 6548–6558. https://doi.org/10.1039/c6ra26437a

Chen Y., Li Z., Qian C., Core–shell structured polystyrene coated silica composite abrasives with homogeneous shells: the effects of polishing pressure and particle size on oxide-CMP, Precision Engineering, 43 (2016) 71–77. https://doi.org/10.1016/j.precisioneng.2015.06.011

Chen Y., Qian C., Miao N., Atomic force microscopy indentation to determine mechanical property for polystyrene–silica core–shell hybrid particles with controlled shell thickness, Thin Solid Films, 579 (2015a) 57–63. https://doi.org/10.1016/j.tsf.2015.02.049

Chen Y., Qin J., Wang Y., Li Z., Core/shell composites with polystyrene cores and meso-silica shells as abrasives for improved chemical mechanical polishing behavior, Journal of Nanoparticle Research, 17 (2015b) 1–11. https://doi.org/10.1007/s11051-015-3172-5

Chen Y., Zuo C., Chen A., Core/shell structured $sSiO_2$/$mSiO_2$ composite particles: the effect of the core size on oxide chemical mechanical polishing, Advanced Powder Technology, 29 (2018) 18–26. https://doi.org/10.1016/j.apt.2017.09.020

Chiriac A.P., Neamtu I., Nita L.E., Nistor M.T., Sol gel method performed for biomedical products implementation, Mini Reviews in Medicinal Chemistry, 10 (2010) 990–1013. https://doi.org/10.2174/1389557511009010990

Choi W., Mahajan U., Lee S.-M., Abiade J., Singh R.K., Effect of slurry ionic salts at dielectric silica CMP, Journal of the Electrochemical Society, 151 (2004) G185. https://doi.org/10.1149/1.1644609

Costa C.A., Leite C.A., Galembeck F., Size dependence of Stöber silica nanoparticle microchemistry, The Journal of Physical Chemistry B, 107 (2003) 4747–4755. https://doi.org/10.1021/jp027525t

Croissant J.G., Butler K.S., Zink J.I., Brinker C.J., Synthetic amorphous silica nanoparticles: toxicity, biomedical and environmental implications, Nature Reviews Materials, 5 (2020) 886–909. https://doi.org/10.1038/s41578-020-0230-0

Dai S., Lei H., Fu J., Preparation of SiC/$SiO_2$ hard core–soft shell abrasive and its CMP behavior on sapphire substrate, Journal of Electronic Materials, 49 (2020) 1301–1307. https://doi.org/10.1007/s11664-019-07683-9

De Keizer A., Van der Ent E., Koopal L., Surface and volume charge densities of monodisperse porous silicas, Colloids and Surfaces A: Physicochemical and Engineering Aspects, 142 (1998) 303–313. https://doi.org/10.1016/s0927-7757(98)00268-4

Debnath D., Khatua B., Preparation by suspension polymerization and characterization of polystyrene (PS)-poly (methyl methacrylate) (PMMA) core-shell nanocomposites, Macromolecular Research, 19 (2011) 519–527. https://doi.org/10.1007/s13233-011-0607-4

Ding R., Lei H., Chen C., Zhang Z., Preparation of the nanodiamond@$SiO_2$ abrasive and its effect on the polishing performance of zirconia ceramics, ECS Journal of Solid State Science and Technology, 11 (2022) 064002. https://doi.org/10.1149/2162-8777/ac757e

Dorobantu L.S., Bhattacharjee S., Foght J.M., Gray M.R., Analysis of force interactions between AFM tips and hydrophobic bacteria using DLVO theory, Langmuir, 25 (2009) 6968–6976. https://doi.org/10.1021/la9001237

Ein-Eli Y., Starosvetsky D., Review on copper chemical–mechanical polishing (CMP) and post-CMP cleaning in ultra large system integrated (ULSI)—An electrochemical perspective, Electrochimica Acta, 52 (2007) 1825–1838. https://doi.org/10.1016/j.electacta.2006.07.039

Eppler A.S., Rupprechter G., Anderson E.A., Somorjai G.A., Thermal and chemical stability and adhesion strength of Pt nanoparticle arrays supported on silica studied by transmission electron microscopy and atomic force microscopy, The Journal of Physical Chemistry B, 104 (2000) 7286–7292. https://doi.org/10.1021/jp0006429

Estel K., Künzelmann U., Bartha J.W., Meyer E.P., Barthel H., Influence of ionic strength and pH-value on the silicon dioxide polishing behaviour of slurries based on pure silica suspensions, MRS Online Proceedings Library, 1249 (2010) 402. https://doi.org/10.1557/proc-1249-e04-02

Feng X., Sayle D.C., Wang Z.L., Paras M.S., Santora B., Sutorik A.C., Sayle T.X., Yang Y., Ding Y., Wang X., Converting ceria polyhedral nanoparticles into single-crystal nanospheres, Science, 312 (2006) 1504–1508. https://doi.org/10.1002/chin.200636200

Fernandes R.S., Raimundo Jr I.M., Pimentel M.F., Revising the synthesis of Stöber silica nanoparticles: a multivariate assessment study on the effects of reaction parameters on the particle size, Colloids and Surfaces A: Physicochemical and Engineering Aspects, 577 (2019) 1–7. https://doi.org/10.1016/j.colsurfa.2019.05.053

Franz A.K., Wilson S.O., Organosilicon molecules with medicinal applications, Journal of Medicinal Chemistry, 56 (2013) 388–405. https://doi.org/10.1021/jm3010114

Fury M.A., The early days of CMP, Solid State Technology, 40 (1997) 81–84.

Garrett P.R., Defoaming: Theory and Industrial Applications, 1st edition, CRC Press, 2017, ISBN: 9780367402617. https://doi.org/10.1201/9781315140827

Ghimire P.P., Jaroniec M., Renaissance of Stöber method for synthesis of colloidal particles: new developments and opportunities, Journal of Colloid and Interface Science, 584 (2021) 838–865. https://doi.org/10.1016/j.jcis.2020.10.014

Giraldo L.F., López B.L., Pérez L., Urrego S., Sierra L., Mesa M., Mesoporous silica applications, Macromolecular Symposia, 258 (2007) 129–141. https://doi.org/10.1002/masy.200751215

Göppert A.-K., Gonzalez-Rubio G., Schnitzlein S., Cölfen H., A nanoparticle-based model system for the study of heterogeneous nucleation phenomena, Langmuir, 39 (2023) 3580–3588. https://doi.org/10.1021/acs.langmuir.2c03034

Green D., Lin J., Lam Y.-F., Hu M.-C., Schaefer D.W., Harris M., Size, volume fraction, and nucleation of Stober silica nanoparticles, Journal of Colloid and Interface Science, 266 (2003) 346–358. https://doi.org/10.1016/s0021-9797(03)00610-6

Guedes M., Ferreira J.M., Ferro A.C., A study on the aqueous dispersion mechanism of CuO powders using Tiron, Journal of Colloid and Interface Science, 330 (2009) 119–124. https://doi.org/10.1016/j.jcis.2008.10.057

Gun'ko V., Zarko V., Leboda R., Voronin E., Chibowski E., Pakhlov E., Influence of modification of fine silica by organosilicon compounds on particle-particle interaction in aqueous suspensions, Colloids and Surfaces A: Physicochemical and Engineering Aspects, 132 (1998) 241–249. https://doi.org/10.1016/s0927-7757(97)00184-2

Guo D., Xie G., Luo J., Mechanical properties of nanoparticles: basics and applications, Journal of Physics D: Applied Physics, 47 (2013) 013001. https://doi.org/10.1088/0022-3727/47/1/013001

Gutiérrez-Climente R., Clavié M., Dumy P., Mehdi A., Subra G., Sol–gel process: the inorganic approach in protein imprinting, Journal of Materials Chemistry B, 9 (2021) 2155–2178. https://doi.org/10.1039/d0tb02941f

Haba S., Fukuda K., Ohta Y., Koubuchi Y., Katouda T., Fumed silica slurry stabilizing methods for chemical mechanical polishing, Japanese Journal of Applied Physics, 42 (2003) 418. https://doi.org/10.1143/jjap.42.418

Hamaker H.C., The London—van der Waals attraction between spherical particles, Physica, 4 (1937) 1058–1072. https://doi.org/10.1016/S0031-8914(37)80203-7

Hayashi Y., Sakurai M., Nakajima T., Hayashi K., Sasaki S., Chikaki S.-i., Kunio T.K.T., Ammonium-salt-added silica slurry for the chemical mechanical polishing of the interlayer dielectric film planarization in ULSI's, Japanese Journal of Applied Physics, 34 (1995) 1037. https://doi.org/10.1143/jjap.34.1037

Hwang H.-S., Kang H.-G., Park J.-H., Paik U., Park H.-S., Park J.-G., Effect of alkaline agent with organic additive in colloidal silica slurry on polishing rate selectivity of polysilicon-to-$SiO_2$ in polysilicon CMP, ECS Transactions, 13 (2008) 67. https://doi.org/10.1149/ma2008-01/17/692

Hyde E.D., Seyfaee A., Neville F., Moreno-Atanasio R., Colloidal silica particle synthesis and future industrial manufacturing pathways: a review, Industrial & Engineering Chemistry Research, 55 (2016) 8891–8913. https://doi.org/10.1021/acs.iecr.6b01839

Ibrahim I.A., Zikry A., Sharaf M.A., Preparation of spherical silica nanoparticles: Stober silica, Journal of American Science, 6 (2010) 985–989. <https://picture.iczhiku.com/resource/paper/WYkdoklpfJzOtCvn.pdf> accessed 08.11.2023.

Ishida N., Craig V., Direct measurement of interaction forces between surfaces in liquids using atomic force microscopy, KONA Powder and Particle Journal, 36 (2019) 187–200. https://doi.org/10.14356/kona.2019013

Janaun J., Ellis N., Role of silica template in the preparation of sulfonated mesoporous carbon catalysts, Applied Catalysis A: General, 394 (2011) 25–31. https://doi.org/10.1016/j.apcata.2010.12.016

Jin Y., Song K., Gellermann N., Huang Y., Printing of hydrophobic materials in fumed silica nanoparticle suspension, ACS Applied Materials & Interfaces, 11 (2019) 29207–29217. https://doi.org/10.1021/acsami.9b07433

Kang Y.-J., Prasad Y.N., Kim I.-K., Jung S.-J., Park J.-G., Synthesis of Fe metal precipitated colloidal silica and its application to W chemical mechanical polishing (CMP) slurry, Journal of Colloid and Interface Science, 349 (2010) 402–407. https://doi.org/10.1016/j.jcis.2010.04.083

Kanungo S.B., Physicochemical properties of $MnO_2$ and $MnO_2$ CuO and their relationship with the catalytic activity for $H_2O_2$ decomposition and CO oxidation, Journal of Catalysis, 58 (1979) 419–435. https://doi.org/10.1016/0021-9517(79)90280-x

Kappl M., Butt H.J., The colloidal probe technique and its application to adhesion force measurements, Particle & Particle Systems Characterization, 19 (2002) 129–143. https://doi.org/10.1002/1521-4117(200207)19:3<129::AID-PPSC129>3.0.CO;2-G

Karnati S.R., Oldham D., Fini E.H., Zhang L., Application of surface-modified silica nanoparticles with dual silane coupling agents in bitumen for performance enhancement, Construction and Building Materials, 244 (2020) 118324. https://doi.org/10.1016/j.conbuildmat.2020.118324

Kawaguchi M., Dispersion stability and rheological properties of silica suspensions in aqueous solutions, Advances in Colloid and Interface Science, 284 (2020) 102248. https://doi.org/10.1016/j.cis.2020.102248

Khan S.A., Günther A., Schmidt M.A., Jensen K.F., Microfluidic synthesis of colloidal silica, Langmuir, 20 (2004) 8604–8611. https://doi.org/10.1002/adma.200700127

Khavryutchenko V., Barthel H., Nikitina E., Fumed silica synthesis: from molecules, protoparticles and primary particles to aggregates and agglomerates, Macromolecular Symposia, 169 (2001) 7–18. https://doiorg/10.1002/1521-3900(200105)169:1<7::AID-MASY7>3.0.CO;2-5

Kim E., Lee J., Park Y., Shin C., Yang J., Kim T., Shape classification of fumed silica abrasive and its effects on chemical mechanical polishing, Powder Technology, 381 (2021) 451–458. https://doi.org/10.1016/j.powtec.2020.11.058

Kim K., Yi D.K., Paik U., CuO embedded silica nanoparticles for tungsten oxidation via a heterogeneous Fenton-like reaction, Microelectronic Engineering, 183 (2017) 58–63. https://doi.org/10.1016/j.mee.2017.10.004

Kosmulski M., Compilation of PZC and IEP of sparingly soluble metal oxides and hydroxides from literature, Advances in Colloid and Interface Science, 152 (2009) 14–25. https://doi.org/10.1016/j.cis.2009.08.003

Krishnan M., Nalaskowski J.W., Cook L.M., Chemical mechanical planarization: slurry chemistry, materials, and mechanisms, Chemical Reviews, 110 (2010) 178–204. https://doi.org/10.1021/cr900170z

Kwon T.-Y., Ramachandran M., Park J.-G., Scratch formation and its mechanism in chemical mechanical planarization (CMP), Friction, 1 (2013) 279–305. https://doi.org/10.1007/s40544-013-0026-y

Lee C.F., The properties of core–shell composite polymer latex.: effect of heating on the morphology and physical properties of PMMA/PS core–shell composite latex and the polymer blends, Polymer, 41 (2000) 1337–1344. https://doi.org/10.1016/s0032-3861(99)00281-5

Lee D., Lee H., Jeong H., Slurry components in metal chemical mechanical planarization (CMP) process: a review, International Journal of Precision Engineering and Manufacturing, 17 (2016) 1751–1762. https://doi.org/10.1007/s12541-016-0201-y

Lee H., Kim M., Jeong H., Effect of non-spherical colloidal silica particles on removal rate in oxide CMP, International Journal of Precision Engineering and Manufacturing, 16 (2015) 2611–2616. https://doi.org/10.1007/s12541-015-0334-4

Lee K., Seo J., Paik U., 12 - Preparation and characterization of slurry for CMP, in: Babu S. (Ed.) Advances in Chemical Mechanical Planarization (CMP) (Second Edition), Woodhead Publishing, 2022, pp. 323–354, ISBN: 978-0-12-821791-7. https://doi.org/10.1016/B978-0-12-821791-7.00005-8

Lei H., Jiang L., Chen R., Preparation of copper-incorporated mesoporous alumina abrasive and its CMP behavior on hard disk substrate, Powder Technology, 219 (2012) 99–104. https://doi.org/10.1016/j.powtec.2011.12.022

Lei H., Liu T., Xu L., Synthesis of Sm-doped colloidal $SiO_2$ composite abrasives and their chemical mechanical polishing performances on sapphire substrates, Materials Chemistry and Physics, 237 (2019) 121819. https://doi.org/10.1016/j.matchemphys.2019.121819

Lei H., Zhang P., Preparation of alumina/silica core-shell abrasives and their CMP behavior, Applied Surface Science, 253 (2007) 8754–8761. https://doi.org/10.1016/j.apsusc.2007.04.079

Li H., Chen X., Shen D., Wu F., Pleixats R., Pan J., Functionalized silica nanoparticles: classification, synthetic approaches and recent advances in adsorption applications, Nanoscale, 13 (2021) 15998–16016. https://doi.org/10.1039/d1nr04048k

Li S., Gaudet G., Sun F., Naman A., ILD CMP with silica abrasive particles: interfacial removal kinetics and effect of pad surface textures, Journal of the Electrochemical Society, 157 (2010) H1061. https://doi.org/10.1149/1.3486806

Lim J.-H., Park J.-H., Park J.-G., Effect of iron(III) nitrate concentration on tungsten chemical-mechanical-planarization performance, Applied Surface Science, 282 (2013) 512–517. https://doi.org/10.1016/j.apsusc.2013.06.003

Liu C.C., Maciel G.E., The fumed silica surface: a study by NMR, Journal of the American Chemical Society, 118 (1996) 5103–5119. https://doi.org/10.1021/ja954120w

Liu T., Lei H., Nd3+-doped colloidal $SiO_2$ composite abrasives: synthesis and the effects on chemical mechanical polishing (CMP) performances of sapphire wafers, Applied Surface Science, 413 (2017) 16–26. https://doi.org/10.1016/j.apsusc.2017.03.270

Lu Y.-W., Shie B., Hsiao S., Yang H., Lee S., CMP filter characterization with leading slurry particles, ICPT 2013, Taiwan, (2013), <https://www.entegris.com/content/dam/product-assets/planargardnmbfilter/appnote-cmp-slurry-particles-7561.pdf> accessed 08.11.2023.

Lunardi C.N., Gomes A.J., Rocha F.S., De Tommaso J., Patience G.S., Experimental methods in chemical engineering: zeta potential, The Canadian Journal of Chemical Engineering, 99 (2021) 627–639. https://doi.org/10.1002/cjce.23914

Luo J., Dornfeld D.A., Effects of abrasive size distribution in chemical mechanical planarization: modeling and verification, IEEE Transactions on Semiconductor Manufacturing, 16 (2003) 469–476. https://doi.org/10.1109/tsm.2003.815199

Ma J., Guo X., Ge H., Tian G., Zhang Q., Seed-mediated photodeposition route to Ag-decorated $SiO_2$@ $TiO_2$ microspheres with ideal core-shell structure and enhanced photocatalytic activity, Applied Surface Science, 434 (2018) 1007–1014. https://doi.org/10.1016/j.apsusc.2017.11.020

Ma P., Lei H., Chen R., Preparation of cobalt-doped colloidal silica abrasives and their chemical mechanical polishing performances on sapphire, Micro & Nano Letters, 10 (2015) 657–661. https://doi.org/10.1049/mnl.2015.0292

Margenau H., Van der waals forces, Reviews of Modern Physics, 11 (1939) 1–35. https://doi.org/10.1103/revmodphys.11.1

Meled A., Optimization of Polishing Kinematics and Consumables during Chemical Mechanical Planarization Processes, doctoral dissertation, The University of Arizona, 2011, http://hdl.handle.net/10150/145385

Mikhaylichenko K., Post CMP cleans evolution and defect improvement approaches, Business of Cleans / SPCC Conference, 2018, <https://www.linx-consulting.com/wp-content/uploads/2018/04/Post-CMP-Cleans-Evolution-and-Defect-Improvement-Approaches-SPCC-2018-presented.pdf> accessed 08.11.2023.

Moore T.L., Rodriguez-Lorenzo L., Hirsch V., Balog S., Urban D., Jud C., Rothen-Rutishauser B., Lattuada M., Petri-Fink A., Nanoparticle colloidal stability in cell culture media and impact on cellular interactions, Chemical Society Reviews, 44 (2015) 6287–6305. https://doi.org/10.1039/C4CS00487F

Mu W., Fu M., Synthesis of non-rigid core–shell structured PS/$SiO_2$ composite abrasives and their oxide CMP performance, Microelectronic Engineering, 96 (2012) 51–55. https://doi.org/10.1016/j.mee.2012.02.047

Nasab M.J., Kiasat A.R., Multifunctional $Fe_3O_4$@ *n*$SiO_2$@ *m*$SiO_2$/Pr-Imi-$NH_2$·Ag core–shell microspheres as highly efficient catalysts in the aqueous reduction of nitroarenes: improved catalytic activity and facile catalyst recovery, RSC Advances, 6 (2016) 41871–41877. https://doi.org/10.1039/C6RA00120C

Nayl A., Abd-Elhamid A., Aly A.A., Bräse S., Recent progress in the applications of silica-based nanoparticles, RSC Advances, 12 (2022) 13706–13726. https://doi.org/10.1039/d2ra01587k

Niibori Y., Kunita M., Tochiyama O., Chida T., Dissolution rates of amorphous silica in highly alkaline solution, Journal of Nuclear Science and Technology, 37 (2000) 349–357. https://doi.org/10.1080/18811248.2000.9714905

Ninham B.W., On progress in forces since the DLVO theory, Advances in Colloid and Interface Science, 83 (1999) 1–17. https://doi.org/10.1016/s0001-8686(99)00008-1

Nowatzki P.J., Franck C., Maskarinec S.A., Ravichandran G., Tirrell D.A., Mechanically tunable thin films of photosensitive artificial proteins: preparation and characterization by nanoindentation, Macromolecules, 41 (2008) 1839–1845. https://doi.org/10.1021/ma071717a

Paik U., Park J.-G., Nanoparticle engineering for chemical-mechanical planarization: fabrication of next-generation nanodevices, Taylor & Francis, 2009, ISBN: 1420059114. https://doi.org/10.1201/9780429291890

Pan K., Zeng X., Li H., Lai X., Synthesis of silane oligomers containing vinyl and epoxy group for improving the adhesion of addition-cure silicone encapsulant, Journal of Adhesion Science and Technology, 30 (2016) 1131–1142. https://doi.org/10.1080/01694243.2016.1142806

Parker J., Next-generation abrasive particles for CMP, Solid State Technology, 47 (2004) 30–32.

Passeri D., Alippi A., Bettucci A., Rossi M., Tamburri E., Terranova M., Indentation modulus and hardness of polyaniline thin films by atomic force microscopy, Synthetic Metals, 161 (2011) 7–12. https://doi.org/10.1016/j.synthmet.2010.10.027

Plumeré N., Ruff A., Speiser B., Feldmann V., Mayer H.A., Stöber silica particles as basis for redox modifications: particle shape, size, polydispersity, and porosity, Journal of Colloid and Interface Science, 368 (2012) 208–219. https://doi.org/10.1016/j.jcis.2011.10.070

Ralston J., Larson I., Rutland M.W., Feiler A.A., Kleijn M., Atomic force microscopy and direct surface force measurements (IUPAC Technical Report), Pure and Applied Chemistry, 77 (2005) 2149–2170. https://doi.org/10.1515/iupac.77.0089

Saka N., Eusner T., Chun J.-H., Nano-scale scratching in chemical–mechanical polishing, CIRP Annals, 57 (2008) 341–344. https://doi.org/10.1016/j.cirp.2008.03.098

Sedev R., Exerowa D., DLVO and non-DLVO surface forces in foam films from amphiphilic block copolymers, Advances in Colloid and Interface Science, 83 (1999) 111–136. https://doi.org/10.1016/s0001-8686(99)00007-x

Seipenbusch M., Rothenbacher S., Kirchhoff M., Schmid H.-J., Kasper G., Weber A., Interparticle forces in silica nanoparticle agglomerates, Journal of Nanoparticle Research, 12 (2010) 2037–2044. https://doi.org/10.1007/s11051-009-9760-5

Selvarajan V., Obuobi S., Ee P., Silica nanoparticles—a versatile tool for the treatment of bacterial infections, Frontiers in Chemistry, 8 (2020) 602. https://doi.org/10.3389/fchem.2020.00602

Seo J., A review on chemical and mechanical phenomena at the wafer interface during chemical mechanical planarization, Journal of Materials Research, 36 (2021) 235–257. https://doi.org/10.1557/s43578-020-00060-x

Seo J., Kim J.H., Lee M., Moon J., Yi D.K., Paik U., Size-dependent interactions of silica nanoparticles with a flat silica surface, Journal of Colloid and Interface Science, 483 (2016a) 177–184. https://doi.org/10.1016/j.jcis.2016.08.041

Seo J., Moon J., Kim K., Kim Y., Kim S., Paik U., Role of surface chemistry of ceria nanoparticles in CMP, ECS Meeting Abstracts, MA2014-01 (2014) 1425. https://doi.org/10.1149/MA2014-01/38/1425

Seo J., Moon J., Kim Y., Kim K., Lee K., Cho Y., Lee D.-H., Paik U., Communication—synergistic effect of mixed particle size on W CMP process: optimization using experimental design, ECS Journal of Solid State Science and Technology, 6 (2016b) P42. https://doi.org/10.1149/2.0171701jss

Serrano-Lotina A., Portela R., Baeza P., Alcolea-Rodriguez V., Villarroel M., Ávila P., Zeta potential as a tool for functional materials development, Catalysis Today, 423 (2023) 113862. https://doi.org/10.1016/j.cattod.2022.08.004

Shin C., Choi J., Kwak D., Kim J., Yang J., Chae S.-k., Kim T., Evaluation of size distribution measurement methods for sub-100 nm colloidal silica nanoparticles and its application to CMP Slurry, ECS Journal of Solid State Science and Technology, 8 (2019) P3195. https://doi.org/10.1149/2.0261905jss

Shluger A., Rohl A., Gay D., Williams R., Atomistic theory of the interaction between AFM tips and ionic surfaces, Journal of Physics: Condensed Matter, 6 (1994) 1825. https://doi.org/10.1007/978-94-011-0049-6_17

Soh S.-Y., Han K.-D., Won H.-Y., Chun Y.-J., Lee B.-J., Yang H.-S., Tetramethyl orthosilicate (TMOS) synthesis by the copper-catalyzed reaction of the metallic silicon with methanol (i)-effect of the manufacturing condition and the composition of contact mass on TMOS synthesis, Applied Chemistry for Engineering, 10 (1999) 252–258.

Song J., Tranchida D., Vancso G.J., Contact mechanics of UV/ozone-treated PDMS by AFM and JKR testing: mechanical performance from nano-to micrometer length scales, Macromolecules, 41 (2008) 6757–6762. https://doi.org/10.1021/ma800536y

Srinivasan R., Dandu P.V., Babu S., Shallow trench isolation chemical mechanical planarization: a review, ECS Journal of Solid State Science and Technology, 4 (2015) P5029. https://doi.org/10.1149/2.0071511jss

Srinivasan S., Datye A., Smith M., Peden C.H., Interaction of titanium isopropoxide with surface hydroxyls on silica, Journal of Catalysis, 145 (1994) 565–573. https://doi.org/10.1006/jcat.1994.1068

Stöber W., Fink A., Bohn E., Controlled growth of monodisperse silica spheres in the micron size range, Journal of Colloid and Interface Science, 26 (1968) 62–69. https://doi.org/10.1016/0021-9797(68)90272-5

Sui T., Song B., Wen Y.-h., Zhang F., Bifunctional hairy silica nanoparticles as high-performance additives for lubricant, Scientific Reports, 6 (2016) 22696. https://doi.org/10.1038/srep22696

Sun S., Lee K., Lee G., Kim Y., Kim S., Hwang J., Kong H., Chung K.Y., Ali G., Song T., Fe-substituted silica via lattice dissolution–reprecipitation replacement for tungsten chemical mechanical planarization, Journal of Industrial and Engineering Chemistry, 111 (2022) 219–225. https://doi.org/10.1016/j.jiec.2022.04.001

Szekeres M., Kamalin O., Schoonheydt R.A., Wostyn K., Clays K., Persoons A., Dékány I., Ordering and optical properties of monolayers and multilayers of silica spheres deposited by the Langmuir–Blodgett method, Journal of Materials Chemistry, 12 (2002) 3268–3274. https://doi.org/10.1039/b204687c

Tamboli D., Seal S., Desai V., Maury A., Studies on passivation behavior of tungsten in application to chemical mechanical polishing, Journal of Vacuum Science & Technology A: Vacuum, Surfaces, and Films, 17 (1999) 1168–1173. https://doi.org/10.1116/1.581790

Tao C., Li J., Zhang Y., Liew K.Y., Effect of isomorphic substitution of zirconium on mesoporous silica as support for cobalt Fischer–

Tropsch synthesis catalysts, Journal of Molecular Catalysis A: Chemical, 331 (2010) 50–57. https://doi.org/10.1016/j.molcata.2010.08.002
Tolias P., Lifshitz calculations of Hamaker constants for fusion relevant materials, Fusion Engineering and Design, 133 (2018) 110–116. https://doi.org/10.1016/j.fusengdes.2018.06.002
van Oss C.J., Chapter three - the extended DLVO theory, in: van Oss C.J. (Ed.) Interface Science and Technology, Vol. 16: The Properties of Water and their Role in Colloidal and Biological Systems, Elsevier, ISBN: 9780123743039, 2008, pp. 31–48. https://doi.org/10.1016/S1573-4285(08)00203-2
Wang C.-X., Zhang X.-F., A non-particle and fluorine-free superhydrophobic surface based on one-step electrodeposition of dodecyltrimethoxysilane on mild steel for corrosion protection, Corrosion Science, 163 (2020) 108284. https://doi.org/10.1016/j.corsci.2019.108284
Wang F., Pi J., Li J.-Y., Song F., Feng R., Wang X.-L., Wang Y.-Z., Highly-efficient separation of oil and water enabled by a silica nanoparticle coating with pH-triggered tunable surface wettability, Journal of Colloid and Interface Science, 557 (2019) 65–75. https://doi.org/10.1016/j.jcis.2019.08.114
Wang J., Wang T., Pan G., Lu X., Effect of photocatalytic oxidation technology on GaN CMP, Applied Surface Science, 361 (2016) 18–24. https://doi.org/10.1016/j.apsusc.2015.11.062
Wang W., Zhang B., Shi Y., Ma T., Zhou J., Wang R., Wang H., Zeng N., Improvement in chemical mechanical polishing of 4H-SiC wafer by activating persulfate through the synergistic effect of UV and $TiO_2$, Journal of Materials Processing Technology, 295 (2021) 117150. https://doi.org/10.1016/j.jmatprotec.2021.117150
Wang W., Zhang B., Shi Y., Zhou D., Wang R., Improvement in dispersion stability of alumina suspensions and corresponding chemical mechanical polishing performance, Applied Surface Science, 597 (2022) 153703. https://doi.org/10.1016/j.apsusc.2022.153703
Wells J., Koopal L., de Keizer A.d., Monodisperse, nonporous, spherical silica particles, Colloids and Surfaces A: Physicochemical and Engineering Aspects, 166 (2000) 171–176. https://doi.org/10.1016/s0927-7757(99)00462-8
Xu B., Dong L., Chen Y., Influence of CuO loading on dispersion and reduction behavior of $CuO/TiO_2$ (anatase) system, Journal of the Chemical Society, Faraday Transactions, 94 (1998) 1905–1909. https://doi.org/10.1039/a801603h
Xu D., Cheng F., Lu Q., Dai P., Microwave enhanced catalytic degradation of methyl orange in aqueous solution over $CuO/CeO_2$ catalyst in the absence and presence of $H_2O_2$, Industrial & Engineering Chemistry Research, 53 (2014) 2625–2632. https://doi.org/10.1021/ie4033022
Zhang B., Lei H., Chen Y., Preparation of $Ag_2O$ modified silica abrasives and their chemical mechanical polishing performances on sapphire, Friction, 5 (2017) 429–436. https://doi.org/10.1007/s40544-017-0156-8
Zhang X., Pan G., Wang W., Guo D., Polishing behavior of $PS/SiO_2$ Core-Shell nanoparticles with different shell thickness on fused silica Chemical Mechanical Polishing, IOP Conference Series: Materials Science and Engineering, 563 (2019) 022048. https://doi.org/10.1088/1757-899X/563/2/022048
Zwicker G., 19 - Applications of chemical mechanical planarization (CMP) to More than Moore devices, in: Babu S. (Ed.), Advances in Chemical Mechanical Planarization (CMP) (Second Edition), Woodhead Publishing, ISBN: 9780128217917, 2022, pp. 533–557. https://doi.org/10.1016/B978-0-12-821791-7.00001-0

## Authors' Short Biographies

**Ganggyu Lee** received his B.S. degree from the Department of Energy Engineering at Hanyang University, South Korea, in 2020. He is currently a Ph.D. candidate in Prof. Ungyu Paik's Nano Device Process Laboratory (NDPL) group at Hanyang University. His research interest mainly focuses on colloid chemistry and the semiconductor manufacturing process, including chemical mechanical polishing.

**Kangchun Lee** received his Ph.D. degree from the Department of Energy Engineering at Hanyang University, South Korea, in 2020. Now, he has been an Assistant Professor in the Department of Electronic Engineering at Kyonggi University, since 2023. Prior to joining Kyonggi University, he was a Staff Engineer at the Semiconductor R&D Center in Samsung Electronics, from 2020 to 2023. His research focuses on Advanced CMP/Post-Cleaning Processes and cutting-edge materials based on Colloid- and Electrochemistry.

**Seho Sun** received his Ph.D. degree from the Department of Energy Engineering, Hanyang University, South Korea, in 2022. He worked as a senior research engineer at Samsung Electronics from August 2022 to August 2023. Since September 2023, he has been an Assistant Professor at the School of Chemical Engineering in Yeungnam University. His current research focuses on semiconductors, energy storage, and electro catalysis.

**Taeseup Song** received his Ph.D. degree from the Department of Materials Science and Engineering at Hanyang University, South Korea, in 2012. He is currently an Associate Professor of the Department of Energy Engineering at Hanyang University. His research interest mainly focuses on synthesizing nanostructured materials for energy and electronic applications.

**Ungyu Paik** is a Distinguished Professor of the Department of Energy Engineering at Hanyang University, South Korea. He received his Ph.D. degree from the Department of Ceramic Engineering at Clemson University in 1991. His research interest is the synthesis and engineering of nanomaterials for applications in energy and electronic devices.

KONA Powder and Particle Journal

KONA Powder and Particle Journal No. 42 (2025) 100–120/https://doi.org/10.14356/kona.2025006 Review Paper

# The Effect of Process Conditions on Powder Flow Properties for Slow Flow Regimes†

**Sina Zinatlou Ajabshir, Diego Barletta* and Massimo Poletto**

*Dipartimento di Ingegneria Industriale, Università degli Studi di Salerno, Italy*

In several industrial units and applications, particulate solids are exposed to peculiar process conditions that significantly affect their flowability. Accurate characterisation and prediction of these effects are crucial for proper design and operation control of the processes. Liquid content, environmental humidity, and temperature can directly modify the type and magnitude of the interparticle forces and, thus, the cohesive behaviour at the bulk scale. This paper reports a critical review of experimental and modelling studies regarding the quantitative assessment of the effect of powder liquid content, environmental gas humidity and temperature on the mechanics of dense particle assemblies. Particular attention is paid to novel setups and experimental protocols that aim to go beyond the limits of standard and commercial instruments. A multiscale approach is followed from the particle level to the bulk level.

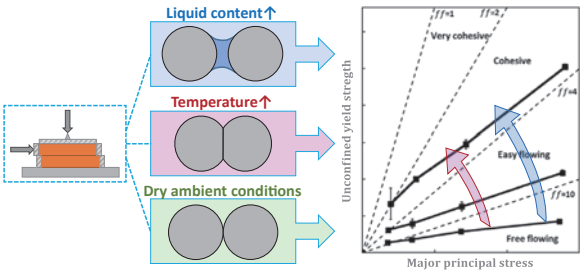


**Keywords:** powder flow properties, cohesion, liquid content, humidity, temperature, capillary condensation

## 1. Introduction

The rheology of dense particle assemblies plays a major role not only in several conventional unit operations (storage, handling, mixing, fluidisation, granulation, and milling) but also in more recent applications such as additive manufacturing (Cordova et al., 2020), pharmaceutical dry powder delivery (Price et al., 2002), calcium looping reactors (Durán-Olivencia et al., 2023), concentrated solar thermal technologies (Tregambi et al., 2021), plastic waste valorisation (Kartik et al., 2022), and dry battery manufacturing (Gyulai et al., 2023). Process conditions relevant to different industrial unit operations significantly impact particle interactions and, thus, average bulk flow properties. First, different flow regimes ranging from slow to intermediate and rapid exhibit very different phenomena and, therefore, are described by peculiar models that relate solid stress and velocity fields depending on the relevant strain rates. Boundaries between different regimes were proposed in terms of dimensionless inertial number as the ratio between the time scale associated with the consolidation stress and the time scale of the strain, as summarised in recent comprehensive surveys (Francia et al., 2021; Mort et al., 2015). Therefore, all these regimes will not be covered in this review work. The focus of the present review will be on the effect of significant process parameters such as temperature and liquid content particulate systems in the quasi-static regime.

Several experimental and theoretical studies have demonstrated that the flow behaviour of particulate systems at the bulk level is the macroscopic result of solid–solid interactions and fluid–solid interactions at the microscopic particle level. As a result, a multiscale approach is required.

### 1.1 Powder flow properties and interparticle forces

Powder flow properties in the quasi-static regime result from the frictional and cohesive interactions of particle assemblies. A macroscopic description of the incipient flow is performed by comparing the state of stress in the granular medium with a plastic yield criterion.

The Mohr circle gives a graphical representation of the distribution of normal stress, $\sigma$, and shear stress, $\tau$, in a plane (**Fig. 1**). The intercepts of the Mohr circle with the $\sigma$ axis correspond to the major principal stress, $\sigma_1$, and the minor principal stress, $\sigma_2$, with $\sigma_1 > \sigma_2$. The first attempt to describe the frictional component was made by Coulomb, who treated the solids as a rigid plastic material. According to this theory, in a simple shear problem, powder yielding occurs only when, along a direction, the shear stress reaches a limit value related to the normal stress:

$$\tau = \sigma \tan\phi + c \tag{1}$$

where $c$ is the material cohesion and $\phi$ is the angle of

† Received 10 June 2023; Accepted 8 November 2023
J-STAGE Advance published online 17 March 2024
* Corresponding author: Diego Barletta;
Add: Via Giovanni Paolo II 132, I-84084 Fisciano SA, Italy
E-mail: dbarletta@unisa.it
TEL: +39-089-96-2499

internal friction. Different mathematical functions accounting for the curvature of the yield locus have been proposed, such as the Warren Spring equation (Orband and Geldart, 1997), but the Coulomb equation remains the most used for its simplicity.

This approach can be generalised to the three-dimensional case in terms of a yield criterion, which indicates the limit stress state corresponding to powder yielding. When cohesion cannot be neglected, the material's cohesive strength can be derived for compressive deformation along one principal direction, assuming that negligible stress is applied along the orthogonal principal directions or, alternatively, for traction deformation. The corresponding values are the unconfined yield strength, $f_c$, and the uniaxial tensile strength, $\sigma_t$, as shown in **Fig. 1**. A common representation of flowability is presented in terms of a plot of $f_c$ vs $\sigma_1$, referred to as flow function, which can be compared to the flowability class bounded by constant values of the flow factor, $ff_c = \sigma_1/f_c$, according to the classification proposed by Jenike (1964) and completed by Tomas and Schubert (1985) (**Fig. 2**).

Several defined consolidation methods, including shear testers, tensile testers, and rheometers, have been developed to measure bulk powder flow properties, as recently surveyed by Barletta et al. (2019). There are open issues for further scientific research and technical development regarding the characterisation of small powder samples under low consolidation stress (below 1 kPa) (Ghadiri et al., 2020).

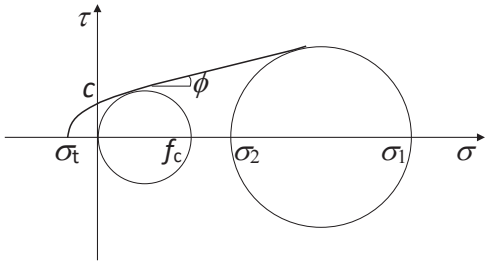


**Fig. 1** Mohr-Coulomb analysis on a yield locus to derive powder flow properties.

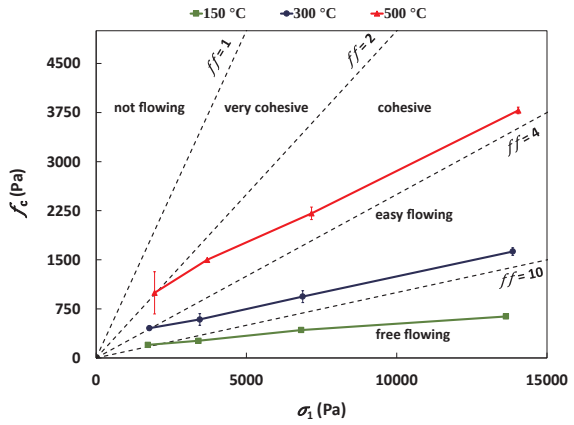


**Fig. 2** Flow functions of zeolite T804 at changing temperatures (150, 300 and 500 °C) ranked according to the Jenike flowability classification. Reprinted from Ref. (Zinatlou Ajabshir et al., 2022) under the terms of the CC BY-NC-ND 4.0 license. Copyright: (2022) The Authors, published by Elsevier.

Interparticle forces affecting bulk-scale behaviour are of three main types: van der Waals, capillary and electrostatic forces (Seville et al., 1997). Their intensity is conveniently related to the gravitational force acting on a single particle of the reference size by the dimensionless granular Bond number (Capece et al., 2015, 2016; Castellanos, 2005).

The direct measurement of interparticle adhesive forces appeared challenging; the pull-off experiment with atomic force microscopy was extensively used, but the results are often affected by limited repeatability mainly due to particle surface roughness and asperities, causing wide dispersion of the characteristic size of the interparticle contact and, therefore, of the resulting force (Castellanos, 2005; Rabinovich et al., 2000a).

A theoretical link between the forces at the particle level and the strength of the material at the bulk level can be derived for spherical particles assuming a simplified isostatic state of stress (Rumpf, 1962). This approach has often been applied to estimate the average values of interparticle forces from bulk-scale experimental data (Sofia et al., 2018; Tomas, 2003). In this case, the role of nanoscale asperities must also be properly accounted for to obtain correct quantification (Jallo et al., 2012; LaMarche et al., 2016; Rabinovich et al., 2000b).

## 2. Effect of liquid content and environmental humidity

### 2.1 Liquid content

By adding water, moisture, or any other liquid to the powder sample, liquid bridges can form between particles, giving rise to capillary interparticle forces (Mason and Clark, 1965). However, the intensity of capillary forces does not increase monotonically with increasing liquid amount because different liquid distributions arise depending on the liquid saturation amount (Pietsch et al., 1969), which is defined as the volumetric fraction of interparticle voids occupied by the liquid and can be derived from the liquid content on a dry basis, $x_w$, as follows:

$$S = \frac{1-\varepsilon}{\varepsilon}\frac{\rho_s}{\rho_l}x_w \tag{2}$$

where $\varepsilon$ is the volumetric fraction of interparticle voids in the powder, $\rho_s$ is the particle density and $\rho_l$ is the liquid density. In fact, by progressively increasing $S$, isolated liquid bridges between neighbouring particles can first form (pendular state); then, liquid bridges and liquid menisci on the particle surface roughness co-exist (funicular state); finally, the liquid fills all the available interparticle voids (capillary state) (**Fig. 3**) (Chen and Roberts, 2018; Coelho

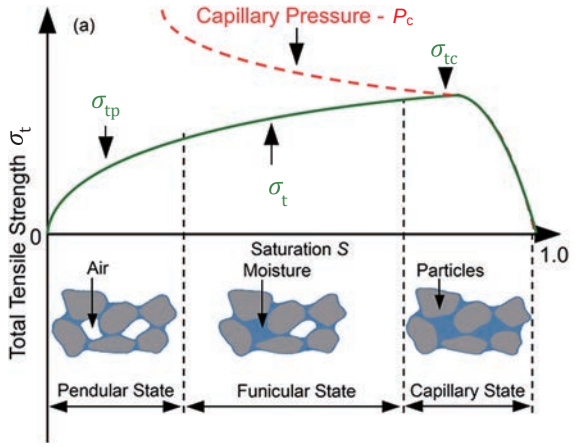


**Fig. 3** Tensile strength at increasing saturation. Adapted with permission from Ref. (Chen and Roberts, 2018). Copyright: (2018) Elsevier.

and Harnby, 1978a; Pietsch, 1968). Moreover, the spatial distribution of interparticle voids depends on the particle size distribution, particle shapes, and packing level and thus plays an important role in the capillary networks and on the effective saturation level, as highlighted by 2D and 3D images obtained by X-ray microtomography (Badetti et al., 2018; Louati et al., 2017). The presence of liquid can play a role in the formation of interparticle solid bridges. This phenomenon, referred to as caking, not covered in this paper, is deeply surveyed in the literature (Zafar et al., 2017).

The effect of the presence of liquid in the interparticle voids on cohesive powder properties was investigated using tensile testers, shear cells, and rheometers.

### 2.1.1 Measurement of the tensile strength and modelling

Experimental studies on the tensile strength of wet powder samples, by direct measurement or by split-cell testers (Eaves and Jones, 1972a, 1972b; Pierrat and Caram, 1997a; Pietsch et al., 1969; Schubert et al., 1975) or derivation from yield loci (Louati et al., 2017), highlighted different behaviours depending on the liquid content and the dry powder properties. Generally, for coarse or fine inorganic powders (particle size distribution, PSD, between 30 and 350 μm) not showing cohesive strength under dry conditions, an increase of the tensile strength was observed with increasing liquid content until a plateau was reached for a range of values of the amount of liquid and then, for much higher liquid saturation, a further significant rise of the strength was registered (Eaves and Jones, 1972a; Louati et al., 2017; Schubert, 1984). This result was explained by a physical interpretation based on the transition between different saturation states and the consequent effect on the forces acting at the particle level.

The tensile strength $\sigma_t$ can be estimated at low saturation levels, assuming a pendular state, using the Rumpf equation:

$$\sigma_{tp} = (1-\varepsilon)\frac{kF_c}{\pi d^2} \tag{3}$$

where $F_c$ is the capillary force, $k$ is the coordination number, and $d$ is the mean particle size (Pietsch et al., 1969; Rumpf, 1962).

For very high saturation levels, particles are surrounded by the liquid in the capillary state; thus, the tensile strength is proportional to the capillary pressure, $P_c$, by a factor equal to the saturation:

$$\sigma_{tc} = SP_c \tag{4}$$

For intermediate saturation levels corresponding to the funicular state, both contributions are present with a weighing factor that depends on the saturation value:

$$\sigma_t = \sigma_{tp}\frac{S_2 - S}{S_2 - S_1} + \sigma_{tc}\frac{S - S_1}{S_2 - S_1} \tag{5}$$

where $S_1$ is the critical liquid saturation between the pendular and the funicular state while $S_2$ is the critical liquid saturation between the funicular and capillary states. $S_1$ can vary between 0.25 and 0.5, while $S_2$ is generally larger than 0.9 (Pierrat and Caram, 1997a).

The capillary pressure $P_c$, present in **Eqn. (4)**, can be estimated by the following equation:

$$P_c = a'\frac{1-\varepsilon}{\varepsilon}\frac{\gamma}{d} \tag{6}$$

where $\gamma$ is the liquid surface tension and $a'$ is a constant depending on the particulate material, assuming a value between 6 and 8 and between 1.9 and 14.5 for narrow and wide particle size distributions, respectively (Schubert, 1984).

For particles below 1 mm, the capillary force $F_c$, appearing in **Eqn. (3)**, can be estimated as the sum of two main contributions: the first is the axial component of the surface tension force, $F_c$, at the interface between solid, liquid, and gas, which always results in an attractive force; the second is the force, $F_p$, caused by the change in pressure in the liquid bridge with respect to the atmospheric value due to the curvature of the liquid interface:

$$F_c = F_s + F_p \tag{7}$$

Assuming a saddle-shaped liquid bridge according to the Laplace–Young equation, the pressure difference between air and liquid is given by

$$\Delta p = \gamma\left(\frac{1}{R_1} - \frac{1}{R_2}\right) \tag{8}$$

where $R_1$ and $R_2$ are the characteristic curvature radii of a liquid bridge (one is convex and is related to the narrowest circular cross-section of the bridge; the other approximates the curvature radius of the toroidal concavity, **Fig. 4**). The

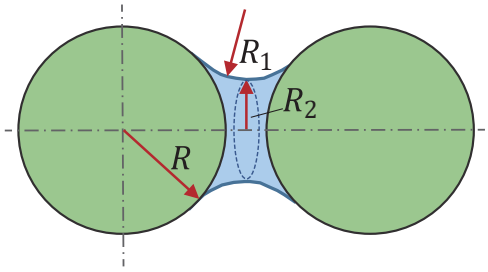


**Fig. 4** Liquid bridge and characteristic radii in **Eqn. (8)**.

pressure force turns out to be generally attractive because a pressure reduction is established in the liquid bridge (in fact $R_2 > R_1$), but it could be repulsive if a pressure increase arose.

Gradually increasing the liquid content to the funicular state, the attractive force $F_p$ due to suction at the gas–liquid interface can reduce the distance (Chen and Roberts, 2018) between the particles connected by the liquid and create an uneven spatial distribution of the interparticle voids. Generally, the resulting average bondage also reduces (Louati et al., 2017).

In the pendular regime, several theoretical equations for the capillary force proposed in the literature differ for the assumptions made regarding the size and shape of the two particles in contact with the liquid bridge and the geometry of the liquid bridge itself, including the liquid contact angle of the liquid on solid surfaces. Equations were more easily derived by assuming spherical particles, zero contact angles, and a toroidal bridge. The general form of the total capillary force is

$$F_c = K\gamma r \tag{9}$$

where $r$ is a characteristic curvature radius of the particle surface in contact with the liquid bridge, and $K$ is a complex function of several geometrical parameters of the liquid bridge, such as the interparticle distance, the half-angle of the liquid bridge (also referred to as filling angle), and the contact angle. More details on capillary forces between surfaces of different shapes (between sphere and sphere, between sphere, cone, cylinder and plane), with and without microscale roughness, can be found elsewhere (Butt and Kappl, 2009).

The combination of **Eqns. (3)** to **(9)** predicts the possible existence of the plateau of the tensile strength experimentally observed in the pendular regime. Moreover, following the analysis for a single liquid bridge forming between two equal spherical particles, the capillary force may increase up to a plateau value with increasing filling angle, which is related to the overall liquid saturation (Weigert and Ripperger, 1999) since the contribution due to the surface tension rises monotonically while the force due to the suction initially assumes increasing positive values (attractive) then, after reaching a maximum, decreases down to negative values (repulsive) for a range of values of the ratio between the interparticle distance and the particle size between $5 \times 10^{-2}$ and 0.5 (Pierrat and Caram, 1997a; Pietsch and Rumpf, 1967). Moreover, by increasing the liquid saturation in a powder sample, the average number of liquid bridges per particle increases until a roughly constant value is reached in the pendular regime (Kohonen et al., 2004). However, micro cracks and roughness on the particle surface could absorb liquid from the surface, reducing the probability of liquid bridge formation and, thus, the capillary force (Johanson et al., 2003).

Peculiar observations have been made for very fine powders (PSD mostly below 15 μm) with cohesive properties at very low moisture contents (Eaves and Jones, 1972a; 1972b). In fact, the tensile strength reaches a maximum value at a very limited amount of liquid (lower than 1–2 % w/w dry basis), then decreases with increasing liquid amount up to 50 % of the maximum value for liquid content between 5 % and 10 % w/w dry basis. This trend was interpreted by Eaves et al. (1972b), assuming that free water on the particle surface could swamp microcontacts between particles and, thus, cause a reduction in the intensity of van der Waals forces not balanced by the increase in capillary forces. In fact, this trend is in qualitative agreement with the prediction that the capillary force decreases as a function of the filling angle for the case where the ratio between the interparticle distance and the particle size tends to zero for equal spherical particles (Pietsch and Rumpf, 1967).

### 2.1.2 Measurement of the yield loci

Direct shear tests with translational and rotational cells confirmed the effect of capillary forces on bulk flow properties on a range of fine powders with increasing content of different liquids such as water, aqueous solutions, and oil (Althaus and Windhab, 2012; Badetti et al., 2018; Emery et al., 2009; Johanson et al., 2003; Louati et al., 2017; Lu et al., 2018; Pierrat et al., 1998; Pierrat and Caram, 1997a).

Inspection of experimental yield loci highlighted that the cohesion increased with increasing liquid content in the low range (<5–10 % w/w), whereas the internal friction angle remained almost unchanged. The increase in cohesion appears to be more pronounced for higher consolidation stress values (Johanson et al., 2003; Louati et al., 2017). A quantitative prediction of the cohesion increase was proposed with the so-called theory of shift of a linearised yield locus, assuming a constant value of the angle of friction $\phi$ (Pierrat et al., 1998). The shift of the yield locus is estimated in terms of the reduction of the normal stress, $\Delta\sigma$, providing the same shear strength in the dry condition. An expression of $\Delta\sigma$ as a function of the changes in the tensile strength, $\Delta\sigma_t$, is proposed:

$$\Delta\sigma = \Delta\sigma_t \frac{1+\sin\phi}{2\sin\phi} \tag{10}$$

This equation shows that a wet powder yield locus shifts to the left compared to that for dry conditions. $\Delta\sigma_t$ can be directly measured by a split cell or derived from model predictions according to **Eqn. (5)**.

An irregular particle shape can drive a different effect of the liquid presence on the cohesive strength (Emery et al., 2009). In fact, for needle-shaped particles (e.g. aspartame powders), an optimal moisture content value was found to improve flowability. By increasing the liquid content, an improvement of flowability (increase of the flow factor or decrease of cohesive strength) was observed because of the formation of round-shaped agglomerates, while going beyond this critical moisture value (e.g. 5 % w/w), the flowability decreased because of increments of capillary forces of liquid bridges between agglomerates. In contrast, for particles ranging from spheres to elongated shapes with smooth edges (e.g., Hydroxypropyl Methylcellulose powders), a more cohesive behaviour was obtained by increasing the water content (5 % w/w). Then, an improvement in flowability for higher moisture contents (10 % w/w) was interpreted, considering the possible lubricating effect of a thick layer of liquid on the particle surface.

Prediction of the effect of moisture on powders consisting of porous particles appeared to be more challenging because it is necessary to estimate the amount of liquid penetrating the particle porosity and, thus, not available for the formation of liquid bridges (Lu et al., 2018).

A more complete survey of the experimental and modelling results on the effect of liquid content is reported in **Table 1**.

## 2.2 Effect of capillary condensation

Liquid water or moisture content in powders can be caused by the exposition of the sample to a humid atmosphere and the consequent capillary condensation leading to liquid bridge formation (Coelho and Harnby, 1978b). Such phenomena typically occur in storage containers and process units such as dryers and fluidised bed reactors. Capillary condensation was studied by directly observing liquid bridges between particles and indirectly measuring the induced cohesive properties at the bulk level.

Capillary condensation is possible for the reduction of the vapour pressure of water due to the reduced pressure within the liquid bridge determined by the surface tension acting over a curved concave interfacial surface with air. The modified vapour pressure is described by the Kelvin equation:

$$p_s = p_{s0}\exp\left[-\frac{M_w\Delta p}{\rho_l R_g T}\right] \tag{11}$$

where $p_{s0}$ is the vapour pressure of the liquid, $p_s$ is the vapour pressure over a curved surface, $M_W$ is the molecular weight of water, $R_g$ is the universal gas constant, and $T$ is temperature. $\Delta p$ is the pressure difference between gas and liquid, as predicted by the Laplace–Young equation, **Eqn. (8)**.

As a result, regardless of the relative (air) humidity (*RH*), condensation occurs in liquid bridges or other liquid menisci with concave curvature radii small enough to provide a decrease in the liquid pressure sufficient to lower $p_s$ below the water partial pressure. At equilibrium, it is

$$RH = \frac{p_s}{p_{s0}} = \exp\left[-\frac{M_w\Delta p}{\rho_l R_g T}\right] \tag{12}$$

Experiments using a simplified translational shear cell were performed on various powders with different PSD limits and particle shapes under controlled air humidity conditions in a climatic chamber (Elbirli et al., 1982). The results highlighted that the effect of humidity on the powder shear strength varies significantly with the geometrical features of the particle surface and the resulting curvature of interparticle contact points, as well as with the surface hydrophilic/hydrophobic properties. In fact, for silane-coated glass beads and $TiO_2$ particles with almost spherical contact points (PSD range 125–190 μm) and hydrophobic surfaces, the effect of air humidity was nearly negligible, and a small reduction in cohesive strength was observed for $RH < 90$ %. These results do not contradict the theoretical prediction of the capillary force due to capillary condensation at increasing *RH* on spherical particles, obtained by combining the Kelvin and Laplace–Young equations with the capillary force equation as the sum of the surface tension force and the pressure force (Coughlin et al., 1982). Instead, for powder with more irregularly shaped particles and rough surfaces, such as amorphous silica (PSD range 0.4–15 μm), an increase in cohesive strength was found with increasing *RH*. However, different trends were observed, including the observation of a minimum or maximum strength for critical humidity values. Interpretations can be attempted on a case-by-case inspection of SEM images of the particles, revealing very irregular shapes, including flat sides, elongated shapes, and eventually agglomerates of particles that play a complex role in the contact point distribution and effective capillary condensation.

The role of the roughness of the particle surface on capillary condensation has been widely studied by several authors on theoretical grounds. The presence of asperities must be taken into account when modelling liquid condensation at the contact point between a conical asperity and a flat surface, highlighting the prevailing contribution of the capillary suction force (Coughlin et al., 1982). The resulting adhesive force increased with increasing relative humidity (*RH*). A more significant increase was predicted for larger cone half-angle values. However, because the characteristic size of the calculated liquid bridge did not exceed a few nanometers, a length comparable with the molecular scale, until $RH > 0.3$, quantitative values are affected by

**Table 1** Overview of case studies on the effect of liquid content on powder strength, friction and cohesion (chronological order).

| Reference | Liquid content (%) | Powders/Tester/Properties | Main results |
|---|---|---|---|
| (Pietsch et al., 1969) | 0–21 (Water) | Limestone/agglomerate TS tester/TS | TS increases with moisture up to a plateau and then continues to increase. Model for pendular and capillary regimes. |
| (Eaves and Jones, 1972a) | 0–17 (Water) | Sodium chloride/split-cell TS tester/TS | PSD influence: for coarse powders, TS increases with moisture up to a plateau; for fine powders, a maximum value is found at a very limited amount of liquid (<1–2 % w/w dry basis), then decreases with increasing liquid amount up to 50 % for liquid content between 5 % and 10 % w/w dry basis. |
| (Eaves and Jones, 1972b) | 0–15 (Water) | Ca phosphate, glass beads, potassium chloride/split-cell Parfitt TS tester/TS | The TS of calcium phosphate is almost constant with moisture due to porous particles. |
| (Pierrat and Caram, 1997b) | 0.7–8 (Water, surfactants) | Glass beads/Parfitt TS tester with a larger split cell/YL | TS increases with liquid content up to a plateau in the pendular regime and strongly depends on powder bed voidage; a correlation is proposed. |
| (Pierrat et al., 1998) | 1.3–25 (Water) | Crushed limestone, Super D catalyst, Leslie coal, glass beads/translational ST/YL | Increase in cohesion with moisture. AIF is almost independent of moisture. Proposed equation for the yield locus shift with moisture. |
| (Johanson et al., 2003) | 0–0.12 (Oil) | Glass beads/Schulze ST/FF | Increase in UYS with oil content. UYS decreases with increasing particle size. |
| (Richefeu et al., 2006) | 0–3 (Distilled water) | Sand grains, glass beads/ Translational ST/YL | Increase of cohesion to a plateau value with moisture. |
| (Althaus and Windhab, 2012) | 18–30 (Aq. solution with dextrin) | Glass beads and silica/ Schulze ring ST/YL | Cohesion and uniaxial TS increase with moisture and as a function of the different identified saturation regimes. |
| (Althaus et al., 2012) | 16, 18, 20 (Aq. solution with dextrin) | Glass beads/Schulze RST/YL | Limited effect of dextrin concentration on YL. A semi-empirical model linking capillary forces and YL. |
| (Louati et al., 2017) | 0, 0.5, 3.5, and 40 (PEG) | Glass beads/Hosokawa MPT, Schulze RST/AOR, YL | TS is more affected by liquid at consolidation stress > 4 kPa. X-ray tomographic images highlight saturation levels. |
| (Lu et al., 2018) | 1.6–29 (Water) | Pulverized coal/Hosokawa MPT, Freeman FT4 Powder Rheometer/AOR, HR, Carr flowability index, Cohesion, Angle of internal friction, FF | Increase in AOR and HR with moisture. Increase in cohesion and decrease in flowability for moisture higher than a critical value (15–20 % w/w). |
| (Badetti et al., 2018) | 1.5–7.5 (Silicone oil) | Polystyrene beads/Stress-controlled rheometers with an annular shear cell/Apparent friction coefficient | The apparent friction coefficient ($\tau/\sigma$) increases with moisture and with the inertia number. Proposed equation for apparent friction coefficient as a function of reduced pressure and inertia number. |
| (Chen et al., 2018) | 3.5–17 (Water) | Coal, Bauxite, Iron ore/Jenike ST/TS, FF | FF vertical shift (flowability decreases) with moisture. Proposed modification of the flowability classification for high consolidation. |

significant uncertainty at low *RH*. An extension of the analysis to a couple of generic curved asperities in contact highlighted the significant effect of curvature on the acting force. For smooth micrometric spherical particles, the capillary force is mainly proportional to the particle radius and is not significantly affected by the relative humidity (Bocquet et al., 1998). Instead, capillary condensation is relevant to asperities of nanometric size, comparable to the Kelvin length, that is, the concave curvature radii allowing condensation at $RH \approx 0.1$ (Butt, 2008), explaining the onset of capillary forces. A more comprehensive model, experimentally validated by AFM measurements, has been

proposed for an asperity in contact with a larger spherical particle (Rabinovich et al., 2002). The results revealed that adhesive forces increased and the critical relative humidity decreased with decreasing root mean square roughness. An extension of this analytical approach also considered the roughness distribution on irregularly shaped particles (Butt, 2008). The predicted capillary force increased with *RH* up to a maximum value close to that of the force estimated for a smooth particle (**Fig. 5**). The complete picture of the physical interpretation is that at low *RH*, a single capillary bridge forms by condensation between close nanometric asperities of particles in contact and, therefore, the van der Waals force that is proportional to the overall particle size (order from tens to few hundreds microns) prevails. At intermediate *RH*, the number of capillary bridges increases and the sum of acting capillary force increases. At high *RH*, liquid water fills all the voids between asperities to obtain a large capillary meniscus with a larger curvature radius comparable with the overall particle size. This situation corresponds to the maximum intensity of the capillary force (**Fig. 6**) (Butt and Kappl, 2009).

Experiments performed at the bulk level confirmed the conclusions of force analysis at the particle level. In fact, powder cohesion varied only for air humidity values higher than a critical value by analysing the results of shear tests (Elbirli et al., 1982; Karde and Ghoroi, 2015; Landi et al., 2011; Salehi et al., 2021; Stevens et al., 2009; Teunou and Fitzpatrick, 1999), torque and energy measurements in rheometers (Groen et al., 2020; Landi et al., 2012; Lu et al., 2017; Marchetti et al., 2022), and flowability indices in rotating drums (Lumay et al., 2016).

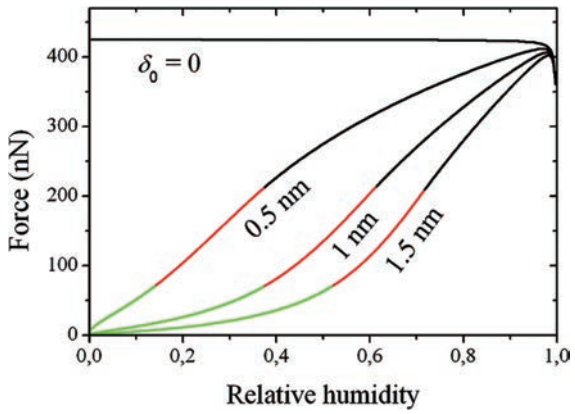


**Fig. 5** Capillary forces at various humidity amounts and surface roughness. Same rough spheres with 1 μm radius and constant contact angle $\theta = 20°$. $\delta_0$ is the characteristic roughness. Reprinted with permission from Ref. (Butt, 2008). Copyright: (2008) Elsevier.

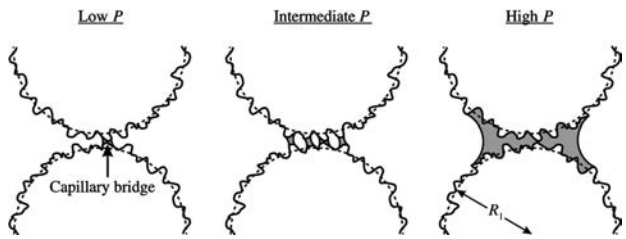


**Fig. 6** Capillary bridge patterns between particles with asperities at increasing relative humidity. Reprinted with permission from Ref. (Butt and Kappl, 2009). Copyright: (2009) Elsevier.

For instance, the results of shear tests on glass beads previously conditioned in a fluidised state by humid air showed an increase in cohesion for $RH > 70$ %, while the angle of internal friction was less affected (Landi et al., 2011). Moreover, by considering the presence of asperities with a curvature radius equal to about one hundred of the bead radius (two samples with 50 μm and 90 beads μm mean size), predictions of the tensile strength by a model combining the Rumpf, Laplace–Young, and Kelvin equations showed good agreement with the values derived from experimental yield loci. A tiny fraction of the condensed moisture between particles could form capillary bridges that play an active role in increasing the powder's cohesion.

As mentioned above for the interparticle forces, relative humidity also affects the unconfined yield strength of powders, depending not only on the particle size and shape but also on the hydrophilic/hydrophobic properties of the particle surface (Karde and Ghoroi, 2015; Stevens et al., 2009). In fact, the moisture content and cohesive strength of hydrophobic ibuprofen powder did not increase with *RH*. In contrast, the increase in the unconfined yield strength of hydrophilic starch and Avicel powders was directly correlated with the measured specific surface energy component increasing at *RH* higher than a critical value (**Fig. 7**). At lower *RH* values, cohesive strength was correlated with the Lifshitz–van der Waals forces due to the dispersive surface energy component. The coexistence of electrostatic charging may explain the minimum unconfined yield strength of starch powder by a possible reduction of electrostatic forces with increasing *RH*.

The cohesion force between particles in different ranges of air relative humidity could provide interesting results. In the range below the critical air relative humidity, particle–particle friction might generate electrostatic forces, which cause cohesive forces between the particles (Harnby et al., 1987; Lumay et al., 2016). In contrast, above the critical air relative humidity, the condensed air moisture determines the cohesion forces (Landi et al., 2011; Lumay et al., 2016). The tensile strength and adhesion forces between particles increase as the relative humidity content increases. At the same time, the consolidation pressures could vary the contribution of the adhesion force. For instance, capillary forces play an important role at low consolidation pressures, but contact forces prevail at high consolidation pressures (Karde et al., 2017).

**Table 2** reports a wider overview of the experimental and modelling studies on the effect of air humidity.

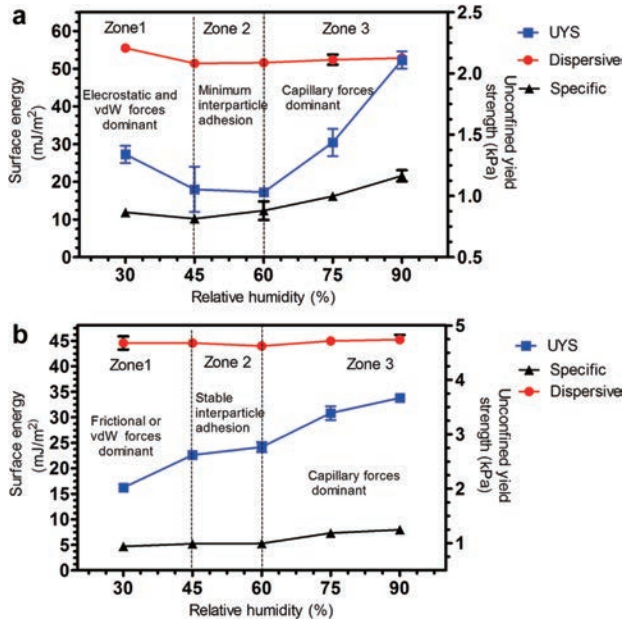


**Fig. 7** Correlation between unconfined yield strength (UYS), dispersive and specific surface energy components for **a)** starch powder and **b)** Avicel powder. Reprinted with permission from Ref. (Karde and Ghoroi, 2015). Copyright: (2015) Elsevier.

## 3. Effect of temperature

The effect of temperature on the mechanical properties of powders was tested by considering the direct measure of binary interparticle forces at the microscopic level and bulk scale properties at defined bulk consolidation, such as tensile strength or shear testing properties.

### 3.1 Direct measurement of the interparticle forces

#### 3.1.1 Experimental setup and procedures

The direct measurement of interparticle forces at changing temperatures is a complex task, and the literature reports only the high-temperature micro-force balance developed by Pagliai et al. (Pagliai et al., 2004). The setup included a system of micromanipulators to set the position of two particles in an electric oven to heat the system to 1000 °C, where a camera allowed image recording for visual observation. The relative motion between the couple of tested particles was regulated by a linear displacement actuator moving one of the two particles. The pulling force between the two particles in contact was derived from the cantilever deflection of a calibrated bending strip mounted on the static micromanipulator while pulling.

A micromanipulation system for measuring interparticle forces under controlled humidity and temperature was also developed by Haider et al. (2012) to measure the increase of adhesion force between amorphous maltodextrin particles when the temperature approached the glass transition temperature. The mechanism involved is related to the desired particle agglomeration, which is beyond the scope of this review.

#### 3.1.2 Main observed phenomena

Pagliai et al. (2004) performed measurements on particles of E-cat powder (a powder similar to those used in fluid catalytic cracking reactors). This powder was withdrawn from the process, where it exhibited defluidization at high temperatures. The change in interparticle forces with increasing temperature was observed with a liquid bridge forming between the tested particles at 90 °C due to low melting compounds. However, the low surface tension of the formed liquid made the intensity of the capillary force not very high. In fact, a hydrocarbon liquid phase is formed. The liquid evaporated at 180 °C and up to 300 °C, and a solid bridge formed between the two particles. Correspondingly, the measured force increased significantly.

### 3.2 Experimental setup and procedures for the bulk solids properties

The effect of temperature on bulk flow properties was investigated by conventional characterisation techniques in different apparatuses properly modified for high-temperature experiments.

#### 3.2.1 Direct evaluation of the tensile strength

Several studies have exploited the split cell tensile testers developed for tests up to 1100 °C by Kamiya et al. (2002b). This apparatus (**Fig. 8a**) was made of a circular vertically split cell consisting of a fixed part and a horizontally moving part suspended by a very thin metal plate. The cell was heated by radiation from the top and bottom in a furnace purposely prepared. The cell was made of silica glass to limit thermal expansion. The experimental procedure was similar to a conventional tensile test, with the only difference being the heating and monitoring of the powder sample temperature by a thermocouple. It consisted of a vertical consolidation step with a normal stress of 2.5 kPa and a successive tensile failure step during which the pull-off force and displacement of the movable part were measured.

Different apparatuses for a vertical uniaxial tensile test have been recently proposed (Liu et al., 2022; Luan and You, 2015). In the high-temperature solid bridge force device (Luan and You, 2015) (**Fig. 8b**), the ash sample was divided into two parts, which were separately heated in two cylindrical cells at high temperatures between 750 °C and 1250 °C and then put in contact under vertical compressive stresses between 9.5 and 19.9 kPa for a period between 1 and 20 min. After this phase, the two cylinders were vertically separated by a traction motor, and the tensile force was measured. Different specimen preparations were proposed by Liu et al. (2022): a coal ash powder sample was extruded through a cylindrical die under 20 MPa pressure, then it was vertically suspended between two clamping tools and heated at varying temperatures between ambient and 1200 °C for 1 h. Finally, the tensile force to obtain the

**Table 2** Overview of case studies on the effect of air humidity on powder strength, friction, and cohesion (chronological order).

| References | *RH* (%) | Powders/Tester/Properties | Main results |
|---|---|---|---|
| (Elbirli et al., 1982) | 10–96 | $TiO_2$, glass beads, polycarbonate, amorphous silica, and alumina/translational ST/YL | The effect of humidity on cohesive strength varies with particle shape, surface, hydrophilic/hydrophobic properties, surface roughness, and material hardness. |
| (Harnby et al., 1987) | 11–87 | Glass beads/Hosokawa MPT/bulk density, HR | The aerated and tapped bulk density slightly decreases with *RH*. Fluctuating trend in HR. |
| (Teunou and Fitzpatrick, 1999) | 0–97 | Food powders (Flour, skim-milk, tea, whey-permeate)/RST/FF | General increase in UYS with *RH* except for flour powder. Food powder composition and wide PSD affect interaction with water. Caking at high *RH*. |
| (Stevens et al., 2009) | 20, 50, 80 | Aluminium powder (as received and surface modified)/Schulze RST/FF | Particle coating mitigates the *RH* impact, especially for low hydrophobicity. Further water adsorption did not affect the capillary forces and UYS. Higher humidity may induce lubrication, leading to a reduction in particle friction and lower UYS. |
| (Emery et al., 2009) | 0–10 | Pharmaceutical powders (API, Aspartame, HPMC, Respitose)/density meter, translational ST/HR, Carr index, AOR, FF | The effect of *RH* on the flow factor depends on particle shape. Increasing or decreasing flowability depends on the powder nature. |
| (Landi et al., 2011) | 13–98 | Glass beads/Schulze RST/YL | Cohesion and AIF increase only at high *RH*. Model linking bulk and particle scales. |
| (Landi et al., 2012) | 0–70 | Glass beads/Couette fluidized bed rheometer, Schulze RST/torque | Torque decreases with air velocity, and exhibits a non-monotonous trend with *RH*. The proposed rheological model is a function of flow properties. |
| (Karde et al., 2015) | 30–90 | Pharmaceutical powders: (Corn starch, Avicel PH 105, ibuprofen)/Freeman FT4 Powder Rheometer, Surface energy analyser/UYS, specific surface energy | Specific surface energy and flow behaviour are correlated. Hydrophilic powders are influenced by *RH*, in contrast to hydrophobic powders. |
| (Lumay et al., 2016) | 0–95 | Lactose/GranuDrum/Cohesive index | The cohesive index increases at very high *RH*. |
| (Lu et al., 2017) | 0, 30, 58, 85 | Lactose powders/Freeman FT4 powder rheometer/Flow energy | Flow energy increases with increasing relative humidity and fraction of fine particles. |
| (Karde et al., 2017) | 30–90 | Corn starch/Freeman FT4 powder rheometer/YL | Cohesion increases gradually with *RH* at low consolidation stress (<2 kPa), while it shows a minimum value for an intermediate value of *RH* at higher consolidation stress (3–9 kPa). |
| (Groen et al., 2020) | 5–90 | Coffee creamer, Citric acid monohydrate/Anton Paar powder rheometer/torque | Moderate increase of torque for $RH < 60$ %; for higher significant change of the slope. Temperature increase reduces the critical *RH* value. |
| (Salehi et al., 2021) | 0–90 | Mannitol powder/Brookfield powder flow tester, surface energy analyser/YL, FF, specific surface energy | Flowability remains unchanged for $RH < 60$ % with a temperature effect observed in the range 25–35 °C. A comparison of estimated interparticle forces is made using different theories (Rumpf model and a combination of the Kelvin model with the Laplace–Young equation). |
| (Marchetti et al., 2022) | 40, 60, 80 | Steel powder/Freeman FT4 powder rheometer/Flow energy, UYS | Flow energy and specific energy increase with *RH* beyond a critical value. Limited effect of *RH* on UYS. |

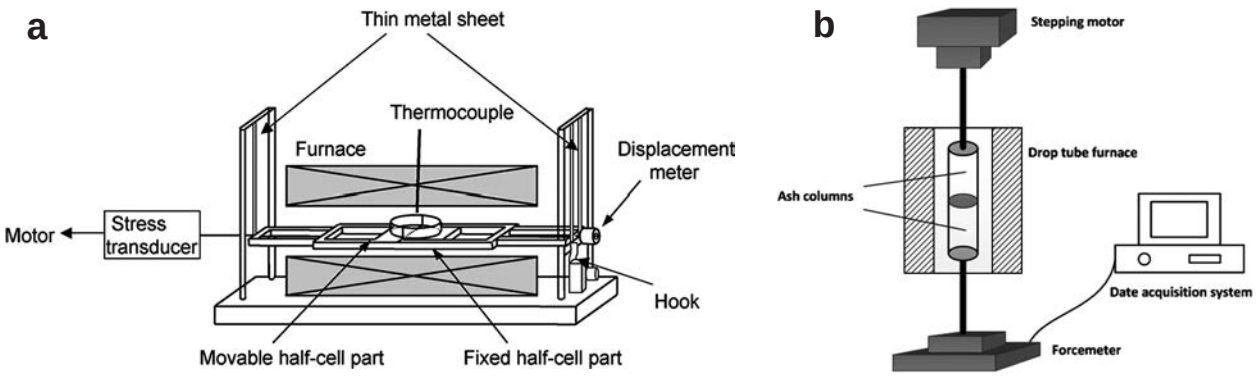


**Fig. 8** **a)** Split-type tensile-strength testing system, reprinted with permission from Ref. (Kamiya et al., 2002b). Copyright: (2002) Elsevier; **b)** High-temperature solid bridge force device, reprinted with permission from Ref. (Luan and You, 2015). Copyright: (2015) Elsevier.

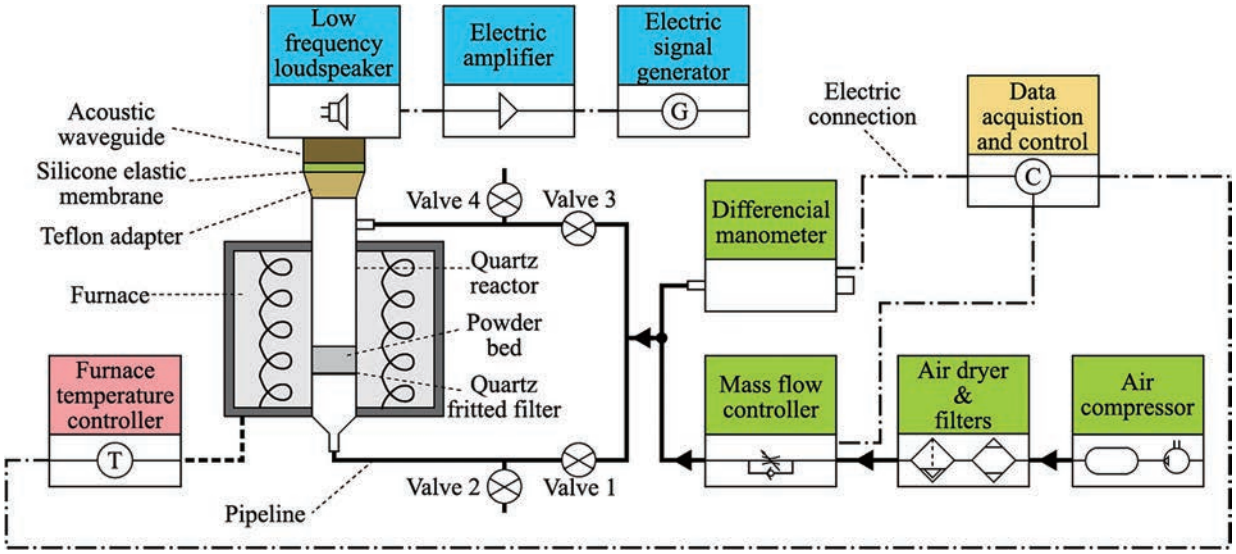


**Fig. 9** Setup of the high-temperature Sevilla powder tester. Reprinted with permission from Ref. (Durán-Olivencia et al., 2020). Copyright: (2020) Elsevier.

specimen failure was measured.

The high-temperature Sevilla powder tester (HTSPT) is a modified version of the Sevilla Powder Tester that can reach temperatures up to 500 °C using a quartz fluidisation column surrounded by an electrical furnace (Durán-Olivencia et al., 2021; Espin et al., 2020) (**Fig. 9**). A low-frequency sound wave generation system was implemented on top of the powder bed to obtain the fluidisation state even with very cohesive powders. The tensile strength measurement was based on the measurement of the maximum pressure drop value during a fluidisation test at increasing gas velocity, as in the original apparatus for tests at ambient temperature. An initial preparation of the powder bed with a downward gas flow allowed consolidation of the sample under set values of resulting normal stress (Durán-Olivencia et al., 2020; Gannoun et al., 2022).

Tests were performed for various fly ashes derived from the combustion of coal and biomass particles (Horiguchi et al., 2018; Kamiya et al., 2002b; Liu et al., 2022; Tsukada et al., 2003, 2008) for mixes of silica coated with alkali metals (Kamiya et al., 2002a) and for calcium carbonate particles (Horiguchi et al., 2021b; 2022).

### 3.2.2 Shear testing experiments

First attempts at the conduction of shear experiments at high temperatures were performed using conventional shear cells heated before or during the test by placing a translational cell in an oven (Kanaoka et al., 2001; Smith et al., 1997) or in a muffle furnace (Maarup et al., 2014). Afterwards, the rheometers and shear cells were modified for conditions different from the ambient temperature. Zimmerlin et al. (2008) developed a rheometer based on a viscosimeter design to measure the torque necessary for the rotation of an impeller formed by a thin shaft with some orthogonal pins in a cylindrical cell heated by a coaxial furnace up to 700 °C. Ripp and Ripperger (2010) modified a Schulze annular shear cell to obtain temperatures lower and higher than ambient by introducing the flow of a heat transfer medium in a double casing of the though at the bottom of the ring cell (internal volume about 900 mL).

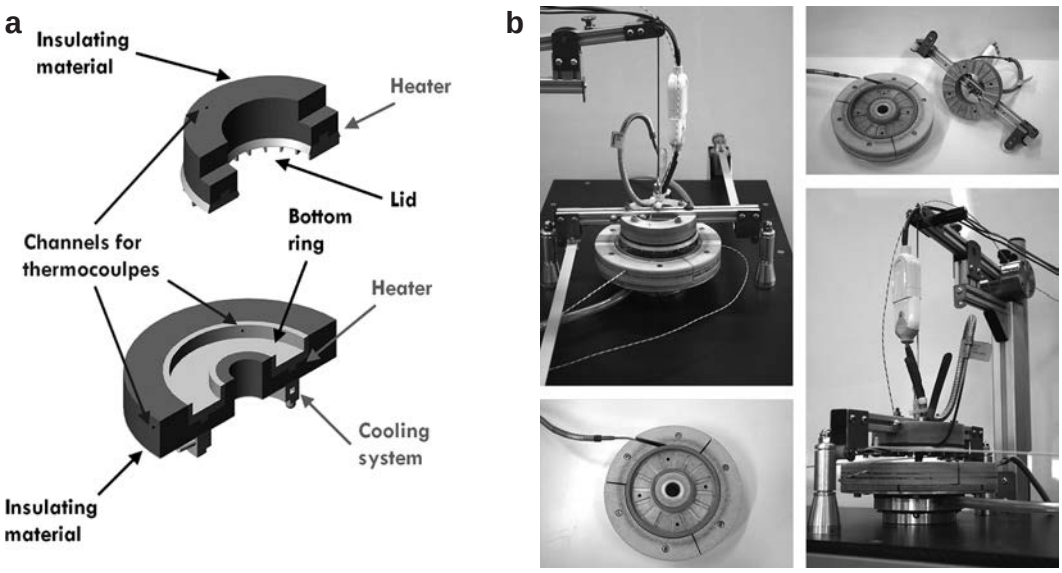


**Fig. 10** High-temperature annular shear cell: **a)** cell and lid sketch; **b)** whole setup. Reprinted with permission from Ref. (Tomasetta et al., 2013). Copyright: (2013) Elsevier.

The setup was provided with conductive plates to achieve a uniform temperature distribution. The lid was provided with a thermal insulation layer for the cooling case and electric resistances for the heating case. Shear tests at temperatures between –80 °C and 120 °C were reported.

Tomasetta et al. (2013) developed a high-temperature annular shear cell (HT-ASC) (**Fig. 10**) by designing a ring bottom cell (internal volume of about 85 mL) and a lid electrically heated provided with a thermal insulation system consisting of a layer of ceramic material and a casing with flowing cooling water for the bottom cell in contact with a Schulze ring shear tester bench. Operating conditions allowed reaching temperatures from ambient to 500 °C.

More recently, a commercial shear cell with temperature and relative humidity control was developed by Anton Paar GmbH. It consists of an annular shear cell (internal volume: small cell 4.3 mL and large cell 18.9 mL) positioned in a heat transfer system based on combined convection and radiation to cover the temperature range from –160 °C to 600 °C (Barletta et al., 2019).

Investigations by shear testing at high temperatures have considered several powders with very different chemical natures, particle size distributions, and particle shapes, including fly ashes (Kanaoka et al., 2001; Liu et al., 2018), $MgSO_4$ and $CaSO_4$ powders (Smith et al., 1997), food powders (Ripp and Ripperger, 2010), ceramic powders (Chirone et al., 2016, 2018; Tomasetta et al., 2013), catalyst and catalyst support powders (Tomasetta et al., 2013; Zinatlou Ajabshir et al., 2022), titanium dioxide powders (Macrì et al., 2017b), and polymer powders for additive manufacturing (Ruggi et al., 2020a; 2020b).

In addition to measuring complete yield loci and flow functions according to the shear testing standards, a simplified experimental procedure for quicker scrutiny of the effect of temperature on flowability was proposed by Chirone et al. (2018). The shear stress was measured in the HT-ASC during a single sequence of pre-shear and shear steps under decreasing normal stress, as it is recommended to measure a single point for a static yield locus at increasing temperature values (**Fig. 11**). This protocol allowed the preliminary detection of critical temperature values for the change in interparticle forces. As a result, complete shear tests can be focussed on a narrower temperature interval to obtain the corresponding flow functions. Experimental results were generally reported in terms of yield loci and flow functions at consolidation stresses between 1 and 14 kPa, but more often at low consolidation stresses between 0.75 and 2 kPa, to reproduce the typical range of stresses experienced by the powders in process units such as fluidised beds

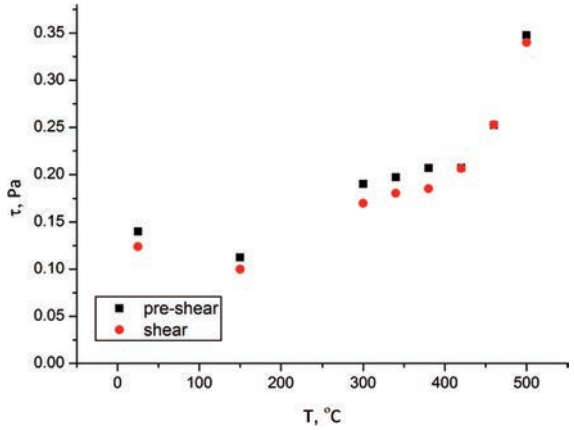


**Fig. 11** Shear stress as a function of temperature for a ceramic powder with low-melting impurities. Reprinted with permission from Ref. (Chirone et al., 2018). Copyright: (2018) Elsevier.

(Chirone et al., 2020; Macrì et al., 2020) and selective laser sintering machines (Ruggi et al., 2020a; 2020b).

### 3.3 Effect of temperature on bulk flow properties in the presence of capillary forces

When powders are characterised by some moisture content at ambient temperature and are not melting at relatively low temperatures, the prevailing phenomena affecting flow properties are related to water evaporation. By increasing the temperature above 100 °C, capillary forces vanish, and the only active interactions remaining are van der Waals forces. At the bulk scale, these changes can be detected as a decrease in tensile strength, cohesion, and unconfined yield strength between ambient and temperatures just above 100 °C (Chirone et al., 2018; Ruggi et al., 2020a).

For higher temperatures or dry powders, a temperature increase is generally associated with an increase in cohesion and tensile strength, which can be related to either the rise of van der Waals forces or the eventual formation of a liquid phase. Given the high intensity of capillary forces, a melting phase is generally associated with a sharp increase in powder cohesion or tensile strength. Such phenomena have been observed in shear testing experiments with polymeric powders (Ruggi et al., 2020a; 2020b) or ceramic powder mixtures containing salt impurities (Chirone et al., 2018). It is remarkable that while for polymeric powders, DSC revealed that the increase in powder cohesion is related to the approach to the polymer melting temperature (Ruggi et al., 2020a; 2020b), for ceramic powder mixtures with salt impurities, neither DTA nor TGA could show the phase transition of low melting salts due to the minimal quantities of these salts present only on the particle surface. Such salt presence could be indirectly proven by EDX analysis and information on the reactive system to which the particles had been exposed. In this respect, the single-point pre-shear/shear analysis proposed above and reported in **Fig. 11** appeared to be more sensitive to phase changes limited to the particle surface than the established thermal analysis procedures (Chirone et al., 2018).

Similar phenomena linked to capillary forces were observed in tensile strength experiments on ash materials containing low melting compounds associated with the presence of eutectic oxides (Horiguchi et al., 2021b) or the addition of highly reacting calcium carbonate nanoparticles (Horiguchi et al., 2022). Proof of this interpretation is found in the similar behaviour found in artificial mixtures of silica particles coated with alkali metals, such as sodium and potassium (Kamiya et al., 2002a), or phosphorous (Horiguchi et al., 2021a). Care should be taken when using such a model system because it was also noted that when the interparticle liquid phase is formed by the fusion of low melting compounds, some evaporation due to the increasing temperature can occur and result in a slight decrease in the tensile strength (Tsukada et al., 2003).

Chirone et al. (2018) proved that the significant increase in the cohesive strength of ceramic powders at high temperatures (500 °C) was due to the rise of capillary forces using a model approach similar to that proposed by Pierrat and Caram (1997), assuming the partial melting of all salts present in the powder. The characteristic size of the contact area where the capillary bridge formed was estimated using the Rumpf model applied to the tensile strength value measured at low temperature for the dry powder, assuming the presence of van der Waals forces only.

In general, clear indications of a molten capillary phase come from the effects of system cooling, which may transform bridges from liquid to solid at interparticle contact surfaces. The result is a stronger bond between particles and, thus, a higher strength at the bulk level, as found in tensile testing experiments (Hurley and Dockter, 2003; Luan and You, 2015). Another coherent phenomenon is the observed shrinkage of the hot powder bed, which can be explained by the partial sintering of the particle surfaces in contact with the mobility of the molten phase (Kamyabi et al., 2017).

### 3.4 Effect of temperature on bulk flow properties in the presence of van der Waals forces

#### 3.4.1 Theoretical background

The intensity of van der Waal forces tends to be a few orders of magnitude smaller than capillary forces (e.g. $10^{-8}$, vs $10^{-6}$ N) and is more strongly dependent on the local contact geometry (Chirone et al., 2018), thus significantly changing from particle to particle. Perhaps, for this reason, no direct measurement of the effect of temperature on van der Waals forces is available, as reported in **Section 3.1** above.

Van der Waals forces, $F_{vdW}$, between spheres of radiuses $r_1$ and $r_2$ are well described by the following simple equation:

$$F_{vdWs} = \frac{A}{6a^2}\left(\frac{r_1 r_2}{r_1 + r_2}\right) = \frac{A}{12a^2} r \tag{13}$$

where $A$ is the Hamaker constant, $a$ is the shortest distance between the particle surfaces, and $r$ represents the average radius. For contacting spheres $a = a_0 = 4 \cdot 10^{-10}$ $m$, the conventional distance is assumed between atomic layers in crystals (Israelachvili, 2011). The short-range characteristics of van der Waals interactions allow the extension of **Eqn. (13)** to the shapes of real particles, assuming for $r_1$ and $r_2$ the local curvature radius of the particle surfaces at the contact point. However, in real particles, the surface at the contact point can deform due to the attraction force, eventually combined with external compaction forces. A simplified but comprehensive approach in the presence of a consolidation force, $F_N$, was proposed by Tomas (Tomas, 2004), who proposed a simple static force balance between the contacting particles, assuming that the attractive van

der Waals force is obtained by simply summing the contributions of the van der Waals force between the undeformed particles and the attractive force, $F_{vdWp}$, developed by the area of the flattened surface at the contact point:

$$F_N + F_{vdWs} + F_{vdWp} = F_{el} + F_{pla} \tag{14}$$

where $F_{el}$ and $F_{pla}$ are the repulsive force components due to the contact's elastic and plastic deformation, respectively. In particular, assuming a circular footprint of the contact area of radius $r_c$, it is

$$F_{vdWp} = \pi r_c^2 \frac{A}{6a_0^3} \tag{15}$$

**Eqn. (15)** is derived from the general expression for van der Waals interactions between two planar surfaces. The complete calculations for $F_{el}$ and $F_{pla}$ were given by Tomas (Tomas, 2004) and depended on the material elasticity and the limiting yield strength of the particle surface. Under tensile conditions, the minimum force $F_P = -F_N$ necessary to separate the particle (pull-off) can be obtained from **Eqn. (14)** under conditions in which the contribution of the repulsive forces is nil:

$$F_P = F_{vdWs} + F_{vdWp} \tag{16}$$

In this situation, the flattened portion of the contact is limited to the portion permanently deformed during consolation. The $F_{vdWp}$ and the $r_c$ values at consolidation and pull-off coincide only for purely plastically deformable particles with an equal curvature radius at contact $r$. In this case, the Molerus equation (Molerus, 1975) is obtained as follows:

$$F_P = \frac{A}{12a_0^2} r \frac{1+(2F_N/\pi p_f r a_0)}{1-(A/6\pi p_f a_0^3)} \tag{17}$$

where $p_f$ is the material yield strength in a confined situation, such as that in the contact region, which can be related to the material hardness. In the case of simple isometric particle shapes with relatively narrow and unimodal particle size distributions, a single contact point between neighbouring particles can be assumed, and the Rumpf equation can provide a reasonable relationship between interparticle forces and major principal stress or strength, as follows:

$$\sigma_1 = (1-\varepsilon)\frac{kF_N}{\pi d^2} \tag{18}$$

$$\sigma_t = (1-\varepsilon)\frac{kF_P}{\pi d^2} \tag{19}$$

The Hamaker constant is scarcely dependent on temperature changes within the proper ranges of chemical processes. Therefore, the effect of temperature on van der Waals forces is mostly related to changes in the material hardness with temperature. Lower material hardness corresponds to larger permanent deformations at the contacts, larger values of $F_{vdWp}$ at pull-off, and larger material cohesion, both in the case of purely plastic deformation and elastic–plastic deformations of contacts.

### 3.4.2 Experiments qualitatively supporting the theory

Quantitative verification of the above-described theory requires knowledge of several physical parameters such as the geometry and number of binary particle contacts, effective material hardness and elasticity at the contact points and test temperature, and their distribution in the powder sample. Therefore, the theory can often be used only for qualitatively interpreting the observed results of experiments in which the effect of temperature on tensile strength or shear testing is measured. Experiments are limited to systems in which cohesion is dominated by van der Waals forces, i.e., for materials that do not exhibit any liquid formation, such as calcium carbonate and silicon carbide powders and soda-lime glass beads. In these systems, it has been verified that temperature changes significantly combine with consolidation and particle size to determine changes in the directly measured tensile strength (Durán-Olivencia et al., 2020, 2021; Espin et al., 2020). At a consolidation stress of 2 kPa, the tensile strength showed a much greater increase (up to ten times for $CaCO_3$) for $T > 300$ °C compared with that at very low consolidation (1 kPa) (Durán-Olivencia et al., 2020). Regression of experimental results over a range of temperatures between ambient and 500 °C and at a low range of consolidation stresses between 0.37 and 2 kPa allowed the derivation of different empirical correlations of the tensile strength as a function of temperature and consolidation stress (Durán-Olivencia et al., 2020; 2021). Considering powders of the same material and different mean particle sizes, the same order of magnitude percentage increase in the tensile strength was observed at lower temperatures (Espin et al., 2020) with smaller particle sizes. Increases of different magnitudes of the tensile strength for different materials were justified with a changing effect of temperature on the material hardness: the larger the hardness reduction, the more significant was the necessary pull-off force at the particle level and, therefore, the larger was the tensile strength at high temperature (Durán-Olivencia et al., 2021). The intensity of the temperature effect was also qualitatively correlated with the glass transition temperature and the Tamman temperature for glassy and non-glassy materials, respectively. For example, for soda lime glass beads, approaching the glass transition temperature, a significant hardness reduction could occur, and the surface particle could undergo some "softening" corresponding to a larger pulling force for particles in contact.

In shear testing experiments, elevated temperature mainly affected powder cohesion, whereas changes in the angle of internal friction were generally negligible. The

increase of cohesion with increasing temperature resulted in a vertical shift of the yield locus, corresponding to a rise in the unconfined yield strength $f_c$ and of the extrapolated tensile strength $\sigma_t$, but to a much more limited extent in the major principal stress $\sigma_1$. Consequently, when a thermal effect was observed, the flow functions at higher temperatures shifted upward with respect to those at ambient temperature, and the flow factor $\sigma_1/f_c$ values increased. The effect of voidage changes due to temperature appeared to be much less significant in affecting interparticle forces and, thus, cohesive powder strength.

For ceramic powders, catalyst powders, and glass beads without low melting components, the increase in the unconfined yield strength was between 50 % and 100 % (Chirone et al., 2016; Macrì et al., 2017b; Tomasetta et al., 2013). The highest increase values were recorded at higher consolidation stress (Tomasetta et al., 2013) and for finer particles. The corresponding growth of the flow factor could shift the flowability class of the powder, especially when the flow function at ambient temperature lies close to the borders of neighbouring classes. For instance, this happened to the fine-cut 20–38 μm of silicon powders, resulting in an easy-flowing classification at ambient temperature while becoming cohesive at 500 °C (Chirone et al., 2016). A more substantial change in class of flowability was observed for zeolites passing gradually, with increasing temperature, from free-flowing at 150 °C to easy-flowing at 300 °C and to cohesive behaviour at 500 °C (Zinatlou Ajabshir et al., 2022) (**Fig. 2**). Thermal analysis excluded the occurrence of any melting in the powder sample.

In the literature, different explanations than those given at the beginning of this section are provided to justify the observed changes in the measured flow properties with temperature. Tensile strength experiments on complex materials, such as ashes, were coupled with X-ray diffractometry, Fourier transform infrared analysis (FTIR), field emission scanning electron microscopy (FESEM), and thermomechanical characterisation to deeply investigate the chemical composition and particle morphology changes with temperature. According to Horiguchi et al. (2022; 2021b), the increase in van der Waals forces was mainly due to the thermal expansion of particles, which may cause an increase in the interparticle contact area and a reduction in the distance between particles. Moreover, in some cases, temperature could change the molecular characteristics (e.g. the amount of free silanol group on silica) on the surface of the particles, which affects the intensity of the van der Waals forces (Kamiya et al., 2002b).

On the other hand, the presence of several additives, such as diatomite microparticles (Tsukada et al., 2008), alumina nanoparticles (Horiguchi et al., 2018), iron oxide ($Fe_3O_4$) microparticles (Horiguchi et al., 2021a), and kaolin and vermiculite microparticles (Liu et al., 2022), was demonstrated to decrease the tensile strength of ashes due to the increase of interparticle porosity or to prevent the generation of eutectic compounds. These findings indicate that a strategic choice of additives to coal can reduce the increase in cohesive strength at high temperatures due to the formation of a liquid phase.

### 3.4.3 Experiments quantitatively supporting the theory

Tomasetta et al. (2014) showed that the assumption of plastic deformation of the interparticle contact area due to the local consolidation force, according to Molerus (1975), was necessary to correctly predict the change in cohesive strength with consolidation stress under dry conditions. Chirone et al. (2016) demonstrated that the temperature effect on the intensity of van der Waals forces mainly depends on the increase in the interparticle contact area, which is determined by a decrease in the yield strength of the particle material with increasing temperature. Similar conclusions were drawn by Macrì et al. (2017b), who replaced the Molerus model with the Tomas equations (Tomas, 2000) for the interparticle adhesive forces in the framework of the Rumpf approach, and by Macrì et al. (2017a), who applied the Tomas model relating flow factors and angles of internal friction, derived from the yield locus, directly to the elastic–plastic contact consolidation coefficient (Tomas, 2004). More recently, this interpretation was also confirmed by Espin et al. (2020), who derived the relationship between microscopic consolidation force and adhesion force from data on consolidation stress and tensile strength experimentally measured using HTSPT.

Zinatlou Ajabshir et al. (2022) highlighted the role of the presence of fines for a zeolite powder with a wide particle size distribution in the definition of a more or less significant effect of temperature on flowability. This finding was explained with the Rumpf model corrected to consider the effect of a bimodal distribution with micrometric-sized core host particles coated by smaller satellite or guest particles in the form of agglomerates. The satellite particles act as spacers between the core particles and define the actual geometry and distribution of the interparticle contacts. In particular, for these powders, a key role is played by the increased number of active contacts between two neighbouring agglomerates. Therefore, the more cohesive powder resulted in the one with smaller satellites, which ensured a higher number of active contacts between particles. Even if singularly taken at the satellite level, the consolidation forces and the cohesion forces are relatively small. Instead, the material with a more limited number of larger satellite particles in the agglomerate showed better flow properties for the limited number of contacts between adjacent agglomerates. However, both the contact force and consolidation forces calculated for the contact points between satellite particles were larger than those in the other powder and, likely, more affected by contact

**Table 3** Overview of case studies on the effect of temperature on powder strength, friction, and cohesion (chronological order). (Continued on next page)

| References | Temp. (°C) | Powders/Tester/Properties | Main results |
|---|---|---|---|
| (Smith et al., 1997) | 22, 750 | $CaSO_4$, $MgSO_4$, alone and mixtures/Jenike ST/FF | Increase in the UYS at higher temperatures. |
| (Kanaoka et al., 2001) | 20–950 | Coal fly ashes/Heated translational ST/YL | Increase in cohesion beyond a critical temperature value depending on the lime content in the ashes and on the gas component exposition ($N_2$ or $CO_2$) due to solid bridges (sintering). |
| (Kamiya et al., 2002b) | 25–850 | Silica and fly ashes/Heated split-cell TS tester/TS | Moderate increase of TS up to 1000 K, sharp increase at higher temperatures. |
| (Kamiya et al., 2002a) | 25–850 | Silica coated with alkali metals/Heated split-cell TS tester/TS | Melting of alkali metals causes a dramatic increase in TS for $T > 700$ °C. |
| (Hurley and Dockter, 2003) | 700–750 | Combustion gas filter dust/Heated split-cell TS tester/TS | The ratio between TS and the density of the ashes cake on the hot gas filter is presented as a key parameter. |
| (Tsukada et al., 2003) | 25–900 | Biomass combustion ashes/Heated split-cell TS tester/TS | TS increases from 400 to 700 °C due to liquid phase formation, while it decreases above 700 °C due to liquid evaporation. |
| (Hurley et al., 2006) | 300–800 | Combustion gas filter dust/Heated split-cell TS tester/TS | TS increase depends on the temperature and pressure drop across the filter, acting as a consolidation stress. The higher strength increase is due to partial melting. Role of the reactions at intermediate temperatures. |
| (Tsukada et al., 2008) | 20–600 | Fly ashes with additives/Heated split-cell TS tester/TS | Addition of 100 µm diatomite and silica sand particles reduces TS at $T > 700$ °C, while water-quenched molten slag particles with aluminium increase it. |
| (Zimmerlin et al., 2008) | | Soda-lime glass, gypsum, sodium chloride, potassium chloride/High temperature rheometer/Torque | Torque increases above 400–450 °C. The component mixture reproduces the ashes' behaviour with temperature. |
| (Ripp and Ripperger, 2010) | –78–220 | Polyester granulates, lactose, ground coffee, polyphosphates, cocoa powder, dry ice/Modified Schulze RST/YL, FF | Different temperature effects depending on the material. |
| (Tomasetta et al., 2013) | 25, 500 | Fluid cracking catalysts, Fly ashes, Corundum, Synthetic α-alumina, Glass beads, Mix of glass beads and 1 % HDPE/HT-ASC/YL, FF | Very limited effect of temperature on flow properties, except for glass beads with 1 % HDPE exhibiting a significant increase in cohesion at 500 °C. |
| (Maarup et al., 2014) | 22–850 | Cement raw meal/Translational ST in a muffle/UYS | UYS increases above 550 °C. |
| (Luan et al., 2015) | 750–1250 | Ashes/High-temperature solid bridge force device (HTSBFD)/TS | Significant increase in TS above 1150 °C. TS is correlated with the solid bridge force. |
| (Shao et al., 2016) | 25–800 | Biomass combustion ashes/Heated split-cell TS tester/TS | DEM model predictions compared with the experiments. |
| (Chirone et al., 2016) | 25, 500 | Ceramic powders/HT-ASC/YL, FF | A simplified experimental procedure allows quicker preliminary detection of the critical temperature for flowability change. Temperature mainly affects cohesion, whereas the AIF results remain independent of temperature. A proposed model links interparticle forces to TS. |
| (Macrì et al., 2017a, b) | 25, 500 | Titanium dioxide synthetic rutile and natural rutile/HT-ASC/YL, FF | More significant decrease in flowability at 500 °C for synthetic rutile. Proposed model linking interparticle forces to TS. |

**Table 3** Overview of case studies on the effect of temperature on powder strength, friction, and cohesion (chronological order). (Continued from previous page)

| References | Temp. (°C) | Powders/Tester/Properties | Main results |
|---|---|---|---|
| (Chirone et al., 2018) | 25, 500 | Ceramic powders/HT-ASC/YL, FF | The presence of low-melting impurities determines a significant reduction in flowability with temperature. A proposed model aims to link capillary forces and TS. |
| (Horiguchi et al., 2018) | 25–900 | Fly ashes with alumina additives/Heated split-cell TS tester/TS | The addition of alumina nanoparticles reduces the increase in TS of ashes due to their positive effect on porosity and chemical composition. |
| (Liu et al., 2018) | 25, 500 | Fly ashes/HT-ASC/YL, FF | Moderate decrease in flowability at 500 °C. A proposed model links interparticle forces to TS considering PSD. |
| (Espin et al., 2020) | 25–500 | Limestone/HTSPT/TS | The increase in TS with temperature is more significant for finer powders. |
| (Ruggi et al., 2020a, b) | 25–160 | Polyamide 12 and 6/HT-ASC/YL, FF | Dramatic increase in UYS at temperatures approaching the melting point. The Bond number provides a qualitative correlation with spreading behaviour. |
| (Durán-Olivencia et al., 2020) | 25–500 | Calcium carbonate/HTSPT/TS | TS increases above 200 °C, and is more pronounced at consolidation stress > 1 kPa due to softening caused by hardness reduction. |
| (Durán-Olivencia et al., 2021) | 25–500 | Soda-lime glass beads, silicon carbide, limestone/HTSPT/TS | TS increases with temperature for all materials, emphasizing the temperature dependence of material hardness. |
| (Horiguchi et al., 2021a) | 25–800 | Synthetic ashes/Heated split-cell TS tester/TS | Phosphorus leads to a marked increase in the adhesiveness of synthetic ashes at temperatures > 600 °C, whereas the presence of $Fe_3O_4$ reduces the strength, withparticular relevance to ashes from incinerated sewage sludge. |
| (Horiguchi et al., 2021b) | 25–500 | Calcium carbonate, alumina, silica/Heated split-cell TS tester/TS | Temperature affects the TS of $CaCO_3$ at $T$ > 500 °C, with negligible effect on alumina and silica microparticle. The addition of alumina to calcium carbonate hinders the temperature effect on strength. |
| (Horiguchi et al., 2022) | 25–900 | Silica, kaolin, calcium carbonate, alumina/Heated split-cell TS tester/TS | The addition of calcium carbonate nanoparticles to kaolin powder at 900 °C increases TS. However, this effect is not observed when added to silica powder. The presence of alumina in mixtures suppresses the strength increase with temperature. |
| (Liu et al., 2022) | 800–1200 | High calcium coal ash powders/High-temperature TS tester/TS | Tensile strength increases above 800 °C, with a steep rise at 1100 °C. Additives with a low-temperature eutectic enhance the ash TS. |
| (Zinatlou Ajabshir et al., 2022) | 150, 300, 500 | Zeolite/Anton Paar shear cell/YL, FF | Flowability decreases with temperature, and the more significant effect on one sample is theoretically explained by the different PSDs. |

plasticisation, resulting in a larger temperature effect on the flowability of this material.

Macrì et al. (2017a) and Zinatlou Ajabshir et al. (2022) provided quantitative evidence that the most relevant material property related to the effect of temperature on the change in van der Waals interparticle forces is the hardness of the particle material.

Ruggi et al. (2020b) estimated the interparticle force for some polyamide powders used in additive manufacturing, exhibiting a change in flowability class from easy flowing to very cohesive when the temperature increased to values close to their melting point. These authors found that the ratio between the granular Bond number value close to the melting temperature and that at 100 °C under dry conditions was greater than 100.

**Table 3** reports a detailed survey of the studies on the effect of temperature.

## 4. Conclusions and perspectives

Process conditions inducing the presence of liquid in the interparticle volume due to either liquid addition, partial melting of solids, or capillary condensation from a humid gas atmosphere give rise to capillary bridges and capillary forces. The intensity of the forces depends on the liquid

saturation level. The resulting cohesive strength of a powder, free flowing or easy flowing under dry conditions, can increase when liquid bridges are in the pendular regime until the achievement of a plateau value. Then, for the funicular regime, the strength continues to grow. Pendular and funicular regimes typically correspond to liquid contents between 1 % and 15 % or between 15 % and 40 %, respectively, assuming a specific gravity of approximately 1.5. Only in the capillary regime is a dramatic decrease in cohesive strength observed due to the dominant reduction of capillary pressure. Instead, for a powder exhibiting cohesion due to van der Waals forces, a limited amount of liquid can initially reduce the strength, but the previously described trend is recovered by further increasing the liquid content.

Temperature rise above 100 °C under atmospheric conditions can dry the moisture eventually present between particles in bulk. Vanishing of capillary forces makes the powder less cohesive because of the lower intensity of van der Waals forces. Further temperature rise can strengthen these interactions due to the enhancement of plastic deformation at interparticle contacts, especially for high consolidation stress due to reduced particle material hardness. The consequent flattening of the contact and increase of the contact area is the main cause of the rise in van der Waals forces and of the reduction of powder flowability, which in general is limited to a shift from one class to the adjacent one (e.g. from free flowing to easy flowing, from easy flowing to cohesive). Low melting components or thermally activated reactions generating a liquid phase can determine the onset of capillary forces at critical temperatures, dramatically affecting powder flowability, which can change from free-flowing to cohesive behaviour. The significant influence of liquid content, humidity, and temperature on interparticle forces and bulk flow properties can explain the change in powder behaviour in units with peculiar process conditions. In fact, it was possible to qualitatively relate the increase in cohesive flow properties at low consolidation and the fluidisation behaviour, in terms of minimum velocity for fluidisation and bed expansion, due to the higher temperature effect on van der Waals forces (Chirone et al., 2020; Macrì et al., 2020). A direct link between interparticle forces and fluidisation properties was also demonstrated for the effect of environmental relative humidity (LaMarche et al., 2016).

Although general phenomenology has been explained qualitatively and quantitatively for various materials and different process conditions, the variability in particle shape, material composition, physical state, and temperature change of all relevant material properties in real systems make it challenging to theoretically predict the effect of a liquid phase or temperature. In fact, this requires a detailed characterisation of the surface morphological properties of particles (i.e. roughness and asperities size), which can be affected by wide distributions in real samples of industrial processes. Moreover, theoretical equations linking microscale forces and macroscale stresses, such as the Rumpf equation, could be affected by a certain degree of uncertainty in the case of non-ideal particles. Developing a completely predictive model is even more challenging in the case of low-melting impurities or chemical reactions activated by heating. As a result, direct characterisation of the flow properties of powder samples under conditions reproducing those of process units appears to be the main method for quantitative purposes. In this respect, conditioning a powder sample by adding liquid or exposure to humid air before performing any type of flow property test (e.g. tensile tester or shear tester) requires particular care to obtain uniform and stable liquid distribution in the specimen. This latter issue might be overcome in the near future by the use of purposely generated and calibrated discrete element method (DEM) models. However, the right way to proceed would require dedicated studies that are yet to be conducted.

As widely discussed in this review, suitable testers with reliable temperature control are presently available in the academic community to directly measure flow properties at high temperatures. However, nowadays, only one commercial instrument is known to reach temperatures up to 600 °C. Other instruments will likely come in the future to address wider needs. In particular, it might be of great scientific and industrial interest because of the possibility of reaching temperatures around 1000 °C, which is typical of several thermal and solar applications.

## Acknowledgments

Sina Zinatlou Ajabshir research grant and part of the research were supported by MATHEGRAM, a Marie Sklodowska-Curie Innovative training network MATHEGRAM funded through the People Programme (Marie Sklodowska-Curie Actions) of the European Union's Horizon 2020 Programme H2020 under REA grant agreement No. 813202.

## Nomenclature

| | |
|---|---|
| AIF | angle of internal friction |
| AOR | angle of repose |
| FF | flow function |
| HR | Hausner ratio |
| HT-ASC | high-temperature annular shear cell |
| HTSPT | high-temperature Sevilla powder tester |
| MPT | Micron powder tester |
| PSD | particle size distribution |
| RST | ring shear tester |
| ST | shear tester |
| TS | tensile strength |
| UYS | unconfined yield strength |
| YL | yield loci |
| $a$ | closest distance between particles (m) |
| $A$ | Hamaker constant (J) |

| | |
|---|---|
| $a'$ | constant in **Eqn. (6)** (-) |
| $a_0$ | minimum distance at contact (m) |
| $c$ | cohesion (Pa) |
| $d$ | mean particle size (m) |
| $f_c$ | unconfined yield strength (Pa) |
| $F_c$ | capillary force (N) |
| $F_{el}$ | elastic deformation repulsion force (N) |
| $F_N$ | contact consolidation force (N) |
| $F_p$ | pressure force (N) |
| $F_{pla}$ | plastic deformation repulsion force (N) |
| $F_s$ | surface tension force (N) |
| $F_{vdWp}$ | van der Waals force for a flat surface (N) |
| $F_{vdWs}$ | van der Waals force for a sphere or spherical contact (N) |
| $ff_c$ | flow factor (-) |
| $k$ | coordination number (-) |
| $K$ | constant in **Eqn. (9)** (-) |
| $M_W$ | molecular weight of water (kg/mol) |
| $P_c$ | capillary pressure (Pa) |
| $p_f$ | material hardness (Pa) |
| $p_s$ | vapour pressure over a curved surface (Pa) |
| $p_{s0}$ | vapour pressure of the liquid (Pa) |
| $r$ | characteristic curvature radius of the particle surface at contact (m) |
| $r_1$; $r_2$ | radii of particles 1 and 2 (m) |
| $R_1$ | liquid bridge convex curvature radius (m) |
| $R_2$ | liquid bridge concave curvature radius (m) |
| $r_c$ | radius of the flattened surface at contact (m) |
| $R_g$ | universal gas constant (J $K^{-1}$ $mol^{-1}$) |
| $RH$ | relative humidity (-) |
| $S$ | liquid saturation (-) |
| $S_1$ | critical liquid saturation between the pendular and funicular states (-) |
| $S_2$ | critical liquid saturation between the funicular and capillary states (-) |
| $T$ | temperature (K) |
| $x_w$ | liquid content by mass on a dry basis (-) |
| $\gamma$ | liquid surface tension (N/m) |
| $\delta_0$ | characteristic roughness (m) |
| $\varepsilon$ | powder bed voidage (-) |
| $\theta$ | liquid bridge contact angle (deg) |
| $\Delta p$ | pressure difference between air and liquid (Pa) |
| $\rho_l$ | liquid density (kg/$m^3$) |
| $\rho_s$ | particle density (kg/$m^3$) |
| $\sigma$ | normal stress (Pa) |
| $\sigma_1$ | major principal stress (Pa) |
| $\sigma_2$ | minor principal stress (Pa) |
| $\sigma_t$ | tensile strength (Pa) |
| $\sigma_{tc}$ | tensile strength in the capillary regime (Pa) |
| $\sigma_{tp}$ | tensile strength in the pendular regime (Pa) |
| $\tau$ | shear stress (Pa) |
| $\phi$ | static angle of internal friction (deg) |

## References


Althaus T.O., Windhab E.J., Characterization of wet powder flowability by shear cell measurements and compaction curves, Powder Technology, 215–216 (2012) 59–65. https://doi.org/10.1016/j.powtec.2011.09.007

Althaus T.O., Windhab E.J., Scheuble N., Effect of pendular liquid bridges on the flow behavior of wet powders, Powder Technology, 217 (2012) 599–606. https://doi.org/10.1016/j.powtec.2011.11.026

Badetti M., Fall A., Hautemayou D., Chevoir F., Aimedieu P., Rodts S., Roux J.-N., Rheology and microstructure of unsaturated wet granular materials: experiments and simulations, Journal of Rheology, 62 (2018) 1175–1186. https://doi.org/10.1122/1.5026979

Barletta D., Poletto M., Santomaso A.C., Chapter 4. bulk powder flow characterisation techniques, in: Hare C., Hassanpour A., Pasha M. (Eds.), Powder Flow, Royal Society of Chemistry, Cambridge, UK, 2019, pp. 64–146, ISBN: 978-1-78801-224-9. https://doi.org/10.1039/9781788016100-00064

Bocquet L., Charlaix E., Ciliberto S., Crassous J., Moisture-induced ageing in granular media and the kinetics of capillary condensation, Nature, 396 (1998) 735–737. https://doi.org/10.1038/25492

Butt H.J., Capillary forces: influence of roughness and heterogeneity, Langmuir, 24 (2008) 4715–4721. https://doi.org/10.1021/la703640f

Butt H.-J., Kappl M., Normal capillary forces, Advances in Colloid and Interface Science, 146 (2009) 48–60. https://doi.org/10.1016/j.cis.2008.10.002

Capece M., Ho R., Strong J., Gao P., Prediction of powder flow performance using a multi-component granular Bond number, Powder Technology, 286 (2015) 561–571. https://doi.org/10.1016/j.powtec.2015.08.031

Capece M., Silva K.R., Sunkara D., Strong J., Gao P., On the relationship of inter-particle cohesiveness and bulk powder behavior: flowability of pharmaceutical powders, International Journal of Pharmaceutics, 511 (2016) 178–189. https://doi.org/10.1016/j.ijpharm.2016.06.059

Castellanos A., The relationship between attractive interparticle forces and bulk behaviour in dry and uncharged fine powders, Advances in Physics, 54 (2005) 263–376. https://doi.org/10.1080/17461390500402657

Chen W., Roberts A.W., A modified flowability classification model for moist and cohesive bulk solids, Powder Technology, 325 (2018) 639–650. https://doi.org/10.1016/j.powtec.2017.11.054

Chirone R., Barletta D., Lettieri P., Poletto M., Bulk flow properties of sieved samples of a ceramic powder at ambient and high temperature, Powder Technology, 288 (2016) 379–387. https://doi.org/10.1016/j.powtec.2015.11.040

Chirone R., Barletta D., Poletto M., Lettieri P., Detection and estimation of capillary interparticle forces in the material of a fluidized bed reactor at high temperature by powder flow characterization, Powder Technology, 330 (2018) 371–385. https://doi.org/10.1016/j.powtec.2018.02.024

Chirone R., Poletto M., Barletta D., Lettieri P., The effect of temperature on the minimum fluidization conditions of industrial cohesive particles, Powder Technology, 362 (2020) 307–322. https://doi.org/10.1016/j.powtec.2019.11.102

Coelho M.C., Harnby N., Moisture bonding in powders, Powder Technology, 20 (1978a) 201–205. https://doi.org/10.1016/0032-5910(78)80049-7

Coelho M.C., Harnby N., The effect of humidity on the form of water retention in a powder, Powder Technology, 20 (1978b) 197–200. https://doi.org/10.1016/0032-5910(78)80048-5

Cordova L., Bor T., de Smit M., Campos M., Tinga T., Measuring the spreadability of pre-treated and moisturized powders for laser powder bed fusion, Additive Manufacturing, 32 (2020) 101082. https://doi.org/10.1016/j.addma.2020.101082

Coughlin R.., Elbirli B., Vergara-Edwards L., Interparticle force conferred by capillary-condensed liquid at contact points, Journal of Colloid and Interface Science, 87 (1982) 18–30. https://doi.org/10.1016/0021-9797(82)90368-X

Durán-Olivencia F.J., Ebri J.M.P., Espín M.J., Valverde J.M., The cohesive behavior of granular solids at high temperature in solar energy storage, Energy Conversion and Management, 240 (2021) 114217. https://doi.org/10.1016/j.enconman.2021.114217

Durán-Olivencia F.J., Espín M.J., Valverde J.M., Cross effect between temperature and consolidation on the flow behavior of granular materials in thermal energy storage systems, Powder Technology, 363 (2020) 135–145. https://doi.org/10.1016/j.powtec.2019.11.125

Durán-Olivencia F.J., Gannoun R., Pérez A.T., Valverde J.M., Efficacy of nanosilica coatings in calcium looping reactors, Industrial & Engineering Chemistry Research, 62 (2023) 1373–1389. https://doi.org/10.1021/acs.iecr.2c03490

Eaves T., Jones T.M., Effect of moisture on tensile strength of bulk solids i: sodium chloride and effect of particle size, Journal of

Pharmaceutical Sciences, 61 (1972a) 256–261. https://doi.org/10.1002/jps.2600610226
Eaves T., Jones T.M., Effect of moisture on tensile strength of bulk solids ii: fine particle-size materials with varying inherent coherence, Journal of Pharmaceutical Sciences, 61 (1972b) 342–348. https://doi.org/10.1002/jps.2600610304
Elbirli B., Vergara-Edwards L., Coughlin R.W., Interparticle force conferred by capillary-condensed liquid at contact points, Journal of Colloid and Interface Science, 87 (1982) 31–45. https://doi.org/10.1016/0021-9797(82)90369-1
Emery E., Oliver J., Pugsley T., Sharma J., Zhou J., Flowability of moist pharmaceutical powders, Powder Technology, 189 (2009) 409–415. https://doi.org/10.1016/j.powtec.2008.06.017
Espin M.J., Duran-Olivencia F.J., Valverde J.M., Role of particle size on the cohesive behavior of limestone powders at high temperature, Chemical Engineering Journal, 391 (2020) 123520. https://doi.org/10.1016/j.cej.2019.123520
Francia V., Ait Ali Yahia L., Ocone R., Ozel A., From quasi-static to intermediate regimes in shear cell devices: theory and characterisation, KONA Powder and Particle Journal, 38 (2021) 3–25. https://doi.org/10.14356/kona.2021018
Gannoun R., Ebrí J.M.P., Pérez A.T., Valverde J.M., The Sevilla powder tester: a tool for measuring the flow properties of cohesive powders at high temperatures, KONA Powder and Particle Journal, 39 (2022) 29–44. https://doi.org/10.14356/kona.2022008
Ghadiri M., Pasha Mehrdad, Nan W., Hare C., Vivacqua V., Zafar U., Nezamabadi S., Lopez A., Pasha Massih, Nadimi S., Cohesive powder flow: trends and challenges in characterisation and analysis, KONA Powder and Particle Journal, 37 (2020) 3–18. https://doi.org/10.14356/kona.2020018
Groen J.C., Kooijman W., van Belzen D., Meesters G.M.H., Schütz D., Aschl T., Verolme P., Real-time in-situ rheological assessment of sticky point temperature and humidity of powdered products, KONA Powder and Particle Journal, 37 (2020) 176–186. https://doi.org/10.14356/kona.2020006
Gyulai A., Bauer W., Ehrenberg H., Dry electrode manufacturing in a calender: the role of powder premixing for electrode quality and electrochemical performance, ACS Applied Energy Materials, 6 (2023) 5122–5134. https://doi.org/10.1021/acsaem.2c03755
Haider C.I., Althaus T., Niederreiter G., Hounslow M.J., Palzer S., Salman A.D., A micromanipulation particle tester for agglomeration contact mechanism studies in a controlled environment, Measurement Science and Technology, 23 (2012) 105904. https://doi.org/10.1088/0957-0233/23/10/105904
Harnby N., Hawkins A.E., Vandame D., The use of bulk density determination as a means of typifying the flow characteristics of loosely compacted powders under conditions of variable relative humidity, Chemical Engineering Science, 42 (1987) 879–888. https://doi.org/10.1016/0009-2509(87)80046-5
Horiguchi G., Fujii R., Yamauchi Y., Okabe H., Tsukada M., Okada Y., Kamiya H., Toward stable operation of coal combustion plants: the use of alumina nanoparticles to prevent adhesion of fly ash, Energy & Fuels, 32 (2018) 13015–13020. https://doi.org/10.1021/acs.energyfuels.8b03043
Horiguchi G., Fujimoto T., Yoshinaga K., Okada Y., Kamiya H., Particle adhesion induced by calcium carbonate nanoparticles at 900 °C, Powder Technology, 405 (2022) 117514. https://doi.org/10.1016/j.powtec.2022.117514
Horiguchi G., Ito M., Ito A., Kamiya H., Okada Y., Role of phosphorus and iron in particle adhesiveness at high temperatures using synthetic ashes, ACS Sustainable Chemistry & Engineering, 9 (2021a) 15315–15321. https://doi.org/10.1021/acssuschemeng.1c05676
Horiguchi G., Kamiya H., García-Triñanes P., Evaluation and control of the adhesiveness of cohesive calcium carbonate particles at high temperatures, Advanced Powder Technology, 32 (2021b) 283–289. https://doi.org/10.1016/j.apt.2020.12.009
Hurley J.P., Dockter B.A., Factors affecting the tensile strength of hot-gas filter dust cakes, Advanced Powder Technology, 14 (2003) 695–705. https://doi.org/10.1163/15685520360731981
Hurley J.P., Mukherjee B., Mann M.D., Assessment of filter dust characteristics that cause filter failure during hot-gas filtration, Energy & Fuels, 20 (2006) 1629–1638. https://doi.org/10.1021/ef050303k
Israelachvili J.N., Intermolecular and Surface Forces, third edition, Academic Press, 2011, ISBN: 978-0-12-375182-9. https://doi.org/10.1016/C2009-0-21560-1
Jallo L.J., Ghoroi C., Gurumurthy L., Patel U., Davé R.N., Improvement of flow and bulk density of pharmaceutical powders using surface modification, International Journal of Pharmaceutics, 423 (2012) 213–225. https://doi.org/10.1016/j.ijpharm.2011.12.012
Jenike A.W., Storage and flow of solids, Bulletin No. 123, Bulletin of the University of Utah, 53 (1964) 56–56. <https://digital.library.unt.edu/ark:/67531/metadc1067072/> accessed28122023.
Johanson K., Rabinovich Y., Moudgil B., Breece K., Taylor H., Relationship between particle scale capillary forces and bulk unconfined yield strength, Powder Technology, 138 (2003) 13–17. https://doi.org/10.1016/j.powtec.2003.08.037
Kamiya H., Kimura A., Tsukada M., Naito M., Analysis of the high-temperature cohesion behavior of ash particles using pure silica powders coated with alkali metals, Energy & Fuels, 16 (2002a) 457–461. https://doi.org/10.1021/ef0102081
Kamiya H., Kimura A., Yokoyama T., Naito M., Jimbo G., Development of a split-type tensile-strength tester and analysis of mechanism of increase of adhesion behavior of inorganic fine powder bed at high-temperature conditions, Powder Technology, 127 (2002b) 239–245. https://doi.org/10.1016/S0032-5910(02)00117-1
Kamyabi M., Sotudeh-Gharebagh R., Zarghami R., Saleh K., Principles of viscous sintering in amorphous powders: a critical review, Chemical Engineering Research and Design, 125 (2017) 328–347. https://doi.org/10.1016/j.cherd.2017.06.009
Kanaoka C., Hata M., Makino H., Measurement of adhesive force of coal flyash particles at high temperatures and different gas compositions, Powder Technology, 118 (2001) 107–112. https://doi.org/10.1016/S0032-5910(01)00300-x
Karde V., Dixit D., Ghoroi C., Adhesion force approximation at varying consolidation stresses for fine powder under humid conditions, Advanced Powder Technology, 28 (2017) 346–355. https://doi.org/10.1016/j.apt.2016.09.023
Karde V., Ghoroi C., Fine powder flow under humid environmental conditions from the perspective of surface energy, International Journal of Pharmaceutics, 485 (2015) 192–201. https://doi.org/10.1016/j.ijpharm.2015.03.021
Kartik S., Balsora H.K., Sharma M., Saptoro A., Jain R.K., Joshi J.B., Sharma A., Valorization of plastic wastes for production of fuels and value-added chemicals through pyrolysis – a review, Thermal Science and Engineering Progress, 32 (2022) 101316. https://doi.org/10.1016/j.tsep.2022.101316
Kohonen M.M., Geromichalos D., Scheel M., Schier C., Herminghaus S., On capillary bridges in wet granular materials, Physica A: Statistical Mechanics and its Applications, 339 (2004) 7–15. https://doi.org/10.1016/j.physa.2004.03.047
LaMarche C.Q., Miller A.W., Liu P., Hrenya C.M., Linking micro-scale predictions of capillary forces to macro-scale fluidization experiments in humid environments, AIChE Journal, 62 (2016) 3585–3597. https://doi.org/10.1002/aic.15281
Landi G., Barletta D., Lettieri P., Poletto M., Flow properties of moisturized powders in a Couette fluidized bed rheometer, International Journal of Chemical Reactor Engineering, 10 (2012) A28. https://doi.org/10.1515/1542-6580.2993
Landi G., Barletta D., Poletto M., Modelling and experiments on the effect of air humidity on the flow properties of glass powders, Powder Technology, 207 (2011) 437–443. https://doi.org/10.1016/j.powtec.2010.11.033
Liu Y., Lu H., Barletta D., Poletto M., Guo X., Gong X., Jin Y., Bulk flow properties of fly ashes at ambient and high temperature, Particuology, 38 (2018) 113–125. https://doi.org/10.1016/j.partic.2017.04.013
Liu Z., Jin J., Zheng L., Zhang R., Wang Y., He X., Kong S., Zhai Z., Controlling the ash adhesion strength of Zhundong high-calcium coal by additives at high temperature, Fuel, 323 (2022) 124342. https://doi.org/10.1016/j.fuel.2022.124342
Louati H., Oulahna D., de Ryck A., Effect of the particle size and the

liquid content on the shear behaviour of wet granular material, Powder Technology, 315 (2017) 398–409. https://doi.org/10.1016/j.powtec.2017.04.030

Lu H., Guo X., Jin Y., Gong X., Effect of moisture on flowability of pulverized coal, Chemical Engineering Research and Design, 133 (2018) 326–334. https://doi.org/10.1016/j.cherd.2018.03.023

Lu X.-Y., Chen L., Wu C.-Y., Chan H.-K., Freeman T., The effects of relative humidity on the flowability and dispersion performance of lactose mixtures, Materials, 10 (2017) 592. https://doi.org/10.3390/ma10060592

Luan C., You C., A novel experimental investigation into sintered neck tensile strength of ash at high temperatures, Powder Technology, 269 (2015) 379–384. https://doi.org/10.1016/j.powtec.2014.09.031

Lumay G., Traina K., Boschini F., Delaval V., Rescaglio A., Cloots R., Vandewalle N., Effect of relative air humidity on the flowability of lactose powders, Journal of Drug Delivery Science and Technology, 35 (2016) 207–212. https://doi.org/10.1016/j.jddst.2016.04.007

Maarup C., Hjuler K., Dam-Johansen K., High temperature cement raw meal flowability, Powder Technology, 253 (2014) 686–690. https://doi.org/10.1016/j.powtec.2013.12.040

Macrì D., Barletta D., Lettieri P., Poletto M., Experimental and theoretical analysis of $TiO_2$ powders flow properties at ambient and high temperatures, Chemical Engineering Science, 167 (2017a) 172–190. https://doi.org/10.1016/j.ces.2017.03.057

Macrì D., Poletto M., Barletta D., Lettieri P., An investigation of the flow properties of rutile particles: fluidization behaviour linked with shearing studies, Powder Technology, 374 (2020) 544–559. https://doi.org/10.1016/j.powtec.2020.07.082

Macrì D., Poletto M., Barletta D., Sutcliffe S., Lettieri P., Analysis of industrial reactive powders flow properties at high temperature, Powder Technology, 316 (2017b) 131–138. https://doi.org/10.1016/j.powtec.2016.10.064

Marchetti L., Mellin P., Neil Hulme C., Negative impact of humidity on the flowability of steel powders, Particulate Science and Technology, 40 (2022) 722–736. https://doi.org/10.1080/02726351.2021.1995091

Molerus O., Theory of yield of cohesive powders, Powder Technology, 12 (1975) 259–275. https://doi.org/10.1016/0032-5910(75)85025-X

Mort P., Michaels J.N., Behringer R.P., Campbell C.S., Kondic L., Kheiripour Langroudi M., Shattuck M., Tang J., Tardos G.I., Wassgren C., Dense granular flow—a collaborative study, Powder Technology, 284 (2015) 571–584. https://doi.org/10.1016/J.POWTEC.2015.06.006

Orband J.L.R., Geldart D., Direct measurement of powder cohesion using a torsional device, Powder Technology, 92 (1997) 25–33. https://doi.org/10.1016/S0032-5910(97)03212-9

Pagliai P., Simons S.J.R., Rhodes D., Towards a fundamental understanding of defluidisation at high temperatures: a micro-mechanistic approach, Powder Technology, 148 (2004) 106–112. https://doi.org/10.1016/j.powtec.2004.09.004

Pierrat P., Agrawal D.K., Caram H.S., Effect of moisture on the yield locus of granular materials: theory of shift, Powder Technology, 99 (1998) 220–227. https://doi.org/10.1016/S0032-5910(98)00111-9

Pierrat P., Caram H.S., Tensile strength of wet granular materials, Powder Technology, 91 (1997a) 83–93. https://doi.org/10.1016/S0032-5910(96)03179-8

Pierrat P., Caram H.S., Tensile strength of wet granula materials, Powder Technology, 91 (1997b) 83–93. https://doi.org/10.1016/S0032-5910(96)03179-8

Pietsch W., Hoffman E., Rumpf H., Tensile strength of moist agglomerates, Industrial & Engineering Chemistry Product Research & Development, 8 (1969) 58–62. https://doi.org/10.1021/i360029a009

Pietsch W., Rumpf H., Haftkraft, kapillardruck, flüssigkeitsvolumen und grenzwinkel einer flüssigkeitsbrücke zwischen zwei kugeln, Chemie Ingenieur Technik, 39 (1967) 885–893. https://doi.org/10.1002/cite.330391502

Pietsch W.B., Tensile strength of granular materials, Nature, 217 (1968) 736–737. https://doi.org/10.1038/217736a0

Price R., Young P.M., Edge S., Staniforth J.N., The influence of relative humidity on particulate interactions in carrier-based dry powder inhaler formulations, International Journal of Pharmaceutics, 246 (2002) 47–59. https://doi.org/10.1016/S0378-5173(02)00359-9

Rabinovich Y.I., Adler J.J., Ata A., Singh R.K., Moudgil B.M., Adhesion between nanoscale rough surfaces: ii. measurement and comparison with theory, Journal of Colloid and Interface Science, 232 (2000a) 17–24. https://doi.org/10.1006/jcis.2000.7168

Rabinovich Y.I., Adler J.J., Ata A., Singh R.K., Moudgil B.M., Adhesion between nanoscale rough surfaces: i. role of asperity geometry, Journal of Colloid and Interface Science, 232 (2000b) 10–16. https://doi.org/10.1006/jcis.2000.7167

Rabinovich Y.I., Adler J.J., Esayanur M.S., Ata A., Singh R.K., Moudgil B.M., Capillary forces between surfaces with nanoscale roughness, Advances in Colloid and Interface Science, 96 (2002) 213–230. https://doi.org/10.1016/S0001-8686(01)00082-3

Richefeu V., El Youssoufi M.S., Radjaï F., Shear strength properties of wet granular materials, Physical Review E, 73 (2006) 051304. https://doi.org/10.1103/PhysRevE.73.051304

Ripp M., Ripperger S., Influence of temperature on the flow properties of bulk solids, Chemical Engineering Science, 65 (2010) 4007–4013. https://doi.org/10.1016/j.ces.2010.03.046

Ruggi D., Barrès C., Charmeau J.-Y., Fulchiron R., Barletta D., Poletto M., A quantitative approach to assess high temperature flow properties of a PA 12 powder for laser sintering, Additive Manufacturing, 33 (2020a) 101143. https://doi.org/10.1016/j.addma.2020.101143

Ruggi D., Lupo M., Sofia D., Barrès C., Barletta D., Poletto M., Flow properties of polymeric powders for selective laser sintering, Powder Technology, 370 (2020b) 288–297. https://doi.org/10.1016/j.powtec.2020.05.069

Rumpf H., The strength of granules and agglomerates, in: Knepper W.A. (ed.), Agglomeration, Wiley, New York, 1962, pp. 379–418.

Salehi H., Karde V., Hajmohammadi H., Dissanayake S., Larsson S.H., Heng J.Y.Y., Bradley M., Understanding flow properties of mannitol powder at a range of temperature and humidity, International Journal of Pharmaceutics, 596 (2021) 120244. https://doi.org/10.1016/j.ijpharm.2021.120244

Schubert H., Capillary forces - modeling and application in particulate technology, Powder Technology, 37 (1984) 105–116. https://doi.org/10.1016/0032-5910(84)80010-8

Schubert H., Herrmann W., Rumpf H., Deformation behaviour of agglomerates under tensile stress, Powder Technology, 11 (1975) 121–131. https://doi.org/10.1016/0032-5910(75)80037-4

Seville J., Tüzün U., Clift R., Processing of Particulate Solids, Springer Netherlands, Dordrecht, 1997, ISBN: 9780751403763. https://doi.org/10.1007/978-94-009-1459-9

Shao Y., Aoki N., Tong Z., Zhong W., Yu A., Kamiya H., Numerical and experimental study of tensile stresses of biomass combustion ash with temperature variation, Advanced Powder Technology, 27 (2016) 215–222. https://doi.org/10.1016/j.apt.2015.12.007

Smith D.H., Haddad G.J., Ferer M., Shear Strengths of heated and unheated mixtures of $MgSO_4$ and $CaSO_4$ powders. Model pressurized fluidized bed combustion filter cakes, Energy & Fuels, 11 (1997) 1006–1011. https://doi.org/10.1021/ef970037d

Sofia D., Chirone R., Lettieri P., Barletta D., Poletto M., Selective laser sintering of ceramic powders with bimodal particle size distribution, Chemical Engineering Research and Design, 136 (2018) 536–547. https://doi.org/10.1016/j.cherd.2018.06.008

Stevens N., Tedeschi S., Powers K., Moudgil B., El-Shall H., Controlling unconfined yield strength in a humid environment through surface modification of powders, Powder Technology, 191 (2009) 170–175. https://doi.org/10.1016/j.powtec.2008.10.001

Teunou E., Fitzpatrick J.., Effect of relative humidity and temperature on food powder flowability, Journal of Food Engineering, 42 (1999) 109–116. https://doi.org/10.1016/S0260-8774(99)00087-4

Tomas J., Particle adhesion fundamentals and bulk powder consolidation, KONA Powder and Particle Journal, 18 (2000) 157–169. https://doi.org/10.14356/kona.2000022

Tomas J., Mechanics of nanoparticle adhesion—A continuum approach, in: Mittal K.L. (ed.), Particles on Surfaces: Detection, Adhesion and Removal, Volume 8, 1st edition, CRC Press, 2003, pp. 183–229, ISBN: 9780429088131. https://doi.org/10.1201/9789047403333

Tomas J., Fundamentals of cohesive powder consolidation and flow, Granular Matter, 6 (2004) 75–86. https://doi.org/10.1007/s10035-004-0167-9

Tomas J., Schubert H., Fliessverhalten von feuchten Schüttgütern, Aufbereitungs-Technik, 26 (1985) 399–404.

Tomasetta I., Barletta D., Poletto M., The high temperature annular shear cell: a modified ring shear tester to measure the flow properties of powders at high temperature, Advanced Powder Technology, 24 (2013) 609–617. https://doi.org/10.1016/j.apt.2012.11.007

Tomasetta I., Barletta D., Poletto M., Correlation of powder flow properties to interparticle interactions at ambient and high temperatures, Particuology, 12 (2014) 90–99. https://doi.org/10.1016/j.partic.2013.02.002

Tregambi C., Troiano M., Montagnaro F., Solimene R., Salatino P., Fluidized beds for concentrated solar thermal technologies—a review, Frontiers in Energy Research, 9 (2021). https://doi.org/10.3389/fenrg.2021.618421

Tsukada M., Kawashima K., Yamada H., Yao Y., Kamiya H., Analysis of adhesion behavior of waste combustion ash at high temperatures and its control by the addition of coarse particles, Powder Technology, 180 (2008) 259–264. https://doi.org/10.1016/j.powtec.2007.04.005

Tsukada M., Yamada H., Kamiya H., Analysis of biomass combustion ash behavior at elevated temperatures, Advanced Powder Technology, 14 (2003) 707–717. https://doi.org/10.1163/15685520360731990

Weigert T., Ripperger S., Calculation of the liquid bridge volume and bulk saturation from the half-filling angle, Particle & Particle Systems Characterization, 16 (1999) 238–242. https://doi.org/10.1002/(SICI)1521-4117(199910)16:5<238::AID-PPSC238>3.0.CO;2-E

Zafar U., Vivacqua V., Calvert G., Ghadiri M., Cleaver J.A.S., A review of bulk powder caking, Powder Technology, 313 (2017) 389–401. https://doi.org/10.1016/j.powtec.2017.02.024

Zimmerlin B., Leibold H., Seifert H., Evaluation of the temperature-dependent adhesion characteristics of fly ashes with a HT-rheometer, Powder Technology, 180 (2008) 17–20. https://doi.org/10.1016/j.powtec.2007.03.014

Zinatlou Ajabshir S., Gucuyener C., Vivacqua V., Gobby D., Stitt H., Barletta D., Poletto M., Flow behaviour of zeolite powders at high process temperatures, Powder Technology, 409 (2022) 117818. https://doi.org/10.1016/j.powtec.2022.117818

## Authors' Short Biographies

**Dr. Sina Zinatlou Ajabshir** is currently a Postdoctoral Fellow at the Department of Industrial Engineering of the University of Salerno (UNISA), working on powder properties for powder-based Laser 3D printing. He earned his BSc and MSc in materials science and engineering from the University of Tabriz and Sharif University of Technology (SUT), respectively. He completed his Ph.D. in Industrial Engineering with a concentration in Chemical Engineering from UNISA. Prior to joining the Powder Technology Group at UNISA, he worked as a research assistant at the SUT, focusing on additive manufacturing and welding. Sina's research interests encompass particle characterization, powder flow, and powder behaviour for powder bed Fusion methods, as well as the development of computational approaches using the Discrete/Finite Element methods.

**Dr. Diego Barletta** is Associate Professor of Chemical Engineering at the Department of Industrial Engineering of the University of Salerno. Member and from 2020 elected Chairman of the Working Party on Mechanics of Particulate Solids of the European Federation of Chemical Engineering. Member of editorial board of international journals (*KONA, Processes, Powders*) and of scientific committees of international conferences. Involved in research projects (FECUNDUS, MATHEGRAM, TUSAIL) funded by the European Commission. He is engaged in experimentally based research on mechanics of particulate solids, flow properties of powders at process conditions and on design and optimisation of biorefineries and of chemical processes with reduced $CO_2$ emissions.

**Prof. Massimo Poletto** is a Professor of Chemical Engineering at the Department of Industrial Engineering of the University of Salerno and has been a Guest Professor at East China University of Science and Technology Shanghai (2016–2022). Member and past Chairman of the Working Party Mechanics of Particulate Solids of the European Federation of Chemical Engineering. Subject editor (Powder technology) of Chemical Engineering Research and Design. He is presently involved in research concerning the study of flow properties of powders and particulates, including lignocellulosic biomass, fluidization and flow of cohesive powders, and powder spreading in the laser sintering process.

KONA Powder and Particle Journal

KONA Powder and Particle Journal No. 42 (2025) 121–133/https://doi.org/10.14356/kona.2025008 Review Paper

# Strategies to Overcome Undesired Physicochemical Changes in Particle Engineering for Inhalation †

**Mariana Romero-Gonzalez [1], Julia Crowther [1], Mani Ordoubadi [2] and Ashlee D. Brunaugh [1]***

[1] *Department of Pharmaceutical Sciences, University of Michigan, USA*
[2] *Department of Mechanical Engineering, University of Alberta, Canada*

Particle engineering broadly refers to the controlled production of drug particles optimized for size, morphology, and structure. It encompasses both destructive (top-down) and constructive (bottom-up) particle formation processes, of which the most used for commercial dry powder inhaler (DPI) products are milling and spray drying. In both cases, undesirable physicochemical changes may occur because of thermal and mechanical stresses and through interactions with solvents, and can be further potentiated through storage and interaction with atmospheric water. The occurrence and extent of these phenomena are dependent upon the process parameters and the starting material, which necessitates a thorough understanding of these factors to create a stable product with the necessary characteristics for lung deposition. This review covers commonly arising issues in particle engineering and mechanisms of prevention. Topics to be discussed relating to physical changes include (1) the unintended generation of crystalline disorder and amorphous regions in particles; (2) polymorphic transformations; (3) unintended crystallization when amorphization is desired; and (3) triboelectric charging. Topics to be discussed relating to chemical changes include (1) thermal and mechanically activated chemical reactions; and (2) crystalline disorder and chemical reactivity.

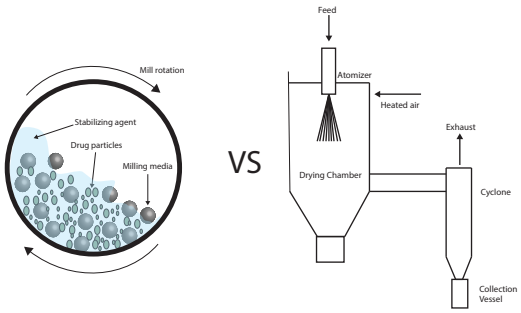


**Keywords:** powder, particle engineering, amorphous, solid-state, spray drying, milling

## 1. Introduction

The location of inhaled particle deposition within the airways and post-deposition interactions with the lung milieu are influenced by particle properties such as size, density, morphology, hygroscopicity, surface area, and energetics. Particles with desirable properties for inhalation can be generated via particle engineering techniques, which in this article we define as both destructive (top-down) and constructive (bottom-up) particle formation processes. The most used technologies for each respective method are milling and spray drying, both of which have been employed in commercial dry powder inhaler (DPI) drug products. Although these processes can produce particles with the necessary characteristics for inhaled drug delivery, they may also induce undesirable physical and chemical changes in the drugs and excipients due to the inherent stresses and interactions involved during particle formation. These include mechanical stresses, thermal stresses, and interactions with solvents, which can result in surface and bulk changes in the crystalline structure, triboelectric charging, and chemical reactions that may adversely affect aerosol performance and drug efficacy and safety. Moreover, the influence of storage conditions and interactions with atmospheric water can potentiate these effects. Minimization of undesired or unanticipated physicochemical changes during particle engineering requires a thorough understanding of the process, its potential interactions with drug molecules, and subsequent effects on the final process. Careful optimization and control of particle formation processes and rational formulation design must then be employed to minimize and mitigate these undesired changes. By adopting appropriate methods and process parameters, pharmaceutical researchers can produce stable drug particles with the desired characteristics for efficient drug delivery and therapeutic effectiveness.

Destructive or "top-down" particle formation techniques encompass the production of respirable drug particles through the application of mechanical forces that result in particle breakage. Destructive particle engineering approaches include milling and homogenization technologies. In milling, particle breakage is achieved through particle–particle collisions and between the particles and the surrounding equipment. Homogenization also involves impact forces, but particle breakage is also achieved via the application of shear forces, cavitation, and pressure and flow forces. This review will focus on milling as a prototypical destructive particle engineering technique based on its wide use in the manufacturing of respirable powders.

† Received 31 July 2023; Accepted 17 August 2023
J-STAGE Advance published online 6 April 2024
* Corresponding author: Ashlee D. Brunaugh;
Add: 428 Church St, Ann Arbor 48109, USA
E-mail: brunaugh@med.umich.edu
TEL: +1-734-647-9910

Constructive or "bottom-up" particle formation processes encompass controlled precipitation approaches for forming particles, such as spray drying, spray freeze drying, thin film freezing, and antisolvent precipitation. In these approaches, the drug and/or excipients are typically dissolved in a solvent and exposed to either a drying medium (spray drying), cryogenic environment (spray freeze drying/thin film freezing), or solvent in which the drug has very little to no solubility (antisolvent precipitation). In the case of spray drying and antisolvent precipitation, this results in rapid precipitation of the drug. Rapid freezing occurs during spray freeze drying and thin film freezing, and the feed solvent is subsequently removed in a secondary lyophilization procedure. Compared to destructive particle engineering techniques, constructive particle engineering techniques can offer more control over particle size, morphology, shape, and surface characteristics but carry unique considerations with regard to thermal stability and interactions between the drug/excipients and solvents. Similar to milling, undesired transformations in the solid-state structure and chemical instability can occur. This review will focus on spray drying as a prototypical constructive particle formation process based on its wide use in the pharmaceutical industry.

This review is structured to provide insight into how the unique stresses occurring in milling and spray drying affect the solid-state properties of the end particles, which in turn affect chemical stability, stickiness, and triboelectric charging, all of which can impact the safety and performance of inhaled drug products. For each process, the impact of the starting material properties on the solid state transformations is discussed. Thus, we intend to provide a guide for formulation scientists to select an appropriate processing approach and adjust process parameters according to the risks associated with a given molecule. Given the unique considerations for the dry state stability of biological products such as proteins, the scope of this review will primarily focus on small molecules.

## 2. Mitigation of undesired physicochemical changes in milled particles

### 2.1 Effects of milling process on particle solid state

Particle size reduction in milling occurs through the fracture of particles following collisions with each other, the milling equipment, or the milling media. Fracture mechanisms include impaction (force is applied normal to the particle surface), attrition (force is applied parallel to the particle surface), compression (slow application of force), and shear and cavitation forces when liquid medium is used (Parrott, 1974). The mills used most frequently for orally inhaled drug products are fluid energy mills, in which particle fracture occurs via the application of high-velocity air jets and the generation of turbulence and particle–particle collisions; and ball mills, in which balls or beads are incorporated and cause grinding through collisions with particles (Yokoyama and Inoue, 2007). For either mill, the rates and type of collision impact the end particle size distribution and can result in solid state transformations.

When mechanical stresses are applied to a particle during the milling process, the energy is initially stored as strain energy, and the solid undergoes reversible deformation. Further application of stress beyond the yield point of the solid results in permanent deformation and the initiation of cracking (Brunaugh and Smyth, 2018; Parrott, 1974). For semi-brittle and ductile materials, plastic deformation precedes fracture. The energy balance in particle fracture and the creation of new surfaces can be defined by the first law of thermodynamics (**Eqn. (1)**) (Zeleny and Piret, 1962):

$$W_s = Q_S + \bar{\sigma}_s \Delta A + \Delta D_s \tag{1}$$

where $W_s$ is the work input to the material, $Q_S$ is the heat produced in the material, $\bar{\sigma}_s$ is the average surface energy per unit area of the material, $\Delta A$ is the surface area change, and $\Delta D_s$ is the deformation energy of the material. Thus, the work required to fracture a particle is dependent upon the surface energy or surface tension of the material. For fracture to occur, the cohesive forces of the molecules on either side of the crack must be overcome. For this reason, cracks will initiate and propagate along existing microflaws in the material, as described by Griffith's theory for crack propagation (Griffith and Taylor, 1921). If a crystal were completely perfect, the applied mechanical forces would be distributed uniformly across the structure, resulting in breakage into uniform, individual units. However, all crystalline solids contain defects in their lattice structure, which results in fracture into a few larger particles and many fine particles and contributes to the typical asymmetrical size distribution of milled materials (Parrott, 1974).

It is well established that comminution via milling can result in the unintentional generation of molecular disorder in the crystalline structure or the generation of amorphous regions (De Gusseme et al., 2008; Feng et al., 2008; Ward and Schultz, 1995). The extent of this disorder is dependent upon the amount of energy imputed into the process (pressure employed in the mill, or the efficiency of the mill). This has several consequences for milled drugs, including changes in solubility, increased particle cohesion, deviations in blend uniformity, and reduction in aerosol performance (Shur et al., 2013). Additionally, disordered surfaces will have a thermodynamic tendency for recrystallization, which can lead to the formation of solid bridges between particles and irreversible aggregation (Dunber et al., 1998).

When the mechanical forces generated in milling exceed the intermolecular forces in the crystal lattice structure (e.g., electrostatic interactions, van der Waals forces, and

hydrogen bonding), disruption and disorder of the crystal lattice structure will occur (York, 1983). Crystal fracture is postulated to occur when the lattice dislocations accumulate and attain a critical density (Olusanmi et al., 2011). In addition to fracture, depending on the material properties and the magnitude of the applied forces, small point defects to complete disruption of the lattice order may occur, resulting in the formation of amorphous or partially disordered structures (Iyer et al., 2023). The resulting increase in entropy of the disordered system increases the free energy of the system and produces solids that are in a so-called "mechanically activated" state in which acceleration of chemical and physical reactions can occur (Hüttenrauch et al., 1985). Crystal to amorphous phase transition during milling is hypothesized to occur as a result of mechanical or thermodynamic destabilization (Crowley and Zografi, 2002). Mechanical destabilization theorizes that if mechanical forces and the resulting anharmonicity of phonons in the material violate the Born stability criteria of the crystal lattice, the lattice will collapse to yield an amorphous form (Tse, 1992). Thermodynamic destabilization theorizes that amorphous transformation occurs when the concentration of defects in the crystal lattice induced by the mechanical energy input exceeds a critical limit beyond which the amorphous form has greater thermodynamic stability than the disordered crystal (Fecht, 1992).

Process optimization to control solid-state transformations in milling has primarily focused on the effects of temperature and milling intensity. The breakage propensity of aspirin during milling was found to increase with temperature (Olusanmi et al., 2010), and it is possible that this could be applied to other materials to improve milling efficiency. However, if the goal is to produce amorphous particles, milling should be performed at temperatures well below the glass transition temperature ($T_g$) of the expected amorphous state (Descamps et al., 2007; Tsukushi et al., 1995). Milling at temperatures above $T_g$ can lead to polymorphic transformation of the disordered material (Descamps et al., 2007). For some high $T_g$ materials (e.g., trehalose), this can be accomplished under ambient conditions; however, materials with lower $T_g$ may benefit from cryogenic milling. An additional benefit of cryogenic milling is that it can be used to make semi-brittle or ductile materials more brittle. At higher temperatures, thermal activation enables greater movement of crystal lattice dislocations by diffusion, thus enhancing plastic flow (Olusanmi et al., 2010). Indomethacin has provided a useful model for examining the effect of milling intensity on solid-state transformations, as it exhibits multiple polymorphs as well as the formation of a glassy state. In a study using amorphous indomethacin, Desprez et al. (Desprez and Descamps, 2006) found that different milling durations and intensities led to the transformation into different crystalline forms, which was hypothesized to be due to successive solid-state transformations as the milling time progressed. Milling at low intensity or short duration at higher intensity promoted direct crystallization of the stable γ crystalline form, wherease milling at high intensity and long duration promoted crystallization of the metastable α phase, either during the milling process itself or upon reheating the glass. These trends followed those observed with temperature effects on the crystallization of amorphous indomethacin, in which the stable γ form crystallizes at lower temperatures (near the $T_g$), whereas the metastable α form crystallizes at higher temperatures. Material properties (e.g., hardness, morphology) can confound the impact of the type of mill used on the tendency toward crystalline disorder. Chikhalia et al. (2006) found that specifically for the plate morphology of β-succinic acid, ball milling resulted in greater crystalline disorder than jet milling, although the opposite trend occurred for needle-like morphology.

Several patents (Lee, 2012; Vemuri et al., 2003) describe the incorporation of humidified air into the fluid energy milling process to produce a powder with little to no amorphous content. Alternatively, several formulators (Brodka-Pfeiffer et al., 2003; Depasquale et al., 2015; Ward and Schultz, 1995) have used a process of "curing" or "conditioning" of milled powders, in which recrystallization of partially amorphous solids is induced in a controlled manner through storage under high humidity conditions for a specified duration. In humid environments, water molecules adsorb onto the amorphous regions of the particle surfaces and function as plasticizers, thereby reducing the $T_g$ (Price and Young, 2005). Provided that the surrounding environment maintains a temperature above $T_g$, the increased molecular mobility within the surface amorphous regions will promote accelerated crystallization. Given that it can alleviate unexpected solid-state transformations and changes in quality attributes during storage, the FDA recommends a conditioning step for micronized drug products in their draft guidance for dry powder inhalers (DPIs) (Food and Drug Administration, 2018), although a specific method is not provided and is probably product dependent. The inclusion of humidified air is critical to the conditioning process for milled powders (Brodka-Pfeiffer et al., 2003); dry conditioning of micronized albuterol for 24 h at 70 °C did not result in recrystallization, whereas a relative humidity above 50 % did produce crystallization. This was hypothesized to be due to the expulsion of water from particle surfaces at high, dry temperatures, which would have a deplasticizing effect. Importantly, in this study, it was found that a combination of higher temperature (40 °C) and high humidity increased particle growth during storage relative to a lower temperature (25 °C) storage. This could have been due to increased molecular mobility at higher temperatures, leading to the formation of crystal bridges.

### 2.2 Impact of starting material on solid state of milled particles

Mechanical properties such as Young's modulus, hardness, and fracture toughness impact fracture strength, deformation behavior, and subsequently particle breakage in milled materials (Brunaugh and Smyth, 2018). Feed material properties have also been correlated with the propensity to crystal disorder during milling. The molar volume of a crystalline solid has been theoretically (Wildfong et al., 2006) and experimentally (Lin et al., 2009) correlated with amorphization because it relates to geometric constraints on crystal dislocation before a critical density is obtained. A higher $T_g$ has also been correlated with increased amorphization by milling (Lin et al., 2009), likely due to stabilization of the amorphous state during processing.

Hydrates and solvates affect solid-state transformations during milling. Crowley and Zografi (2002) examined the differing propensity of two indomethacin solvates (methanol and t-butanol) toward solid-state transformations during grinding. Although indomethacin is generally recognized as a good glass former, amorphization was initially unobserved upon grinding although desolvation of methanol was. This was hypothesized to be due to the plasticization effects of methanol contributing to the rapid recrystallization of a transient amorphous form, which was confirmed through a modified, cryogenic grinding experiment where an amorphous phase containing residual methanol was formed and required additional drying to stabilize. T-butanol, in contrast, resisted desolvation or solid-state transformation. Similar plasticization effects have been observed with the milling of hydrates; while the milling of anhydrous forms of trehalose and glucose results in amorphization, trehalose dihydrate and glucose monohydrate remain crystalline (Willart et al., 2010). Hydrates have also shown greater susceptibility to particle breakage than anhydrates because of alterations in molecular packing (Schneider-Rauber et al., 2021). Therefore, the use of hydrates and solvates can be a useful approach when avoidance of amorphization is desired.

The inclusion of excipients to prevent amorphization during milling has been explored (Balani et al., 2010; Lau et al., 2017). Balani et al. (2010) found that co-milling of salbutamol sulfate with crystalline alpha-lactose monohydrate, adipic acid, or magnesium stearate was effective in reducing the amorphization of the drug, as assessed by X-ray powder diffraction (XRPD), dynamic vapor sorption (DVS), and differential scanning calorimetry (DSC). Based on XRPD patterns obtained after different milling durations, the stabilizing effect of the excipients was hypothesized to be due to the excipient particles acting as seed crystals to induce recrystallization of the amorphous drug. As confirmed by co-milling crystalline lactose with an amorphous sample of salbutamol sulfate resulted in complete recrystallization. The ability of drug seed crystals to induce recrystallization during milling has been reported in other studies (De Gusseme et al., 2008; Otsuka and Kaneniwa, 1986). It is important to note in this study that an excipient in the crystalline state is necessary to induce recrystallization during the milling process; co-milling with amorphous polyvinylpyrrolidone (PVP) had no effect on drug crystallinity.

### 2.3 Effects of milling on chemical reactivity

The work of generating new surfaces in milling produces heat. Thus, localized temperature increases during milling (Schmalzried, 1995) may contribute to thermal degradation. Cryogenic milling has also been used to reduce the effect of heat generation on micronized compounds (Chamarthy and Pinal, 2008); however, Adrjanowicz et al. (2011) found that compared with room temperature processing, milling under cryogenic conditions resulted in a duration-dependent chemical degradation of furosemide, with an identical degradation product produced as reported for thermal degradation. This is unusual because the rate of thermally activated chemical reactions typically increases with increasing temperature (Adrjanowicz et al., 2011), and it was hypothesized that the reaction instead occurred through a pathway activated by mechanical energy provided through a combination of high-energy collisions and the increased surface area and amorphous content of the milled material (Adrjanowicz et al., 2011). Thus, milling under cryogenic conditions is not necessarily a guarantee against chemical degradation, and the product must still be carefully monitored.

Regions of crystal lattice damage or amorphousness generated during milling can also increase the chemical degradation rate of the product, particularly when exposed to water (Ahlneck and Zografi, 1990; Weers and Miller, 2015). Amorphous solids take up more water than their crystalline form. Because of the disordered state of the solid, it is possible for water to dissolve in the solid, where it acts as a plasticizer and reduces the $T_g$. As the ambient temperature increases above $T_g$, the viscoelasticity of the solid decreases and the molecular mobility of both water and the solid increases. This increased mobility increases the chemical decomposition rate for amorphous solids as well as partially damaged crystal lattice structures (Ahlneck and Zografi, 1990; Pikalet al., 1977). To avoid this risk, the duration and energy of the milling process may be reduced to attenuate crystal lattice disorder.

## 3. Mitigation of undesired physicochemical changes in spray-dried particles

### 3.1 Effect of spray-drying process on particle solid state

Spray drying is a manufacturing technique suitable for the large-scale production of powders with ideal characteristics for pulmonary delivery. These properties, which are

generally straightforward to design for different scales, include well-defined particle size with a narrow distribution, good flowability, improved bioavailability resulting from higher aqueous solubility, and enhanced stability of biologics achieved through glass stabilization (Alhajj et al., 2021; Baumann et al., 2021). The aerodynamic size of spray-dried particles can be predicted from a mass-balance equation (**Eqn. (2)**) (Vehring R., 2008a):

$$d_a = d_0 \sqrt[3]{\frac{C_F}{\rho^*}} \sqrt[6]{\frac{\rho_p}{\rho^*}} \quad (2)$$

where $d_a$ and $d_0$ represent the aerodynamic diameter of the particles and the diameter of the initial atomized droplets, respectively, while $C_F$, $\rho_p$, and $\rho^*$ denote the total feed concentration, particle density, and unit density (1000 g/mL), respectively. According to this equation, the final particle size distribution is primarily influenced by the size of the atomized droplets and, to a lesser extent, by the total feed concentration of the solutes.

**Fig. 1** illustrates a schematic representation of the spray-drying process, which involves atomizing a solution or suspension into a fine spray within a chamber in the presence of a hot gas flow. Evaporation of a droplet involves the transfer of heat from a hot gas via conduction and convection to the droplet surface and the transfer of vapor from the droplet surface into the gas stream via diffusion and convection. The rate of this transfer is dependent upon the properties of both the drying gas (temperature, humidity, transport properties) and the droplet (diameter, temperature, relative velocity) (Ranz, 1952). Droplet evaporation

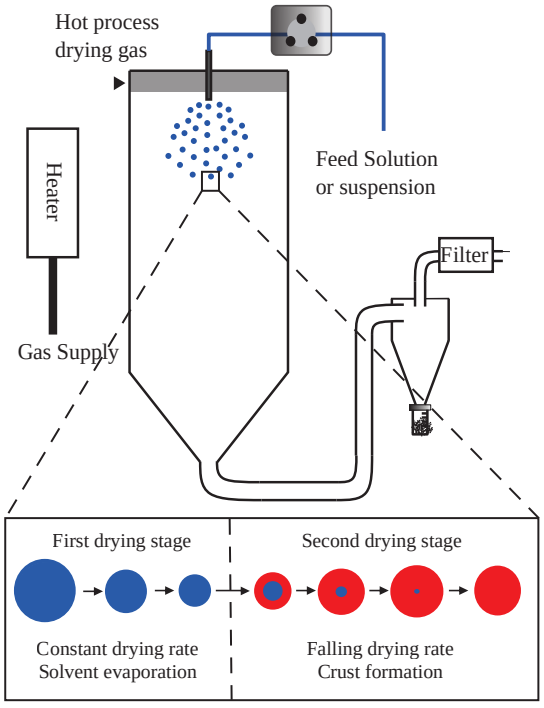


**Fig. 1** Schematic of the spray dryer and particle formation in the open mode.

in spray drying is thermodynamically driven by the difference in chemical potential between the solvent in the solidifying droplet and in the carrier gas/vapor phase; thus, the drying rate is proportional to the magnitude of the difference between solvent activity adjacent to the droplet surface and that of the bulk carrier gas (Handscomb et al., 2009a; Singh and Van den Mooter, 2016). This necessitates careful control of humidity during the spray-drying process and efficient solvent removal if operating in a "closed-loop" mode to maintain this differential and if a rapid drying rate is desired. Similarly, the droplet surface must remain saturated with solvent, and the drying rate will begin to decrease once the solvent molecules can no longer diffuse to the surface at a sufficient rate to maintain saturation (Handscomb et al., 2009a). Drying continues until the solvent activity in the solid and vapor phases has reached equilibrium.

The process of solvent removal during spray drying can be broadly classified into two states: 1) a constant drying rate period and 2) a declining drying rate period. During the constant drying rate period, the droplet temperature initially equilibrates to the wet bulb temperature and then begins to increase as the amount of solids at the surface of the droplet increases (Nešić and Vodnik, 1991). Toward the end of this period, the accumulation of solids at the droplet surface causes a reduction in the vapor partial pressure at the surface and a reduced rate of evaporation; the transferred heat is instead used for droplet heating. This marks the start of the declining drying rate period, where the formation of a crust increases the resistance to heat and mass transfer. Depending on the permeability of the crust for vapor diffusion, whether the bulk carrier gas temperature is greater than the solution boiling temperature, and the mechanical properties of the crust, an increase in internal pressure can lead to inflation, cracking, or explosion. Conversely, shrinkage or buckling of the shell may occur because of the capillary pressure of the receding continuous phase (Handscomb et al., 2009b). Thus, manipulation of the drying rate offers some degree of control over particle morphology, as the morphology of the produced particles is strongly dependent on the properties of the formed crust (Handscomb et al., 2009a). Upon bulk solvent removal from the particle core, the drying rate continues to decrease as the residual solvent is evaporated from the pores and micropores until the temperature of the droplet approaches that of the surrounding carrier gas (Nešić and Vodnik, 1991). Once formed, particles are then typically separated from the gas flow using cyclonic separation for further processing (Carrigy and Vehring, 2019; Ordoubadi et al., 2022). The spray-dried powder may be subjected to additional drying processes to further reduce the residual solid content.

Ultimately, whether a spray-dried particle will be amorphous, partially amorphous, or crystalline depends on

whether nucleation and crystal growth can occur before the droplet dries. The time length of this critical period can be decreased through adjustments of process parameters that impact the droplet evaporation rate and surface saturation of the droplet components, which include the inlet temperature, feed flow rate, and feed solid concentration. Given that adjustment of these parameters can have confounding effects on the drying capacity of the spray dryer and the temperatures to which the drying particle is exposed, which can conversely impact molecular mobility, the most efficient mechanism for optimization is probably a multifactorial experimental approach. Mathematical models for particle formation have been extensively presented by Vehring and colleagues (Hoe et al., 2013; Vehring et al., 2007; Vehring, 2008a), an overview of which is presented here. **Eqn. (3)** describes the time it takes for a droplet to dry completely ($\tau_D$):

$$\tau_D = \frac{d_0^2}{\kappa} \tag{3}$$

where $d_0$ is the initial droplet diameter and $\kappa$ is the evaporation rate. **Eqn. (4)** describes the time for a component, $i$, to reach surface saturation:

$$\tau_{sat,i} = \tau_D \left[ 1 - \left( \frac{c_{0,i} E_i}{c_{sol,i}} \right)^{\frac{2}{3}} \right] \tag{4}$$

where $c_{0,i}$ is the initial concentration of the component $i$ in the droplet, $c_{sol,i}$ is the equilibrium solubility of component $i$, and $E_i$ describes surface enrichment of component $i$, that is, the surface concentration of component $i$ in relation to its concentration in the bulk droplet. The time remaining between saturation and complete droplet drying describes the time available for crystallization of component $i$, referred to as the precipitation time ($\tau_{p,i}$), and is described in **Eqn. (5)**:

$$\tau_{p,i} = \tau_D \left[ 1 - \left( \frac{c_{0,i}}{\rho_{t,i}} * E_i \right)^{\frac{2}{3}} \right] \tag{5}$$

where $\rho_{t,i}$ is the true density for component $i$. Depending on whether the component has sufficient time to crystallize before droplet drying is complete, a crystalline, partially amorphous, or amorphous particle will form.

Crystallization kinetics have been modeled in the spray-drying process through several different methods, including those related to the thermodynamic drivers for nucleation and crystal growth kinetics and solid-state transformation that can occur from a transient amorphous to crystalline state as solvent contents change in the drying droplet. For a saturation-based approach to crystallization, each individual droplet can be considered a crystallizer. A thermodynamic drive for nucleation and crystal growth is provided by the difference between the chemical potential of the solute in solution and the crystal form (**Eqn. (6)**) (Dirksen and Ring, 1991):

$$\Delta G = -RT \ln\left(\frac{a}{a^*}\right) = -RT \ln\left(\frac{C}{C_{eq}}\right) \tag{6}$$

where $R$ is the universal gas constant, $T$ is the absolute temperature, and a and $a^*$ are the activities of the solute in supersaturated and saturated conditions, respectively. For an ideal solution, this can be expressed in terms of the ratio of the solute concentration ($C$) to the equilibrium solubility ($C_{eq}$) at a given temperature and pressure. Evaporation of solvent during the spray-drying process increases $C$ and the degree of supersaturation, thus increasing the thermodynamic drive for crystallization. The rate of nucleation can be described using an Arrhenius equation (**Eqn. (7)**) according to Classical Nucleation Theory (Thakur et al., 2022):

$$J = A \exp\left(-\frac{\Delta G^*}{k_B T}\right) \tag{7}$$

where $A$ is a constant that depends on the stochastic process of attachment and detachment of the solute from the surface of the nucleus, $k_B$ is Boltzmann's constant, $\Delta G^*$ is the change in free energy required for critical cluster formation, and $T$ is the nucleation temperature. The frequency of molecular transport ($v$) to the nucleus–liquid interface is related to the bulk viscosity ($\eta$) using the Stokes–Einstein equation (**Eqn. (8)**) (Rodríguez-Hornedo and Murphy, 1999):

$$v = \frac{kT}{3\pi a_o^3 \eta(T)} \tag{8}$$

where $a_o$ is the mean effective diameter of the diffusing species. Further crystal growth can be controlled by volume diffusion, i.e., it is rate-limited by the diffusion of the solute from the bulk solution to the crystal surface, or it can be controlled by surface integration, i.e., incorporation of the molecule into the crystal lattice is the rate-limiting step (Rodríguez-Hornedo and Murphy, 1999). Ultimately, crystallization is limited by the extent of molecular rearrangement in the liquid adjacent to the interface (Turnbull, 1969). If this molecular rearrangement is slowed and if the clusters cannot assemble into crystals during the timeframe of droplet drying (e.g., through an increase in viscosity), then an amorphous solid will be formed. Unintended polymorph transformations can also occur in bottom-up particle engineering techniques such as spray drying. Ostwald's Rule of Stages states that crystallization from a solution typically occurs in a manner in which the least thermodynamically stable polymorph is formed first, followed by subsequent transitions into more stable forms (Nývlt, 1995). However, the rapid drying times that occur during spray drying may not enable full conversion to the most stable polymorph and can instead result in a metastable

crystalline form or a mixture of polymorphs (Vehring, 2008b). The polymorph in the final product can be influenced by both the process parameters and feed formulation. The length of the drying time has been used as a mechanism of controlling the crystalline state produced, as well as the variation in droplet size (Lee et al., 2011). Lee et al. (2011) found that variation in mannitol polymorphs occurred as a function of droplet size, which was theorized to be due to the slower drying of larger droplets, as the retention of moisture facilitates crystallization to the stable polymorph. Inclusion of excipients in the spray dryer feed solution can control polymorph transition because excipient molecules will adsorb onto crystal surfaces and affect the direction of crystal growth (Kitamura, 2009). Likewise, incorporation of a co-solvent in the feed solution can be used as a mechanism to control the polymorphism, as this will alter the nucleation and crystallization rate (Kitamura, 2009; Lee et al., 2011; Roelands et al., 2006).

Spray drying is unique in that it involves concurrent evaporation and particle formation processes. Using single droplet drying data of lactose solution, Woo et al. determined that before the formation of a solid crust in the drying droplet, a saturation-based analysis similar to that provided above can be used to predict the extent of crystallization; however, upon the formation of the crust, crystallization is more aptly modeled using solid-state approaches (Woo et al., 2012). Solid-phase crystallization in semi-dried or dried particles during the spray-drying process can be modeled using the Williams–Landel–Ferry (WLF) equation, which describes viscosity ($v$) and thus molecular relaxation as a function of temperature difference from $T_g$ (**Eqn. (9)**) (Williams et al., 1955):

$$\log\left(\frac{v_{\text{ref}}}{v_{\text{max}}}\right)=\frac{-C_1\left(T-T_g\right)}{C_2+T-T_g} \tag{9}$$

where $C_1$ and $C_2$ are material-dependent constants. The $T_g$ during the various time steps in the drying process can be estimated using the Gordon–Taylor equation (**Eqn. (10)**) (Gordon and Taylor, 1952):

$$T_g=\frac{w_1T_{g,1}+kw_2T_{g,2}}{w_1+kw_2} \tag{10}$$

The WLF equation can be integrated against the drying time to describe the driving force for crystallization based on changes in molecular mobility, where a larger value indicates that the particle has experienced more crystallization (Woo et al., 2012). Process drying efficiency and trends toward recrystallization of drying particles have been predicted using characteristic drying curves, in which a relative drying rate (the actual drying rate of the solids relative to the unhindered drying rate) is calculated as a function of the characteristic moisture content over the drying process as process parameters are adjusted (Chiou et al., 2007).

Ultimately, whether a spray-dried particle will be amorphous, partially amorphous, or crystalline depends on whether nucleation and crystal growth can occur before the droplet dries. The time length of this critical period can be decreased through adjustments of process parameters that impact the droplet evaporation rate and surface saturation of the droplet components, which include the inlet temperature, feed flow rate, and feed solid concentration. Given that adjustment of these parameters can have confounding effects on the drying capacity of the spray dryer and the temperatures to which the drying particle is exposed (e.g., the outlet temperature), which can conversely impact molecular mobility, the most efficient mechanism for optimization is probably a multifactorial experimental approach.

The inlet temperature, feed flow rate, and solid content are directly related to the heat and mass transfer efficiency in spray drying. Increasing the inlet temperature will increase the evaporation rate because the heat transfer to the droplet surface increases the average kinetic energy of the solvent molecules, enabling them to break free into the vapor phase. As such, the surface saturation rate will also increase and can produce particles with smaller crystals and lower overall crystalline content (Baldelli et al., 2016). More efficient solvent removal can also reduce its plasticization effects and increase the $T_g$ of the solids, although the residual solvent content cannot be reduced below zero. Increasing the temperature to increase drying efficiency must be balanced against the potential for drug degradation at higher outlet/dry bulb temperatures. Furthermore, if an amorphous product is desired, increasing the inlet temperature may also increase the temperature of the drying particle above $T_g$, thereby increasing molecular mobility and increasing the rate of recrystallization according to the WLF equation. Using experimental and modeling approaches based on the WLF equation, Langrish (2008) found that the rate of crystallization was greatly enhanced when the particle temperature was more than 30 K higher than the $T_g$ of the material. Spray drying above the $T_g$ has also been associated with a significant reduction in production yield because of particles sticking to the walls of the cyclone (Camino-Sánchez et al., 2020).

If an amorphous end product is the goal, the outlet temperature should be maintained below $T_g$. In the case of molecules with low $T_g$, this may necessitate the incorporation of anti-plasticizing excipients to increase the $T_g$ of the mixture or the use of highly volatile solvents such as dichloromethane. Conversely, maximizing the positive temperature differential between the particle and its $T_g$ can be an efficient mechanism to induce crystallization. Increasing the feed flow rate results in a decrease in the outlet temperature and decreases the drying efficiency as more mass is added to the system and evaporative cooling occurs. This can produce an increase in residual solvent content in the

dried particles, which can cause plasticization and impact storage stability. While increasing solids content will decrease the time to surface saturation and precipitation, this can also impede solvent removal depending on the permeability of the crust formed during droplet drying.

### 3.2 Effect of starting material on solid state of spray-dried particles

The formation of amorphous or crystalline particles depends not only on the operating conditions and process variables employed in spray drying but also on the materials that are being fed to the spray drier. Whether a material forms a glass or an ordered crystalline structure depends on the efficiency and timescale of molecular packing as it relates to phase transition into the solid state. Various structural features that affect the packing efficiency of molecules have been identified through experimental and statistical approaches. Identifying these features and understanding their impact on the thermodynamic drive and kinetics of crystallization can provide early guidance on the need for stabilizing excipients or adjustment of spray drying parameters, depending on the desired product outcomes. Generally, the presence of benzene rings in a molecule is associated with a planar structure and increased opportunities for non-specific van der Waals interactions between the aromatic rings, which promote a tightly packed, energetically favorable crystal structure (Mahlin et al., 2011; Yu et al., 2000). A higher molecular weight is associated with increased glass-forming ability, although this may be confounded by the typically higher complexity of these molecules and increased configurational entropy (Yu et al., 2000). Drugs with a molecular weight greater than 300 g/mol exhibit good glass-forming ability using different processing technologies, including spray drying, which may provide a quick screening tool for the tendency to crystalize (Mahlin and Bergström, 2013). Other molecular features that support glass formation during spray drying include a highly branched structure or asymmetry (Mahlin et al., 2011). Molecules with more rotatable bonds exhibit slower crystallization kinetics because of the decreased probability that a molecule conformer will be in the proper orientation to undergo nucleation or be incorporated into the growing lattice structure (Baird et al., 2010; Yu et al., 2000). Increased electronegativity in a molecule also increases the tendency toward amorphization upon spray drying (Mahlin et al., 2011), as it promotes hydrogen bonding between molecules, which has previously been linked with the generation of molecular aggregates that pack poorly and limit the rate of molecular reorganization into the crystalline state (Wang et al., 2009).

For drugs that are poor glass formers, excipients can be incorporated into the feed to stabilize the amorphous state, e.g., through the formation of an amorphous solid dispersion (ASD) in which a matrix-like structure is formed that hinders the molecular mobility of any molecules incorporated into it. Even in the case of drugs that readily form amorphs, an ASD development approach can be a useful strategy to overcome the thermodynamic instabilities of the amorphous form and raise the $T_g$ to a level sufficient for storage stability, e.g., greater than ~50 K of the anticipated storage temperature (Hancock et al., 1995). In the context of spray-drying ASDs for administration via dry powder inhalers, it is important to check that the excipients display properties to ensure that they are well tolerated in humans and are amenable to scale-up production. These properties include an established safety profile, biocompatibility, no displayed toxicity, and polymer processability, e.g., sufficient solubility in solvents for spray drying. Sugar-based excipients and polymers such as HPMC, HPMCAS, and PVPs are generally considered to be biologically inert, are generally recognized as safe, and are present in commercial products (Anane-Adjei et al., 2022). This review will provide a brief discussion on the use of polymers as glass-stabilizing excipients as a case example based on their wide use in the stabilization of amorphous small molecules, although saccharides such as trehalose are commonly used for the stabilization of biological spray-dried products.

The specific polymer used in ASDs directly impacts physical stability and dissolution properties; therefore, it is imperative to understand the interactions between the drug and polymer in ASDs. The most common physicochemical property used to predict the compatibility of drugs and polymers is their miscibility, or ability to form a stable single phase. Intermolecular bonds, primarily hydrogen bonds and ionic interactions, between the polymer and the drug impact miscibility. *In silico* models are often used as a preliminary method for determining the miscibility of an ASD, usually by evaluating the surface charge characteristics of both molecular entities. Models such as COSMO-Rank use this method to determine the miscibility of an API with various established polymers, which are then ranked based on the enthalpy of the predicted interaction. Typically, the more negative the calculated enthalpy is between the API and polymer, the higher the ASD ranking (Anane-Adjei et al., 2022). Hydrophobicity also plays an important role in the success of a polymer in forming an ASD because it affects the strength of interactions between the polymer, the drug, and the feed solvent. Ilevbare et al. (2013) found that a moderate level of polymer hydrophobicity was ideal for inhibiting drug crystal growth in supersaturated solutions, as it enabled non-specific interactions and promoted adsorption of the polymer to the surface of the crystalline drugs (Ilevbare et al., 2013). Excessive polymer hygroscopicity, particularly when coupled with weak polymer–drug interactions, can negatively impact the storage stability of ASDs through moisture-induced amorphous–amorphous phase separation (Rumondor and Taylor, 2010). For polymers, an increase in the molecular weight

of the polymer generally results in an increase in $T_g$, according to the Flory–Fox equation (Fox and Flory, 1950). Thus, one potential mechanism for stabilizing amorphous spray-dried products is to substitute a polymer with a higher molecular weight in the solid dispersion. However, it must also be considered that increasing the molecular weight will increase droplet viscosity during drying and impede solvent transport from the bulk to the surface (Wu et al., 2011). This can increase the amount of residual solvent and result in plasticization.

Feed solvent selection can impact drug solubility and saturation, thermodynamic drive for crystallization and polymer behavior. The solubility of feed components in the feed solvent can impact crystallinity, as it affects the supersaturation ratio. Harjunen et al. (2002) determined the effects of the ethanol-to-water ratio in the feed solution on the crystallinity of spray-dried lactose. Crystallinity was evaluated by isothermal microcalorimetry and differential scanning calorimetry. The solubility of lactose in water at room temperature is 0.21 mg/mL, whereas it is practically insoluble in ethanol. The authors found that the crystallinity of spray-dried lactose varies from 0% to 100% depending upon the composition of the feed, where an increase in the proportion of ethanol in the feed produced a corresponding decrease in the amorphous content of the spray-dried products. The lactose spray dried from pure ethanol was 100 % crystalline, whereas the lactose spray dried from pure water was 100 % amorphous. Li et al. (2020) examined the phase behavior of ritonavir–copovidone spray-dried dispersions from methanol and methanol–water mixtures. The prepared ASDs were characterized using differential scanning calorimetry (DSC), fluorescence spectroscopy, X-ray photoelectron spectroscopy (XPS), and surface-normalized dissolution rate (SNDR) measurements. Their results indicate that the addition of water to the solvent system could lead to phase separation during the spray-drying process, and even slight modifications in the composition of the solvent mixture resulted in notable alterations in the phase behavior of the ASDs during drying. These findings are relevant because the addition of water to organic solvents is often used to increase the solubility of drugs or polymers in feed and because the use of hygroscopic solvents, such as methanol or acetone, in spray drying can pick up atmospheric moisture, leading to heterogeneity or phase separation of spray-dried ASD particles.

### 3.3 Effect of spray drying on chemical reactivity

Thermal degradation can be an issue in spray drying of thermolabile compounds, particularly proteins and peptides or biodegradable polymers (Cheow et al., 2011). Although largely beyond the scope of this review, for macromolecular biologics, degradation mechanisms that require the most attention during the formulation development of spray-dried powders are denaturation and aggregation (Mensink et al., 2017). Denaturation of proteins is the unfolding and disruption of their tertiary and secondary structures, which generally occurs due to external stresses, with thermal, interfacial, and dehydration-related stresses being significant during drying processes (Haque and Adhikari, 2015). Protein aggregation is a series of structural changes involving protein–protein interactions that can lead to the formation of reversible or non-reversible clusters (Wang and Roberts, 2018). The formation of these protein clusters can reduce their therapeutic efficacy and potentially increase their immunogenicity and cause immune response after delivery (Lundahl et al., 2021).

Oxidation and hydrolysis are common factors contributing to the chemical degradation of labile drugs and excipients during spray drying and subsequent storage, and these reactions can be catalyzed by the high temperatures present during processing. Although many of these chemical degradation studies have been conducted on food products, the results are likely applicable to certain excipient classes relevant to inhaled drug products, e.g., phospholipids. For example, high (>180 °C) inlet temperatures during spray drying were found to result in increased lipid oxidation in spray-dried egg powder (Javed et al., 2018). Antioxidants have been included in a spray-dried HPMCAS-based ASD to prevent oxidation during storage (Kotha et al., 2022) and could provide similar protective benefits during processing. Sodium caseinate–lactose powders containing an increased percentage of hydrolyzed sodium caseinate exhibited increased powder sticking during processing, increased particle breakage/friability, and a lower $T_g$ and higher percentage lactose crystallinity upon storage, indicating increased moisture sorption behavior (Mounsey et al., 2012). Thus, the chemical reactions such as hydrolysis may have impacts on the physical properties of powders as well as product safety.

## 4. Triboelectric charging of engineered particles

Because organic compounds typically consist of insulating material (Karner et al., 2014), engineered particles may accumulate electrostatic charges (triboelectrification) during processing as particles move against the solid surfaces of equipment and each other (Kwok and Chan, 2013; Rasenack and Müller, 2004). The extent of triboelectrification depends on ambient relative humidity, temperature, surface impurities, surface roughness, area of contact, and other physicochemical factors (Karner et al., 2014; Kwok and Chan, 2013). Attractive forces produced during particle charging can lead to particle agglomeration and adhesion to equipment surfaces. This may result in alterations in particle size or blocking of powder flow pathways through equipment (Kwok and Chan, 2013). In contrast, if repulsive forces are produced from particle charging, blend

stability and bulk powder density will be reduced, which may in turn affect dose metering (Bailey, 1993). The material from which equipment is constructed will influence charge (stainless steel versus polymers) (Elajnaf et al., 2006), as well as contamination of equipment surfaces over time, which could lead to variations from batch to batch if equipment is not properly cleaned or if detergent residue is left on equipment (Kwok and Chan, 2013). Furthermore, particle charging can be affected by relative humidity (RH), the magnitude of which is dependent on the hygroscopicity of the material. For particles with low hygroscopicity, RH appears to have a negligible effect; however, for particles with high hygroscopicity, electrostatic charging is inversely related to RH (Kwok and Chan, 2013). This is hypothesized to be due to the reduction in surface contact as water is adsorbed.

In addition to altering the equipment material, avoidance of electrostatic charging can be achieved through the addition of certain excipients, such as fillers or lubricants, to the micronized drug powder (Kwok and Chan, 2013). For example, Zhang et al. (2010) included an anti-electrostatic agent (Poloxamer 188) in an azithromycin formulation for inhalation to reduce the effect of charging. The solid state properties of particles can also influence charging behavior. Wong et al. (2014) found that amorphous salbutamol sulfate exhibited more variability in surface charge compared with the crystalline form, which was hypothesized to be due to the less defined molecular arrangement of the amorphous form. According to molecular modeling, the dominant surface face of crystalline salbutamol sulfate contains electronegative sulfate counter-ions which impact the work function (the minimum energy required to remove an electron from the solid surface).

## 5. Conclusions

Undesirable physicochemical changes in particles engineered for inhalation can be attributed to unanticipated transformations in the solid state due to processing conditions. By understanding material-dependent propensity toward solid-state transformations and how these may be amplified by unique stresses present in top-down particle engineering approaches (e.g., milling) or bottom-up particle engineering approaches (e.g., spray drying), rational decisions can be made regarding the choice of processing approach, limitations of the process design space, and inclusion of stabilizing excipients. Although much research in this area has focused on empirical approaches toward the mitigation of undesirable physicochemical changes in particle engineering, future research directions may incorporate advanced statistical models and artificial intelligence to guide processing and formulation decisions.

## References

Adrjanowicz K., Kaminski K., Grzybowska K., Hawelek L., Paluch M., Gruszka I., Zakowiecki D., Sawicki W., Lepek P., Kamysz W., Guzik L., Effect of cryogrinding on chemical stability of the sparingly water-soluble drug furosemide, Pharmaceutical Research, 28 (2011) 3220–3236. https://doi.org/10.1007/s11095-011-0496-4

Ahlneck C., Zografi G., The molecular basis of moisture effects on the physical and chemical stability of drugs in the solid state, International Journal of Pharmaceutics, 62 (1990) 87–95. https://doi.org/10.1016/0378-5173(90)90221-O

Alhajj N., O'Reilly N.J., Cathcart H., Designing enhanced spray dried particles for inhalation: a review of the impact of excipients and processing parameters on particle properties, Powder Technology, 384 (2021) 313–331. https://doi.org/10.1016/j.powtec.2021.02.031

Anane-Adjei A.B., Jacobs E., Nash S.C., Askin S., Soundararajan R., Kyobula M., Booth J., Campbell A., Amorphous solid dispersions: utilization and challenges in preclinical drug development within AstraZeneca, International Journal of Pharmaceutics, 614 (2022) 121387. https://doi.org/10.1016/j.ijpharm.2021.121387

Bailey A.G., Charging of solids and powders, Journal of Electrostatics, 30 (1993) 167–180. https://doi.org/10.1016/0304-3886(93)90072-F

Baird J.A., Van Eerdenbrugh B., Taylor L.S., A classification system to assess the crystallization tendency of organic molecules from undercooled melts, Journal of Pharmaceutical Sciences, 99 (2010) 3787–3806. https://doi.org/10.1002/jps.22197

Balani P.N., Ng W.K., Tan R.B.H., Chan S.Y., Influence of excipients in comilling on mitigating milling-induced amorphization or structural disorder of crystalline pharmaceutical actives, Journal of Pharmaceutical Sciences, 99 (2010) 2462–2474. https://doi.org/10.1002/jps.21998

Baldelli A., Power R.M., Miles R.E.H., Reid J.P., Vehring R., Effect of crystallization kinetics on the properties of spray dried microparticles, Aerosol Science and Technology, 50 (2016) 693–704. https://doi.org/10.1080/02786826.2016.1177163

Baumann J.M., Adam M.S., Wood J.D., Engineering advances in spray drying for pharmaceuticals, Annual Review of Chemical and Biomolecular Engineering, 12 (2021) 217–240. https://doi.org/10.1146/annurev-chembioeng-091720-034106

Brodka-Pfeiffer K., Häusler H., Graß P., Langguth P., Conditioning following powder micronization: influence on particle growth of salbutamol sulfate, Drug Development and Industrial Pharmacy, 29 (2003) 1077–1084. https://doi.org/10.1081/DDC-120025865

Brunaugh A., Smyth H.D.C., Process optimization and particle engineering of micronized drug powders via milling, Drug Delivery and Translational Research, 8 (2018) 1740–1750. https://doi.org/10.1007/s13346-017-0444-x

Camino-Sánchez F.J., López-López H., Gutierrez-Rodríguez J.M., The development and application of sticky-point models to spray drying processes for the manufacturing of nutritional powder products and infant formulas, Journal of Food Engineering, 279 (2020) 109947. https://doi.org/10.1016/j.jfoodeng.2020.109947

Carrigy N., Vehring R., Engineering stable spray-dried biologic powder for inhalation, in: Hickey A.J., & da Rocha S.R. (Eds.), Pharmaceutical Inhalation Aerosol Technology, Third Edition, CRC Press, 2019, pp. 291–326, ISBN: 9780429055201. https://doi.org/10.1201/9780429055201

Chamarthy S.P., Pinal R., The nature of crystal disorder in milled pharmaceutical materials, Colloids and Surfaces A: Physicochemical and Engineering Aspects, 331 (2008) 68–75. https://doi.org/10.1016/j.colsurfa.2008.06.040

Cheow W.S., Ng M.L.L., Kho K., Hadinoto K., Spray-freeze-drying production of thermally sensitive polymeric nanoparticle aggregates for inhaled drug delivery: effect of freeze-drying adjuvants, International Journal of Pharmaceutics, 404 (2011) 289–300. https://doi.org/10.1016/j.ijpharm.2010.11.021

Chikhalia V., Forbes R.T., Storey R.A., Ticehurst M., The effect of crystal morphology and mill type on milling induced crystal disorder, European Journal of Pharmaceutical Sciences, 27 (2006) 19–26. https://doi.org/10.1016/j.ejps.2005.08.013

Chiou D., Langrish T.A.G., Braham R., Partial crystallization behavior during spray drying: simulations and experiments, Drying Technol-

ogy, 26 (2007) 27–38. https://doi.org/10.1080/07373930701781181
Crowley K.J., Zografi G., Cryogenic grinding of indomethacin polymorphs and solvates: assessment of amorphous phase formation and amorphous phase physical stability, Journal of Pharmaceutical Sciences, 91 (2002) 492–507. https://doi.org/10.1002/jps.10028
De Gusseme A., Neves C., Willart J.F., Rameau A., Descamps M., Ordering and disordering of molecular solids upon mechanical milling: the case of fananserine, Journal of Pharmaceutical Sciences, 97 (2008) 5000–5012. https://doi.org/10.1002/jps.21472
Depasquale R., Lee S.L., Saluja B., Shur J., Price R., The influence of secondary processing on the structural relaxation dynamics of fluticasone propionate, AAPS PharmSciTech, 16 (2015) 589–600. https://doi.org/10.1208/s12249-014-0222-8
Descamps M., Willart J.F., Dudognon E., Caron V., Transformation of pharmaceutical compounds upon milling and comilling: the role of Tg, Journal of Pharmaceutical Sciences, 96 (2007) 1398–1407. https://doi.org/10.1002/jps.20939
Desprez S., Descamps M., Transformations of glassy indomethacin induced by ball-milling, Journal of Non-Crystalline Solids, 352 (2006) 4480–4485. https://doi.org/10.1016/j.jnoncrysol.2006.02.130
Dirksen J.A., Ring T.A., Fundamentals of crystallization: kinetic effects on particle size distributions and morphology, Chemical Engineering Science, 46 (1991) 2389–2427. https://doi.org/10.1016/0009-2509(91)80035-W
Dunber C.A., Hickey A.J., Holzner P., Dispersion and characterization of pharmaceutical dry powder aerosols, KONA Powder and Particle Journal, 16 (1998) 7–45. https://doi.org/10.14356/kona.1998007
Elajnaf A., Carter P., Rowley G., Electrostatic characterisation of inhaled powders: effect of contact surface and relative humidity, European Journal of Pharmaceutical Sciences, 29 (2006) 375–384. https://doi.org/10.1016/j.ejps.2006.07.006
Fecht H.J., Defect-induced melting and solid-state amorphization, Nature, 356 (1992) 133–135. https://doi.org/10.1038/356133a0
Feng T., Pinal R., Carvajal M.T., Process induced disorder in crystalline materials: differentiating defective crystals from the amorphous form of griseofulvin, Journal of Pharmaceutical Sciences, 97 (2008) 3207–3221. https://doi.org/10.1002/jps.21219
Food and Drug Administration, Metered Dose Inhaler (MDI) and Dry Powder Inhaler (DPI) Drug Products—Quality Considerations, 2018. <https://www.regulations.gov/docket/FDA-2018-D-1098> accessed04032024.
Fox T.G., Flory P.J., Second-order transition temperatures and related properties of polystyrene. i. influence of molecular weight, Journal of Applied Physics, 21 (1950) 581–591. https://doi.org/10.1063/1.1699711
Gordon M., Taylor J.S., Ideal copolymers and the second-order transitions of synthetic rubbers. i. non-crystalline copolymers, Journal of Applied Chemistry, 2 (1952) 493–500. https://doi.org/10.1002/jctb.5010020901
Griffith A.A., Taylor G.I., VI. The phenomena of rupture and flow in solids, Philosophical Transactions of the Royal Society of London Series A, Containing Papers of a Mathematical or Physical Character, 221 (1921) 163–198. https://doi.org/10.1098/rsta.1921.0006
Hancock B.C., Shamblin S.L., Zografi G., Molecular mobility of amorphous pharmaceutical solids below their glass transition temperatures, Pharmaceutical Research, 12 (1995) 799–806. https://doi.org/10.1023/A:1016292416526
Handscomb C.S., Kraft M., Bayly A.E., A new model for the drying of droplets containing suspended solids, Chemical Engineering Science, 64 (2009a) 628–637. https://doi.org/10.1016/j.ces.2008.04.051
Handscomb C.S., Kraft M., Bayly A.E., A new model for the drying of droplets containing suspended solids after shell formation, Chemical Engineering Science, 64 (2009b) 228–246. https://doi.org/10.1016/j.ces.2008.10.019
Haque M.A., Adhikari B., Drying and denaturation of proteins in spray drying process, Handbook of Industrial Drying, 33 (2015) 971–983.
Harjunen P., Lehto V.-P., Välisaari J., Lankinen T., Paronen P., Järvinen K., Effects of ethanol to water ratio in feed solution on the crystallinity of spray-dried lactose, Drug Development and Industrial Pharmacy, 28 (2002) 949–955. https://doi.org/10.1081/DDC-120006427
Hoe S., Ivey J.W., Boraey M.A., Shamsaddini-Shahrbabak A., Javaheri E., Matinkhoo S., Finlay W.H., Vehring R., Use of a fundamental approach to spray-drying formulation design to facilitate the development of multi-component dry powder aerosols for respiratory drug delivery, Pharmaceutical Research, 31 (2013) 449–465. https://doi.org/10.1007/s11095-013-1174-5
Hüttenrauch R., Fricke S., Zielke P., Mechanical activation of pharmaceutical systems, Pharmaceutical Research, 2 (1985) 302–306. https://doi.org/10.1023/a:1016397719020
Ilevbare G.A., Liu H., Edgar K.J., Taylor L.S., Impact of polymers on crystal growth rate of structurally diverse compounds from aqueous solution, Molecular Pharmaceutics, 10 (2013) 2381–2393. https://doi.org/10.1021/mp400029v
Iyer J., Brunsteiner M., Modhave D., Paudel A., Role of crystal disorder and mechanoactivation in solid-state stability of pharmaceuticals, Journal of Pharmaceutical Sciences, 112 (2023) 1539–1565. https://doi.org/10.1016/j.xphs.2023.02.019
Javed A., Imran M., Ahmad N., Hussain A.I., Fatty acids characterization and oxidative stability of spray dried designer egg powder, Lipids in Health and Disease, 17 (2018) 282. https://doi.org/10.1186/s12944-018-0931-1
Karner S., Littringer E.M., Urbanetz N.A., Triboelectrics: the influence of particle surface roughness and shape on charge acquisition during aerosolization and the DPI performance, Powder Technology, 262 (2014) 22–29. https://doi.org/10.1016/j.powtec.2014.04.025
Kitamura M., Strategy for control of crystallization of polymorphs, CrystEngComm, 11 (2009) 949–964. https://doi.org/10.1039/B809332F
Kotha R.R., Zhang K., Yehl P., Kumar A., Oxidative degradation in pharmaceuticals: mechanism and stabilization of a spray-dried amorphous drug – A case study, Journal of Pharmaceutical and Biomedical Analysis, 220 (2022) 114962. https://doi.org/10.1016/j.jpba.2022.114962
Kwok P., Chan H., Electrostatic charge in pharmaceutical systems, in; Swarbrick, J. (Ed.), Encyclopedia of Pharmaceutical Science and Technology, Six Volume Set (Print), 4th ed., CRC Press, 2013, pp. 1394–1407. https://doi.org/10.1081/E-EPT4
Langrish T.A.G., Assessing the rate of solid-phase crystallization for lactose: the effect of the difference between material and glass-transition temperatures, Food Research International, 41 (2008) 630–636. https://doi.org/10.1016/j.foodres.2008.04.010
Lau M., Young P.M., Traini D., Co-milled API-lactose systems for inhalation therapy: impact of magnesium stearate on physico-chemical stability and aerosolization performance, Drug Development and Industrial Pharmacy, 43 (2017) 980–988. https://doi.org/10.1080/03639045.2017.1287719
Lee R.C., Nonequilibrium humidity control for jet milling, US Patent, (2012) US8235314B2. https://patents.google.com/patent/US8235314B2/en
Lee Y.-Y., Wu J.X., Yang M., Young P.M., van den Berg F., Rantanen J., Particle size dependence of polymorphism in spray-dried mannitol, European Journal of Pharmaceutical Sciences, 44 (2011) 41–48. https://doi.org/10.1016/j.ejps.2011.06.002
Li N., Cape J.L., Mankani B.R., Zemlyanov D.Y., Shepard K.B., Morgen M.M., Taylor L.S., Water-induced phase separation of spray-dried amorphous solid dispersions, Molecular Pharmaceutics, 17 (2020) 4004–4017. https://doi.org/10.1021/acs.molpharmaceut.0c00798
Lin Y., Cogdill R.P., Wildfong P.L.D., Informatic calibration of a materials properties database for predictive assessment of mechanically activated disordering potential for small molecule organic solids, Journal of Pharmaceutical Sciences, 98 (2009) 2696–2708. https://doi.org/10.1002/jps.21647
Lundahl M.L.E., Fogli S., Colavita P.E., Scanlan E.M., Aggregation of protein therapeutics enhances their immunogenicity: causes and mitigation strategies, RSC Chemical Biology, 2 (2021) 1004–1020. https://doi.org/10.1039/d1cb00067e
Mahlin D., Bergström C.A.S., Early drug development predictions of glass-forming ability and physical stability of drugs, European Journal of Pharmaceutical Sciences, 49 (2013) 323–332. https://doi.org/10.1016/j.ejps.2013.03.016

Mahlin D., Ponnambalam S., Heidarian Höckerfelt M., Bergström C.A.S., Toward in silico prediction of glass-forming ability from molecular structure alone: a screening tool in early drug development, Molecular Pharmaceutics, 8 (2011) 498–506. https://doi.org/10.1021/mp100339c

Mensink M.A., Frijlink H.W., van der Voort Maarschalk K., Hinrichs W.L., How sugars protect proteins in the solid state and during drying (review): mechanisms of stabilization in relation to stress conditions, Eur J Pharm Biopharm, 114 (2017) 288–295. https://doi.org/10.1016/j.ejpb.2017.01.024

Mounsey J.S., Hogan S.A., Murray B.A., O'Callaghan D.J., Effects of hydrolysis on solid-state relaxation and stickiness behavior of sodium caseinate-lactose powders, Journal of Dairy Science, 95 (2012) 2270–2281. https://doi.org/10.3168/jds.2011-4674

Nešić S., Vodnik J., Kinetics of droplet evaporation, Chemical Engineering Science, 46 (1991) 527–537. https://doi.org/10.1016/0009-2509(91)80013-O

Nývlt J., The Ostwald rule of stages, Crystal Research and Technology, 30 (1995) 443–449. https://doi.org/10.1002/crat.2170300402

Olusanmi D., Roberts K.J., Ghadiri M., Ding Y., The breakage behaviour of Aspirin under quasi-static indentation and single particle impact loading: effect of crystallographic anisotropy, International Journal of Pharmaceutics, 411 (2011) 49–63. https://doi.org/10.1016/j.ijpharm.2011.03.039

Olusanmi D., Wang C., Ghadiri M., Ding Y., Roberts K.J., Effect of temperature and humidity on the breakage behaviour of Aspirin and sucrose particles, Powder Technology, 201 (2010) 248–252. https://doi.org/10.1016/j.powtec.2010.04.003

Ordoubadi M., Wang H., Vehring R., Mechanistic formulation design of spray-dried powders, KONA Powder and Particle Journal, 40 (2023) 149–171. https://doi.org/10.14356/kona.2023012

Otsuka M., Kaneniwa N., Effect of seed crystals on solid-state transformation of polymorphs of chloramphenicol palmitate during grinding, Journal of Pharmaceutical Sciences, 75 (1986) 506–511. https://doi.org/10.1002/jps.2600750517

Parrott E.L., Milling of pharmaceutical solids, Journal of Pharmaceutical Sciences, 63 (1974) 813–829. https://doi.org/10.1002/jps.2600630603

Pikal M.J., Lukes A.L., Lang J.E., Thermal decomposition of amorphous β-lactam antibacterials, Journal of Pharmaceutical Sciences, 66 (1977) 1312–1316. https://doi.org/10.1002/jps.2600660927

Price R., Young P.M., On the physical transformations of processed pharmaceutical solids, Micron, 36 (2005) 519–524. https://doi.org/10.1016/j.micron.2005.04.003

Ranz W.E., Evaporation from drops, Chemical Engineering Progress, 48 (1952) 141–146.

Rasenack N., Müller B.W., Micron-size drug particles: common and novel micronization techniques, Pharmaceutical Development and Technology, 9 (2004) 1–13. https://doi.org/10.1081/PDT-120027417

Rodríguez-Hornedo N., Murphy D., Significance of controlling crystallization mechanisms and kinetics in pharmaceutical systems, Journal of Pharmaceutical Sciences, 88 (1999) 651–660. https://doi.org/10.1021/js980490h

Roelands C.M., Jiang S., Kitamura M., ter Horst J.H., Kramer H.J., Jansens P.J., Antisolvent crystallization of the polymorphs of L-histidine as a function of supersaturation ratio and of solvent composition, Crystal Growth & Design, 6 (2006) 955–963. https://doi.org/10.1021/cg050529d

Rumondor A.C.F., Taylor L.S., Effect of polymer hygroscopicity on the phase behavior of amorphous solid dispersions in the presence of moisture, Molecular Pharmaceutics, 7 (2010) 477–490. https://doi.org/10.1021/mp9002283

Schmalzried H., Influence of mechanical stress, Chemical Kinetics of Solids, Wiley-VCH Verlag GmbH, 1995, pp. 331–354, ISBN: 9783527615537. https://doi.org/10.1002/9783527615537

Schneider-Rauber G., Arhangelskis M., Goh W.-P., Cattle J., Hondow N., Drummond-Brydson R., Ghadiri M., Sinha K., Ho R., Nere N.K., Bordawekar S., Sheikh A.Y., Jones W., Understanding stress-induced disorder and breakage in organic crystals: beyond crystal structure anisotropy, Chemical Science, 12 (2021) 14270–14280. https://doi.org/10.1039/D1SC03095G

Shur J., Pitchayajittipong C., Rogueda P., Price R., Effect of processing history on the surface interfacial properties of budesonide in carrier-based dry-powder inhalers, Therapeutic Delivery, 4 (2013) 925–937. https://doi.org/10.4155/tde.13.69

Singh A., Van den Mooter G., Spray drying formulation of amorphous solid dispersions, Advanced Drug Delivery Reviews, 100 (2016) 27–50. https://doi.org/10.1016/j.addr.2015.12.010

Thakur A.K., Kumar R., Vipin Kumar V.K., Kumar A., Kumar Gaurav G., Naresh Gupta K., A critical review on thermodynamic and hydrodynamic modeling and simulation of liquid antisolvent crystallization of pharmaceutical compounds, Journal of Molecular Liquids, 362 (2022) 119663. https://doi.org/10.1016/j.molliq.2022.119663

Tse J.S., Mechanical instability in ice $I_h$. A mechanism for pressure-induced amorphization, The Journal of Chemical Physics, 96 (1992) 5482–5487. https://doi.org/10.1063/1.462732

Tsukushi I., Yamamuro O., Matsuo T., Solid state amorphization of organic molecular crystals using a vibrating mill, Solid State Communications, 94 (1995) 1013–1018. https://doi.org/10.1016/0038-1098(95)00161-1

Turnbull D., Under what conditions can a glass be formed?, Contemporary Physics, 10 (1969) 473–488. https://doi.org/10.1080/00107516908204405

Vehring R., Pharmaceutical particle engineering via spray drying, Pharmaceutical Research, 25 (2008a) 999–1022. https://doi.org/10.1007/s11095-007-9475-1

Vehring R., Pharmaceutical particle engineering via spray drying, Pharmaceutical Research, 25 (2008b) 999–1022. https://doi.org/10.1007/s11095-007-9475-1

Vehring R., Foss W.R., Lechuga-Ballesteros D., Particle formation in spray drying, Journal of Aerosol Science, 38 (2007) 728–746. https://doi.org/10.1016/j.jaerosci.2007.04.005

Vemuri N.M., Brown A.B., Authelin J.R., Hosek P., Milling process for the production of finely milled medicinal substances, US Patent, (2003) US6641063B2. https://patents.google.com/patent/US6641063B2/en

Wang R., Pellerin C., Lebel O., Role of hydrogen bonding in the formation of glasses by small molecules: a triazine case study, Journal of Materials Chemistry, 19 (2009) 2747–2753. https://doi.org/10.1039/B820294J

Wang W., Roberts C.J., Protein aggregation – Mechanisms, detection, and control, International Journal of Pharmaceutics, 550 (2018) 251–268. https://doi.org/10.1016/j.ijpharm.2018.08.043

Ward G.H., Schultz R.K., Process-induced crystallinity changes in albuterol sulfate and its effect on powder physical stability, Pharmaceutical Research, 12 (1995) 773–779. https://doi.org/10.1023/a:1016232230638

Weers J.G., Miller D.P., Formulation design of dry powders for inhalation, Journal of Pharmaceutical Sciences, 104 (2015) 3259–3288. https://doi.org/10.1002/jps.24574

Wildfong P.L.D., Hancock B.C., Moore M.D., Morris K.R., Towards an understanding of the structurally based potential for mechanically activated disordering of small molecule organic crystals, Journal of Pharmaceutical Sciences, 95 (2006) 2645–2656. https://doi.org/10.1002/jps.20672

Willart J.F., Dujardin N., Dudognon E., Danède F., Descamps M., Amorphization of sugar hydrates upon milling, Carbohydrate Research, 345 (2010) 1613–1616. https://doi.org/10.1016/j.carres.2010.04.014

Williams M.L., Landel R.F., Ferry J.D., The temperature dependence of relaxation mechanisms in amorphous polymers and other glass-forming liquids, Journal of the American chemical society, 77 (1955) 3701–3707. https://doi.org/10.1021/ja01619a008

Wong J., Kwok P.C., Noakes T., Fathi A., Dehghani F., Chan H.K., Effect of crystallinity on electrostatic charging in dry powder inhaler formulations, Pharmaceutical Research, 31 (2014) 1656–1664. https://doi.org/10.1007/s11095-013-1270-6

Woo M.W., Fu N., Moo F.T., Chen X.D., Unveiling the mechanism of in situ crystallization in the spray drying of sugars, Industrial & Engineering Chemistry Research, 51 (2012) 11791–11802. https://doi.org/10.1021/ie3007402

Wu J.X., Yang M., Berg F.v.d., Pajander J., Rades T., Rantanen J., Influence of solvent evaporation rate and formulation factors on solid dispersion physical stability, European Journal of Pharmaceutical Sciences, 44 (2011) 610–620. https://doi.org/10.1016/j.ejps.2011.10.008

Yokoyama T., Inoue Y., Chapter 10 selection of fine grinding mills, in: Salman A.D., Ghadiri M., Hounslow M.J. (Eds.), Handbook of Powder Technology, Elsevier Science B.V., 2007, pp. 487–508, ISBN: 0167-3785. https://doi.org/10.1016/S0167-3785(07)12013-3

York P., Solid-state properties of powders in the formulation and processing of solid dosage forms, International Journal of Pharmaceutics, 14 (1983) 1–28. https://doi.org/10.1016/0378-5173(83)90111-4

Yu L., Reutzel-Edens S.M., Mitchell C.A., Crystallization and polymorphism of conformationally flexible molecules: problems, patterns, and strategies, Organic Process Research & Development, 4 (2000) 396–402. https://doi.org/10.1021/op000028v

Zeleny R.A., Piret E.L., Dissipation of energy in single particle crushing, Industrial & Engineering Chemistry Process Design and Development, 1 (1962) 37–41. https://doi.org/10.1021/i260001a007

Zhang Y., Wang X., Lin X., Liu X., Tian B., Tang X., High azithromycin loading powders for inhalation and their in vivo evaluation in rats, International Journal of Pharmaceutics, 395 (2010) 205–214. https://doi.org/10.1016/j.ijpharm.2010.05.043

## Authors' Short Biographies

**Mariana Romero-Gonzalez** is currently a third-year Ph.D. candidate in the Department of Pharmaceutical Sciences at the University of Michigan. Mariana holds a master's degree in Pharmaceutical Sciences from Universidad Autonoma de Nuevo Leon, where she worked on oral controlled-release pharmaceutical dosage forms. Mariana's doctoral research at the University of Michigan is focused on the development of inhalable pharmaceutical interventions that help treat opportunistic lung infections and restore microbiome diversity in chronic disease states.

**Julia Crowther** is a second-year Ph.D. student at the University of Michigan studying Pharmaceutical Sciences. Julia attended the University of Michigan for her undergraduate degree, obtaining a B.S. in Pharmaceutical Sciences with honors. During her undergraduate studies, Julia investigated the impact of lipid composition on atheroprotective properties of HDL-mimetic micelles. Her doctoral research is focused on the role of the gut microbiome in traumatic brain injury.

**Dr. Mani Ordoubadi** serves as a Postdoctoral Fellow in the Department of Mechanical Engineering at the University of Alberta. He obtained his Ph.D. from the same institution, focusing on the development of predictive tools for assisting in the formulation design of spray-dried inhalable microparticles. This aids in cost and risk reduction during the initial stages of product development for emerging therapeutics in solid dosage forms. His expertise encompasses numerical simulations, computational fluid dynamics, heat and mass transfer, multiphase flows, and aerosol mechanics.

**Dr. Ashlee Brunaugh** is an Assistant Professor in the University of Michigan Pharmaceutical Sciences department. She obtained her Pharm.D. and Ph.D. degrees at the University of Texas at Austin. Prior to joining the faculty at the University of Michigan, she managed start-up companies related to translational pre-clinical development of drug products for respiratory infections. Her lab focuses on the elucidation of the underlying mechanisms for respiratory disease progression to determine appropriate therapeutic targets and develop novel formulation and pulmonary drug delivery approaches to improve patient outcomes.

KONA Powder and Particle Journal

KONA Powder and Particle Journal No. 42 (2025) 134–155/https://doi.org/10.14356/kona.2025011 Review Paper

# Progress in the Application of Multidimensional Particle Property Distributions: The Separation Function†

**Edgar Schach[1], Thomas Buchwald[1], Orkun Furat[2], Florentin Tischer[3], Alexandra Kaas[1], Laura Kuger[4], Matthias Masuhr[5], Johanna Sygusch[6], Thomas Wilhelm[2], Ralf Ditscherlein[1] and Urs Alexander Peuker[1]***

[1] *Institute of Mechanical Process Engineering and Mineral Processing, TU Bergakademie Freiberg, Germany*
[2] *Institute of Stochastics, Ulm University, Germany*
[3] *Department of Chemical and Biological Engineering, Friedrich-Alexander-Universität Erlangen-Nürnberg, Germany*
[4] *Institute of Functional Interfaces, Karlsruhe Institute of Technology, Germany*
[5] *Institute of Technology for Nanostructures, Universität Duisburg-Essen, Germany*
[6] *Helmholtz Institute Freiberg for Resource Technology, Helmholtz-Zentrum Dresden-Rossendorf, Germany*

In KONA 2022, the fundamentals of two- and multidimensional particle size distributions were introduced. The next question in the field of two- and multidimensional distributions addresses their application to describe a particle process, e.g., agglomeration or separation. A multidimensional separation can be seen as retrieving only particles with a specific set of properties from a multidimensionally distributed system, e.g., retrieving only small particles (below a certain threshold in size) with a compact spherical shape (above a certain threshold in sphericity). The multidimensional separation allows the generation of functional particle systems with specific properties, e.g., semiconducting, optical, or electronic properties, which are required for high-technology applications. Starting from so-called particle-discrete information, i.e., an information vector for each particle containing its compositional, geometrical, and physical properties, it is possible to describe a multidimensional separation in full detail based on various properties. Each particle can be evaluated according to different separation properties, e.g., size, shape, and material composition. With this database, it is possible to define and work with separation functions to describe the multidimensional separation and quantify the separation results. For example, in the two-dimensional case, the median cut size becomes a median cut line, where the probability for a particle to belong to the concentrate is 0.5. Some case studies and examples show different approaches and possibilities to achieve a multidimensional separation in one or several connected process steps.

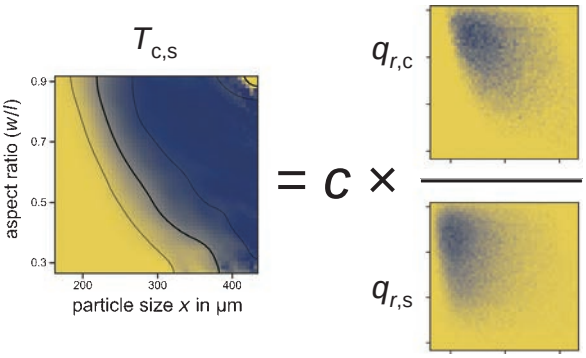


**Keywords:** separation function, Tromp curve, partition curve, multidimensional, particle property distribution

## 1. Introduction

In KONA 2022, Frank et al. presented the fundamentals of two- and multidimensional particle size distributions, allowing for a more detailed description of particle systems than combining a constant shape factor with a particle size distribution. They also demonstrated the challenges in measuring and retrieving multidimensional particle size distributions (Frank et al., 2022). Particle-discrete information is necessary to generate particle property distributions of any dimension. For the one-dimensional distribution, which we all know as particle size distribution (PSD), the starting point is the information about the size, i.e., the equivalent diameter, of each discrete particle. This information is grouped into size classes and weighted by number, cord length, surface, or volume. To compute particle property distributions of higher dimensions, which show the distributed values of size, shape, composition, crystallinity, and others simultaneously, particle-discrete information has to be extracted (**Fig. 1**). Thus, each particle is described by an information vector containing the relevant particle-discrete data of its properties.

In addition to the multidimensional information about particle geometry, the composition of the individual particles provides additional dimensions in the description of particle systems. These dimensions are central aspects in the field of primary and secondary raw materials, where ores, slags, or anthropogenic waste materials (**Fig. 2**) have to be characterized, processed, and separated (Werner et al., 2020). Individual multicomponent particles are intergrown, i.e., they have a complex microstructure consisting of more than one material phase.

The cassiterite ore shown here (**Fig. 3**) consists of four

† Received 29 June 2023; Accepted 6 October 2023
J-STAGE Advance published online 29 June 2024
* Corresponding author: Urs Alexander Peuker;
Add: Agricolastraße 1, KKB-1057, 09599 Freiberg, Germany
E-mail: urs.peuker@mvtat.tu-freiberg.de
TEL: +49-3731-39-2795

main materials, i.e., minerals. Each particle within the ore sample is composed of one or more of these minerals. Material classes are chosen to reduce complexity, i.e., the dimension of the problem. For example, all iron-containing phases are grouped together in the material class iron oxides. Using the color code, it becomes apparent that there is a vast diversity among the individual particles, even with just four different material phases. This behavior is also observed in the slag sample in **Fig. 3 (right)**, which exhibits multiple material phases.

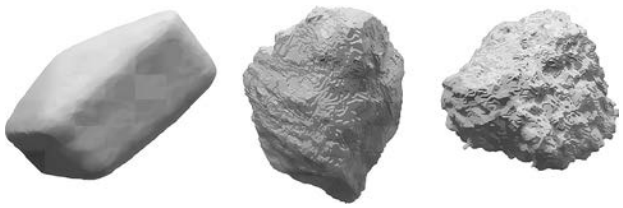

**Fig. 1** 3D particles of different materials from which geometrical data can be retrieved, determined by 3D scanning **(left)** and by µ-CT **(middle and right)**.

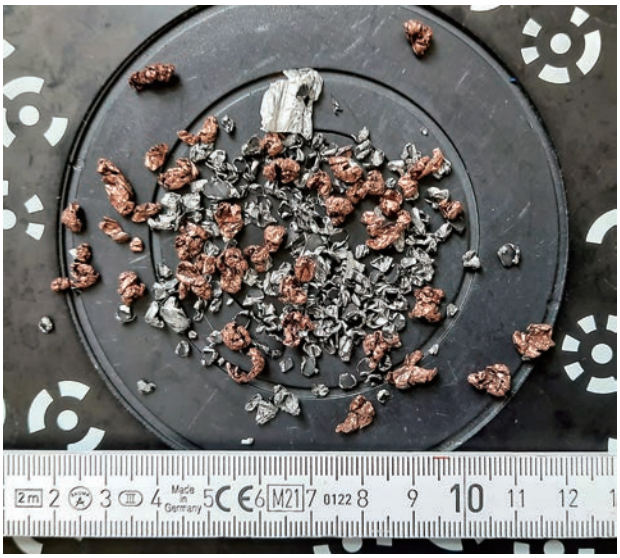

**Fig. 2** Particles from the mechanical recycling process of lithium-ion-batteries as explained in Ref. (Werner et al., 2020), showing particles with non-compact irregular and significantly distributed shape properties.

Multimaterial particles also become increasingly important in the field of particle design, when particles are coated (**Fig. 4**), encapsulated, co-precipitated, or integrated into composite materials (Hickstein and Peuker, 2009). The interplay between different properties of a particle collective has therefore come into focus of research in recent years (Bagheri et al., 2015).

In summary, the concept of particle-discrete information forms the basis for generating multidimensional particle property distributions. These distributions are created by constructing property vectors for individual particles, which include various properties such as characteristic length, volume, shape factor, composition, porosity, roughness, and crystallinity. The more elements are included in the vector, the higher becomes the potential dimensionality of the property distribution that can be generated from the particle-discrete data set. Common measuring techniques producing particle-discrete, multidimensional data are computed tomography (Çiçek et al., 2016; Ditscherlein et al., 2020; Egan et al., 2015; Leißner et al., 2020), dynamic image analysis (Bujak and Bottlinger, 2008; Kuzmanić and Mikoš, 2022; Oliver et al., 2019), and mineral liberation analysis (Leißner et al., 2016), as shown in **Fig. 3**. Other measuring techniques in which multidimensionality poses a particular problem include the shape influence in laser diffraction analysis (Matsuyama and Yamamoto, 2005; Peciar et al., 2022).

The properties in the vector may originate from different sources. Initially, these are the original measurement data obtained from different characterization methods and principles. It is crucial to ensure that the data is thoroughly linked to the corresponding particle when combining or correlating measurements from different principles. Some properties in the vector, such as equivalent diameters and shape factors, are calculated or aggregated parameters (Heywood, 1961). These properties can be added to the

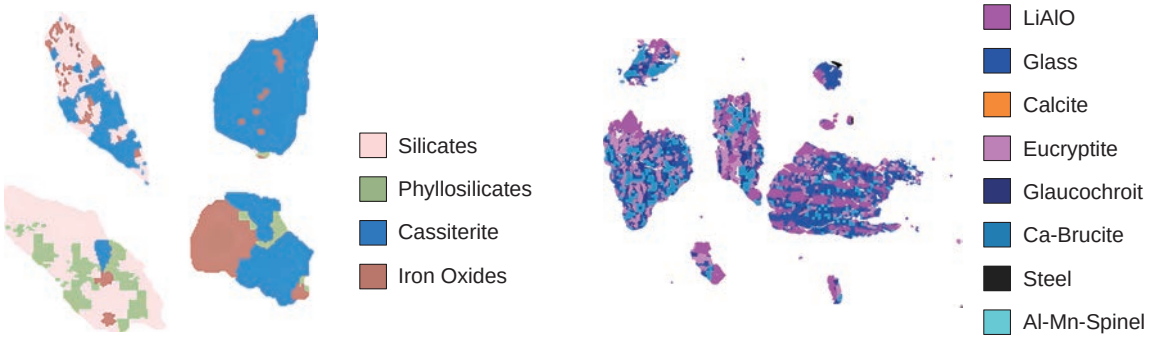


**Fig. 3** Material-related properties of individual particles, measured by mineral liberation analysis (MLA), which is a SEM-EDX-system, coupled with a mineral data base. Adapted with permission from Ref. (Buchmann et al., 2020b). **Left**: particles from different material streams in the processing of a cassiterite ore (Ehrenfriedersdorf, Saxony); **right**: particles from a lithium-aluminate slag (RWTH Aachen IME), which occurs in lithium-ion-battery recycling.

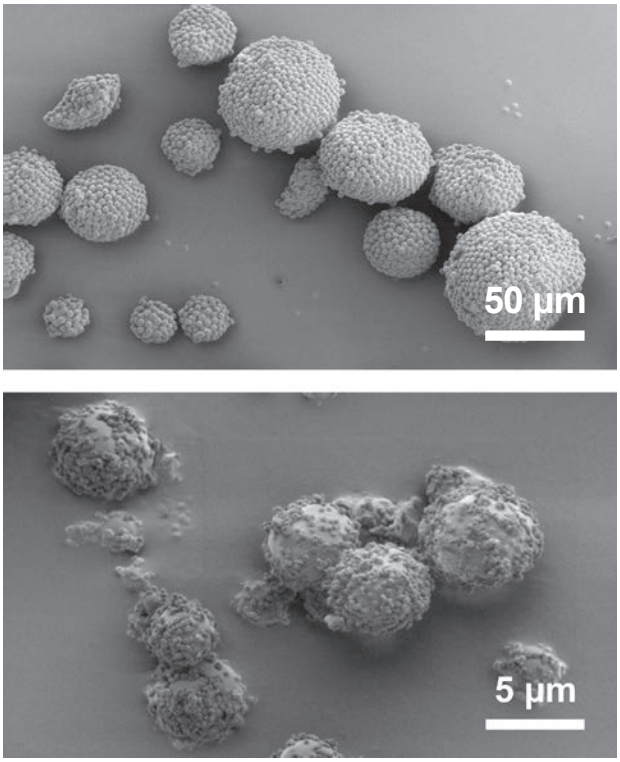


**Fig. 4** SEM pictures of surface coated particles. The particles were produced by mechano-fusion (Alonso et al., 1989; Pfeffer et al., 2001; Tanno, 1990). **Top**: carrier particle ($Al_2O_3$ - DAW-45, Denka) with a polystyrene particle coating (Chemisnow SX-350 H, Soken Chemical); **bottom**: carrier particles (Alumina - DAW-05, Denka) coated with PMMA (Chemisnow MP2801, Soken Chemical) (Friebel et al., 2024).

vector, resulting in a rapid increase in the number of elements. From the methodological perspective, particle-discrete multidimensional data sets are essential for creating multidimensional property distributions since they contain all necessary information. Only with additional information or assumptions, such as precise knowledge of particle geometry in the case of synthesized nanoparticles, it is possible to directly generate the corresponding unique multidimensional distribution from several one-dimensional distributions (marginal distributions) (Demeler et al., 2014). Imaging techniques and correlative imaging methods, such as X-ray computed tomography, are often preferred for generating particle-discrete data sets (Frank et al., 2019; 2022).

The multidimensional description of the particle collective then provides the methods to investigate many common separation processes. On most classification and sorting machines, particles are sorted according to more than one parameter. While some of these properties are perceived to have an influence, they have yet to be thoroughly investigated. A perfect example is the sieving process, in which results are displayed as a separation according to particle size, but where particle shape plays a vital role (Blott and Pye, 2008; Dehghani et al., 2002; Nakajima et al., 1979; Whiteman and Ridgway, 1986). Other examples are sedimentation (Wadell H., 1932a,b; 1933) and the aero- (Furchner and Zampini, 2009), and hydrodynamic separation processes (Fontein, 1961), as well as processes for shape separation (Furuuchi and Gotoh, 1992).

Often, the multidimensionality of a separation process is implicitly shown by researchers without highlighting the multidimensionality explicitly (Tang and Puri, 2007). Examples include the separation of PET flakes from plastic bottle recycling on zig-zag sifters and air jigs (Friedländeret al., 2006) and separation by thermo-adhesion, where particles are selectively heated by microwaves until they stick to a surface (Baloun. et al., 2005).

In other separation processes, most importantly some analytical methods, the multidimensionality of the separation process is of key interest, for example, in flow-field fractionation, where particles are separated hydrodynamically inside a flat channel (Baalousha et al., 2011). Recently, separation processes have been shown to become comparable by calculation of a statistic entropy that describes the degree of disorder in a particle collective (Buchmann et al., 2020a).

In the following, a description of multidimensional particle property distributions is given, followed by a description of how two-dimensional separation processes can be presented in a convenient manner. The text ends with a review of some examples of multidimensional separation.

## 2. Theoretical background

### 2.1 Working with particle-discrete datasets

When particle-discrete datasets are available, it is possible to generate the corresponding multidimensional particle property distributions. As in the one-dimensional case, property classes are defined with appropriate boundaries. In the multidimensional case, a property class addresses more than one property (**Fig. 5**). For the two-dimensional example, with the properties $x$ (equivalent diameter/particle size) and $y$ (shape factor), each class contains the fraction of all particles, which fulfill the specifications:

- equivalent diameter: $x_{i-1} < x \leq x_i$
- shape factor: $y_{j-1} < y \leq y_j$

The two-dimensional particle density distribution uses a definition similar to the one-dimensional case. The following example considers a set of particle data in which the volume of each particle is known. Only under the assumption of constant density, a volume- or mass-weighted distribution can be computed. Where length- and area-based distributions will sometimes occur in the description of one-dimensional property distributions, in practice, multidimensional distributions will either be number- or volume-/mass-weighted.

To obtain the two-dimensional density distribution, the mass of the particles in class $[i, j]$, $m_{i,j}$, is divided by the

overall mass $m_{total}$ and the area of that class, which now involves two dimensions, $\Delta x_i$ for the property $x$ and $\Delta y_j$ for the property $y$:

$$q_3\left(\overline{x}_i, \overline{y}_j\right) = \frac{m_{i,j}}{m_{\text{total}}\ \Delta x_i\ \Delta y_j} = \frac{\Delta Q_{3,i,j}}{\Delta x_i \Delta y_j} \tag{1}$$

The width of the property classes is the difference between the upper and lower limits for each property:

$$\Delta x_i = x_i - x_{i-1} \tag{2}$$
$$\Delta y_i = y_j - y_{j-1} \tag{3}$$

Using d$x$ and d$y$ for the size of the classes, the two-dimensional property distribution can be written in a differential form as well:

$$q_3(x,y) = \frac{\mathrm{d}^2 Q_3}{\mathrm{d}x\mathrm{d}y} \tag{4}$$

The normalization condition that the sum or the integral of a density distribution is equal to one is also valid for the two- and multidimensional cases. In the two-dimensional case, the density distribution has to be summed up over both $x$ and $y$:

$$\sum_{j=1}^{m}\sum_{i=1}^{n} q_3(x_i, y_j) = 1 \tag{5}$$

The definition range of a two-dimensional property distribution describes a defined area in the $x$-$y$-plane. Outside this area, the density distribution is by definition:

$$q_3(x,y) = 0 \quad \text{if } x \le x_{\min} \text{ and / or } y \le y_{\min} \tag{6}$$
$$q_3(x,y) = 0 \quad \text{if } x > x_{\max} \text{ and / or } y > y_{\max} \tag{7}$$

The cumulative sum is calculated via summing up or integrating the density distribution from the minimal values $x_{min}$ and $y_{min}$ up to a point ($x$, $y$):

$$\begin{aligned} Q_{3,i,j} &= \sum_{\mu=1}^{j}\sum_{\nu=1}^{i} \Delta Q_{3,\nu,\mu} \\ &= \sum_{\mu=1}^{j}\sum_{\nu=1}^{i} q_{3,\nu,\mu}\, \Delta x_\nu\, \Delta y_\mu \end{aligned} \tag{8}$$

$$Q_3(x,y) = \int_{y_{\min}}^{y}\int_{x_{\min}}^{x} q_3(x,y)\mathrm{d}x\mathrm{d}y \tag{9}$$

For the two-dimensional case, the cumulative sum is zero when both properties are below their minimal values and is 1 if both properties are above their maximum value:

$$Q_3(x,y) = 0 \quad \text{if } x \le x_{\min} \text{ or } y \le y_{\min} \tag{10}$$
$$Q_3(x,y) = 1 \quad \text{if } x > x_{\max} \text{ and } y > y_{\max} \tag{11}$$

For better visualization heat plots, which project the third dimension, i.e., the numerical value of the distribution, in a color code, should be used instead of the 3D-plots (**Fig. 6**). For example, **Fig. 7** shows the same two-dimensional data-set (**Fig. 6, right**) as a heat map. Of course, this type of visualization can also be implemented for the density distribution (**Fig. 6, left**).

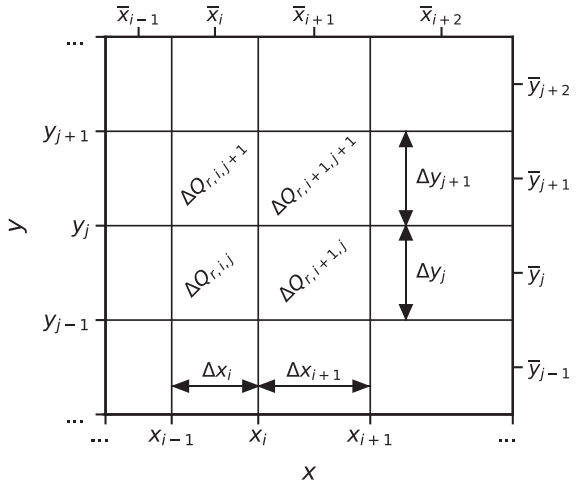


**Fig. 5** Schematic representation of the two-dimensional definition of property classes for the properties $x$ and $y$.

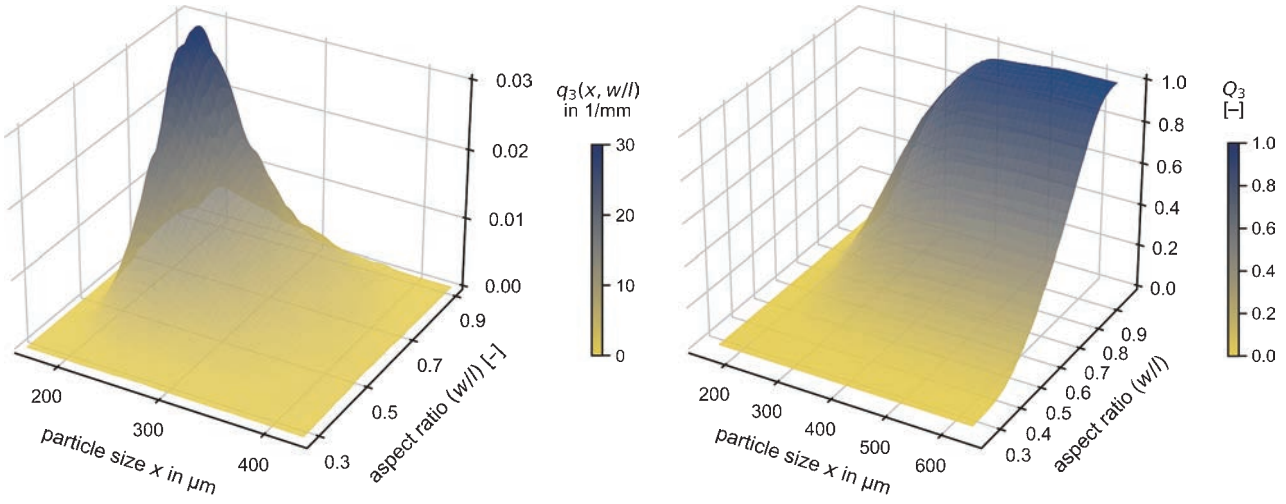


**Fig. 6** 3D-plot of a two-dimensional size-shape-distribution of 56500 particles, measured with the dynamic image analysis system PartAn 3D; **left**: probability density function; **right**: cumulative sum.

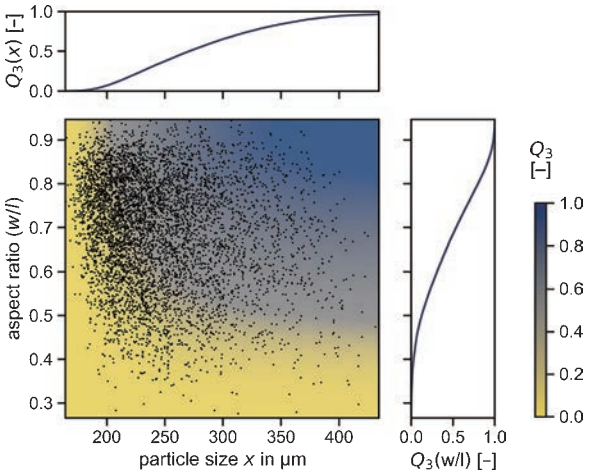


**Fig. 7** Two-dimensional plot of the cumulative sum (mass-weighted), also displaying the discrete particles' data points. The outer one-dimensional distributions are the corresponding marginal distributions for size $x$ and aspect ratio $y = w/l$.

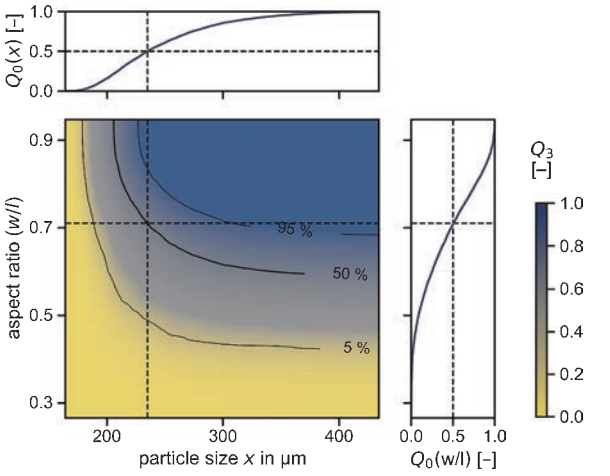


**Fig. 8** Cumulative sum distribution showing the isolines for 5 %, 50 %, and 95 %. Visualization of the median particle size ($x_{50}$, $y_{50}$) as the intercept of the median values of the marginal distributions.

Marginal distributions are distributions of lower dimensionality. For the exemplary two-dimensional case ($x$, $y$), the corresponding marginal distributions are the one-dimensional distributions of the individual properties $x$ and $y$. These derive from an integration over the other property, i.e., for $q_3(x)$ derives from $q_3(x, y)$ as integration over $y$ in the entire variable range $y_{min}$ to $y_{max}$:

$$q_3(x) = \int_{y_{min}}^{y_{max}} q_3(x, y)\,\mathrm{d}y \tag{12}$$

$$q_3(y) = \int_{x_{min}}^{x_{max}} q_3(x, y)\,\mathrm{d}x \tag{13}$$

The marginal one-dimensional distributions can be visualized at the individual axis of the heat-plot of the two-dimensional distribution (**Fig. 7**), either as histograms for discrete property classes or as smooth functions, when the heat plot shows a differential presentation of the distribution. The latter typically uses an interpolation between the property classes or even between the individual data points. Suitable interpolation methods are kernel density estimation (Schach et al., 2019) and copulas (Czado, 2019; Furat et al., 2019; Joe H., 2014).

## 2.2 Characteristic particle sizes of the multidimensional distribution

One-dimensional particle size distributions are commonly described by the median particle size or the modal particle size as characteristic values, which are used to represent the entire particle size distribution with a single parameter, e.g., in empirical models. The identification of the modal particle property within the two- or multidimensional property distribution is quite simple, since the modal property is the peak in the 3D plot, i.e., the element of the multidimensional property matrix (**Fig. 5**) with the highest numerical value. Regarding the complexity of the multidimensional property distributions, multimodal distributions (with several distinct peaks) are expected to occur much more frequently than in the one-dimensional case.

The definition of the median particle property requires a detailed view of the distribution itself. In the two-dimensional case, there is an isoline, which contains all points that split the particle system into two fractions of same quantity. For example, in **Fig. 8**, which shows the distribution by number, 50 % of the particles derive from a fraction with an aspect ratio below 0.63 and particle-equivalent diameter below 350 µm; however, 50 % of particles are also contained in the fraction of particles below an aspect ratio of 0.8 and a particle-equivalent diameter of 230 µm and smaller. The isoline itself cannot serve as one single characteristic parameter, but it is clear that the median of the cumulative sum of this particle system is located on this isoline. For the definition of the median particle size of a two-dimensional particle property distribution, we look at the intercept of the marginal property distributions. The median ($x_{50}$, $y_{50}$) is the point which fulfills the following two conditions:

1. 50 % of the particles originate from particles below this size, which is the $x_{50}$ of the marginal size distribution.
2. 50 % of the particles originate from particles below this shape factor, which is the $y_{50}$ of the marginal shape distribution.

Looking at the heat plot with the curved and monotonically decreasing isoline (**Fig. 8**), the median represents in the two-dimensional case the point that creates the rectangle having the maximum area $A$. Thus, the median ($x_{50}$, $y_{50}$) additionally fulfills the following condition:

$$A = (x_{max} - x_{50})(y_{max} - y_{50}) = \max. \tag{14}$$

## 3. Fundamentals of mixing and separation of multidimensionally distributed particle systems

Having defined the multidimensional property distribution, it has to be investigated how they can be used to describe particle-based processes.

### 3.1 Mixing of particle collectives

The mixing of two or more multidimensionally distributed particle systems still follows a simple mass balance, e.g., for the mixture of two samples:

$$m_{\mathrm{res}} = m_1 + m_2 \tag{15}$$

Using the relative mass $v$, i.e., the mass fraction, allows for a normalized discussion of the mixing process, where all relative masses $v_i$ sum up to one:

$$v_1 = \frac{m_1}{m_{\mathrm{res}}} \tag{16}$$

$$v_2 = \frac{m_2}{m_{\mathrm{res}}} \tag{17}$$

$$v_1 + v_2 = 1 \tag{18}$$

The resulting probability density distribution of the mixture can then be calculated from the density distributions of the individual samples:

$$q_{\mathrm{res}}(x,y) = v_1 q_1(x,y) + v_2 q_2(x,y) \tag{19}$$

$$Q_{\mathrm{res}}(x,y) = v_1 Q_1(x,y) + v_2 Q_2(x,y) \tag{20}$$

It has to be stated that it is only possible to mix particle property distributions of the same dimension, i.e., the particle property distribution of the mixture will have the dimensions of the particle property distribution with the lowest dimensionality.

When a three-dimensional property distribution is mixed with a two-dimensional distribution, the three-dimensional distribution has to be marginalized to a two-dimensional distribution prior to the calculation of the mixing process. Consider, for example, a dataset in which a multidimensional distribution of particle size, shape, and density is known. For the second product, density was not determined explicitly. In calculating the probability density of the resulting mixture, the information on density is lost. The marginalization therefore leads to a loss in information, which cannot be reversed later on, unless the resulting distributions are measured again.

The generalized form, which describes the mixing of $n$ different distributions with the dimensionality $m$, is the weighted sum of the $n$ distributions:

$$q_{\mathrm{res}}(x_1,\ldots,x_m) = \sum_{i=1}^{n} \left(v_i\, q_i(x_1,\ldots,x_m)\right) \tag{21}$$

### 3.2 Multidimensional separation function / Tromp curve

A multidimensional separation is defined as a separation according to more than one property. Independent of the dimensionality of the feed, the separation step creates two product fractions that vary in more than one property. Since this separation is not only a separation according to size parameters, the nomenclature of “concentrate” ($c$; mass fraction of concentrate) and “reject” ($r$; mass fraction of retentate) is used for the two product fractions, the first containing the product (valuable material), the latter containing particles of lesser interest. The indices are derived from the sorting nomenclature with C for “concentrate” and R for “refuse” or “reject”. Correspondingly, the index S is used for the feed material (“supply”) (c.f. ISO 9276-4).

As an example, for the two-dimensional case, the mass balance of the distribution densities can be written using the corresponding mass fractions:

$$1 = \frac{m_{\mathrm{C}}}{m_{\mathrm{S}}} + \frac{m_{\mathrm{R}}}{m_{\mathrm{S}}} = c + r \tag{22}$$

$$q_{\mathrm{S}}(x,y) = c\, q_{\mathrm{C}}(x,y) + r\, q_{\mathrm{R}}(x,y) \tag{23}$$

The correlation of the integral mass balance and the class-wise mass balance allows for the recalculation of the concentrate and reject mass fractions using the data from the three density distributions involved in the separation, i.e., supply, concentrate, and reject:

$$c = \frac{q_{\mathrm{S}}(x,y) - q_{\mathrm{R}}(x,y)}{q_{\mathrm{C}}(x,y) - q_{\mathrm{R}}(x,y)} \tag{24}$$

$$r = \frac{q_{\mathrm{S}}(x,y) - q_{\mathrm{C}}(x,y)}{q_{\mathrm{R}}(x,y) - q_{\mathrm{C}}(x,y)} \tag{25}$$

The separation function $T$ indicates the probability whether a particle will be transferred to the concentrate or stay in the reject. The separation function $T$ is defined in the interval [0, 1]. If the function equals $T = 1$, then the feed with these properties is entirely discharged into the concentrate. If it equals to $T = 0$, the concentrate fraction contains no particles from the feed in that area, and all feed material is discharged into the reject. Values of the separation function between 0 and 1 are a measure of the probability of the feed material ending up in the concentrate in a specific interval.

Since the degree of separation is the fraction of the particle mass in each class ($i$, $j$) that passes into the concentrate fraction, it can also be calculated from the respective distribution densities for the two-dimensional case. The calculation of the degree of separation for the higher-dimensional cases requires three discrete pieces of information, either all three property distributions of feed ($s$), concentrate ($c$) and reject ($r$), or two property distributions and a mass ratio $c$ or $r$.

Like the one-dimensional separation functions, the multidimensional separation function has a definition range in

which they can take values between 0 and 1, in which the separation is subject to a degree of uncertainty. This definition range is for $T(x, y)$ in the range between $x_{min}$ and $x_{max}$ as well as between $y_{min}$ and $y_{max}$. However, individual classes in this two-dimensional area can take the values 0 or 1, because for them a complete separation into concentrate or reject can occur. Furthermore, the calculation of $T(x, y)$ can give values outside the definition range of 0 and 1. The reason for such values is, in most cases an erroneous balance between the products and the feed material. An appropriate mass balance of the particle classes might be necessary to obtain reasonable results as e.g., proposed by Lamberg et al. (Lamberg and Vianna, 2007). Furthermore, balances can be biased due to analytical errors, which might require a correction of the results (Buchmann et al., 2018).

If one defines the two-dimensional separation function on the basis of the associated two-dimensional density distributions of feed material and concentrate and the mass balance, it leads to the separation function $T_{SC}(x, y)$:

$$T_{SC}(x,y) = \frac{c\,q_C(x,y)}{q_S(x,y)} \tag{26}$$

Using the mass balance to replace $c\,q_C(x, y)$ with $q_S(x, y) - r\,q_R(x, y)$, a different definition of the separation function is obtained, which uses the information of the reject and feed material:

$$T_{SR}(x,y) = \frac{q_S(x,y) - r\cdot q_R(x,y)}{q_S(x,y)} = 1 - r\frac{q_R(x,y)}{q_S(x,y)} \tag{27}$$

The marginal separation function is a lower-dimensional separation function of a multidimensional separation function. For the two-dimensional case, the one-dimensional separation function, i.e., a Tromp curve, is the corresponding marginal separation function. For each two-dimensional partition function there are two marginal distributions, each of which represents the one-dimensional partition function with respect to the associated property:

$$T_{SC}(x) = c\cdot\frac{\int_{y_{min}}^{y_{max}} q_C(x,y)\,dy}{\int_{y_{min}}^{y_{max}} q_S(x,y)\,dy} \tag{28}$$

$$T_{SC}(y) = c\cdot\frac{\int_{x_{min}}^{x_{max}} q_C(x,y)\,dx}{\int_{x_{min}}^{x_{max}} q_S(x,y)\,dx} \tag{29}$$

## 4. Separation functions

Before discussing the model cases of multidimensional separation, the one-dimensional separation function (Tromp curve) for a classification step is depicted in **Fig. 9 (left)**. The graph shows the distribution of the fine ($f$) and coarse ($c$) material, weighted by the mass split of the separation, the resulting Tromp curve with a typical sigmoidal shape and the separation cut size ($x_T$).

Because it will be an effect in the following discussion, **Fig. 9 (right)** shows a Tromp curve that exhibits the well-known fishhook, starting at values greater than 0. There are different explanations for such a process behavior, including, e.g., entrainment, adhesion of fine particles on coarse particles or measurement errors (Bourgeois and Majumder, 2013; Nageswararao, 2000).

### 4.1 Examples of separation functions

Buchwald et al. (2023) discussed the deduction of the two-dimensional separation function for a virtually separated particle system, where the particle-discrete data on the equivalent particle diameter and the shape factor aspect ratio were known. In that paper, the dataset coming from a dynamic image analysis (PartAn 3D) was presented as a mass distribution with a low resolution using 6 × 6 property classes. Increasing the resolution to 50 × 50 property classes provides a smoother view of the same dataset and allows for a more accurate description of the separation function with isolines. Furthermore, some special details of the separation become visible, e.g., the two-dimensional equivalent of the fishhook effect.

### 4.2 Model cases of separation

To evaluate and classify a two- or higher-dimensional separation function, it is necessary to discuss the model cases of a two-dimensional separation (**Fig. 10**). Starting with the presentation of the ideal one-dimensional separation in the two-dimensional plot, the heat plot shows either

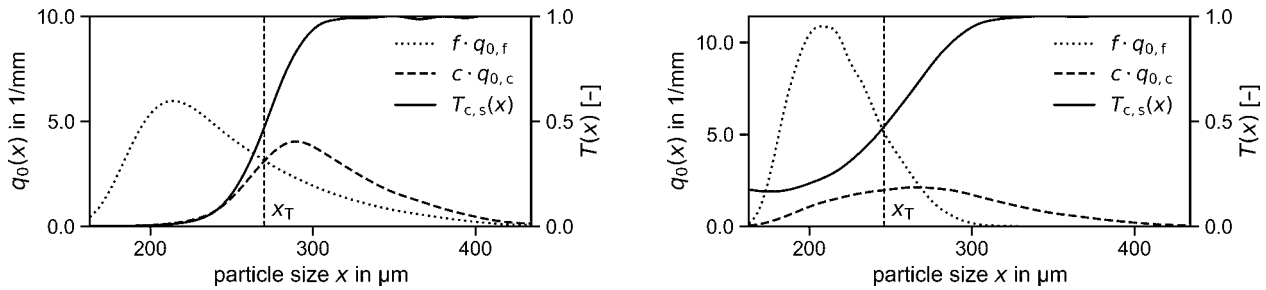


**Fig. 9** Two one-dimensional separation functions for size separations (classifications) with the underlying density functions of both the fine and the coarse fractions. The density functions have been multiplied by the respective mass fraction to better represent the mass share graphically. **Left**: ideal separation function of sigmoidal shape; **right**: separation function with "fishhook".

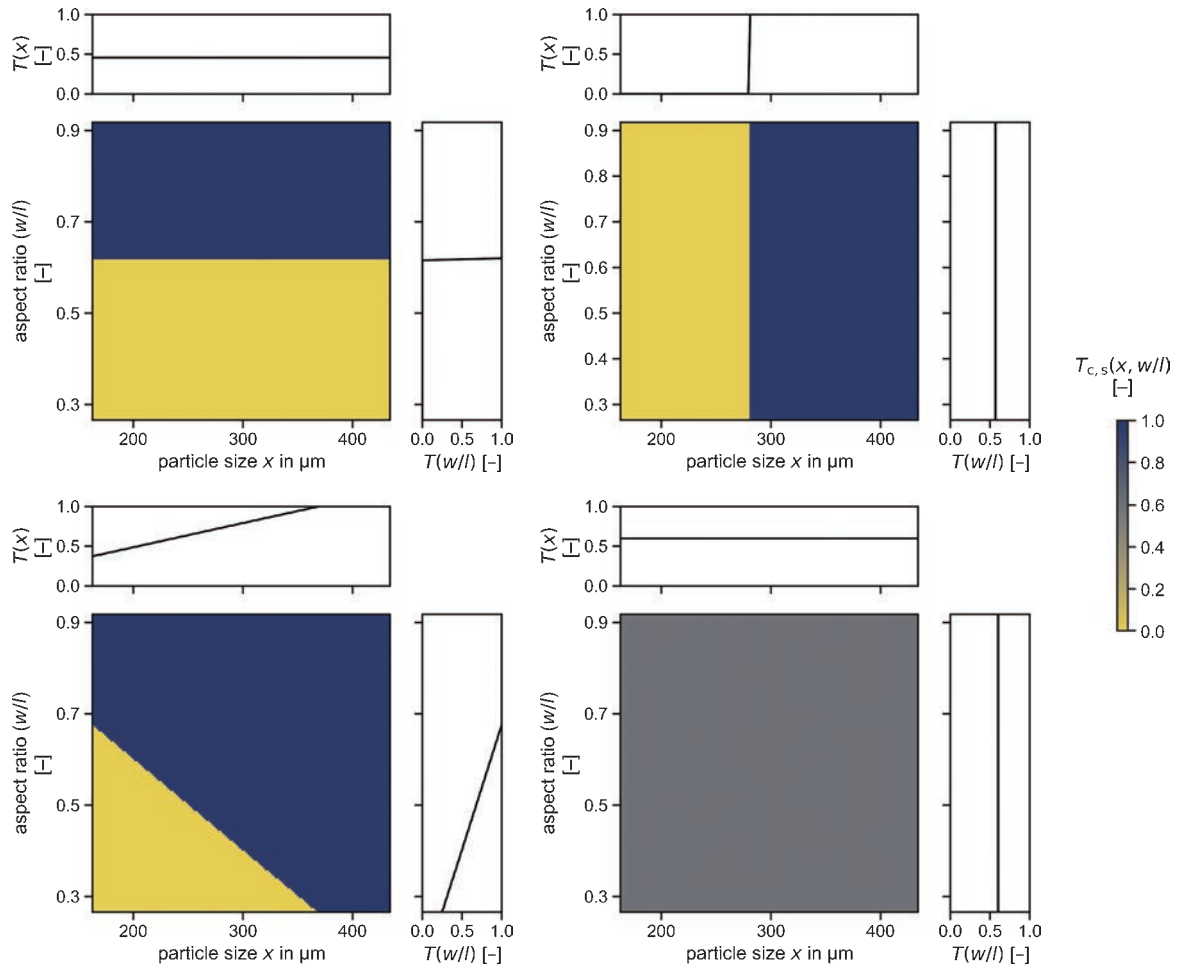


**Fig. 10** Ideal cases of the two-dimensional separation function for the parameters $x$ (size) and $y = w/l$ (aspect ratio); **upper left**: ideal one-dimensional separation according to aspect ratio; **upper right**: ideal one-dimensional separation according to particle size; **lower left**: two-dimensional separation according to a linear combination of both parameters; **lower right**: ideal splitting without any influence of either size or aspect ratio.

a horizontal (**Fig. 10, upper left**) for a separation only according to the particle aspect ratio, with the reject at the bottom and the concentrate on the top, or a vertical isoline for the separation (**Fig. 10, upper right**) with the reject on the left and the concentrate on the right. Because the separation is only due to a single parameter, the marginal separation function of this parameter will show the step function of an ideal separation function, whereas the other marginal separation function will exhibit the behavior of ideal splitting with a constant value over the entire parameter range.

A perfectly sharp separation that involves both parameters separates the parameter field into two areas of concentrate and reject (**Fig. 10, lower left**). The concentrate is situated in the upper right part of the plot, whereas the reject is found in the lower left. Even though the two-dimensional separation function shows a perfectly steep increase, the marginal one-dimensional separation functions show imperfectness: both marginal separation functions increase from a starting value above zero and reach one within the definition range of the particle property distribution. This effect can be described as fishhook, as briefly explained in **Section 3.2**. The multidimensional case in **Fig. 10** shows that fishhook effects in the one-dimensional margin distributions might be caused by an underlying multidimensional behavior. This effect can be found, e.g., for separation processes in fluid flows, in which, in addition to size and shape, the particle density has an impact on the particle process response.

The case of perfect splitting (**Fig. 10, lower right**), where feed, concentrate, and reject have an identical particle property distribution, results in a homogenous color over the entire definition range of the separation function in the heat plot.

## 4.3 Application of model cases

Particles were analyzed by dynamic image analysis in the PartAn 3D (now Camsizer 3D) by Microtrac. The device tracks particles while they fall through the measuring window, which allows for a recreation of the 3D appearance of the particle from several rotated views. In contrast to conventional dynamic image analysis, which solely

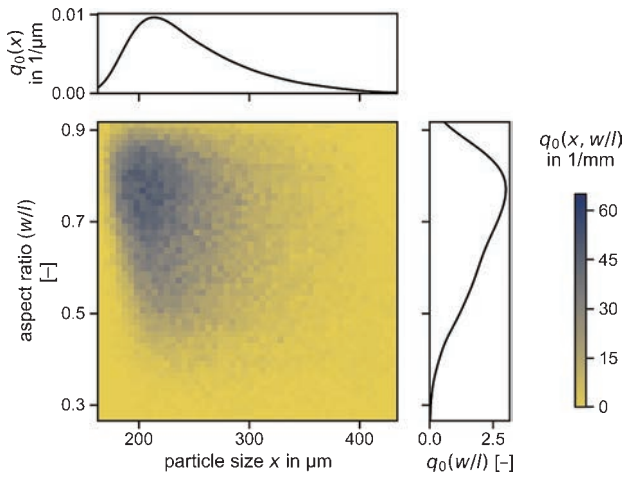


**Fig. 11** Feed particle system discussed virtually separated in the model cases described in the text.

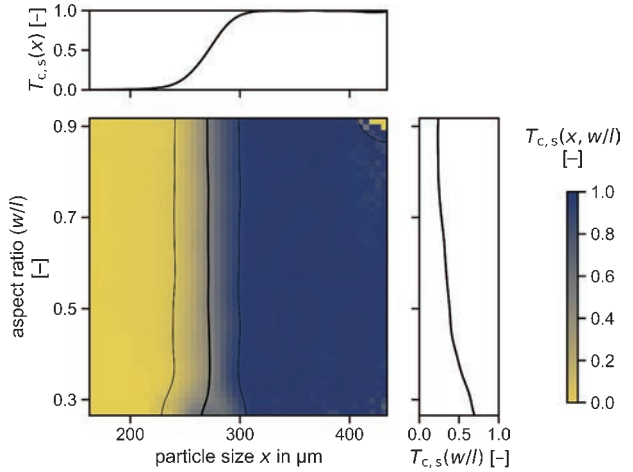


**Fig. 12** Separation function for a one-dimensional separation according to size. The separation function is calculated from the probability distributions in **Figs. 11** and **12**. Isolines display a separation degree of 25 %, 50 %, and 75 %.

measures 2D projection areas of particles, this technique has the advantage of providing true volume and shape data for each particle.

The feed particle system (**Fig. 11**) shows a wide distribution of the particles in the definition range of size and shape. The distribution will be separated one- and multidimensionally.

## 4.4 Separation according to size

The separation according to size is virtually generated using a certain imperfection that leads to an interstitial regime and a certain spread of the separation function (**Fig. 12**). For the example given in **Fig. 13**, the marginal size fractions of concentrate and reject overlap in the size range between 200 µm and 300 µm.

The resulting separation function (**Fig. 12**) principally behaves like the model case for the separation according to size, showing a vertical slope. In addition to the median isoline, two further isolines are plotted, which represent the 25 % and 75 % values of the separation function. Looking at the marginal separation function, the function for size separation shows the known s-shaped form of a Tromp curve, whereas the function for shape separation in the real case is widely distributed and differs considerably from the ideal split behavior, which is due to a certain size dependency of the shape factor in the feed material.

## 4.5 Separation according to shape

The separation of the feed distribution according to shape generates a concentrate with higher aspect ratio and a reject with lower aspect ratio. The marginal distributions of the particle shape overlap for aspect ratios between 0.5 and 0.6. The marginal distributions in size appear to be quite similar (**Fig. 14**).

The resulting two-dimensional separation function (**Fig. 15**) shows a horizontal median isoline at an aspect ratio of approximately 0.55. The marginal separation

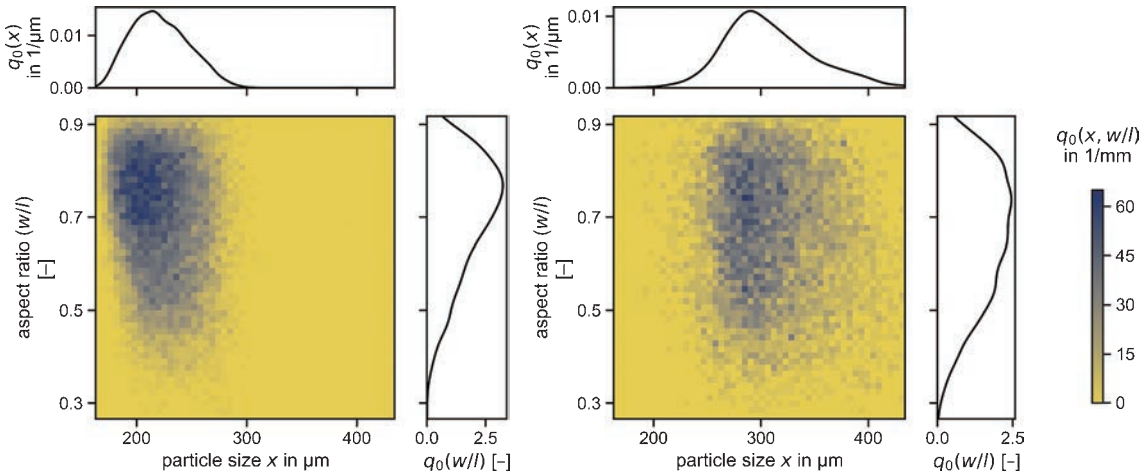


**Fig. 13** Particle property distributions for the ideal separation according to particle size; **left**: reject; **right**: concentrate. The distributions sum to the feed displayed in **Fig. 10**.

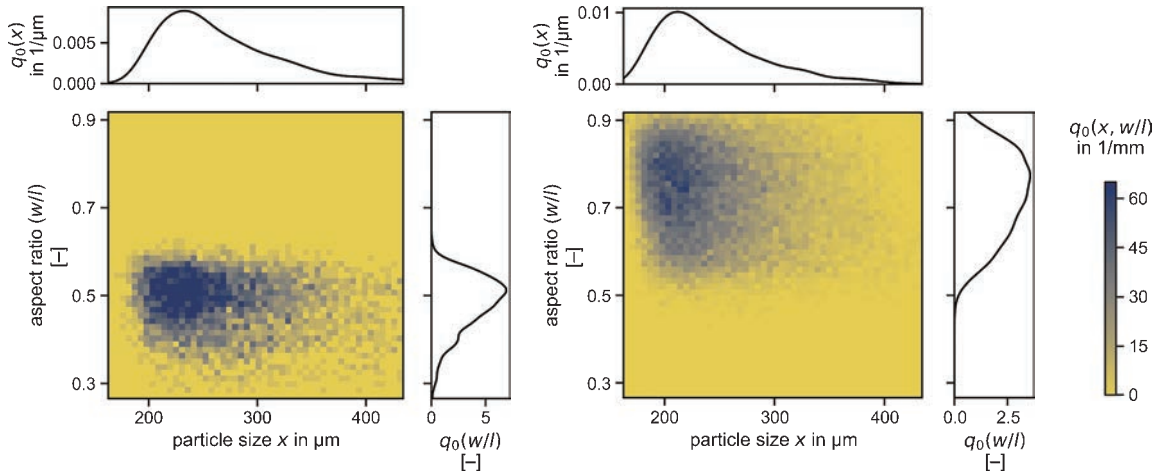


**Fig. 14** Particle property distributions for the ideal separation according to particle shape; **left**: reject; **right**: concentrate. The distributions sum to the feed displayed in **Fig. 11**.

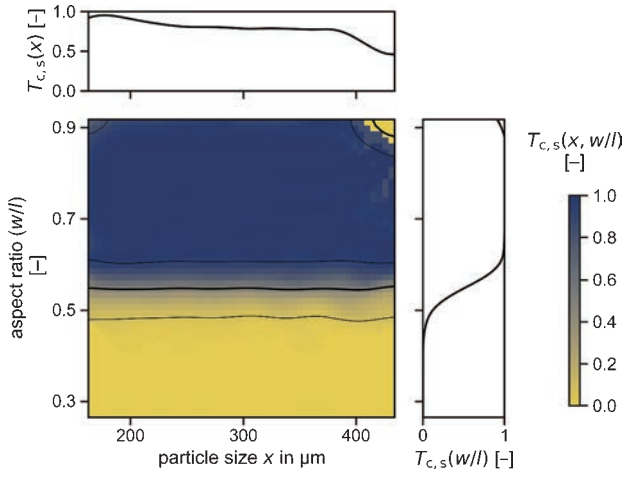


**Fig. 15** Separation function for a separation according to particle shape, derived from the probability distributions of concentrate and feed in **Fig. 14** and **Fig. 11**, respectively. Isolines display a separation degree of 25 %, 50 %, and 75 %.

function for the aspect ratio shows the typical S-shape. The marginal separation function for the size separation has a quite high value of about 0.85 in the interval from 200 µm to 400 µm, indicating that only 15 % of the particles in this size class will end up in the reject. This result is due to the correlation between size and shape in the feed particle property distribution. In this size range, the size separation can be described as ideal split; however, above 400 µm the marginal separation function for size drops to below 0.5. In this size range the shape distribution of the particles changes and more particles will end up in the concentrate. The two-dimensional separation function also shows a second median isoline in the upper right corner, which is the two-dimensional analogion of the (one-dimensional) fishhook effect.

## 4.6 Two-step separation according to size and shape in series

In particle processing, the processing of a particle stream often involves several process steps in series to generate the required specifications of the particle system. When separation according to size and shape is performed in series, the final product, i.e., the concentrate, will contain all particles above a certain particle size and having an aspect ratio above a certain threshold (**Fig. 16, left**). The reject will contain all other particles.

The resulting separation function (**Fig. 17**) is the superposition of the two individual separation functions for the size and shape separation steps. The superposition generates a separation function that eliminates the upper right corner of the two-dimensional feed distribution. Due to this positioning of the two-dimensional function, the marginal separation functions appear to be quite imperfect. Both show an S-shaped increase near their individual threshold value, but this increase does not reach the value of 1, which is due to the fact that each particle has to fulfill two conditions to belong in the concentrate. Large particles with a small aspect ratio and small particles with high aspect ratio will therefore end up in the reject, making the one-dimensional separation functions never reach the value of 1.

## 4.7 Two-dimensional simultaneous separation according to size and shape

Most separation apparatuses will not separate particles according to a single feature. A real two-dimensional separation occurs when the combination of two or more features determines the separation result, i.e., when more than one properties become a separation feature in the separation process. The separation function can then have any geometrical appearance in the two- or multidimensional plot.

In the two-dimensional example, the concentrate

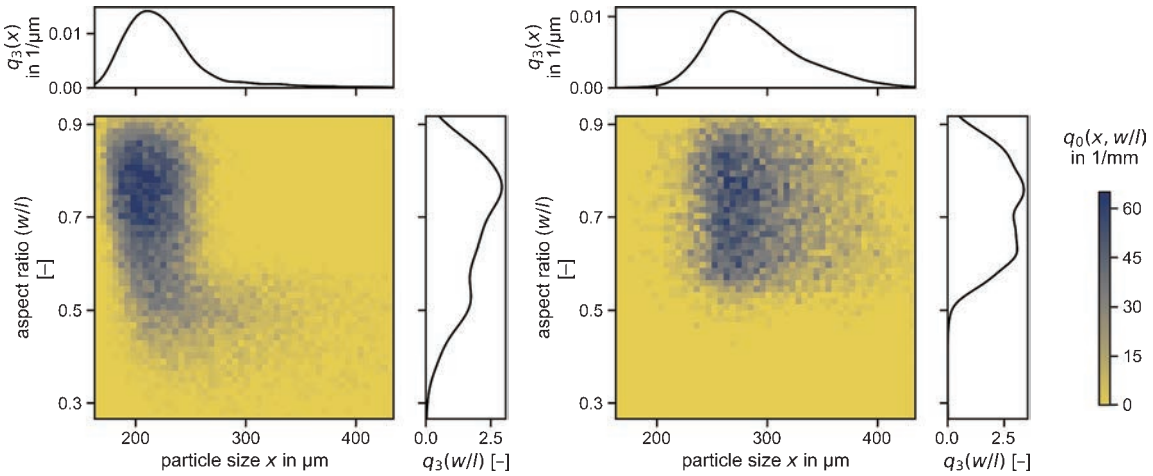


**Fig. 16** Particle property distributions of concentrate **(left)** and reject **(right)** for a two-step separation according to size and shape, one after the other.

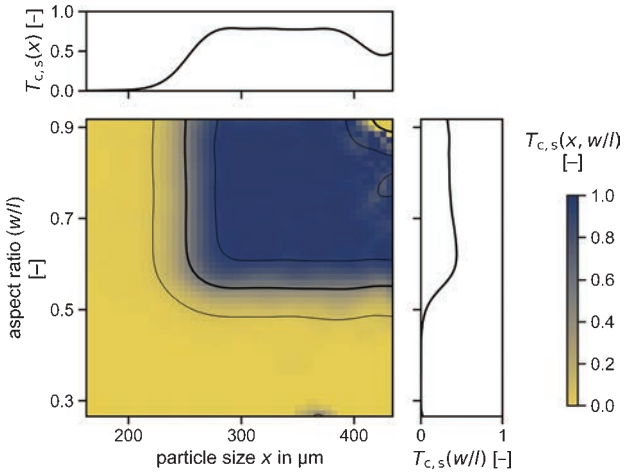


**Fig. 17** Separation function of a two-step separation consisting of a first separation according to size and a second separation step according to shape, i.e., aspect ratio. Isolines display a separation degree of 25 %, 50 %, and 75 %.

contains larger particles with a higher aspect ratio (**Fig. 18**). The appearance of particles in the concentrate with a lower aspect ratio increases with increasing particle size.

The two-dimensional separation (**Fig. 19**) shows several effects. Firstly, because the median separation isoline has a certain slope, the two-dimensional function is influenced by both parameters: size and aspect ratio. Secondly, the distance between the isolines for the separation degrees of 25 %, 50 %, and 75 % is not constant; thus, the local sharpness of the separation is not constant within the definition range of the separation function.

The marginal separation function for particle size looks very much like a normal one-dimensional size separation. It is therefore not always apparent from one-dimensional separation functions, if there is an influence of another parameter. In contrast, the marginal separation function for aspect ratio looks very much nonideal, hinting at the effect of another parameter.

In the upper right corner of the diagram, the separation function decreases and does not have a value of 1. This can

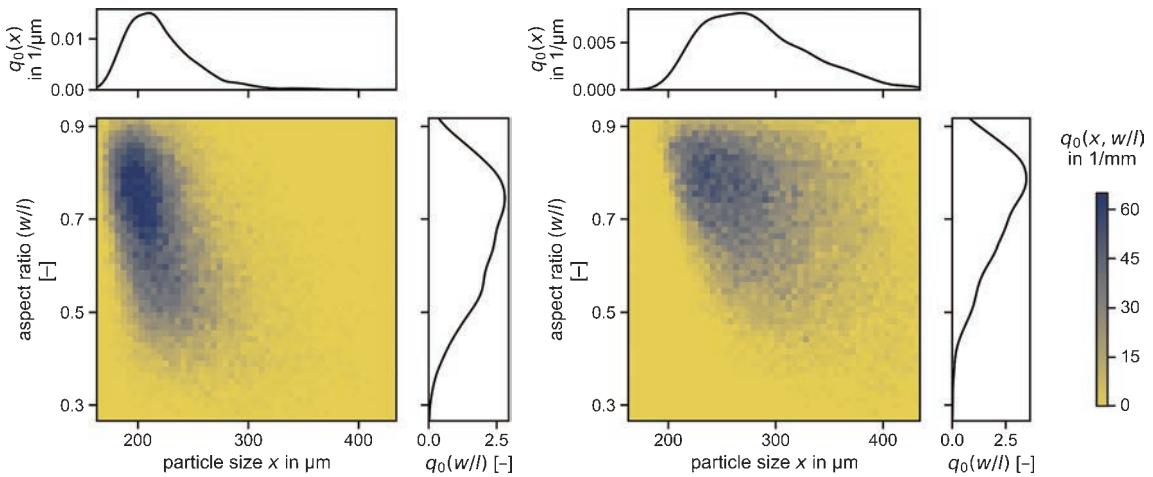


**Fig. 18** Reject **(left)** and concentrate **(right)** fractions for a (single step) multidimensional separation that depends on both particle shape and size.

be a real property related to a decrease in the separation efficiency or an artifact, which derives from the fact that in that region the particle property distribution only contains a very small number of particles or does even contain no particles. The uncertainty of the separation function is also low in the lower right corner (large particle sizes and low aspect ratio), since that region does not contain many particles.

## 5. Application examples: two- and multi-dimensional separation

### 5.1 Analysis of the performance of an air classifier for lithium battery recycling

An air classifier, as described by Kaas A. et al. (2022), was used to separate different material fractions from the recycling process of lithium-ion batteries. The mechanical recycling route results in cathode and anode foils being separated from other material fractions like cell housing, wiring, and separator foil (Werner et al., 2022). The resulting fractions from the separation experiments were analyzed using an RGB-camera system and two-dimensional image analysis techniques. The air classifier in this step was supposed to generate at different gas velocities several material fractions out of the crushed battery cell, where besides the electrode coatings, aluminum and copper are the main valuable materials (Kaas et al., 2023).

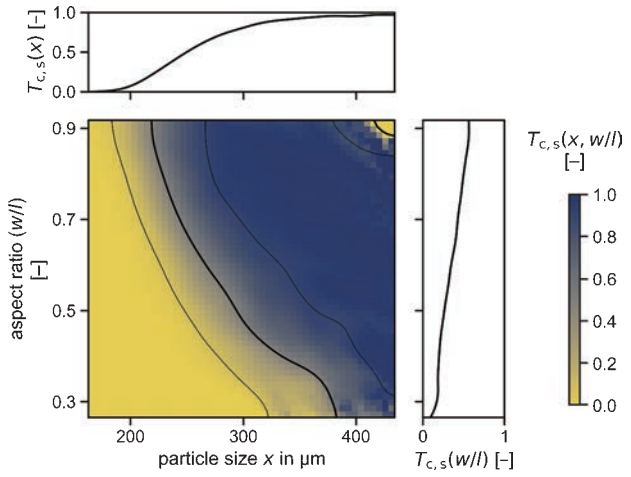


**Fig. 19** Separation function for a single step two-dimensional separation, with both particle shape and particle size having an effect on the separation process.

**Fig. 20** shows the resulting two-dimensional partition curves for particle size and shape, taking solely aluminum and copper or all fractions into account. From the first partition curve, aluminum results in the concentrate fraction within a specific variable area in the heat plot with relatively coarse, slightly compacted or platy particles. The smaller, more compacted particles are aluminum housing particles (**Fig. 20, left**). From the second partition curve (**Fig. 20, middle**), it can be seen that copper reports to the concentrate over a wide variable area of size and shape, including small compacted particles and coarse particles with low circularity. The last map (**Fig. 20, right**) shows the overall partition values weighted by the general particle area. It can be found that particles, in general, report to the concentrate at a particle size of > 40 mm and a circularity of < 0.6. In summary, the graphs show that separating shredded and compacted aluminum and copper foils as one of the main separation tasks in battery recycling can be successfully conducted using an air classifier. However, small copper particles with a low circularity are problematic, as they are recovered into the reject product stream. Actually, the dataset reflects a separation of a higher dimensionality than two-dimensional, since particle size, particle shape, and material composition are involved. To allow a consistent presentation of the results, no three-dimensional heat plots are used here.

### 5.2 Froth flotation

Froth flotation is a well-established and efficient processing technique for the separation of fine particle fractions. The method has gained attention in recycling applications recently (Vanderbruggen et al., 2021). It relies on the difference in particle wettability, i.e., hydrophobic particles attach to gas bubbles and are recovered in the froth, whereas hydrophilic particles remain suspended. Because of the complex interactions between the particles and the bubbles, further properties such as particle size, particle shape (Chen et al., 2022; Hassas et al., 2016; Koh

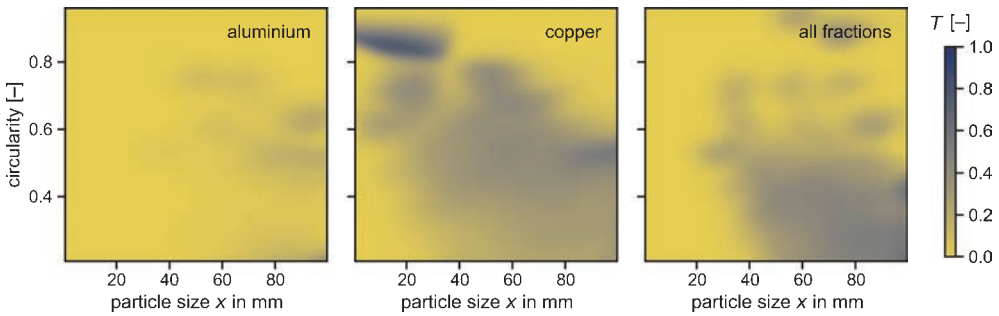


**Fig. 20** Separation of crushed battery debris particles in a zig-zag air classifier; **left** separation function for aluminum; **middle** separation function for copper; **right** separation function for all materials.

et al., 2009; Verrelli et al., 2014; Wang et al., 2015; Xia, 2017), morphology, or composition affect the separation process as well. Therefore, generally speaking, the separation function of flotation is multidimensional. The size dependence of flotation is caused by inefficient particle attachment due to the lack of inertia for fine particles (approx. < 10 µm) and caused by high particle detachment rates for coarse particles (approx. −>200 µm). Although this size dependence can be found for all material systems, the optimal particle size for flotation depends on additional properties such as particle density (Farrokhpay et al., 2021; Hassanzadeh et al., 2022).

The modified flotation cell used in this study was designed specifically for the separation of particles below 10 µm. It combines the advantages of a mechanical flotation cell with a high particle-bubble collision rate (thus a high recovery) with those from a flotation column with a secondary fractionating effect due to its deep froth (thus a high grade). A schematic drawing of the newly designed *MultiDimFlot* cell is presented in **Fig. 21**, and more detailed information can be found in literature (Wilhelm et al., 2023).

To investigate the influence of specific particle properties on the separation process, tailored mixtures of particle fractions with defined properties are used to evaluate, e.g., the influence of particle shape and size on the separation efficiency in flotation. The mixture consists of either glass spheres or glass fragments as the floatable particle fraction mixed with magnetite as the non-floatable particle fraction. The wettability of the glass particles is modified via an esterification reaction with alcohols before flotation, thus resulting in glass particles with defined wettability states (C0—hydrophilic, C6—mildly hydrophobic, C10—strongly hydrophobic) (Sygusch and Rudolph, 2021).

Because of the detailed characterization of the separation products, which involves. XRF (X-ray fluorescence), SEM, and SEM–EDX, information on particle size, shape and composition is available.

The separation results are plotted for the different particle systems as two-dimensional heat plots, highlighting particle-equivalent diameter and aspect ratio as the main particle parameters, since these are available per particle, i.e., particle-discrete in **Fig. 22**. The further parameters, the surface energy, i.e., the wetting properties of the glass, and the predominant particle shape are investigated and presented as a parameter study. The multidimensional separation functions differ between the spherical and the irregular glass particles significantly. The definition range, where the separation function has the value of one, i.e., where the particles are transferred to the concentrate, is larger for the

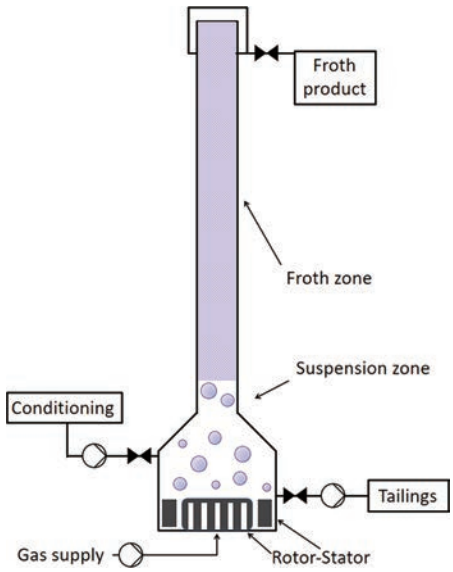


**Fig. 21** Schematic drawing of the newly designed *MultiDimFlot* separation apparatus combining mechanical and column flotation. Adapted from Ref. (Sygusch et al., 2023) under the terms of the CC-BY 4.0 license. Copyright: (2023) The Authors, published by MDPI (Basel, Switzerland).

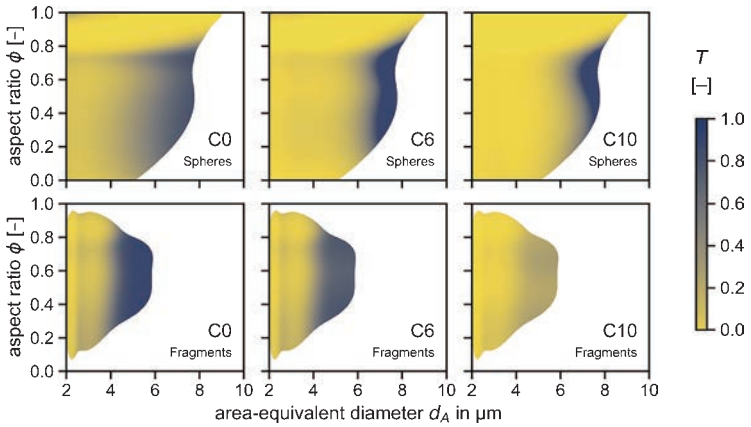


**Fig. 22** Two-dimensional separation functions showing the combined influence of the shape (aspect ratio) and size (area-equivalent diameter) on the separation process; **upper row**: glass spheres and **lower row**: glass fragments. The hydrophobicity of the used glass particles increases from left to right (C0 = hydrophilic, C6 = mildly hydrophobic, C10 = strongly hydrophobic). Adapted from Ref. (Frank et al., 2023) under the terms of the CC-BY 4.0 license. Copyright: (2023) The Authors, published by MDPI (Basel, Switzerland).

predominant spherical shape of the feed (**Fig. 22**). The influence of the particle hydrophobicity is revealed when comparing separation functions of the same row, i.e spheres-C0 vs. spheres-C6 vs. spheres-C10, as the hydrophobicity of the glass particles increases from left to right in **Fig. 22**. It becomes visible that the sharpness of the separation increases along with the hydrophobicity of the spherical glass particles.

## 5.3 Beneficiation of a tin-bearing complex skarn ore

Recently, multiple research consortia have explored the extraction and beneficiation of the polymetallic Tellerhäuser deposit in Germany's Erzgebirge area (Werner and Axel, 2012). The deposit contains iron oxides, valuable sulfide minerals, and cassiterite, a crucial tin-bearing mineral that plays a significant role in its economic feasibility. Because of the high specific density of cassiterite (approx. 7 g/cm$^3$), gravity separation is one of the most critical processing steps in a possible beneficiation flowsheet, whereas the significant content of iron oxides in the ore is separated by magnetic separation. Gravity separation tests for ore samples obtained from the Tellerhäuser deposit were performed on a laboratory scale using a falcon density separator. In a pilot plant test with 140 t of material, a drum-type magnetic separator was used to produce a magnetic concentrate.

Furthermore, a shaking table was used to separate cassiterite from lighter mineral phases (Pereira et al., 2021). For all cases, including the falcon separator, the shaking table and the drum-type magnetic separator, samples of the products were investigated using MLA, allowing for particle-based analysis of the separation process by calculating two-dimensional distributions based on kernel density estimates. All three separation processes will be discussed in the following sections, showcasing the application of two-dimensional partition curves. The data for the processes described here are available online (Schach et al., 2021).

### 5.3.1 Magnetic separation in the pilot plant

In most magnetic separators, the electromagnetic characteristics of a particle collective are superposed by the particle mass (Oberteuffer, 1974; Oder, 1976; Svoboda and Fujita, 2003). Separation of the iron oxide phases is essential to achieve a high-quality cassiterite concentrate (Buchmann et al., 2018). The iron oxides present in the ore primarily consist of magnetite and hematite (Kern et al., 2019). Even though MLA can distinguish between magnetite and hematite using backscattered electron values (Figueroa et al., 2012), it cannot be employed in this study's ore because of fluctuations in BSE values caused by varying amounts of Sn and other elements in the crystal lattice (Kern et al., 2018). As a consequence of the inability to easily differentiate between the iron oxide phases, the magnetic susceptibility of the particles cannot be calculated, and the iron oxide content in the particles is used as a proxy for the separation property.

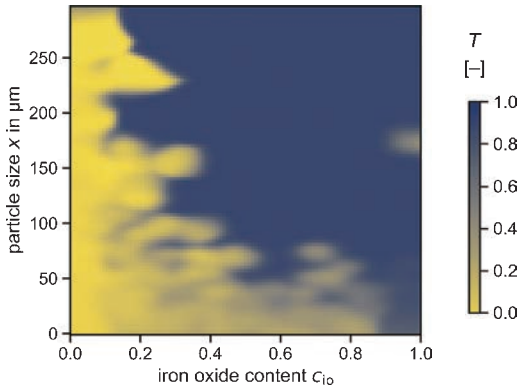


**Fig. 23** Two-dimensional partition curve for the magnetic separation of a cassiterite ore.

A weak wet drum-type separator was installed in the pilot plant. The diameter of the drum was 900 mm at a drum width of 300 mm. During operation, the volume flow of the feed suspension was adjusted to 1.5 m$^3$/h with a solid content of 0.2 kg/m$^3$, and the drum speed was set to 18 rpm. The partition curve based on the MLA data is depicted in **Fig. 23**. The graph shows that coarse particles (> 150 µm) with an iron oxide content of more than 0.2–0.3 report to the magnetic concentrate. At smaller particle sizes, the threshold content of iron oxides within a particle to be recovered into the magnetic product increases. At particle sizes below 50 µm, the separation becomes unsharp even at high iron oxide contents of 0.6–0.8, which is indicated by *T*-values in the range of 0.4–0.6.

This behavior might be explained by fine hematite particles in the ore that do not respond to the drum-type separator's relatively low magnetic field density and gradient. Another explanation could be an inefficient extraction at such fine particle sizes due to agglomeration or slime-coating effects.

### 5.3.2 Gravity separation on a shaking table

Gravity separation technologies, with the exception of dense media separation, are fundamentally multidimensional separation processes, where the effects of density, particle size, and particle shape often influence the separation efficiency (Burt and Mills, 1984), since drag forces and field forces interact. Density separation in this example was realized using a shaking table that produced four streams: one product stream with a high content of liberated dense cassiterite, iron oxides, and arsenopyrite (Product 1), a product stream mainly comprising iron oxides but also significant amounts of cassiterite (Product 2), a middling stream containing intergrown cassiterite, and finally a tailing stream consisting of light mineral phases such as silicates.

The particles on the shaking table are separated by density and size along the width of the table, with small and heavy particles collected at one end of the separator followed by heavy-coarse particles and small-light particles contained in the middle of the shaking table. On the other end of the table, coarse-light particles are collected (Wills and Finch, 2016). The dimensions of the shaking table used in the pilot test is 3500 × 1500 mm. The volume flows of the feed suspension and the wash water were 0.3 $m^3$/h and 1.3 $m^3$/h, respectively, and the solid content of the feed suspension was 700 kg/$m^3$.

**Fig. 24** shows a schematic of the used shaking table and the obtained streams. Based on MLA analysis, a mass-weighted distribution over particle density and particle size is plotted in **Fig. 25**. It is noteworthy that, especially prominent for the two product streams, the distribution shows distinct lines at certain density values representing the respective liberated mineral phases, e.g., cassiterite with a density of about 7 g/$cm^3$, iron oxides with a density of 4–5 g/$cm^3$, and arsenopyrite with a density of around 6 g/$cm^3$. Whereas product 1 mainly comprises particles below 100 µm with a significant concentration of cassiterite particles, product 2 mainly contains iron oxide particles in larger size fractions. For the feed, middling and tailing stream, particles are distributed over a wider size range at low particle densities indicating light mineral phases such as silicates.

For the calculation of the two-dimensional Tromp curve depicted in **Fig. 26**, product 1 was defined as concentrate stream and all other products were summarized as the reject. The graph shows that the shaking table has a cut point within the density range of 4–5 g/$cm^3$.

However, at particle sizes below 25 µm, particles have a high probability to be recovered in the tailing stream independent of their density. For particles within this size range, the shaking table is not able to effectively separate the minerals according to density and as a consequence fine cassiterite is lost in the reject in this application. Due to the brittle nature of cassiterite and its favorable enrichment in fine particle fractions, this behavior leads to unwanted losses of fine cassiterite.

## 5.4 Gravity separation in a Falcon separator

Gravity separation at laboratory scale with a Falcon Separator (Falcon L40 concentrator, **Fig. 27**) was used with 500 g ore samples as feed material and a water flow of 5 l/min. The riffled bowl of the separator rotated at a speed of 2300 rpm. Due to the resulting gravitational force, the heavy material was deposited in the riffles of the separator and scraped off at the end of the test. The light tailing material was discharged continuously.

The resulting partition curve (Schach et al., 2019) for the falcon separator is presented in **Fig. 28**. Both particle

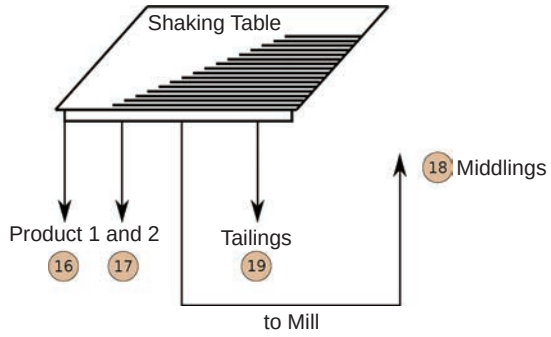


**Fig. 24** Schematic of the shaking table with the respective product streams.

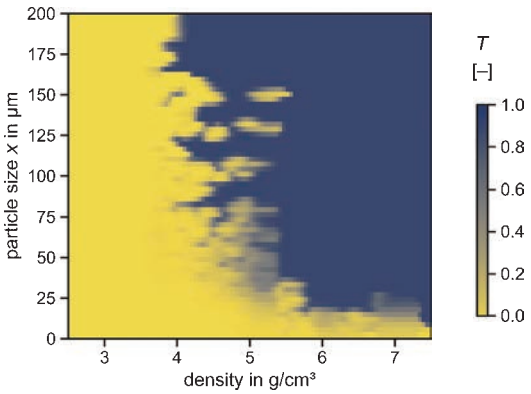


**Fig. 26** Partition map for the shaking table over density and size defining product 1 as concentrate and the remaining streams as reject, tailing stream respectively.

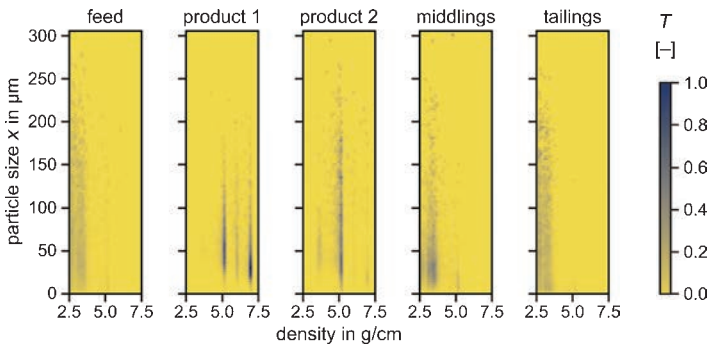


**Fig. 25** Distributions for the feed and output streams of the shaking table over particle size and density.

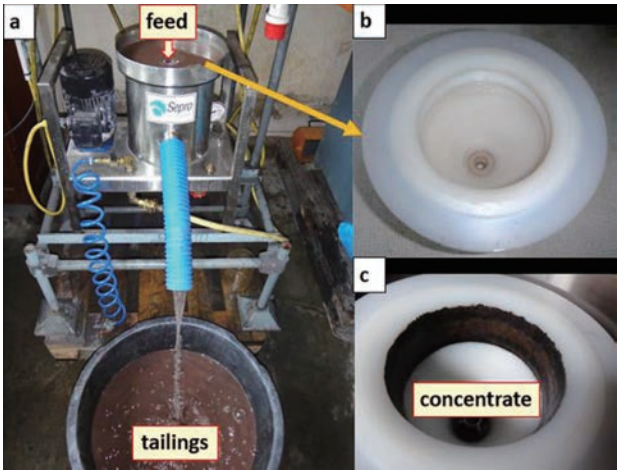


**Fig. 27** Falcon separator: **(a)** experimental set up; **(b)** inner riffled bowl without material; **(c)** riffles filled with heavy material.

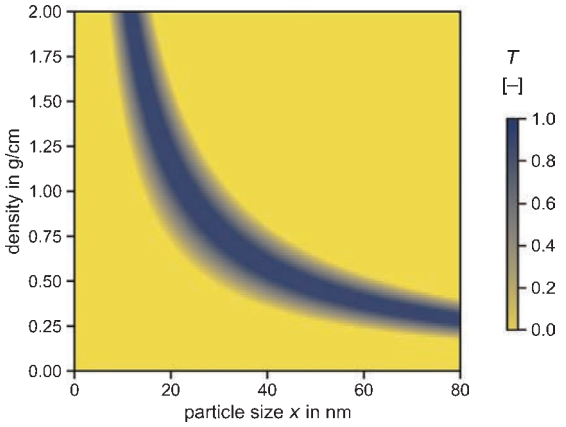


**Fig. 29** Two-dimensional separation function of an aerodynamic lens. Adapted with permission from Ref. (Furat et al., 2020). Copyright: (2020) Elsevier B.V.

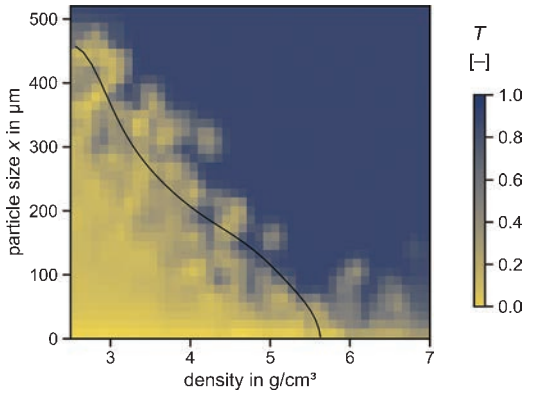


**Fig. 28** Two-dimensional partition curve for the gravity separation via falcon concentrator. The line represents the cut function fitted to the points with a partition value of 50 %, displayed as points in the graph. Adapted with permission from Ref. (Schach et al., 2019). Copyright: (2019) Elsevier B.V.

properties—density and size—influence the partition of particles (Rao et al., 2003). It can be concluded that the separation process is rather dependent on the particle mass, resulting in higher inertia during separation, than solely on particle density or particle size (Nayak et al., 2021). Below a particle size in the range of 20–30 µm, the partition remains low for all density values. In this size range, the separation device cannot effectively separate cassiterite from the light minerals due to, e.g., slime coating of the fine cassiterite particles on coarser silica particles. Here, the drag forces determine the movement of all particles.

## 5.5 Aerodynamic lens

A classifying aerodynamic lens can be used to fractionate aerosols by particle size and particle density at the same time (Kiesler et al., 2019; Wang et al., 2005a, 2005b). The window of application of such a separation system depends on the flow regime and the geometry of the lens itself and is located in the upper nm range. The operation parameters allow the tailoring of the separation function, i.e., the product received as concentrate.

Classifying aerodynamic lenses are orifices that constrict aerosol flow through a radially symmetric pipe. If the flow is laminar, and the starting position of a particle upstream of the lens is known, the end position downstream of the lens is a function of its specific relaxation time. Therefore, the feed is injected at a defined central position. The relaxation time is a function of different parameters, such as the pressure upstream of the lens, the flow rate through the lens, and the lens diameter, and it further depends on the particle properties, e.g., the particle size, shape, and density. In the setup discussed in Furat et al. (2020), the aerosol particles are injected into a laminar sheath gas flow at an off-axis position. Extracting aerosol downstream of the lens at a central position gives the separating aerodynamic lens a differential transfer characteristic, where only particles within a small range of particle properties such as size and solid density are collected. This becomes clearly visible in the two-dimensional plot for the separation function (**Fig. 29**), which has only a small and defined area of particle properties, where the separation function is one.

## 5.6 Hydrocyclone

The two-dimensional separation for plate-shaped particles having different aspect ratios has been discussed by Frank et al. for a hydrocyclone (Frank et al., 2023). The particle shape is assumed to be a flat regular cylinder with diameter $d$ and thickness $l$. The separation efficiency presented uses a theoretical model that contains the shape dependency by taking its dependency on the drag force into account. The separation function (**Fig. 30**) based on this model shows over a long range of the thickness $l$ of the plates only a dependence on the particle diameter $d$, resulting in a vertical isoline similar to the discussion of the respective ideal one-dimensional case in **Fig. 9**. The separation becomes two-dimensional with decreasing

particle thickness. Below about 1 µm there is a significant dependency of the separation function on both parameters: diameter and plate thickness, which is indicated by a deviation of the isoline from the ideal behavior of the one-dimensional case. Nevertheless, it can be stated that the hydrocyclone described by this model is predominantly a classification apparatus with only small capacities in two- or multidimensional separation. The effect of particle shape on the separation is not pronounced for the range of particle dimensions investigated. This might change for coarser particles. Real experiments to validate this model approach are still lacking.

## 5.7 Disc-stack centrifuge

Applying theoretical models for the separation efficiency by sedimentation, Frank et al. generated a two-dimensional separation function for a disc-stack centrifuge (**Fig. 31**) (Frank et al., 2023). As it is fundamentally known that the sedimentation velocity depends on the particle-equivalent diameter to the square as well as to the particle density difference between carrier media and solids, the multidimensional separation probability can be plotted using these two influencing parameters. The results show a slight negative slope of the 50 % isoline in the separation function, which states that separation by size is the predominant effect and there is only a smaller influence of the particle density in this machine. Thus, the sedimentation in the disc-stack centrifuge still is a classification process with a certain contribution of the effect of equal settling velocity for small dense and large light particles.

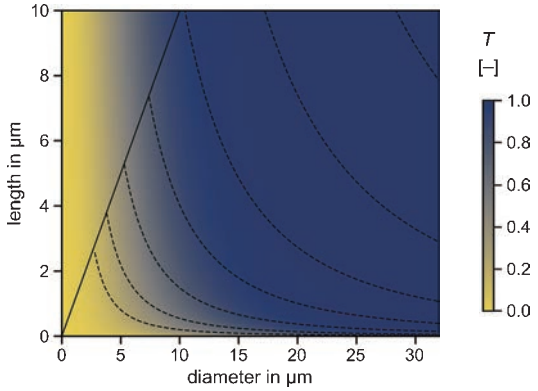


**Fig. 30** Theoretically deducted two-dimensional separation function for the separation of plate shaped cylindrical particles in a hydrocyclone. Adapted from Ref. (Frank et al., 2023) under the terms of the CC-BY 4.0 license. Copyright: (2023) The Authors, published by MDPI (Basel, Switzerland).

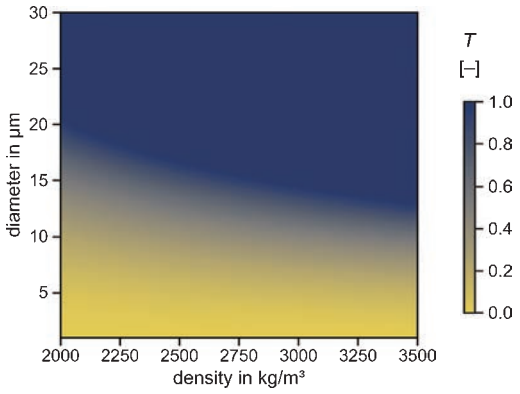


**Fig. 31** Theoretically deducted two-dimensional separation function for the separation of model particles being distributed in size and density in a disk-stack centrifuge. Adapted from Ref. (Frank et al., 2023) under the terms of the CC-BY 4.0 license. Copyright: (2023) The Authors, published by MDPI (Basel, Switzerland).

## 5.8 High-gradient magnetic separation

Three commercially available, rare-earth-doped lamp phosphor particle collectives obtained from Leuchtstoffwerk Breitungen GmbH (Breitungen, Germany) were used. These included a cerium/terbium-doped lanthanum phosphate ($LaPO_4$:$Ce^{3+}$, $Tb^{3+}$, LAP), a europium-doped barium magnesium aluminate ($BaMgAl_{10}O_{17}$:$Eu^{2+}$, BAM), and a europium-doped yttrium oxide ($Y_2O_3$:$Eu^{3+}$, YOX). Due to their rare earth content, the particles exhibit paramagnetic properties, with LAP having the highest magnetic susceptibility at $3.69 \times 10^{-3}$, followed by BAM at $1.19 \times 10^{-3}$ and YOX at $0.516 \times 10^{-3}$. Their use as illuminants and the associated fluorescence of the compounds allowed for quantitative analysis through fluorimetry.

For conducting fractionation experiments of the particle mixture, a fast protein liquid chromatography (FPLC) system (ÄKTA purifier, Cytiva, Buckinghamshire, UK) equipped with polyetheretherketone (PEEK) tubing was employed. The schematic flow diagram in **Fig. 32** illustrates the process of magnetic field-controlled chromatography. A defined mixture of low salt (1a) and high salt (1b) buffer was pumped into the system, mixed (2), and injection pulses ($V = 0.5$ mL) were introduced to the fluid stream through an injection loop and valve (3). The mobile phase, along with the injected particle suspension, flowed onto the column, which was surrounded by an external magnetic field source (4) connected to a power supply (5). The effluent was then collected and separated into distinct

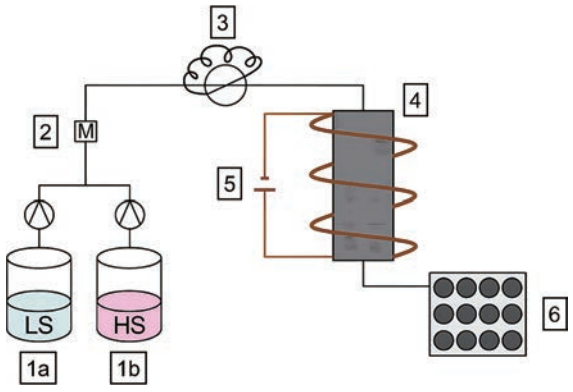


**Fig. 32** General flow diagram for the fractionation experiment.

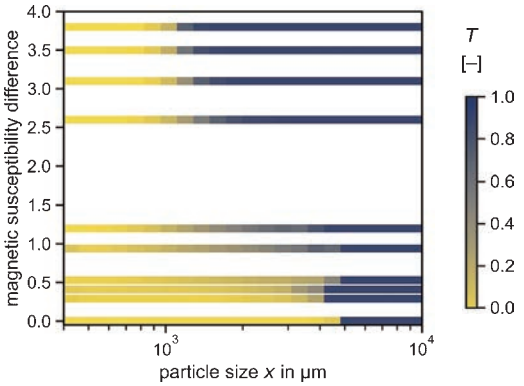


**Fig. 33** The separation function for magnetic chromatography retrieved from different particle systems consisting of distinct materials with distinct magnetic properties.

fractions at the outlet of the column using a fraction collector (6). Continuous monitoring of the process was performed using an in-line UV/VIS cell at 280 nm.

The magnetic force induced between the paramagnetic particles and the magnetized chromatography matrix elements is influenced by the particle size as well as the intrinsic magnetic susceptibilities of the particles and the magnetic susceptibility of the surrounding fluid. Consequently, when the susceptibility difference between the dispersed and continuous phases decreases, the magnitude of the magnetic force diminishes. Therefore, by dissolving paramagnetic salts such as manganese(II)-chloride in the continuous phase and employing various particle types with distinct magnetic susceptibilities, which prevent a continuous display of the two-dimensional degree of separation (see **Fig. 33**), it is possible to deliberately adjust the magnetic susceptibility difference. However, the solubility of the salt in the solution constrains this approach. In theory, by maintaining constant process parameters (such as flow rate and magnetic flux intensity), the size fractionation result can be altered by adjusting the salt concentration in the buffer.

## 6. Conclusions

Particle separation processes are, in most cases, influenced by multiple particle properties such as size, shape, and composition. However, the conventional one-dimensional separation function or Tromp curve fails to capture the multidimensional distribution of particles and their effect on separation. Therefore, it's crucial to account for and define the Tromp curve for the multidimensional space. Knowing the multidimensional property distribution of feed, concentrate, and reject, it is possible to define and express the multidimensional separation function in a formal manner. This separation function has the same dimensionality as the property distributions of the related material streams. Furthermore, it is possible to define characteristic values for a multidimensional property distribution, like the median particle size ($x_{50}$, $y_{50}$) and a median isoline, where the value of the separation function equals $T(x, y) = 0.5$. Several application examples and the discussion of model cases of the two-dimensional separation function show that multidimensional separation occurs in many applications and that it can be described, quantified, and discussed using the methods shown.

## Acknowledgements

This scientific work was mainly financed from projects within the Priority Programme 2045 of the German Science Foundation (DFG), with the project No. 313858373. Some scientific results stem as well from the projects DIGISORT (No. 03XP0337A) and AFK (No. 033R128) funded by the German Ministry for Education and Research (BMBF).

## Nomenclature

| | |
|---|---|
| $A$ | area of plot (pixel$^2$) |
| C | index for concentrate (-) |
| $c$ | mass fraction of concentrate (kg/kg) |
| $c_{io}$ | iron oxide content (kg/kg) |
| $d_A$ | area-equivalent diameter (m) |
| $i$ | class index for first parameter ($x$) (-) |
| $j$ | class index for second parameter ($y$) (-) |
| $m$ | mass (kg) |
| $m_i$ | mass of particle class $i$ (kg) |
| $q_r$ | density distribution weighted by quantity of dimension $r$ (variable) |
| $q_3$ | volume-/mass-based density distribution (variable) |
| $q_{res}$ | sum of density distributions, distribution of mixture (variable) |
| $Q_3$ | volume-/mass-based cumulative sum function (-) |
| $\Delta Q_{3,i,j}$ | volume-/mass-based fraction of particles in a two-dimensional distribution (-) |
| R | index for retentate (-) |
| $r$ | mass fraction of retentate (kg/kg) |
| S | index for supply, feed (-) |
| $T$ | separation function, partition value (-) |
| $x$ | particle size (equivalent diameter) (m) |
| $x_i$ | upper particle size of a given class (m) |
| $\overline{x_i}$ | average particle size of a given class (m) |
| $\Delta x_i$ | particle size interval of a given class (m) |
| $x_{min}$ | minimum particle size of a distribution (m) |
| $x_{max}$ | maximum particle size of a distribution (m) |
| $y$ | second parameter, e.g., shape factor (variable) |
| $\mu$ | integrating index for first parameter ($x$) (-) |
| $\nu$ | mass fraction (kg/kg), integrating index for second parameter ($y$) (-) |

## References

Alonso M., Satoh M., Miyanami K., Mechanism of the combined coating-mechanofusion processing of powders, Powder Technology, 59 (1989) 45–52. https://doi.org/10.1016/0032-5910(89)80094-4

Baalousha M., Stolpe B., Lead J.R., Flow field-flow fractionation for the analysis and characterization of natural colloids and manufactured nanoparticles in environmental systems: a critical review, Journal of Chromatography A, 1218 (2011) 4078–4103. https://doi.org/10.1016/j.chroma.2011.04.063

Bagheri G.H., Bonadonna C., Manzella I., Vonlanthen P., On the characterization of size and shape of irregular particles, Powder Technology, 270 (2015) 141–153.

https://doi.org/10.1016/j.powtec.2014.10.015
Baloun T.A., Schoenherr J.I., Zocher M., Schubert G., Studies on thermoadhesion-based sorting, Aufbereitungstechnik, 46 (2005) 12–27.
Blott S.J., Pye K., Particle shape: a review and new methods of characterization and classification, Sedimentology, 55 (2008) 31–63. https://doi.org/10.1111/j.1365-3091.2007.00892.x
Bourgeois F., Majumder A.K., Is the fish-hook effect in hydrocyclones a real phenomenon?, Powder Technology, 237 (2013) 367–375. https://doi.org/10.1016/j.powtec.2012.12.017
Buchmann M., Schach E., Leißner T., Kern M., Mütze T., Rudolph M., Peuker U.A., Tolosana-Delgado R., Multidimensional characterization of separation processes – Part 2: comparability of separation efficiency, Minerals Engineering, 150 (2020a) 106284. https://doi.org/10.1016/j.mineng.2020.106284
Buchmann M., Schach E., Rudolph M., Peuker U., Boogaart G., Tolosana-Delgado R., Multidimensional particle-based process characterization, Proceedings of the IMPC (International Mineral Processing Congress), 2020b, pp10.
Buchmann M., Schach E., Tolosana-Delgado R., Leißner T., Astoveza J., Kern M., Möckel R., Ebert D., Rudolph M., van den Boogaart K., Peuker U., Evaluation of magnetic separation efficiency on a cassiterite-bearing skarn ore by means of integrative SEM-based image and XRF–XRD data analysis, Minerals, 8 (2018) 390. https://doi.org/10.3390/min8090390
Buchwald T., Ditscherlein R., Peuker U.A., Beschreibung von Trennoperationen mit mehrdimensionalen Partikeleigenschaftsverteilungen, Chemie Ingenieur Technik, 95 (2023) 199–209. https://doi.org/10.1002/cite.202200109
Bujak B., Bottlinger M., Three-dimensional measurement of particle shape, Particle & Particle Systems Characterization, 25 (2008) 293–297. https://doi.org/10.1002/ppsc.200800027
Burt R.O., Mills C., Gravity Concentration Technology, Elsevier, 1984, ISBN: 9780444424112.
Chen Y., Zhuang L., Zhang Z., Effect of particle shape on particle-bubble interaction behavior: a computational study using discrete element method, Colloids and Surfaces A: Physicochemical and Engineering Aspects, 653 (2022) 130003. https://doi.org/10.1016/j.colsurfa.2022.130003
Çiçek Ö., Abdulkadir A., Lienkamp S.S., Brox T., Ronneberger O., 3D U-Net: learning dense volumetric segmentation from sparse annotation, Medical Image Computing and Computer-Assisted Intervention – MICCAI 2016, Cham, Springer International Publishing, (2016). https://doi.org/10.1007/978-3-319-46723-8_49
Czado C., Analyzing Dependent Data with Vine Copulas, Springer International Publishing, 2019, ISBN: 9783030137847.
Dehghani A., Monhemius A.J., Gochin R.J., Evaluating the Nakajima et al. model for rectangular-aperture screens, Minerals Engineering, 15 (2002) 1089–1094. https://doi.org/10.1016/s0892-6875(02)00225-x
Demeler B., Nguyen T.-L., Gorbet G.E., Schirf V., Brookes E.H., Mulvaney P., El-Ballouli A.a.O., Pan J., Bakr O.M., Demeler A.K., Uribe B.I.H., Bhattarai N., Whetten R.L., Characterization of size, anisotropy, and density heterogeneity of nanoparticles by sedimentation velocity, Analytical Chemistry, 86 (2014) 7688–7695. https://doi.org/10.1021/ac501722r
Ditscherlein R., Furat O., de Langlard M., de Souza e Silva J.M., Sygusch J., Rudolph M., Leißner T., Schmidt V., Peuker U.A., Multiscale tomographic analysis for micron-sized particulate samples, Microscopy and Microanalysis, 26 (2020) 676–688. https://doi.org/10.1017/s1431927620001737
Egan C.K., Jacques S.D.M., Wilson M.D., Veale M.C., Seller P., Beale A.M., Pattrick R.A.D., Withers P.J., Cernik R.J., 3D chemical imaging in the laboratory by hyperspectral X-ray computed tomography, Scientific Reports, 5 (2015) 15979. https://doi.org/10.1038/srep15979
Farrokhpay S., Filippov L., Fornasiero D., Flotation of fine particles: a review, Mineral Processing and Extractive Metallurgy Review, 42 (2021) 473–483. https://doi.org/10.1080/08827508.2020.1793140
Figueroa G., Moeller K., Buhot M., Gloy G., Haberla D., Advanced discrimination of hematite and magnetite by automated mineralogy, Proceedings of the 10th International Congress for Applied Mineralogy (ICAM), Berlin, Heidelberg, Springer Berlin Heidelberg, (2012).
Fontein F.J., Wirkung des hydrozyklons und des bogensiebs sowie deren anwendungen, Aufbereitungs-Technik, 2 (1961) 85–89.
Frank U., Dienstbier J., Tischer F., Wawra S.E., Gromotka L., Walter J., Liers F., Peukert W., Multidimensional fractionation of particles, Separations, 10 (2023) 252. https://doi.org/10.3390/separations10040252
Frank U., Uttinger M.J., Wawra S.E., Lübbert C., Peukert W., Progress in multidimensional particle characterization, KONA Powder and Particle Journal, 39 (2022) 3–28. https://doi.org/10.14356/kona.2022005
Frank U., Wawra S.E., Pflug L., Peukert W., Multidimensional particle size distributions and their application to nonspherical particle systems in two dimensions, Particle & Particle Systems Characterization, 36 (2019) 1800554. https://doi.org/10.1002/ppsc.201800554
Friebel J.M., Ditscherlein R., Ditscherlein L., Peuker U.A., Three-dimensional characterization of dry particle coating structures originating from the mechano-fusion process, Microscopy and Microanalysis, 30 (2024) 179–191. https://doi.org/10.1093/mam/ozae009
Friedländer T., Kuyumcu H.Z., Rolf L., Investigations into sorting PET flakes by particle shape, Aufbereitungstechnik, 47 (2006) 24–35.
Furat O., Leißner T., Bachmann K., Gutzmer J., Peuker U., Schmidt V., Stochastic modeling of multidimensional particle properties using parametric copulas, Microscopy and Microanalysis, 25 (2019) 720–734. https://doi.org/10.1017/s1431927619000321
Furat O., Masuhr M., Kruis F.E., Schmidt V., Stochastic modeling of classifying aerodynamic lenses for separation of airborne particles by material and size, Advanced Powder Technology, 31 (2020) 2215–2226. https://doi.org/10.1016/j.apt.2020.03.014
Furchner B., Zampini S., Air classifying, in: Wiley-VCH (Ed.), Ullmann's Ecyclopedia of Industrial Chemistry, Wiley-VCH Verlag GmbH & Co. KGaA, Weinheim, 2009, ISBN: 9783527306732. https://doi.org/10.1002/14356007.b02_17.pub2
Furuuchi M., Gotoh K., Shape separation of particles, Powder Technology, 73 (1992) 1–9. https://doi.org/10.1016/0032-5910(92)87001-Q
Hassanzadeh A., Safari M., Hoang D.H., Khoshdast H., Albijanic B., Kowalczuk P.B., Technological assessments on recent developments in fine and coarse particle flotation systems, Minerals Engineering, 180 (2022) 107509. https://doi.org/10.1016/j.mineng.2022.107509
Hassas B.V., Caliskan H., Guven O., Karakas F., Cinar M., Celik M.S., Effect of roughness and shape factor on flotation characteristics of glass beads, Colloids and Surfaces A: Physicochemical and Engineering Aspects, 492 (2016) 88–99. https://doi.org/10.1016/j.colsurfa.2015.12.025
Heywood H., Techniques for the evaluation of powders. i. fundamental properties of particles and methods of sizing analysis, Powder Metallurgy, 4 (1961) 1–28. https://doi.org/10.1179/pom.1961.4.7.001
Hickstein B., Peuker U.A., Modular process for the flexible synthesis of magnetic beads—Process and product validation, Journal of Applied Polymer Science, 112 (2009) 2366–2373. https://doi.org/10.1002/app.29655
Joe H., Dependence Modeling with Copulas, 1st edition, Taylor & Francis Group, 2014, ISBN: 9780429103186. https://doi.org/10.1201/b17116
Kaas A., Mütze T., Peuker U.A., Review on Zigzag Air Classifier, Processes, 10 (2022) 764. https://doi.org/10.3390/pr10040764
Kaas A., Wilke C., Vanderbruggen A., Peuker U.A., Influence of different discharge levels on the mechanical recycling efficiency of lithium-ion batteries, Waste Management, 172 (2023) 1–10. https://doi.org/10.1016/j.wasman.2023.08.042
Kern M., Kästner J., Tolosana-Delgado R., Jeske T., Gutzmer J., The inherent link between ore formation and geometallurgy as documented by complex tin mineralization at the Hämmerlein deposit (Erzgebirge, Germany), Mineralium Deposita, 54 (2019) 683–698. https://doi.org/10.1007/s00126-018-0832-2
Kern M., Möckel R., Krause J., Teichmann J., Gutzmer J., Calculating the deportment of a fine-grained and compositionally complex Sn skarn with a modified approach for automated mineralogy, Minerals

Engineering, 116 (2018) 213–225. https://doi.org/10.1016/j.mineng.2017.06.006
Kiesler D., Bastuck T., Kennedy M.K., Kruis F.E., Development of a high flow rate aerodynamic lens system for inclusion of nanoparticles into growing PVD films to form nanocomposite thin films, Aerosol Science and Technology, 53 (2019) 630–646. https://doi.org/10.1080/02786826.2019.1587149
Koh P.T.L., Hao F.P., Smith L.K., Chau T.T., Bruckard W.J., The effect of particle shape and hydrophobicity in flotation, International Journal of Mineral Processing, 93 (2009) 128–134. https://doi.org/10.1016/j.minpro.2009.07.007
Kuzmanić T., Mikoš M., Effect of coarse gravel and cobble size particles shape on their dynamic image analysis results, EGU General Assembly 2022, (2022) EGU22-4865. https://doi.org/10.5194/egusphere-egu22-4865
Lamberg P., Vianna S., A Technique for Tracking Multiphase Mineral Particles in Flotation Circuits, XXII ENTMME / VII MSHMT, (2007) pp9.
Leißner T., Bachmann K., Gutzmer J., Peuker U.A., MLA-based partition curves for magnetic separation, Minerals Engineering, 94 (2016) 94–103. https://doi.org/10.1016/j.mineng.2016.05.015
Leißner T., Diener A., Löwer E., Ditscherlein R., Krüger K., Kwade A., Peuker U.A., 3D ex-situ and in-situ X-ray CT process studies in particle technology – A perspective, Advanced Powder Technology, 31 (2020) 78–86. https://doi.org/10.1016/j.apt.2019.09.038
Matsuyama T., Yamamoto H., Particle shape and laser diffraction: a discussion of the particle shape problem, Journal of Dispersion Science and Technology, 25 (2005) 409–416. https://doi.org/10.1081/dis-200025692
Nageswararao K., A critical analysis of the fish hook effect in hydrocyclone classifiers, Chemical Engineering Journal, 80 (2000) 251–256. https://doi.org/10.1016/S1383-5866(00)00098-8
Nakajima Y., Whiten W.J., White M.E., Behaviour of non-spherical particles in screening, Transactions of Institution of Mining and Metallurgy, 88 (1979) C88–92.
Nayak A., Jena M.S., Mandre N.R., Application of enhanced gravity separators for fine particle processing: an overview, Journal of Sustainable Metallurgy, 7 (2021) 315–339. https://doi.org/10.1007/s40831-021-00343-5
Oberteuffer J., Magnetic separation: a review of principles, devices, and applications, IEEE Transactions on Magnetics, 10 (1974) 223–238. https://doi.org/10.1109/tmag.1974.1058315
Oder R., High gradient magnetic separation theory and applications, IEEE Transactions on Magnetics, 12 (1976) 428–435. https://doi.org/10.1109/tmag.1976.1059076
Oliver M., Matúš Č., Ľudmila G., Martin J., Radovan R., Peter P., Dynamic image analysis to determine granule size and shape, for selected high shear granulation process parameters, Strojnícky časopis - Journal of Mechanical Engineering, 69 (2019) 57–64. https://doi.org/10.2478/scjme-2019-0043
Peciar P., Jezso K., Kohutova M., GustafÃ-k A., Kratky L., Fekete R., Jirout T., Peciar M., Particle size distribution analysis of beech chips depending on the measurement method, Chemical Engineering Transactions, 92 (2022) 43–48. https://doi.org/10.3303/CET2292008
Pereira L., Frenzel M., Khodadadzadeh M., Tolosana-Delgado R., Gutzmer J., A self-adaptive particle-tracking method for minerals processing, Journal of Cleaner Production, 279 (2021) 123711. https://doi.org/10.1016/j.jclepro.2020.123711
Pfeffer R., Dave R.N., Wei D., Ramlakhan M., Synthesis of engineered particulates with tailored properties using dry particle coating, Powder Technology, 117 (2001) 40–67. https://doi.org/10.1016/s0032-5910(01)00314-x
Rao B.V., Kapur P.C., Konnur R., Modeling the size–density partition surface of dense-medium separators, International Journal of Mineral Processing, 72 (2003) 443–453. https://doi.org/10.1016/s0301-7516(03)00118-2
Schach E., Buchmann M., Tolosana-Delgado R., Leißner T., Kern M., van den Boogaart K.G., Rudolph M., Peuker U.A., Multidimensional characterization of separation processes – Part 1: introducing kernel methods and entropy in the context of mineral processing using SEM-based image analysis, Minerals Engineering, 137 (2019) 78–86. https://doi.org/10.1016/j.mineng.2019.03.026
Schach E., Padula F., Buchmann M., Möckel R., Ebert D., Pereira L., Kern M., Leißner T., Pashkevich D., Sousa R., Bremerstein I., Breuer B., Oliver K., Seltmann R., …van den Boogaart K.G., Data from a pilot plant experiment for the processing of a complex tin skarn ore - 19.11.2018, Dataset, Rodare, 2021. https://doi.org/10.14278/rodare.715
Svoboda J., Fujita T., Recent developments in magnetic methods of material separation, Minerals Engineering, 16 (2003) 785–792. https://doi.org/10.1016/s0892-6875(03)00212-7
Sygusch J., Rudolph M., A contribution to wettability and wetting characterisation of ultrafine particles with varying shape and degree of hydrophobization, Applied Surface Science, 566 (2021) 150725. https://doi.org/10.1016/j.apsusc.2021.150725
Sygusch J., Stefenelli N., Rudolph M., Ultrafine particle flotation in a concept flotation cell combining turbulent mixing zone and deep froth fractionation with a special focus on the property vector of particles, Minerals, 13 (2023) 1099. https://doi.org/10.3390/min13081099
Tang P., Puri V.M., Segregation quantification of two-component particulate mixtures: effect of particle size, density, shape, and surface texture, Particulate Science and Technology, 25 (2007) 571–588. https://doi.org/10.1080/02726350701783977
Tanno K., Current status of the mechanofusion process for producing composite particles, KONA Powder and Particle Journal, 8 (1990) 74–82. https://doi.org/10.14356/kona.1990014
Vanderbruggen A., Sygusch J., Rudolph M., Serna-Guerrero R., A contribution to understanding the flotation behavior of lithium metal oxides and spheroidized graphite for lithium-ion battery recycling, Colloids and Surfaces A: Physicochemical and Engineering Aspects, 626 (2021) 127111. https://doi.org/10.1016/j.colsurfa.2021.127111
Verrelli D.I., Bruckard W.J., Koh P.T.L., Schwarz M.P., Follink B., Particle shape effects in flotation. Part 1: microscale experimental observations, Minerals Engineering, 58 (2014) 80–89. https://doi.org/10.1016/j.mineng.2014.01.004
Wadell H., Sedimentation and sedimentology, Science, 75 (1932a) 20. https://doi.org/10.1126/science.75.1931.20.a
Wadell H., Volume, shape, and roundness of rock particles, The Journal of Geology, 40 (1932b) 443–451.
Wadell H., Sphericity and roundness of rock particles, The Journal of Geology, 41 (1933) 310–331. https://doi.org/10.1086/624040
Wang L., Peng Y., Runge K., Bradshaw D., A review of entrainment: mechanisms, contributing factors and modelling in flotation, Minerals Engineering, 70 (2015) 77–91. https://doi.org/10.1016/j.mineng.2014.09.003
Wang X., Gidwani A., Girshick S.L., McMurry P.H., Aerodynamic focusing of nanoparticles: ii. numerical simulation of particle motion through aerodynamic lenses, Aerosol Science and Technology, 39 (2005a) 624–636. https://doi.org/10.1080/02786820500181950
Wang X., Kruis F.E., McMurry P.H., Aerodynamic focusing of nanoparticles: i. guidelines for designing aerodynamic lenses for nanoparticles, Aerosol Science and Technology, 39 (2005b) 611–623. https://doi.org/10.1080/02786820500181901
Werner D., Peuker U.A., Mütze T., Recycling chain for spent lithium-ion batteries, Metals, 10 (2020) 316. https://doi.org/10.3390/met10030316
Werner D.M., Mütze T., Peuker U.A., Influence of cell opening methods on electrolyte removal during processing in lithium-ion battery recycling, Metals, 12 (2022) 663. https://doi.org/10.3390/met12040663
Werner S., Axel H., Die Komplexlagerstätten Tellerhäuser und Hämmerlein, 2012, ISBN: 9783981142143.
Whiteman M., Ridgway K., Particle shape discrimination using slotted sieves, Drug Development and Industrial Pharmacy, 12 (1986) 1995–2013. https://doi.org/10.3109/03639048609042621
Wilhelm T., Sygusch J., Furat O., Bachmann K., Rudolph M., Schmidt V., Parametric stochastic modeling of particle descriptor vectors for studying the influence of ultrafine particle wettability and

morphology on flotation-based separation behavior, Powders, 2 (2023) 353–371. https://doi.org/10.3390/powders2020021
Xia W., Role of particle shape in the floatability of mineral particle: an overview of recent advances, Powder Technology, 317 (2017) 104–116. https://doi.org/10.1016/j.powtec.2017.04.050

## Authors' Short Biographies

**Edgar Schach** is a PhD candidate in Mechanical Process Engineering and Mineral Processing at the University of Freiberg, Germany. His current work focuses on battery recycling and entropy analysis of raw material processes. He previously worked at Helmholtz-Institute Freiberg for Resource Technology, where he tested new reagents for sulfide flotation, contributed to research concerning the processing of complex and finely intergrown cassiterite ores, and developed characterization techniques for multidimensional separation processes.

**Dr. Thomas Buchwald** got his M.Sc. in chemical engineering from the University of Applied Sciences Bremerhaven in 2016 and has since been employed at the Institute of Mechanical Process Engineering and Mineral Processing and got his PhD there at TU Bergakademie Freiberg in 2021. He is currently doing research in particle characterization and mechanical solid-liquid separation processes as well as digitization and handling of experimental data.

**Dr. Orkun Furat** studied Mathematics at Ulm University and received his PhD there in 2022. In his research as a postdoc at the Institute of Stochastics at Ulm University he deals with structural segmentation of tomographic image data using methods from machine learning, statistical image analysis, multidimensional probabilistic modeling based on copulas, and stochastic geometry models with a focus on morphological, textural and elemental characterization of particle systems.

**Florentin Tischer** is a research assistant at the Institute of particle technology at the University of Erlangen-Nuremberg, Germany. He obtained his Bachelor's degree in chemical reaction engineering and his Master's degree in particle technology at the Friedrich-Alexander-University Erlangen (Germany). His research interest is around the production of optimised polymer powders for the powder bed fusion process (additive manufacturing). This involves the use of cold wet comminution, melt emulsification and precipitation of polymers.

**Alexandra Kaas** is a PhD candidate at the Institute of Mechanical Process Engineering and Mineral Processing, Freiberg University of Mining and Technology, Germany. She holds a diploma degree in Mechanical Process Engineering and Particle Technology. Focusing on Potash granulation in her diploma thesis she shifted in her professional career in 2021 to the recycling of Lithium-Ion-Batteries. Alexandra is currently focusing on several projects on secondary raw material processing, such as digitalization and modelling of sorting processes.

**Laura Kuger** is a research associate at the Institute for Functional Interfaces (IFG) at Karlsruhe Institute of Technology (KIT) in Karlsruhe, Germany. She has a Master's degree in Bioprocess Engineering from KIT and is currently pursuing her PhD, focusing on the multidimensional fractionation of nanoparticles using magnetic field controlled continuous chromatography.

**Matthias Masuhr** is a PhD candidate researcher at the Institute of Technology for Nanostructures (NST) at the University of Duisburg-Essen. He has a background in Nanoengineering and Nano process technology. His research interests include nano- and submicron particles, aerosols and their classification and characterization based on multiple properties. Parts of his research were published in "Advanced Powder Technology" and at multiple conferences including European Aerosol Conference (EAC), International Congress on Particle Technology (PARTEC) and World Congress on Particle Technology (WCPT).

**Johanna Sygusch** studied chemistry at the Technische Universität Braunschweig and received her Master's degree in 2016 in the field of technical chemistry. Since November 2017, she has been part of the processing department of the Helmholtz Institute Freiberg for Resource Technology of the Helmholtz-Zentrum Dresden-Rossendorf. As part of her research, she investigates the surface modification and characterisation of ultrafine particles as well as the multidimensional separation of fine particulate systems via flotation.

## Authors' Short Biographies

**Thomas Wilhelm** studied Mathematics and Economics at Ulm University and finished his Master's degree in 2021. Currently he is working as a PhD student at the Institute of Stochastics at Ulm University. His current research primarily revolves around employing machine learning techniques, statistical image analysis, multidimensional probabilistic modelling using copulas, and stochastic geometry models. The main objective of his research is to extract structural information from tomographic image data, with a specific emphasis on characterizing particle systems in terms of morphology and texture in order to optimize processes such as cooling, comminution and separation.

**Dr. Ralf Ditscherlein** studied physical engineering at the University of Applied Sciences in Zwickau. In his diploma thesis he dealt with the evaluation of oceanographic measurement data and was subsequently responsible for the metrological monitoring of two offshore measurement platforms in the North Sea and the Baltic Sea. In 2008, he then moved to the photovoltaic industry, where he was responsible for the coating of ceramic crucibles and the crystallization of polycrystalline silicon. Since 2017, he has been at the TU Bergakademie Freiberg at the Institute of Mechanical Process Engineering and Mineral Processing where he received his PhD in 2022 in the field of three-dimensional particle analysis using X-ray computed tomography.

**Prof. Urs Alexander Peuker** has been appointed Full Professor (chair) for particle technology and mineral processing in 2008 at TU Bergakademie Freiberg, Germany. In 2002 he was awarded a PhD in chemical and process engineering from the university of Karlsruhe, Germany, now KIT. From 2002 to 2008 he worked as junior professor at TU Clausthal, Germany. His main fields of work are separation processes in particle technology, mineral processing and recycling. In 2016 he became spokesman of the Priority Programme 2045 of the German Science Foundation (DFG) with the title: "Highly specific and multidimensional fractionation of fine particle systems", which was a unique possibility to have a deeper look into particle property distributions of higher dimensionality.

KONA Powder and Particle Journal

KONA Powder and Particle Journal No. 42 (2025) 156–169/https://doi.org/10.14356/kona.2025003 Review Paper

# Synthesis of Functional Nanoparticles Using a Microreactor†

**Satoshi Watanabe* and Minoru T. Miyahara#**

*Department of Chemical Engineering, Kyoto University, Japan*

Fine particles are widely used as intermediate and final products in industrial processes. Because particle properties are directly linked to the function and quality of the products, synthesizing monodispersed particles is a key technology. A microreactor, which comprises microchannels typically narrower than 1 mm, is a promising reaction tool because it offers excellent mixing and heat transfer performance. We used a microreactor for the synthesis of single-component and composite nanoparticles. This review introduces our synthetic results for functional nanoparticles including nickel, platinum–cobalt alloys, gold and silver nanoshells, patchy particles, core–shell clusters, and metal–organic frameworks. The microreactor we used is of the central-collision type and exhibits a characteristic mixing time 100~1,000 times shorter than that of the conventional batch mixing. The excellent mixing ability of the microreactor enables the synthesis of monodisperse particles in size and shape as well as core–shell particles with uniform shell thickness through instantaneous nucleation. More importantly, the microreactor realizes syntheses, which are not possible with batch reactors, by trapping reaction intermediates in a sequential reaction process and by rapidly changing the reaction temperature. These results demonstrate great advantages of using the microreactor for nanoparticle synthesis.

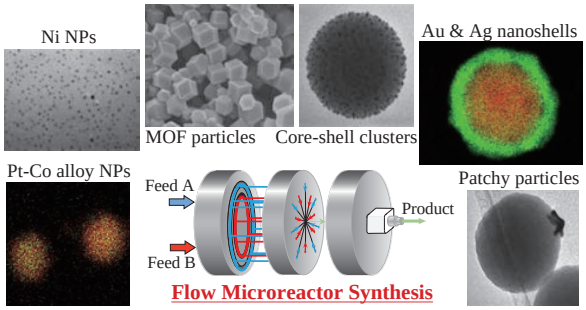


**Keywords:** microreactor, alloy nanoparticles, core–shell particles, metal–organic frameworks, nucleation, mixing time

## 1. Introduction

Fine particles are core materials in various industries, including chemistry, cosmetics, electronics, food, pharmaceuticals, photonics, and printing. Even if the final products are not in the particulate form, particles are contained in liquid and solid form products, including sunscreens, paint, and colored glasses, and they are involved in many products as intermediates in industrial processes. Notably, nanoparticles (NPs) play key roles in various applications, including electrode catalysts for fuel cells (Hou J. et al., 2020), conductive pastes (Abhinav K V. et al., 2015), bioimaging (Wolfbeis O.S., 2015), and sensing devices (Saha K. et al., 2012). In these applications, particle properties are directly linked to the function and quality of the products, and accordingly, the synthesis of monodispersed NPs in size and shape is a crucial issue.

Among various synthetic processes of NPs reported so far, liquid-phase synthesis using chemical reactions is promising in terms of versatility in reaction conditions and ease of process handling (Fiévet F. et al., 2018; Wang D. and Li Y., 2011; Xia Y. et al., 2009). A general strategy for synthesizing monodispersed particles is to shorten the nucleation period so that the particle growth period starts after the completion of nucleation. However, conventional batch-type synthesis often allows overlap between nucleation and growth periods because of its weak mixing intensity, which causes concentration distribution after mixing reaction solutions, resulting in the formation of particles with a wide size distribution. “Slowing reaction rates” is a possible solution because the effect of mixing becomes less significant, but typically leads to the formation of particles of submicrometer size or larger. In contrast, “quickening mixing rates” is a more direct and promising approach that is suitable for NP synthesis, which typically involves rapid reactions.

To achieve the latter approach, a microreactor is the first candidate because rapid mixing is a primary feature of microreactors (Yoshida J. et al., 2013). Microreactors comprise microchannels typically narrower than 1 mm, in which chemical reactions occur. Not only mixing ability but also heat transfer is excellent in microspaces, and accordingly exploiting these properties dramatically improves the precision and efficiency of chemical reactions (Mae K., 2007). Microreactors with different architectures have been successfully applied to the synthesis of various types of NPs, including gold using a chip-based interdiffusion microreactor (Wagner J. et al., 2004) and a chip-shaped three-layer assembly (Wagner J. and Köhler J.M., 2005), silver using a tubular (Lin X.Z. et al., 2004) and helical microreactors (Wu K.-J. et al., 2017), platinum using a droplet junction chip (Luty-Błocho M. et al., 2013)

† Received 5 July 2023; Accepted 28 September 2023
J-STAGE Advance published online 24 February 2024
* Corresponding author: Satoshi Watanabe;
Add: Katsura, Nishikyo, Kyoto 615-8510, Japan
E-mail: nabe@cheme.kyoto-u.ac.jp
TEL: +81-75-383-2682 FAX: +81-75-383-2652
# Minoru T. Miyahara passed away on August 11, 2022.

and a spiral tubular microreactor (Suryawanshi P.L. et al., 2016), palladium using a Y-junction microreactor (Sharada S. et al., 2016) and a slit interdigital microstructured mixer (Gioria E. et al., 2019), nickel using a T-shaped microreactor (Xu L. et al., 2015), and silica in a slit interdigital microstructured mixer (Gutierrez L. et al., 2011). Not only single-component NPs and composite particles have been synthesized, including palladium@platinum core–shell nanoparticles using T-mixers (Hashiguchi Y. et al., 2021), gold nanoshells in microfluidic slug flow (Duraiswamy S. and Khan S.A., 2010), and patchy particles using a T-mixer (Meincke T. et al., 2017; Völkl A. and Klupp Taylor R.N., 2022). Microreactors combined with acoustic waves to enhance mixing intensity, which are so-called acoustic microreactors, have also been demonstrated to synthesize various types of NPs (Chen Z. et al., 2022). These synthetic results demonstrate the advantages of applying microreactors to NP synthesis.

Focusing especially on the excellent mixing ability of microreactors, we have been working on the synthesis of functional NPs such as nickel (Ni) and bimetallic alloy (Watanabe S. et al., 2021), nanoporous metal–organic frameworks (MOFs) (Fujiwara A. et al., 2021; Watanabe S. et al., 2017b), gold and silver nanoshells (Maw S.S. et al., 2019; Watanabe S. et al., 2015), and patchy particles (Watanabe S. et al., 2016). Our concept is to achieve highly supersaturated conditions by quickly mixing reaction solutions, thereby enabling instantaneous nucleation and subsequent growth. In this review article, we introduce our synthetic results using a microreactor.

## 2. Central-collision-type microreactor

The microreactor we used is a central-collision-type reactor (Nagasawa H. et al., 2005), which comprises three plates (inlet, mixing, and outlet plates), as illustrated in **Fig. 1**. Each of the two inlet fluids is divided into seven streams on the inlet plate (**Fig. 1(B)**), and the fourteen streams (seven from inlet A indicated by black circles and the other seven from inlet B indicated by black squares as illustrated in **Fig. 1(C)**) collide with each other into a single stream at the center of the mixing plate and then outflow from the outlet. We used the microreactor with fourteen streams because the mixing intensity was confirmed to increase with the number of streams (Nagasawa H. et al., 2005) and fourteen streams were almost the highest possible number in terms of channel geometry. The intensive collision breaks the fluids into small segments, thereby shortening the diffusion distance to achieve quick mixing.

We evaluated the mixing ability of the microreactor using a chemical test reaction (Watanabe S. et al., 2017a). We adopted the Villermaux–Dushman (VD) method (Ehrfeld W. et al., 1999; Fournier M.C. et al., 1996), which comprises parallel competing neutralization and redox reactions. Because the neutralization reaction is much faster than the redox reaction, only the neutralization reaction would proceed under ideal mixing conditions. However, in the case of poor mixing, the mixed fluid is segregated, and accordingly, the redox reaction proceeds. Thus, the amount of the product from the redox reaction is a measure of the mixing intensity (smaller production indicates better mixing). We obtained the mixing time from the VD experiments following the procedure reported by Commenge et al. (Commenge J.-M. and Falk L., 2011). **Fig. 2** shows the relationship between the mixing time $t_m$ and the flow rate. The increase in the flow rate shortens the mixing time of the microreactor, and a flow rate of 10 mL/min attains the shortest mixing time of 0.3 ms, which indicates that complete mixing is achieved in 0.3 ms. For comparison purposes, **Fig. 2** also shows a series of mixing times of a Y-shaped mixer with an inner diameter of 1.5 mm. At the

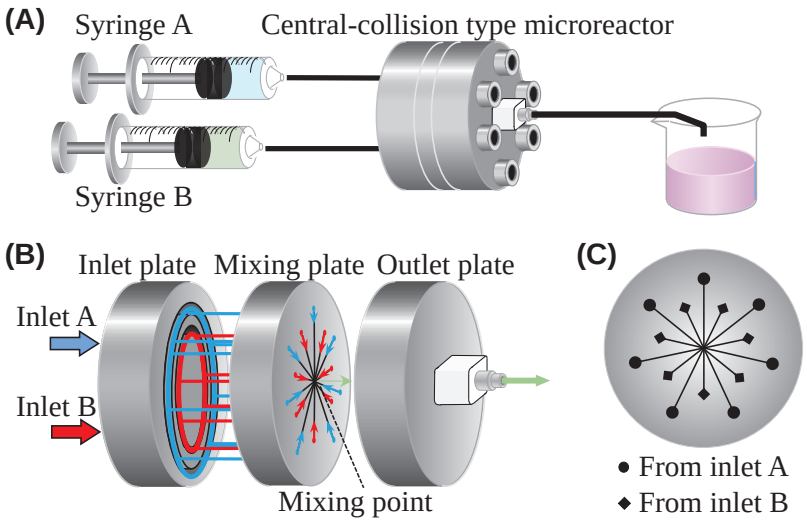


**Fig. 1** Schematic illustrations of **(A)** experimental setup for nanoparticle synthesis, **(B)** central-collision-type microreactor (disassembly image), and **(C)** mixing plate. Adapted with permission from Ref. (Watanabe S. et al., 2017a). Copyright: (2017) Elsevier B.V.

same flow rates, the mixing time of the microreactor is 100~1,000 times shorter than that of the Y-shaped mixer, clearly demonstrating the advantage of the microreactor. Comparison of the microreactor with the Y-shaped mixer and batch-type reactor under the same Reynolds numbers from 300 to 1200 also confirmed the superiority of the microreactor in terms of mixing intensity. A short mixing time leads to a uniform reaction field with the desired concentration condition, thereby enabling the formation of monodisperse particles.

## 3. Synthesis of metallic nanoparticles

Metallic particles exhibit excellent chemical and physical properties, and are thus promising in various applications, including catalysts, electronics, photonics, sensing, and imaging (Xia Y. et al., 2009). Downsizing them to the nanoscale is crucial to fully exploit their properties. Here we focus on Ni, and Ni NPs with average diameters of 3–10 nm have been synthesized by several techniques, including a water-in-oil microemulsion technique (Chen D.-H. and Wu S.-H., 2000; Wu X. et al., 2012), an organometallic approach (Domínguez-Crespo M.A. et al., 2009; Ely T.O. et al., 1999), and a polyol process (Couto G.G. et al., 2007; Eluri R. and Paul B., 2012; Wu S.-H. and Chen D.-H., 2003). However, these techniques rely on organic solvents and involve heating during the synthesis, which can be a problem in terms of environmental protection and energy consumption. Although aqueous syntheses have been reported (Chen D.-H. and Hsieh C.-H., 2002; Jiang Z. et al., 2013), the resultant size of Ni particles was larger (>10 nm) with wider size distributions than those synthesized using organic solvents. Why is it so difficult to synthesize monodisperse Ni NPs in aqueous systems? This is because the reduction reaction of Ni ions does not uniformly proceed due to insufficient mixing, and if this is the case, the central-collision-type microreactor is a suitable reactor to overcome this difficulty.

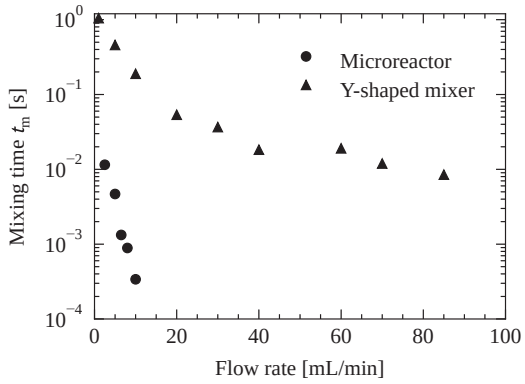


**Fig. 2** Dependence of the characteristic mixing time ($t_m$) estimated from the VD experiments on the flow rate for different mixing procedures of the microreactor and Y-shaped mixer. Adapted with permission from Ref. (Watanabe S. et al., 2017a). Copyright: (2017) Elsevier B.V.

**Fig. 3** shows the experimental setup for Ni NPs synthesis, in which two microreactors are sequentially connected through a tube with varying lengths of 1, 3, 20, and 40 cm (Watanabe S. et al., 2021). Varying the tube length corresponded to the change in residence times between the two microreactors (0.053, 0.16, 1.1, and 2.1 s). We first mixed aqueous solutions of $NiCl_2$ and a surfactant (cetyltrimethylammonium bromide; CTAB). We used CTAB because it has been reported to serve as an effective capping agent suitable for the Ni NP synthesis (Wu S.-H. and Chen D.-H., 2004). The premixed solution was mixed with a hydrazine ($N_2H_4$) aqueous solution in microreactor A, and the mixed solution from the outlet, which was directly injected into microreactor B, was mixed with a sodium hydroxide (NaOH) solution. The flow rate was set to 10 mL/min for each syringe using syringe pumps, and the synthesis was conducted at room temperature. In this sequential flow process, the following reaction scheme is assumed (Park J.W. et al., 2006). The reaction in microreactor A produces nickel–hydrazine complexes.

$$Ni^{2+} + xN_2H_4 \rightarrow \left[Ni\left(N_2H_4\right)_x\right]^{2+}, x = 1,2,3 \quad (1)$$

Subsequent mixing with NaOH in microreactor B induces a ligand exchange reaction to yield nickel hydroxide ($Ni(OH)_2$) and $N_2H_4$.

$$\left[Ni\left(N_2H_4\right)_x\right]^{2+} + 2OH^- \rightarrow Ni\left(OH\right)_2 + xN_2H_4 \quad (2)$$

$Ni(OH)_2$ was then reduced to zero-valent Ni by freed $N_2H_4$, followed by nucleation and growth to produce Ni

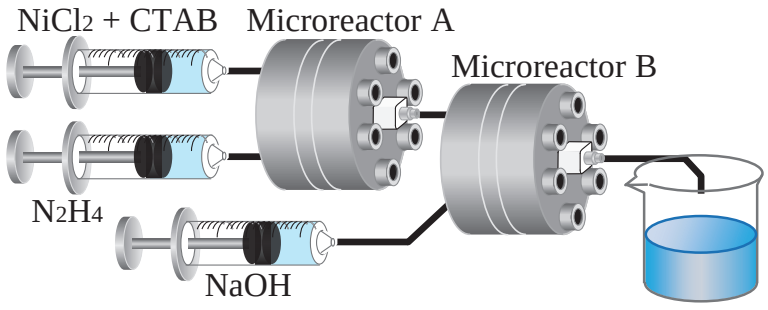


**Fig. 3** Schematic of the sequential flow process for the synthesis of Ni NPs. Reprinted from Ref. (Watanabe S. et al., 2021) under the terms of the CC-BY 4.0 license. Copyright: (2021) The Authors, published by Frontiers.

NPs.

A typical synthetic result is presented in **Fig. 4**, where the residence time between microreactors A and B was set to 0.053 s. NPs with a sharp size distribution (3.8 ± 0.6 nm) were successfully formed, as confirmed by transmission electron microscopy (TEM) images and particle size distributions (**Figs. 4(A) and 4(B)**). X-ray photoelectron spectroscopy (XPS) and powder X-ray diffraction (XRD) measurements demonstrated the formation of Ni NPs with face-centered cubic (fcc) crystal structures (**Figs. 4(C) and 4(D)**). The synthesized Ni NPs were comparable to those synthesized using organic solvents in terms of average particle size and size distribution, demonstrating the excellent performance of the microreactor that enables aqueous and room-temperature synthesis of Ni NPs. Note that the use of a Y-shaped mixer with a weaker mixing intensity in place of either microreactor A or B did not produce monodisperse Ni NPs, further demonstrating the importance of the instantaneous and homogeneous mixing provided by the microreactor for the synthesis of monodisperse NPs.

In this flow sequential process, the residence time between microreactors A and B was found to have a critical effect on the size distribution; a longer residence time resulted in a wider distribution. This is closely related to the formation of nickel–hydrazine complexes. Ni ions are reported to react with $N_2H_4$ molecules to form stable three-coordinate complex structures $[Ni(N_2H_4)_3]^{2+}$, by way of intermediate species with one- and two-coordinate structures $[Ni(N_2H_4)]^{2+}$ and $[Ni(N_2H_4)_2]^{2+}$ (Gilbert E.C. and Evans W.H., 1951; Li Y.D. et al., 1999). A residence time of more than 2 s is assumed to be sufficiently long to allow the formation of stable three-coordinate complex structures before mixing with NaOH. In this case, the ligand exchange reaction would be slow, possibly because of the high activation energy required to replace $N_2H_4$ molecules with $OH^-$ ions (**Eqn. (2)**), which leads to a slow reduction and consequently results in a wide size distribution. In contrast, under residence times shorter than ca. 1 s, less stable intermediate species react with NaOH to quickly free $N_2H_4$ molecules through the ligand exchange reaction, thereby leading to a quick reduction of Ni ions. In this manner, for the formation of monodisperse Ni NPs, it is necessary to trap less stable intermediate complex structures so that they react with NaOH at microreactor B. To satisfy this requirement, precise control of the residence time, on the order of milliseconds, is critical, which is enabled by the excellent mixing performance of the microreactor.

The synthesis of bimetallic alloy NPs is also possible using a central-collision-type microreactor. We synthesized platinum (Pt)–cobalt (Co) alloy NPs by the simultaneous reduction of Pt and Co ions. We mixed a premixed aqueous solution of Pt and Co ions and polyvinylpyrrolidone (PVP, molecular weight of 1,300,000) with an aqueous solution of a strong reducing agent, $NaBH_4$, in the microreactor (**Fig. 1(A)**). We opted for PVP for two reasons: firstly, it is

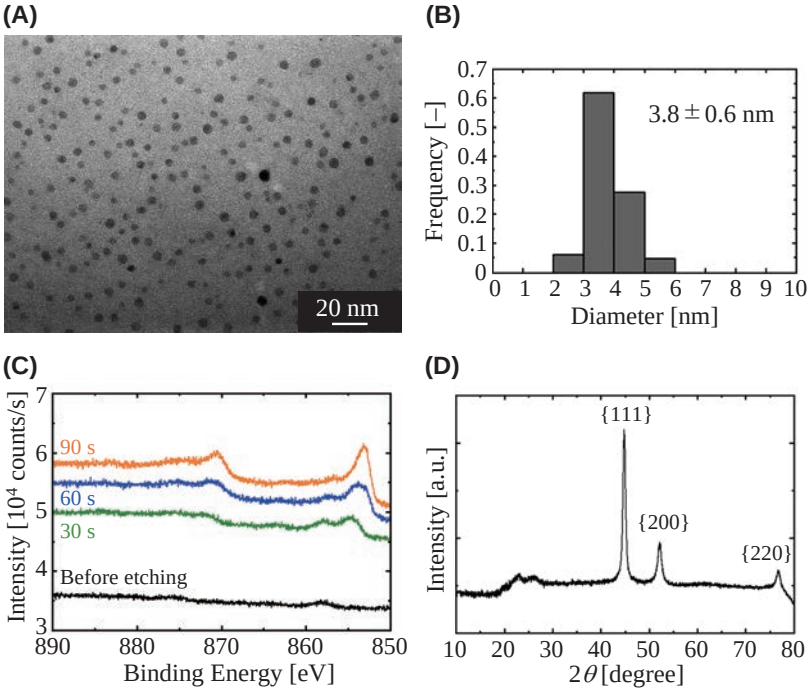


**Fig. 4** Synthetic result of Ni NPs with a residence time of 0.053 s. **(A)** TEM image, **(B)** particle size distribution, **(C)** XPS result, and **(D)** XRD pattern. In the XPS result, the peaks at 870 and 853 eV were attributed to Ni $2p_{1/2}$ and Ni $2p_{3/2}$, respectively, which appeared after Ar ion etching, possibly because the etching removed CTAB molecules surrounding the resultant particle surfaces. Reprinted from Ref. (Watanabe S. et al., 2021) under the terms of the CC-BY 4.0 license. Copyright: (2021) The Authors, published by Frontiers.

widely used as a stabilizer for various metallic NPs, and secondly, being a nonionic polymer, it is suitable for investigating the effects of different metal precursors—details of which are discussed later. This choice prevents the dissolution of different ions from stabilizers. **Fig. 5** presents TEM images, particle size distributions, and scanning TEM (STEM) and energy-dispersive X-ray (EDX) mapping images of the resultant particles synthesized using the microreactor (**Fig. 5(A)**) and a batch reactor (**Fig. 5(B)**) for comparison, in which $K_2PtCl_4$ and $CoCl_2$ were used as precursors. The microreactor produced NPs with a monomodal distribution, which is in contrast to batch reactor synthesis, which results in a wide size distribution with a rather bimodal shape. As shown in the STEM and EDX mapping images, in the case of the microreactor, Pt and Co elements were uniformly mixed in single particles to form solid solutions, whereas the batch reactor yielded segregated structures composed of smaller (Co) and larger (Pt) NPs.

The results shown in **Fig. 5** again demonstrate the importance of the mixing process in NP synthesis because the mixing procedure (microreactor vs. batch reactor) is the only difference in the synthetic processes. The formation of segregated particles from the batch reactor can be explained as follows: because of the weak mixing ability of the batch reactor, a reaction solution immediately after mixing two solutions is non-uniform and has domains of the original solutions with different sizes. In this situation, reducing agents can be locally deficient relative to metal ions, and accordingly, Pt ions are preferentially reduced because of their lower ionization tendency than that of Co ions to promote the nucleation of Pt and subsequent growth. This results in the formation of larger Pt NPs. Consequently, the resultant particles exhibit segregated bimodal structures composed of larger Pt and smaller Co NPs. In contrast, complete mixing is achieved much faster in the microreactor, and the reaction solution is more uniform. In this homogeneously mixed solution, the reduction reaction of both Pt and Co ions simultaneously proceeds to produce Pt–Co solid solution alloys.

For the synthesis of Pt–Co solid solution alloy NPs, the choice of precursors was critical (**Fig. 6**). For a fixed Co precursor of $CoCl_2$, the resultant particles were Pt–Co solid solution alloys when $K_2PtCl_4$ was used as a Pt precursor (**Fig. 6(A)**), whereas the use of $H_2PtCl_6$ resulted in the formation of smaller NPs mainly composed of Pt as well as larger Pt–Co alloy NPs (**Fig. 6(C)**). We also used $K_2PtCl_6$ and confirmed a similar result to that of $H_2PtCl_6$. A different Co precursor ($Co(NO_3)_2$) yielded similar results to those of $CoCl_2$ (**Figs. 6(B) and 6(D)**). These results demonstrate that the valence number of Pt ions is more critical than the type of Co precursors and counter cations in Pt precursors; for synthesizing monodisperse Pt–Co alloy NPs, the use of $PtCl_4^{2-}$ ions is more desirable than $PtCl_6^{2-}$ ions. $PtCl_4^{2-}$ ions

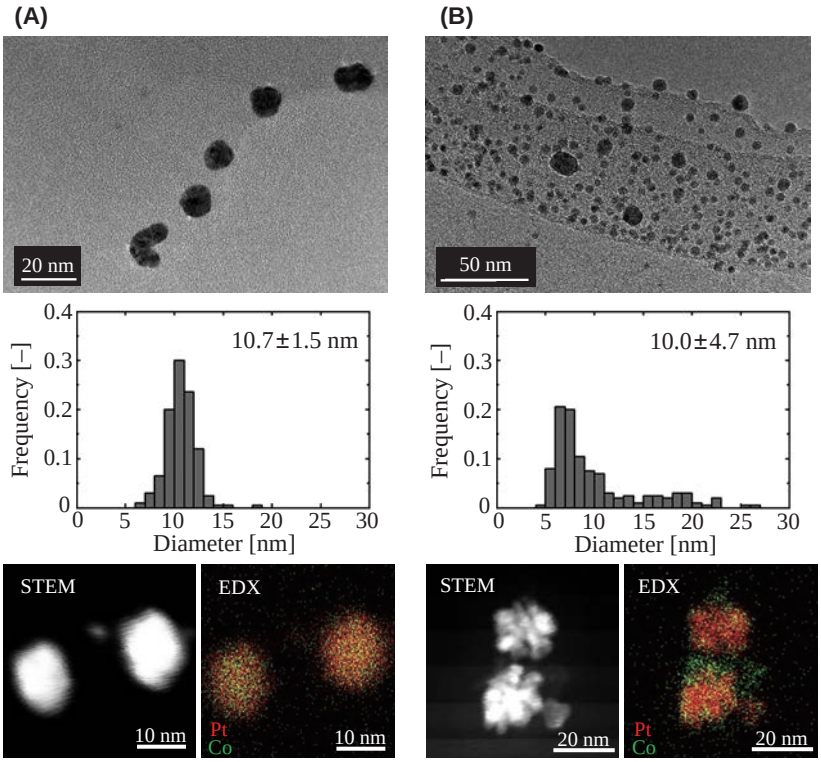


**Fig. 5** TEM image, particle size distribution, and STEM and EDX mapping images of Pt and Co bimetallic particles synthesized by **(A)** microreactor and **(B)** batch reactor. Reprinted from Ref. (Watanabe S. et al., 2021) under the terms of the CC-BY 4.0 license. Copyright: (2021) The Authors, published by Frontiers.

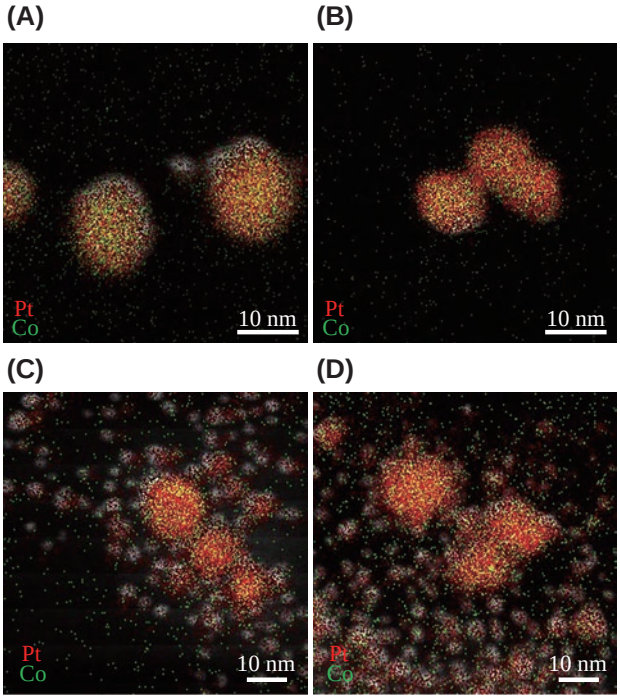


**Fig. 6** EDX mapping images of Pt and Co bimetallic particles synthesized from different combinations of precursors of **(A)** $K_2PtCl_4$ and $CoCl_2$, **(B)** $K_2PtCl_4$ and $Co(NO_3)_2$, **(C)** $H_2PtCl_6$ and $CoCl_2$, and **(D)** $H_2PtCl_6$ and $Co(NO_3)_2$. Reprinted from Ref. (Watanabe S. et al., 2021) under the terms of the CC-BY 4.0 license. Copyright: (2021) The Authors, published by Frontiers.

are directly reduced to zero-valent Pt, while $PtCl_6^{2-}$ ions follow a two-step sequential route by way of $PtCl_4^{2-}$ ions. Because the standard reduction potentials of $PtCl_6^{2-}$/$PtCl_4^{2-}$ and $PtCl_4^{2-}$/Pt are similar (Jiang B. et al., 2015), the reduction reaction of $PtCl_6^{2-}$ ions would be slower than that of $PtCl_4^{2-}$ to have a rate difference in the reduction reaction of Co ions. Because of the difference in the reduction rate, $PtCl_6^{2-}$ is later reduced to produce smaller NPs with a main component of Pt. Therefore, matching the reduction rates of constituent metal ions is another key factor for synthesizing solid solution alloy NPs.

## 4. Synthesis of metallic shells and patches

Core–shell-type particles with metallic shells and dielectric cores, or so-called metallic nanoshells, are quite promising for optical and biomedical applications because of their tunable surface plasmon resonances (Yang W. et al., 2019). Not only metallic nanoshells but also core–shell clusters (CSC; core particles uniformly covered with nanoparticles) and patchy particles (core particles partially covered with shell portion) exhibit attractive optical properties due to discreteness and/or anisotropy in the particle structure (Han J.H. et al., 2022; Mühlig S. et al., 2011). What is intriguing about these composite particles is that they not only possess multiple different properties, which is impossible with single-component particles, but also demonstrate peculiar characteristics due to synergetic effects, interfacial properties, and morphologies of core and shell materials. However, because of the complexity of their structures, the synthesis of these structured particles is generally not straightforward, and typically requires multiple steps and/or templates. In core–shell-type particle synthesis, controlling reactions on core particle surfaces is a major difficulty. It is generally challenging to promote reactions selectively at interfaces because reactions in the bulk phase can proceed in parallel, especially when reactions are quick.

Here, we take gold nanoshells as an example. A typical synthetic method is seed-mediated growth, which comprises three steps: surface modification of core silica particles, gold NP decoration of the modified silica surface as "seeds" to form CSCs, and growth of gold NP seeds into a shell by the reduction of gold ions (Oldenburg S.J. et al., 1998). Although this method allows good control in the shell thickness, it takes a long time, often on the order of days, to complete the preparation process. The bottleneck step is the CSC formation process, in which gold NPs are separately prepared by the reduction of gold ions, aged for a certain period of several days, and then mixed with a suspension of surface-modified silica particles to proceed with the adsorption of gold NPs on the modified silica surface, followed by the separation of unattached gold NPs (Rasch M.R. et al., 2009). Most of the syntheses of gold nanoshells are conducted in batch-type processes, and the intrinsic weak mixing ability of batch reactors is one of the reasons for the requirement of the multistep time-consuming procedure in the CSC formation process. This leads to the idea of using a microreactor to simplify and intensify the CSC formation process.

Our concept to achieve a one-step process for CSC formation was to simply use the principle that, under an ideally uniform reaction field, heterogeneous nucleation at interfaces is energetically more favored than homogeneous nucleation in the bulk phase. Following this concept, we mixed a premixed aqueous suspension of surface-modified silica particles and $HAuCl_4$ with an aqueous solution of $NaBH_4$ in a central-collision-type microreactor (**Fig. 1(A)**) (Watanabe S. et al., 2015). The surface modification of silica particles was conducted by using 3-aminopropyl trimethoxysilane to positively charge the particle surface. **Figs. 7(A) and 7(B)** present typical TEM images of the resultant particles, in which the core silica particles are uniformly decorated with monodisperse gold NPs. In our TEM measurements, we observed no unattached free gold NPs, indicating the preferential formation of gold NPs on the surface of core silica particles. In contrast, the use of a batch reactor and Y-shaped mixer (inner diameter of 1.5 mm) instead of the microreactor resulted in non-uniform deposition of gold NPs with wide size distributions, as shown in **Figs. 7(C) and 7(D)**. Another feature of **Figs. 7(C) and 7(D)** is that the gold NP coverages of

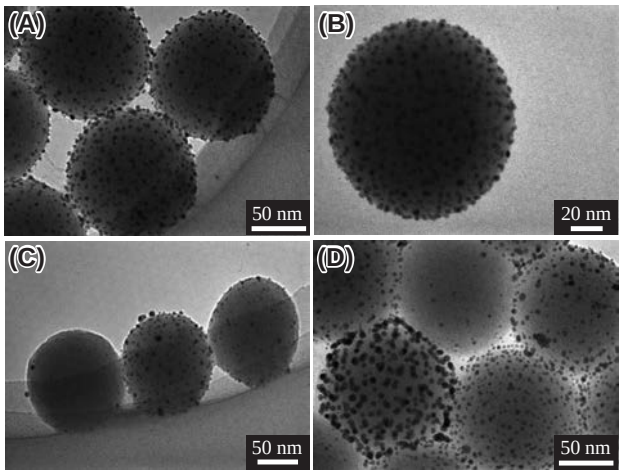


**Fig. 7** Representative TEM images of CSCs prepared **(A,B)** with the microreactor, **(C)** with a batch reactor, and **(D)** with a Y-shaped mixer. Adapted with permission from Ref. (Watanabe S. et al., 2015). Copyright: (2015) Wiley.

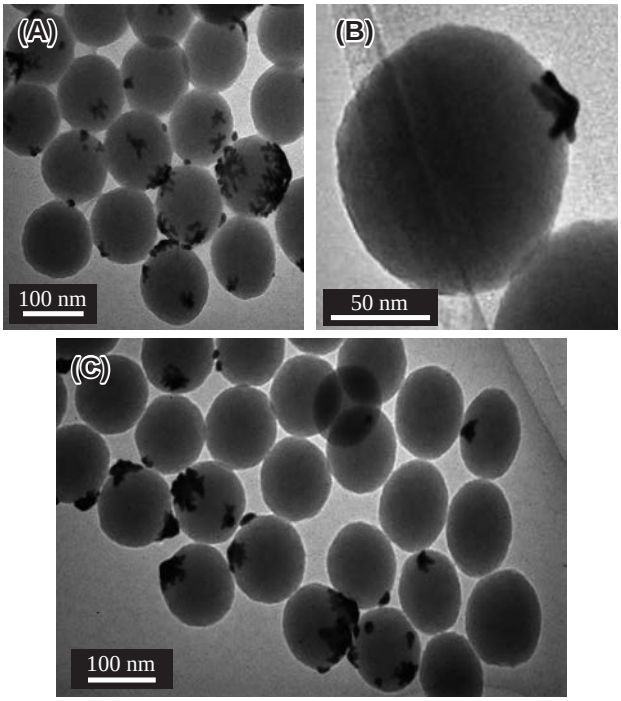


**Fig. 8** Representative TEM images of patchy particles prepared **(A,B)** with the microreactor and **(C)** with a batch reactor. Adapted with permission from Ref. (Watanabe S. et al., 2016). Copyright: (2016) Elsevier B.V.

individual resultant CSCs are remarkably different between a state almost devoid of NPs and that with full decoration. Therefore, gold NP seeding through the in situ reduction of gold ions requires intensive mixing provided by the microreactor.

The in situ reduction of gold ions described above produced core silica particles uniformly decorated with gold NPs, which is possibly attributable to the use of a strong reducing agent, $NaBH_4$, which induced a rapid increase in the degree of supersaturation to produce many small nuclei. Based on this discussion, the use of a weaker reducing agent would lead to the formation of patchy particles. We accordingly used ascorbic acid as a reducing agent instead of $NaBH_4$, and as expected, we successfully obtained patchy particles (**Fig. 8(A)**) (Watanabe S. et al., 2016). Core particles are partially covered with gold patches with a dendritic shape (**Fig. 8(B)**), which is quite a contrast to the CSCs obtained using $NaBH_4$. Meanwhile, the batch-type reactor produced particles with a larger variation in the number of patches than the microreactor, as shown in **Fig. 8(C)**. These results demonstrate that even though a weaker reductant was used, the reduction reaction remained so rapid that intensive mixing by the microreactor was still necessary to obtain uniform patchy particles.

Based on these results, we propose possible formation mechanisms of CSCs and patchy particles, schematic representations of which are shown in **Fig. 9**. Before starting the reduction reaction in both cases, it is reasonable to assume that negatively charged gold complex ions form electric double layers by crowding around surface-modified silica particles with positive charges, as depicted in **Fig. 9(A)-(i)**. For CSC formation, upon mixing with a strong reducing agent, $NaBH_4$, the reduction of gold ions quickly proceeds to increase the degree of supersaturation of the reduced gold atoms. Due to the formation of electric double layers, the degree of supersaturation is higher in the vicinity of the particle surface than that of the bulk solution, thus leading to increased nucleation at the interface. Because gold NPs are negatively charged, they are stabilized on the surface of the surface-modified silica particles, which facilitates heterogeneous nucleation (**Fig. 9(A)-(ii)**). The nuclei formed on the silica particle surface grow larger through the diffusion of reduced gold atoms remaining in the vicinity of the core silica particles to complete the formation of CSCs (**Fig. 9(A)-(iii)**). In the case of ascorbic acid with a weak reducing ability, the degree of supersaturation is lower than that of $NaBH_4$; accordingly, a much fewer number of nuclei are formed on the core particle surface (**Fig. 9(B)-(i)**). In the subsequent growth process, the surface diffusion of reduced gold atoms along the core particle surface is dominant over that from the bulk phase because of the higher concentration of gold ions forming electric double layers (**Fig. 9(B)-(ii)**). Because the surface reaction of the patches is assumed to be quick, the growth reaction proceeds under diffusion-limited conditions. In this case, the protruding portions of patches preferentially grow, resulting in dendritic structures (**Fig. 9(B)-(iii)**).

According to this mechanism, not only the supply rate of gold, which is affected by the gold ion concentration and the reducing ability, but also the zeta potential of core particles is a critical factor for the resultant structure because the zeta potential dominantly determines the affinity with negatively charged gold ion complexes. To change the zeta

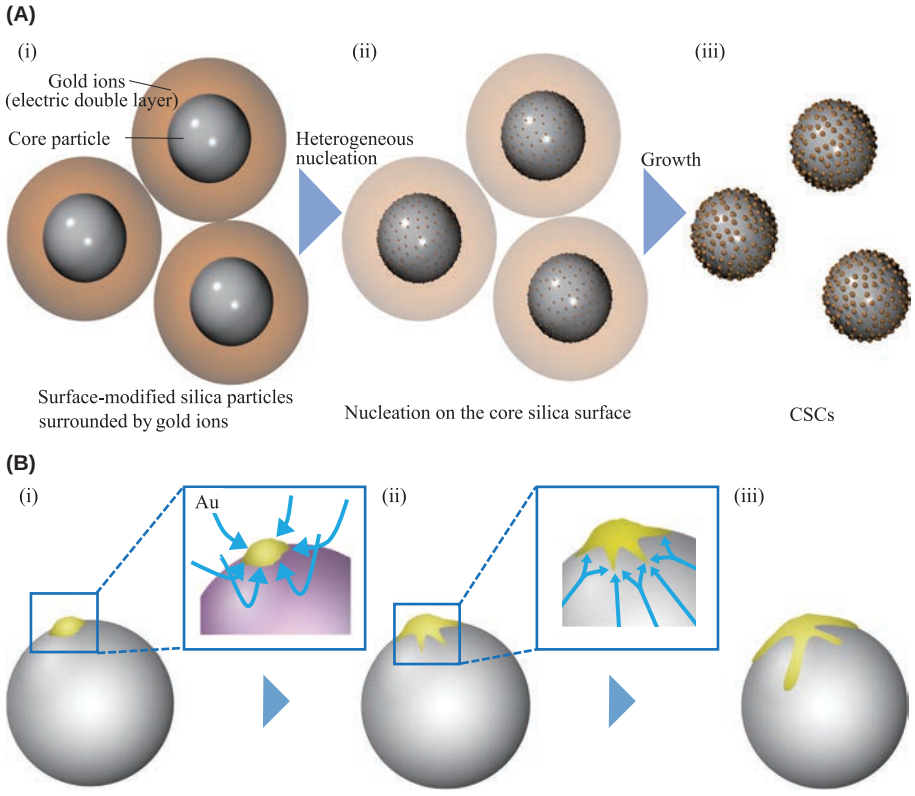


**Fig. 9** Schematic of possible formation mechanisms of **(A)** CSCs and **(B)** patchy particles through the in situ reduction of gold ions. Adapted with permission from Refs. (Watanabe S. et al., 2015) and (Watanabe S. et al., 2016) for **(A)** and **(B)**, respectively. Copyrights: (2015) Wiley and (2016) Elsevier B.V.

potential and the supply rate, we used trisodium citrate, which has a much weaker reducing ability. The zeta potential of core silica particles decreased under higher pH conditions of a trisodium citrate solution. Under an increased temperature of 95 °C, we obtained "snowman-like" particles in which a gold NP with a diameter of approximately 30 nm was deposited on a core silica particle (Watanabe S. et al., 2016). The formation of these particles occurs because the use of a far weaker reducing agent highly suppressed nucleation and because the lowered zeta potential allowed diffusion from the bulk phase to form spherical patches. In this manner, the coating structure of the core silica particles can be manipulated by the supply rate of gold and the interaction between the core particles and gold ions.

Growing gold NP seeds from a CSC into a continuous shell leads to the formation of gold nanoshells. In the experiment, we mixed a premixed aqueous suspension of CSCs and gold ions with an aqueous solution of a reducing agent in a central-collision-type microreactor (**Fig. 1(A)**). Gold ions were obtained by preaging a $HAuCl_4$ solution with $K_2CO_3$, which is referred to as K-gold. In the shell growth process, the use of $NaBH_4$ as a reducing agent did not produce complete shells; seed gold NPs grew larger, although gold NPs newly formed in the bulk solution phase before completing shell formation (Watanabe S. et al., 2013). This is possibly because the energy barrier to self-nucleation in the bulk phase can be easily surmounted by the strong reducing ability of $NaBH_4$. We accordingly used a weaker reducing agent, ascorbic acid, and successfully synthesized complete gold nanoshells without self-nucleation in the bulk phase (**Fig. 10(A)**) (Watanabe S. et al., 2015). The shell thickness varied from 17 nm to 50 nm by changing the concentration of K-gold. In contrast, the use of a Y-shaped mixer (inner diameter of 1.5 mm) instead of the microreactor resulted in a mixture composed of unreacted particles (CSCs; the upper right particle in **Fig. 10(B)**), particles in the process of growing (the lower left particle in **Fig. 10(B)**), and gold nanoshells (the centered particle in **Fig. 10(B)**). The batch reaction also failed.

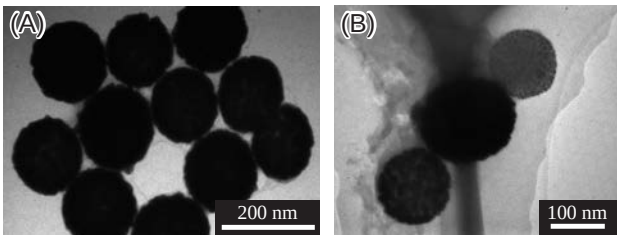


**Fig. 10** Representative TEM images of the resultant particles after the shell growth reaction using **(A)** the microreactor and **(B)** a Y-shaped mixer. Adapted with permission from Ref. (Watanabe S. et al., 2015). Copyright: (2015) Wiley.

These results are similar to the case of the formation of CSCs and patchy particles, thereby demonstrating that strong mixing by the microreactor is necessary for the synthesis of uniform gold nanoshells. By using $AgNO_3$ mixed with ammonia instead of K-gold and formaldehyde as a reducing agent, silver nanoshells can be synthesized (**Fig. 11**) (Maw S.S. et al., 2019), demonstrating the versatility of the synthetic process using a microreactor.

Taking advantage of the flow processes, we combined the synthetic processes for CSCs and gold nanoshells into a sequential process (**Fig. 12(A)**). A premixed suspension of surface-modified silica particles and $HAuCl_4$ was mixed with $NaBH_4$ in the first microreactor to produce CSCs, followed by mixing with K-gold in a Y-shaped mixer. The mixed suspension from the Y-shaped mixer was directly injected into the second microreactor to react with ascorbic acid to yield gold nanoshells. Residence times between the first microreactor and the Y-shaped mixer and between the Y-shaped mixer and the second microreactor were set to be

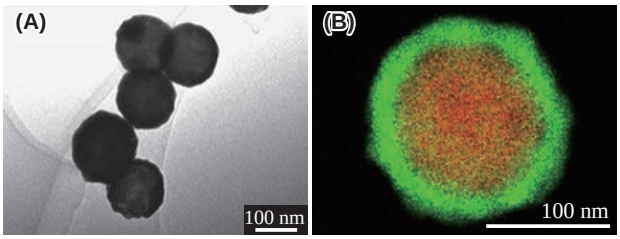


**Fig. 11** **(A)** TEM and **(B)** STEM-EDX mapping (Si: red, Ag: green) images of the resultant silver nanoshells synthesized using the microreactor. Adapted with permission from Ref. (Maw S.S. et al., 2019). Copyright: (2019) Elsevier B.V.

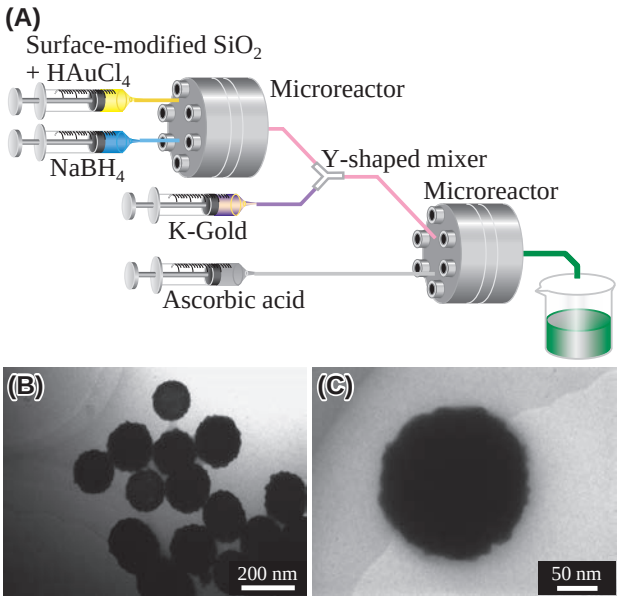


**Fig. 12** **(A)** Schematic of the experimental setup for the sequential flow synthesis of gold nanoshells from surface-modified silica particles. **(B,C)** TEM images of the resultant gold nanoshells. Adapted with permission from Ref. (Watanabe S. et al., 2015). Copyright: (2015) Wiley.

2 s and 1 s, respectively, which are considerably longer than the mixing times (~0.3 ms for the microreactor and ~50 ms for the Y-shaped mixer). This attempt was successful because uniform gold nanoshells were synthesized without the formation of gold NPs in the bulk solution phase, as shown in **Figs. 12(B)** and **12(C)** (Watanabe S. et al., 2015). Our sequential flow process not only enables a high throughput of 60 mL/min compared with typical microfluidic systems but also reduces tedious efforts such as post-synthetic washing steps to remove free unattached gold NPs. For the silver nanoshell synthesis, a sequential flow process similar to the case of the gold nanoshells was attempted but resulted in the formation of free silver NPs, possibly because silver ions were reduced by the remaining $NaBH_4$ after the CSC formation reaction. To deactivate $NaBH_4$, we found that a longer residence time of ~30 min between the CSC formation and the shell growth reactions was necessary, and with that setting of a long residence time, the flow sequential synthesis of silver nanoshells is in principle possible. This type of flow sequential process enables the facile and scalable synthesis of metallic nanoshells and is accordingly promising for industrial applications in various fields.

## 5. Synthesis of nanoporous particles

MOFs are emerging nanoporous crystals with attractive features, including large surface area, highly regular and tunable pore structure, and structural flexibility inherent to specific types of MOFs (Furukawa H. et al., 2013; Kitagawa S. et al., 2004). In contrast to most conventional adsorbents, such as carbon-based materials and zeolites, which are rigid and typically yield type I isotherms, the structural flexibility of such MOFs is particularly intriguing because their crystal structures transform in response to external stimuli, leading to peculiar adsorption behaviors (Horike S. et al., 2009). Because the peculiar adsorption behaviors are particle size- and shape-dependent (Ehrling S. et al., 2021), controlling the size and shape of MOF particles is an important technology for the practical use of MOFs, and if the mixing matters in the synthetic processes of MOFs, the microreactor is believed to contribute to the development of the technology.

As a model MOF system, we focused on the zeolitic imidazolate framework-8 (ZIF-8), which comprises zinc ions and 2-methylimidazole (2-MIM) linkers (Park K.S. et al., 2006). Although solvothermal syntheses are popular, we selected an environmentally friendly aqueous synthesis process. In the experiment, we mixed aqueous solutions of $Zn(NO_3)_2$ and 2-MIM in a central-collision-type microreactor (**Fig. 1(A)**) (Watanabe S. et al., 2017b). The mixed solution turned turbid within 1 min after being collected from the outlet in a vial. The mixture was allowed to stand for 1 h. **Fig. 13** shows the SEM image and XRD patterns of the resultant particles synthesized at room temperature.

The average diameter of the resultant particles in **Fig. 13(A)** is 434 ± 94 nm with chamfered cubic (CC) shapes composed of square and hexagonal faces. The measured XRD pattern (denoted as "434 nm, CC") agrees fairly well with the simulated pattern for ZIF-8 (Moggach S.A. et al., 2009), demonstrating the successful formation of ZIF-8 particles. The combinations of the concentration of Zn ions, concentration ratio ([2-MIM]/[$Zn^{2+}$]), and reaction temperature varied the particle size from 51 nm to 1.8 μm and the shape from cubes to CC to rhombic dodecahedron (RD). All of those resultant particles were ZIF-8, as confirmed by the agreement of the XRD patterns with the simulated pattern (**Fig. 13(B)**). The results indicate that the concentration conditions determine the particle size, whereas the reaction temperature defines the particle shape.

The microreactor produced ZIF-8 particles with a sharper size distribution than those synthesized using the batch-type reactor, although the total synthetic period was 1 h, which was much longer than the mixing time. This result is because instantaneous nucleation occurred immediately after quick and homogeneous mixing in the microreactor, which enabled uniform particle growth after collection in a vial. Furthermore, the results also indicate that the reaction conditions in the microreactor govern nucleation, and the temperature in the vial after mixing controls the growth process. Therefore, we developed a concept of setting different temperatures in the microreactor and vial to further control the ZIF-8 particle size and shape. In the experiment, we set the temperature of the microreactor to 5 °C, rapidly increased the temperature of the mixed solution to 80 °C using the central-collision-type microreactor as a microchannel heat exchanger, and collected the heated solution in a vial immersed in a water bath maintained at 80 °C (**Fig. 14(A)**). The size and shape of the resultant particles were 410 ± 86 nm and rhombic dodecahedron, respectively, as shown in **Fig. 14(B)**. The resultant size was almost identical to that synthesized at a temperature of 5 °C throughout the entire synthetic process, but the resultant shape was different (cube at 5 °C). This result demonstrates that the mixing process in the microreactor governs the particle size, whereas the aging process in the vial determines the particle shape. It also exhibits the possibility of separate control of the ZIF-8 particle size and shape by setting different temperatures during nucleation at the microreactor and growth in the

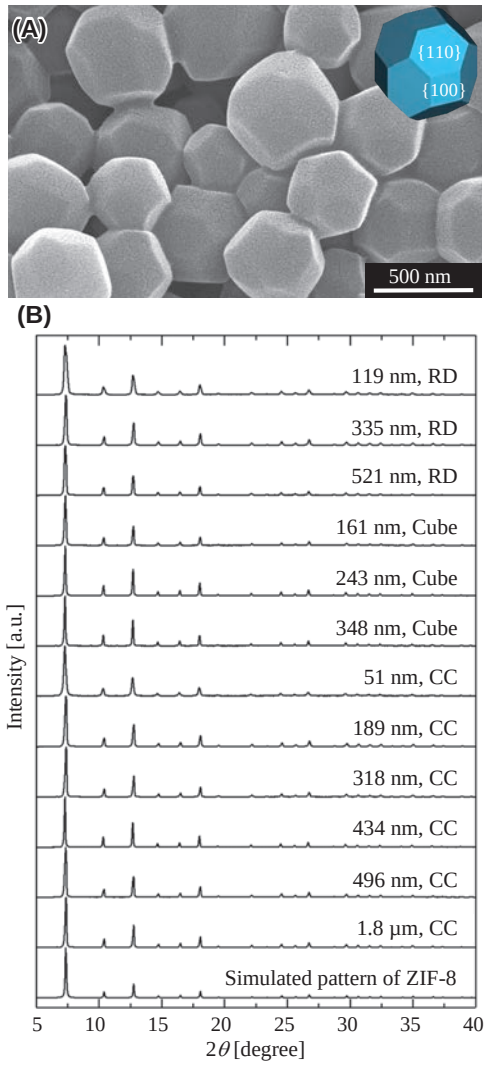


**Fig. 13** Synthesis results for ZIF-8 particles using the microreactor. **(A)** Typical SEM image of the resultant particles and **(B)** measured XRD patterns of ZIF-8 particles of various sizes and shapes. Adapted with permission from Ref. (Watanabe S. et al., 2017b). Copyright: (2017) Elsevier B.V.

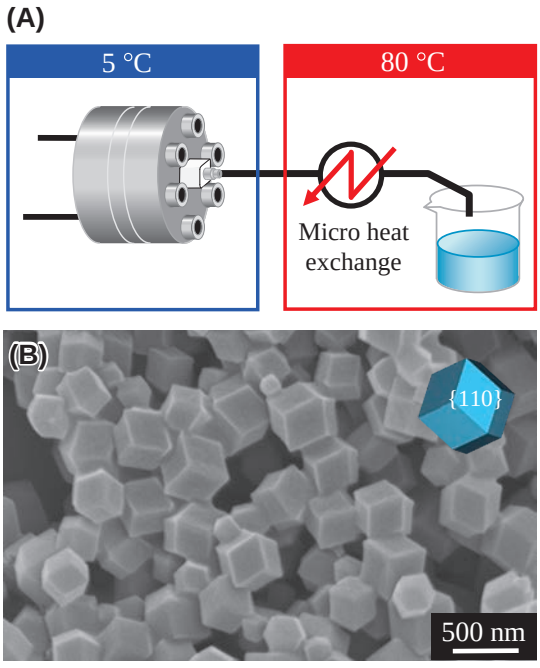


**Fig. 14** **(A)** Schematic illustration of the experimental setup with different temperatures set in the microreactor and vial using a micro-heat exchanger. **(B)** SEM image of the ZIF-8 particles prepared at a temperature of 5 °C in the microreactor, followed by rapid temperature increase up to 80 °C. Reprinted with permission from Ref. (Watanabe S. et al., 2017b). Copyright: (2017) Elsevier B.V.

vial. We emphasize that the rapid temperature change was realized by taking full advantage of the characteristics of the flow microreactor process, which would not be possible with batch reactors.

Further functionalization of ZIF-8 particles is possible by encapsulating them in another nanoporous material to form core–shell structures. As a shell material, we used ZIF-67, which is a structural analog of ZIF-8 with cobalt ions instead of zinc ions (Banerjee R. et al., 2008). Because of the crystal structure similarity, seamless growth of ZIF-67 shells was expected on core ZIF-8 particles. In the experiment, we mixed a methanol solution of $Co(NO_3)_2$ with a premixed methanol suspension of ZIF-8 particles and 2-MIM in the central-collision-type microreactor, collected the reaction suspension in a vial, and allowed it to stand for 1 h (Fujiwara A. et al., 2021). We used methanol as the solvent instead of water because ZIF-8 crystals partly dissolve in water. Typical synthetic results are displayed in **Fig. 15**. Polyhedral particles were obtained (**Fig. 15(A)**), and the STEM-EDX mapping image showed that Zn domains were covered with Co domains in single particles (**Fig. 15(B)**), demonstrating the successful synthesis of ZIF-8@ZIF-67 core–shell particles. The ZIF-67 shell thickness increased from 32 nm to 66 nm with decreasing the core particle concentration (**Figs. 15(C)–(E)**). This was possibly because an increased number of Co ions was used for the formation of shells per core particle. Furthermore, the shell thickness was found to be uniform because the particle size distributions simply shifted to larger sizes with coefficient of variance (CV) values remaining almost unchanged after the shell formation reaction (**Figs. 15(F)–(H)**), whereas the size distribution of the ZIF-8@ZIF-67 particles synthesized using the batch reactor was much wider. In addition, no single-component ZIF-67 particles were observed during microreactor synthesis. These results were attributable to the uniform reaction field provided by the microreactor, which facilitated the uniform distribution of Co ions around the core ZIF-8 particles during the shell formation reaction, thereby demonstrating that rapid and homogeneous mixing was critical to realize uniform shell thickness.

By using ZIF-67 particles as the core material and

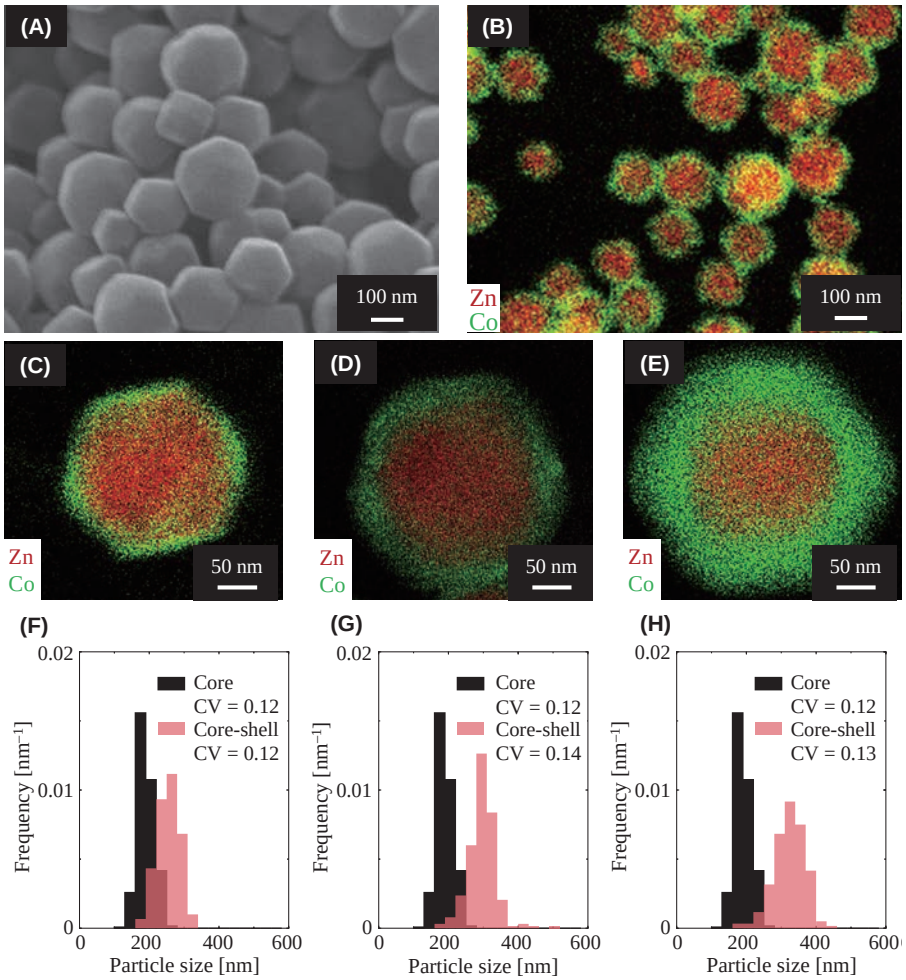


**Fig. 15** **(A)** SEM and **(B)** STEM-EDX mapping images of ZIF-8@ZIF-67 particles. **(C–E)** SETM-EDX mapping images and **(F–H)** corresponding size distributions of the resultant particles synthesized at various concentrations. Adapted with permission from Ref. (Fujiwara A. et al., 2021). Copyright: (2021) American Chemical Society.

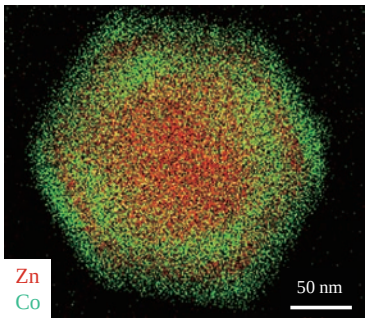


**Fig. 16** STEM-EDX mapping image of a ZIF-8@ZIF-67@ZIF-8@ZIF-67 multilayered particle. Adapted with permission from Ref. (Fujiwara A. et al., 2021). Copyright: (2021) American Chemical Society.

$Zn(NO_3)_2$ as the shell source, a swapped structure of ZIF-67@ZIF-8 core–shell particles can also be synthesized using the same synthetic procedure. Furthermore, by repeating the formation processes of the ZIF-67 and ZIF-8 shells, more complex ZIF-8@ZIF-67@ZIF-8@ZIF-67 multilayered structures can be obtained (**Fig. 16**). Zn and Co domains alternately formed shells of similar thickness in a single particle. Because shell formation is initiated by a universal heterogeneous reaction on the core surface, our technique can be extended to the synthesis of "mixed" MOFs with three or more components, aiming at further functionalization of the resultant composites.

## 6. Conclusions

In this review, we introduced the synthesis of functional NPs, including single-component Ni, Pt–Co alloys, gold and silver nanoshells, patchy particles, CSCs, and nanoporous MOF particles and their core–shell derivatives, using a central-collision-type microreactor. In the case of quick reactions, where the mixing process is often a rate-controlling step, the use of a microreactor with excellent mixing performance is demonstrated to be effective in synthesizing uniform particles in size, shape, and shell thickness. The microreactor is mobile and enables the on-site and on-demand syntheses of functional NPs. Another advantage of the microreactor is its high reproducibility in contrast to conventional batch syntheses, which sometimes suffer from poor reproducibility. A key factor is the relative rate of mixing to the reaction. By adjusting the mixing intensity by the flow rate and reactor geometry according to the reaction rates, synthetic processes can be further optimized in terms of throughput and energy consumption. We hope that this review conveys the advantages of the microreactor and accelerates its industrial use for the precise synthesis of functional NPs.

## Nomenclature

| | |
|---|---|
| CC | Chamfered cube |
| CSC | Core–shell cluster |
| CTAB | Cetyltrimethylammonium bromide |
| CV | Coefficient of variance |
| EDX | Energy-dispersive X-ray |
| fcc | Face-centered cubic |
| MOF | Metal–organic framework |
| NP | Nanoparticles |
| PVP | Polyvinylpyrrolidone |
| RD | Rhombic dodecahedron |
| STEM | Scanning transmission electron microscopy |
| TEM | Transmission electron microscopy |
| VD | Villermaux–Dushman |
| XPS | X-ray photoelectron spectroscopy |
| XRD | Powder X-ray diffraction |
| ZIF | Zeolitic imidazolate framework |
| $t_m$ | Mixing time (s) |

## References

Abhinav K.V., Rao R.V.K., Karthik P.S., Singh S.P., Copper conductive inks: synthesis and utilization in flexible electronics, RSC Advances, 5 (2015) 63985–64030. https://doi.org/10.1039/c5ra08205f

Banerjee R., Phan A., Wang B., Knobler C., Furukawa H., O'Keeffe M., Yaghi O.M., High-throughput synthesis of zeolitic imidazolate frameworks and application to $CO_2$ capture, Science, 319 (2008) 939–943. https://doi.org/10.1126/science.1152516

Chen D.-H., Hsieh C.-H., Synthesis of nickel nanoparticles in aqueous cationic surfactant solutions, Journal of Materials Chemistry, 12 (2002) 2412–2415. https://doi.org/10.1039/b200603k

Chen D.-H., Wu S.-H., Synthesis of nickel nanoparticles in water-in-oil microemulsions, Chemistry of Materials, 12 (2000) 1354–1360. https://doi.org/10.1021/cm991167y

Chen Z., Pei Z., Zhao X., Zhang J., Wei J., Hao N., Acoustic microreactors for chemical engineering, Chemical Engineering Journal, 433 (2022) 133258. https://doi.org/10.1016/j.cej.2021.133258

Commenge J.-M., Falk L., Villermaux–Dushman protocol for experimental characterization of micromixers, Chemical Engineering and Processing: Process Intensification, 50 (2011) 979–990. https://doi.org/10.1016/j.cep.2011.06.006

Couto G.G., Klein J.J., Schreiner W.H., Mosca D.H., de Oliveira A.J., Zarbin A.J., Nickel nanoparticles obtained by a modified polyol process: synthesis, characterization, and magnetic properties, Journal of Colloid and Interface Science, 311 (2007) 461–468. https://doi.org/10.1016/j.jcis.2007.03.045

Domínguez-Crespo M.A., Ramírez-Meneses E., Montiel-Palma V., Torres Huerta A.M., Dorantes Rosales H., Synthesis and electrochemical characterization of stabilized nickel nanoparticles, International Journal of Hydrogen Energy, 34 (2009) 1664–1676. https://doi.org/10.1016/j.ijhydene.2008.12.012

Duraiswamy S., Khan S.A., Plasmonic nanoshell synthesis in microfluidic composite foams, Nano Letters, 10 (2010) 3757–3763. https://doi.org/10.1021/nl102478q

Ehrfeld W., Golbig K., Hessel V., Löwe H., Richter T., Characterization of mixing in micromixers by a test reaction: single mixing units and mixer arrays, Industrial & Engineering Chemistry Research, 38 (1999) 1075–1082. https://doi.org/10.1021/ie980128d

Ehrling S., Miura H., Senkovska I., Kaskel S., From macro- to nanoscale: finite size effects on metal–organic framework switchability, Trends in Chemistry, 3 (2021) 291–304. https://doi.org/10.1016/j.trechm.2020.12.012

Eluri R., Paul B., Synthesis of nickel nanoparticles by hydrazine reduction: mechanistic study and continuous flow synthesis, Journal of Nanoparticle Research, 14 (2012) 800. https://doi.org/10.1007/s11051-012-0800-1

Ely T.O., Amiens C., Chaudret B., Snoeck E., Verelst M., Respaud M., Broto J.-M., Synthesis of nickel nanoparticles. influence of aggregation induced by modification of poly(vinylpyrrolidone) chain length on their magnetic properties, Chemistry of Materials, 11 (1999) 526–529. https://doi.org/10.1021/cm980675p

Fiévet F., Ammar-Merah S., Brayner R., Chau F., Giraud M., Mammeri F.,

Peron J., Piquemal J.Y., Sicard L., Viau G., The polyol process: a unique method for easy access to metal nanoparticles with tailored sizes, shapes and compositions, Chemical Society Reviews, 47 (2018) 5187–5233. https://doi.org/10.1039/c7cs00777a

Fournier M.C., Falk L., Villermaux J., A new parallel competing reaction system for assessing micromixing efficiency—Determination of micromixing time by a simple mixing model, Chemical Engineering Science, 51 (1996) 5187–5192. https://doi.org/10.1016/S0009-2509(96)00340-5

Fujiwara A., Watanabe S., Miyahara M.T., Flow microreactor synthesis of zeolitic imidazolate framework (ZIF)@ZIF core-shell metal-organic framework particles and their adsorption properties, Langmuir, 37 (2021) 3858–3867. https://doi.org/10.1021/acs.langmuir.0c03378

Furukawa H., Cordova K.E., O'Keeffe M., Yaghi O.M., The chemistry and applications of metal-organic frameworks, Science, 341 (2013) 1230444. https://doi.org/10.1126/science.1230444

Gilbert E.C., Evans W.H., Complex formation between nickel ion and hydrazine in solution, Journal of the American Ceramic Society, 73 (1951) 3516–3518. https://doi.org/10.1021/ja01151a518

Gioria E., Wisniewski F., Gutierrez L., Microreactors for the continuous and green synthesis of palladium nanoparticles: enhancement of the catalytic properties, Journal of Environmental Chemical Engineering, 7 (2019) 103136. https://doi.org/10.1016/j.jece.2019.103136

Gutierrez L., Gomez L., Irusta S., Arruebo M., Santamaria J., Comparative study of the synthesis of silica nanoparticles in micromixer–microreactor and batch reactor systems, Chemical Engineering Journal, 171 (2011) 674–683. https://doi.org/10.1016/j.cej.2011.05.019

Han J.H., Kim D., Kim J., Kim G., Fischer P., Jeong H.H., Plasmonic nanostructure engineering with shadow growth, Advanced Materials, (2022) e2107917. https://doi.org/10.1002/adma.202107917

Hashiguchi Y., Watanabe F., Honma T., Nakamura I., Poly S.S., Kawaguchi T., Tsuji T., Murayama H., Tokunaga M., Fujitani T., Continuous-flow synthesis of Pd@Pt core-shell nanoparticles, Colloids and Surfaces A: Physicochemical and Engineering Aspects, 620 (2021) 126607. https://doi.org/10.1016/j.colsurfa.2021.126607

Horike S., Shimomura S., Kitagawa S., Soft porous crystals, Nature Chemistry, 1 (2009) 695–704. https://doi.org/10.1038/nchem.444

Hou J., Yang M., Ke C., Wei G., Priest C., Qiao Z., Wu G., Zhang J., Platinum-group-metal catalysts for proton exchange membrane fuel cells: from catalyst design to electrode structure optimization, EnergyChem, 2 (2020) 100023. https://doi.org/10.1016/j.enchem.2019.100023

Jiang B., Li C., Imura M., Tang J., Yamauchi Y., Multimetallic mesoporous spheres through surfactant-directed synthesis, Advanced Science, 2 (2015) 1500112. https://doi.org/10.1002/advs.201500112

Jiang Z., Xie J., Jiang D., Wei X., Chen M., Modifiers-assisted formation of nickel nanoparticles and their catalytic application to *p*-nitrophenol reduction, CrystEngComm, 15 (2013) 560–569. https://doi.org/10.1039/c2ce26398j

Kitagawa S., Kitaura R., Noro S., Functional porous coordination polymers, Angewandte Chemie International Edition, 43 (2004) 2334–2375. https://doi.org/10.1002/anie.200300610

Li Y.D., Li L.Q., Liao H.W., Wang H.R., Preparation of pure nickel, cobalt, Nickel-cobalt and nickel-copper alloys by hydrothermal reduction, Journal of Materials Chemistry, 9 (1999) 2675–2677. https://doi.org/10.1039/A904686K

Lin X.Z., Terepka A.D., Yang H., Synthesis of silver nanoparticles in a continuous flow tubular microreactor, Nano Letters, 4 (2004) 2227–2232. https://doi.org/10.1021/nl0485859

Luty-Błocho M., Wojnicki M., Pacławski K., Fitzner K., The synthesis of platinum nanoparticles and their deposition on the active carbon fibers in one microreactor cycle, Chemical Engineering Journal, 226 (2013) 46–51. https://doi.org/10.1016/j.cej.2013.04.008

Mae K., Advanced chemical processing using microspace, Chemical Engineering Science, 62 (2007) 4842–4851. https://doi.org/10.1016/j.ces.2007.01.012

Maw S.S., Watanabe S., Miyahara M.T., Flow synthesis of silver nanoshells using a microreactor, Chemical Engineering Journal, 374 (2019) 674–683. https://doi.org/10.1016/j.cej.2019.05.210

Meincke T., Bao H., Pflug L., Stingl M., Klupp Taylor R.N., Heterogeneous nucleation and surface conformal growth of silver nanocoatings on colloidal silica in a continuous flow static T-mixer, Chemical Engineering Journal, 308 (2017) 89–100. https://doi.org/10.1016/j.cej.2016.09.048

Moggach S.A., Bennett T.D., Cheetham A.K., The effect of pressure on ZIF-8: increasing pore size with pressure and the formation of a high-pressure phase at 1.47 GPa, Angewandte Chemie International Edition, 48 (2009) 7087–7089. https://doi.org/10.1002/anie.200902643

Mühlig S., Cunningham A., Scheeler S., Pacholski C., Bürgi T., Rockstuhl C., Lederer F., Self-assembled plasmonic core-shell clusters with an isotropic magnetic dipole response in the visible range, ACS Nano, 5 (2011) 6586–6592. https://doi.org/10.1021/nn201969h

Nagasawa H., Aoki N., Mae K., Design of a new micromixer for instant mixing based on the collision of micro segments, Chemical Engineering and Technology, 28 (2005) 324–330. https://doi.org/10.1002/ceat.200407118

Oldenburg S.J., Averitt R.D., Westcott S.L., Halas N.J., Nanoengineering of optical resonances, Chemical Physics Letters, 288 (1998) 243–247. https://doi.org/10.1016/S0009-2614(98)00277-2

Park J.W., Chae E.H., Kim S.H., Lee J.H., Kim J.W., Yoon S.M., Choi J.-Y., Preparation of fine Ni powders from nickel hydrazine complex, Materials Chemistry and Physics, 97 (2006) 371–378. https://doi.org/10.1016/j.matchemphys.2005.08.028

Park K.S., Ni Z., Cote A.P., Choi J.Y., Huang R., Uribe-Romo F.J., Chae H.K., O'Keeffe M., Yaghi O.M., Exceptional chemical and thermal stability of zeolitic imidazolate frameworks, Proceedings of the National Academy of Sciences, 103 (2006) 10186–10191. https://doi.org/10.1073/pnas.0602439103

Rasch M.R., Sokolov K.V., Korgel B.A., Limitations on the optical tunability of small diameter gold nanoshells, Langmuir, 25 (2009) 11777–11785. https://doi.org/10.1021/la901249j

Saha K., Agasti S.S., Kim C., Li X., Rotello V.M., Gold nanoparticles in chemical and biological sensing, Chemical Reviews, 112 (2012) 2739–2779. https://doi.org/10.1021/cr2001178

Sharada S., Suryawanshi P.L., Kumar P R., Gumfekar S.P., Narsaiah T.B., Sonawane S.H., Synthesis of palladium nanoparticles using continuous flow microreactor, Colloids and Surfaces A: Physicochemical and Engineering Aspects, 498 (2016) 297–304. https://doi.org/10.1016/j.colsurfa.2016.03.068

Suryawanshi P.L., Gumfekar S.P., Kumar P.R., Kale B.B., Sonawane S.H., Synthesis of ultra-small platinum nanoparticles in a continuous flow microreactor, Colloid and Interface Science Communications, 13 (2016) 6–9. https://doi.org/10.1016/j.colcom.2016.05.001

Völkl A., Klupp Taylor R.N., Investigation and mitigation of reagent ageing during the continuous flow synthesis of patchy particles, Chemical Engineering Research and Design, 181 (2022) 133–143. https://doi.org/10.1016/j.cherd.2022.03.016

Wagner J., Kirner T., Mayer G., Albert J., Köhler J.M., Generation of metal nanoparticles in a microchannel reactor, Chemical Engineering Journal, 101 (2004) 251–260. https://doi.org/10.1016/j.cej.2003.11.021

Wagner J., Köhler J.M., Continuous synthesis of gold nanoparticles in a microreactor, Nano Letters, 5 (2005) 685–691. https://doi.org/10.1021/nl050097t

Wang D., Li Y., Bimetallic nanocrystals: liquid-phase synthesis and catalytic applications, Advanced Materials, 23 (2011) 1044–1060. https://doi.org/10.1002/adma.201003695

Watanabe S., Asahi Y., Omura H., Mae K., Miyahara M.T., Flow microreactor synthesis of gold nanoshells and patchy particles, Advanced Powder Technology, 27 (2016) 2335–2341. https://doi.org/10.1016/j.apt.2016.08.013

Watanabe S., Hiratsuka T., Asahi Y., Tanaka A., Mae K., Miyahara M.T., Flow synthetic process of $SiO_2$@Au core-shell nanoparticles by using microreactor, Journal of the Society of Powder Technology, Japan, 50 (2013) 478–484. https://doi.org/10.4164/sptj.50.478

Watanabe S., Hiratsuka T., Asahi Y., Tanaka A., Mae K., Miyahara M.T., Flow synthesis of plasmonic gold nanoshells via a microreactor, Particle & Particle Systems Characterization, 32 (2015) 234–242.

https://doi.org/10.1002/ppsc.201400126
Watanabe S., Koshiyama T., Watanabe T., Miyahara M.T., Room-temperature synthesis of Ni and Pt-Co alloy nanoparticles using a microreactor, Frontiers in Chemical Engineering, 3 (2021) 780384. https://doi.org/10.3389/fceng.2021.780384
Watanabe S., Ohsaki S., Fukuta A., Hanafusa T., Takada K., Tanaka H., Maki T., Mae K., Miyahara M.T., Characterization of mixing performance in a microreactor and its application to the synthesis of porous coordination polymer particles, Advanced Powder Technology, 28 (2017a) 3104–3110. https://doi.org/10.1016/j.apt.2017.09.005
Watanabe S., Ohsaki S., Hanafusa T., Takada K., Tanaka H., Mae K., Miyahara M.T., Synthesis of zeolitic imidazolate framework-8 particles of controlled sizes, shapes, and gate adsorption characteristics using a central collision-type microreactor, Chemical Engineering Journal, 313 (2017b) 724–733. https://doi.org/10.1016/j.cej.2016.12.118
Wolfbeis O.S., An overview of nanoparticles commonly used in fluorescent bioimaging, Chemical Society Reviews, 44 (2015) 4743–4768. https://doi.org/10.1039/c4cs00392f
Wu K.-J., De Varine Bohan G.M., Torrente-Murciano L., Synthesis of narrow sized silver nanoparticles in the absence of capping ligands in helical microreactors, Reaction Chemistry & Engineering, 2 (2017) 116–128. https://doi.org/10.1039/c6re00202a
Wu S.-H., Chen D.-H., Synthesis and characterization of nickel nanoparticles by hydrazine reduction in ethylene glycol, Journal of Colloid and Interface Science, 259 (2003) 282–286. https://doi.org/10.1016/s0021-9797(02)00135-2
Wu S.-H., Chen D.-H., Synthesis and stabilization of Ni nanoparticles in a pure aqueous CTAB solution, Chemistry Letters, 33 (2004) 406–407. https://doi.org/10.1246/cl.2004.406
Wu X., Xing W., Zhang L., Zhuo S., Zhou J., Wang G., Qiao S., Nickel nanoparticles prepared by hydrazine hydrate reduction and their application in supercapacitor, Powder Technology, 224 (2012) 162–167. https://doi.org/10.1016/j.powtec.2012.02.048
Xia Y., Xiong Y., Lim B., Skrabalak S.E., Shape-controlled synthesis of metal nanocrystals: simple chemistry meets complex physics?, Angewandte Chemie International Edition, 48 (2009) 60–103. https://doi.org/10.1002/anie.200802248
Xu L., Srinivasakannan C., Peng J., Zhang D., Chen G., Synthesis of nickel nanoparticles by aqueous reduction in continuous flow microreactor, Chemical Engineering and Processing: Process Intensification, 93 (2015) 44–49. https://doi.org/10.1016/j.cep.2015.04.010
Yang W., Liang H., Ma S., Wang D., Huang J., Gold nanoparticle based photothermal therapy: development and application for effective cancer treatment, Sustainable Materials and Technologies, 22 (2019) e00109. https://doi.org/10.1016/j.susmat.2019.e00109
Yoshida J., Takahashi Y., Nagaki A., Flash chemistry: flow chemistry that cannot be done in batch, Chemical Communications, 49 (2013) 9896–9904. https://doi.org/10.1039/c3cc44709j

## Authors' Short Biographies

**Dr. Satoshi Watanabe** is an Associate Professor of Department of Chemical Engineering at Kyoto University. He earned his B.S., M.S., and Ph.D. (Chemical Engineering) from Kyoto University. He has worked for Kyoto University as an Assistant Professor, Junior Associate Professor, and Associate Professor. His research is in the field of colloid science and engineering, especially focusing on material design and technologies to bridge functions and structures from micro- to macroscale.

**Prof. Minoru T. Miyahara** was a Professor of Department of Chemical Engineering at Kyoto University. He earned his Ph.D. from Kyoto University. He had held key senior positions in academic societies in areas of powder technology, adsorption science and technology, and chemical engineering. He had devoted all his efforts to research and education. He unfortunately passed away in August 2022.

KONA Powder and Particle Journal

KONA Powder and Particle Journal No. 42 (2025) 170–187/https://doi.org/10.14356/kona.2025004 Review Paper

# Review of the Gas-Phase Synthesis of Particle Heteroaggregates and Their Applications†

**Suman Pokhrel[1,2,3], Udo Fritsching[1,2,3] and Lutz Mädler[1,2,3]***

[1] *Particles and Process Engineering, Faculty of Production Engineering, University of Bremen, Germany*
[2] *Leibniz Institute for Materials Engineering, Germany*
[3] *MAPEX Center for Materials and Processes, University of Bremen, Germany*

Custom-made nanomaterials are indispensable in the production of high-value goods in almost any industry. For many applications, materials with defined functional contacts on the nanoscale between different components are crucial. In heterogeneous catalysis, active nanoparticles are often dispersed on a support, and defined interfaces facilitate the stabilization of the active materials. This leads to strong metal-support interactions (SMSI), which determine the activity and selectivity of the catalytic reactions. In photocatalysts, hetero-contacts can significantly reduce electron–hole recombination after light excitation, leading to improved photoefficiency. By choosing materials with appropriate band levels, the redox window can be tuned for a specific reaction. In batteries, mixing the active material and carbon leads to improved electrochemical characteristics. All these applications have in common that different nanomaterials need to be mixed at the nano-level with defined interfaces. This review highlights the most suitable routes for gas-phase synthesis of particle heteroaggregates, their modeling, and their applications.

**Keywords:** double flame spray pyrolysis, aerosol mixing, heteroaggregates, heterojunctions, charge transfer

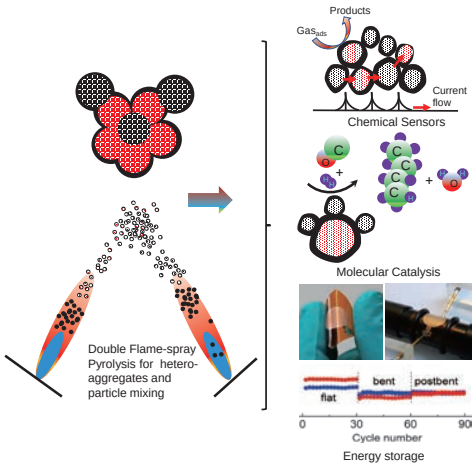


## 1. Introduction

Various synthesis techniques are possible to produce highly defined particle mixtures at the nanoscale (Minnermann et al., 2011; 2013). These can be broadly distinguished in processes where readily produced nanoparticles are mixed in the liquid phase (Grossmann, 2017; Grossmann et al., 2015; Shi and Russell, 2018). To mix these two dissimilar nanoparticles in the liquid, the break-up of agglomerated and even aggregated nanoparticles needs to be achieved, e.g., by milling, dispersion in a sonic nozzle, or ultrasonification of nanoparticles in liquid (Wang et al., 2015). In the second step, a heat treatment process leads to the formation of interfaces in a single step during solid-state particle synthesis (Yu et al., 2021). In well-known wet-chemical approaches, such as sol–gel, precipitation, or incipient wetness techniques, the formation of an interface is achieved by modifying the temperature, pressure, solvent composition (Munnik et al., 2015). A major drawback of wet-chemical approaches is achieving good crystallinity and the requirement of additional calcination/heat treatment steps for the modification of the material interface (Sun et al., 2015; 2016). Gas-phase preparation, especially coupled with high-temperature synthesis of nanoparticles, offers a scalable, single-step alternative to established wet-chemical synthesis routes (Lovell et al., 2019; Pokhrel et al., 2013). A promising technique for designing such heterointerfaces is the double flame spray pyrolysis (DFSP) approach (Gäßler et al., 2022; Stahl et al., 2021). Here, nanoparticle components are synthesized in two individual flame sprays that are mixed at a certain distance above the burners (Kim et al., 2016; Wang et al., 2013). Parameters such as nozzle distances, air entrainment rate, turbulence of the mixing jets, and temperature distribution are important for controlling the mixing process (Minnermann et al., 2011; 2013). High-temperature gradients in the process from ~2800 °C in the flames to almost room temperature in just a few milliseconds and lateral scales of millimeter lead to highly crystalline primary particles (Balakrishnan et al., 2021; Li et al., 2020; Pokhrel et al., 2023). Gas-phase synthesis of multicomponent nanomaterials has huge potential, but a review of different gas-phase mixing approaches is still lacking.

In this contribution, we discuss the routes and process parameters for determining aggregation in gas-phase

† Received 4 July 2023; Accepted 5 September 2023
J-STAGE Advance published online 24 February 2024
* Corresponding author: Lutz Mädler;
[1,3] Add: Badgasteiner Straße 1, 28359 Bremen, Germany
[2] Add: Badgasteiner Straße 3, 28359 Bremen, Germany
E-mail: lmaedler@iwt.uni-bremen.de
TEL: +49-421-21851200

mixing processes. Here, computational fluid dynamics (CFD) simulations coupled with discrete element methods (DEM) or population balance methods (PBM) that can simulate interface formation between nanoparticles in the gas phase are discussed. Techniques for experimentally determining the mixing state of multiple particles are introduced. Currently, different communities studying gas-phase mixing of nanomaterials often use different definitions, leading to possible misunderstandings. Thus, the review will recommend some unification and common definitions for core concepts such as interfaces, heteroaggregates, (functional) hetero-contacts/junctions, and even aggregation. Applications of heteroaggregates designed using double flame spray pyrolysis are discussed, validating that gas-phase mixing research serves as a common reference point for the future. Heterojunctions in aggregates are created by physically mixing dissimilar particles such as A and B or directly nucleating one dissimilar particle on the other during the synthesis process. The number density of the hetero-contacts and their distribution determine the reaction kinetics, adsorption sites, and reaction centers (Lovell et al., 2019). In addition to the chemical composition of the particles, the shape and surface morphology of the heteroaggregates are key to the overall material performance.

## 2. Gas-phase in situ mixing to design heteroaggregates

An aggregate confines multiple, and chemically tight, sintered primary particle—a characteristic property of gas-phase synthesized materials (Eggersdorfer et al., 2012). The degree of mixing indicates the number density of hetero-contacts between different dissimilar particles and is abundant when all particles are bonded via hetero-contacts. The high thermal gradient due to radiation, evaporation, and collision of the saturated aerosol stream (particle clusters/nuclei) allows efficient particle mixing. Feng et al. (2015; 2016) described continuous gas-phase synthesis using lasers or electric discharge to produce vapor through material ablation. The vapor was quenched using an inert gas co-flow. While supersaturation is realized in such quenched vapor, the critical nucleus size is reduced to the atomic scale, causing strong coagulation and particle growth. A key paradigm is singlets, i.e., single particles grow from clusters to sizes up to a few nanometers, forming primary particles in aggregates. In another report, Voloshko et al. (2015) studied the particle formation process in spark discharge and nanosecond- (ns-)laser ablation, focusing on the plasma influence on particle formation. In both techniques, Cu was used as the target material. Although the plasma density and time evolution were different, the particles were similar because of the larger evaporation rate in ns-laser ablation and supersaturated vapor formation in the spark. In the spark discharge process, nanoparticles are generated by evaporation followed by condensation. First, the spark enables the evaporation of the target material, followed by subsequent rapid quenching via adiabatic expansion of the plasma radiation, and mixes with the carrier gas to result in supersaturation of the vapor. As stated earlier, higher saturation triggers nucleus formation, coagulation, and particle growth. Tabrizi et al. (2009) postulated that the co-evaporation of different materials from the target electrodes leads to the formation of mixed particles. Based on this hypothesis, Pfeiffer et al. (2014) investigated the formation of Pd-doped Mg heteroaggregates using a double spark mixing process. The vapor generated from each individual spark was rapidly cooled via adiabatic expansion and instantly mixed with one another using co-flow gas. While a very high-temperature gradient and vapor supersaturation are achieved in the spark-generated vapor, the Smoluchowski-type coagulation process dominates. This process allows simultaneous evaporation of different materials, which combine to form new heteroaggregates. Hence, gas-phase aerosol mixing is very attractive for heteroaggregate systems where a wide range of precursors with low volatility and high energy combustion density are available (Marine et al., 2000). In addition, homogeneity of the particle–particle mixture is realized when the hetero-contacts are uniformly distributed from the surface to the bulk of the particle ensemble. Note that two or more multicomponent mixtures at the atomic scale lead either to the formation of a mixed metal oxide or to a doped system (Adeleye et al., 2018; Naatz et al., 2017). Such a system represents an individual particle (classified as binary, ternary and quaternary) with a crystal structure of at least two different elements having a covalent bond with the ligand. The ternary forms include perovskites ($ABO_3$), scheelites ($ABO_4$), spinels ($AB_2O_4$), and even ternary metastable phases that are used in a variety of catalytic systems (Dreyer et al., 2016; Grossmann, 2017; Kemmler et al., 2012). As an example, these heteroaggregates are obtained in the gas phase by double flame spray pyrolysis (DFSP), which can synthesize a variety of heteroaggregates.

Two aerosol streams (containing independent components) from two separate spray flames at different temperatures and at different stages of particle formation within the individual aerosol stream can be mixed (**Fig. 1**). The materials nucleate in different flames, and the intersection of the two flames at a defined distance and angle results in a certain mixing state. The geometric configuration and the corresponding process conditions (e.g. temperature) in the mixing zone significantly influence the material properties. The concentration ratio of the sprayed components and the adjustment of the flame geometry allow tailored synthesis of mixing states within a single and/or agglomerated particle. A single-step synthesis of these different mixing stages is achieved when DFSP is applied. The particle residence

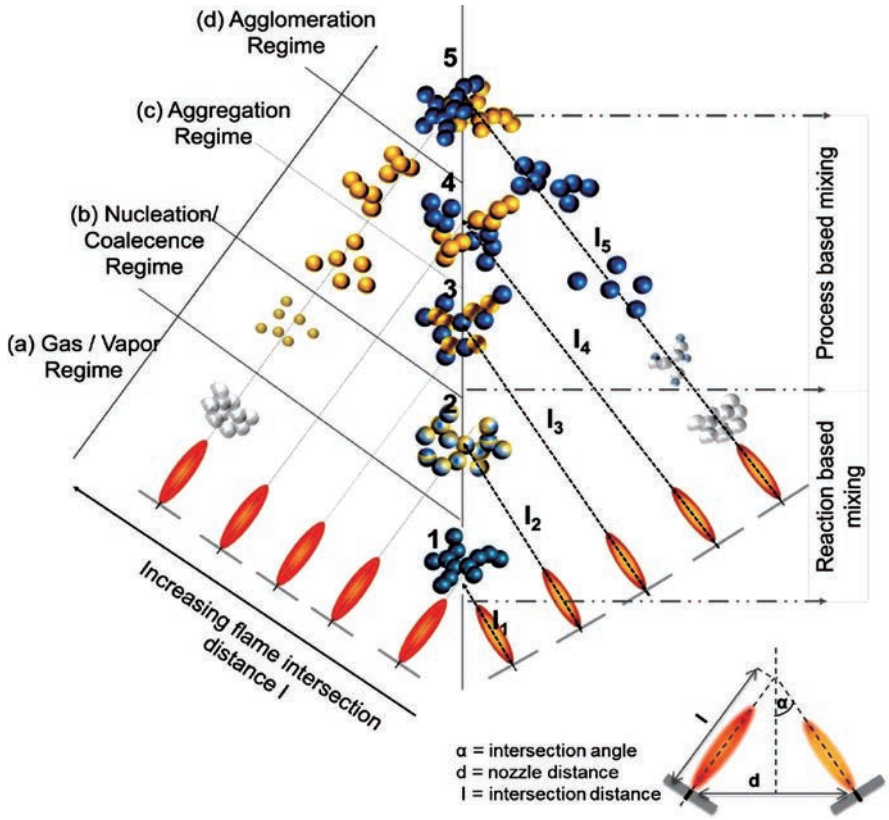


**Fig. 1** Illustration of the influence of the intersection distance and mixing within the aggregated systems. **(a)** The intersection distance of the flames when both precursors are in the gas/vapor phase results in atomic mixing to form heteroaggregates. **(b)** Mixing in a zone, where nucleation and primary particle formation start, can result in the formation of polycrystalline particles. The characteristics of the synthesized particles highly depend on the miscibility of the material. High miscibility favors polycrystalline particle formation due to diffusion processes. **(c)** An increase in the flame intersection distance up to the aggregation regime favors the formation of individual oxide particles, which form a mixture on the particle scale. **(d)** A further increase in the intersection distance, associated with a decrease in the temperature in the mixing zone, leads to a mixture on the agglomerate scale. The aggregates physically bond to one another. Adapted from Grossmann (2017). Copyright Universität Bremen Library, open access (URN: urn:nbn:de:gbv:46-00106641-10).

times of the two streams through symmetrical and/or non-symmetrical mixing can be exploited to vary the particle properties. External temperature control at the mixing point is possible by installing a quenching ring at the point of aerosol mixing. The high thermal gradient of individual aerosol streams enables independent control of the specific surface area of the particles and their crystallinity (Kemmler et al., 2012). The hetero-contact of different binary, ternary, mixed binary, and mixed ternary materials obtained in the gas phase is crucial for particle performance. The in situ synthesis of the materials using different flame symmetries and nozzle placements enabled the formation of such heteroaggregates. Integrated high-temperature aerosol synthesis with multiple flames is a promising route for complex and heteroaggregated materials via various precursor/solvent combinations, concentrations, temperature profiles, and residence times in the flame (Buss et al., 2019; Meierhofer and Fritsching, 2021; Meierhofer et al., 2017; Pokhrel et al., 2010; Pokhrel and Mädler, 2020). Each flame producing the desired oxide mixtures and/or single metastable phases is characterized by its own temperature profile along the axis of the gas flow. This results in a specific temperature–time history during nanoparticle formation. It is known that increasing the precursor flow rate and decreasing the dispersion gas lead to a longer flame and residence time, resulting in the production of larger particles. The gas composition (air or oxygen) and the energy provided by the supporting flame are further measures to tune the temperature–time history. In the direct mixing of existing particle systems, particle concentration plays a key role. The particle formation process using large nozzle distances allows the physical mixing of the two heteroaggregates at the mixing zone. Aerosol mixing within the nucleation phase leads to atomic mixing producing ternary and/or metastable phases. However, when the mixing process occurs later, i.e., when the two aerosol streams mix at a higher distance above the nozzle, heteroaggregates are obtained. If the respective aerosol streams are mixed even later, the particles and agglomerates produce fewer hetero-contacts. Based on this strategy, $Co/Al_2O_3$ Fischer–Tropsch catalysts were synthesized using Co and Al aerosol streams (Schubert et al., 2016). When these two streams

were mixed before the nucleation phase, a very stable but catalytically inactive mixed phase ($Co_{3-x}Al_xO_4$, $0 < x \leq 2$) was formed. However, mixing the two aerosol streams after the nucleation phase gives rise to homogeneously mixed heteroaggregates, allowing a very active Co catalyst in stable $Al_2O_3$ support. Hetero-contact plays an essential role, especially in the dry reforming of $CH_4$, which was demonstrated by the selective mixing of even three-component systems (Horlyck et al., 2019). Note that the mismatch of the primary particle size induces random collisions during aerosol mixing between two dissimilar particles, resulting in heteroaggregates. The formation of larger particles could be counteracted by reducing the precursor concentration and increasing the oxidant flow. Recently, the degree of mixing as a function of time was acquired via DEM simulation in a rotary drum. This new strategy is based on cross-correlation development from a learning set consisting of 17 sets of simulation data representing a variation in the revolution frequency. The results showed good predictions for binary mixtures of particles with different densities rather than sizes within the parametric conditions (Wu et al., 2022). Therefore, double flame FSP is a versatile technique in which each precursor component is subjected to the same temperature–time history, leading to atomically mixed metal oxide NPs. However, the quantification of hetero-contacts generated from such gas-phase synthesis is challenging and requires extensive theoretical and mathematical models to clarify. In addition, the type of hetero-contact (physical and/or chemical with respect to a contact energy) and the possibilities for flexible adjustment allow the extraction of material properties.

## 3. Modeling and theoretical characterization of heteroaggregation

The modeling approaches of aerosol particle formation are based on gas-to-particle growth mechanisms depicted in **Figs. 2(a) and (b)**, where the time scales of chemical reactions are much shorter than the particle residence time in the reactor (Pratsinis, 1998). Although DEM for the analysis of particle processes is already developed (Pöschel and Schwager, 2005) and used for the description of large particle systems (Fischer et al., 2016; Parteli and Pöschel, 2016), the modeling of aerosol reactors for the description of homogenization and aggregation processes on the sub-micron scale appears to be a challenge. This concerns the inclusion of short-range surfaces (e.g., van der Waals) and electrostatic forces, which are dominant for these particle sizes and heteroaggregates (Endres et al., 2021; Parteli et al., 2014). Very recently, Endres et al. (2021) reported particle–particle interactions in flame-made agglomerates. Such interactions were described using a particle–particle contact model assuming inherent material properties such as but not limited to mechanical stiffness, plasticity, polarizability, surface charge, and chemistry (Endres et al., 2021; Parteli et al., 2014). Numerical modeling of such particles and aggregates of very different sizes and complex geometric shapes requires the development of new approaches in DEM and much more elaborate algorithmic description for high-performance computing (HPC) (Endres et al., 2022; Gunkelmann et al., 2014; Topic and Pöschel, 2016).

In a very early work on combustion, Ulrich and Subramanian (1977) reported a model for coagulation and sintering mechanisms as growth-limiting and process-controlling mechanisms. Later, Kruis et al. (1993) modified the model by considering a characteristic sintering time and introducing a fractal dimensional parameter to describe the particle aggregates. Johannessen et al. (2000) reported a mathematical model for the dynamics of particle growth during the synthesis of ultrafine particles in diffusion flames. The velocity, temperature, and gas composition in a diffusion flame for $Al_2O_3$ synthesis were calculated by

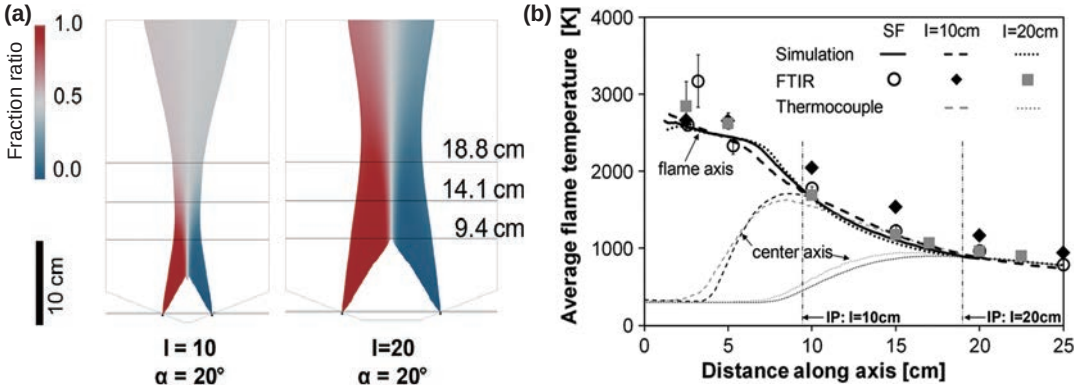


**Fig. 2** Numerical simulations of two-particle aerosol mixing (from double flame spray pyrolysis) reported by Grossmann et al. **(a)** Central plane contour plots of the fraction ratio released from nozzles 1 (red) and 2 (blue) for the $l = 10$ cm and $l = 20$ cm settings are inclined at 20°. **(b)** FTIR-measured line-of-sight (symbols) and CFD-predicted centerline flame temperatures (thick black lines) along the flame axis for the single flame (circles, solid line) as well as the DF with $l = 10$ cm (diamonds, dashed line) and $l = 20$ cm (squares, dotted line) inclined at 20°. The specific influence of the process flow and the process conditions are decisive for the resulting heteroaggregates and their properties. Adapted from Grossmann et al. (2015). Copyright 2015, Springer.

simplification of 2D simulations of the aerosol model. The model was a key to developing an aerosol solver that allows detailed representation of particle evolution within the calculated process domain (Gröhn et al., 2011). To control the particle growth and mixing processes of heteroaggregation, complex simulation models for different aerosol flame reactor configurations have been analyzed (Meierhofer et al., 2014; Noriler et al., 2014). Meierhofer et al. (2014) reported numerical simulations of the air entrainment and droplet trajectory of the flame spray. At very low swirl angles (0°), droplets explicitly splashed on the nozzle plate. A similar calculation at 5° showed that the recirculation of the particles forced the small droplets toward the flame. The increase in the swirl angle to 15° directed all the droplets toward the flame with completely reduced recirculation. The simulation data showed that the stronger swirling flow prolonged the mean residence time of the droplets in the combustion domain for aggregate formation (Mädler et al., 2002; Meierhofer et al., 2014). Grossmann et al. (2015) reported a mathematical model describing the reactive spray dynamics of xylene using a two-phase Euler–Lagrange approach describing the continuous gas phase and discrete liquid droplets. The simulation for the temperature is underestimated, whereas the FTIR data shows the average temperature in regions with steep radial gradients. Lowering the intersection distances of the two aerosol streams increases the temperature up to 300 K along the flame axis between 10 and 20 cm [**Figs. 2(a) and (b)**]. Hence, the fundamental understanding of gas-phase particle production is through simulation and modeling of the process, enabling tailor-made functional particles with an enhanced number of hetero-contacts.

While reactor geometry and process parameter models are important for understanding particle production, theoretical characterization of nanosized heteroaggregates requires mixing characteristics during such processes. Baric et al. (2018) studied the mixing properties of flame-made particles using a combination of particle simulations and image analysis to derive correlations for the quantification of particle mixing. The acquired simulation method predicted the 3D coordination number from 2D images of binary and/or ternary mixtures of aggregated particles. This method is valid for cluster aggregation with primary particles >4. The results of binary particle mixing (between the simulations and experimental imaging) showed that the coordination numbers and cluster sizes deviate from the simulated values by ~10 % (mixing ratio 0.6 and 0.7) and below 30 % (mixing ratio 0.8), respectively.

Very recently, Gerken et al. (2023) validated the work reported by Baric et al. They used double flame-sprayed $TiO_2$ and $WO_3$ heteroaggregates to quantify hetero-contacts using high-angle annular dark-field scanning transmission electron microscopy (HAADF-STEM) images. The heteroaggregates shown in **Fig. 3** were generated as 3D objects in the computer. The figure is a corresponding 2D projection of the 3D aggregates from the simulation. In contrast to the 2D image analysis in the experiment, it is possible to simulate 3D particle systems and subsequently convert them into a 2D projection to mimic the image analysis by TEM. This allows a direct correlation between 2D and 3D cluster sizes and coordination numbers (Baric et al., 2018). The approach based on a geometric model considered the ratio of sample thickness and logarithmically scaled colored intensity. The data showed that in all the cases, each primary nanoparticle had ~10 % of another particles (either $WO_3$ during $TiO_2$ quantification or vice versa) during EDX measurements. The tool developed was reported as generic, which could be used for any such

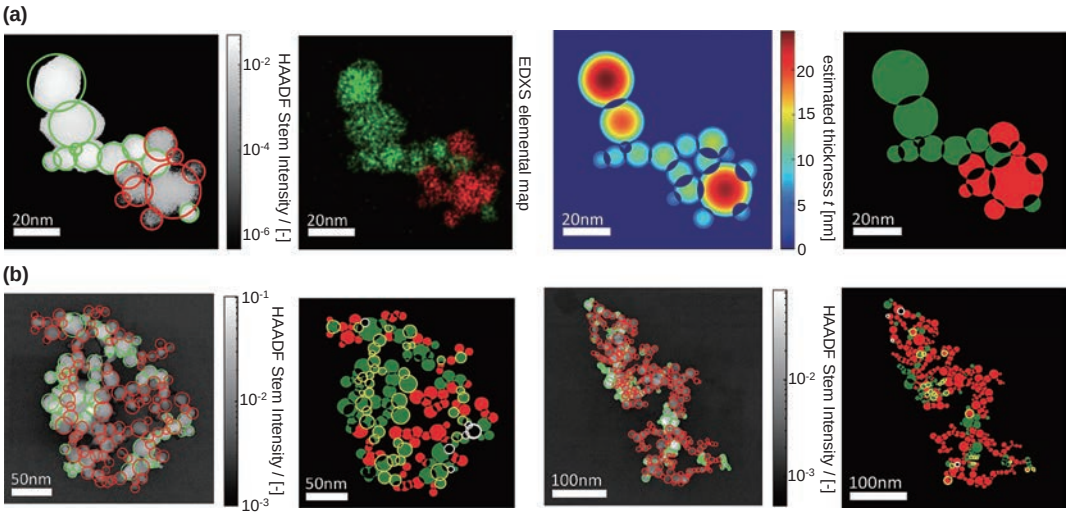


**Fig. 3** HAADF STEM image of an exemplary $TiO_2$–$WO_3$ heteroaggregate. From left to right, the particle ($TiO_2$/$WO_3$) positions are marked manually; the red circle represents $TiO_2$ while the green circle represents $WO_3$. The elemental map was scanned using EDXS and the particle thickness was estimated by a geometric model assuming spherical particles **(a)** for small heteroaggregates and **(b)** large heteroaggregates. Adapted from Gerken et al. (2023). Copyright 2023 Wiley.

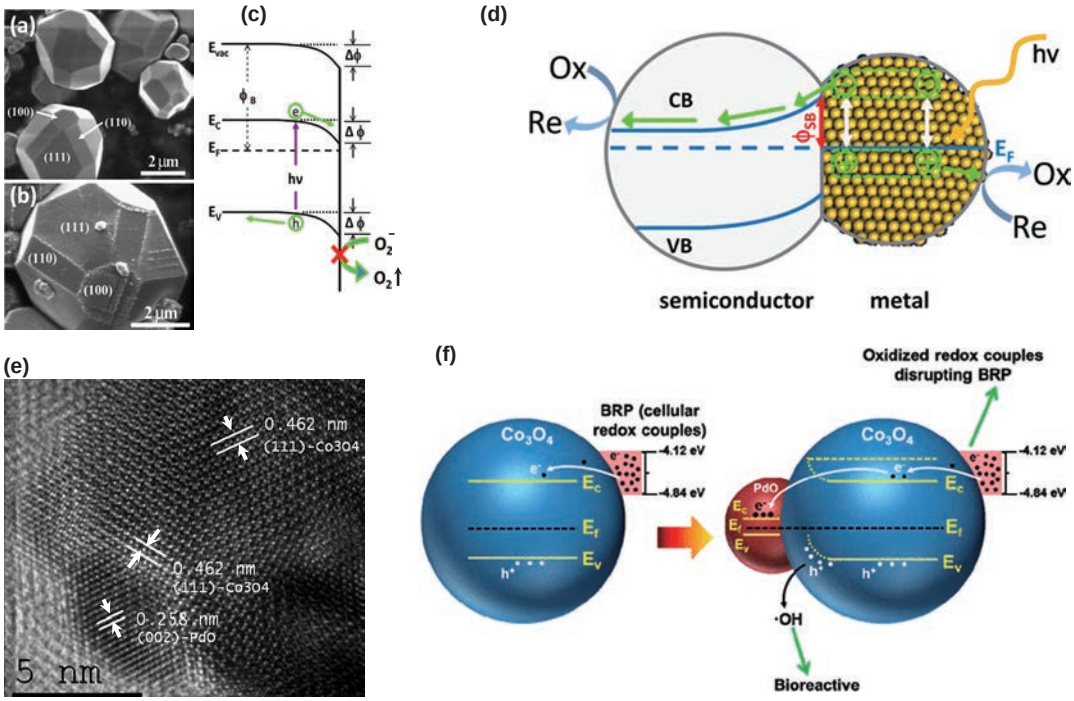


**Fig. 4** SEM images of highly crystalline $BaTiO_3$ produced in **(a)** KCl and **(b)** after reaction in aqueous $AgNO_3$. Schematic of **(c)** band bending by Au and **(d)** plasmon-induced charge separation due to photochemical reactions at the metal/semiconductor heterojunctions. Here, heterocomponents (Ti and Ba) and white contrast due to silver deposition could act as a site for surface reaction. The striped pattern of these deposits is consistent with the domain structure and polarization-specific reactivity flux. The crystallographic orientations of the faces are labeled. **(e)** HRTEM images showing chemically tight heterojunctions between PdO–$Co_3O_4$ nanoparticles synthesized in the gas phase. Such heterojunction is clearly observed between the single-crystalline PdO particle, oriented in the (002) direction, and a single-crystalline $Co_3O_4$ particle, oriented in the (111) direction. **(f)** A *p*-type semiconductor (holes are charge carriers) showing charge transfer from $Co_3O_4$ to PdO via heterojunctions for surface reaction. Adapted with permission from Zhang et al. (2014) and Zhang and Yates (2012). Copyright 2012 and 2014, American Chemical Society.

heteroaggregates provided that the two dissimilar particles have large differences in atomic numbers (high atomic number particles are usually brighter) in HAADF-STEM images (**Fig. 4**).

## 4. Heteroaggregation, interface properties, and applications

### 4.1 Band bending at the heteroaggregate interface

Heteroaggregation at the nanoscale (heterojunctions) allows the development of unique functional properties that are essential for many industrial applications. The presence of heterojunctions between two dissimilar particles allows Femi level equilibration and transfer of charge via the space charge layer to the particle with high work function energy. Hence, such tight hetero-contacts are key to these applications, including but not limited to catalysis (hydrocarbon cracking, dry reforming of methane, organic molecular degradation etc.), chemical sensors, electronics, and energy storage technologies (Carlsson et al., 2023; Wang et al., 2021). The number of hetero-contacts in the aggregates depends on the production routes for heteroaggregates, and the degree of mixing is further understood via mathematical modeling of the mixing processes followed by experimental verification of the heteroaggregate formation (Gerken et al., 2023).

The degree of mixing in the gas-phase process depends on the composition, metal components, and their concentration in the solid solution (Liu et al., 2020). Many particles, including but not limited to doping, solid solution, and mixed metal oxide phases, have been produced following this route (Kho et al., 2011; Manshian et al., 2017; Stark et al., 2003; Teoh et al., 2007; Xiao et al., 2011, 2013). The synthesis of particles may be limited by their thermodynamic properties, e.g., differences in vapor pressures, boiling points, and solid–solid miscibility. These are important in high-temperature synthesis where solid-state reactions and/or the formation of complex oxide mixtures are obtained. Although the mixing of heteroatoms is a parameter inclusive of mathematical variance as a measure of inhomogeneity, a description of the functionality of heteroaggregated particle systems is necessary (Grossmann, 2017). The particle–particle and/or hetero-atomic interaction originates through the contact between different particles, through the resulting interface, or via contacts, as depicted in **Fig. 4** (Zhang et al., 2014). Properties such as charge, mass, heat transfer, and even chemical reactions are realized through such hetero-contacts, explaining the involvement of the number of contact regions/interfaces in controlling the material properties of the overall system (Gerken et al., 2023). For instance, charge transfer across

heterojunctions determines the mechanism involved in surface reactions such as chemical sensors, catalysis and biological redox assessment, and nanomedicines (Minnermann et al., 2011; Möller et al., 2013; Naatz et al., 2020; Takenaka et al., 2012; Xiao et al., 2011).

### 4.2 Charge transfer across the particle–particle heterojunction

Metal–metal oxide heterojunctions are also important because the charges can be transferred through the resulting band bending supporting the $e^{-}h^{+}$ pair separation. The key properties of such catalysts include (1) eluding $e^{-}h^{+}$ pair recombination during the photocatalytic reaction, (2) enhanced reactive sites on the large specific surface, and (3) shifting the optical absorption edge via particle engineering (Yu et al., 2018; Zhang et al., 2012). Zhang et al. (2011) reported the photoreduction of $Ag^{+}$ on $BaTiO_3$ microcrystals physically visualized via white particles in hetero-contact with the (100) and (111) planes [**Figs. 4(a) and (b)**]. The reactivity of the surfaces in the order of (100) > (111) > (110) was related to the heterojunction in the Ag-ferroelectric crystal. The charge transfer and band bending due to the heterojunction at the Au/$TiO_2$ surface are shown in **Fig. 4(c)**. The presence of downward band bending via electropositive Au on the $O_2$/$TiO_2$ (110) heterojunction surface slows down the hole transport via the space charge layer. In both cases, the separated $e^{-}$ and $h^{+}$ participate in the chemical reactions [see **Fig. 4(d)**]. The valence electrons in the metal particle are collectively excited via photon adsorption (surface plasmon resonance). Excited electrons with energy higher than the Schottky barrier cross metal/semiconductor heterojunctions and transfer to the valence band of the semiconductor (Zhang et al., 2011; Zhang and Yates, 2012). In another report, George et al. (2011) reported the photochemical properties of Fe-doped $TiO_2$ synthesized in the gas phase using flame spray pyrolysis. The increasing dopant (via hetero-contact) in $TiO_2$ reciprocally decreased the band gap energy of the particles and was able to excite electrons at the absorption edge near visible light (George et al., 2011; Gomes et al., 2023). Such an effect demonstrates the importance of band energy in photocatalysis. Zhang et al. functionalized PdO on $Co_3O_4$ to create surface PdO/$Co_3O_4$ heterojunctions (Lin et al., 2011). The Fermi energy alignment between PdO and $Co_3O_4$ triggered $e^{-}$ transfer from $Co_3O_4$ to PdO at the interface, resulting in $h^{+}$ generation, as shown in **Figs. 4(e) and (f)**. While surface engineering and modification strategies ease the separation of $e^{-}h^{+}$ pairs on the surface for enhanced photocatalytic efficiency, the significant number density of such charge pairs recombines in the bulk before surface migration for the redox process. The success of the photocatalytic process relies on the effective separation of the photogenerated charges $e^{-}h^{+}$ in the bulk before they take part in the surface redox reaction (George et al., 2011; Lin et al., 2011). The charge transfer concepts described above are also valid in catalysis/photocatalysis and electrochemical processes. Such transfer is particularly attractive when *p*- and *n*-type junctions are realized, for example, in chemical sensors (Frisenda et al., 2018).

### 4.3 Particle–particle heterojunction in chemical sensors

Jeong et al. reported the formation of $Cr_2O_3$–$SnO_2$ sensors for the detection of ethylene at low concentrations. The cross-sectional imaging showed a uniform sensor thickness of ~21 μm [**Fig. 5(a)**]. High-magnification images of the top layer showed spherical $SnO_2$ covered by $Cr_2O_3$ nanoparticles, resulting in a rough surface shown in **Figs. 5(b) and (c)**. The layer composition of the sensor had a uniform distribution of the metals and oxygen, as depicted in **Figs. 5(d) and (e)**, while the Cr distribution was on top of the Sn layer with a heterojunction. The cross-responses of the $Cr_2O_3$–$SnO_2$ to amines such as dimethylene and/or trimethylamine and $NH_3$ (meat or fish usually emit these amines when stored) is a unique sensing marker. The sensing data showed that the specific distances between the fruit and the sensing system successfully discriminated bananas for different levels of ripening. The ethylene recognition test for a banana in the absence and presence of seafood and/or meat using $0.3Cr_2O_3$–$SnO_2$ sensor showed that the ethylene response was unaffected during storage. In addition, $Cr_2O_3$–$SnO_2$ bilayer sensor potentially monitored in real-time and onsite fruit freshness via a portable sensing device was connected to a mobile phone via WLAN, as shown in **Figs. 5(f) and (g)**. A strategy for detecting ethylene at a low ppm concentration shows the importance of heterojunction for efficient gas sensing. The analyte gas adsorption behavior and/or surface reactions are quite different for various molecules on solid surfaces. For instance, a surface with sufficient adsorption energy might support molecular cleavage and allow intermediate species to diffuse to the neighboring particle for further reaction via hetero-contact (Jeong et al., 2020). The $SnO_2$–$Cr_2O_3$ heterojunction was highly selective and sensitive toward ethylene due to the catalytic oxidation of reactive interfering gases, without sacrificing the transport of the analyte gas to the lower sensing region across the heterojunction.

The sintering of the powder sample is another process that intensifies the particle–particle heterojunction via heat treatment. During exothermic surface reactions, heat transport occurs from one component to the other and propagates to neighboring surfaces through hetero-contacts. For example, heat transfer in gas sensors provides suitable adsorption and reaction conditions, leading to improved sensitivity (Gardner et al., 2023). Naik et al. reported the gas sensing properties of $WO_3$–ZnO system and showed that the sintering of grains seemed easier in composites rich in

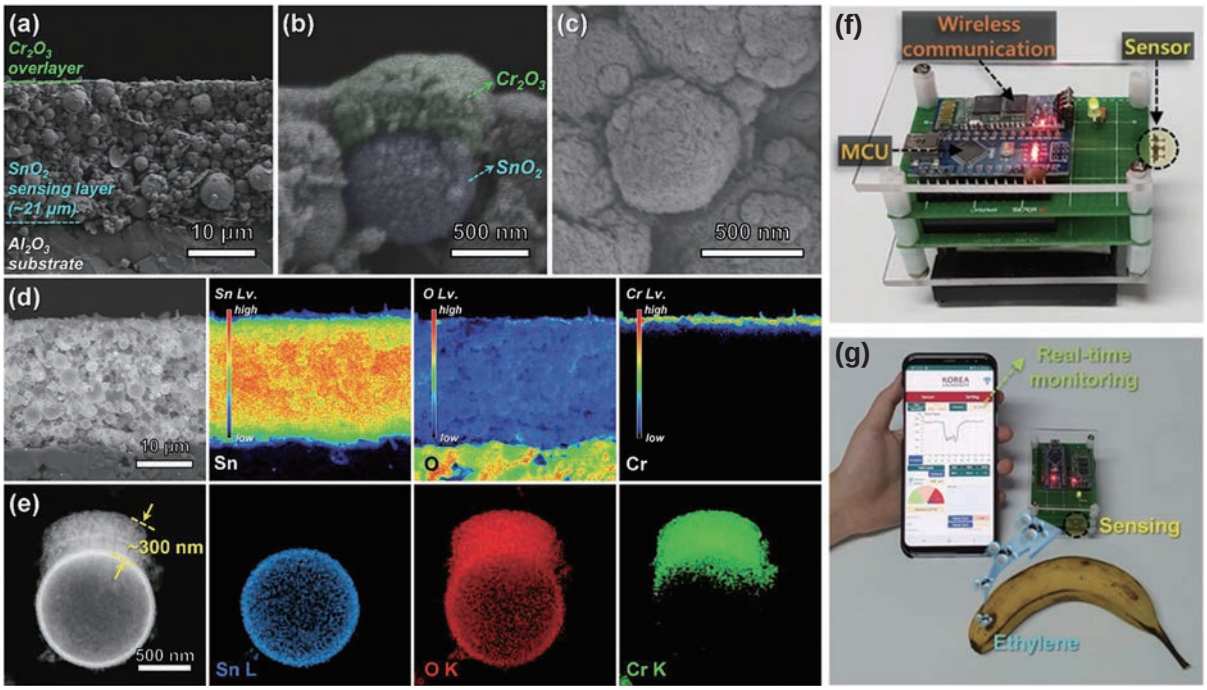


**Fig. 5** Imaging and hetero-contact characterization of $Cr_2O_3$-$SnO_2$ based sensor detecting ethylene ($C_2H_4$) gas: **(a)** cross-sectional image of the heterostructured film, **(b)** magnified SEM image clearly showing $Cr_2O_3$-$SnO_2$ heterojunction, **(c)** top-view image, **(d)** elemental mapping images of Sn, O, and Cr mapping, **(e)** elemental mapping images of Sn, O, and Cr with color codes showing detachment of a particle from the top region of the sensing film, **(f)** wireless sensor module used to assess and monitor fruit freshness using $Cr_2O_3$-$SnO_2$ sensing film, **(g)** photograph of the in situ gas-sensing test. Adapted with permission from a reference (Jeong et al., 2020). Copyright 2020, WILEY-VCH Verlag.

either $WO_3$ or ZnO. The extent of hetero-contacts was higher in the mixture with low and high amounts of oxides, e.g., 10%ZnO and 90%$WO_3$, rather than 50%$WO_3$ and 50%ZnO where inhomogeneity in the mixing was observed. This observation is in line with the highest sensing response by 10%ZnO–90%$WO_3$ for $NO_2$ at an operating temperature of 300 °C (Naik et al., 2013). In another report, Shimizu et al. (2001) significantly increased the NO response of 5.0 wt.% $Cr_2O_3$–$SnO_2$ hetero-contacts via the formation of *p*–*n* junctions. Tuning particle–particle heterojunction allows direct adjustment of the accumulation or depletion layer, surface catalytic activity, Lewis–Bronsted acid–base properties, and polarity, which are key to catalytic application (Jo et al., 2022).

## 4.4 Heteroaggregation and its application in catalysis

While the gas sensing property of heteroaggregates depends on the mixing and increased number of hetero-contacts, such particle geometry is also important for catalytic reactions. As stated in **Section 2**, heteroaggregates can be tailor-made using a double flame system, and the particles are controlled via homogeneous mixing of the aerosol streams (Gockeln et al., 2018b; Kemmler et al., 2012; Manshian et al., 2018; Naatz et al., 2017, 2020; Pokhrel and Mädler, 2020). To realize catalytic performance based on mixing and/or with an increased number of hetero-contacts [see **Fig. 6 (upper panel)**], a series of Pt–Ba/$Al_2O_3$ and Pt/Ba/$Ce_xZr_{1-x}O_2$ multicomponent catalysts with various Ba loadings (4.5–33 wt%) were prepared using a double flame unit and tested for NOx storage capacity (Strobel et al., 2006). The in situ HT-$BaCO_3$ phase leads to improved NO*x* storage potential at higher Ba loadings (Piacentini et al., 2006). In another report, the hetero-contacts between catalytically active Co and $Al_2O_3$ support and their defined particle size were controlled using different intersection distances of the particle streams in the two independent nozzles. The catalytic material was stable on the $Al_2O_3$ support during FT synthesis with enhanced performance (Minnermann et al., 2013). Høj et al. (2013) used multiple flame systems to prepare a heterogeneous catalyst including (CoMo) in $Al_2O_3$ support. The hydrodenitrogenation activity of the catalysts without heat treatment improved from 71 % to 91 % after mixing two aerosol streams. The chemoselective hydrogenation of aromatic ketones was performed using double flame-generated Pd/silica–alumina catalysts. The Pd particles offered identical electronic properties on the Pd surface, contributing similar chemoselectivity for the hydrogenation of carbonyl groups on all double-flame-derived catalysts. Hydrogenation was strongly enhanced by tuning the density of the surface Brønsted acid sites on the catalytic support by varying the Si/Al hetero-contact density (Wang et al., 2013). Very recently, Gäßler et al. (2022) reported the methylation activity of catalysts, namely Co/$SiO_2$, Co/$TiO_2$, and Co/$TiO_2$–$SiO_2$. The synthesis technique and in situ mixing

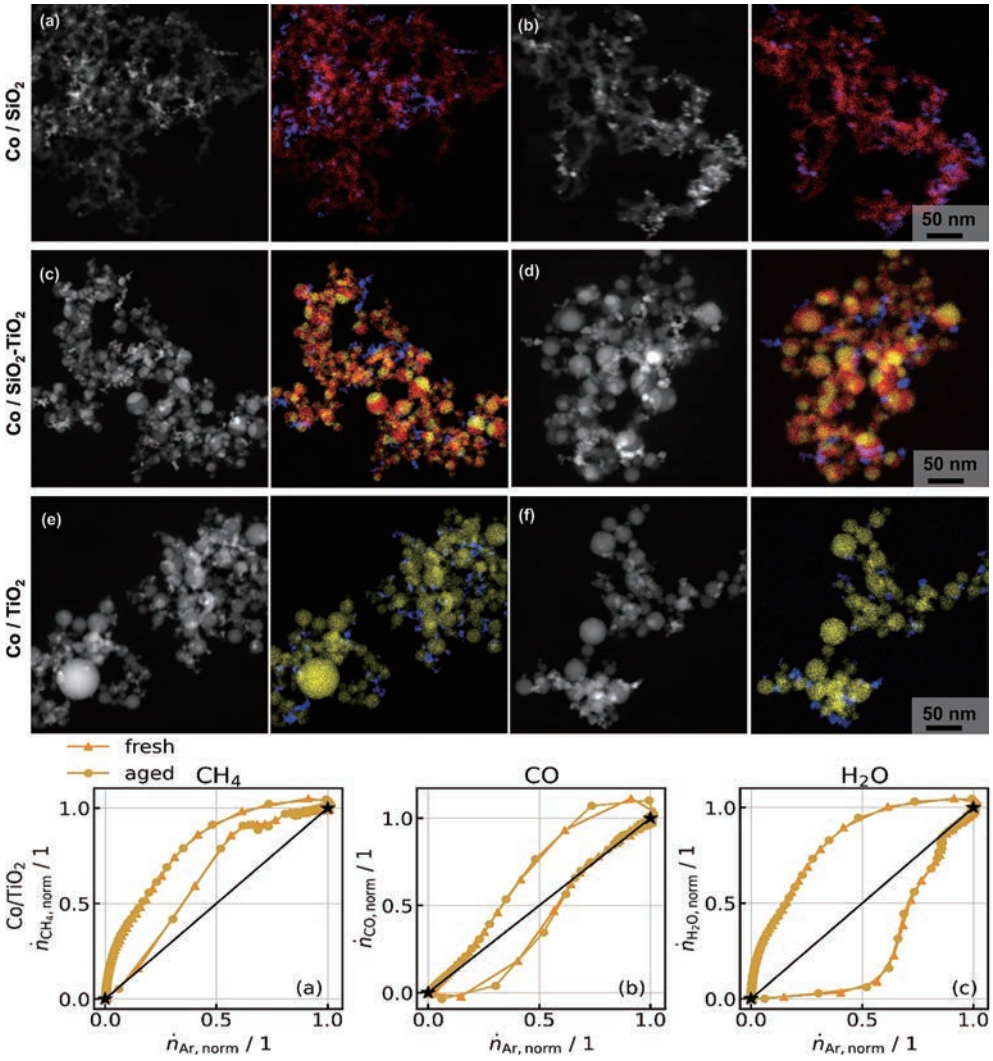


**Fig. 6** **(upper panel)** TEM micrographs of $Co/SiO_2$ **(a,b)**, $Co/SiO_2$-$TiO_2$ **(c,d)**, and $Co/TiO_2$ **(e,f)** catalysts. The micrographs in HAADF mode and EDX mappings of the elements show Co in blue, Si in red, and Ti in yellow. **(lower panel)** State-space plots for outlet molar flow rates of $CH_4$, CO, and $H_2O$ for $Co/TiO_2$ catalysts at 300 °C and 2 bar. Adapted from Gäßler et al. (2022). Copyright 2022 Wiley.

were suitable for well-defined heteroaggregates catalysts. The separation of the individual nanoparticle formation into two independent flames and varying nozzle distances allowed for the defined mixing of active metal and support.

Dynamic catalytic testing showed that the support material is affected by adsorbed $H_2O$ on the support surface, leading to a significant delay in $H_2O$ response. In contrast, the data showed fast formation of stoichiometric $CH_4$ [**Fig. 6 (lower panel)**]. While the formation of CO is increased with $Co/TiO_2$–$SiO_2$, the rate of $CH_4$ formation increases with higher $TiO_2$ fractions in the support (Gäßler et al., 2022). In another report, Stahl et al. (2021) studied $Co/Al_2O_3$, Co/Pt, $Co/ZrO_2$, and $Co/Sm_2O_3$ heteroaggregated catalysts synthesized by double-flavor gas phase mixing. The results of different surface promoters, including Pt, $ZrO_2$ and $Sm_2O_3$, showed overall improvement of methanation at operation temperature compared with unpromoted catalyst. In the case of CO methanation, Pt performed the best methanation activation, and all the catalysts deactivated rapidly above 310 °C. The combination of well-defined catalysts obtained from the gas phase provides the basis to correlate material properties with catalytic performance (Stahl et al., 2021). In the future, experiments with doping on the reactive surface might even lead to the formation of catalytically very active heteroaggregates. Hence, the particle properties depend on the degree of mixing and are directly proportional to the number of hetero-contacts in the aggregates. Selectivity, which is essential in heterogeneous catalysis, e.g., layered double hydroxide (LDH), allows polymerization of propylene oxide on the hydroxide surface. Laycock et al. (1991) reported that inorganic or organometallic coordination is possible on the specific orientation of the LDH surface for heterojunction.

The optimal functionality of the material also depends on the contact area, atomic structure of the interface, lattice strain, and defect chemistry of the two dissimilar particles. The variation in the process parameters during double

flame spray pyrolysis allows efficient mixing and results in improved functionalities in various other applications.

### 4.5 Particle–particle heteroaggregation in photocatalysis

The heterojunctions in the aggregates improve the photocatalytic activity by enhancing charge carrier separation and reducing recombination. Selective deposition with active co-catalysts allows enhancement of the number of heterojunctions. Apart from the $e^{-}h^{+}$ pair separation, the extension of light absorption by the combination of at least one visible light-absorbing semiconductor hetero-contact also enhances the catalytic property (Marschall, 2014). The photocatalytic reaction of sucrose with excess oxygen favors a reductive pathway in Pt/$TiO_2$ heteroaggregates (Teoh et al., 2005). However, the photocatalytic reaction of methanol was absent, clearly indicating the beneficial effects of Pt(0) and/or Pt(IV) hetero-contact with $TiO_2$ (Teoh et al., 2005; 2007). The photocatalysis using different Pt functionalized hetero-contacts showed an optimum photocatalytic effect for 0.5 % Pt loading. At a lower Pt distribution (0.1 %), the activity was even lower than that of pure $TiO_2$ due to the high photocurrent density of the Pt particles enhancing the electron–hole recombination process (Teoh et al., 2005). To test this effect, Kho et al. (2010) studied photocatalytic $H_2$ evolution over aqueous $TiO_2$ using methanol as a hole scavenger. The variation in the band energies of the anatase and rutile phases poses a synergic barrier and electron transfer across the anatase–rutile junction, as depicted in **Figs. 7(A) and (C)**. Such synergistic behavior (charge separation mechanism in the interface of the heteroaggregates) is responsible for the photoactivity of the particles. The other possibility of $e^{-}h^{+}$ pair generation in the $TiO_2$ based nanoparticles is via re-engineering oxides by doping (hetero-contacts), as shown in **Figs. 7(B) and (D)**(George et al., 2011). The effect in the mixed anatase–rutile phases originated through efficient charge separation across the interface. In another report, Sasikala et al. (2009) reported $TiO_2$–$SnO_2$ heteroaggregates with enhanced photocatalytic activity for hydrogen generation compared with pure $TiO_2$ via effective charge separation in the aggregate system. Similarly, Jia et al. (2014) studied $BiVO_4$–$SrTiO_3$: Rh heterojunction system and reported that a stable interface between components is essential for charge separation. The heteroaggregation and structural complexity of the photocatalyst components described above offer many

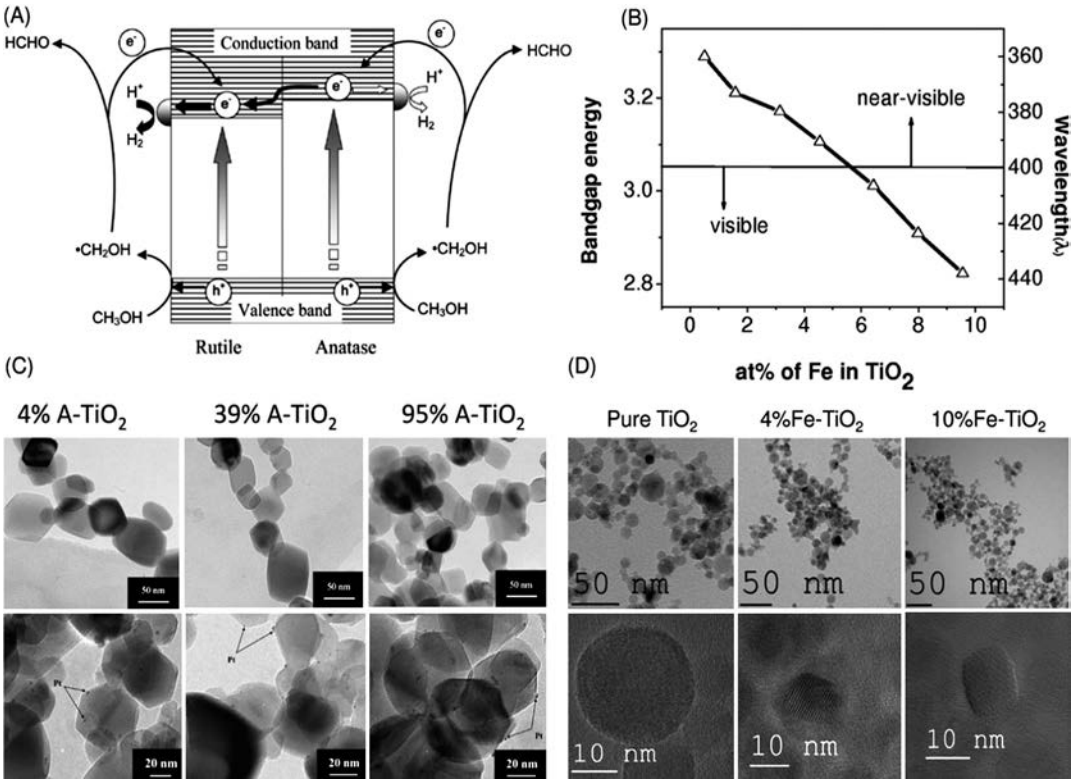


**Fig. 7** **(A)** Proposed photocatalytic route for $H_2$ evolution via electron transfer in the anatase–rutile heterojunction. The oxidation of methanol results in the formation of hydroxymethyl radicals ($^{\cdot}CH_2OH$) via hydroxyl radicals ($^{\cdot}OH$). **(B)** Decrease in the band gap energy by Fe doping in $TiO_2$. With an increase in the doping content, the band gap energy decreases. **(C)** (**Top**): Images of $TiO_2$ nanoparticles with 4, 39 and 95 % anatase contents. **Bottom**: Images of Pt/$TiO_2$ (4, 39 and 95 % anatase) with Pt dispersion after photocatalytic reaction. **(D)** Microscopic images of undoped and Fe-doped $TiO_2$ nanoparticles. Low-resolution (**top row**) and high-resolution (**bottom row**) images of single particles of undoped $TiO_2$, 4 % Fe doped $TiO_2$ and 10 % Fe-doped $TiO_2$, respectively. Adapted with permission from references (George et al., 2011; Kho et al., 2010). Copyright 2010 and 2011, American Chemical Society.

degrees of freedom for tuning their catalytic properties (Schauermann et al., 2013).

### 4.6 Heteroaggregation in energy storage applications

Apart from the performance of the catalysis, heteroaggregates with tight chemical contact are also known to be very novel for the development of energy storage materials (designed from the double flame spray pyrolysis). While single-phase $LiMn_2O_4$ has a high energy density and rate capability, the dissolution of $Mn^{2+}$ in the electrolyte via disproportionation causes cell degradation and fast capacity fading (Erichsen et al., 2020). The use of double flame gas phase synthesis, efficient mixing of two aerosol streams inclined at constant 20° (one with $AlPO_4$ and the second with $LiMn_2O_4$), produced $AlPO_4/LiMn_2O_4$ heteroaggregates in the gas phase. The electrochemical performances of these energy storage materials showed a capacity retention of 93 % and an outstanding initial capacity of 116.1 mAh $g^{-1}$ for 1 % $AlPO_4$, as depicted in **Figs. 8(a)–(c)** (Li et al., 2021).

In another report, novel battery systems were fabricated using double flame spray pyrolysis followed by a role-to-role lamination technique. The C–$Li_4Ti_5O_{12}$ heterojunction was obtained by combusting xylene in one independent flame and $Li_4Ti_5O_{12}$ in the other flame , as illustrated in **Figs. 8(d) and (e)**. The carbon stream was mixed with the active energy storage material above the

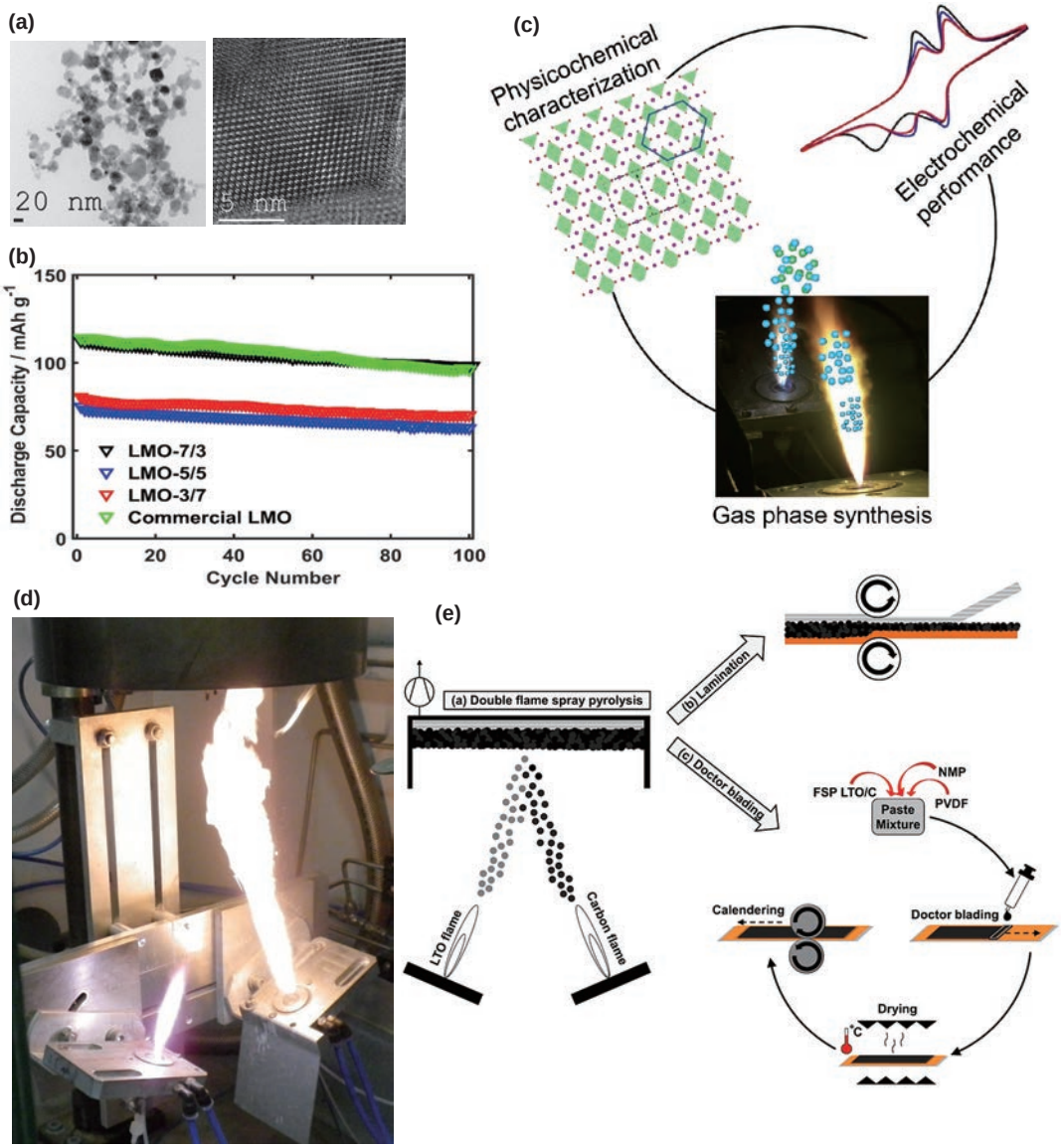


**Fig. 8** Energy storage heteroaggregated materials: **(a)–(c)** particle characterization and energy storage application of heteroaggregated $AlPO_4$ with spinel $LiMn_2O_4$. The material is a promising cathode for rechargeable Li-ion batteries because of its cost effectiveness, eco-friendliness, high energy density, and rate capability. **(d)** Synthesis of C–$Li_4Ti_5O_{12}$ using double-flavor aerosol mixing, **(e)** realization of role-to-role layer transfer technology and doctor blading for battery layer fabrication. Adapted from references (Gockeln et al., 2018b; Li et al., 2021). Copyright: 2018 American Chemical Society 2018 and 2021 Elsevier.

flame. The C–$Li_4Ti_5O_{12}$ powder was transferred to the current collector directly from the role-to-role laminator.

The development of this in situ gas-phase process avoids (1) the use of organic binder and/or solvent and (2) the traditional multiple steps necessary for battery fabrication (Ernst et al., 2007; Li et al., 2021). As described above for $AlPO_4$–$LiMn_2O_4$ and C–$Li_4Ti_5O_{12}$ lithium-ion batteries, these batteries have come into industrial focus with high interest. The investment in cathode, anode, and electrolytic research has been realized due to solid–liquid hetero-contact (Groß, 2022). The results showed that the solid electrolytes interfaced with the solid electrodes were free from leakage, free from Li-dendrite growth, and non-flammable during cycling, as depicted in **Figs. 9(a)–(d)**. These advantages allowed feasible battery operation at a wide range of temperatures (Meng et al., 2022). All solid-state batteries covering a large class of materials including but not limited to polymeric, inorganic ceramic, or glassy materials such as oxides, halides, and sulfides with tight hetero-contact are commercially attractive, and a few of them are already under operation and use (Manthiram et al., 2017; Naatz et al., 2018; Pokhrel et al., 2023; Zou et al., 2020).

### 4.7 Particle–particle heterojunction in superconductors and medicine

The physical properties, including but not limited to charge transfer, specific band energy position changes, spin–orbit, and spin–spin coupling, can be altered by increasing the number of hetero-contacts through doping, pressing, and sintering. Gan et al. (2023) designed an oxide hetero-contact using $Hf_{0.5}Zr_{0.5}O_2$ interfaced with a selective orientation (110) of $KTaO_3$, allowing light-induced giant spin–orbit coupling-based superconducting interfaces. Such hetero-contacts are promising efficient spintronic devices and topological superconductors. While heteroaggregation is a key to many physical properties and applications, such heteroaggregation is equally important in medicinal and pharmaceutical processes for efficient treatment. Meng et al. (2010) used mesoporous $SiO_2$ nanoparticles as a solid support for controlled drug delivery using their large surface for functionalization (solid–solid hetero-contact) to control the nanopore openings. These particles were used as a novel delivery system based on the function of such hetero-contacts. In recent years, various approaches such as deep-eutectic systems (Sánchez-Leija et al., 2014), solid crystal suspensions, and nanoparticulate formulations (Ely et al., 2014) have been shown to have the best performance due to the interaction effect in the

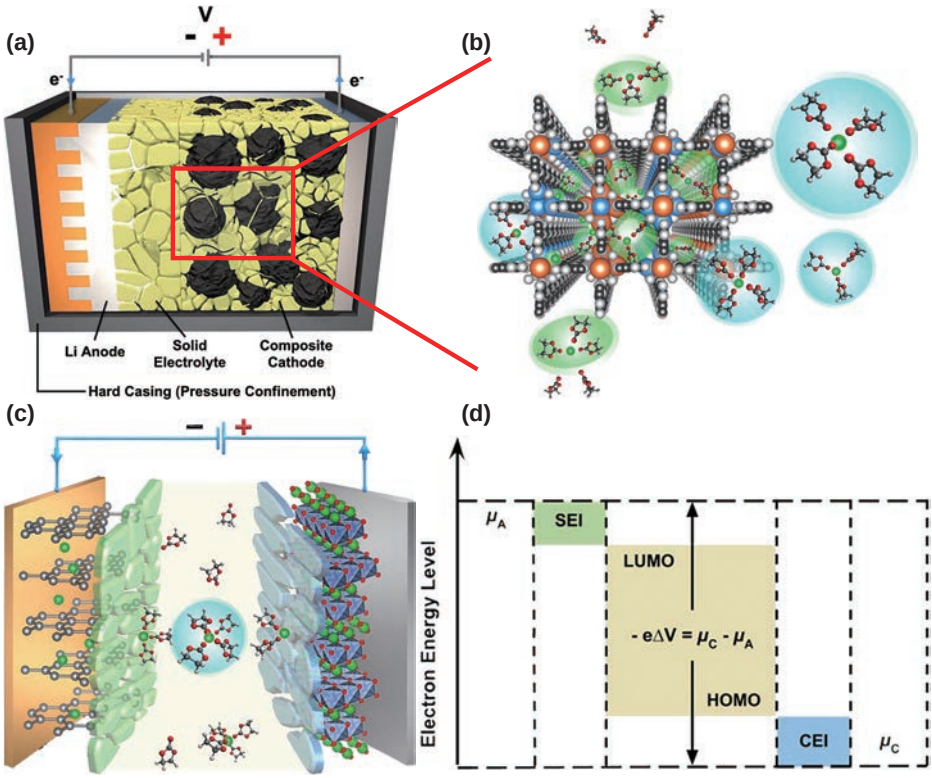


**Fig. 9** **(a)** All solid-state lithium ion batteries showing hetero-contacts between the electrodes and electrolyte, **(b)** solvation in nanoconfinement within the cells with hetero-junctions, **(c)** Schematic diagram showing hetero-junctions with all battery components with stable ionic conduction in the electrolyte, **(d)** electrodes operating at potentials beyond the region enclosed between energy levels followed by interphase formation for the reversibility of the cell chemistry. Adapted with permission from a reference (Meng et al., 2022). Copyright 2022, American Association for the Advancement of Science.

colloidal size (Priemel et al., 2012). This effect is achieved by the local hetero-contact of the multicomponent substances at the nanoscale.

### 4.8 Layer fabrication with heteroaggregates

The transfer of forces and moments at the hetero-contact occurs during the densification and layering of the powders. To design such systems, the combination of ductile and brittle particles offers a high-strength granular system that allows deformations at the interfaces. Baric et al. (2019) modeled nanoparticle aggregate film compaction (considering elastic sinter bridges between primary particles) using DEM. The results showed deviation from the experimentally determined porosity and pore size distribution against applied pressure when non-covalence, adhesion, very rigid, and strong agglomerates were considered [**Figs. 10(a)–(e)**]. Such porosity of the films arises from low mechanical resistance. The thermal stability of the films was realized via sintering/annealing to enhance electrical conductivity; however, this was at the expense of the reduced porosity and specific surface area. In the gas phase, in situ thermophoresis for the development of heterojunctions involves high-velocity particle streams colliding with the substrates placed above the spray. The post treatments,

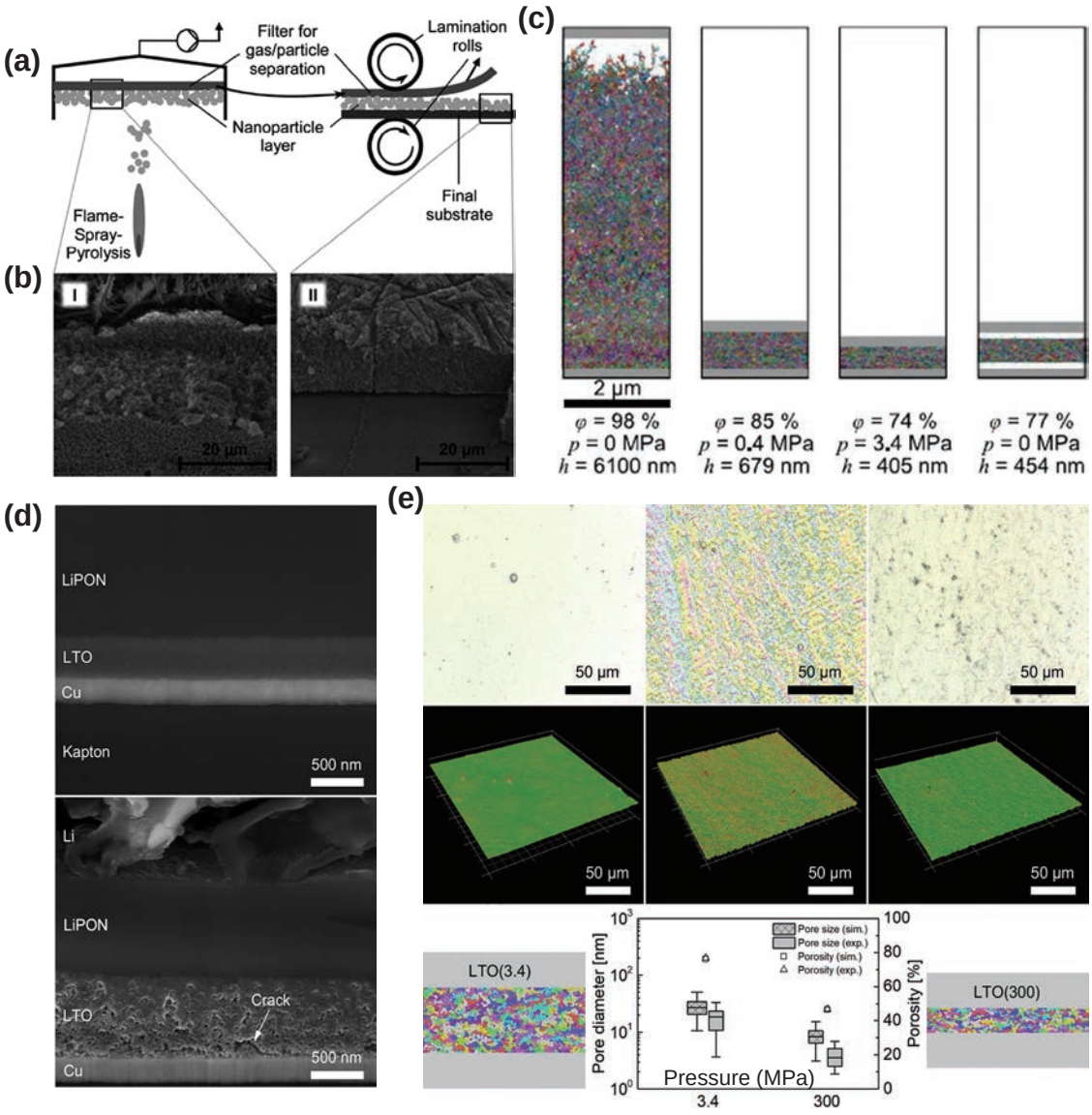


**Fig. 10** **(a)–(c)** Role-to-role layer transfer of in situ deposited particles. **(a)** Gas phase synthesis of heteroaggregates and layer transfer via lamination. **(b)** SEM images of the fabricated layer **(I)** before and **(II)** after layer transfer. **(c)** Simulation of the thermophoretic particle layer. The $\varphi$, $p$, and $h$ denote the porosity, pressure, and film height, respectively. **(d)** Thin-film lithium-ion batteries overview and $Li_4Ti_5O_{12}$ close-up images of SEM/FIB cuts for $Li_4Ti_5O_{12}$ at 300 **(top)** and 3.4 **(lower)** MPa pressure. The higher pressured $Li_4Ti_5O_{12}$ at 300 MPa is dense, homogeneous, and thin, whereas the lower pressured layer is porous, irregular, and thicker. **(e)** 2D **(top)** and 3D **(middle)** representations of the surface sections of $Li_4Ti_5O_{12}$ powder, compacted at 0, 3.4, and 300 MPa **(e-lower panel)** illustrate the coherence of the simulated and experimental porosities and pore size distributions of $Li_4Ti_5O_{12}$ at 3.4 and 300 MPa, respectively. The colored images on the left and right in **(e)** demonstrate the simulated thin films. Adapted with permission from references (Gockeln et al., 2020; Pokhrel and Mädler, 2020). Copyright 2020, American Chemical Society.

i.e., sintering the resulting particle–particle heteroaggregates, are unnecessary because organic binders are avoided at all process steps and the temperature of combustion is ~3000 °C. While particle–substrate bonding strength (loose hetero-contact of the layer with the substrate) is weaker for the in situ deposited layers, Schopf et al. (2013) developed a role-to-role lamination process enabling compact dry nanoparticle films at pressures up to 3.4 MPa. Such role-to-role layer fabrication technology allowed stronger and mechanically stable hetero-contact between the substrate and the particle layer, as shown in **Figs. 10(a) and (b)**.

The compaction led to a significant increase in the compressive Young's modulus (from 0.8 MPa to 1.9 MPa) and a decrease in porosity from 84 % to 79 % while preserving the specific surface area of the film, as depicted in **Figs. 10(d) and (e)**. In addition, it has been reported that compact particle–particle films retain their physical properties, e.g., structure and morphology, against capillary forces resulting from an air–liquid interface during liquid imbibition (Schopf et al., 2017). It must be noted that particles of 10 nm size at 3.4 MPa compaction pressure producing brittle fractures is highly unlikely. To validate this finding, flexible $Li_4Ti_5O_{12}$ layers (LTO) were in situ deposited on Cu substrates (LTO–Cu hetero-contact) followed by compacting at pressures of 3.4 and 300 MPa. The hetero-contact at higher pressure was dense, homogeneous, and thin, whereas the contact compacted at lower pressure was highly porous, more irregular, and thicker, as shown in **Figs. 10(d) and (e)**. The LTO–Cu hetero-contact compressed at 300 MPa and 3.4 MPa showed porosities of 46.6 % and 76.7 %, matching the DEM-simulated porosities of 46.4 % and 75.9 %, respectively (Gockeln et al., 2018a; 2018b; 2020). Gottschalk et al. (2023) reported high-energy hetero-contacts of C–Si. The data showed that the balanced ratio of the active heteroaggregates and compaction drives the battery performance optimally.

## 5. Conclusion and outlook

The development of process parameters to design a large number of particle–particle hetero-contacts during production is a key to many innovative applications. The generation of hetero-contacts within the heteroaggregates allows specific charge distributions in the particle–particle interface, providing a great opportunity to develop new materials in the gas phase. However, unresolved challenges such as but not limited to surface adsorption, particle shape/size, and turbulence in the gas phase affect the actual realization of particle mixing. While larger process time length, particle concentrations, and homogeneity gradients of the mixing are particularly challenging, the quantification of such heteroaggregates and the determination of parameters for such aggregation create new opportunities and resolve the drawbacks, i.e., heteromixing, which is difficult via liquid phase and/or physical mixing processes. The non-uniform heteroaggregation is caused by different mixing zones during the spray, while the mixing of two aerosol streams crossing at an angle differs significantly in the flow direction. Two identical free jets at different distances from each other result in very different mixing patterns in the flow direction. This makes it possible to mix particles that meet at very different growth stages, control over heteroaggregation. This review aims to establish functional correlationsbetween the process design, modeling, particle–particle mixing, and uniformity of the heteroaggregates. These aggregates at the nanoscale are a very important class of materials, especially in catalysis, sensor, and battery development. Charge transport between different components and different heterojunctions is the driving factor for enhanced performance. The same applies to semiconducting materials, where the *n*–*p* transition within heteroaggregates is another emerging field of research. On this basis, new concepts for gas sensors and photoreactors have been developed. In addition, in catalysis, mass and charge transfers in multicomponent materials are important. Hence, to realize an advancement in science, especially in materials science, particle formulation and the characterization of heteroaggregates are research topics with high relevance.

## Acknowledgments

The authors thank the German Research Foundation (DFG) for funding through the priority program SPP 2289 Hetero-Aggregates. SP and LM would like to thank the European Research Council (ERC) for Grant Agreement 786487.

## References

Adeleye A.S., Pokhrel S., Mädler L., Keller A.A., Influence of nanoparticle doping on the colloidal stability and toxicity of copper oxide nanoparticles in synthetic and natural waters, Water Research, 132 (2018) 12–22. https://doi.org/10.1016/j.watres.2017.12.069

Balakrishnan A., Groeneveld J.D., Pokhrel S., Mädler L., Metal sulfide nanoparticles: precursor chemistry, Chemistry – A European Journal, 27 (2021) 6390–6406. https://doi.org/10.1002/chem.202004952

Baric V., Ciacchi L.C., Mädler L., Compaction-induced restructuring of aggregated nanoparticle films using the discrete element method, Powder Technology, 342 (2019) 773–779. https://doi.org/10.1016/j.powtec.2018.10.038

Baric V., Grossmann H.K., Koch W., Mädler L., Quantitative characterization of mixing in multicomponent nanoparticle aggregates, Particle & Particle Systems Characterization, 35 (2018) 1800177. https://doi.org/10.1002/ppsc.201800177

Buss L., Meierhofer F., Bianchi Neto P., França Meier H., Fritsching U., Noriler D., Impact of co-flow on the spray flame behaviour applied to nanoparticle synthesis, The Canadian Journal of Chemical Engineering, 97 (2019) 604–615. https://doi.org/10.1002/cjce.23386

Carlsson A., Rosen J., Dahlqvist M., Finding stable multi-component materials by combining cluster expansion and crystal structure predictions, npj Computational Materials, 9 (2023) 21. https://doi.org/10.1038/s41524-023-00971-3

Dreyer J.A.H., Pokhrel S., Birkenstock J., Hevia M.G., Schowalter M., Rosenauer A., Urakawa A., Teoh W.Y., Mädler L., Decrease of the required dopant concentration for δ-$Bi_2O_3$ crystal stabilization through thermal quenching during single-step flame spray pyrolysis,

CrystEngComm, 18 (2016) 2046–2056. https://doi.org/10.1039/c5ce02430g

Eggersdorfer M.L., Kadau D., Herrmann H.J., Pratsinis S.E., Aggregate morphology evolution by sintering: number and diameter of primary particles, Journal of Aerosol Science, 46 (2012) 7–19. https://doi.org/10.1016/j.jaerosci.2011.11.005

Ely D.R., Edwin García R., Thommes M., Ostwald–Freundlich diffusion-limited dissolution kinetics of nanoparticles, Powder Technology, 257 (2014) 120–123. https://doi.org/10.1016/j.powtec.2014.01.095

Endres S.C., Avila M., Mädler L., A discrete differential geometric formulation of multiphase surface interfaces for scalable multiphysics equilibrium simulations, Chemical Engineering Science, 257 (2022) 117681. https://doi.org/10.1016/j.ces.2022.117681

Endres S.C., Ciacchi L.C., Mädler L., A review of contact force models between nanoparticles in agglomerates, aggregates, and films, Journal of Aerosol Science, 153 (2021) 105719. https://doi.org/10.1016/j.jaerosci.2020.105719

Erichsen T., Pfeiffer B., Roddatis V., Volkert C.A., Tracking the diffusion-controlled lithiation reaction of $LiMn_2O_4$ by in situ TEM, ACS Applied Energy Materials, 3 (2020) 5405–5414. https://doi.org/10.1021/acsaem.0c00380

Ernst F.O., Kammler H.K., Roessler A., Pratsinis S.E., Stark W.J., Ufheil J., Novák P., Electrochemically active flame-made nanosized spinels: $LiMn_2O_4$, $Li_4Ti_5O_{12}$ and $LiFe_5O_8$, Materials Chemistry and Physics, 101 (2007) 372–378. https://doi.org/10.1016/j.matchemphys.2006.06.014

Feng J., Biskos G., Schmidt-Ott A., Toward industrial scale synthesis of ultrapure singlet nanoparticles with controllable sizes in a continuous gas-phase process, Scientific Reports, 5 (2015) 15788. https://doi.org/10.1038/srep15788

Feng J., Huang L., Ludvigsson L., Messing M.E., Maisser A., Biskos G., Schmidt-Ott A., General approach to the evolution of singlet nanoparticles from a rapidly quenched point source, The Journal of Physical Chemistry C, 120 (2016) 621–630. https://doi.org/10.1021/acs.jpcc.5b06503

Fischer D., Börzsönyi T., Nasato D.S., Pöschel T., Stannarius R., Heaping and secondary flows in sheared granular materials, New Journal of Physics, 18 (2016) 113006. https://doi.org/10.1088/1367-2630/18/11/113006

Frisenda R., Molina-Mendoza A.J., Mueller T., Castellanos-Gomez A., van der Zant H.S.J., Atomically thin p–n junctions based on two-dimensional materials, Chemical Society Reviews, 47 (2018) 3339–3358. https://doi.org/10.1039/c7cs00880e

Gan Y., Yang F., Kong L., Chen X., Xu H., Zhao J., Li G., Zhao Y., Yan L., Zhong Z., Chen Y., Ding H., Light-induced giant Rashba spin–orbit coupling at superconducting $KTaO_3$(110) heterointerfaces, Advanced Materials, 35 (2023) 2300582. https://doi.org/10.1002/adma.202300582

Gardner E.L.W., Gardner J.W., Udrea F., Micromachined thermal gas sensors—a review, Sensors, 23 (2023) 681. https://doi.org/10.3390/s23020681

Gäßler M., Stahl J., Schowalter M., Pokhrel S., Rosenauer A., Mädler L., Güttel R., The impact of support material of cobalt-based catalysts prepared by double flame spray pyrolysis on $CO_2$ methanation dynamics, ChemCatChem, 14 (2022) e202200286. https://doi.org/10.1002/cctc.202200286

George S., Pokhrel S., Ji Z., Henderson B.L., Xia T., Li L., Zink J.I., Nel A.E., Mädler L., Role of Fe doping in tuning the band gap of $TiO_2$ for the photo-oxidation-induced cytotoxicity paradigm, Journal of the American Chemical Society, 133 (2011) 11270–11278. https://doi.org/10.1021/ja202836s

Gerken B., Mahr C., Stahl J., Grieb T., Schowalter M., Krause F.F., Mehrtens T., Mädler L., Rosenauer A., Material discrimination in nanoparticle hetero-aggregates by analysis of scanning transmission electron microscopy images, Particle & Particle Systems Characterization, 40 (2023) 2300048. https://doi.org/10.1002/ppsc.202300048

Gockeln M., Glenneberg J., Busse M., Pokhrel S., Mädler L., Kun R., Flame aerosol deposited $Li_4Ti_5O_{12}$ layers for flexible, thin film all-solid-state Li-ion batteries, Nano Energy, 49 (2018a) 564–573. https://doi.org/10.1016/j.nanoen.2018.05.007

Gockeln M., Pokhrel S., Meierhofer F., Glenneberg J., Schowalter M., Rosenauer A., Fritsching U., Busse M., Mädler L., Kun R., Fabrication and performance of $Li_4Ti_5O_{12}$/C Li-ion battery electrodes using combined double flame spray pyrolysis and pressure-based lamination technique, Journal of Power Sources, 374 (2018b) 97–106. https://doi.org/10.1016/j.jpowsour.2017.11.016

Gockeln M., Ruiter T., Palacios Saura A., Baric V., Glenneberg J., Busse M., Pokhrel S., Kun R., Mädler L., Enhancing the utilization of porous $Li_4Ti_5O_{12}$ layers for thin-film lithium-ion batteries, ACS Applied Energy Materials, 3 (2020) 9667–9675. https://doi.org/10.1021/acsaem.0c01231

Gomes S.I.L., Roca C.P., Pokhrel S., Mädler L., Scott-Fordsmand J.J., Amorim M.J.B., $TiO_2$ nanoparticles' library toxicity (UV and non-UV exposure) – high-throughput in vivo transcriptomics reveals mechanisms, NanoImpact, 30 (2023) 100458. https://doi.org/10.1016/j.impact.2023.100458

Gottschalk L., Oertel C., Strzelczyk N., Müller J., Krüger J., Haselrieder W., Kwade A., Improving the performance of lithium-ion batteries using a two-layer, hard carbon-containing silicon anode for use in high-energy electrodes, Energy Technology, 11 (2023) 2200858. https://doi.org/10.1002/ente.202200858

Groß A., Reversible vs standard hydrogen electrode scale in interfacial electrochemistry from a theoretician's atomistic point of view, The Journal of Physical Chemistry C, 126 (2022) 11439–11446. https://doi.org/10.1021/acs.jpcc.2c02734

Grossmann H.K., Tailored aerosol synthesis of nanosized multicomponent catalysts, PhD, University of Bremen, 2017, <https://media.suub.uni-bremen.de/handle/elib/1464> accessed 29122023.

Grossmann H.K., Grieb T., Meierhofer F., Hodapp M.J., Noriler D., Gröhn A., Meier H.F., Fritsching U., Wegner K., Mädler L., Nanoscale mixing during double-flame spray synthesis of heterostructured nanoparticles, Journal of Nanoparticle Research, 17 (2015) 174. https://doi.org/10.1007/s11051-015-2975-8

Gröhn A.J., Buesser B., Jokiniemi J.K., Pratsinis S.E., Design of turbulent flame aerosol reactors by mixing-limited fluid dynamics, Industrial & Engineering Chemistry Research, 50 (2011) 3159–3168. https://doi.org/10.1021/ie1017817

Gunkelmann N., Montaine M., Pöschel T., Stochastic behavior of the coefficient of normal restitution, Physical Review E, 89 (2014) 022205. https://doi.org/10.1103/physreve.89.022205

Høj M., Pham D., Brorson M., Mädler L., Jensen A., Grunwaldt J.-D., Two-nozzle flame spray pyrolysis (FSP) synthesis of CoMo/$Al_2O_3$ hydrotreating catalysts, Catalysis Letters, 143 (2013) 386–394. https://doi.org/10.1007/s10562-013-0990-x

Horlyck J., Pokhrel S., Lovell E., Bedford N.M., Mädler L., Amal R., Scott J., Unifying double flame spray pyrolysis with lanthanum doping to restrict cobalt–aluminate formation in Co/$Al_2O_3$ catalysts for the dry reforming of methane, Catalysis Science & Technology, 9 (2019) 4970–4980. https://doi.org/10.1039/c9cy01293a

Jeong S.-Y., Moon Y.K., Kim T.-H., Park S.-W., Kim K.B., Kang Y.C., Lee J.-H., A new strategy for detecting plant hormone ethylene using oxide semiconductor chemiresistors: exceptional gas selectivity and response tailored by nanoscale $Cr_2O_3$ catalytic overlayer, Advanced Science, 7 (2020) 1903093. https://doi.org/10.1002/advs.201903093

Jia Q., Iwase A., Kudo A., $BiVO_4$–Ru/$SrTiO_3$:Rh composite Z-scheme photocatalyst for solar water splitting, Chemical Science, 5 (2014) 1513–1519. https://doi.org/10.1039/c3sc52810c

Jo Y.-M., Jo Y.K., Lee J.-H., Jang H.W., Hwang I.-S., Yoo D.J., MOF-based chemiresistive gas sensors: toward new functionalities, Advanced Materials, 35 (2022) 2206842. https://doi.org/10.1002/adma.202206842

Johannessen T., Pratsinis S.E., Livbjerg H., Computational fluid-particle dynamics for the flame synthesis of alumina particles, Chemical Engineering Science, 55 (2000) 177–191. https://doi.org/10.1016/S0009-2509(99)00183-9

Kemmler J.A., Pokhrel S., Birkenstock J., Schowalter M., Rosenauer A., Bârsan N., Weimar U., Mädler L., Quenched, nanocrystalline $In_4Sn_3O_{12}$ high temperature phase for gas sensing applications, Sensors and Actuators B: Chemical, 161 (2012) 740–747.

https://doi.org/10.1016/j.snb.2011.11.026
Kho Y.K., Iwase A., Teoh W.Y., Mädler L., Kudo A., Amal R., Photocatalytic $H_2$ evolution over $TiO_2$ nanoparticles. The synergistic effect of anatase and rutile, The Journal of Physical Chemistry C, 114 (2010) 2821–2829. https://doi.org/10.1021/jp910810r
Kho Y.K., Teoh W.Y., Iwase A., Mädler L., Kudo A., Amal R., Flame preparation of visible-light-responsive $BiVO_4$ oxygen evolution photocatalysts with subsequent activation via aqueous route, ACS Applied Materials & Interfaces, 3 (2011) 1997–2004. https://doi.org/10.1021/am200247y
Kim K.D., Pokhrel S., Wang Z., Ling H., Zhou C., Liu Z., Hunger M., Mädler L., Huang J., Tailoring high-performance Pd catalysts for chemoselective hydrogenation reactions via optimizing the parameters of the double-flame spray pyrolysis, ACS Catalysis, 6 (2016) 2372–2381. https://doi.org/10.1021/acscatal.6b00396
Kruis F.E., Kusters K.A., Pratsinis S.E., Scarlett B., A simple model for the evolution of the characteristics of aggregate particles undergoing coagulation and sintering, Aerosol Science and Technology, 19 (1993) 514–526. https://doi.org/10.1080/02786829308959656
Laycock D.E., Collacott R.J., Alan Skelton D., Tchir M.F., Stereospecific polymerization of propylene oxide on thermally activated synthetic hydrotalcite, Journal of Catalysis, 130 (1991) 354–358. https://doi.org/10.1016/0021-9517(91)90119-o
Li H., Erinmwingbovo C., Birkenstock J., Schowalter M., Rosenauer A., La Mantia F., Mädler L., Pokhrel S., Double flame-fabricated high-performance $AlPO_4$/$LiMn_2O_4$ cathode material for Li-Ion batteries, ACS Applied Energy Materials, 4 (2021) 4428–4443. https://doi.org/10.1021/acsaem.1c00024
Li H., Pokhrel S., Schowalter M., Rosenauer A., Kiefer J., Mädler L., The gas-phase formation of tin dioxide nanoparticles in single droplet combustion and flame spray pyrolysis, Combustion and Flame, 215 (2020) 389–400. https://doi.org/10.1016/j.combustflame.2020.02.004
Lin S., Zhao Y., Xia T., Meng H., Ji Z., Liu R., George S., Xiong S., Wang X., Zhang H., Pokhrel S., Mädler L., Damoiseaux R., Lin S., Nel A.E., High content screening in zebrafish speeds up hazard ranking of transition metal oxide nanoparticles, ACS Nano, 5 (2011) 7284–7295. https://doi.org/10.1021/nn202116p
Liu C., Pokhrel S., Tessarek C., Li H., Schowalter M., Rosenauer A., Eickhoff M., Li S., Mädler L., Rare-earth-doped $Y_4Al_2O_9$ nanoparticles for stable light-converting phosphors, ACS Applied Nano Materials, 3 (2020) 699–710. https://doi.org/10.1021/acsanm.9b02231
Lovell E.C., Großman H., Horlyck J., Scott J., Mädler L., Amal R., Asymmetrical double flame spray pyrolysis-designed $SiO_2$/$Ce_{0.7}Zr_{0.3}O_2$ for the dry reforming of methane, ACS Applied Materials & Interfaces, 11 (2019) 25766–25777. https://doi.org/10.1021/acsami.9b02572
Mädler L., Kammler H.K., Mueller R., Pratsinis S.E., Controlled synthesis of nanostructured particles by flame spray pyrolysis, Journal of Aerosol Science, 33 (2002) 369–389. https://doi.org/10.1016/s0021-8502(01)00159-8
Manshian B.B., Pokhrel S., Himmelreich U., Tämm K., Sikk L., Fernández A., Rallo R., Tamm T., Mädler L., Soenen S.J., In silico design of optimal dissolution kinetics of Fe-doped ZnO nanoparticles results in cancer-specific toxicity in a preclinical rodent model, Advanced Healthcare Materials, 6 (2017) 1601379. https://doi.org/10.1002/adhm.201601379
Manshian B.B., Pokhrel S., Mädler L., Soenen S.J., The impact of nanoparticle-driven lysosomal alkalinization on cellular functionality, Journal of Nanobiotechnology, 16 (2018) 85. https://doi.org/10.1186/s12951-018-0413-7
Manthiram A., Yu X., Wang S., Lithium battery chemistries enabled by solid-state electrolytes, Nature Reviews Materials, 2 (2017) 16103. https://doi.org/10.1038/natrevmats.2016.103
Marine W., Patrone L., Luk'yanchuk B., Sentis M., Strategy of nanocluster and nanostructure synthesis by conventional pulsed laser ablation, Applied Surface Science, 154–155 (2000) 345–352. https://doi.org/10.1016/s0169-4332(99)00450-x
Marschall R., Semiconductor composites: strategies for enhancing charge carrier separation to improve photocatalytic activity, Advanced Functional Materials, 24 (2014) 2421–2440. https://doi.org/10.1002/adfm.201303214
Meierhofer F., Fritsching U., Synthesis of metal oxide nanoparticles in flame sprays: review on process technology, modeling, and diagnostics, Energy & Fuels, 35 (2021) 5495–5537. https://doi.org/10.1021/acs.energyfuels.0c04054
Meierhofer F., Hodapp M., Achelis L., Buss L., Noriler D., Meier H.F., Fritsching U., Investigation of atomization concepts for large-scale flame spray pyrolysis (FSP), Materialwissenschaft und Werkstofftechnik, 45 (2014) 765–778. https://doi.org/10.1002/mawe.201400314
Meierhofer F., Li H., Gockeln M., Kun R., Grieb T., Rosenauer A., Fritsching U., Kiefer J., Birkenstock J., Mädler L., Pokhrel S., Screening precursor–solvent combinations for $Li_4Ti_5O_{12}$ energy storage material using flame spray pyrolysis, ACS Applied Materials & Interfaces, 9 (2017) 37760–37777. https://doi.org/10.1021/acsami.7b11435
Meng H., Xue M., Xia T., Zhao Y.-L., Tamanoi F., Stoddart J.F., Zink J.I., Nel A.E., Autonomous in vitro anticancer drug release from mesoporous silica nanoparticles by pH-sensitive nanovalves, Journal of the American Chemical Society, 132 (2010) 12690–12697. https://doi.org/10.1021/ja104501a
Meng Y.S., Srinivasan V., Xu K., Designing better electrolytes, Science, 378 (2022) eabq3750. https://doi.org/10.1126/science.abq3750
Minnermann M., Grossmann H.K., Pokhrel S., Thiel K., Hagelin-Weaver H., Bäumer M., Mädler L., Double flame spray pyrolysis as a novel technique to synthesize alumina-supported cobalt Fischer–Tropsch catalysts, Catalysis Today, 214 (2013) 90–99. https://doi.org/10.1016/j.cattod.2013.04.001
Minnermann M., Pokhrel S., Thiel K., Henkel R., Birkenstock J., Laurus T., Zargham A., Flege J.-I., Zielasek V., Piskorska-Hommel E., Falta J., Mädler L., Bäumer M., Role of palladium in iron based Fischer–Tropsch catalysts prepared by flame spray pyrolysis, The Journal of Physical Chemistry C, 115 (2011) 1302–1310. https://doi.org/10.1021/jp106860d
Möller W., Gibson N., Geiser M., Pokhrel S., Wenk A., Takenaka S., Schmid O., Bulgheroni A., Simonelli F., Kozempel J., Holzwarth U., Wigge C., Eigeldinger-Berthou S., Mädler L., Kreyling W.G., Gold nanoparticle aerosols for rodent inhalation and translocation studies, Journal of Nanoparticle Research, 15 (2013) 1574. https://doi.org/10.1007/s11051-013-1574-9
Munnik P., de Jongh P.E., de Jong K.P., Recent developments in the synthesis of supported catalysts, Chemical Reviews, 115 (2015) 6687–6718. https://doi.org/10.1021/cr500486u
Naatz H., Hoffmann R., Hartwig A., La Mantia F., Pokhrel S., Mädler L., Determination of the flat band potential of nanoparticles in porous electrodes by blocking the substrate–electrolyte contact, The Journal of Physical Chemistry C, 122 (2018) 2796–2805. https://doi.org/10.1021/acs.jpcc.7b11423
Naatz H., Lin S., Li R., Jiang W., Ji Z., Chang C.H., Köser J., Thöming J., Xia T., Nel A.E., Mädler L., Pokhrel S., Safe-by-design CuO nanoparticles via Fe-doping, Cu–O bond length variation, and biological assessment in cells and zebrafish embryos, ACS Nano, 11 (2017) 501–515. https://doi.org/10.1021/acsnano.6b06495
Naatz H., Manshian B.B., Rios Luci C., Tsikourkitoudi V., Deligiannakis Y., Birkenstock J., Pokhrel S., Mädler L., Soenen S.J., Model-based nanoengineered pharmacokinetics of iron-doped copper oxide for nanomedical applications, Angewandte Chemie International Edition, 59 (2020) 1828–1836. https://doi.org/10.1002/anie.201912312
Naik A.J.T., Parkin I.P., Binions R., Gas sensing studies of an n-n heterojunction metal oxide semiconductor sensor array based on $WO_3$ and ZnO composites, Sensors, 2013 IEEE, (2013) 1–4. https://doi.org/10.1109/icsens.2013.6688509
Noriler D., Rosebrock C.D., Madler L., Meier H.F., Fritsching U., Influence of atomization and spray parameters on the flame spray process for nanoparticle production, 24 (2014) 495–524. https://doi.org/10.1615/AtomizSpr.2014008559
Parteli E.J.R., Pöschel T., Particle-based simulation of powder application in additive manufacturing, Powder Technology, 288 (2016) 96–102.

https://doi.org/10.1016/j.powtec.2015.10.035
Parteli E.J.R., Schmidt J., Blümel C., Wirth K.-E., Peukert W., Pöschel T., Attractive particle interaction forces and packing density of fine glass powders, Scientific Reports, 4 (2014) 6227. https://doi.org/10.1038/srep06227
Pfeiffer T.V., Feng J., Schmidt-Ott A., New developments in spark production of nanoparticles, Advanced Powder Technology, 25 (2014) 56–70. https://doi.org/10.1016/j.apt.2013.12.005
Piacentini M., Strobel R., Maciejewski M., Pratsinis S.E., Baiker A., Flame-made Pt–Ba/$Al_2O_3$ catalysts: structural properties and behavior in lean-$NO_x$ storage-reduction, Journal of Catalysis, 243 (2006) 43–56. https://doi.org/10.1016/j.jcat.2006.07.005
Pokhrel S., Birkenstock J., Schowalter M., Rosenauer A., Mädler L., Growth of ultrafine single crystalline $WO_3$ nanoparticles using flame spray pyrolysis, Crystal Growth & Design, 10 (2010) 632–639. https://doi.org/10.1021/cg9010423
Pokhrel S., Mädler L., Flame-made particles for sensors, catalysis, and energy storage applications, Energy & Fuels, 34 (2020) 13209–13224. https://doi.org/10.1021/acs.energyfuels.0c02220
Pokhrel S., Nel A.E., Mädler L., Custom-designed nanomaterial libraries for testing metal oxide toxicity, Accounts of Chemical Research, 46 (2013) 632–641. https://doi.org/10.1021/ar300032q
Pokhrel S., Stahl J., Groeneveld J.D., Schowalter M., Rosenauer A., Birkenstock J., Mädler L., Flame aerosol synthesis of metal sulfides at high temperature in oxygen-lean atmosphere, Advanced Materials, 35 (2023) 2211104. https://doi.org/10.1002/adma.202211104
Pöschel T., Schwager T., Computational Granular Dynamics-Models and Algorithms, Springer, Berlin, Heidelberg, New York, 2005, ISBN: 978-3540214854. https://doi.org/10.1007/3-540-27720-x
Pratsinis S.E., Flame aerosol synthesis of ceramic powders, Progress in Energy and Combustion Science, 24 (1998) 197–219. https://doi.org/10.1016/s0360-1285(97)00028-2
Priemel P.A., Grohganz H., Gordon K.C., Rades T., Strachan C.J., The impact of surface- and nano-crystallisation on the detected amorphous content and the dissolution behaviour of amorphous indomethacin, European Journal of Pharmaceutics and Biopharmaceutics, 82 (2012) 187–193. https://doi.org/10.1016/j.ejpb.2012.05.012
Sánchez-Leija R.J., Pojman J.A., Luna-Bárcenas G., Mota-Morales J.D., Controlled release of lidocaine hydrochloride from polymerized drug-based deep-eutectic solvents, Journal of Materials Chemistry B, 2 (2014) 7495–7501. https://doi.org/10.1039/c4tb01407c
Sasikala R., Shirole A., Sudarsan V., Sakuntala T., Sudakar C., Naik R., Bharadwaj S.R., Highly dispersed phase of $SnO_2$ on $TiO_2$ nanoparticles synthesized by polyol-mediated route: photocatalytic activity for hydrogen generation, International Journal of Hydrogen Energy, 34 (2009) 3621–3630. https://doi.org/10.1016/j.ijhydene.2009.02.085
Schauermann S., Nilius N., Shaikhutdinov S., Freund H.-J., Nanoparticles for heterogeneous catalysis: new mechanistic insights, Accounts of Chemical Research, 46 (2013) 1673–1681. https://doi.org/10.1021/ar300225s
Schopf S.O., Hartwig A., Fritsching U., Mädler L., Imbibition into highly porous layers of aggregated particles, Transport in Porous Media, 119 (2017) 119–141. https://doi.org/10.1007/s11242-017-0876-2
Schopf S.O., Salameh S., Mädler L., Transfer of highly porous nanoparticle layers to various substrates through mechanical compression, Nanoscale, 5 (2013) 3764–3772. https://doi.org/10.1039/c3nr34235b
Schubert M., Pokhrel S., Thomé A., Zielasek V., Gesing T.M., Roessner F., Mädler L., Bäumer M., Highly active Co–$Al_2O_3$-based catalysts for $CO_2$ methanation with very low platinum promotion prepared by double flame spray pyrolysis, Catalysis Science & Technology, 6 (2016) 7449–7460. https://doi.org/10.1039/c6cy01252c
Shi S., Russell T.P., Nanoparticle assembly at liquid–liquid interfaces: from the nanoscale to mesoscale, Advanced Materials, 30 (2018) 1800714. https://doi.org/10.1002/adma.201800714
Shimizu Y., Nakashima N., Hyodo T., Egashira M., $NO_x$ sensing properties of varistor-type gas sensors consisting of micro p-n junctions, Journal of Electroceramics, 6 (2001) 209–217. https://doi.org/10.1023/A:1011448513611
Stahl J., Ilsemann J., Pokhrel S., Schowalter M., Tessarek C., Rosenauer A., Eickhoff M., Bäumer M., Mädler L., Comparing co-catalytic effects of $ZrO_x$, $SmO_x$, and Pt on $CO_x$ methanation over Co-based catalysts prepared by double flame spray pyrolysis, ChemCatChem, 13 (2021) 2815–2831. https://doi.org/10.1002/cctc.202001998
Stark W.J., Maciejewski M., Mädler L., Pratsinis S.E., Baiker A., Flame-made nanocrystalline ceria/zirconia: structural properties and dynamic oxygen exchange capacity, Journal of Catalysis, 220 (2003) 35–43. https://doi.org/10.1016/S0021-9517(03)00235-5
Strobel R., Mädler L., Piacentini M., Maciejewski M., Baiker A., Pratsinis S.E., Two-nozzle flame synthesis of Pt/Ba/$Al_2O_3$ for $NO_x$ storage, Chemistry of Materials, 18 (2006) 2532–2537. https://doi.org/10.1021/cm0600529
Sun B., Pokhrel S., Dunphy D.R., Zhang H., Ji Z., Wang X., Wang M., Liao Y.-P., Chang C.H., Dong J., Li R., Mädler L., Brinker C.J., Nel A.E., Xia T., Reduction of acute inflammatory effects of fumed silica nanoparticles in the lung by adjusting silanol display through calcination and metal doping, ACS Nano, 9 (2015) 9357–9372. https://doi.org/10.1021/acsnano.5b03443
Sun B., Wang X., Liao Y.-P., Ji Z., Chang C.H., Pokhrel S., Ku J., Liu X., Wang M., Dunphy D.R., Li R., Meng H., Mädler L., Brinker C.J., Nel A.E., et al., Repetitive dosing of fumed silica leads to profibrogenic effects through unique structure–activity relationships and biopersistence in the lung, ACS Nano, 10 (2016) 8054–8066. https://doi.org/10.1021/acsnano.6b04143
Tabrizi N.S., Xu Q., van der Pers N.M., Lafont U., Schmidt-Ott A., Synthesis of mixed metallic nanoparticles by spark discharge, Journal of Nanoparticle Research, 11 (2009) 1209–1218. https://doi.org/10.1007/s11051-008-9568-8
Takenaka S., Möller W., Semmler-Behnke M., Karg E., Wenk A., Schmid O., Stoeger T., Jennen L., Aichler M., Walch A., Pokhrel S., Mädler L., Eickelberg O., Kreyling W.G., Efficient internalization and intracellular translocation of inhaled gold nanoparticles in rat alveolar macrophages, Nanomedicine, 7 (2012) 855–865. https://doi.org/10.2217/nnm.11.152
Teoh W.Y., Denny F., Amal R., Friedmann D., Mädler L., Pratsinis S.E., Photocatalytic mineralisation of organic compounds: a comparison of flame-made $TiO_2$ catalysts, Topics in Catalysis, 44 (2007) 489–497. https://doi.org/10.1007/s11244-006-0096-4
Teoh W.Y., Mädler L., Beydoun D., Pratsinis S.E., Amal R., Direct (one-step) synthesis of $TiO_2$ and Pt/$TiO_2$ nanoparticles for photocatalytic mineralisation of sucrose, Chemical Engineering Science, 60 (2005) 5852–5861. https://doi.org/10.1016/j.ces.2005.05.037
Topic N., Pöschel T., Steepest descent ballistic deposition of complex shaped particles, Journal of Computational Physics, 308 (2016) 421–437. https://doi.org/10.1016/j.jcp.2015.12.052
Ulrich G.D., Subramanian N.S., III. Coalescence as a rate-controlling process, Combustion Science and Technology, 17 (1977) 119–126. https://doi.org/10.1080/00102207708946822
Voloshko A., Colombier J.-P., Itina T.E., Comparison of laser ablation with spark discharge techniques used for nanoparticle production, Applied Surface Science, 336 (2015) 143–149. https://doi.org/10.1016/j.apsusc.2014.10.077
Wang F., Harindintwali J.D., Yuan Z., Wang M., Wang F., Li S., Yin Z., Huang L., Fu Y., Li L., Chang S.X., Zhang L., Rinklebe J., Yuan Z., Zhu Q., et al., Technologies and perspectives for achieving carbon neutrality, The Innovation, 2 (2021) 100180. https://doi.org/10.1016/j.xinn.2021.100180
Wang H., Adeleye A.S., Huang Y., Li F., Keller A.A., Heteroaggregation of nanoparticles with biocolloids and geocolloids, Advances in Colloid and Interface Science, 226 (2015) 24–36. https://doi.org/10.1016/j.cis.2015.07.002
Wang Z., Pokhrel S., Chen M., Hunger M., Mädler L., Huang J., Palladium-doped silica–alumina catalysts obtained from double-flame FSP for chemoselective hydrogenation of the model aromatic ketone acetophenone, Journal of Catalysis, 302 (2013) 10–19. https://doi.org/10.1016/j.jcat.2013.02.017
Wu W., Chen K., Tsotsas E., Prediction of particle mixing time in a rotary drum by 2D DEM simulations and cross-correlation, Advanced Powder Technology, 33 (2022) 103512. https://doi.org/10.1016/j.apt.2022.103512
Xiao J., Kuc A., Pokhrel S., Mädler L., Pöttgen R., Winter F., Frauenheim

T., Heine T., Fe-doped ZnO nanoparticles: the oxidation number and local charge on iron, studied by $^{57}$Fe Mößbauer Spectroscopy and DFT calculations, Chemistry – A European Journal, 19 (2013) 3287–3291. https://doi.org/10.1002/chem.201204308

Xiao J., Kuc A., Pokhrel S., Schowalter M., Parlapalli S., Rosenauer A., Frauenheim T., Mädler L., Pettersson L.G.M., Heine T., Evidence for $Fe^{2+}$ in wurtzite coordination: iron doping stabilizes ZnO nanoparticles, Small, 7 (2011) 2879–2886. https://doi.org/10.1002/smll.201100963

Yu J., Sun X., Tong X., Zhang J., Li J., Li S., Liu Y., Tsubaki N., Abe T., Sun J., Ultra-high thermal stability of sputtering reconstructed Cu-based catalysts, Nature Communications, 12 (2021) 7209. https://doi.org/10.1038/s41467-021-27557-1

Yu Z., Chen X.-Q., Kang X., Xie Y., Zhu H., Wang S., Ullah S., Ma H., Wang L., Liu G., Ma X., Cheng H.-M., Noninvasively modifying band structures of wide-Bandgap metal oxides to boost photocatalytic activity, Advanced Materials, 30 (2018) 1706259. https://doi.org/10.1002/adma.201706259

Zhang H., Ji Z., Xia T., Meng H., Low-Kam C., Liu R., Pokhrel S., Lin S., Wang X., Liao Y.-P., Wang M., Li L., Rallo R., Damoiseaux R., Telesca D., et al., Use of metal oxide nanoparticle band gap to develop a predictive paradigm for oxidative stress and acute pulmonary inflammation, ACS Nano, 6 (2012) 4349–4368. https://doi.org/10.1021/nn3010087

Zhang H., Pokhrel S., Ji Z., Meng H., Wang X., Lin S., Chang C.H., Li L., Li R., Sun B., Wang M., Liao Y.-P., Liu R., Xia T., Mädler L., et al., PdO doping tunes band-gap energy levels as well as oxidative stress responses to a $Co_3O_4$ *p*-type semiconductor in cells and the lung, Journal of the American Chemical Society, 136 (2014) 6406–6420. https://doi.org/10.1021/ja501699e

Zhang Z., Tang W., Neurock M., Yates J.T., Jr., Electric charge of single Au atoms adsorbed on $TiO_2$(110) and associated band bending, The Journal of Physical Chemistry C, 115 (2011) 23848–23853. https://doi.org/10.1021/jp2067809

Zhang Z., Yates J.T., Jr., Band bending in semiconductors: chemical and physical consequences at surfaces and interfaces, Chemical Reviews, 112 (2012) 5520–5551. https://doi.org/10.1021/cr3000626

Zou Z., Li Y., Lu Z., Wang D., Cui Y., Guo B., Li Y., Liang X., Feng J., Li H., Nan C.-W., Armand M., Chen L., Xu K., Shi S., Mobile ions in composite solids, Chemical Reviews, 120 (2020) 4169–4221. https://doi.org/10.1021/acs.chemrev.9b00760

## Authors' Short Biographies

**Dr. Suman Pokhrel** is a "Privatdozent" at the Department of Production Engineering, University of Bremen. His research interests include designing oxide/sulfide nanostructured materials using flame spray pyrolysis (FSP) for various physicochemical applications. His innovative re-engineering of nanoparticles has created cutting-edge research within the nanotechnology field worldwide. Dr. Pokhrel was awarded the Jawaharlal Nehru prize in 2000, the George Forster award of the Alexander von Humboldt foundation in 2006, the JSPS award in 2008, and the Habilitation (Venia Legendi) award in 2016 by the Department of Production Engineering, University of Bremen, for his outstanding contribution in research and teaching.

**Prof. Lutz Mädler** is a Professor in the Department of Production Engineering and Director of the Leibniz Institute for Materials Science, University of Bremen, Germany. His research includes particle synthesis in the gas phase, catalytic properties, and bio-nano-interactions and has significant contributions in many academic and industrial laboratories worldwide. Prof. Mädler has been the recipient of many awards such as the BASF Award 2004 in Process Engineering, the SMOLUCHOWSKI Award 2005, the DECHEMA Award 2009 (highest award in Chemical Engineering in Germany), and the Leibniz Award 2017. Prof. Mädler is a member of the German Academy of Science and Engineering (acatech).

**Prof. Udo Fritsching** leads the research group "Multiphase Flow, Heat and Mass Transfer" at the Leibniz Institute for Materials Science, Bremen, Germany, and is a Professor in the Department of Production Engineering at the University of Bremen, Germany. His research interests include multiphase flow, particle technology, atomization, and sprays as well as computational multiphase fluid dynamics and particle and process measurement techniques. Prof. Fritsching serves as the president of ILASS Europe (Institute of Liquid Atomization and Spray Systems) and the chairman of the Multiphase Flow group within VDI/Dechema. He is also a delegate to the Multiphase Flow Working Party of EFCE (European Federation Chemical Engineering).

KONA Powder and Particle Journal

KONA Powder and Particle Journal No. 42 (2025) 188–199/https://doi.org/10.14356/kona.2025013 Review Paper

# Perspectives on Particle Design Strategies for Better Inactivation of Airborne Pathogens†

**Mohaiminul Haider Chowdhury$, Zan Zhu$ and Wei-Ning Wang***

*College of Engineering, Virginia Commonwealth University, USA*

Airborne pathogens such as bacteria, viruses and fungi pose significant threats to human health. Various mitigation strategies have been developed, including air filtration, ventilation, UV irradiation, and photocatalytic oxidative disinfection (POD). In particular, the combination of passive air filtration and active POD has promise for the better inactivation of airborne pathogens. However, the efficiency of POD remains hindered by numerous factors, such as inherent fast charge recombination, limited understanding of the interactions between airborne pathogens and catalyst surfaces, and short migration distances of reactive oxygen species (ROS). This perspective elucidates the fundamental principles and constraints of POD and provides several examples for delineating enhancement strategies. The primary objective of this study is to cultivate a cellular-level understanding of the interactions occurring at the biointerfaces in POD systems, thereby revealing the mechanistic pathways and paving the way for future catalyst designs to improve air quality.

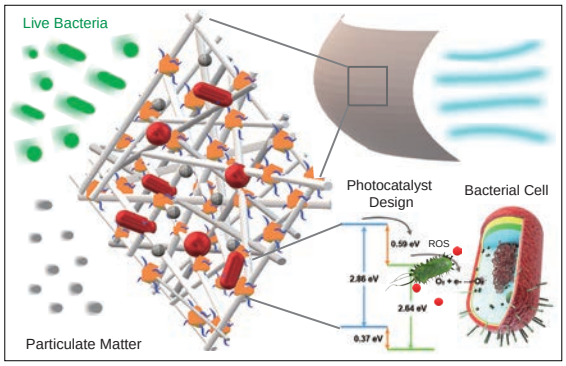


**Keywords:** air filtration, COVID, airborne pathogens, photocatalysis, disinfection

## 1. Introduction

The World Health Organization (WHO) reports that indoor air pollution causes 3.8 million deaths worldwide each year (Balmes, 2019). Indoor air quality, therefore, has increasingly become an alarming concern within the scientific community due to the growing health impacts such as cancer, asthma, and bronchitis, induced by poor air quality (Balakrishnan et al., 2014; Burnett et al., 2014). Indoor air pollutants include particulate matter (PM), volatile inorganic compounds (VIC), and volatile organic compounds (VOC) (Gonzalez-Martin et al., 2021). Of particular concern are airborne pathogens, which are a unique component of PM. They are clustered into three major groups: bacteria, fungi, and viruses (Song et al., 2022). Different airborne pathogens can cause a plethora of diseases, such as common colds, flu, asthma, anthrax, tuberculosis, botulism, and pneumonia (Bhardwaj et al., 2021; Xu Z.Q. et al., 2012) (see **Table 1**).

The recent COVID-19 pandemic was also caused by the airborne SARS-CoV-2 virus, which can spread through airborne transmission. This global health crisis underscored the critical importance of air biosecurity, as the transmission of the SARS-CoV-2 virus through respiratory droplets and aerosol particles emerged as the primary mode of spread (Guo et al., 2023; Vlaskin, 2022).

Over the years, strategies for controlling airborne pathogens have been developed and are generally classified based on two fundamental principles: capture and inactivation, as depicted in **Fig. 1**.

Among these strategies, air filtration using HVAC filters and face masks is the most viable tool to control air quality, protecting people from inhaling PM and airborne pathogens. However, although most commercial filters can capture airborne pathogens on their surfaces, they cannot inactivate them, posing a risk of secondary contamination under high airflow.

In particular, bio-contaminated surfaces in hospital buildings, equipment, and even personal protective equipment (PPE) are considered sources of secondary contamination, leading to hospital-acquired infections (HAI), also known as health-associated infections (Magill et al., 2014; Peleg and Hooper, 2010). Effective disinfection strategies are crucial to prevent these transmissions. Typically, harsh chemicals, e.g., chlorine dioxide and ethylene oxide are used, which, however, are often associated with several adverse effects (Hubbard et al., 2009). Ultraviolet (UV) sterilization by direct UV-C irradiation is also employed, but this involves severe occupational risks (Kühn et al., 2003; Walker and Ko, 2007). Among these control

† Received 29 May 2024; Accepted 17 June 2024
J-STAGE Advance published online 10 August 2024
$ Authors contributed equally to this publication
* Corresponding author: Wei-Ning Wang;
Add: 401 W. Main St., Richmond, Virginia 23284, USA
E-mail: wnwang@vcu.edu
TEL: +1-804-827-4306 FAX: +1-804-827-7030

**Table 1** Airborne pathogens and associated health risks.

| Species | Airborne pathogens (Microorganisms) | Health impacts |
|---|---|---|
| Bacteria (Gram-Negative) | *Escherichia coli* | Gastroenteritis; abdominal cramps; diarrhea; vomiting |
| | *Pseudomonas fluorescens* | Septicemia |
| | *Legionella pneumophila* | Pneumonia; pulmonary infections; influenza |
| Bacteria (Gram-Positive) | *Staphylococcus epidermidis* | Food poisoning |
| | *Staphylococcus aureus* | Septicemia; endocarditis; meningitis; osteomyelitis |
| | *Micrococcus luteus* | Endocarditis; meningitis |
| | *Mycobacterium* | Tuberculosis |
| Fungi | *Aspergillus versicolor* | Gastroenteritis; abdominal cramps; diarrhea; vomiting |
| | *Aspergillus niger* | Ear infections; sore throat; bronchitis; skin infections |
| | *Penicillium citrinum* | Renal tumors |
| | *Penicillium spinulosum* | Septicemia |
| Viruses | Measles virus | Measles |
| | *NWS/G70C (H11N9)* | Pneumonia; pulmonary infections; influenza |
| | *Norovirus* | Gastroenteritis; abdominal cramps; diarrhea; vomiting |
| | *Adenovirus* | Ear, respiratory tract, gastrointestinal, and liver infections |
| | Varicella-zoster virus | Chickenpox |

Source: (Bhardwaj et al., 2021; Xu Z.Q. et al., 2012)

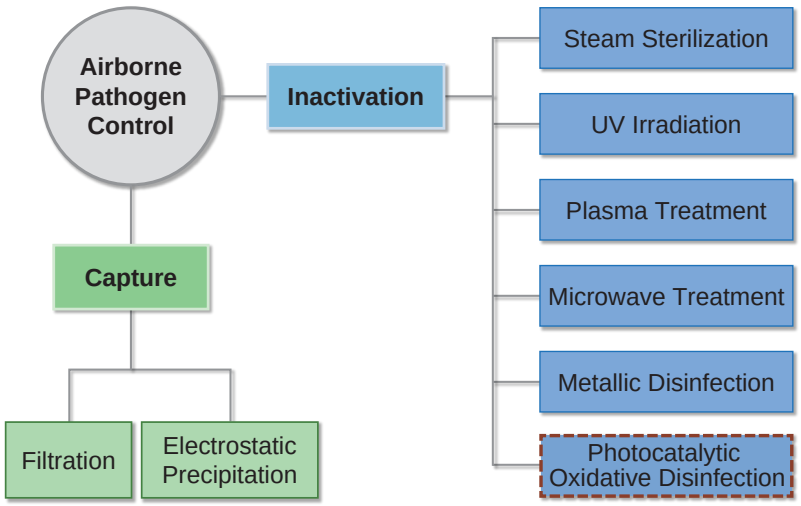


**Fig. 1** Classification of various techniques for controlling airborne pathogens.

strategies, photocatalytic oxidative disinfection (POD) using catalyst particles has emerged as an efficient, cost-effective, environmentally sustainable approach (Hodges et al., 2018; Wang H.L. et al., 2014; Yu J.C. et al., 2005). Notably, combining passive air filtration and active POD may be a promising strategy for capturing airborne pathogens and simultaneously killing them *in situ*.

However, the POD efficiency remains low and is plagued by many factors, such as inherent fast charge recombination, limited understanding of the interactions between the captured pathogen cells and catalyst surface, and short migration distances (also times) of reactive oxygen species (ROS). The rational design of photocatalyst particles by addressing the constraints of the POD technique is thus essential.

In this perspective, we introduce the fundamental principles and constraints of the POD technique and provide several examples to delineate enhancement strategies. We used bacteria as the model airborne pathogens and metal-organic frameworks (MOFs) (Furukawa et al., 2013; Li P. et al., 2019) as supporting materials for efficient catalyst particle design. The primary objective of this study is

to cultivate a cellular-level understanding of the interactions occurring at the biointerfaces in POD systems, thereby revealing the mechanistic pathways and paving the way for future catalyst designs to improve air quality.

## 2. Principles and limitations of photocatalytic oxidative disinfection

Photocatalytic oxidative disinfection (POD) is a promising technology for killing airborne pathogens. In the POD system, the photocatalytic surface is activated by light to generate charge carriers, i.e., electron and hole pairs (**Fig. 2**) (Chen F.N. et al., 2010; Kim et al., 2021; Kumar et al., 2020; Li P. et al., 2019; Nosaka Y. and Nosaka A.Y., 2017; Shi et al., 2020; Wang W.J. et al., 2013).

Taking a water-based POD system as an example, these excited charge carriers react with water or oxygen molecules to form various reactive oxygen species (ROS), such as $\bullet O_2^-$, $^1O_2$, •OH, $\bullet O^-$, and $\bullet OO^-$ (Nosaka Y. and Nosaka A.Y., 2017). When a bacterial cell comes in contact with the photocatalytic surface through different forces such as electrostatic attraction, hydrophobic interactions, van der Waals forces, and receptor-ligand interactions, these ROS impact the bacterial cell membrane and also affect cell metabolism (Regmi et al., 2018). Consequently, these ROS damage bacterial cells, including the cell wall and intracellular components such as proteins, DNA, and lipids (**Fig. 3**) (Shi et al., 2020; You et al., 2019; Zeng et al., 2017). The proposed reactions for representative ROS formation and associated bacterial inactivation are described below (Regmi et al., 2018):

$$\text{Photocatalyst} + h\upsilon \rightarrow h^+ + e^-$$
$$h^+ + H_2O \rightarrow \bullet OH + H^+$$
$$h^+ + OH^- \rightarrow \bullet OH$$
$$e^- + O_2 \rightarrow \bullet O_2^- \xrightarrow{2H^+} H_2O_2 \xrightarrow{e^-} \bullet OH + OH^-$$
$$\bullet OH + \text{pathogen} + O_2 \rightarrow \text{simpler products (salts, } H_2O\text{, etc.)}$$

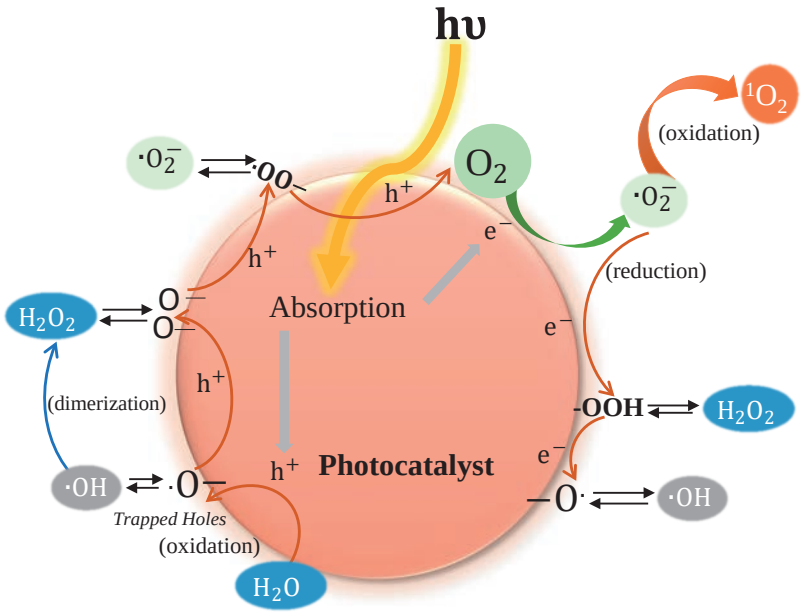


**Fig. 2** Mechanism of ROS generation in the presence of light.

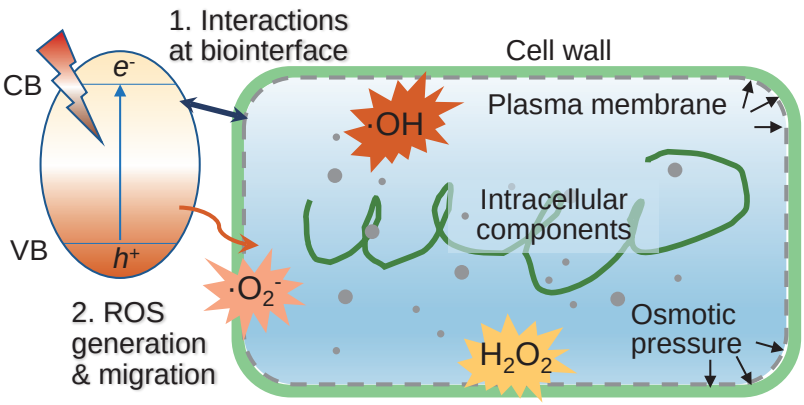


**Fig. 3** Interactions between bacterial cells and photogenerated ROS at the biointerface.

**Table 2** Half-life and migration distance of ROS.

| ROS | Half-life time ($t_{1/2}$) | Migration distance |
|---|---|---|
| Superoxide ($\bullet O_2^-$) | 1–4 μs | 30 nm |
| Singlet Oxygen ($^1O_2$) | 1–4 μs | 30 nm |
| Hydroxyl radicals (•OH) | 1 μs | 1 nm |
| Hydrogen Peroxide ($H_2O_2$) | 1 ms | 1 μm |

Despite being a promising antimicrobial strategy, the POD system is inefficient. The major challenge in this system is the rapid electron–hole ($e^-$–$h^+$) recombination, which typically occurs within nanoseconds, two or three orders of magnitude faster than other charge transfer processes (Fujishima et al., 2008; Hoffmann et al., 1995). Over the past decades, constant efforts have been made to address this critical issue and improve the overall POD efficiency by developing strategies such as incorporating metal sinks and creating heterojunctions (Ahmad et al., 2023; Linsebigler et al., 1995; Serpone and Emeline, 2012).

However, in a typical POD system, ROS are generated on the photocatalyst surface, typically with very short half-life times ($t_{1/2}$) and migration distances (see **Table 2**).

The short lifespans and migration distances of photogenerated ROS often result in their degradation into less potent species before they reach bacterial cells. Consequently, the efficacy of bacterial inactivation is heavily dependent on the overall ROS concentration in the system. For instance, despite being 100 times more potent than $\bullet O_2^-$ and $H_2O_2$, •OH does not achieve its full antimicrobial capability as it has a significantly shorter migration distance compared to others, which restricts overall bactericidal efficacy (Das and Roychoudhury, 2014; Kusiak-Nejman and Morawski, 2019; Nasir et al., 2021).

In addition, bacterial cells are rich in carboxylic and phosphate groups, rendering them negatively charged. This often results in electrical repulsion, preventing bacterial adhesion on the catalytic surface of most metal oxide-based photocatalysts, which are also negatively charged due to the presence of hydroxyl groups. In such scenarios, antimicrobial activity depends on ROS diffusion and penetration into the bacterial cells (Cho et al., 2004). Therefore, the distance between the bacterial cell and catalyst surface can be reduced to further enhance the POD efficiency.

## 3. Particle design strategies

In this perspective, we present specific particle design strategies to address the aforementioned limitations by using metal-organic frameworks (MOFs) and quaternary ammonium compounds (QAC) as model materials. As emerging porous polymers, MOFs exhibit exceptionally high surface areas, rich surface chemistry, and tunable porous structures, making them well-suited for a range of catalytic applications (Jiao et al., 2019; Li D. et al., 2024; Yusuf et al., 2022). Conversely, QAC compounds are widely known for their antibacterial properties due to factors such as low toxicity, structural flexibility, ease of surface fixation, and minimal risk of antibiotic resistance (Ping et al., 2019; Sun et al., 2020; Zander et al., 2018; Zhang et al., 2020). The $N^+$ in QAC electrostatically attracts negatively charged bacterial cells, which ultimately leads to cell lysis (Jennings et al., 2015; Wilson et al., 2001).

Based on these considerations, we implemented two strategies to develop MOF-based particles with QAC coatings, addressing the challenges of shorter ROS lifespan, shorter migration distance, and greater charge-carrier recombination. First, we developed a self-decontaminating nanofibrous filter (UiO-PQDMAEMA@PAN) for enhanced ROS interaction with bacterial cells (Zhu et al., 2021), where UiO refers to a zirconium-based MOF, PQDMAEMA refers to poly[2-(dimethyl decyl ammonium) ethyl methacrylate], and PAN indicates polyacrylonitrile. Second, we rationally designed heterojunction photocatalyst particles by modulating the surface of $g$-$C_3N_4$/MIL-125-$NH_2$ with a positive QAC layer (QAC@$g$-$C_3N_4$/MIL-125-$NH_2$) (Zhu et al., 2023). Here, $g$-$C_3N_4$ is a two-dimensional semiconductor, and MIL-125-$NH_2$ is a titanium-based MOF (Li P. et al., 2019; Ong et al., 2016; Zhou et al., 2020). This design aims to improve its affinity for bacterial cells and enhance electron–hole separation. The details of the design strategies and antimicrobial performance of the two materials are explained here.

### 3.1 UiO-PQDMAEMA@PAN filter

***Synthesis of nanofibers.*** The entire synthesis route of the UiO-PQDMAEMA@PAN filter is schematically illustrated in **Figs. 4(a)** and **4(b)**. Initially, UiO-PQDMAEMA particles were prepared using UiO-66-$NH_2$ as the base material, which was then decorated with 2-bromoisobutyryl bromide (BIBB) to form UiO-66-BIBB. Next, using the atomic transfer radical polymerization (ATRP) method, the monomer 2-(dimethyl decyl ammonium) ethyl methacrylate (QDMAEMA) was polymerized and grafted onto the surface of UiO-66-BIBB to obtain UiO-PQDMAEMA.

The antibacterial nanofibrous filter was then fabricated through a facile electrospinning process by embedding UiO-PQDMAEMA particles in polyacrylonitrile (PAN) polymers. By varying parameters such as concentration, particle/polymer ratio, temperature, and relative humidity (RH), a range of nanofibers can be prepared.

***Optimization of the nanofibers.*** In a typical electrospinning process, a well-mixed polymer solution of filler particles is generally used, resulting in a uniform distribution of filler particles within the polymer backbone in the final

nanofibers (Zhang et al., 2016). However, this homogenous structure is undesirable because it limits the catalytic performance of the embedded particles. To fully exploit the antimicrobial properties of UiO-PQDMAEMA, the particles must be exposed to the fiber surface.

To address this issue, an engineered strategy was implemented. The diameter of the PAN fiber backbone was optimized to be smaller than that of the UiO-PQDMAEMA particles ($d \cong 213$ nm). This optimization was based on understanding the fiber scaling law in electrospinning, where the equilibrium between the liquid's surface tension and the repellent electrostatic force determines the terminal fiber diameter (Schaate et al., 2011):

$$d_f \sim \left(\gamma \frac{Q^2}{I^2}\right)^{\frac{1}{3}} w_p^{\frac{1}{2}} \quad (1)$$

Here, $Q$ is the feeding flowrate, $I$ is the electric current in the system, $w_p$ is the polymer volume fraction, and $\gamma$ is the surface tension of the polymer solution, which can be expressed as follows (Xiao et al., 2017):

$$\gamma = \gamma^0 \left(1 - \frac{T}{T_c}\right)^n \quad (2)$$

where $\gamma^0$ is the constant of each liquid, $n$ is a positive empirical factor, $T_c$ is the critical temperature and $T$ is the working temperature. According to **Eqn. (1)**, a decrease in $\gamma$ will decrease the terminal fiber diameter. In this study, we rationally increased the working temperature of the polymer solution to reduce the surface tension while keeping $Q$, $I$, and $w_p$ constant. The relative humidity (RH) was maintained as low as 10 % to facilitate the production of thinner fibers because a lower RH aids solvent evaporation (Xu J.W. et al., 2015). As shown in **Fig. 4(c)**, the pure PAN fibers have smooth surfaces and an average diameter of ~139 nm. The morphology of the UiO-PQDMAEMA@PAN filter was much rougher, with UiO-PQDAMEMA particles distributed on the fiber surface (**Fig. 4(d)**). This arrangement allows PQDMAEMA particles to come into direct contact with more bacterial cells.

***Particle and Bacterial Filtration Tests.*** The experimental setup of the filtration tests is illustrated in **Fig. 5**. The particle filtration tests were conducted based on the international standard (ISO 21083-1, 2018) using monodispersed NaCl as model particles. The system includes an atomizer to generate NaCl particles, a $Po^{210}$ neutralizer to achieve Boltzmann equilibrium during charging (Tang et al., 2018), a differential mobility analyzer (DMA, Model 3082, TSI Inc.) to select specific particle sizes, and a filter system

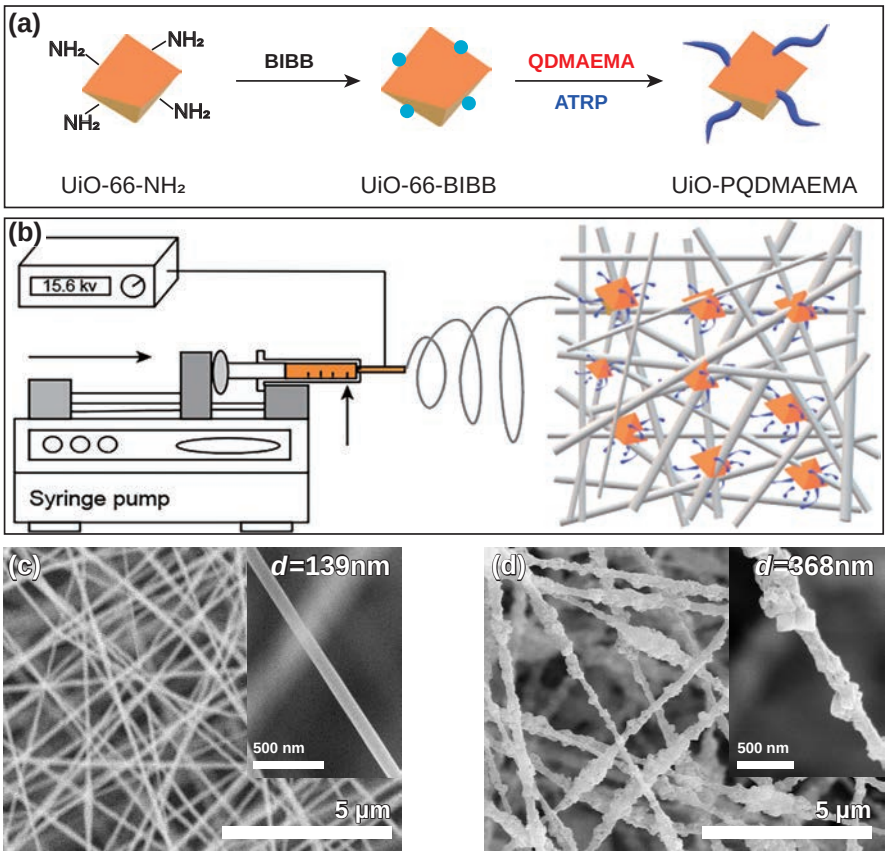


**Fig. 4** **(a)** Synthesis route for UiO-PQDMAEMA from UiO-66-$NH_2$, **(b)** Schematic electrospinning process for nanofiber fabrication, **(c)** SEM image of pure PAN fibers, **(d)** SEM image of UiO-PQDMAEMA@PAN fibers. Reprinted with permission from Ref. (Zhu Z. et al., 2021). Copyright: (2021) The Royal Society of Chemistry.

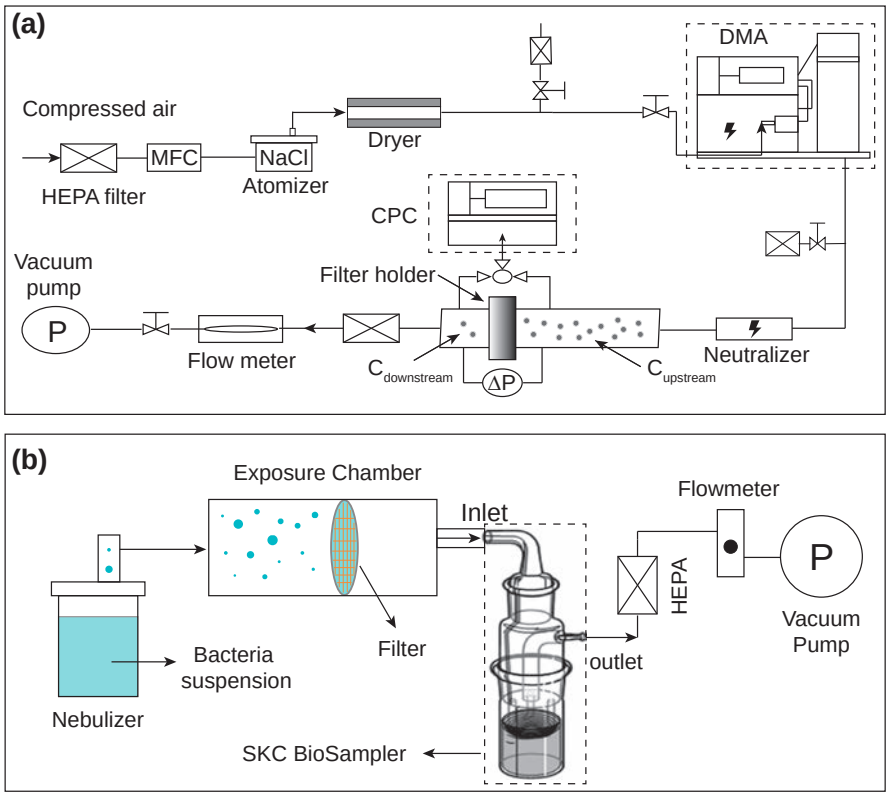


**Fig. 5** Schematic diagram of experimental setup for **(a)** particle and **(b)** bacteria filtration tests. Reprinted with permission from Ref. (Zhu Z. et al., 2021). Copyright: (2021) The Royal Society of Chemistry.

(**Fig. 5(a)**). The particle filtration efficiency was calculated from **Eqn. (3)** using the upstream and downstream particle number concentrations measured using an ultrafine condensation particle counter (UCPC, Model 3776, TSI Inc.). The same calculation was performed using a commercial N95 respirator (VWR Makrite®) for comparison.

$$PFE\,(\%) = \left(1 - \frac{C_{\text{downstream}}}{C_{\text{upstream}}}\right) \times 100\% \tag{3}$$

Filtration tests for *S. epidermidis* (Gram-positive) and *E. coli* (Gram-negative) bacteria were conducted as shown in **Fig. 5(b)**. The bacteria cells were first suspended in phosphate-buffered saline (PBS) solution at a density of $10^7$ CFU/mL. An ultrasonic nebulizer (2.4 MHz) was used to atomize the suspension. The generated bioaerosols were bombarded onto the filter surface at a flow rate of 12.5 L/min for 1 min. The escaped bioaerosols were collected in a sterile PBS solution using a BioSampler (SKC Inc.). **Eqn. (4)** defines the bacterial filtration efficiency (*BFE*) of the filter.

$$BFE = \left[\left(1 - \frac{C_{\text{f}}}{C_{\text{total}}}\right)\right] \times 100\% \tag{4}$$

where $C_{\text{f}}$ and $C_{\text{total}}$ are the bacteria concentrations in the BioSampler with and without a filter, respectively.

As shown in **Fig. 6(a)**, the particle filtration efficiency decreased until it approached the most penetrating particle size (MPPS), which was approximately 80 nm. The efficiency of the UiO-PQDMAEMA@PAN filter in measuring 80 nm PM was found to be ~95.4 %, which is comparable to the conventional N95 respirator standard in terms of PM filtration.

The hierarchical structures within the electrospun fibers of the UiO-PQDMAEMA@PAN filter likely contributed to its superior filtering performance when tested under the same pressure drop (52.3 Pa) as pure PAN filters (Chang et al., 2016), where more active sites for interaction between particles and composite electrospun fibers are available (Chen S.C. et al., 2014).

Another crucial parameter of mask filters is the pressure drop ($\Delta P$), which affects user comfort. The quality factor (*QF*) is used to measure the pressure drop performance of a filter, which is defined as follows:

$$QF = \frac{\ln(1 - PFE)}{\Delta P} \tag{5}$$

As shown in **Fig. 6(b)**, the UiO-PQDMAEMA@PAN fibers exhibit satisfactory *QFs* that are substantially better than those of pure PAN fibers. The minimal *QF* value of 0.058 at an MPPS of 80 nm for the UiO-PQDMAEMA@PAN filter indicates again that its peak filtration performance is comparable to that of commercial N95 respirators (0.056).

In contrast to the particle filtration results, all atomized

bacterial cells were captured using a UiO-PQDMAEMA@PAN filter and a commercial N95 respirator (Zhu et al., 2021). This is expected because bacterial cells typically have sizes in the range of 0.5 to 2 μm, which is much larger than the MPPS of the filter, i.e., 80 nm, as discussed above.

***Bactericidal Evaluation.*** In addition to filtration measurements, bacterial inactivation experiments were conducted. As shown in **Figs. 6(c)** and **6(d)**, the UiO-PQDMAEMA filters outperformed all other control filters, achieving an inactivation efficiency of ~97.4 % for *S. epidermidis* and ~95.1 % for *E. coli*. This indicates that the grafted UiO-PQDMAEMA on the surface of the PAN fibers allows the filter to exhibit efficient bactericidal behavior. Numerous contacting sites of positively charged UiO-PQDMAEMA ($N^+$) are responsible for capturing and killing bacterial cells *in situ* by lysing their cytoplasm (Gozzelino et al., 2013).

## 3.2 QAC@ g-$C_3N_4$/MIL-125-$NH_2$ particles

***Synthesis of photocatalysts.*** The heterojunction QAC@*g*-$C_3N_4$/MIL-125-$NH_2$ (C-M-Q) photocatalyst particles were synthesized in several steps, as shown in **Fig. 7**.

The bare catalyst particles *g*-$C_3N_4$/MIL-125-$NH_2$ (C-M) were first synthesized by a solvothermal method in which pre-synthesized *g*-$C_3N_4$ was suspended in the MIL-125-$NH_2$ precursor. The mixture was then heated in a Teflon-lined steel autoclave at 150 °C for 15 h (Wang H. et al., 2015). The C-M particles were then coated with QAC, where the QDMAEMA monomer was polymerized and grafted on the surface of C-M through ATRP (Hippeli and Elstner, 1997) to obtain QAC@*g*-$C_3N_4$/MIL-125 (C-M-Q) particles.

***Photocatalytic performance.*** Synthesizing heterojunction semiconductor catalysts with proper band gap alignment is a promising approach to mitigate rapid charge recombination, i.e., better $e^-$–$h^+$ separation to enhance photocatalytic performance (Hippeli and Elstner, 1997).

The band alignment between *g*-$C_3N_4$ and MIL-125-$NH_2$ was determined following the Kraut method (Kraut et al., 1980; Zhao et al., 2019) using X-ray photoelectron spectroscopy (XPS) and UV-Vis spectroscopy. As illustrated in **Fig. 8(a)**, the enhanced charge transfer within the heterojunction was achieved.

Bacterial inactivation experiments were conducted in PBS solution under visible light irradiation with *S. epidermidis*, which was selected as the representative bacterium for the POD tests. As shown in **Fig. 8(b)**, the bare photocatalyst C-M exhibited an unnoticeable reduction of bacterial cells in the dark, whereas under light irradiation, it achieved a 1.5 log reduction, suggesting that the

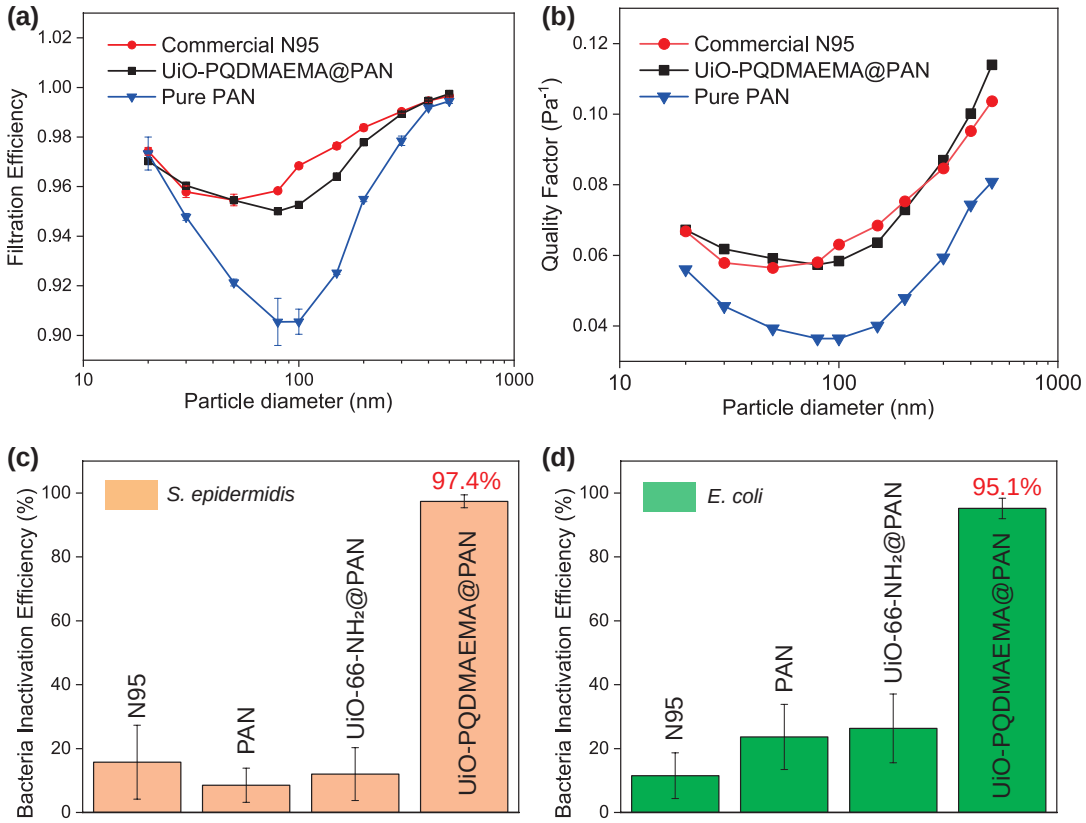


**Fig. 6** **(a)** Particle filtration efficiency and **(b)** quality factor of different filters tested using NaCl particles of 20–500 nm at a face velocity of 9.3 cm/s; the inactivation performance of different filters toward **(c)** *S. epidermidis* and **(d)** *E. coli*. Reprinted with permission from Ref. (Zhu Z. et al., 2021). Copyright: (2021) The Royal Society of Chemistry.

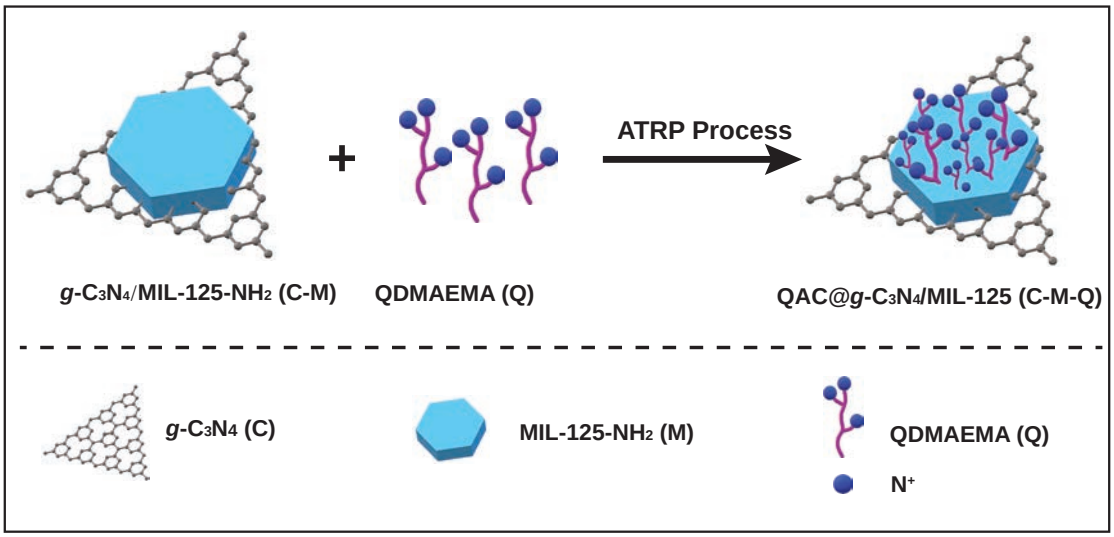


**Fig. 7** Synthesis of QAC@$g$-$C_3N_4$/MIL-125 (C-M-Q) particles. Reprinted with permission from Ref. (Zhu Z. et al., 2023). Copyright: (2023) Elsevier.

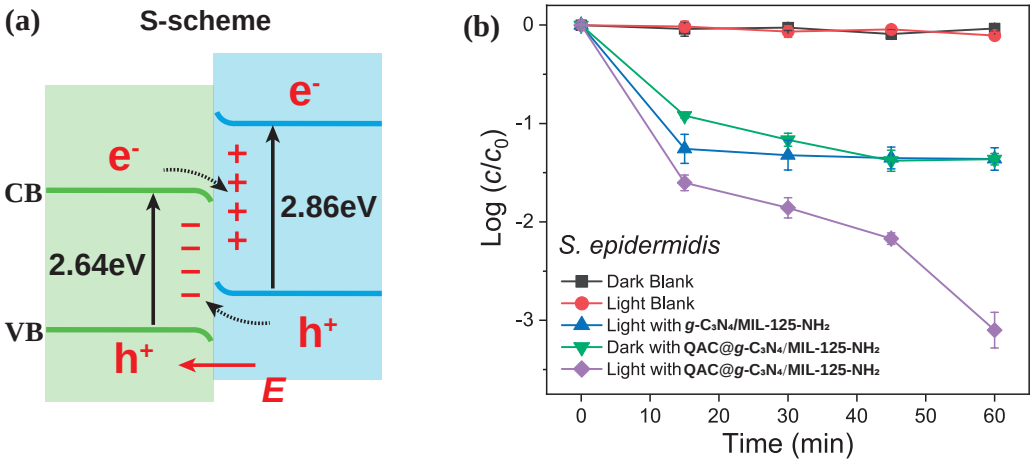


**Fig. 8** **(a)** Schematic illustration of band alignment and charge transfer in C-M-Q and **(b)** time course of the bactericidal activities of C-M-Q in *S. epidermidis* under different conditions. Reprinted with permission from Ref. (Zhu Z. et al., 2023). Copyright: (2023) Elsevier.

bactericidal activity was mainly due to the photogenerated ROS in the solution rather than the toxicity of the catalyst itself. Interestingly, C-M-Q achieved a 1.54 log reduction of *S. epidermis* in the dark via the contact killing mechanism due to the QAC coating (Kaur and Liu, 2016). When light was applied, a significantly enhanced bactericidal efficiency (3.2 log reduction) was obtained. Therefore, at the biointerface, the photogenerated ROS and the positively charged QAC layer exhibit cooperative antibacterial behavior, which significantly improves the overall bactericidal activity.

***Visualization and quantification of bacteria-photocatalyst interactions.*** To further understand the interactions between *S. epidermidis* cells and the C-M-Q surface, the direct visualization and quantification of these interactions at the biointerface were conducted via atomic force microscopy (AFM) using the peak force quantitative nano-mechanical (QNM) mode. As shown in **Fig. 9(a)**, these measurements were performed in PBS solution (pH 7.4) to avoid potential errors due to capillary forces that arose from the humid coverage of both the sample and the AFM tip under ambient conditions (Asri et al., 2014; Hoogenboom et al., 2008).

Specifically, the AFM probe was first functionalized with the C-M-Q particles (**Figs. 9(b)** and **9(c)**), which were then used to measure the adhesion forces. **Figs. 9(d)–9(f)** display the peak force error image, adhesion map, and force curve of S. *epidermidis* cells using the pristine AFM probe as the control. The same results were obtained for the C-M-Q-functionalized probe (**Figs. 9(g)–9(i)**).

As seen from the measurement results, in comparison with the bare probe in the approach curve, the attractive electrostatic effects in C-M-Q were noticed much earlier due to the presence of a positively charged QAC layer. Additionally, a significantly higher adhesion force ($F_{adh}$) of 972 pN was found between C-M-Q and the bacterial cells

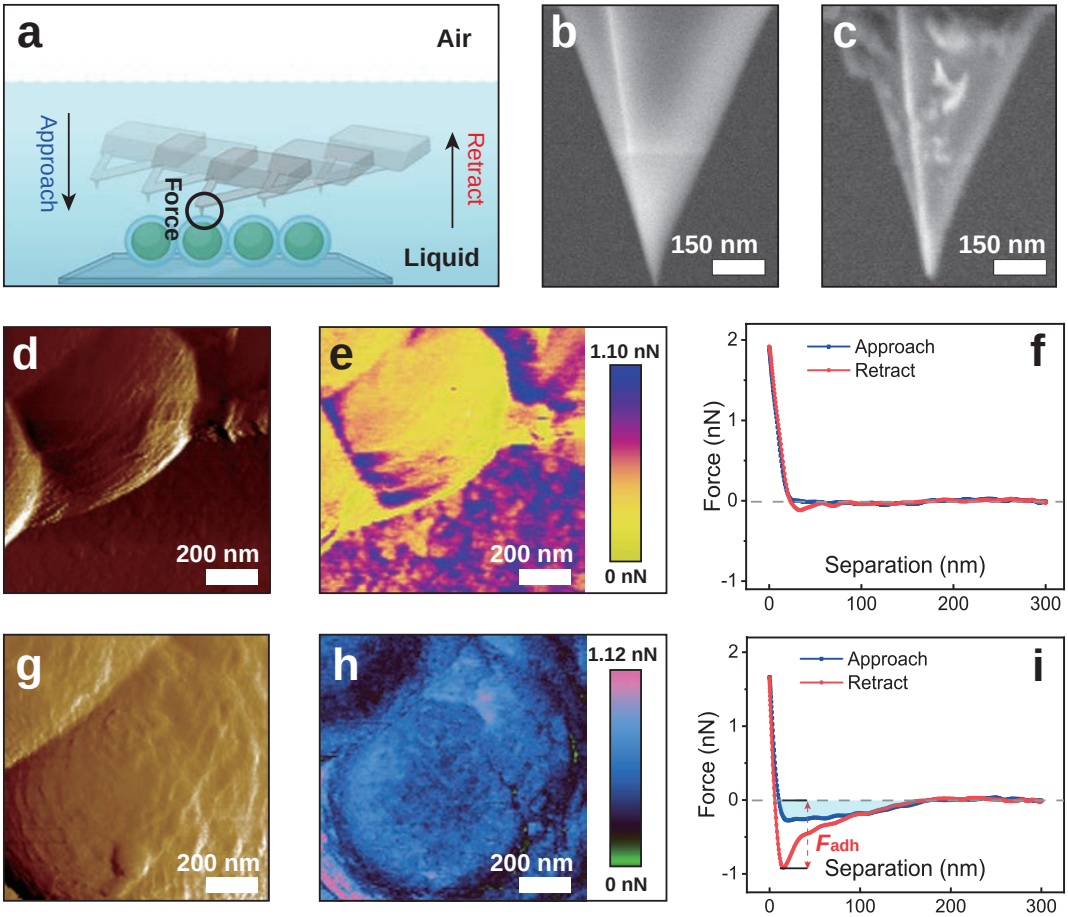


**Fig. 9** AFM measurements of interactions between *S. epidermidis* cells and the C-M-Q photocatalyst. **(a)** Illustration of the AFM force measurement in PBS solution; SEM images of **(b)** the pristine AFM probe and **(c)** the C-M-Q coated probe; **(d,e,f)** and **(g,h,i)** show the peak force error image, adhesion force mapping, and approach-retract force curves of *S. epidermidis* cells measured using the pristine AFM probe and the photocatalyst-coated probe, respectively. Reprinted with permission from Ref. (Zhu Z. et al., 2023). Copyright: (2023) Elsevier.

(**Fig. 9(i)**), whereas only 115 pN was detected between the unmodified probe and the bacterial cells (**Fig. 9(f)**). The results reflect that the positive charge modulation of the photocatalyst surface facilitates bacterial adhesion, which in turn enhances the overall bactericidal performance.

## 4. Conclusions and perspectives

This perspective introduces the fundamental principles of POD and its enhancement strategies by providing several examples. We rationally designed and fabricated several novel antimicrobial MOF-based particles to effectively kill airborne bacterial cells. Specifically, QAC polymer, a broad-spectrum antimicrobial agent, was carefully coated on the surface of MOF-based particles to form active composites capable of attracting and killing bacterial cells *in situ*. These composite particles exhibit excellent antibacterial activity, with contact killing and photogenerated ROS responsible for efficient disinfection. The results also show that the adhesion of bacterial cells to the catalyst surface significantly enhances the photocatalytic bactericidal efficiency.

In addition, several perspectives are provided to further advance the POD technique for combating airborne pathogens as follows:

1) Understanding the mechanistic pathways of POD is crucial for designing photocatalyst particles. In particular, quantifying the characteristic times and migration distances of ROS and other intermediates along with their oxidative capacity in the system should be considered carefully.
2) The interactions between photocatalysts and pathogen cells should also be quantified at the molecular or atomic level using advanced *in situ* techniques, such as AFM and/or TEM.
3) Achieving multifunctional MOF-based materials to mitigate air pollution is promising but challenging. For example, coating polymers around MOF materials reduces specific surface areas and blocks active sites, adversely affecting gas adsorption. Therefore, “trade-off” effects should be seriously considered in material design.
4) Last but not least, the results obtained for bacterial

inactivation may not be easily applied to other airborne pathogens, such as viruses and fungi. Additional work is required in this regard.

## Acknowledgments

This work was supported by the National Science Foundation (CMMI-1727553), the Center for Innovative Technology (CIT) through the Virginia Commonwealth Research Commercialization Fund (CRCF) program, and the COVID-19 Rapid Research Funding Program at Virginia Commonwealth University (VCU). The authors thank Dr. Ping Xu from the VCU School of Dentistry and Dr. Shawn Chen from the VCU College of Engineering for their collaborations on this project. This perspective is based on Dr. Zan Zhu's Ph.D. dissertation entitled "Rational Design of Metal-Organic Frameworks (MOFs)-based Functional Materials Toward Better Air Quality."

## References

Ahmad I., Zou Y., Yan J., Liu Y., Shukrullah S., Naz M.Y., Hussain H., Khan W.Q., Khalid N.R., Semiconductor photocatalysts: a critical review highlighting the various strategies to boost the photocatalytic performances for diverse applications, Advances in Colloid and Interface Science, 311 (2023) 102830. https://doi.org/10.1016/j.cis.2022.102830

Asri L.A.T.W., Crismaru M., Roest S., Chen Y., Ivashenko O., Rudolf P., Tiller J.C., van der Mei H.C., Loontjens T.J.A., Busscher H.J., A shape-adaptive, antibacterial-coating of immobilized quaternary-ammonium compounds tethered on hyperbranched polyurea and its mechanism of action, Advanced Functional Materials, 24 (2014) 346–355. https://doi.org/10.1002/adfm.201301686

Balakrishnan K., Ghosh S., Ganguli B., Sambandam S., Bruce N.G., Barnes D.F., Erratum: "An integrated risk function for estimating the global burden of disease attributable to ambient fine particulate matter exposure", Environmental Health Perspectives, 122 (2014) A235. https://doi.org/10.1289/ehp.122-A235

Balmes J.R., Household air pollution from domestic combustion of solid fuels and health, Journal of Allergy and Clinical Immunology, 143 (2019) 1979–1987. https://doi.org/10.1016/j.jaci.2019.04.016

Bhardwaj S.K., Bhardwaj N., Kumar V., Bhatt D., Azzouz A., Bhaumik J., Kim K.H., Deep A., Recent progress in nanomaterial-based sensing of airborne viral and bacterial pathogens, Environment International, 146 (2021) 106183. https://doi.org/10.1016/j.envint.2020.106183

Burnett R.T., Pope C.A., Ezzati M., Olives C., Lim S.S., Mehta S., Shin H.H., Singh G., Hubbell B., Brauer M., Anderson H.R., Smith K.R., Balmes J.R., Bruce N.G., Kan H., et al., An integrated risk function for estimating the global burden of disease attributable to ambient fine particulate matter exposure, Environmental Health Perspectives, 122 (2014) 397–403. https://doi.org/10.1289/ehp.1307049

Chang D.Q., Chen S.C., Pui D.Y.H., Capture of sub-500 nm particles using residential electret HVAC filter media-experiments and modeling, Aerosol and Air Quality Research, 16 (2016) 3349–3357. https://doi.org/10.4209/aaqr.2016.10.0437

Chen F.N., Yang X.D., Mak H.K.C., Chan D.W.T., Photocatalytic oxidation for antimicrobial control in built environment: a brief literature overview, Building and Environment, 45 (2010) 1747–1754. https://doi.org/10.1016/j.buildenv.2010.01.024

Chen S.C., Wang J., Bahk Y.K., Fissan H., Pui D.Y.H., Carbon nanotube penetration through fiberglass and electret respirator filter and Nuclepore filter media: experiments and models, Aerosol Science and Technology, 48 (2014) 997–1008. https://doi.org/10.1080/02786826.2014.954028

Cho M., Chung H., Choi W., Yoon J., Linear correlation between inactivation of *E. coli* and OH radical concentration in $TiO_2$ photocatalytic disinfection, Water Research, 38 (2004) 1069–1077. https://doi.org/10.1016/j.watres.2003.10.029

Das K., Roychoudhury A., Reactive oxygen species (ROS) and response of antioxidants as ROS-scavengers during environmental stress in plants, Frontiers in Environmental Science, 2 (2014) 53. https://doi.org/10.3389/fenvs.2014.00053

Fujishima A., Zhang X.T., Tryk D.A., $TiO_2$ photocatalysis and related surface phenomena, Surface Science Reports, 63 (2008) 515–582. https://doi.org/10.1016/j.surfrep.2008.10.001

Furukawa H., Cordova K.E., O'Keeffe M., Yaghi O.M., The chemistry and applications of metal-organic frameworks, Science, 341 (2013) 1230444. https://doi.org/10.1126/science.1230444

Gonzalez-Martin J., Kraakman N.J.R., Perez C., Lebrero R., Munoz R., A state-of-the-art review on indoor air pollution and strategies for indoor air pollution control, Chemosphere, 262 (2021) 128376. https://doi.org/10.1016/j.chemosphere.2020.128376

Gozzelino G., Lisanti C., Beneventi S., Quaternary ammonium monomers for UV crosslinked antibacterial surfaces, Colloid Surface A, 430 (2013) 21–28. https://doi.org/10.1016/j.colsurfa.2013.03.061

Guo L., Zhao P.Y., Jia Y.K., Wang Z.F., Chen M., Zhang H., Liu D.X., Zhang Y., Wang X.H., Rong M.Z., Inactivation of airborne pathogenic microorganisms by plasma-activated nebulized mist, Journal of Hazardous Materials, 459 (2023) 132072. https://doi.org/10.1016/j.jhazmat.2023.132072

Hippeli S., Elstner E.F., OH-radical-type reactive oxygen species: a short review on the mechanisms of OH-radical-and peroxynitrite toxicity, Zeitschrift für Naturforschung C, 52 (1997) 555–563. https://doi.org/10.1515/znc-1997-9-1001

Hodges B.C., Cates E.L., Kim J.H., Challenges and prospects of advanced oxidation water treatment processes using catalytic nanomaterials, Nature Nanotechnology, 13 (2018) 642–650. https://doi.org/10.1038/s41565-018-0216-x

Hoffmann M.R., Martin S.T., Choi W.Y., Bahnemann D.W., Environmental applications of semiconductor photocatalysis, Chemical Reviews, 95 (1995) 69–96. https://doi.org/10.1021/cr00033a004

Hoogenboom B.W., Frederix P.L.T.M., Fotiadis D., Hug H.J., Engel A., Potential of interferometric cantilever detection and its application for SFM/AFM in liquids, Nanotechnology, 19 (2008) 384019. https://doi.org/10.1088/0957-4484/19/38/384019

Hubbard H., Poppendieck D., Corsi R.L., Chlorine dioxide reactions with indoor materials during building disinfection: surface uptake, Environmental Science & Technology, 43 (2009) 1329–1335. https://doi.org/10.1021/es801930c

ISO 21083-1,Test method to measure the efficiency of air filtration media against spherical nanomaterials, Part 1: Size range from 20 nm to 500 nm, ISO (International Organization for Standardization), (2018). <https://www.iso.org/standard/69876.html> accessed 25072024.

Jennings M.C., Minbiole K.P.C., Wuest W.M., Quaternary ammonium compounds: an antimicrobial mainstay and platform for innovation to address bacterial resistance, ACS Infectious Diseases, 1 (2015) 288–303. https://doi.org/10.1021/acsinfecdis.5b00047

Jiao L., Seow J.Y.R., Skinner W.S., Wang Z.U., Jiang H.-L., Metal–organic frameworks: structures and functional applications, Materials Today, 27 (2019) 43–68. https://doi.org/10.1016/j.mattod.2018.10.038

Kaur R., Liu S., Antibacterial surface design – Contact kill, Progress in Surface Science, 91 (2016) 136–153. https://doi.org/10.1016/j.progsurf.2016.09.001

Kim Y., Coy E., Kim H., Mrowczynski R., Torruella P., Jeong D.W., Choi K.S., Jang J.H., Song M.Y., Jang D.J., Peiro F., Jurga S., Kim H.J., Efficient photocatalytic production of hydrogen by exploiting the polydopamine-semiconductor interface, Applied Catalysis B-Environmental, 280 (2021) 119423. https://doi.org/10.1016/j.apcatb.2020.119423

Kraut E.A., Grant R.W., Waldrop J.R., Kowalczyk S.P., Precise determination of the valence-band edge in X-ray photoemission spectra—application to measurement of semiconductor interface potentials, Physical Review Letters, 44 (1980) 1620–1623. https://doi.org/10.1103/PhysRevLett.44.1620

Kühn K.P., Chaberny I.F., Massholder K., Stickler M., Benz V.W., Sonntag H.G., Erdinger L., Disinfection of surfaces by photocatalytic oxidation with titanium dioxide and UVA light, Chemosphere, 53 (2003) 71–77. https://doi.org/10.1016/S0045-6535(03)00362-X

Kumar A., Raizada P., Singh P., Saini R.V., Saini A.K., Hosseini-Bandegharaei A., Perspective and status of polymeric graphitic carbon nitride based Z-scheme photocatalytic systems for sustainable photocatalytic water purification, Chemical Engineering Journal, 391 (2020) 123496. https://doi.org/10.1016/j.cej.2019.123496

Kusiak-Nejman E., Morawski A.W., $TiO_2$/graphene-based nanocomposites for water treatment: a brief overview of charge carrier transfer, antimicrobial and photocatalytic performance, Applied Catalysis B-Environmental, 253 (2019) 179–186. https://doi.org/10.1016/j.apcatb.2019.04.055

Li D., Yadav A., Zhou H., Roy K., Thanasekaran P., Lee C., Advances and applications of metal-organic frameworks (MOFs) in emerging technologies: a comprehensive review, Global Challenges, 8 (2024) 2300244. https://doi.org/10.1002/gch2.202300244

Li P., Li J.Z., Feng X., Li J., Hao Y.C., Zhang J.W., Wang H., Yin A.X., Zhou J.W., Ma X.J., Wang B., Metal-organic frameworks with photocatalytic bactericidal activity for integrated air cleaning, Nature Communications, 10 (2019) 2177. https://doi.org/10.1038/s41467-019-10218-9

Linsebigler A.L., Lu G.Q., Yates J.T., Photocatalysis on $TiO_2$ Surfaces - principles, mechanisms, and selected results, Chemical Reviews, 95 (1995) 735–758. https://doi.org/10.1021/cr00035a013

Magill S.S., Edwards J.R., Bamberg W., Beldavs Z.G., Dumyati G., Kainer M.A., Lynfield R., Maloney M., McAllister-Hollod L., Nadle J., Ray S.M., Thompson D.L., Wilson L.E., Fridkin S.K., Multistate point-prevalence survey of health care–associated infections, New England Journal of Medicine, 370 (2014) 1198–1208. https://doi.org/10.1056/NEJMoa1306801

Magill S.S., O'Leary E., Janelle S.J., Thompson D.L., Dumyati G., Nadle J., Wilson L.E., Kainer M.A., Lynfield R., Greissman S., Ray S.M., Beldavs Z., Gross C., Bamberg W., Sievers M., et al., Changes in prevalence of health care–associated infections in U.S. hospitals, New England Journal of Medicine, 379 (2018) 1732–1744. https://doi.org/10.1056/NEJMoa1801550

Nasir A.M., Awang N., Hubadillah S.K., Jaafar J., Othman M.H.D., Salleh W.N.W., Ismail A.F., A review on the potential of photocatalysis in combatting SARS-CoV-2 in wastewater, Journal of Water Process Engineering, 42 (2021) 102111. https://doi.org/10.1016/j.jwpe.2021.102111

Nosaka Y., Nosaka A.Y., Generation and detection of reactive oxygen species in photocatalysis, Chemical Reviews, 117 (2017) 11302–11336. https://doi.org/10.1021/acs.chemrev.7b00161

Ong W.J., Tan L.L., Ng Y.H., Yong S.T., Chai S.P., Graphitic carbon nitride ($g\text{-}C_3N_4$)-based photocatalysts for artificial photosynthesis and environmental remediation: are we a step closer to achieving sustainability?, Chemical Reviews, 116 (2016) 7159–7329. https://doi.org/10.1021/acs.chemrev.6b00075

Peleg A.Y., Hooper D.C., Hospital-acquired infections due to Gram-negative bacteria, New England Journal of Medicine, 362 (2010) 1804–1813. https://doi.org/10.1056/nejmra0904124

Ping M., Zhang X.R., Liu M.X., Wu Z.C., Wang Z.W., Surface modification of polyvinylidene fluoride membrane by atom-transfer radical-polymerization of quaternary ammonium compound for mitigating biofouling, Journal of Membrane Science, 570 (2019) 286–293. https://doi.org/10.1016/j.memsci.2018.10.070

Regmi C., Joshi B., Ray S.K., Gyawali G., Pandey R.P., Understanding mechanism of photocatalytic microbial decontamination of environmental wastewater, Frontiers in Chemistry, 6 (2018) 33. https://doi.org/10.3389/fchem.2018.00033

Schaate A., Roy P., Godt A., Lippke J., Waltz F., Wiebcke M., Behrens P., Modulated synthesis of Zr-based metal-organic frameworks: from nano to single crystals, Chemistry – A European Journal, 17 (2011) 6643–6651. https://doi.org/10.1002/chem.201003211

Serpone N., Emeline A.V., Semiconductor photocatalysis - past, present, and future outlook, The Journal of Physical Chemistry Letters, 3 (2012) 673–677. https://doi.org/10.1021/jz300071j

Shi H.X., Fan J., Zhao Y.Y., Hu X.Y., Zhang X., Tang Z.S., Visible light driven $CuBi_2O_4/Bi_2MoO_6$ p-n heterojunction with enhanced photocatalytic inactivation of *E. coli* and mechanism insight, Journal of Hazardous Materials, 381 (2020) 121006. https://doi.org/10.1016/j.jhazmat.2019.121006

Song L., Zhou J.F., Wang C., Meng G., Li Y.F., Jarin M., Wu Z.Y., Xie X., Airborne pathogenic microorganisms and air cleaning technology development: A review, Journal of Hazardous Materials, 424 (2022) 127429. https://doi.org/10.1016/j.jhazmat.2021.127429

Sun H.G., Du Y.W., Gao C.F., Iftikhar, Long J., Li S.W., Shao L., Pressure-assisted in-depth hydrophilic tailoring of porous membranes achieving high water permeability, excellent fouling resistance and superior antimicrobial ability, Journal of Membrane Science, 604 (2020) 118071. https://doi.org/10.1016/j.memsci.2020.118071

Tang M., Thompson D., Chen S.C., Liang Y., Pui D.Y.H., Evaluation of different discharging methods on HVAC electret filter media, Building and Environment, 141 (2018) 206–214. https://doi.org/10.1016/j.buildenv.2018.05.048

Vlaskin M.S., Review of air disinfection approaches and proposal for thermal inactivation of airborne viruses as a life-style and an instrument to fight pandemics, Applied Thermal Engineering, 202 (2022) 117855. https://doi.org/10.1016/j.applthermaleng.2021.117855

Walker C.M., Ko G., Effect of ultraviolet germicidal irradiation on viral aerosols, Environmental Science & Technology, 41 (2007) 5460–5465. https://doi.org/10.1021/es070056u

Wang H., Yuan X.Z., Wu Y., Zeng G.M., Chen X.H., Leng L.J., Li H., Synthesis and applications of novel graphitic carbon nitride/metal-organic frameworks mesoporous photocatalyst for dyes removal, Applied Catalysis B-Environmental, 174 (2015) 445–454. https://doi.org/10.1016/j.apcatb.2015.03.037

Wang H.L., Zhang L.S., Chen Z.G., Hu J.Q., Li S.J., Wang Z.H., Liu J.S., Wang X.C., Semiconductor heterojunction photocatalysts: design, construction, and photocatalytic performances, Chemical Society Reviews, 43 (2014) 5234–5244. https://doi.org/10.1039/c4cs00126e

Wang W.J., Yu J.C., Xia D.H., Wong P.K., Li Y.C., Graphene and $g\text{-}C_3N_4$ nanosheets cowrapped elemental α-sulfur as a novel metal-free heterojunction photocatalyst for bacterial inactivation under visible-light, Environmental Science & Technology, 47 (2013) 8724–8732. https://doi.org/10.1021/es4013504

Wilson W.W., Wade M.M., Holman S.C., Champlin F.R., Status of methods for assessing bacterial cell surface charge properties based on zeta potential measurements, Journal of Microbiological Methods, 43 (2001) 153–164. https://doi.org/10.1016/S0167-7012(00)00224-4

Xiao Q., Liang Y., Zhu F.W., Lu S.Y., Huang S., Microwave-assisted one-pot synthesis of highly luminescent N-doped carbon dots for cellular imaging and multi-ion probing, Microchimica Acta, 184 (2017) 2429–2438. https://doi.org/10.1007/s00604-017-2242-z

Xu J.W., Wang Y., Yang Y.F., Ye X.Y., Yao K., Ji J., Xu Z.K., Effects of quaternization on the morphological stability and antibacterial activity of electrospun poly(DMAEMA-co-AMA) nanofibers, Colloid Surface B, 133 (2015) 148–155. https://doi.org/10.1016/j.colsurfb.2015.06.002

Xu Z.Q., Shen F.X., Li X.G., Wu Y., Chen Q., Jie X., Yao M.S., Molecular and microscopic analysis of bacteria and viruses in exhaled breath collected using a simple impaction and condensing method, PLOS One, 7 (2012) e41137. https://doi.org/10.1371/journal.pone.0041137

You J.H., Guo Y.Z., Guo R., Liu X.W., A review of visible light-active photocatalysts for water disinfection: features and prospects, Chemical Engineering Journal, 373 (2019) 624–641. https://doi.org/10.1016/j.cej.2019.05.071

Yu J.C., Ho W.K., Yu J.G., Yip H., Wong P.K., Zhao J.C., Efficient visible-light-induced photocatalytic disinfection on sulfur-doped nanocrystalline titania, Environmental Science & Technology, 39 (2005) 1175–1179. https://doi.org/10.1021/es035374h

Yusuf V.F., Malek N.I., Kailasa S.K., Review on metal-organic framework classification, synthetic approaches, and influencing factors: applications in energy, drug delivery, and wastewater treatment, ACS Omega, 7 (2022) 44507–44531. https://doi.org/10.1021/acsomega.2c05310

Zander Z.K., Chen P.R., Hsu Y.H., Dreger N.Z., Savariau L., Mcroy W.C., Cerchiari A.E., Chambers S.D., Barton H.A., Becker M.L., Post-fabrication QAC-functionalized thermoplastic polyurethane for contact-killing catheter applications, Biomaterials, 178 (2018) 339–350. https://doi.org/10.1016/j.biomaterials.2018.05.010

Zeng X.K., Wang Z.Y., Meng N., McCarthy D.T., Deletic A., Pan J.H., Zhang X.W., Highly dispersed $TiO_2$ nanocrystals and carbon dots on reduced graphene oxide: ternary nanocomposites for accelerated photocatalytic water disinfection, Applied Catalysis B-Environmental, 202 (2017) 33–41. https://doi.org/10.1016/j.apcatb.2016.09.014

Zhang Y.D., Zhang X., Zhao Y.Q., Zhang X.Y., Ding X.K., Ding X.J., Yu B.R., Duan S., Xu F.J., Self-adaptive antibacterial surfaces with bacterium-triggered antifouling-bactericidal switching properties, Biomaterials Science, 8 (2020) 997–1006. https://doi.org/10.1039/c9bm01666j

Zhang Y.Y., Yuan S., Feng X., Li H.W., Zhou J.W., Wang B., Preparation of nanofibrous metal-organic framework filters for efficient air pollution control, Journal of the American Chemical Society, 138 (2016) 5785–5788. https://doi.org/10.1021/jacs.6b02553

Zhao Y.X., Cai W., Chen J.X., Miao Y.Y., Bu Y.F., A highly efficient composite catalyst constructed from $NH_2$-MIL-125(Ti) and reduced graphene oxide for $CO_2$ photoreduction, Frontiers in Chemistry, 7 (2019) 789. https://doi.org/10.3389/fchem.2019.00789

Zhou J.L., Hu Z.X., Zabihi F., Chen Z.G., Zhu M.F., Progress and perspective of antiviral protective material, Advanced Fiber Materials, 2 (2020) 123–139. https://doi.org/10.1007/s42765-020-00047-7

Zhu Z., Bao L., Pestov D., Xu P., Wang W.N., Cellular-level insight into biointerface: from surface charge modulation to boosted photocatalytic oxidative disinfection, Chemical Engineering Journal, 453 (2023) 139956. https://doi.org/10.1016/j.cej.2022.139956

Zhu Z., Zhang Y., Bao L., Chen J.P., Duan S., Chen S.C., Xu P., Wang W.N., Self-decontaminating nanofibrous filters for efficient particulate matter removal and airborne bacteria inactivation, Environmental Science: Nano, 8 (2021) 1081–1095. https://doi.org/10.1039/d0en01230k

## Authors' Short Biographies

**Mohaiminul Haider Chowdhury** has been pursuing his Ph.D. in the Department of Mechanical and Nuclear Engineering at Virginia Commonwealth University, USA, under the guidance of Prof. Wei-Ning Wang since Spring 2024. He earned his Master's degree in Renewable Energy Technology from the University of Dhaka, Bangladesh in 2019. His research focuses on the innovative design of efficient photocatalysts for energy- and environmental-sustainable applications.

**Dr. Zan Zhu** obtained his Ph.D. from the Department of Mechanical and Nuclear Engineering at Virginia Commonwealth University, USA, under the guidance of Prof. Wei-Ning Wang in 2022. He received his Master's degree in Optical Engineering from the Beijing Institute of Technology in 2016. His research at VCU focused on the design of metal-organic frameworks (MOFs)-based functional materials for better air quality.

**Prof. Wei-Ning Wang** is an Associate Professor in the Department of Mechanical and Nuclear Engineering at Virginia Commonwealth University. He received a Ph.D. degree in Chemistry and Chemical Engineering from Hiroshima University in 2006 and worked as a JSPS postdoctoral fellow from 2006 to 2007. He served as an Assistant Professor at Hiroshima University from 2007 to 2009. He was a Postdoctoral Research Associate at Washington University in St. Louis from 2009 to 2012 and served as a Research Assistant Professor from 2013 to 2014. His research interests include functional material design, synthesis, and characterization, as well as their applications to address energy and environmental issues.

KONA Powder and Particle Journal

KONA Powder and Particle Journal No. 42 (2025) 200–212/https://doi.org/10.14356/kona.2025016 Review Paper

# Formulation of Bacteriophage for Inhalation to Treat Multidrug-Resistant Pulmonary Infections†

**Vaibhav Pathak[1], Hak-Kim Chan[2] and Qi Tony Zhou[1]***

[1] *Department of Industrial and Molecular Pharmaceutics, College of Pharmacy, Purdue University, USA*
[2] *Advanced Drug Delivery Group, School of Pharmacy, Faculty of Medicine and Health, The University of Sydney, Australia*

Rapid development of antibiotic resistance in pathogenic bacteria and a decline in the pharmaceutical development of new antibiotics are pushing the research community to explore alternative antimicrobials that can replace or complement antibiotics. Bacteriophages (or, phages) are naturally occurring viruses that can kill bacteria with high specificity and can evolve to target resistant bacteria. Phages have been historically employed as antimicrobial agents, but they were overshadowed by the emergence of antibiotics. With a renewed focus on phages, it is important to study their clinical efficacy, safety, and formulation. Pulmonary infections have a large burden of global morbidity and frequently involve multidrug-resistant pathogens such as *Acinetobacter baumannii, Klebsiella pneumoniae, Mycobacterium tuberculosis*, and *Pseudomonas aeruginosa*. Therefore, this can be an important area of application of phages. Dry powder inhalers can be an effective strategy to deliver phages to the lungs because they are easy-to-use, portable, and capable of delivering a higher lung dose than oral or intravenous route. They also have longer shelf life and lower cold storage requirements than solutions. Therefore, the aim of the current review is to summarize recent findings on bacteriophage dry powder formulations, particularly focusing on the effect of various excipients and manufacturing factors on phage titer preservation.

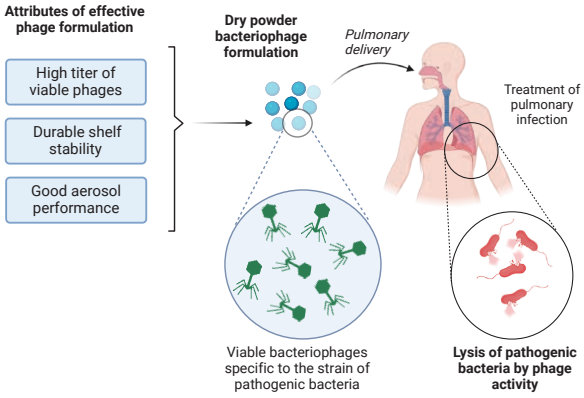


**Keywords:** bacteriophage therapy, dry powder inhalers, antimicrobial resistance, pulmonary infection

## 1. Introduction

Gram-negative bacteria like *Acinetobacter baumannii, Klebsiella pneumoniae*, and *Pseudomonas aeruginosa* are a serious threat to human health due to their ability to develop resistance to a broad range of antibiotics (Livermore, 2003). For instance, a review by Livermore in 2002 reported that 1 % of *P. aeruginosa* isolates in the USA showed resistance against six of the most relevant antibiotics: amikacin, ceftazidime, ciprofloxacin, gentamicin, carbapenems, and piperacillin (Livermore, 2002). In 2014, 51,000 cases of healthcare-associated *P. aeruginosa* infections were reported in the USA, and 13 % were multidrug-resistant (Rossolini et al., 2014).

The problem of antimicrobial resistance is intensified by a steadily decreasing number of new antibiotics under development against Gram-negative pathogens over the last three decades (Ventola, 2015). Developing antibiotics against Gram-negative bacteria is less profitable for the pharmaceutical industry due to a shorter duration of use (Bartlett et al., 2013), cheaper prices, and the unpredictable risk of resistance development that can curtail sales (Gould and Bal, 2013). Given this shortage of new classes of antibiotics, researchers and clinicians are exploring alternative antimicrobial strategies like bacteriophage, antimicrobial peptides, quorum sensing inhibitors, biofilm inhibitors, and antibiotic adjuvants (Scoffone et al., 2024).

Bacteriophages are naturally occurring viruses that infect bacteria. Bacteriophages that are obligately *lytic* infect bacterial cells for self-replication and release progeny phages through cell lysis. Progeny phages can infect other bacterial cells and continue the cycle of infection. Lytic phages can therefore be effective antibacterial agents. Phages have not yet been widely adopted as a treatment option in Western countries, but have several unique characteristics: specificity to bacteria, ability to self-propagate in the presence of bacteria, and ability to co-evolve with bacteria (Loc-Carrillo and Abedon, 2011).

Respiratory infections are one of the leading causes of mortality. Chronic and refractory lung infections often occur in patients with compromised lungs, such as those with chronic obstructive pulmonary disorder (COPD) and cystic fibrosis (CF) (Hauser et al., 2011). The treatment of chronic lung infections can be complicated by inefficient drug delivery to the lungs, the development of multidrug resistance

† Received 22 May 2024; Accepted 28 June 2024
J-STAGE Advance published online 24 August 2024
* Corresponding author: Qi Tony Zhou;
Add: 575 Stadium Mall Drive, West Lafayette, Indiana 47907, USA
E-mail: tonyzhou@purdue.edu
TEL: +1-765-496-0707

in chronic cases, and a shortage of new antibiotics and alternative antimicrobial drugs. Phage therapy can be an alternative treatment option for lung infections resistant to antibiotics.

Phage therapy has several advantages over traditional antibiotics in terms of their ability to treat bacterial infections (Kortright et al., 2019): (1) Phages have a high host specificity, which reduces off-target effects on the natural microbiome of the patient. Moreover, phages do not infect human cells; (2) Because phages can self-replicate via the lytic infection of bacteria, the dose of the phage can be amplified in the presence of the host bacteria. This indicates that phages can be used at lower doses than antibiotics; (3) Phages are naturally capable of evolving to overcome the phage resistance mechanisms of bacteria. Thus, unlike antibiotics, iterations of a phage can be employed to target resistance bacteria; (4) Chronic lung infections often develop biofilms that are practically impermeable to antibiotics. Phages can penetrate biofilms (Chan et al., 2018; Loc-Carrillo and Abedon, 2011), making them highly effective against chronic bacterial infections.

## 2. Efficacy of phage therapy

Phage therapy for lung infections has shown promise in animal studies and clinical cases. Additionally, phage therapy has often been used for the treatment of bacterial infections in eastern European countries for decades (Abedon, 2015). Some recent studies are summarized below.

### 2.1 Phage testing in animal models

Debarbieux et al. (2010) tested the effect of intranasal phage administration in acute lung infection models using bioluminescent *P. aeruginosa* (PAK lumi). The live bacteria population in mice was estimated by quantifying photon emission. Bacteriophage (PAK-P1) pretreatment of mice 24 h before introduction of bacterial infection using phages at a multiplicity of infection (phage-to-bacteria ratio) of 10 resulted in 5 times lower photon emission after 2 h than phosphate buffer saline control pretreatment. All phage-pretreated mice survived for 16 days, whereas all mice in the control group died within 2 days (Debarbieux et al., 2010). This demonstrates the great potential of preventive phage therapy against the known risk of bacterial challenge.

Semler et al. (2014) showed that aerosolized phage delivery (Myoviridae KS12) to mice lungs resulted in a 2-log reduction in the median bacterial load of acute *Burkholderia cenocepacia* (K56-2, highly antibiotic-resistant) infection in mice. Yang et al. (2015) demonstrated complete eradication of *P. aeruginosa* D9 cells in a murine hemorrhagic pneumonia model and 100% survival of mice using a single dose of an N4-like phage (YH6) with an MOI of 0.1 administered intranasally 2 h after infection. Cao et al. (2015) showed that when murine pneumonia induced by the multi-resistant *Klebsiella pneumoniae* strain 1513 was treated intranasally with phages at an MOI of 10, 80 % of the mice survived. In comparison, none of the control-treated mice survived. Phage-treated mice exhibited reduced bacterial cell burden, lower loss of body weight, and exhibited lower levels of inflammatory cytokines in the lungs (Cao et al., 2015).

### 2.2 Clinical application of phages

Hoyle et al. (2018) reported phage treatment of a cystic fibrosis (CF) patient with a multidrug-resistant *Achromobacter xylosoxidans* lung infection. A cocktail of two *Achromobacter* bacteriophages (*Siphoviridae* family) ($6 \times 10^8$ PFU dose) was nebulized for inhalation and orally administered twice daily for 20 days. The course was repeated four times over a year. The patient's lung function improved significantly, dyspnea resolved, and cough reduced (Hoyle et al., 2018). Other clinical and animal studies on bacteriophage treatment have been extensively reviewed by Abedon (2015) and Bhadoriya et al. (2023).

By employing two or more independent modes of bacterial killing, bacterial killing can be improved and the chance of selecting resistant mutants can be reduced (Torres-Barceló and Hochberg, 2016). Thus, phage cocktails containing two or more phages specific to a pathogen can improve bacterial killing and prevent development of resistance. The combination of phages and antibiotics has shown promise (Tagliaferri et al., 2019). Some phage-antibiotics combinations can show synergistic antibacterial action (Comeau et al., 2007; Kamal and Dennis, 2015; Ryan et al., 2012; Uchiyama et al., 2018). Ruest et al. (2023) demonstrated synergistic bacterial killing in some phage-phage and phage-colistin combinations against *B. cenocepacia*. The study also observed "phage steering", where phage resistance can be exploited to re-sensitize bacteria to antibiotics. Some cases of phage-induced resistance in *Burkholderia cenocepacia* altered the structure of its lipopolysaccharide membrane, making it susceptible to the action of immune components in serum and antibiotics that target the membrane, such as colistin (Ruest et al., 2023).

In addition to the clinical use of phage therapies in East Europe, several phage therapies are currently under development in the USA and Europe: BX004 phage by BiomX is under clinical evaluation for treating multi-resistant *P. aeruginosa* involved in cystic fibrosis (ClinicalTrials.gov ID NCT05498363). Armata Pharmaceuticals is currently studying the safety, kinetics, and efficacy of the inhaled AP-PA02 phage in subjects with non-cystic fibrosis bronchiectasis and chronic pulmonary *P. aeruginosa* infection (ID NCT05616221). **Table 1** lists bacteriophage products currently under development.

**Table 1** Bacteriophage products and their status of clinical evaluation as of May 5, 2024.

| Product name | Company | Target pathogen | Site of infection and comorbidity | Mode of delivery | Development stage | Trial ID |
|---|---|---|---|---|---|---|
| BX004 | BiomX | *P. aeruginosa* | Lungs with cystic fibrosis | Not known | Part 2 of Phase 1b/2a was completed successfully | NCT05498363 |
| BX211 | BiomX | *S. aureus* | Diabetic foot osteomyelitis (DFO) | Not known | Ongoing phase 2 study | |
| Tailwind (AP-PA02) | Armata Pharmaceuticals | *P. aeruginosa* | Noncystic fibrotic bronchiectasis | Inhaled | Recruiting patients for phase 2 | NCT05616221 |
| SWARM P.a. (AP-PA02) | Armata Pharmaceuticals | *P. aeruginosa* | Lung with cystic fibrosis | Inhaled | Phase 1b/2a study has been completed | NCT04596319 |
| AP-SA02 | Armata Pharmaceuticals | *S. aureus* | Bacteremia | Not known (Adjunct to antibiotic therapy) | Recruiting patients for phase 1b/2a | NCT05184764 |

## 3. Powder formulation of bacteriophages for inhalation

Successful phage treatment depends on the delivery of a high phage titer to the infection site. Pulmonary delivery of a wide variety of drugs shows higher target site deposition and thus requires a lower dose than parenteral or oral delivery.

Nebulization, pressurized metered-dose inhalers (pMDIs), and dry powder inhalers are the most common pulmonary drug delivery methods. Dry powder inhalers stand out as a dosage form for inhaled delivery because they are portable and easy to use by patients (Kwok and Chan, 2014; Zhou et al., 2014). These can deliver a higher dose of the drug substance to the lungs in a shorter time than nebulizers and pMDIs. Importantly, dry powders tend to be physically and chemically more stable than solutions or suspensions (Ke et al., 2022). It is especially beneficial to formulate labile biological drugs like proteins, viruses, and monoclonal antibodies as dry powders because of their improved storage stability (Santana et al., 2014; Walters et al., 2014). Therefore, this review focused on the formulation of bacteriophages as inhaled dry powders.

Chang et al. (2018) conducted a proof-of-principle study to investigate the *in vivo* effects of phage dry powders on *Pseudomonas aeruginosa* infection (**Fig. 1**). The lungs of neutropenic mice were infected using a suspension of FADDI-PA001 bacteria via intratracheal instillation, which resulted in an average load of $3.4 \times 10^5$ CFU/lung. Phage powders were administered intratracheally at a dose of $1.4 \times 10^7$ to $1.2 \times 10^8$ PFU/lung. After 24 h, the phage-treated mice had a 5.3 $\log_{10}$ lower bacterial count than the untreated mice (Chang et al., 2018).

Dry powders for inhalation are often engineered to have appropriate aerodynamic particle size and physicochemical properties that facilitate their efficient delivery to the lungs

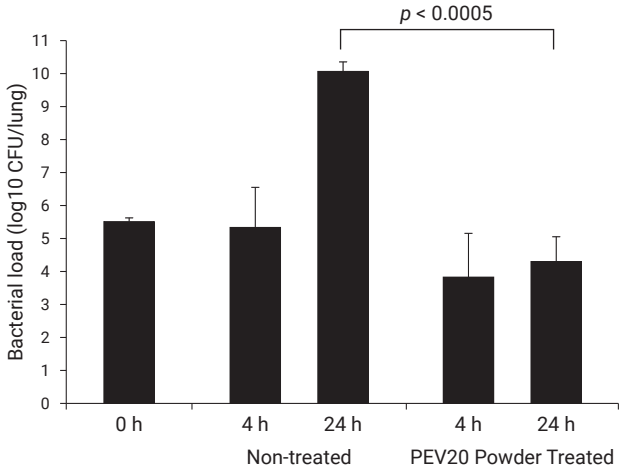


**Fig. 1** Comparison of PEV20 phage dry powder treatment ($1.4 \times 10^7$ to $1.2 \times 10^8$ PFU/lung) and no treatment on the bacterial load of *Pseudomonas aeruginosa* FADDI-PA001 in a mouse lung infection model at 4 and 24 h after infection, reprinted with permission from Ref. (Chang et al., 2018). Copyright (2018) American Society for Microbiology.

(Hoppentocht, 2016; Ke et al., 2022). These powders should resist physical changes that can occur due to moisture sorption and agglomeration during storage because these can affect their dispersion. Furthermore, the formulation of biological drugs as dry powders presents additional requirements. Biologic drug substances, including phages, are highly susceptible to loss of therapeutic activity due to external stresses. It is important to design a manufacturing method and select formulation components that minimize phage inactivation during processing and storage.

Dry powders for inhalation are commonly prepared by spray drying, lyophilization-micronization, spray freeze drying, or blending micronized powders with lactose carrier particles. The requirement for higher antimicrobial drug doses limits the use of lactose carrier blends because

of the high powder burden (Patton and Byron, 2007). Spray drying is a particle engineering technology involving hot air flow to dry an atomized solution or suspension (**Fig. 2**). Lyophilization is the process of freezing and removing moisture from a drug solution at low temperature and pressure via sublimation. Lyophilized dry cake can be micronized to generate inhaled dry powder (Golshahi et al., 2011). Spray freeze drying involves vacuum or atmospheric drying of frozen atomized drug solution droplets generated by rapid exposure to liquid nitrogen or other cryogens (**Fig. 3**).

Several studies have investigated the preparation of dry powder phage formulations using spray drying, wherein they study the effects of manufacturing parameters and excipients on formulation stability and aerosol performance. During spray drying, the phage formulation is exposed to shear, thermal, and desiccation stresses (Leung et al., 2016; Matinkhoo et al., 2011; Vandenheuvel et al., 2013). These stresses can induce denaturation of the capsid protein, breakage of the tail, or loss of enclosed nucleic acid material, which can cause the phage to lose its ability to infect host bacteria.

Sugars like trehalose, lactose, and sucrose are commonly used as lyoprotectants in protein formulations because they prevent protein denaturation in the absence of water. Sugars are believed to have glass-forming ability that can immobilize proteins in their native conformations (Chang and Pikal, 2009). Another mechanism of stabilization attributed to sugars is their ability to form hydrogen bonds with proteins (Grasmeijer et al., 2013). In this way, sugars replace hydrogen-bonding interactions between proteins and water. It is possible for one or both mechanisms to be responsible for protein stabilization. Because a phage body is essentially a complex assembly of proteins enclosing nucleic acids, it can also be stabilized in the dry state using sugars. Several studies have investigated the ability of these sugars to stabilize phages during drying and subsequent storage. Indeed, phages were shown to be stable when the glass transition temperature of the sugar matrix was 46 °C above the storage temperature, which supports the role of immobilization by the glassy matrix in phage stabilization (Chang et al., 2020).

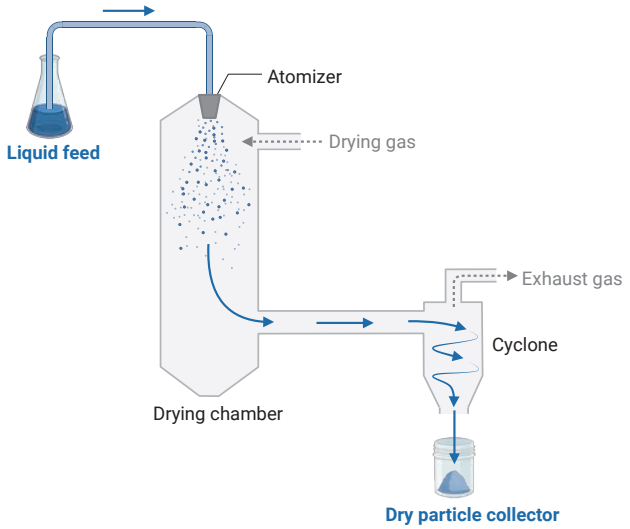


**Fig. 2** Schematic of the spray drying process. Created on BioRender.com.

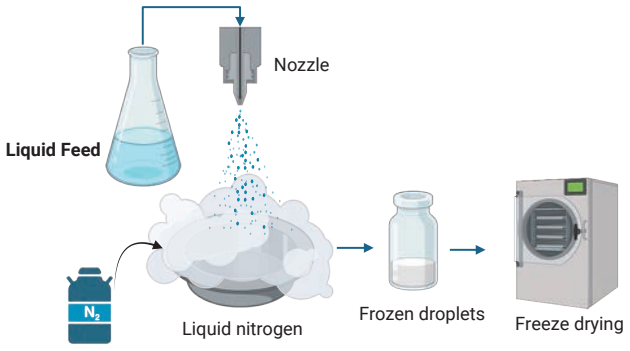


**Fig. 3** Schematic of spray freeze drying. Created on BioRender.com.

There are limited studies on the formulation of bacteriophages as dry powders for inhalation. These studies selected diverse phages that target multidrug-resistant strains of pathogenic bacteria like *Pseudomonas aeruginosa*, *Burkhoderia* complexes, and *Acinetobacter baumannii*. Most of these studies focused on spray drying to manufacture inhalable phage formulations (Chang et al., 2017; Leung et al., 2017; Matinkhoo et al., 2011). Other studies have explored spray freeze drying and a combination process of lyophilization-milling (Golshahi et al., 2011; Leung et al., 2016). The main objective of these studies was to determine processing conditions and excipient combinations that minimized the loss of phage viability during preparation and/or storage.

The number of viable phages is generally quantified using a double-agar plaque assay, which is considered the gold standard biological assay and is based on the interaction of a phage with its host bacteria (Ács et al., 2020). A phage sample is suspended and serially diluted. These diluted suspensions are poured over a lawn of actively growing host bacteria and incubated. The active phages in the solution infect the bacteria and begin the lytic cycle of phage propagation. Over time, bacterial cell lysis can cause visible plaques to appear on the surface of the bacterial lawn; each plaque ideally represents one active parent phage in the sample. The plaque count and dilution factor are then used to determine the active phage titer of the sample. Phage titers are therefore reported as plaque-forming units (PFUs) per mL. Because phage titers can vary over several orders of magnitude, change in phage titer is commonly reported as logarithmic change (base 10).

A subset of dry powder formulation studies on phages also determined the *in vitro* aerosol performance of the phage formulations and estimated the viable phage dose that could be delivered to the lungs. This is commonly

referred to as the lung dose or fine particle dose/fraction (FPF) of the formulation. The lung phage dose of a dry powder formulation is a function of particle aerodynamic diameter, particle morphology, cohesive and adhesive particle forces (Ke et al., 2022), as well as the formulation's capability to protect phages from damage due to shear and impaction forces during powder dispersion and inhalation.

Some of the most important studies on phage formulations are summarized here, with a focus on the most important excipients for phage preservation and aerosol performance in dry inhalable powders (**Table 2**).

### 3.1 Spray drying

Chang et al. (2017) screened a series of excipients to stabilize phages during spray drying: trehalose, lactose, mannitol, glycine, leucine, PEG3000, and Pluronic F68. They employed three phages—PEV1, PEV20, and PEV61—that showed antimicrobial activity against 90 clinical and multidrug-resistant strains of *P. aeruginosa*. Trehalose and lactose were screened as the best excipients for preserving phage viability during spray drying. Then, different sugar-to-leucine ratios were studied for phage preservation during spray drying. Higher sugar concentrations relative to leucine offered better protection. However, the highest sugar concentrations were not the best. The lowest titer loss was observed for all three phages with 20–5 mg/mL and 17–8 mg/mL sugar-leucine formulations for each sugar. Lactose provided better phage protection than trehalose, with titer loss of 0.3–0.4 and 0.5–0.9 logs, respectively. Leucine content in the formulation affected particle size and morphology. In formulations with high leucine concentrations, spherical particles of sizes less than 3 μm were obtained. Without leucine, particles agglomerated, which was unsuitable for inhalation. Aerosol performance analysis (MSLI) of the spray-dried formulations screened for high phage stability exhibited a fine particle fraction (FPF) greater than 50 %. The highest FPFs (65–67 %) were observed in formulations containing 0.0027 mg/mL Pluronic F68 (Chang et al., 2017).

It has been reported that leucine, which is usually included to improve powder dispersibility, can protect phages from thermal and desiccation stress during spray drying by forming a crystalline shell on the particle surface and displacing the phage particles to the core (Ke et al., 2022). It also offers moderate protection from moisture absorption during storage, which prevents crystallization of the amorphous sugar matrix (Li et al., 2016; 2017). However, leucine alone is a poor stabilizer of proteins in dry powders because it has a strong tendency to crystallize, which can cause phase separation of biologics from the protective matrix (Chen et al., 2021).

Spray dried powders containing phage cocktails were studied by Matinkhoo et al. (2011). The excipient matrix included trehalose (76 %), leucine (20 %), and optionally a third excipient (2 % of Pluronic surfactant, tyloxapol surfactant or casein Na salt). Casein was tested as a potential thermal stabilizer of phages based on the protective effect of milk on phages. The two surfactants were added to aid phage dispersion in the feed suspension for spray drying. Different phages showed varying losses from the spray drying process; but all phages in general experienced approximately 0.5 log losses. To measure the delivered lung dose, powder was dispersed through an Aerosolizer® inhaler and an Alberta Idealized throat. The trehalose-leucine-casein matrix with a mass ratio of 0.76:0.19:0.02 provided the most consistent delivery of powder mass to the lungs (approx. 70 %) across all phages/cocktails (Matinkhoo et al., 2011).

Similarly, in a study by Leung et al. (2017), PEV2, a *Pseudomonas* phage, was spray dried into powder matrices with various compositions of trehalose (0–80 %), mannitol (0–80 %), and L-leucine (20 %). Trehalose content >40 % helped preserve phages with 1.3 log loss. At 0 % and 20 % trehalose, log titer losses were 2.4 and 5.1, respectively. Mannitol and leucine did not provide protection when used alone. The recovery and respirable fraction of phages were measured using an Osmohaler at 100 L/min for 2.4 s. All formulations had FPF values of 40–48 %. Low phage recovery was observed during aerosol testing (20–53 %), which was attributed to the inactivation of phages on the particle surface due to impaction with the inhaler and other surfaces (Leung et al., 2017).

These studies highlight the protective effects of sugars, such as trehalose, lactose, and sucrose on proteins and other biological drug materials against the drying and thermal stresses of spray drying.

Another interesting excipient for spray-dried biological formulations is mannitol. Mannitol usually has a poor stabilizing effect because it tends to crystallize swiftly after spray drying and thus does not form an amorphous matrix with biologics. However, when used in a smaller fraction with glassy sugars, it may help prevent protein aggregation and deamidation as long as mannitol does not crystallize in the solid matrix (Cleland et al., 2001; Leung et al., 2017; Yan et al., 2021).

Yan et al. (2021) studied the formulation of the anti-*Acinetobacter baumannii* Myoviridae phage AB406 as spray-dried powders consisting of three excipients: trehalose (40–80 %), mannitol (40–0 %), and L-leucine (20 %). Three total solid contents (20, 40 and 60 mg/mL) were assessed. The titer loss due to spray drying was found to be around 0.3–0.5 log for all compositions. Both trehalose-leucine and trehalose-mannitol-leucine systems were similar in their ability to stabilize the phage. In contrast to the study by Leung et al. (2017), the addition of 40 % mannitol did not reduce the survival of AB406 phages after spray drying. The formulations with mannitol had significantly more stable phage titers during storage at room temperature

**Table 2** Summary of studies on the formulation of bacteriophage dry powders. (Continued on next page)

| Study | Phage studied | Manufacturing method | Excipients studied | Best formulation for lyoprotection (lowest phage $\log_{10}$ loss) | Best formulation for storage (lowest phage $\log_{10}$ loss) | Notable observations and inferences |
|---|---|---|---|---|---|---|
| (Matinkhoo et al., 2011) | *Burkholderia cepacia* KS4-M and KS14 phages; *Pseudomonas* phage ΦKZ/D3 | Spray drying | 76:20 trehalose-leucine<br>3rd excipient: Pluronic surfactant, tyloxapol surfactant, or casein Na salt | No significant differences among the tested compositions (~0.5) | — | Trehalose-leucine-casein (0.76–0.19–0.02) provided the most consistent *in vitro* delivery of powder mass to the lungs (Alberta Idealized Throat). |
| (Chang et al., 2017) | *Pseudomonas* PEV1, PEV20, and PEV61 | Spray drying | Trehalose, lactose, mannitol, glycine, leucine, PEG3000 and Pluronic F68 | 80:20/68:32 lactose-leucine (0.3–0.4)<br>80:20/68:32 trehalose-leucine (0.5–0.9) | — | 92:8 sugar-leucine formulations were not the best stabilizers. |
| (Chang et al., 2020) | PEV20 | Spray drying | 80:20 and 50:50 lactose-leucine | Both excipient systems performed similarly | Storage at 5 °C/15 % relative humidity (RH) resulted in the lowest titer reduction after 250 days (0.4–0.6 log loss). Phage stability was lower at 5 °C/33 %RH and 25 °C/15 %RH (~1.1 log) and lowest at 25 °C/33 %RH (3–4 log). | A higher titer loss during storage was observed at temperature-RH conditions, resulting in a smaller difference between the formulation glass transition temperature and storage temperature. |
| (Li et al., 2021) | Cocktail of PEV1, PEV20 (myoviruses), and PEV2 (a podovirus) | Spray drying | 80:20 lactose-leucine | Phage losses varied with the type of phage: PEV1, PEV2, and PEV20 exhibited titer losses of 0.1, 1.3, and 0.7 log. | — | Powder dispersion testing with a low-resistance Osmohaler (using NGI, 100 L/min) and a high-resistance Osmohaler (using MSLI, 60 L/min) showed fine particle fractions ~ 45% and ~63 %. |
| (Leung et al., 2017) | *Pseudomonas* PEV2 | Spray drying | Trehalose (80–0 %)<br>Mannitol (0–80 %)<br>Leucine (20 %) | Trehalose content > 40 % (1.3) | — | *In vitro* aerosol analysis (MSLI) showed FPF 40–48 %. The low recovery of phages during MSLI testing (20–53 %) was attributed to inactivation due to impaction. |
| (Yan et al., 2021) | *Acinetobacter baumannii* AB406 phage | Spray drying | Trehalose (40–80 %)<br>Mannitol (40–0 %)<br>Leucine (20 %)<br>Total solid of feed: 20, 40, and 60 mg/mL | All compositions exhibited similar phage loss (0.3–0.5) | Mannitol improved storage stability (room temperature, <20 % RH) | *In vitro* aerosol analysis (MSLI) at low RH showed that the FPF was better with higher mannitol content and lower feed total solid content. However, exposure to 65 % RH significantly reduced their FPF. |
| (Vandenheuvel et al., 2013) | *Pseudomonas* LUZ19 phage<br>*Staphylococcus* phage Romulus | Spray drying | Trehalose<br>Lactose<br>Dextran 35 | Trehalose | — | Lower spray-drying inlet temperature and atomization flow rate favored higher formulation phage viability. Romulus phages, owing to their larger and more delicate structure, were more susceptible to inactivation than LUZ19 during spray drying. |
| (Vandenheuvel et al., 2014) | *Pseudomonas* LUZ19 phage<br>*Staphylococcus* phage Romulus | Spray drying | 100 % trehalose | — | Better stability at 4 °C and 0 % RH | At 54 % RH, regardless of temperature, the powder absorbed moisture and trehalose crystallized. Storage at 25 °C caused thermal instability of the phages. |

**Table 2** Summary of studies on the formulation of bacteriophage dry powders. (Continued from previous page)

| Study | Phage studied | Manufacturing method | Excipients studied | Best formulation for lyoprotection (lowest phage $\log_{10}$ loss) | Best formulation for storage (lowest phage $\log_{10}$ loss) | Notable observations and inferences |
|---|---|---|---|---|---|---|
| (LeClair et al., 2016) | Human type 5 adenoviral vector | Spray drying | 100 % leucine<br>90:10 lactose/trehalose,<br>67:33 mannitol/dextran | 67:33 mannitol/dextran (0.3) | 67:33 mannitol/dextran (0.7 after 90 days at 20 °C and 10 %RH) | The mannitol/dextran matrix was the best stabilizer because it possibly encapsulated the virus particles better than other excipients. Surprisingly, trehalose/lactose did not stabilize the virus well during storage (3.1 log loss). |
| (Carrigy et al., 2019) | *Campylobacter jejuni* CP30A and CP20 | Spray drying | Trehalose (22.5 mg/mL)<br>Leucine (7.5 mg/mL) | (*compared atomizing method and the type of spray dryer*) | | The twin-fluid atomizer caused less phage inactivation (0.4 log) than the vibrating mesh atomizer (0.8 log). Desiccation was a more harmful stressor than atomization.<br>Buchi B-90 spray dryer showed a higher loss of phages than B-191 spray dryer. |
| (Carrigy et al., 2020) | *Campylobacter jejuni* CP30A | Spray drying | Trehalose (100 mg/mL) along with pullulan (20 mg/mL), trileucine (4 mg/mL), or leucine (20 mg/mL) as shell formers | Trileucine-trehalose & Pullulan-trehalose | Trileucine-trehalose (4:100 mg/mL) (overall 0.6 log loss after spray drying and 1-month room temperature storage) | Trileucine and pullulan formed amorphous shells around the dried particles during spray drying, which protected phages from direct exposure to desiccation stress. |
| (Merabishvili et al., 2013) | *Staphylococcus aureus* phages | Lyophilization | Sucrose (0.3–1.0 M)<br>Trehalose (0.3–1.0 M)<br>Mannitol<br>Glycine<br>Polyvinylpyrrolidone<br>PEG 6000 | Trehalose and sucrose<br>Sucrose at 0.8 and 1.0 M exhibited the lowest loss (0.4–0.5) | Most trehalose and sucrose solutions showed < 1 log loss after 27 months at 4 °C. | Phage stability in trehalose- and sucrose-lyophilized formulations was comparable to that of Luria Bertani broth during storage at 4 °C. |
| (Golshahi et al., 2011) | *Burkholderia cepacia* phage KS4-M and *Pseudomonas* phage ΦKZ | Lyophilization and milling | 60:40 lactose-lactoferrin | — | — | Powders were inhalable with a mass median aerodynamic diameter of 3.4 μm. For KS4-M, lung phage dose was $3.4 \times 10^6$ from a $9.8 \times 10^6$ PFU inhaler load; for phage ΦKZ, $9.8 \times 10^6$ from a$1.9 \times 10^7$ inhaler load. |
| (Ly et al., 2019) | *Mycobacterium tuberculosis* phage D29 | Atmospheric spray freeze drying | 70:30, 50:50, and 100:0 trehalose-mannitol | 70:30 trehalose-mannitol (0.8) | — | Trehalose remained amorphous and mannitol crystallized in the powder. |
| (Leung et al., 2016) | *Pseudomonas* PEV2 | Spray freeze drying (SFD) and Spray drying (SD) were compared | 60:20:20 (F1) and 40:40:20 (F2) trehalose-mannitol-leucine | F1 and F2 were similar after spray drying. When spray freeze dried, F1 was better than F2. | — | Phage loss during droplet generation was higher with the ultrasonic nozzle (2.00) than with the 2-fluid nozzle (0.75).<br>The drying step of SD was more harmful to phage titer than the drying step of SFD. |
| (Leung et al., 2018) | *Pseudomonas* PEV2 and PEV40 | Spray drying | 70:30 and 60:40 trehalose-leucine | The loss of phage titer did not differ between the two excipient combinations. After spray drying, the PEV2 and PEV40 titers decreased by 0.7 log and PEV40 titer decreased by 0.2 log. | Tested at 4 °C and 20 °C under vacuum over 12 months. Both PEV2 formulations were stable at 4 °C. At 20 °C, 70:30 trehalose-leucine exhibited better PEV2 stability than 60:40 trehalose-leucine. | MSLI dispersion tests showed high variability in the percentage recovery of phages. PEV40 formulations lost 0.50 log phages after storage regardless of temperature. The dispersion flow rate (100 vs. 60 L/min) and contact with the dispersion surfaces were ruled out as factors associated with low recovery. |

and <20 % relative humidity (RH) than trehalose-leucine only formulations (Yan et al., 2021). This result was attributed to the superior ability of mannitol to prevent protein aggregation and deamidation compared with disaccharides alone (Cleland et al., 2001). Contrary to the expectations of higher protein stabilization in a glassy matrix, the 40 % mannitol formulation with a low glass transition temperature ($T_g$) (~15 °C) was more stable than the 80 % trehalose formulation ($T_g$~110 °C), indicating that $T_g$ alone may not be a good indicator of phage stability in dry powders. The aerosol performance of the formulations was measured at low humidity: formulations with higher mannitol content and lower total solid content showed higher FPF (Yan et al., 2021). The authors explain this trend to be due to the ability of mannitol to prevent particle merging under dry conditions and the slightly smaller particle sizes of the formulations with lower total solid content. However, exposure to 65 % moisture for 1 h before aerosol testing caused a composition-dependent reduction in FPF: the highest reduction was observed with 20 % mannitol (>30 %), followed by 40 % mannitol (15 %) and 0 % mannitol (~ 5 %). This was attributed to higher moisture uptake and recrystallization of mannitol in the formulation with 20 % mannitol (and 60 % trehalose), which could have led to the formation of strong agglomerates or aggregates (Arte et al., 2024).

In a study by Vandenheuvel et al. (2013), *Pseudomonas* phage LUZ19 and *Staphylococcus* phage Romulus were formulated using spray drying. Trehalose showed good phage stabilization, whereas lactose and dextran 35 exhibited poor phage stabilization. The authors concluded that the reducing property of lactose can damage the protein structure of phage particles and reduce their infectivity. Poor phage survival in the presence of Dextran 35 was related to insufficient H-bonding capacity of dextran to phage particles after dehydration (Vandenheuvel et al., 2013). The effects of two inlet temperatures (85 °C vs. 100 °C) and two atomization air flow rates (6 L/min vs. 12 L/min) on the formulation phage titer were tested. Lower inlet temperature and atomization flow rates favored phage viability. At identical spray drying parameters and excipient compositions, the Romulus phage experienced much higher titer loss than the LUZ19 phage. This could be attributed to the larger and more delicate structure of the former, which increased its susceptibility to the shear stress of spray drying (Vandenheuvel et al., 2013).

This group later studied the storage stabilities of spray-dried LUZ19 and Romulus phage formulations at two temperatures (4 °C and 25 °C) and two humidity conditions (0 % and 54 %RH) for 12 months (Vandenheuvel et al., 2014). Trehalose 4 % w/v was used as the stabilizer. At 54 %RH, regardless of temperature, the powders absorbed moisture and trehalose crystallized (forming trehalose dihydrate), resulting in the loss of phage viability over time. Storage at 25 °C caused thermal instability of the phages; phage loss was observed at both 0 % and 54 %RHs. At 0 % RH and 25 °C, phage loss occurred in the absence of trehalose crystallization.

In a study by LeClair et al. (2016), a human type 5 adenoviral vector (AdHu5) was formulated as a dry powder via spray drying to improve storage stability. Three excipient systems were tested: 100 % leucine, 90/10 lactose/trehalose, and 67/33 mannitol/dextran. The loss of viability of the viral vector due to spray drying were 2.6 ± 0.5 log for leucine, 0.7 ± 0.1 for trehalose/lactose, and 0.3 ± 0.1 log for mannitol/dextran. The authors explained this to be due to different degrees of encapsulation within the excipient matrix shell during droplet drying. The mannitol/dextran matrix encapsulated the virus particles better than other excipients because of the lower diffusion rate of dextran than disaccharides, which can cause it to precipitate at the surface (LeClair et al., 2016). The morphological analysis showed that the encapsulation of the virus was better in the trehalose/lactose matrix than the crystalline leucine matrix. The effects of temperature and ambient humidity on the storage stability of phages in the solid matrix were also studied. The mannitol/dextran matrix provided the best thermal stability for the vector, showing 0.7 log loss at 20 °C and 10 %RH after 90 days, followed by trehalose/lactose with 3.1 log loss and leucine with 4.0 log loss. The lower phage stability observed in the lactose/trehalose matrix than in the mannitol/dextran matrix was attributed to the mobile amorphous state of the lactose/trehalose matrix. When the formulations were exposed to 45 %RH, all three formulations showed dramatically higher titer losses, which was attributed to moisture absorption and increased matrix mobility (LeClair et al., 2016). Excellent stabilization of phage in the mannitol/dextran matrix was in contrast with their poor stabilizing properties reported in other studies (Leung et al., 2017; Vandenheuvel et al., 2013). This result indicates that virus identity and manufacturing conditions strongly affect the stabilizing potential of excipient combinations.

Carrigy et al. (2019) studied the effects of atomizing method and type of spray dryer on the formulation of *Myoviridae* bacteriophages CP30A and CP20 that target *Campylobacter jejuni*. Trehalose (22.5 mg/mL) and leucine (7.5 mg/mL) were used as excipient matrix to stabilize the phage. The twin-fluid atomizer caused less phage inactivation (0.4 $\log_{10}$) than the vibrating mesh atomizer (0.8 $\log_{10}$). Desiccation was more detrimental to phage viability than atomization (for both mesh nebulization and two-fluid atomizer): ~ 2.0 log loss was attributed to the drying process alone (Carrigy et al., 2019). This loss was quantitatively equivalent to room-temperature air drying loss (for 48 h), indicating high phage sensitivity to desiccation stress. The study also compared the titer loss between two spray dryers, B-90 and B-191. B-90, which does not have a cyclone

for particle collection and uses electrostatic separation technology, showed a higher loss of phages than B-191. The authors inferred that cyclone separation of dry particles caused less damage to phage viability than electrostatic separation.

Another study by this group investigated the effect of trileucine, pullalan, or leucine in combination with trehalose on phage viability loss due to spray drying (Carrigy et al., 2020). Pullalan (1.0 log PFU reduction) exhibited significantly less viability loss than leucine (1.7 log) when used in combination with trehalose (20–100 mg/mL). Trileucine-trehalose (4–100 mg/mL) combination showed excellent phage stabilization: overall, 0.6 log PFU loss was observed after spray drying and 1 month of dry storage at room temperature. The authors attribute the phage stabilization of trileucine and pullulan to their ability to form amorphous shells around phage particles during spray drying, which can protect phages from direct exposure to desiccation stress. On the other hand, leucine-trehalose formulation showed a higher titer loss than trileucine and pullulan. This phage loss is likely due to destabilization associated with phase separation from the crystalline leucine and possible breakage by the growing crystals. Compared with the combination, trehalose and pullulan alone resulted in a higher phage loss of 2.4 log during spray drying.

### 3.2 Lyophilization and spray freeze drying

*S. aureus* phage (ISP) was developed into solids using lyophilization (Merabishvili et al., 2013). The effects of different excipients and their concentrations on phage stability during lyophilization and storage were studied. Trehalose and sucrose were found to be the best stabilizers among the different excipients studied. The smallest phage losses after lyophilization were observed with 0.8 and 1 M sucrose, showing only 0.4–0.5 log loss. Activity reduction over 27 months of storage at 4 °C for all trehalose and sucrose formulations was within 1 log, except for 0.3 M trehalose. The storage stability of phage in solid lyophilized formulations was compared to that in Luria Bertani broth and 0.9% saline. (Merabishvili et al., 2013). ISP was stable in LB showing only 1 log loss after 21 months. However, phage loss occurred steadily in the saline: 1 log loss after 12 months and, a further 1 log loss after 21 months. Lyophilized formulation with glycine provided minimal protection because glycine crystallized during lyophilization. After lyophilization with 0.1 or 0.5 M mannitol, high loss of phages (8 and 4 log, respectively) was observed. This result was attributed to the crystallization of mannitol.

Polymers may stabilize lyophilized proteins due to their preferential exclusion, surface activity, steric hindrance to protein interaction, and increased solution viscosity (Wang, 2000). However, 1 % and 5 % PVP solutions showed complete phage inactivation before lyophilization, as reported by Merabishvili et al. (2013). Lyophilization with polyhydric polymeric solvent PEG 6000 at 1 % and 5 % showed log titer losses of 1.8 and 5.0, respectively. The authors also found that the type of phage significantly affects their survival after drying, and processing conditions are not the sole determinants of phage stability. Therefore, lyophilization conditions must be optimized for each individual phage (Merabishvili et al., 2013).

Golshahi et al. (2011) prepared inhalable phage formulations via lyophilization followed by milling. Bacteriophages KS4-M and ΦKZ were lyophilized in a 60–40 w/w lactose-lactoferrin matrix and milled in a mixer mill (without beads) for 5 min to generate respirable powders. Lactoferrins are antimicrobial peptides naturally found in the secretory fluids of mammals. The combination of lactoferrin and phages for treating persistent bacterial infections has been a topic of interest (Kosznik-Kwaśnicka et al., 2022; Zarzosa-Moreno et al., 2020; Zimecki et al., 2008). No significant loss of viability was observed for either phage after lyophilization-milling processing (Golshahi et al., 2011). The mass median aerodynamic diameter and geometric standard deviation of the powder were 3.4 and 1.9 μm as measured using Anderson Cascade Impactor.

A novel technique called atmospheric spray freeze drying was used to prepare dry powders of D29 phages with trehalose and mannitol (Ly et al., 2019). The process involved two steps: (i) spray freezing of the phage-excipient suspension in a chamber cooled to −130 °C using liquid nitrogen, and (ii) atmospheric drying of the frozen solution by streaming progressively warmer air through the chamber, starting with a 2 h hold at −20 °C. The phage titer losses were 3.0 log for 1:1 trehalose-mannitol, 0.8 log for 7:3 trehalose-mannitol, and 1.5 log for 1:0 trehalose-mannitol (Ly et al., 2019). The presence of a lower concentration of mannitol appears to improve phage protection in the matrix; a higher fraction of mannitol in the matrix may lead to significant mannitol crystallization, leading to phase separation of the phages from the matrix.

In a study by Leung et al. (2016), the *Pseudomonas* PEV2 phage was formulated using two manufacturing methods: spray drying (SD) and spray freeze drying (SFD). For each method, two formulations were tested: 60-20-20 (F1) and 40-40-20 (F2) trehalose-mannitol-leucine. Phage titer loss and *in vitro* aerosol performance were studied for each formulation. Phage loss during droplet generation was higher with the ultrasonic nozzle (used for SFD) than the 2-fluid nozzle (used for SD) (2 log vs 0.75 log). However, the evaporative drying step (post-spraying) of SD caused greater damage to phage titer than the freeze-drying step of SFD. It is interesting to note that overall, phage titer loss was lower for spray-dried formulations than for spray freeze-dried formulations in this study (Leung et al., 2016). When different compositions were considered, SFD-F1 exhibited better phage preservation than SFD-F2. This

result was attributed to a higher amount of trehalose in F1 than F2. However, SD-F1 and SD-F2 did not differ in terms of overall phage titer loss. The recovery of phages during *in vitro* aerosol testing varied substantially between SD and SFD (20 % vs 80 %) (Leung et al., 2016). Nonetheless, higher total lung phage doses (in PFU) were obtained for SD than for SFD.

## 4. Current challenges in phage therapy

Phages are an effective treatment option for difficult bacterial infections because of their specificity and adaptability. However, phage therapy has certain drawbacks and faces important hurdles: (1) Despite some animal studies and clinical cases that support the efficacy and safety of phages, they are a unique and novel class of drugs for which the regulatory pathway of development is yet to be paved (Kortright et al., 2019). (2) Phages need to be selected specifically for a patient's needs because phages have a narrow host range. This can limit the accessibility of phage treatments and complicate the design of phage products for broader applications (Bhadoriya et al., 2023). It is also critical to select a phage that obligately infects and kills bacteria. (3) The FDA requires phages to be thoroughly evaluated for possible safety concerns. For instance, phages should not contain genes that express metabolites toxic to humans (Kortright et al., 2019), and they should not be able to transfer genes between bacteria (Doub, 2021). Finally, it is important to assess the risk of endotoxin release from lysed bacterial cells during phage product preparation and during its action in humans (Kortright et al., 2019). (4) Research on the interaction of phages with the human immune system is still in its infancy (Loc-Carrillo and Abedon, 2011; Roach et al., 2017). (5) Due to the omnipresence of phages in the environment, humans may possess neutralizing antibodies. Thus, therapeutic phages may be rendered ineffective by human immune mechanisms (Kortright et al., 2019). However, a recent article by Roach et al. (2017) showed that the innate immune response is important for the treatment of respiratory bacterial infection using phages. The results also highlight the ability of the host innate immune response to kill phage-resistant subpopulations of bacteria if a substantial fraction of the bacteria is phage-sensitive. Moreover, phages were well tolerated by the subject and were not neutralized by the immune system (Roach et al., 2017). (6) Phages are deemed unfit to target intracellular bacteria such as *Mycobacterium tuberculosis* (Kortright et al., 2019). (7) Bacteria can inevitably develop mechanisms to evade a specific phage, and in turn, the phage would need to be modified to target resistant bacteria. Therefore, it is important to employ strategies such as phage cocktails (Gordillo Altamirano and Barr, 2021) and phage-antibiotic combinations (Tagliaferri et al., 2019) that can delay resistance development and improve bacterial killing.

There are currently important challenges associated with the formulation of phages as dry powders: (1) Based on the review of reported literature on phage formulation, each phage is unique in its stability properties in the solid state; thus, its manufacturing and formulation must be optimized on a case-by-case basis. This can make developing dry powders cumbersome for phages. Due to the relative ease of formulation, most clinical applications of phages employ nebulization (Chang et al., 2018); (2) There is limited understanding of optimal phage dose, dose frequency, administration timing, and suitable combinations (phage–phage or phage–antibiotics) for a plethora of indications. Specifically, optimal phage therapy for treating polymicrobial or chronic infections has yet to be thoroughly investigated in animal or human subjects; (3) Plaque assay is an essential test for quantifying active phages in a formulation. However, due to its inherent variability, it is difficult to quantify small reductions in phage titers caused by destabilization during storage (Bodier-Montagutelli et al., 2017). This can make long-term storage stability data ambiguous. The variability of this assay also affects the accuracy of viable phages in the fine particle fraction of a dry powder, which is an important indicator of the efficiency of lung delivery; (4) The correlation between real-time and accelerated storage stability of phages is not well established, so storage stability assessment of formulations requires long durations of time; (5) Finally, the characterization of phage cocktails and phage-antibiotic combinations using plaque assays is complex. It is challenging to differentiate phages and determine their individual stability in a phage cocktail using plaque assays. For phage-antibiotic combination formulations, the antibiotic component can eradicate the host bacteria used for plaque assay before phage infection, which can interfere with plaque formation.

## 5. Conclusion

Bacteriophages are important alternative antimicrobial agents against multidrug-resistant pathogens. Although phages have a long path to regulatory approval as therapeutic agents, they hold great promise as adjuvants to antibiotics. Therefore, it is important to determine formulation strategies that preserve bacteriophage activity and stabilize them for long-term storage. Inhalable dry powders could be a viable treatment option for pulmonary infections. The dry state of the formulation better preserves biological activity than solutions or suspensions. This review summarized some important findings on the formulation of bacteriophages as inhaled dry powders.

The formulation of phages as dry powders with different excipients and processing conditions resulted in different outcomes in previous studies. Some general trends are observed in these studies, such as the prominence of trehalose, lactose, and sucrose as lyoprotectants compared with other excipients, such as mannitol, leucine, glycine, and

polymers. Mannitol may not be a good stabilizer on its own, but its tendency to crystallize after drying may improve the particle structural integrity. Leucine is widely used in dry powder formulations to improve aerosol performance. Because the amphiphilic nature of leucine leads to its mobilization to the droplet surface during spray drying, it may reduce the accumulation of phage units on the particle surface. Phages present on the surface can be deactivated by thermal, desiccation, and mechanical stresses; thus, leucine may reduce phage inactivation during spray drying and dose delivery (dispersion). The hydrophobic and crystalline shell of leucine also reduces moisture adsorption by the particles. In addition to these general trends, the effects of excipient composition and drying process on the viability loss of phages appeared to depend on the type of phage. Screening of excipients and optimization of processing conditions for phage stabilization in dry powder must be performed for each phage product individually. Overall, phage therapy development is still in infancy, and more fundamental and clinical studies are warranted to make full use of its therapeutic potential in tackling the global healthcare crisis of antibiotic resistance.

## Nomenclature

| | |
|---|---|
| CFU | Colony-forming units |
| FPF | Fine particle fraction |
| PFU | Plaque-forming units |
| RH | Relative humidity |
| SD | Spray drying |
| SFD | Spray freeze drying |

## References


Abedon S.T., Phage therapy of pulmonary infections, Bacteriophage, 5 (2015) e1020260. https://doi.org/10.1080/21597081.2015.1020260

Ács N., Gambino M., Brøndsted L., Bacteriophage enumeration and detection methods, Frontiers in Microbiology, 11 (2020) 594868. https://doi.org/10.3389/fmicb.2020.594868

Arte K.S., Tower C.W., Mutukuri T.T., Chen Y., Patel S.M., Munson E.J., Zhou Q., Understanding the impact of mannitol on physical stability and aerosolization of spray-dried protein powders for inhalation, International Journal of Pharmaceutics, 650 (2024) 123698. https://doi.org/10.1016/j.ijpharm.2023.123698

Bartlett J.G., Gilbert D.N., Spellberg B., Seven ways to preserve the miracle of antibiotics, Clinical Infectious Diseases, 56 (2013) 1445–1450. https://doi.org/10.1093/cid/cit070

Bhadoriya P., Sharma R., Mehrotra R., Kaur S., Srivastava I., Jain M., Kaushik P., A review on re-emerging bacteriophage therapy in the era of XDR, Biocell, 47 (2023) 1915–1930. https://doi.org/10.32604/biocell.2023.029564

Bodier-Montagutelli E., Morello E., L'Hostis G., Guillon A., Dalloneau E., Respaud R., Pallaoro N., Blois H., Vecellio L., Gabard J., Heuzé-Vourc'h N., Inhaled phage therapy: a promising and challenging approach to treat bacterial respiratory infections, Expert Opinion on Drug Delivery, 14 (2017) 959–972. https://doi.org/10.1080/17425247.2017.1252329

Cao F., Wang X., Wang L., Li Z., Che J., Wang L., Li X., Cao Z., Zhang J., Jin L., Xu Y., Evaluation of the efficacy of a bacteriophage in the treatment of pneumonia induced by multidrug resistance *Klebsiella pneumoniae* in mice, BioMed Research International, 1 (2015) 752930. https://doi.org/10.1155/2015/752930

Carrigy N.B., Liang L., Wang H., Kariuki S., Nagel T.E., Connerton I.F., Vehring R., Spray-dried anti-*Campylobacter* bacteriophage CP30A powder suitable for global distribution without cold chain infrastructure, International journal of pharmaceutics, 569 (2019) 118601. https://doi.org/10.1016/j.ijpharm.2019.118601

Carrigy N.B., Liang L., Wang H., Kariuki S., Nagel T.E., Connerton I.F., Vehring R., Trileucine and pullulan improve anti-campylobacter bacteriophage stability in engineered spray-dried microparticles, Annals of Biomedical Engineering, 48 (2020) 1169–1180. https://doi.org/10.1007/s10439-019-02435-6

Chan B.K., Turner P.E., Kim S., Mojibian H.R., Elefteriades J.A., Narayan D., Phage treatment of an aortic graft infected with Pseudomonas aeruginosa, Evolution, Medicine, and Public Health, 2018 (2018) 60–66. https://doi.org/10.1093/emph/eoy005

Chang L., Pikal M.J., Mechanisms of protein stabilization in the solid state, Journal of Pharmaceutical Sciences, 98 (2009) 2886–2908. https://doi.org/10.1002/jps.21825

Chang R.Y., Wong J., Mathai A., Morales S., Kutter E., Britton W., Li J., Chan H.-K., Production of highly stable spray dried phage formulations for treatment of *Pseudomonas aeruginosa* lung infection, European Journal of Pharmaceutics and Biopharmaceutics, 121 (2017) 1–13. https://doi.org/10.1016/j.ejpb.2017.09.002

Chang R.Y.K., Chen K., Wang J., Wallin M., Britton W., Morales S., Kutter E., Li J., Chan H.-K., Proof-of-principle study in a murine lung infection model of antipseudomonal activity of phage PEV20 in a dry-powder formulation, Antimicrobial Agents and Chemotherapy, 62 (2018). https://doi.org/10.1128/aac.01714-17

Chang R.Y.K., Kwok P.C.L., Khanal D., Morales S., Kutter E., Li J., Chan H.-K., Inhalable bacteriophage powders: glass transition temperature and bioactivity stabilization, Bioengineering & Translational Medicine, 5 (2020) e10159. https://doi.org/10.1002/btm2.10159

Chen Y., Ling J., Li M., Su Y., Arte K.S., Mutukuri T.T., Taylor L.S., Munson E.J., Topp E.M., Zhou Q.T., Understanding the impact of protein–excipient interactions on physical stability of spray-dried protein solids, Molecular Pharmaceutics, 18 (2021) 2657–2668. https://doi.org/10.1021/acs.molpharmaceut.1c00189

Cleland J.L., Lam X., Kendrick B., Yang J., Yang T.h., Overcashier D., Brooks D., Hsu C., Carpenter J.F., A specific molar ratio of stabilizer to protein is required for storage stability of a lyophilized monoclonal antibody, Journal of Pharmaceutical Sciences, 90 (2001) 310–321. https://doi.org/10.1002/1520-6017(200103)90:3<310::AID-JPS6>3.0.CO;2-R

Comeau A.M., Tétart F., Trojet S.N., Prère M.-F., Krisch H.M., Phage-antibiotic synergy (PAS): β-lactam and quinolone antibiotics stimulate virulent phage growth, PLOS ONE, 2 (2007) e799. https://doi.org/10.1371/journal.pone.0000799

Debarbieux L., Leduc D., Maura D., Morello E., Criscuolo A., Grossi O., Balloy V., Touqui L., Bacteriophages can treat and prevent pseudomonas aeruginosa lung infections, The Journal of Infectious Diseases, 201 (2010) 1096–1104. https://doi.org/10.1086/651135

Doub J., Risk of bacteriophage therapeutics to transfer genetic material and contain contaminants beyond endotoxins with clinically relevant mitigation strategies, Infection and Drug Resistance, 14 (2021) 5629–5637. https://doi.org/10.2147/IDR.S341265

Golshahi L., Lynch K.H., Dennis J.J., Finlay W.H., In vitro lung delivery of bacteriophages KS4-M and ΦKZ using dry powder inhalers for treatment of Burkholderia cepacia complex and Pseudomonas aeruginosa infections in cystic fibrosis, Journal of Applied Microbiology, 110 (2011) 106–117. https://doi.org/10.1111/j.1365-2672.2010.04863.x

Gordillo Altamirano F.L., Barr J.J., Unlocking the next generation of phage therapy: the key is in the receptors, Current Opinion in Biotechnology, 68 (2021) 115–123. https://doi.org/10.1016/j.copbio.2020.10.002

Gould I.M., Bal A.M., New antibiotic agents in the pipeline and how they can help overcome microbial resistance, Virulence, 4 (2013) 185–191. https://doi.org/10.4161/viru.22507

Grasmeijer N., Stankovic M., de Waard H., Frijlink H.W., Hinrichs W.L., Unraveling protein stabilization mechanisms: vitrification and water replacement in a glass transition temperature controlled system, Biochim Biophys Acta, 1834 (2013) 763–769.

https://doi.org/10.1016/j.bbapap.2013.01.020
Hauser A.R., Jain M., Bar-Meir M., McColley S.A., Clinical significance of microbial infection and adaptation in cystic fibrosis, Clinical Microbiology Reviews, 24 (2011) 29–70. https://doi.org/10.1128/cmr.00036-10
Hoppentocht M., Dry powder inhalation of antibiotics: a promising approach for treatment of infectious diseases, doctoral thesis, University of Groningen, 2016, ISBN: 978-94-90791-44-5.
Hoyle N., Zhvaniya P., Balarjishvili N., Bolkvadze D., Nadareishvili L., Nizharadze D., Wittmann J., Rohde C., Kutateladze M., Phage therapy against Achromobacter xylosoxidans lung infection in a patient with cystic fibrosis: a case report, Research in Microbiology, 169 (2018) 540–542. https://doi.org/10.1016/j.resmic.2018.05.001
Kamal F., Dennis J.J., Burkholderia cepacia complex phage-antibiotic synergy (PAS): antibiotics stimulate lytic phage activity, Applied and Environmental Microbiology, 81 (2015) 1132–1138. https://doi.org/10.1128/AEM.02850-14
Ke W.-R., Chang R.Y.K., Chan H.-K., Engineering the right formulation for enhanced drug delivery, Advanced Drug Delivery Reviews, 191 (2022) 114561. https://doi.org/10.1016/j.addr.2022.114561
Kortright K.E., Chan B.K., Koff J.L., Turner P.E., Phage therapy: a renewed approach to combat antibiotic-resistant bacteria, Cell Host & Microbe, 25 (2019) 219–232. https://doi.org/10.1016/j.chom.2019.01.014
Kosznik-Kwaśnicka K., Kaźmierczak N., Piechowicz L., Activity of phage–lactoferrin mixture against multi drug resistant staphylococcus aureus biofilms, Antibiotics, 11 (2022) 1256. https://doi.org/10.3390/antibiotics11091256
Kwok P.C.L., Chan H.-K., Delivery of inhalation drugs to children for asthma and other respiratory diseases, Advanced Drug Delivery Reviews, 73 (2014) 83–88. https://doi.org/10.1016/j.addr.2013.11.007
LeClair D.A., Cranston E.D., Xing Z., Thompson M.R., Evaluation of excipients for enhanced thermal stabilization of a human type 5 adenoviral vector through spray drying, International Journal of Pharmaceutics, 506 (2016) 289–301. https://doi.org/10.1016/j.ijpharm.2016.04.067
Leung S.S.Y., Parumasivam T., Gao F.G., Carrigy N.B., Vehring R., Finlay W.H., Morales S., Britton W.J., Kutter E., Chan H.-K., Production of inhalation phage powders using spray freeze drying and spray drying techniques for treatment of respiratory infections, Pharmaceutical Research, 33 (2016) 1486–1496. https://doi.org/10.1007/s11095-016-1892-6
Leung S.S.Y., Parumasivam T., Gao F.G., Carter E.A., Carrigy N.B., Vehring R., Finlay W.H., Morales S., Britton W.J., Kutter E., Chan H.-K., Effects of storage conditions on the stability of spray dried, inhalable bacteriophage powders, International Journal of Pharmaceutics, 521 (2017) 141–149. https://doi.org/10.1016/j.ijpharm.2017.01.060
Leung S.S.Y., Parumasivam T., Nguyen A., Gengenbach T., Carter E.A., Carrigy N.B., Wang H., Vehring R., Finlay W.H., Morales S., Britton W.J., Kutter E., Chan H.-K., Effect of storage temperature on the stability of spray dried bacteriophage powders, European Journal of Pharmaceutics and Biopharmaceutics, 127 (2018) 213–222. https://doi.org/10.1016/j.ejpb.2018.02.033
Li L., Leung S.S.Y., Gengenbach T., Yu J., Gao G., Tang P., Zhou Q., Chan H.-K., Investigation of L-leucine in reducing the moisture-induced deterioration of spray-dried salbutamol sulfate power for inhalation, International Journal of Pharmaceutics, 530 (2017) 30–39. https://doi.org/10.1016/j.ijpharm.2017.07.033
Li L., Sun S., Parumasivam T., Denman J.A., Gengenbach T., Tang P., Mao S., Chan H.-K., L-Leucine as an excipient against moisture on in vitro aerosolization performances of highly hygroscopic spray-dried powders, European Journal of Pharmaceutics and Biopharmaceutics, 102 (2016) 132–141. https://doi.org/10.1016/j.ejpb.2016.02.010
Li M., Chang R.Y.K., Lin Y., Morales S., Kutter E., Chan H.-K., Phage cocktail powder for Pseudomonas aeruginosa respiratory infections, International Journal of Pharmaceutics, 596 (2021) 120200. https://doi.org/10.1016/j.ijpharm.2021.120200
Livermore D.M., Multiple mechanisms of antimicrobial resistance in pseudomonas aeruginosa: our worst nightmare?, Clinical Infectious Diseases, 34 (2002) 634–640. https://doi.org/10.1086/338782
Livermore D.M., The threat from the pink corner, Annals of Medicine, 35 (2003) 226–234. https://doi.org/10.1080/07853890310001609
Loc-Carrillo C., Abedon S.T., Pros and cons of phage therapy, Bacteriophage, 1 (2011) 111–114. https://doi.org/10.4161/bact.1.2.14590
Ly A., Carrigy N.B., Wang H., Harrison M., Sauvageau D., Martin A.R., Vehring R., Finlay W.H., Atmospheric spray freeze drying of sugar solution with phage D29, Frontiers in Microbiology, 10 (2019) 488. https://doi.org/10.3389/fmicb.2019.00488
Matinkhoo S., Lynch K.H., Dennis J.J., Finlay W.H., Vehring R., Spray-dried respirable powders containing bacteriophages for the treatment of pulmonary infections, Journal of Pharmaceutical Sciences, 100 (2011) 5197–5205. https://doi.org/10.1002/jps.22715
Merabishvili M., Vervaet C., Pirnay J.-P., De Vos D., Verbeken G., Mast J., Chanishvili N., Vaneechoutte M., Stability of staphylococcus aureus phage ISP after freeze-drying (lyophilization), PLOS ONE, 8 (2013) e68797. https://doi.org/10.1371/journal.pone.0068797
Patton J.S., Byron P.R., Inhaling medicines: delivering drugs to the body through the lungs, Nature Reviews Drug Discovery, 6 (2007) 67–74. https://doi.org/10.1038/nrd2153
Roach D.R., Leung C.Y., Henry M., Morello E., Singh D., Di Santo J.P., Weitz J.S., Debarbieux L., Synergy between the host immune system and bacteriophage is essential for successful phage therapy against an acute respiratory pathogen, Cell Host & Microbe, 22 (2017) 38–47.e34. https://doi.org/10.1016/j.chom.2017.06.018
Rossolini G.M., Arena F., Pecile P., Pollini S., Update on the antibiotic resistance crisis, Current Opinion in Pharmacology, 18 (2014) 56–60. https://doi.org/10.1016/j.coph.2014.09.006
Ruest M.K., Supina B.S.I., Dennis J.J., Bacteriophage steering of Burkholderia cenocepacia toward reduced virulence and increased antibiotic sensitivity, Journal of Bacteriology, 205 (2023) e00196–00123. https://doi.org/10.1128/jb.00196-23
Ryan E.M., Alkawareek M.Y., Donnelly R.F., Gilmore B.F., Synergistic phage-antibiotic combinations for the control of Escherichia coli biofilms in vitro, FEMS Immunology & Medical Microbiology, 65 (2012) 395–398. https://doi.org/10.1111/j.1574-695X.2012.00977.x
Santana H., Sotolongo J., González Y., Hernández G., Chinea G., Gerónimo H., Amarantes O., Beldarraín A., Páez R., Stabilization of a recombinant human epidermal growth factor parenteral formulation through freeze-drying, Biologicals, 42 (2014) 322–333. https://doi.org/10.1016/j.biologicals.2014.07.005
Semler D.D., Goudie A.D., Finlay W.H., Dennis J.J., Aerosol phage therapy efficacy in Burkholderia cepacia complex respiratory infections, Antimicrobial Agents and Chemotherapy, 58 (2014) 4005–4013. https://doi.org/10.1128/aac.02388-13
Scoffone V.C., Barbieri G., Irudal S., Trespidi G., Buroni S., New antimicrobial strategies to treat multi-drug resistant infections caused by gram-negatives in cystic fibrosis, Antibiotics, 13 (2024) 71. https://doi.org/10.3390/antibiotics13010071
Tagliaferri T.L., Jansen M., Horz H.-P., Fighting pathogenic bacteria on two fronts: phages and antibiotics as combined strategy, Frontiers in Cellular and Infection Microbiology, 9 (2019) 22. https://doi.org/10.3389/fcimb.2019.00022
Torres-Barceló C., Hochberg M.E., Evolutionary rationale for phages as complements of antibiotics, Trends in Microbiology, 24 (2016) 249–256. https://doi.org/10.1016/j.tim.2015.12.011
Uchiyama J., Shigehisa R., Nasukawa T., Mizukami K., Takemura-Uchiyama I., Ujihara T., Murakami H., Imanishi I., Nishifuji K., Sakaguchi M., Matsuzaki S., Piperacillin and ceftazidime produce the strongest synergistic phage–antibiotic effect in Pseudomonas aeruginosa, Archives of Virology, 163 (2018) 1941–1948. https://doi.org/10.1007/s00705-018-3811-0
Vandenheuvel D., Meeus J., Lavigne R., Van den Mooter G., Instability of bacteriophages in spray-dried trehalose powders is caused by crystallization of the matrix, International Journal of Pharmaceutics, 472 (2014) 202–205. https://doi.org/10.1016/j.ijpharm.2014.06.026
Vandenheuvel D., Singh A., Vandersteegen K., Klumpp J., Lavigne R., Van den Mooter G., Feasibility of spray drying bacteriophages into

respirable powders to combat pulmonary bacterial infections, European Journal of Pharmaceutics and Biopharmaceutics, 84 (2013) 578–582. https://doi.org/10.1016/j.ejpb.2012.12.022

Ventola C.L., The antibiotic resistance crisis: part 1: causes and threats, Pharmacy and Therapeutics, 40 (2015) 277–283. https://www.ncbi.nlm.nih.gov/pmc/articles/PMC4378521/

Walters R.H., Bhatnagar B., Tchessalov S., Izutsu K.-I., Tsumoto K., Ohtake S., Next generation drying technologies for pharmaceutical applications, Journal of Pharmaceutical Sciences, 103 (2014) 2673–2695. https://doi.org/10.1002/jps.23998

Wang W., Lyophilization and development of solid protein pharmaceuticals, International Journal of Pharmaceutics, 203 (2000) 1–60. https://doi.org/10.1016/S0378-5173(00)00423-3

Yan W., He R., Tang X., Tian B., Liu Y., Tong Y., To K.K.W., Leung S.S.Y., The influence of formulation components and environmental humidity on spray-dried phage powders for treatment of respiratory infections caused by *Acinetobacter baumannii*, Pharmaceutics, 13 (2021) 1162. https://doi.org/10.3390/pharmaceutics13081162

Zarzosa-Moreno D., Avalos-Gómez C., Ramírez-Texcalco L.S., Torres-López E., Ramírez-Mondragón R., Hernández-Ramírez J.O., Serrano-Luna J., de la Garza M., Lactoferrin and its derived peptides: an alternative for combating virulence mechanisms developed by pathogens, Molecules, 25 (2020) 5763. https://doi.org/10.3390/molecules25245763

Zhou Q., Tang P., Leung S.S.Y., Chan J.G.Y., Chan H.-K., Emerging inhalation aerosol devices and strategies: where are we headed?, Advanced Drug Delivery Reviews, 75 (2014) 3–17. https://doi.org/10.1016/j.addr.2014.03.006

Zimecki M., Artym J., Kocieba M., Weber-Dabrowska B., Lusiak-Szelachowska M., Górski A., The concerted action of lactoferrin and bacteriophages in the clearance of bacteria in sublethally infected mice, Postepy Hig Med Dosw (Online), 62 (2008) 42–46. https://pubmed.ncbi.nlm.nih.gov/18268472/

## Authors' Short Biographies

**Vaibhav Pathak** is a Ph.D. candidate in the department of Industrial and Molecular Pharmaceutics at Purdue University, USA. He earned a M.S in Agricultural and Biological Engineering at Purdue University in 2018. He completed his B. Tech in Biochemical Engineering at the Indian Institute of Technology, Banaras Hindu University in 2016. His research interests include pharmaceutical formulation of antibacterial agents for dry powder inhalers.

**Prof. Hak-Kim Chan**, Professor in Pharmaceutics, is leading the Advanced Drug Delivery Group at the Sydney Pharmacy School, University of Sydney. Prof. Chan is a world leader in respiratory drug and phage delivery, with a research program ranging from powder production by novel processes, particle engineering and aerosol formulation, to scintigraphic imaging of lung deposition and clinical outcome. He is a Fellow of American Association of Pharmaceutical Scientists, was Vice President of Asian Federation for Pharmaceutical Science, Executive Editor of Advanced Drug Delivery Reviews, and recipient of the 2023 Career Achievement Award of The International Society for Aerosols in Medicine. He has more than 500 scientific publications (>25,000 citations, h-index 86) on pharmaceutical formulation and drug delivery.

**Dr. Qi (Tony) Zhou** is an associate professor at Purdue University. He is a recognized expert in inhalation dosage forms and pulmonary drug delivery systems. He is an Editor of AAPS PharmSciTech and Editorial Board Member of 10 pharmaceutical journals including International Journal of Pharmaceutics, Pharmaceutical Research and Journal of Pharmaceutical Sciences. He has published more than 120 journal articles, and filed 9 patents/applications. Dr. Zhou's research has attracted more than $12 million funding including NIH R01 grants and many industrial projects. Dr. Zhou's significant contribution to the field of pharmaceutical science has been recognized by many prestigious awards including 2021 AAPS Emerging Leader Award.

KONA Powder and Particle Journal

KONA Powder and Particle Journal No. 42 (2025) 213–226/https://doi.org/10.14356/kona.2025005 Review Paper

# Recent Advances in Nitride Composites for Effective Removal of Organic Dyes in Wastewater Treatment†

**Wenjea J. Tseng**

*Department of Materials Science and Engineering, National Chung Hsing University, Taiwan*

The presence of organic dyes from industrial effluents has caused growing environmental and human health concerns. Various remediation methods and materials are available to minimize the environmental impact and ensure safe drinking water. Nitride composite particles have recently emerged as one of the promising materials for the efficient and selective removal of toxic and hazardous substances (including organic and inorganic compounds) from industrial wastewater. This review summarizes recent advances in the disposal of organic dyed wastewater using advanced nitride composite particles, including graphitic carbon nitride-based nanocomposites, boron nitride composites, and two-dimensional transition metal nitrides. The selection of appropriate materials remains largely a trial-and-error approach at present. This review highlights multiple dye-removal mechanisms, such as photocatalytic degradation, dye-sorption behavior, and computational analysis, to aid the material selection and shed light on the interactions between organic dye contaminants and nitride composites.

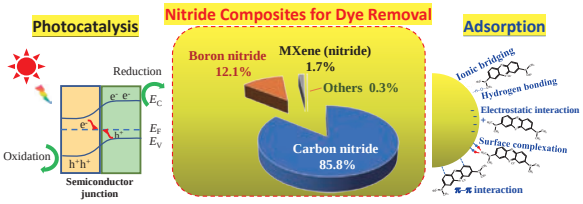


**Keywords:** nitride, composite, dye removal, adsorption, photocatalysis

## 1. Introduction

Water is an essential resource for life on Earth, and its quality is vital for the health and well-being of both humans and the environment. According to a United Nations report, an estimated 47 % of the world's population will face a clean-water shortage by 2030 (Connor, 2015). Population growth, urbanization, and anthropogenic activities contribute to the increasing global water demand by 50 % by the year 2050 (Connor, 2015). Wastewater, the water discharged after use in households, industries, and agriculture, has already become a significant source of pollution that might have severe consequences for the environment and human health. Failure to treat the wastewater properly may harm public health since the untreated wastewater might contain harmful microorganisms, viruses, and chemicals that can cause diseases (Dickin et al., 2016; Adegoke et al., 2018; Choudri and Charabi, 2019). Removal of these harmful contaminants reduces the risk of waterborne illnesses. In addition, eutrophic wastewater may contain nutrients like nitrogen and phosphorus that can cause excessive algae growth in water bodies, leading to oxygen depletion and fish kills (Lapointe et al., 2015; Preisner et al., 2020, 2021). Toxic chemicals in untreated wastewater may also harm aquatic life, damage ecosystems, and enter the food chain (Al-Tohamy et al., 2022; Hamidian et al., 2021; Islam et al., 2021; Saravanan et al., 2021). Treating wastewater protects the environment and helps conserve water resources by reducing the demand for freshwater resources, ensuring sufficient water to meet the needs of people and industries.

Textile and pigment industries significantly contribute to the global economy and environmental pollution. The global market of dyes and pigments was valued at USD 38.2 billion in 2022 and may grow at a compound annual growth rate of 5.3 % from 2023 to 2030 (Market Analysis Report, 2023). The market forecast indicates a growing demand for colorants worldwide, which consume over a million tons of dyes annually (Singh and Arora, 2011; Al-Tohamy et al., 2022). Using organic dyes in textile and pigment industries can thus have negative environmental and health impacts if not properly managed (Lellis et al., 2019). Industries must adopt sustainable and responsible practices, such as eco-friendly dyes and proper wastewater treatment, to minimize environmental and health impacts.

More than 100,000 commercial dyes have been reported on the market (Yagub et al., 2014). Some of the most common organic dyes used in textile industries include: i) reactive dyes for their color fastness and ability to bond with a wide range of fabric fibers, ii) acid dyes for their bright and vibrant colors to wool, silk, and nylon fibers in fabrics, iii) disperse dyes for their ability to bond with the synthetic fibers with color fastness, iv) direct dyes for dyeing cellulosic fibers with their ease of use and affordability, v) vat dyes for their excellent color fastness to stain cotton, rayon, and other cellulosic fibers, and vi) sulfur dyes for dyeing

† Received 3 July 2023; Accepted 23 August 2023
J-STAGE Advance published online 17 March 2024
Add: Taichung 402, Taiwan
E-mail: wenjea@dragon.nchu.edu.tw
TEL: +886-4-22870720 FAX: +886-4-22857017

cellulosic fibers such as cotton and rayon with affordable price and good color fastness (Bechtold et al., 2007; Degano et al., 2009; Zollinger, 2003). Similarly, the pigment industry uses a wide range of organic dyes to produce colorants, including: i) azo dyes consisting of the azo group (–N=N–) as the chromophore for their bright and vibrant colors, ii) phthalocyanine dyes for their blue and green hues, iii) anthraquinone dyes for their lightfastness and color fastness, iv) quinacridone dyes for their bright and vivid colors, v) indigo dyes for their blue color in the production of denim, and vi) perylene dyes for their lightfastness and good color fastness (Zollinger, 2003).

The vast compositional diversity and structural complexity of the organic colorants used in the textile and pigment industries inevitably make complete dye removal an insurmountable task in wastewater treatment. Various methods are available for treating synthetic dyes, e.g., physical, chemical, and biological approaches (Al-Tohamy et al., 2022; Forgacs et al., 2004; Martıńez-Huitle and Brillas, 2009; Singh and Arora, 2011; Yaseen and Sholz, 2019). **Table 1** highlights the advantages and disadvantages of the most frequently used dye removal techniques. Having a method that can effectively remove various types of dyes is challenging. Still, the method's effectiveness depends primarily on specific dyes present in the wastewater and the characteristics of the method used. Some processes may be more effective for removing specific dyes, depending mainly on their chemical properties, such as their molecular structure, solubility, and reactivity. In practice, a combination of methods may become necessary to achieve the desired level of dye removal.

For the materials used in organic dye removal, there have been some excellent reviews covering a wealth of natural and synthetic materials for wastewater remediation (Forgacs et al., 2004; Islam et al., 2021; Martıńez-Huitle and Brillas, 2009; Singh and Arora, 2011; Yagub et al., 2014). Some commonly used natural materials include activated carbon, clay minerals, zeolite, agricultural by-products (e.g., husk, leaf, sawdust, and peel from the plant, chitosan made from the shell of crustaceans), and industrial by-products (e.g., mud, fly ash). Many of these materials purify the dyed wastewater by adsorption (Yagub et al., 2014). Materials possessing high porosity and large surface area are highly desirable as effective sorbents and photocatalysts for selective dye removal. With the rapid development of nanostructured synthetic materials in recent decades, nitride composite particles have emerged as promising materials for efficiently removing organic dye pollutants from industrial wastewater. **Fig. 1a** shows a chronological evolution of reported scientific papers on

**Table 1** Pros and cons of methods used for organic dye removal.

| Methods | Pros | Cons |
|---|---|---|
| *Physical Approach* | | |
| (i) Adsorption | Applicable for treating a wide variety of dyes | Needs regular adsorbent replenishment and sludge cleaning |
| (ii) Ion exchange | Able to handle a large volume of wastewater; requires no chemicals | Impractical to remove some dyes and contaminants that are not ionizable |
| (iii) Membrane filtration | Applicable for treating a wide variety of dyes efficiently in large volumes | Needs periodic replacement of fouled membrane; often requires energy supply to maintain the pressure needed for filtration |
| *Chemical Treatment* | | |
| (i) Coagulation and flocculation | Effective in removing various dyes in large volumes | Often pH sensitive; requires the use of chemicals, and generates sludges |
| (ii) Advanced chemical oxidation | Removes target dyes selectively in large volumes by the formation of $OH^{\bullet}$ | Requires the use of chemicals and may generate harmful by-products; may require longer reaction time |
| (iii) Electrochemical method | Fast and effective at removing a wide range of both synthetic and natural dyes; able to use renewable energy sources | High electricity consumption; requires specialized knowledge in system design and operation |
| *Biological Approach* | | |
| (i) Enzyme-based method | Selective dye removal with energy-saving and environmentally friendly features; less sludge formation | Limited effectiveness and slow processing for large volumes |
| (ii) Microbial method | Natural and low cost; may have a high removal efficiency for certain types of dyes | Limited effectiveness and slow processing for large volumes; may be sensitive to environmental conditions |

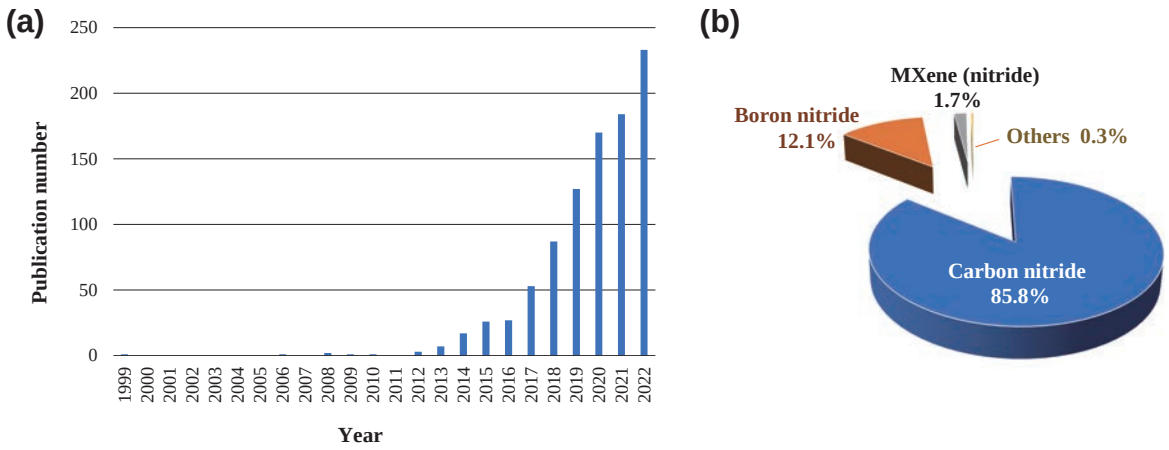


**Fig. 1** **(a)** Publication numbers on nitrides in chronological order for dye removal (Data from Web of Science search using keywords of "nitride", "dye", and "rem*"). **(b)** Publications sorted by materials illustrating the weighted fractions.

nitrides for dye removal. Intensive research has been directed toward wastewater treatment using nitride nanomaterials since about a decade ago. This result is attributable to the emergence of two-dimensional (2D) semiconducting graphitic carbon nitride (g-$C_3N_4$) nanosheets and their three-dimensional (3D) porous counterparts. The g-$C_3N_4$ nanostructures show promise of harnessing visible light for the photocatalytic degradation of organic dyes together with adsorption capability toward selective organic pollutants (Acharya and Parida, 2020; Hu et al., 2019; Lam et al., 2016; Santoso et al., 2020). The fact that g-$C_3N_4$ gained significant attention is demonstrated by the publication of the first highly cited article in 2012 (Cui et al., 2012) from the Web of Science search. **Fig. 1b** further illustrates the prevalent dominance of the g-$C_3N_4$ in published nitride-related water-remediation papers with a substantial 85.8 %. Boron nitride (BN) and transition metal carbide/nitride (MXene) with 2D layered structures follow in the distant second and third positions of 12.1 % and 1.7 %, respectively.

While literature reviews have extensively focused on carbon nitride-based nanomaterials, we envision that a more comprehensive understanding of nitride-based nanocomposites will significantly contribute to developing next-generation multi-purpose dye-removal solutions. Considering their potential use in wastewater treatment, this review aims to cover the recent progress in material design, fabrication method, and dye-removal performance of various nitride nanocomposites. Selecting appropriate dye-removal materials largely remains a trial-and-error approach at present. The review highlights multiple dye-removal mechanisms, such as the photocatalytic degradation and dye-sorption behavior of the composite nitride nanoparticles, together with computational analyses that show promises of shedding light on the nature of interactions between organic dye contaminants and nitrides. Finally, some future perspectives will be addressed.

## 2. g-$C_3N_4$-based nanocomposites

Carbon nitride is a class of compound materials composed of carbon and nitrogen atoms with various structures and properties. Different allotropes exist for the carbon nitride, including alpha, beta, cubic, pseudo-cubic, amorphous, and g-$C_3N_4$ (Aspera et al., 2010; Wang et al., 2017). Among them, g-$C_3N_4$ possesses a repeating unit of stacked carbon atoms and nitrogen-rich functional groups arranged in a honeycomb-like structure resembling graphite. The unique combination of features includes an n-type semiconductor with a tunable optical bandgap around 2.7 eV suitable for harnessing visible light, excellent chemical and thermal stability because of the covalent nature of the carbon–nitrogen bonding for use in harsh environments, facile preparation with environmental friendliness, a metal-free chemical attribute with earth abundance, and low cytotoxicity (Ahmadi et al., 2023; Dong et al., 2014; Jiang et al., 2017; Teter and Hemley, 1996; Thomas et al., 2008; Xu et al., 2018; Zhao et al., 2015). **Fig. 2** shows the primary tectonic units of g-$C_3N_4$, which include two major substructures, i.e., triazine and tri-s-triazine (heptazine). The tri-s-triazine-based structure is the most stable allotrope in the ambient environment (Dong et al., 2014; Thomas et al., 2008).

The stacking layer structure in the g-$C_3N_4$ allotrope consists of the $sp^2$ hybridization of carbon and nitrogen heteroatoms with features of tunable interlayer spacing through changing the localization of electrons and the binding energy between neighboring layers. The structure generates the π-conjugated graphitic planes with tunable positions of the highest occupied molecular orbital (HOMO) and the lowest unoccupied molecular orbital (LUMO) as a semiconducting photocatalyst for the purification of dye-contaminated wastewater (Zhao et al., 2021).

Intrinsic drawbacks, such as insufficient absorption of light energy, low surface area, and fast recombination of photogenerated electrons and holes, suppress the

photocatalytic efficiency of bulk g-$C_3N_4$ photocatalyst. The photoelectronic conversion of g-$C_3N_4$ would enhance substantially by increasing the nitrogen content, as the presence of nitrogen atoms impacts the spin density and charge distribution of the carbon atoms. This creates active sites on the surface to remove organic dyes and pigments efficiently under light illuminations (Ahmadi et al., 2023). Various strategies have been explored to overcome the shortcomings of g-$C_3N_4$ photocatalysts, including doping of metal or non-metal elements, creation of semiconducting junctions with suitable band structures at the interface, morphological control, and defect-modulating engineering (Acharya and Parida, 2020; Kumar et al., 2022; Luo et al., 2023; Xu et al., 2018). The construction of heterojunction involving g-$C_3N_4$ nanosheet composite with a semiconductor having a matched band-edge potential is promising for enhancing the separation efficiency of photoinduced charge carriers together with synergistically enriching light-harvest ability. For example, **Fig. 3a** shows a hypothetical charge-transfer route when two coupled semiconductor photocatalysts display the staggered band structure at the interface. The photogenerated electrons are thought to flow from photocatalyst 2 to photocatalyst 1 under light irradiation, while the opposite is true for the photogenerated holes, facilitating the separation of charge carriers. The idealized recombination suppression occurs at the expense of reduced redox activity for photocatalysis. In addition, the electrostatic repulsion between the like charges may inhibit the continuous accumulation of charge carriers from transferring (Xu et al., 2020). In this regard, the Z-scheme photocatalyst with a suitable intermediate couple between two contacting semiconductors provides a promising alternative to facilitate the charge separation while retaining a strong redox ability in **Fig. 3b** (Kudo and Miseki, 2009; Li et al., 2016). In a typical all-solid-state Z-scheme photocatalyst, a solid conductor is used to replace the shuttle-redox ion pairs in traditional Z-scheme for imparting the transfer of charge carriers at the semiconductor junction. The evolvement toward direct Z-scheme later occurs, as demonstrated in a g-$C_3N_4$/$TiO_2$ composite photocatalyst by Yu et al. in 2013, which does not require an intermediate electron mediator to attain a robust photocatalytic capability. They have shown that the disparity in the work functions of g-$C_3N_4$ and $TiO_2$ renders the formation of an internal electric field at the junction so that an inherent actuating force takes place to replace the intermediate electron mediator. This development leads to a step-scheme (known as the S-scheme) heterojunction involving a

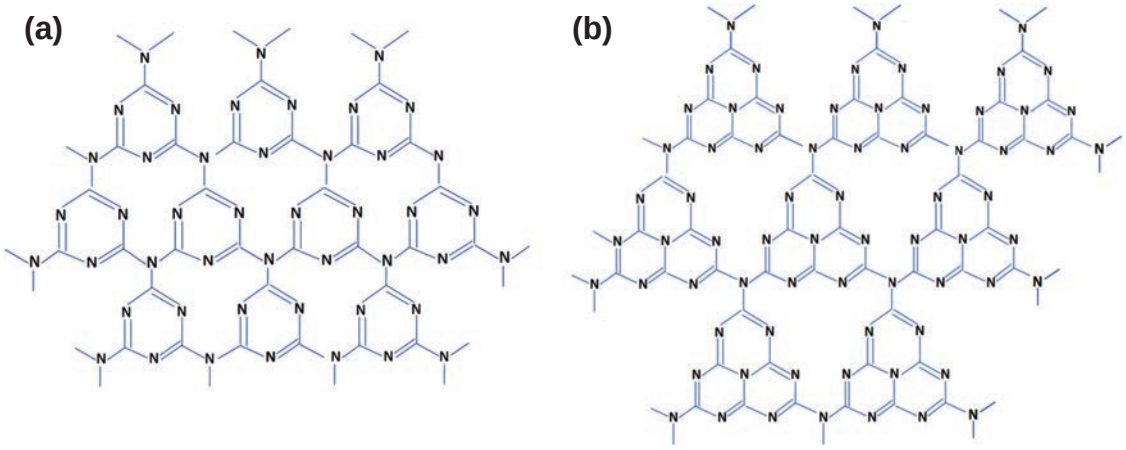


**Fig. 2** Primary tectonic units of **(a)** triazine and **(b)** tri-s-triazine for g-$C_3N_4$ allotropes.

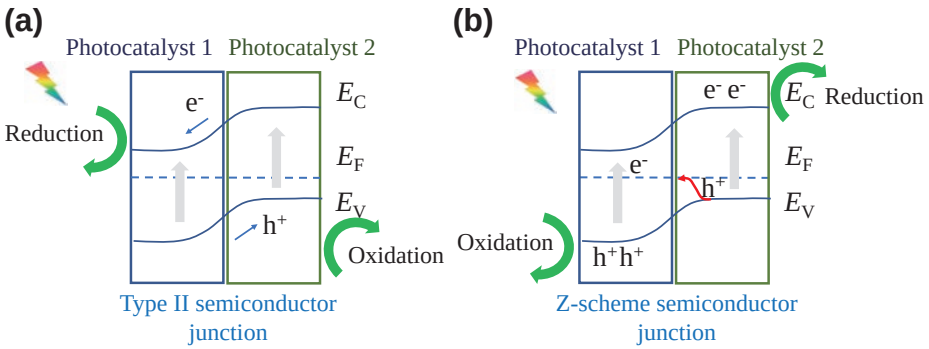


**Fig. 3** Examples of possible charge-transfer routes at the semiconductor junction for **(a)** Type II (staggered gap) and **(b)** direct Z-scheme/S-scheme heterojunctions.

semiconducting couple containing an oxidation photocatalyst (i.e., photocatalyst 1 in **Fig. 3b**) and a reduction counterpart (i.e., photocatalyst 2 in **Fig. 3b**) to form the staggered band structure with a charge-transfer route resembling that of the Z-scheme while remaining a strong redox capability (Xu et al., 2020; Zhang et al., 2022).

**Table 2** lists selected examples of dye-removal performance using g-$C_3N_4$ nanocomposite photocatalysts in dyed water treatment. Various g-$C_3N_4$ nanocomposites have been examined for the photocatalytic removal of organic dye pollutants. In view of the literature in **Table 2**, we may conclude that heterojunction with a suitable band alignment allows simultaneously the creation of active sites and efficient separation of photoinduced charge carriers for facilitating dye decomposition under light illuminations.

The pursuit of highly efficient g-$C_3N_4$-based composite photocatalyst depends critically on the synthesis process since the attainment of mesoporous 2D g-$C_3N_4$-based nanocomposites with high surface area, tailored pore size and pore shape is advantageous in providing active chemical sites on the surface for the selective photodegradation of organic dyes. Appropriate defects residing at the surface are potentially beneficial for enhanced photocatalysis (Acharya and Parida, 2020; Darkwah and Ao, 2018; Ismael et al., 2019; Zhao et al., 2018; Zhu et al., 2014). Various nitrogen-rich organic precursors containing C–N bonding structure without direct C–C bonding have been used as the precursor compound for the g-$C_3N_4$ synthesis, e.g., cyanamide, dicyandiamide, melamine, thiourea, urea, or their mixtures, via the polycondensation route. A low surface area often results due mainly to the formation of a layered graphitic structure. Two main process strategies have been proposed to resolve this shortcoming, i.e., the hard- and soft-templating routes for the g-$C_3N_4$ synthesis. The prepared g-$C_3N_4$ nanosheets often favor depositing on a template with a high surface area. **Table 3** lists the differences between the hard- and soft-templating methods. The hard-templating approach involves using a sacrificial hard template, such as mesoporous silica, for the impregnation with a precursor compound (Groenewolt and Antonietti, 2005; Wang et al., 2009). The removal of the template by calcination or chemical etching forms g-$C_3N_4$ with a porous structure that replicates the shape of the template. On the other hand, the soft-templating approach involves using a soft template, such as surfactants or block copolymers, which self-assemble to form a template for the organic precursor (Lu et al., 2014; Yan, 2012). After deposition of the precursor onto the template, the template can be removed by washing or mild calcination, leaving behind g-$C_3N_4$ with a mesoporous structure that replicates the shape of the template.

A large surface area with a suitable pore structure for allowing organic dye molecules more access to the surface moiety of g-$C_3N_4$ nanocomposite is one important parameter affecting dye removal in wastewater treatment. Surface characteristics of the mesoporous g-$C_3N_4$-based nanocomposite are also essential for imparting high activity as an efficient adsorbent. Aspera et al. (2010) have shown that bonding occurs favorably between the hydrogen atom of the water molecule and the two-coordinated nitrogen atom of the tri-s-triazine-based g-$C_3N_4$ with a chemisorption energy of –0.82 eV by *ab initio* density functional theory (DFT) computations. Modwi et al. (2022) verified recently that hydrogen-bonding interactions occur favorably between OH groups of mesoporous MgO/g-$C_3N_4$ nanocomposite and lone-pair electrons of amine groups of basic fuchsin (BF) dyes, resulting in a pronounced adsorptive uptake selectively.

In addition to the hydrogen bonding, mechanisms involved in the dye adsorption of g-$C_3N_4$ nanocomposites include electrostatic interaction, π–π interaction, surface complexation, and cation bridge (Chen et al., 2020; Fronczak, 2020). **Table 4** lists selected examples of adsorptive dye removal using g-$C_3N_4$ nanocomposites in dyed water treatment. The electrostatic interaction occurs preferentially when g-$C_3N_4$ and dye molecules bear surface charges of different signs in water. Zhu et al. (2015) measured the isoelectric point (IEP) around 4 to 5 for g-$C_3N_4$ prepared using melamine, thiourea, and urea as the precursor compounds, respectively. The experimentally determined IEP reflects the chemical equilibrium between hydrogen ions, hydroxyl ions, and amine groups on the g-$C_3N_4$ surface in an aqueous medium. The adsorption activity increases when the negatively charged g-$C_3N_4$ surface encounters cationic methylene blue (MB) dye molecules at a solution pH more positive than the $pH_{IEP}$. At the same time, the opposite is true for the anionic methyl orange (MO) dye molecules. The π–π interaction occurs when both g-$C_3N_4$ and organic dye structures contain aromatic pendant groups, so adsorption occurs via non-covalent bonding. Meng and Nan recently reported the rapid and selective adsorption of organic MB dyes in water using Na and Fe co-doped g-$C_3N_4$ (Meng and Nan, 2022). The infrared spectra verified the π–π conjugation between MB dyes and g-$C_3N_4$ adsorbents for selective removal. The conjugation, electrostatic interactions, and hydrogen bonding contribute to the synergistic adsorptive MB removal. The complexation mechanism arises primarily from the metal doping to the g-$C_3N_4$ structure, which creates binding sites and functional groups that can firmly adhere to the dye molecules by forming surface complexes.

Similarly, the cation-bridge mechanism involves the ion exchange of charged metal compounds in the g-$C_3N_4$ structure with the ionized cations of the dye molecules. Nnadiekwe et al. (2023) have recently employed DFT computations to examine the adsorption behavior of alkali ions (including $Li^+$, $Na^+$, $K^+$) doped heptazine-based g-$C_3N_4$ nanocomposites to the cationic MB dyes in water.

**Table 2** Selected examples of photocatalytic dye-removal performance using g-$C_3N_4$ nanocomposites in dyed water treatment.

| Catalyst | Dye | Light source | Catalyst dosage (mg) | Dye-removal performance | Reference |
|---|---|---|---|---|---|
| g-$C_3N_4$/$WO_3$ | MB (100 mL, 10 mg·$L^{-1}$) | 300 W Xe lamp with 400 nm cutoff filter | 100 | 97 %, 120 min | Huang et al., 2013 |
| g-$C_3N_4$/BiOI | Rhodamine B (RhB), MB, MO (all 100 mL, 10 mg·$L^{-1}$) | 300 W Xe lamp with 400 nm cutoff filter | 10–20 | ca. 99 %, 50 min for RhB, >95 % for MB and MO | Di et al., 2014 |
| g-$C_3N_4$/$SnO_{2-x}$ | RhB (100 mL, 10 mg·$L^{-1}$) | 350 W Xe lamp with UV and IR cutoff filters | 40 | ca. 99 %, 60 min | He et al., 2015 |
| g-$C_3N_4$/reduced graphene oxide (RGO) | MB (100 mL with 1 mL $H_2O_2$, 5 mg·$L^{-1}$) | 500 W Xe lamp | 2.5 (membrane) for flow-through dye degradation | >95 %, 150 min | Li et al., 2017 |
| g-$C_3N_4$/$TiO_2$ (black) | MO (30 mL, 10 mg·$L^{-1}$) | 300 W Xe lamp with 420 nm cutoff filter | 30 | 95 %, 150 min | Shen et al., 2017 |
| g-$C_3N_4$/BiOCl | 4-chlorophenol (an intermediate for dye synthesis, 100 mL, 10 mg·$L^{-1}$) | 300 W Xe lamp with 420 nm cutoff filter | 50 | ca. 95 %, 150 min | Wang et al., 2018 |
| CoAl-LDH/g-$C_3N_4$/RGO (LDH: Layered double hydroxide) | Congo red (CR) | | | ca. 95 %, 30 min | Jo and Tonda, 2019 |
| g-$C_3N_4$/RGO | RhB (40 mL, 5 mg·$L^{-1}$) | 300 W Xe lamp with 420 nm cutoff filter | 40 | >98 %, 30 min | Wei et al., 2019 |
| g-$C_3N_4$/ZnO/$ZnFe_2O_4$ and g-$C_3N_4$/ZnO/$CoFe_2O_4$ | MO, Malachite green (MG) (150 mL, 10 mg·$L^{-1}$) | 10 W LED lamp (400–700 nm) | 50 | ca. 95 %, 70 min (MG), 140 min (MO) | Chandel et al., 2020 |
| g-$C_3N_4$/$MoS_2$ | MB (20 mL, 5 ppm) | UV, visible, and sun light | 1 | 98.7 % | Monga et al., 2020 |
| Phosphorus sulfur co-doped g-$C_3N_4$/BiOBr/Ag/AgCl | Phenol | 35 W LED lamp | | 98 %, 60 min | Raizada et al., 2020 |
| g-$C_3N_4$/red mud | MB, MG (10 mg·$L^{-1}$) | 300 W Xe lamp with 420 nm cutoff filter | 50 | ca. 95 %, 80 min (MB), 120 min (MG) | Shi et al., 2020 |
| g-$C_3N_4$/CuI | RhB, MO (150 mL, 10 ppm) | 400 W UV, 150 W visible light | 150 | Up to 98.5 % under UV, and 78.6 % under visible irradiations | Ghanbari and Salavati-Niasari, 2021 |
| Sulfur-doped g-$C_3N_4$/Ag/ZnO | MB (100 mL, 10 mg·$L^{-1}$) | Sunlight (57–63 Klux) | 10 | >90 %, 60 min | Iqbal et al., 2021 |
| g-$C_3N_4$/Ni/ZnO | MB (200 mL, 10 mg·$L^{-1}$) | Sunlight (68–73 Klux) | 200 | ca. 99 %, 70 min | Qamar et al., 2021 |
| g-$C_3N_4$/Cd/ZnO | MB (100 mL, 10 mg·$L^{-1}$) | Sunlight | 10 | >90 %, 90 min | Sher et al., 2021 |
| Fe-doped g-$C_3N_4$ | RhB (50 mL, 10 mg·$L^{-1}$) | Visible light | 25 | ca. 98.2 %, 60 min | Ding et al., 2022 |
| g-$C_3N_4$/BiOBr | RhB (25 mL, 20 mg·$L^{-1}$) | 300 W Xe lamp with 420 nm cutoff filter | 20 | 87 %, 30 min | Tian et al., 2022 |

**Table 3** Pros and cons of hard- and soft-templating methods used to synthesize mesoporous 2D g-$C_3N_4$-based nanocomposite.

| Methods | Pros | Cons |
|---|---|---|
| Hard-templating approach | Reasonable control over pore size and distribution; high stability; easily scaled up for industrial production | The range of pore size is typically limited by the available template materials; time-consuming process; limited flexibility in terms of the variety of pore shapes and structures that can be produced. |
| Soft-templating approach | High flexibility for a wide range of pore shapes and structures to be produced; relatively fast for the template removal; cost-effective in terms of the soft-template material | Poor control over pore size and distribution; less stable due to the weaker interaction between the carbon nitride and the soft template material; limited scalability |

**Table 4** Selected examples of g-$C_3N_4$ nanocomposites for the adsorptive organic dye removal in water treatment.

| Adsorbent | Dye | Adsorbent dosage (mg) | Adsorption removal | Reference |
|---|---|---|---|---|
| Fe-doped g-$C_3N_4$/graphitized mesoporous carbon | Acid red 73, RhB (50 mg·$L^{-1}$, $H_2O_2$ 40 mM) | 200* | >99 %, 40 min (pH = 6.9) | Ma et al., 2017 |
| g-$C_3N_4$/red mud | MB, MG (10 mg·$L^{-1}$) | 50 | ca. 35 %, 30 min (MB), ca. 70 %, 30 min (MG) | Shi et al., 2020 |
| g-$C_3N_4$/$TiO_2$ | MO (50 mg·$L^{-1}$, 10 mg·$L^{-1}$) | 10 | ca. 80 %, 15 min (pH ca. 7) | Wang et al., 2020 |
| g-$C_3N_4$/$TiO_2$/GO | MO, MB, CR, RhB (10 mg·$L^{-1}$) | Foam | >97 % | Zhan et al., 2021 |
| g-$C_3N_4$/MgO | CR, Basic Fuchsin (BF) (25 mL, 50 mg·$L^{-1}$) | 10 | 96 %, 24 h (CR); 99 %, 24 h (BF) | Modwi et al., 2022 |
| Na and Fe co-doped g-$C_3N_4$ | MB (50 mL, 50 mg·$L^{-1}$) | 5 | ca. 90 %, 5 min (MB, pH = 6.5) | Meng and Nan, 2022 |

*: Estimated using 250 mL for the dyed solution.

Their calculation shows that the $Li^+$-doped g-$C_3N_4$ exhibits the smallest HOMO–LUMO gap and the highest charge potential compared to the $K^+$ and $Na^+$ counterparts. The predicted adsorption performance is in an ascending order of $K^+$-doped g-$C_3N_4$ < $Na^+$-doped g-$C_3N_4$ < $Li^+$-doped g-$C_3N_4$, depending mainly on the protonation of the g-$C_3N_4$ nanosheets.

Although the selected examples of adsorptive dye removal in **Table 4** appear fewer than those of photocatalytic degradation in **Table 2**, it may be interesting to note that organic dye removal often involves photocatalysis and adsorption mechanisms being both operative simultaneously for many g-$C_3N_4$ nanocomposites in wastewater treatment (Shi et al., 2020). The observation is reasonably justifiable since redox interactions between charge carriers and dye molecules likely favorably occur upon exposure to light irradiation when the organic dye pollutants adsorb on the surface of g-$C_3N_4$ photocatalysts. Accordingly, organic adsorption and photodegradation may be regarded as an integral interaction route for overall pollutant removal. In this regard, attempts at real-time monitoring of the in-situ adsorption and photodegradation of dye molecules are challenging. Recently, Qin et al. (2021) reported their finding using attenuated total reflectance induced evanescent spectroscopy (ATR-ES). The ATR-ES involves the formation of a g-$C_3N_4$ coating layer on a silica optical fiber (SOF) surface coupled to a light-emitting diode (LED). The ATR-ES then interacts with MB adsorbed on the g-$C_3N_4$ interface to produce ATR-ES signal change. They have shown that, in the context of adsorption investigation using a red LED, the observed alteration in the "red" ATR-ES signified the spontaneous nature of the adsorption process. During the initial phase, rapid adsorption predominantly occurred due to electronic attraction. Subsequently, the slower adsorption was primarily driven by π–π interactions during the second phase. For the photodegradation, the change in the "violet" ATR-ES indicated that the adsorption–desorption equilibrium of MB was disrupted through oxidation by hydroxyl radicals (•OH) and superoxide radicals ($•O^{2-}$). Notably, the surface's apparent adsorption rate was 16 times higher than the apparent photodegradation rate constant. This discrepancy reveals that the photodegradation process is the primary rate-controlling step in the photocatalytic degradation reaction.

Finally, the feasibility of using the g-$C_3N_4$ composites in large-scale operations depends mainly on the material cost, disposal, and regeneration. The practical use of g-$C_3N_4$ composites for treating organic dyed wastewater needs to be improved by resolving the difficulties in separating and recovering the recycled sludge. Practices used most frequently, including filtration or centrifugation methods, are tedious, time-consuming, low-efficiency, and costly. Magnetically recoverable g-$C_3N_4$ composites by hybridizing with magnetic $Fe_3O_4$ or spinel ferrite (such as $NiFe_2O_4$) offer a promising means for easy recyclability and multiple reusable capabilities (Kumar et al., 2013; Guo et al., 2018; Sudhaik et al., 2018). Fixation of the g-$C_3N_4$ nanocomposite on mechanically robust and flexible filtration membranes, such as polyacrylonitrile porous substrates or carbon-fiber clothes, is another attractive alternative for resolving the regeneration issue in wastewater treatment (Lei et al., 2021; Li R. et al., 2019; Li X. et al., 2021). In addition, most of the studies are based on small-scale laboratory tests under reasonably well-controlled conditions. Scale-up research with testing conditions close to the actual situation is highly desirable to fill the knowledge gap for practical applications.

## 3. BN-based nanocomposites

BN is analogous to carbon in structure and consists of various crystalline polymorphs, including hexagonal form (h-BN) with honeycomb-like 2D layer structure together with rhombohedral (r-BN), cubic (c-BN), and wurtzite (w-BN) types with hybridized B–N bonds of either $sp^2$ or $sp^3$ types (Pakdel et al., 2014; Yu et al., 2018). The discovery of various carbon nanostructures, including fullerenes, nanowires, nanotubes, nanosheets, etc., has triggered the exploration of other nanostructured counterparts based on the similar honeycomb-like structure. The nanostructures include the layered graphene-like h-BN, with a wide range of nanostructures from 0D to 2D through synthesis methods such as exfoliation (mechanical or chemical), chemical vapor deposition, epitaxial growth, solid-state reaction, nanotube unzipping, or high-energy irradiation (Pakdel et al., 2014). Tuning the morphology of BN nanostructures gives rise to a unique combination of many advantageous properties, including high surface area, high-temperature oxidation resistance, high chemical inertness, possible low friction coefficient, high dielectric constant, tunable structural defect, and surface functionality. The morphological tunability renders BN nanostructures in wide-ranging potential applications, including electronic, optical, thermal, mechanical, wetting, and tribological uses. Depending on the atomic stacking configuration, the layered h-BN generally exhibits a considerable bandgap value of around 6 eV (Wickramaratne et al., 2018), prohibiting BN from being an efficient photocatalyst. However, BN-containing nanocomposites show a dual adsorptive and photocatalytic role. For example, AgI nanocomposites consisting of a minor addition of BN nanosheets have been shown to exhibit substantially enhanced photocatalytic activity and photocorrosion resistance, together with dye adsorption capability against aqueous RhB solutions under simulated sunlight irradiations when compared to pure AgI (Choi et al., 2015). BN–AgI heterojunction increases the charge transportation and separation efficiency for facilitating the photocatalytic degradation of RhB dyes. Similar synergistic findings have also been reported in the literature. As shown in **Table 5**, Wang et al. (2016) prepared porous h-BN fibers with their surface decorated by $Ta_3N_5$ nanoparticles of various fractions. The composite fibers showed preferential adsorption for selected dye molecules while facilitating the separation of photogenerated charge carriers.

In addition to the photocatalytic dye removal, porous BN nanosheets with high specific surface area, selective sorption capability, super-hydrophobicity, and facile regeneration have also received increasing attention as effective adsorbents in wastewater treatment (Lei et al., 2013; Park et al., 2022). For example, Liu et al. (2018) combined the adsorption advantage of BN and carbon by forming a highly porous, cheese-like 3D structure with pore sizes ranging from 2 nm to 100 nm. The BN/C composites showed a fast adsorption rate by removing cationic MB (>80 %) and anionic CR (>70 %) dyes in water (200 mL, 50 mg·$L^{-1}$) within merely ca. 5 min and over 95 % in 2 h duration. More importantly, the BN/C composites were reusable after heating in the air at 500 °C. After ten cycles of recycling, the reused composites maintained more than 70 % of their original adsorption capability. Recent advances in theoretical computations have revealed details about the adsorption process and molecular interactions between the adsorbent and adsorbate. Bangari et al. (2021) have used DFT calculations to examine the adsorption of MO dyes using BN nanosheets. Their results show that negative charge transfer occurred from MO to the nanosheets with high chemical potential. The finding suggests high chemical activity and a substantial decrease in the bandgap (up to 2.9 eV) after the adsorption. More importantly, theoretical computations have advanced to predict the simultaneous removal of multiple organic pollutants, including the adsorption affinity and adsorptive capacity, from the change of bandgap, geometrical bond distance, the molecular orientation of the adsorbate, adsorption energy, etc. (Bangari et al., 2022b; Yadav et al., 2022).

## 4. MXene-based nanocomposites

MXene belongs to the 2D materials family and finds enormous interest due to its proficient structural characteristics (e.g., large surface area, hydrophilic character, abundant active surface sites, etc.) and unique properties (e.g., high chemical stability, high electrical conductivity, quick

**Table 5** Selected recent examples of BN nanocomposites for the adsorptive and/or photocatalytic dye removal in water treatment.

| Composite | Dye | Light source | Dosage (mg) | Dye removal | Reference |
|---|---|---|---|---|---|
| BN/AgI | RhB (100 mL, 10 mg·L$^{-1}$) | Simulated sun light (150 W Xe lamp with AM 1.5G filter) | 100 | ca. 60 %, 30 min by adsorption; >35 %, 70 min by photocatalysis | Choi et al., 2015 |
| BN/$Ta_3N_5$ | RhB, MB (100 mL, 50 mg·L$^{-1}$) | 300 W Xe lamp with 400 nm cutoff filter | 50 | ca. 20 %, 30 min by adsorption; >98 %, 120 min by photocatalysis | Wang et al., 2016 |
| BN/C | MB, CR (200 mL, 50 mg·L$^{-1}$) | Not used | 100 | >95 %, 120 min by adsorption | Liu et al., 2018 |
| BN/Carbon nitride | Neutral red (NR), MG (30 mL, 200 mg·L$^{-1}$) | Not used | 5 | 1350.1 mg·g$^{-1}$ (NR), 1040.6 mg·g$^{-1}$ (MG) by adsorption | Guo et al., 2019 |
| BN/polyvinyl alcohol foam | MB, CR, MO (6 mL, 25 mg·L$^{-1}$) | Not used | N.A. | ca. 11.5, 5.1, 5.2 mg·g$^{-1}$ for adsorption of MB, CR, MO, respectively | Gao et al., 2020 |
| BN/$TiO_2$ | RhB (20 mL, 10 mg·L$^{-1}$) | 300 W Xe lamp with 400 nm cutoff filter | 15 | 95 %, 120 min by photocatalysis | Li et al., 2020 |
| BN/$SnO_2$ | MO (50 mL, 10 mg·L$^{-1}$) | Visible light | 1.25 | 92 %, ca. 7 min by photocatalysis | Singh et al., 2020 |
| BN/chitosan/graphene | MB, Acid orange II | Simulated sun light | Up to 0.05 | 87 % (MB), 57 % (Acid orange II), 20 min by photocatalysis | Khose et al., 2021 |
| BN/α-$Fe_2O_3$ | MB (100 mL, 2.5 mg·L$^{-1}$) | 250 W tungsten-halogen lamp | 10 or 20 | ca. 91 %, 180 min by photocatalysis | Shenoy et al., 2021 |
| BN/polyvinylidene fluoride | MB (150 ppm) | Not used | 133* | 100 % by membrane adsorption | Bangari et al., 2022a |

N.A.: Not available. *: Estimated using 100 mL for the dyed solution.

ion-exchange capability, enriched surface functionality, environmentally benignity, etc.) (Naguib et al., 2014). The structure of MXene with a formula of $M_{n+1}X_nT_x$ (where $n$ generally equals 1 to 3) consists of $n$+1 layers of transitional metal elements M, $n$ layers of X (i.e., carbon and/or nitrogen), and a surface-terminal group of $T_x$ (such as oxygen, fluorine, and hydroxyl) in periodic stacking configuration. The tunable surface termination renders MXene nanosheets potentially effective adsorbents for dyed wastewater treatment (Khandelwal and Darbha, 2021; Kumar et al., 2022; Rasool et al., 2019; Zhang et al., 2018). Mashtalir et al. first demonstrated preferential adsorption of $Ti_3C_2T_x$ for cationic MB dyes over anionic acid blue 80 in water primarily due to electrostatic interactions (Mashtalir et al., 2014). Interestingly, the photodegradation of both dyes occurred under UV light irradiation, revealing the instability of $Ti_3C_2T_x$ in water to form $TiO_2$ favorably for photocatalysis.

**Table 6** lists examples of MXene composites using nitride for organic dye removal in wastewater remediation. All are g-$C_3N_4$ hybridized with MXene carbide of $Ti_3C_2$, showing enhanced photocatalytic dye degradation compared to the pure g-$C_3N_4$ counterpart. Although successful synthesis of MXene nitrides such as $Ti_4N_3$ (Urbankowski et al., 2016) and $Ti_2N$ (Soundiraraju and George, 2017) has been reported, there has been no report on their use in the wastewater remediation to the author's best knowledge. Preparation of nitride MXene by selective acid etching from the MAX phase remains challenging and becomes one of the limiting factors for exploring its use in environmental water remediation.

## 5. Other nitride nanocomposites

Some other nitride-based nanocomposites are promising to become next-generation multi-purpose dye-removal solutions. For example, Tsai and Tseng recently prepared TiN–$TiO_2$ composite nanoparticles by a facile urea-glass route (Tsai and Tseng, 2020). The presence of TiN in the composites imparts a pronouncedly enhanced preferential adsorption against MB dyes in water in addition to their

**Table 6** Selected recent examples of MXene nanocomposites using nitride for the adsorptive and/or photocatalytic dye removal in water treatment.

| Composite | Dye | Light source | Dosage (mg) | Dye removal | Reference |
|---|---|---|---|---|---|
| $Ti_3C_2$/Ag/g-$C_3N_4$ | RhB (200 mL, 10 mg·L$^{-1}$) | 300 W Xe lamp with 420 nm cutoff filter | 100 | ca. 20 %, 30 min by adsorption; 69.2 %, 70 min by photocatalysis | Huang et al., 2021 |
| $Ti_3C_2$/g-$C_3N_4$ | RhB (80 mL, 20 mg·L$^{-1}$) | 500 W metal halide lamp with 420 nm cutoff filter; 300 mW·cm$^{-2}$ | 40 | ca. 99 %, 25 min by photocatalysis | Liu et al., 2022 |
| $Ti_3C_2$/g-$C_3N_4$ | MB (100 mL, 10 mg·L$^{-1}$) | 500 W halogen lamp | 500 | ca. 60 %, 180 min by photocatalysis | Nasri et al., 2022 |
| $Ti_3C_2$-derived Ti-peroxo/g-$C_3N_4$ | RhB (100 mL, 20 mg·L$^{-1}$) | Visible light | 20 | ca. 55 %, 30 min by adsorption; 45 %, 110 min by photocatalysis | Tu et al., 2022 |

photocatalytic property under visible-light illuminations. The adsorption enhancement is directly proportional to the TiN fraction. Up to 95 % of the initial $10^{-5}$ M MB concentration can be removed by the adsorptive composites in less than 90 min. The composite particles show synergistic photocatalysis; in addition, niobium doping in the composite particles also facilitates dye removal, indicating that the creation of ionized defective sites may critically tune surface characteristics for adsorption and energy band offset at the interface for photocatalytic dye degradation.

A following report by Chen and Tseng revealed that TiN–WN composite nanoparticles also exhibit selective adsorption against cationic MB dyes in water. The adsorption under dark conditions reached as much as 90 % within 90 minutes when using an initial MB concentration of $10^{-5}$ M by tuning the TiN–WN composition. In comparison, virtually minimal adsorption (less than 10 %) resulted in the anionic MO dye solution under identical situations (Chen and Tseng, 2022). Similarly, the composite particles rendered a moderate photocatalytic degradation to the MB molecules under visible-light illuminations. Their results also suggest that the composite particles may be suitable for long-term wastewater treatment.

A recent finding further reveals that forming a $TiO_{2-x}N_x$ layer around $Fe_3O_4$@Ag core–shell nanoparticles is sufficient to impart preferential adsorption toward MB dyes in water (Lin and Tseng, 2022). By tuning the $x$ value ($x$ = 0.056 to 0.15) in the $Fe_3O_4$@Ag@$TiO_{2-x}N_x$ core–shell composite via the nitridation temperature, the composites with an $x$ value of about 0.12 show dark adsorption of 54.8 % and an additional visible-light photodegradation of 25.1 % when using dyed wastewater with an initial MB concentration of $5\times10^{-6}$ M. The composites with $x$ about 0.15 can even exhibit dark adsorption of 99.1 % against the MB solution within 30 min, depending on the nitridation level. The nitrogen-dependent MB adsorption may involve multiple concurrent mechanisms, including the electrostatic interaction, formation of hydrogen bridges, electron donor–acceptor relationship, and the π–π electron dispersion force. In addition, the composite particles are magnetically responsive. The recycled particles retain over 72 % of their initial MB removal capability after five use cycles.

## 6. Summary and challenges

Nitride composites as a material group remain vastly unexplored for environmental remediation, despite intensive research endeavors devoted to wastewater treatment in the last decades. We have witnessed enormous groundbreaking advances in 2D nitrides (including g-$C_3N_4$, BN, and MXene) as an efficient photocatalyst through innovative synthesis, tailored morphological structure, bandgap engineering, optimal band alignment, defect tuning, etc. Many nitrides exhibit a strong affinity to adsorb specific dye attributes preferentially in a relatively short time. This dual role with synergistic dye-removal capability is pervasive among nitrides and is less common for other material counterparts. With the help of theoretical computations, we anticipate that the domain knowledge toward understanding the synergistic removal mechanism at the interface between nitride and dye molecules will advance at a faster speed in the coming future.

The effort to assess nitride composites' dye-removal performance in pilot-scale or field-scale experiments using actual wastewater samples is critically important to advance their practical use. So far, the practical use of nitride nanocomposites in large-scale wastewater treatment remains an unsurpassable hurdle to overcome. One must address pollutant-removal efficiency, scalability, long-term stability, cost-effectiveness, and regulatory consideration. To resolve this challenge, nitride composites with advantageous features such as reduced sludge formation, antifouling capability, facile recycle operation, and multiple regeneration usability are highly desirable. Developing effective dye-removal systems that integrate the nitride

composites into existing wastewater-treatment processes may provide a viable route for practical application. The transition from laboratory research to practical implementation in large-scale industrial or municipal wastewater treatment can be complex. The challenges may foster innovative new ideas and become opportunities in the near future.

## Conflict of Interest

The author declares no known competing financial interests or personal relationships that could have appeared to influence the work reported in this paper.

## Acknowledgments

Financial support from the National Science and Technology Council (NSTC) of Taiwan under contract numbers 110-2221-E-005-015-MY3 and 110-2221-E-005-016-MY3 is gratefully acknowledged. Assistance from the Taiwan Instrument Research Institute is much appreciated.

## Credit Author Statement

W.J. Tseng contributed to conceptualization, literature search, data curation, writing, reviewing, editing, and funding acquisition.

## Data Availability Statement

Available upon reasonable request.

## References

Acharya R., Parida K., A review on $TiO_2$/g-$C_3N_4$ visible-light-responsive photocatalysts for sustainable energy generation and environmental remediation, J. Environ. Chem. Eng., 8 (2020) 103896. https://doi.org/10.1016/j.jece.2020.103896

Adegoke A.A., Amoah I.D., Stenström T.A., Verbyla M.E., Mihelcic J.R., Epidemiological evidence and health risks associated with agricultural reuse of partially treated and untreated wastewater: a review, Front. Public Health, 6 (2018) 337. https://doi.org/10.3389/fpubh.2018.00337

Ahmadi A., Hajilou M., Zavari S., Yaghmaei S., A comparative review on adsorption and photocatalytic degradation of classified dyes with metal/non-metal-based modification of graphitic carbon nitride nanocomposites: Synthesis, mechanism, and affecting parameters, J. Clean. Prod., 382 (2023) 134967. https://doi.org/10.1016/j.jclepro.2022.134967

Al-Tohamy R., Ali S.S., Li F., Okasha K.M., Mahmoud Y.A.-G., Elsamahy T., Jiao H., Fu Y., Sun J., A critical review on the treatment of dye-containing wastewater: ecotoxicological and health concerns of textile dyes and possible remediation approaches for environmental safety, Ecotoxicol. Environ. Saf., 231 (2022) 113160. https://doi.org/10.1016/j.ecoenv.2021.113160

Aspera S.M., David M., Kasai H., First-principles study of the adsorption of water on tri-s-triazine-based graphitic carbon nitride, Jap. J. Appl. Phys., 49 (2010) 115703. https://doi.org/10.1143/JJAP.49.115703

Bangari R.S., Yadav A., Sinha N., Experimental and theoretical investigations of methyl orange adsorption using boron nitride nanosheets, Soft Matter, 17 (2021) 2640–2651. https://doi.org/10.1039/d1sm00048a

Bangari R.S., Yadav A., Bharadwaj J., Sinha N., Boron nitride nanosheets incorporated polyvinylidene fluoride mixed matrix membranes for removal of methylene blue from aqueous stream, J. Environ. Chem. Eng., 10 (2022a) 107052. https://doi.org/10.1016/j.jece.2021.107052

Bangari R.S., Yadav A., Awasthi P., Sinha N., Experimental and theoretical analysis of simultaneous removal of methylene blue and tetracycline using boron nitride nanosheets as adsorbent, Colloid. Surf. A, 634 (2022b) 127943. https://doi.org/10.1016/j.colsurfa.2021.127943

Chandel N., Sharma K., Sudhaik A., Raizada P., Hosseini-Bandegharaei A., Thakur V.K., Singh P., Magnetically separable ZnO/$ZnFe_2O_4$ and ZnO/$CoFe_2O_4$ photocatalysts supported onto nitrogen doped graphene for photocatalytic degradation of toxic dyes, Arab. J. Chem., 13 (2020) 4324–4340. https://doi.org/10.1016/j.arabjc.2019.08.005

Chen C.-Y., Tseng W.J., Preparation of TiN-WN composite particles for selective adsorption of methylene blue dyes in water, Adv. Powder Technol., 33 (2022) 103423. https://doi.org/10.1016/j.apt.2021.103423

Chen Z., Zhang S., Liu Y., Alharbi N.S., Rabah S.O., Wang S., Wang X., Synthesis and fabrication of g-$C_3N_4$-based materials and their application in elimination of pollutants, Sci. Total Environ., 731 (2020) 139054. https://doi.org/10.1016/j.scitotenv.2020.139054

Choi J., Reddy D.A., Kim T.K., Enhanced photocatalytic activity and anti-photocorrosion of AgI nanostructures by coupling with graphene-analogue boron nitride nanosheets, Ceram. Int., 41 (2015) 13793–13803. https://doi.org/10.1016/j.ceramint.2015.08.062

Choudri B.S., Charabi Y., Health effects associated with wastewater treatment, reuse, and disposal, Water Environ. Res., 91 (2019) 976–983. https://doi.org/10.1002/wer.1157

Connor R., The United Nations World Water Development Report 2015: Water for a Sustainable World (Vol. 1), UNESCO Publishing, 2015. ISBN 978-92-3-100071-3.

Cui Y., Ding Z., Liu P., Antonietti M., Fu X., Wang X., Metal-free activation of $H_2O_2$ by g-$C_3N_4$ under visible light irradiation for the degradation of organic pollutants, Phys. Chem. Chem. Phys., 14 (2012) 1455–1462. https://doi.org/10.1039/c1cp22820j

Darkwah W.K., Ao Y., Mini review on the structure and properties (photocatalysis), and preparation techniques of graphitic carbon nitride nano-based particle, and Its applications, Nanoscale Res. Lett., 13 (2018) 388. https://doi.org/10.1186/s11671-018-2702-3

Degano I., Ribechini E., Modugno F., Colombini M.P., Analytical methods for the characterization of organic dyes in artworks and in historical textiles, Appl. Spectrosc. Rev., 44 (2009) 363–410. https://doi.org/10.1080/05704920902937876

Di J., Xia J., Yin S., Xu H., Xu L., Xu Y., He M., Li H., Preparation of sphere-like g-$C_3N_4$/BiOI photocatalysts via a reactable ionic liquid for visible-light-driven photocatalytic degradation of pollutants, J. Mater. Chem. A, 2014, 2, 5340–5351. https://doi.org/10.1039/c3ta14617k

Dickin S.K., Schuster-Wallace C.J., Qadir M., Pizzacalla K., A review of health risks and pathways for exposure to wastewater use in agriculture, Environ. Health Perspect., 124 (2016) 900–909. https://doi.org/10.1289/ehp.1509995

Ding C., Kang S., Li W., Gao W., Zhang Z., Zheng L., Cui L., Mesoporous structure and amorphous Fe-N sites regulation in Fe-g-$C_3N_4$ for boosted visible-light-driven photo-Fenton reaction, J. Colloid Interf. Sci., 608 (2022) 2515–2528. https://doi.org/10.1016/j.jcis.2021.10.168

Dong G., Zhang Y., Pan Q., Qiu J., A fantastic graphitic carbon nitride (g-$C_3N_4$) material: electronic structure, photocatalytic and photoelectronic properties, J. Photochem. Photobiol. C, 20 (2014) 33–50. https://doi.org/10.1016/j.jphotochemrev.2014.04.002

Forgacs E., Cserháti T., Oros G., Removal of synthetic dyes from wastewaters: a review, Environ. Int., 30 (2004) 953–971. https://doi.org/10.1016/j.envint.2004.02.001

Fronczak M., Adsorption performance of graphitic carbon nitride-based materials: current state of the art, J. Environ. Chem. Eng., 8 (2020) 104411. https://doi.org/10.1016/j.jece.2020.104411

Gao X., Li R., Hu L., Lin J., Wang Z., Yu C., Fang Y., Gao X., Li R., Hu L., Lin J., Wang Z., Yu C., Fang Y., Preparation of boron nitride nanofibers/PVA composite foam for environmental remediation, Colloid. Surf. A, 604 (2020) 125287. https://doi.org/10.1016/j.colsurfa.2020.125287

Ghanbari M., Salavati-Niasari M., Copper iodide decorated graphitic

carbon nitride sheets with enhanced visible-light response for photocatalytic organic pollutant removal and antibacterial activities, Ecotoxicol. Environ. Saf., 208 (2021) 111712. https://doi.org/10.1016/j.ecoenv.2020.111712

Groenewolt M., Antonietti M., Synthesis of g-$C_3N_4$ nanoparticles in mesoporous silica host matrices, Adv. Mater., 17 (2005) 1789–1792. https://doi.org/10.1002/adma.200401756

Guo F., Lu J., Liu Q., Zhang P., Zhang A., Cai Y., Wang Q., Degradation of acid orange 7 by peroxymonosulfate activated with the recyclable nanocomposites of g-$C_3N_4$ modified magnetic carbon, Chemosphere 205 (2018) 297–307. https://doi.org/10.1016/j.chemosphere.2018.04.139 0045-6535

Guo Y., Wang R., Wang P., Rao L., Wang C., Developing a novel layered boron nitride−carbon nitride composite with high efficiency and selectivity to remove protonated dyes from water, ACS Sustain. Chem. Eng. 2019, 7, 5727–5741. https://doi.org/10.1021/acssuschemeng.8b05150

Hamidian A.H., Ozumchelouei E.J., Feizi F., Wu C., Zhang Y., Yang M., A review on the characteristics of microplastics in wastewater treatment plants: a source for toxic chemicals, J. Clean. Prod., 295 (2021) 126480. https://doi.org/10.1016/j.jclepro.2021.126480

He Y., Zhang L., Fan M., Wang X., Walbridge M.L., Nong Q., Wu Y., Zhao L., Z-scheme $SnO_{2-x}$/g-$C_3N_4$ composite as an efficient photocatalyst for dye degradation and photocatalytic $CO_2$ reduction, Sol. Energy Mater. Sol. Cells, 137 (2015) 175–184. https://doi.org/10.1016/j.solmat.2015.01.037

Hu C., Lin Y.-R., Yang H.-C., Recent developments in graphitic carbon nitride based hydrogels as photocatalysts, ChemSusChem, 12 (2019) 1794–1806. https://doi.org/10.1002/cssc.v12.9

Huang K., Li C., Wang L., Wang W., Meng X., Layered $Ti_3C_2$ MXene and silver co-modified g-$C_3N_4$ with enhanced visible light-driven photocatalytic activity, Chem. Eng. J., 425 (2021) 131493. https://doi.org/10.1016/j.cej.2021.131493

Huang L., Xu H., Li Y., Li H., Cheng X., Xia J., Xu Y., Cai G., Visible-light-induced $WO_3$/g-$C_3N_4$ composites with enhanced photocatalytic activity, Dalton Trans., 42 (2013) 8606–8616. https://doi.org/10.1039/c3dt00115f

Iqbal S., Ahmad N., Javed M., Qamar M.A., Bahadur A., Ali S., Ahmad Z., Irfan R.M., Liu G., Akbar M.B., Qayyum M.A., Designing highly potential photocatalytic comprising silver deposited ZnO NPs with sulfurized graphitic carbon nitride (Ag/ZnO/S-g-$C_3N_4$) ternary composite, J. Environ. Chem. Eng., 9 (2021) 104919. https://doi.org/10.1016/j.jece.2020.104919

Islam A, Teo S.H., Taufiq-Yap Y.H., Ng C.H., Vo D.-V.N., Ibrahim M.L., Hasan M.M., Khan M.A.R., Nur A.S.M., Awual M.R., Step towards the sustainable toxic dyes removal and recycling from aqueous solution—A comprehensive review, Resour. Conserv. Recycl., 175 (2021) 105849. https://doi.org/10.1016/j.resconrec.2021.105849

Ismael M., Wu Y., Taffa D.H., Bottke P., Wark M., Graphitic carbon nitride synthesized by simple pyrolysis: the role of the precursor on the photocatalytic hydrogen production, New J. Chem., 43 (2019) 6909–6920. https://doi.org/10.1039/C9NJ00859D

Jiang L., Yuan X., Pan Y., Liang J., Zeng G., Wu Z., Wang H., Doping of graphitic carbon nitride for photocatalysis: a review, Appl. Catal. B: Environ., 217 (2017) 388–406. https://doi.org/10.1016/j.apcatb.2017.06.003

Jo W.-K., Tonda S., Novel CoAl-LDH/g-$C_3N_4$/RGO ternary heterojunction with notable 2D/2D/2D configuration for highly efficient visible-light-induced photocatalytic elimination of dye and antibiotic pollutants, J. Hazard. Mater., 368 (2019) 778–787. https://doi.org/10.1016/j.jhazmat.2019.01.114

Khandelwal N., Darbha G.K., A decade of exploring MXenes as aquatic cleaners: covering a broad range of contaminants, current challenges and future trends, Chemosphere, 279 (2021) 130587. https://doi.org/10.1016/j.chemosphere.2021.130587

Khose R.V., Lokhande K.D., Bhakare M.A., Dhumal P.S., Wadekar P.H., Some S., Boron nitride doped chitosan functionalized graphene for an efficient dye degradation, ChemistrySelect, 6 (2021) 7956–7963. https://doi.org/10.1002/slct.202101611

Kudo A, Miseki Y., Heterogeneous photocatalyst materials for water splitting, Chem. Soc. Rev., 38 (2009) 253–278. https://doi.org/10.1039/b800489g

Kumar J.A., Prakash P., Krithiga T., Amarnath D.J., Premkumar J., Rajamohan N., Vasseghian Y., Saravanan P.y, Rajasimman M., Methods of synthesis, characteristics, and environmental applications of MXene: a comprehensive review, Chemosphere, 286 (2022) 131607. https://doi.org/10.1016/j.chemosphere.2021.131607

Kumar S., T. Surendar, Kumar B., Baruah A., Shanker V., Synthesis of magnetically separable and recyclable g-$C_3N_4$–$Fe_3O_4$ hybrid nanocomposites with enhanced photocatalytic performance under visible-light irradiation, J. Phys. Chem. C, 117 (2013) 26135–26143. https://doi.org/10.1021/jp409651g

Lam S.-M., Sin J.-C., Mohamed A.R., A review on photocatalytic application of g-$C_3N_4$/semiconductor (CNS) nanocomposites towards the erasure of dyeing wastewater, Mater. Sci. Semicond. Process., 47 (2016) 62–84. https://doi.org/10.1016/j.mssp.2016.02.019

Lapointe B.E., Herren L.W., Debortoli D.D., Vogel M.A., Evidence of sewage-driven eutrophication and harmful algal blooms in Florida's Indian River Lagoon, Harmful Algae, 43 (2015) 82–102. https://doi.org/10.1016/j.hal.2015.01.004

Lei L., Wang W., Wang C., Zhang M., Zhong Q., Fan H., In situ growth of boron doped g-$C_3N_4$ on carbon fiber cloth as a recycled flexible film-photocatalyst, Ceram. Int., 47 (2021) 1258–1267. https://doi.org/10.1016/j.ceramint.2020.08.246

Lei W., Portehault D., Liu D., Qin S., Chen Y., Porous boron nitride nanosheets for effective water cleaning, Nature Commun., 4 (2013) 1777. https://doi.org/10.1038/ncomms2818

Lellis B., Fávaro-Polonio C.Z., Pamphile J.A., Polonio J.C., Effects of textile dyes on health and the environment and bioremediation potential of living organisms, Biotechnol. Res. Innov., 3 (2019) 275–290. https://doi.org/10.1016/j.biori.2019.09.001

Li F., Yu Z., Shi H., Yang Q., Chen Q., Pan Y., Zeng G., Yan L., A Mussel-inspired method to fabricate reduced graphene oxide/g-$C_3N_4$ composites membranes for catalytic decomposition and oil-in-water emulsion separation, Chem. Eng. J., 322 (2017) 33–45. https://doi.org/10.1016/j.cej.2017.03.145

Li H., Tu W., Zhou Y., Zou Z., Z-Scheme photocatalytic systems for promoting photocatalytic performance: recent progress and future challenges, Adv. Sci., (2016) 1500389. https://doi.org/10.1002/advs.201500389

Li Q., Hou X., Fang Z., Yang T., Chen J., Cui X., Liang T., Shi J., Construction of layered h-BN/$TiO_2$ hetero-structure and probing of the synergetic photocatalytic effect, Sci. China Mater., 63 (2020) 276–287. https://doi.org/10.1007/s40843-019-1180-8

Li R., Ren Y., Zhao P., Wang J., Liu J., Zhang Y., Graphitic carbon nitride (g-$C_3N_4$) nanosheets functionalized composite membrane with self-cleaning and antibacterial performance, J. Hazard. Mater., 365 (2019) 606–614. https://doi.org/10.1016/j.jhazmat.2018.11.033

Li X., Huang G., Chen X., Huang J., Li M., Yin J., Liang Y., Yao Y., Li Y., A review on graphitic carbon nitride (g-$C_3N_4$) based hybrid membranes for water and wastewater treatment, Sci. Total Environ., 792 (2021) 148462. https://doi.org/10.1016/j.scitotenv.2021.148462

Lin Y.-H., Tseng W.J., Multifunctional $Fe_3O_4$@Ag@$TiO_{2-x}N_x$ core-shell composite particles for dye adsorption and visible-light photocatalysis, Ceram. Int., 48 (2022) 13906–13913. https://doi.org/10.1016/j.ceramint.2022.01.275

Liu D., Li C., Ge J., Zhao C., Zhao Q., Zhang F., Ni T., Wu W., 3D interconnected g-$C_3N_4$ hybridized with 2D $Ti_3C_2$ MXene nanosheets for enhancing visible light photocatalytic hydrogen evolution and dye contaminant elimination, Appl. Surf. Sci., 579 (2022) 152180. https://doi.org/10.1016/j.apsusc.2021.152180

Liu Z., Fang Y., Jia H., Wang C., Song Q., Li L., Lin J., Huang Y., Yu C., Tang C., Novel multifunctional cheese-like 3D carbon-BN as a highly efficient adsorbent for water purification, Sci. Rep., 8 (2018) 1104. https://doi.org/10.1038/s41598-018-19541-5

Lu X., Xu K., Chen P., Jia K., Liu S., Wu C., Facile one step method realizing scalable production of g-$C_3N_4$ nanosheets and study of their photocatalytic $H_2$ evolution activity, J. Mater. Chem. A, 2 (2014) 18924–18928. https://doi.org/10.1039/c4ta04487h

Luo Y., Zhu Y., Han Y., Ye H., Liu R., Lan Y., Xue M., Xie X., Yu S.,

Zhang L., Yin Z., Gao B., g-$C_3N_4$-based photocatalysts for organic pollutant removal: acritical review, Carbon Res., 2 (2023) 14. https://doi.org/10.1007/s44246-023-00045-5

Ma J., Yang Q., Wen Y., Liu W., Fe-g-$C_3N_4$/graphitized mesoporous carbon composite as an effective Fenton-like catalyst in a wide pH range, Appl. Catal. B, 201 (2017) 232–240. https://doi.org/10.1016/j.apcatb.2016.08.048

Market Analysis Report, Dyes and pigments market size, share & trends analysis report by product (dyes (reactive, vat, acid, direct, disperse), pigment (organic, inorganic)), by application, by region, and segment forecasts, 2023–2030, Grand View Research, (2023) Report ID: GVR-1-68038-545-8.

Martıńez-Huitle C.A., Brillas E., Decontamination of wastewaters containing synthetic organic dyes by electrochemical methods: a general review, Appl. Catal. B – Environ. 87 (2009) 105–145. https://doi.org/10.1016/j.apcatb.2008.09.017

Mashtalir O., Cook K.M., Mochalin V.N., Crowe M., Barsoum M.W., Gogotsi Y., Dye adsorption and decomposition on two-dimensional titanium carbide in aqueous media, J. Mater. Chem. A, 2 (2014) 14334–14338. https://doi.org/10.1039/c4ta02638a

Meng S., Nan Z., Rapid and selective adsorption of organic dyes with ultrahigh adsorption capacity using Na and Fe co-doped g-$C_3N_4$, Sep. Purif. Technol., 297 (2022) 121420. https://doi.org/10.1016/j.seppur.2022.121420

Modwi A., Khezami L., Ghoniem M.G., Nguyen-Tri P., Baaloudj O., Guesmi A., AlGethami F.K., Amer M.S., Assadi A.A., Superior removal of dyes by mesoporous MgO/g-$C_3N_4$ fabricated through ultrasound method: adsorption mechanism and process modeling, Environ. Res., 205 (2022) 112543. https://doi.org/10.1016/j.envres.2021.112543

Monga D., Ilager D., Shetti N.P., Basu S., Aminabhavi T.M., 2D/2d heterojunction of $MoS_2$/g-$C_3N_4$ nanoflowers for enhanced visible-light-driven photocatalytic and electrochemical degradation of organic pollutants, J. Environ. Manage., 274 (2020) 111208. https://doi.org/10.1016/j.jenvman.2020.111208

Naguib M., Mochalin V.N., Barsoum M.W., Gogotsi Y., MXenes: a new family of two-dimensional materials, Adv. Mater., 26 (2014) 992–1005. https://doi.org/10.1002/adma.201304138

Nasri M.S.I., Samsudin M.F.R., Tahir A.A., Sufian S., Effect of MXene loaded on g-$C_3N_4$ photocatalyst for the photocatalytic degradation of methylene blue, Energies, 15 (2022) 955. https://doi.org/10.3390/en15030955

Nnadiekwe C.C., Mustapha U., Abdulazeez I., Alhooshani K., Al-Saadi A.A., Alkali metal ion-doped heptazine-based g-$C_3N_4$ quantum dots for efficient adsorption of methyl blue: a DFT perspective, Surf. Interf., 38 (2023) 102852. https://doi.org/10.1016/j.surfin.2023.102852

Park Y.-G., Nam S.-N., Jang M., Park C.M., Her N., Sohn J., Cho J., Yoon Y., Boron nitride-based nanomaterials as adsorbents in water: a review, Sep. Purif. Technol., 288 (2022) 120637. https://doi.org/10.1016/j.seppur.2022.120637

Pakdel A., Bando Y., Golberg D., Nano boron nitride flatland, Chem. Soc. Rev., 43 (2014) 934–959. https://doi.org/10.1039/c3cs60260e

Preisner M., Neverova-Dziopak E., Kowalewski Z., Analysis of eutrophication potential of municipal wastewater, Water Sci. Technol., 81 (2020) 1994–2003. https://doi.org/10.2166/wst.2020.254

Preisner M., Neverova-Dziopak E., Kowalewski Z., Mitigation of eutrophication caused by wastewater discharge: a simulation-based approach, Ambio, 50 (2021) 413–424. https://doi.org/10.1007/s13280-020-01346-4

Qamar M.A., Shahid S., Javed M., Iqbal S., Sher M., Bahadur A., AL-Anazy M.M., Laref A., Li D., Designing of highly active g-$C_3N_4$/Ni-ZnO photocatalyst nanocomposite for the disinfection and degradation of the organic dye under sunlight radiations, Colloids Surf., 614 (2021) 126176. https://doi.org/10.1016/j.colsurfa.2021.126176

Qin S., Xiong Y., Li J., Wan H., Fang S., Duan M., Li R., Liao D., Real-time adsorption and photodegradation investigation of dye removal on g-$C_3N_4$ surface by attenuated total reflectance induced evanescent spectroscopy, J. Phys. Chem. C, 125 (2021) 4027–4040. https://doi.org/10.1021/acs.jpcc.0c11482

Raizada P., Thakur P., Sudhaik A., Singh P., Thakur V.K., Hosseini-Bandegharaei A., Fabrication of dual Z-scheme photocatalyst via coupling of BiOBr/Ag/AgCl heterojunction with P and S co-doped g-$C_3N_4$ for efficient phenol degradation, Arab. J. Chem., 13 (2020) 4538–4552. https://doi.org/10.1016/j.arabjc.2019.10.001

Rasool K., Pandey R.P., Rasheed P.A., Buczek S., Gogotsi Y., Mahmoud K.A., Water treatment and environmental remediation applications of two-dimensional metal carbides (MXenes), Mater. Today, 30 (2019) 80–102. https://doi.org/10.1016/j.mattod.2019.05.017

Santoso E., Ediati R., Kusumawati Y., Bahruji H., Sulistiono D.O., Prasetyoko D., Review on recent advances of carbon based adsorbent for methylene blue removal from waste water, Mater. Today Chem., 16 (2020) 100233. https://doi.org/10.1016/j.mtchem.2019.100233

Saravanan A., Kumar P.S., Jeevanantham S., Karishma S., Tajsabreen B., Yaashikaa P.R., Reshma B., Effective water/wastewater treatment methodologies for toxic pollutants removal: processes and applications towards sustainable development, Chemosphere, 280 (2021) 130595. https://doi.org/10.1016/j.chemosphere.2021.130595

Shen L., Xing Z., Zou J., Li Z., Wu X., Zhang Y., Zhu Q., Yang S., Zhou W., Black $TiO_2$ nanobelts/g-$C_3N_4$ nanosheets laminated heterojunctions with efficient visible-light-driven photocatalytic performance, Sci. Rep., 7 (2017) 41978. https://doi.org/10.1038/srep41978

Shenoy M.R., Ayyasamy S., Bhojan V., Swaminathan R., Raju N., Kumar P.S., Sasikumar M., Kadarkarai G., Tamilarasan S., Thangavelu S., Suryakanth J., Reddy M.V., Visible light sensitive hexagonal boron nitride (hBN) decorated $Fe_2O_3$ photocatalyst for the degradation of methylene blue, J. Mater. Sci. Mater. Electron., 32 (2021) 4766–4783. https://doi.org/10.1007/s10854-020-05215-4

Sher M., Javed M., Shahid S., Iqbal S., Qamar M.A., Bahadur A., Qayyum M.A., The controlled synthesis of g-$C_3N_4$/Cd-doped ZnO nanocomposites as potential photocatalysts for the disinfection and degradation of organic pollutants under visible light irradiation, RSC Adv., 11 (2021) 2025–2039. https://doi.org/10.1039/d0ra08573a

Shi W., Ren H., Huang X., Li M., Tang Y., Guo F., Low cost red mud modified graphitic carbon nitride for the removal of organic pollutants in wastewater by the synergistic effect of adsorption and photocatalysis, Sep. Purif. Technol., 237 (2020) 116477. https://doi.org/10.1016/j.seppur.2019.116477

Singh B., Singh K., Kumar M., Thakur S., Kumar A., Insights of preferred growth, elemental and morphological properties of BN/$SnO_2$ composite for photocatalytic applications towards organic pollutants, Chem. Phys., 531 (2020) 110659. https://doi.org/10.1016/j.chemphys.2019.110659

Singh K., Arora S., Removal of synthetic textile dyes from wastewaters: a critical review on present treatment technologies, Crit. Rev. Environ. Sci. Technol., 41 (2011) 807–878. https://doi.org/10.1080/10643380903218376

Soundiraraju B., George B.K., Two-dimensional titanium nitride ($Ti_2N$) MXene: synthesis, characterization, and potential application as surface-enhanced Raman scattering substrate, ACS Nano, 11 (2017) 8892–8900. https://doi.org/10.1021/acsnano.7b03129

Sudhaik A., Raizada P., Shandilya P., Singh P., Magnetically recoverable graphitic carbon nitride and $NiFe_2O_4$ based magnetic photocatalyst for degradation of oxytetracycline antibiotic in simulated wastewater under solar light, J. Environ. Chem. Eng., 6 (2018) 3874–3883. https://doi.org/10.1016/j.jece.2018.05.039

Teter D.M., Hemley R.J., Low-compressibility carbon nitrides, Science, 271 (1996) 53–55. https://doi.org/10.1126/science.271.5245.53

Thomas A., Fischer A., Goettmann F., Antonietti M., Müller J.-O., Schlögl R., Carlsson J.M., Graphitic carbon nitride materials: variation of structure and morphology and their use as metal-free catalysts, J. Mater. Chem., 18 (2008) 4893–4908. https://doi.org/10.1039/b800274f

Tian Y., Zhang J., Wang W., Liu J., Zheng X., Li J., Guan X., Facile assembly and excellent elimination behavior of porous BiOBr-g-$C_3N_4$ heterojunctions for organic pollutants, Environ. Res., 209 (2022) 112889. https://doi.org/10.1016/j.envres.2022.112889

Tsai C.-G., Tseng W.J., Preparation of TiN–$TiO_2$ composite nanoparticles for organic dye adsorption and photocatalysis, Ceram. Int., 46 (2020) 14529–14535. https://doi.org/10.1016/j.ceramint.2020.02.252

Tu W., Liu Y., Chen M., Zhou Y., Xie Z., Ma L., Li L., Yang B., Carbon nitride coupled with $Ti_3C_2$-Mxene derived amorphous Ti-peroxo heterojunction for photocatalytic degradation of rhodamine B and tetracycline, Colloid. Surf. A, 640 (2022) 128448. https://doi.org/10.1016/j.colsurfa.2022.128448

Urbankowski P., Anasori B., Makaryan T., Er D., Kota S., Walsh P.L., Zhao M., Shenoy V.B., Barsouma M.W., Gogotsi Y., Synthesis of two-dimensional titanium nitride $Ti_4N_3$ (MXene), Nanoscale, 8 (2016) 11385–11391. https://doi.org/10.1039/c6nr02253g

Wang A., Wang C., Fu L., Wong-Ng W., Lan Y., Recent advances of graphitic carbon nitride-based structures and applications in catalyst, sensing, imaging, and LEDs, Nano-Micro Lett., 9 (2017) 47. https://doi.org/10.1007/s40820-017-0148-2

Wang Q., Wang W., Zhong L., Liu D., Cao X., Cui F., Oxygen vacancy-rich 2D/2D BiOCl-g-$C_3N_4$ ultrathin heterostructure nanosheets for enhanced visible-light-driven photocatalytic activity in environmental remediation, Appl. Catalys. B: Environ., 220 (2018) 290–302. https://doi.org/10.1016/j.apcatb.2017.08.049

Wang Q., Zhang L., Guo Y., Shen M., Wang M., Li B., Shi J., Multifunctional 2D porous g-$C_3N_4$ nanosheets hybridized with 3D hierarchical $TiO_2$ microflowers for selective dye adsorption, antibiotic degradation and $CO_2$ reduction, Chem. Eng. J., 396 (2020) 125347. https://doi.org/10.1016/j.cej.2020.125347

Wang S., Luo H., Xu X., Bai Y., Song X., Zhang J., Li J., Zhao J., Tang C., Enhanced organic dye removal of porous BN fibers supported $Ta_3N_5$ nanoparticles under visible light irradiation, Surf. Interf., 5 (2016) 39–46. https://doi.org/10.1016/j.surfin.2016.10.001

Wang X., Maeda K., Chen X., Takanabe K., Domen K., Hou Y., Fu X., Antonietti M., Polymer semiconductors for artificial photosynthesis: hydrogen evolution by mesoporous graphitic carbon nitride with visible light, J. Am. Chem. Soc., 131 (2009) 1680–1681. https://doi.org/10.1021/ja809307s

Wei Y., Zhu Y., Jiang Y., Photocatalytic self-cleaning carbon nitride nanotube intercalated reduced graphene oxide membranes for enhanced water purification, Chem. Eng. J., 356 (2019) 915–925. https://doi.org/10.1016/j.cej.2018.09.108

Wickramaratne D., Weston L., Van de Walle C.G., Monolayer to bulk properties of hexagonal boron nitride, J. Phys. Chem. C, 122 (2018) 25524–25529. https://doi.org/10.1021/acs.jpcc.8b09087

Xu B, Ahmed M.B., Zhou J.L., Altaee A., Xu G., Wu M., Graphitic carbon nitride based nanocomposites for the photocatalysis of organic contaminants under visible irradiation: progress, limitations and future directions, Sci. Total Environ., 633 (2018) 546–559. https://doi.org/10.1016/j.scitotenv.2018.03.206

Xu Q., Zhang L., Cheng B., Fan J., Yu J., S-scheme heterojunction photocatalyst, Chem, 6 (2020) 1543–1559. https://doi.org/10.1016/j.chempr.2020.06.010

Yadav A., Dindorkar S.S., Ramisetti S.B., Sinh N., Simultaneous adsorption of methylene blue and arsenic on graphene, boron nitride and boron carbon nitride nanosheets: Insights from molecular simulations, J. Water Proc. Eng., 46 (2022) 102653. https://doi.org/10.1016/j.jwpe.2022.102653

Yagub M.T., Sen T.K., Afroze S., Ang H.M., Dye and its removal from aqueous solution by adsorption: a review, Adv. Colloid Interf. Sci., 209 (2014) 172–184. https://doi.org/10.1016/j.cis.2014.04.002

Yan H., Soft-templating synthesis of mesoporous graphitic carbon nitride with enhanced photocatalytic $H_2$ evolution under visible light, Chem. Commun., 48 (2012) 3430–3432. https://doi.org/10.1039/c2cc00001f

Yaseen D.A., Scholz M., Textile dye wastewater characteristics and constituents of synthetic effluents: a critical review, Int. J. Environ. Sci. Technol., 16 (2019) 1193–1226. https://doi.org/10.1007/s13762-018-2130-z

Yu J., Wang S., Low J., Xiao W., Enhanced photocatalytic performance of direct Z-scheme g-$C_3N_4$/$TiO_2$ photocatalyst for decomposition of formaldehyde in air, Phys. Chem. Chem. Phys., 15 (2013) 16883–16890. https://doi.org/10.1039/C3CP53131G

Yu S., Wang X., Pang H., Zhang R., Song W., Fu D., Hayat T., Wang X., Boron nitride-based materials for the removal of pollutants from aqueous solutions: a review, Chem. Eng. J., 333 (2018) 343–360. https://doi.org/10.1016/j.cej.2017.09.163

Zhan B., Liu Y., Zhou W.-T., Li S.-Y., Chen Z.-B., Stegmaier T., Aliabadi M., Han Z.-W., Ren L.-Q., Multifunctional 3D GO/g-$C_3N_4$/$TiO_2$ foam for oil-water separation and dye adsorption, Appl. Surf. Sci., 541 (2021) 148638. https://doi.org/10.1016/j.apsusc.2020.148638

Zhang L., Zhang J., Yu H., Yu J., Emerging S-scheme photocatalyst, Adv. Mater., 34 (2022) 2107668. https://doi.org/10.1002/adma.202107668

Zhang Y., Wang L., Zhang N., Zhou Z., Adsorptive environmental applications of MXene nanomaterials: a review, RSC Adv., 8 (2018) 19895–19905. https://doi.org/10.1039/c8ra03077d

Zhao G.-Q., Zou J., Hu J., Long X., Jiao F.-P., A critical review on graphitic carbon nitride (g-$C_3N_4$)-based composites for environmental remediation, Sep. Purif. Technol., 279 (2021) 119769. https://doi.org/10.1016/j.seppur.2021.119769

Zhao Z., Sun Y, Dong F., Graphitic carbon nitride based nanocomposites: a review, Nanoscale, 7 (2015) 15–37. https://doi.org/10.1039/c4nr03008g

Zhao Z., Ma Y., Fan J., Xue Y., Chang H., Masubuchi Y., Yin S., Synthesis of graphitic carbon nitride from different precursors by fractional thermal polymerization method and their visible light induced photocatalytic activities, J. Alloys Compd., 735 (2018) 1297–1305. https://doi.org/10.1016/j.jallcom.2017.11.033

Zhu B., Xia P., Ho W., Yu J., Isoelectric point and adsorption activity of porous g-$C_3N_4$, Appl. Surf. Sci., 344 (2015) 188–195. https://doi.org/10.1016/j.apsusc.2015.03.086

Zhu J., Xiao P., Li H., Carabineiro S.A.C., Graphitic carbon nitride: synthesis, properties, and applications in catalysis, ACS Appl. Mater. Interf., 6 (2014) 16449–16465. https://doi.org/10.1021/am502925j

Zollinger H., Color Chemistry: Syntheses, Properties, and Applications of Organic Dyes and Pigments, Third Edition, Wiley VCH 2003, ISBN: 9783906390239.

## Author's Short Biography

**Prof. Wenjea J. Tseng** is a Distinguished Professor in the Materials Science and Engineering Department of the National Chung Hsing University. He graduated with a diploma in Metallurgy from the National Taipei Institute of Technology, Taiwan, and his M.S. and Ph.D. degrees in Materials Science from the University of Rochester, New York, U.S.A. His research interests include colloidal processing of fine particles, chemical synthesis of functionalized nanostructures, organic-inorganic hybrid materials, photocatalysis, and gas sensing. He has published more than 100 technical papers and holds over 10 patents. He served as a council member and committee commissioner for the Taiwan Ceramic Society.

KONA Powder and Particle Journal

KONA Powder and Particle Journal No. 42 (2025) 227–240/https://doi.org/10.14356/kona.2025002 Original Research Paper

# An Empirical Equation for Rapid Validation of the Performance of Commercial N95 Equivalent Respirators†

**Sheng-Chieh Chen*, Yu Zhang, Genhui Jing, Peng Wang and Da-Ren Chen**

*Department of Mechanical and Nuclear Engineering, Virginia Commonwealth University, USA*

The COVID-19 pandemic has underscored the importance of wearing effective facepiece filtering respirators (FFRs) to reduce infection and disease transmission. One of the reasons causing the widespread prevalence was found to be the failure of N95-Equivalent FFRs (N95-EFs), i.e., efficiency <<95 %, during the pandemic. To investigate the reasons causing the ineffectiveness of commercial N95-EFs, this study measured the efficiency of several dozens of commercially available N95-EFs following standard testing protocols. The specifications of the N95-EF including fiber diameter, solidity and surface potential of the main layer media of N95-EFs were also determined. We provide a simple method for manufacturers to quickly screen the efficiencies of their N95-EF products before distributing them to the market. We found that the failures of N95-EF are majorly attributed to overprediction of the efficiency due to i) missing neutralization of challenging particles, ii) too small or oversize of challenging particles, and iii) particle detectors with large sizing limits (>500 nm). Based on the pressure drop, respirator area, and surface potential of the N95-EFs, an empirical equation is developed to fast screen and help design effective N95-EFs.

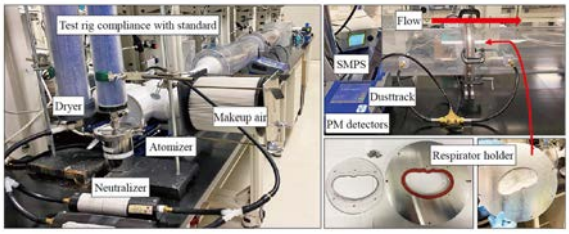


**Keywords:** COVID-19, N95, facepiece filtering respirators, pressure drop, efficiency, empirical equation

## 1. Introduction

Since the outbreaks of the COVID-19 pandemic, the novel coronavirus (SARS-CoV-2) has caused nearly a billion infections and 7 million deaths due to its high transmission and severe fatality rate (Dhand and Li, 2020; Jayaweera et al., 2020; Prather et al., 2020; Yan et al., 2018). In addition to contacting surfaces with fomite, SARS-CoV-2 had a high airborne transmission through virus-laden droplets and aerosols, which are released by sneezing, coughing, speaking, and breathing of the infected person. These droplets and aerosols can travel up to 8 m, and the desiccated residue or droplet nuclei may stay suspended for hours (CDC, 2021; Dhand and Li, 2020), which significantly enlarged the transmission rate. To provide protection for individuals and lower the transmission of SARS-CoV-2 through aerosol transmissions, face masks and filtering facepiece respirators (FFRs) are required or highly recommended by the Centers for Disease Control and Prevention, CDC, since the outbreak of COVID-19 in March 2020 (CDC, 2020). N95, KN95, FPP2, and KF94 respirators, etc., whose filtration efficiencies against laboratory-produced NaCl particles are required to be larger than 94–95 %, are commercially available and affordable for the general public. It is of great importance that these N95 Equivalent-Facepiece filtering respirators (N95-EFs) have good quality to protect people from infection and spreading of viruses.

### 1.1 Failure of FFRs

According to the CDC, approximately 60 % of KN95, the most widely available N95-EFs on the market during the COVID-19 pandemic in 2020 and 2021, did not meet the requirement, i.e., filtration efficiency (FE) ≥95 % (CDC, 2021). Aiming to determine the reasons for the unsatisfactory performance of FFRs or to develop easy screening methods, quite many research teams evaluated commercially available FFRs (e.g., Duncan et al., 2021; Plana et al., 2021; Schilling et al., 2021).

As is known, the standard testing protocols by the National Institute for Occupational Safety and Health (NIOSH) and by the National Standards of the People's Republic of China (GB 2626, 2006) require rigorous procedures and designated or recommended equipment and conditions such as particle type and size distribution, particle charging state, particle detector, filtration flow rate, sample conditioning, environmental control chamber, etc. Because of the strict and time-consuming testing procedures and the expensiveness of the required facilities, any simplifications and noncompliance with the procedures would lead to incorrect filtration efficiency results. Additionally, the urgent demands of tremendous quantities during the early period of the pandemic caused the failures

† Received 11 June 2023; Accepted 11 July 2023
J-STAGE Advance published online 13 January 2024
* Corresponding author: Sheng-Chieh Chen;
Add: 401 West Main St., Richmond, VA, 23284, USA
E-mail: scchen@vcu.edu
FAX: +1-804-827-0306

of quality assurance and control of the N95-EFs by the manufacturers. However, it was very difficult for the public to distinguish between legitimate and counterfeit products. The wearing of counterfeit products would be a reason for speeding the spread of SARS-CoV-2 during the pandemic.

## 1.2 Reasons for N95-EF failure

The efficiency of N95-EFs was often largely overestimated if standard procedures were not followed. In the evaluations of N95-EFs, the required size distribution, charging state, and deliquesce of challenging particles were often not considered (Cai and Floyd, 2020; Duncan et al., 2021; Patra et al., 2022; Schilling et al., 2021; Stahl et al., 2021). For instance, some researchers did not neutralize the challenging particles, which could lead to the overprediction of the Columbic force and the FE. Because particles will carry a higher mean number of charges after they are aerosolized than the neutralized state, as required. During particle dispersion (e.g., aerosolization by atomizer), a triboelectric or contact charge develops along the particle surface because of mechanical friction from the surface and particle contact. This energy transfer could generate an excess charge of 1~$10^5$ elementary units (Forsyth et al., 1998). For example, it was found that 200 nm NaCl particles carried a mean elementary charge of ~3.7 compared to ~1.0 charge of neutralized particles (Forsyth et al., 1998). According to the theoretical model (Chang et al., 2016; 2018), the FE for a neutralized 100 nm NaCl particle through a charged filter media (~75 μC/$m^2$) can be increased from ~60 % to over 95 % if it is not neutralized. This indicates the importance of a completed neutralization before challenging the respirator to prevent a significant overprediction of FE.

While the recommended particle detector by the NIOSH was a mass-based laser light scattering photometer detector having a sizing limit of ~0.1 μm, some researchers applied detectors with a limit larger than 300–500 nm (e.g., optical particle counter), thus, the high penetration from small particles, i.e., <100 nm, was neglected. Indeed, the most penetrating particle size (MPPS) of charged filter media normally falls at 20–50 nm (Chang et al., 2015; Tang et al., 2018a, b, c). The overestimation of EFs becomes more significant when the challenging aerosol particles have a larger number (or count) median diameter (NMD) due to the inherent relatively higher EF of larger particles. For example, the FE of a neutralized 500 nm by charged media could reach ~95 % but it reduced to ~88 % and ~80 % when the size was reduced to 100 nm and 50 nm (MPPS), respectively (Chen et al., 2014). Without taking the high penetration of small particles into account, the overall efficiency was thus overestimated. This analysis also reveals the importance of complying with the specified size distribution of challenging particles by the standards, which was an NMD of 0.075 ± 0.02 μm and geometric standard deviation (GSD) of smaller than 1.86. The more shifting of size distribution to larger size ranges, the more significant overestimation of FE will be. To note, there exists a lack of correspondence between the specified size distribution (NMD ~0.075 μm) and particle detector (>0.1 μm) in the standard, which should be addressed in the future.

The filtration flow rate (or flow face velocity through media) designated by the standards was 85 L/min (or ~10 cm/s face velocity). Some researchers performed the FE test with a face velocity lower than 10 cm/s, especially when a flat sheet of the FFR media instead of a whole FFR was evaluated. For an N95-rated FFR, the FE can increase from ~88 to 95 % for MPPS when reducing the face velocity from 10 to 5 cm/s (Chen et al., 2014). From the foregoing discussion, simplifications and noncompliance with standard methods could produce significant overestimations of FE.

Given the limited access to required facilities and compliance with complex experimental procedures, theoretical models based on the single fiber theory may be applied to predict the FEs (Chang et al., 2016). However, this method can also be problematic as it requires accurate specifications of the FFRs, i.e., fiber diameter, thickness, packing density (solidity), charge density, and face velocity. Among them, charge density is the most inaccessible parameter due to the complexity of charge figuration and its measurement. Thus, it is commonly seen that an estimated value of charge density was used in the calculation to match experimental FE data (Balazy et al., 2006; Chang et al., 2016; Hao et al., 2021). However, the empirically-theoretically fitted charging density is accurate only when other filter parameters are correctly determined. Even if other parameters are correct, an incorrect charging density may be obtained if any filtration equations for each deposition mechanism are incorrect, typically occurring for the equation of electrostatic deposition.

For a good preparation for future respiratory pandemics, it is urgent to develop a fast, convenient, and accurate method for manufacturers and certification laboratories to quickly qualify and prove the effectiveness of N95-EFs before distributing them to the market. Using a modified three-layer model based on the measured and calculated particle depositions through the cracks, researchers successfully developed an empirical equation to predict the penetration rate of outdoor particles into buildings (Chen et al., 2012; You et al., 2012). Similarly, an empirical equation model combining experimental data and filtration theory and describing the relationship between variables is a potentially useful method to quickly provide reliable predictions and insights into the performance of N95-EFs.

## 1.3 Objectives

In this study, a rigorous test rig and strict measurement procedure in compliance with Chinese Standard GB 2626

(GB 2626, 2006) were applied to measure the efficiency of 50 different commercial N95-EFs. The GB 2626 method was chosen because it was similar to the NIOSH standard and the majority (30 out of 50) of the tested respirators were KN95. In addition to the mass-based FE by a photometer, the number-based size-fractioned FE was also determined by a scanning mobility particle sizer (SMPS, Model 3938, TSI Inc., Shoreview, MN) for the 50 N95-EFs. In addition to the FE, the thickness, fiber size, solidity and surface potential of main filtration layer were measured. The charge density of N95-EF media was obtained by comparing the experimental and theoretical efficiency according to Chang et al. (2016). The correlation between calculated charging density and surface potential was investigated. If a good linear correlation is seen, the easily accessible surface potential can substitute the charging density as a representative filtration parameter.

This study is trying to develop an empirical equation to predict the FEs of N95-EFs. Because FEs are size-dependent and number-based according to filtration theory (Hinds, 1999), the FE for MPPS measured by SMPS was selected as the target. The N95-EF can pass the evaluation if its FE at MPPS is higher than 95 %. The qualified N95-EF thus has a minimum FE of 95 % against any size of particles.

Considering many filter parameters that cannot be easily obtained, including solidity, charging density, and fiber diameter, they may be excluded from the empirical equation. Instead, three easily accessible but essential parameters, including pressure drop, mask area, and surface potential, should be good representative variables of FE at MPPS and be applied in the empirical equation. The pressure drop of the respirator is the product of fiber diameter, solidity,, and thickness; thus, it should be an important parameter of FE. Since most N95-EFs are charged, the feasibility of using the surface potential in the empirical equation will be investigated. The respirator area was included because under a constant testing flow rate of 85 L/min, the face velocity and thus the FE would vary significantly. In fact, the area varies largely for commercial N95-EFs.

The developed equation will be evaluated by comparing its predictions with the experimental efficiency of MPPS particles. The model will be further validated by predicting the FE for 5 extra N95-EF samples. The final goal of this study is to provide this validated equation and its constraints for the use of manufacturers or certified laboratories to quickly qualify N95-EFs to secure their quality.

## 2. Materials and methods

### 2.1 N95-EF sources and selection

The N95-EFs evaluated in this study included N95, KN95, KF94, and FFP2 respirators purchased from Amazon, Costco Wholesale, Walmart, Kroger, and CVS. A total of 50 samples were collected and investigated for their FEs and specifications. Before the FE measurement, the first examination was to check their appearance. Samples that appeared to have any damage, deformation and defects on the surface were excluded. Besides, those N95-EFs containing both nanofiber and microfiber layers (by SEM analysis) were also removed because their FE could not be easily predicted by filtration theory. Moreover, samples were also excluded when the variation of FEs for 5 randomly picked respirators from the same box (usually sold with 20–50 packs per box) was too significant. For example, when one standard derivation of FE (the measurement method will be shown later) from 5 samples was higher than 20 % of average efficiency. A high deviation means their average FEs were not statistically significant to be adopted. Finally, a total of 15 samples were excluded from the first examination.

Among the qualified 35 N95-EFs, the evaluation results of 30 samples were used to develop the empirical equation for predicting the FE at MPPS. The rest 5 samples were used to validate the equation. All samples were measured with their thickness, solidity (packing density), fiber diameter, filtration area, charge density and pressure drop. To note, some N95-EFs contain more than one charged (major) layer, so the above specifications should be determined based on all charged layers.

### 2.2 Thickness

The thickness of the main filter layer (excluding the top and bottom layers having very coarse fibers without charges, for support only) was measured by a digital caliper with a resolution of 0.001 mm. To increase the accuracy, 5 pieces of the main layer cut from different locations were combined for their average thickness. The measurement was repeated for 5 runs for 5 respirators from the same box to obtain the representative thickness.

### 2.3 Solidity

Solidity was obtained by taking the ratio of the fiber volume to the total volume of the main filtration layer (usually meltblown of polypropylene) of the respirator. The total volume was determined by the product of media thickness and sample size (cut with 40 mm in diameter). The volume of the filtration layer was determined from the ratio of their weight to the sample volume. The solidity, $\alpha$, is calculated as:

$$\alpha = \frac{W / \rho_f}{t \times \pi \times 4^2 / 4} \quad (1)$$

where $W$ is the weight of the flat sheet [g], $\rho_f$ is the density of the filter media (0.855 g/cm$^3$ for polypropylene) and $t$ is the thickness.

The fiber diameter applied in this study was the effective fiber diameter based on the solidity and pressure drop measured (Davies, 1973). Chang et al. (2016) have proven that

effective fiber diameter was applicable and suitable for the prediction of FE using single fiber efficiency theory.

## 2.4 Filtration area

In the determination of total filtration area of N95-EFs that exhibited different shapes and sizes, a simple method was developed. First, the pressure drop for the whole respirator under 85 L/min was measured. Then, a flat circular sheet of 4 cm in diameter (or 12.56 $cm^2$) was cut from the respirator and measured for its pressure drop under 10 cm/s (or 7.54 L/min). The pressure drop is linearly increased with face velocity for the same filter media. If the measured pressure drop of the whole respirator is $P1$ and that of the 4 cm circular sheet is $P2$, the area of the whole respirator, $A$, is calculated as:

$$\frac{P1}{P2}=\frac{85/A}{7.54/12.56}\Rightarrow A=\frac{141.6\times P2}{P1} \tag{2}$$

## 2.5 Theoretical filtration efficiency

The theoretical single fiber efficiency model was developed to predict the FE of both charged (or electret) and uncharged (or mechanical) filter media under clean conditions (Chang et al., 2016; Hinds, 1999). It is widely applied, and here we summarize the models that can accurately predict the FEs for researchers' reference (Chang et al., 2016, 2018; Liu et al., 2023; Tien et al., 2020). The theoretical particle penetration, $P_{theo}$, is calculated as (Bahk et al., 2013; Hinds, 1999; Wang et al., 2007, 2011):

$$P_{theo}=\exp\left(-\frac{4\alpha E_T t}{\pi d_f(1-\alpha)}\right) \tag{3}$$

where $d_f$ is the fiber diameter in the filter media and $E_T$ is the total single fiber efficiency due to diffusion ($E_D$), interception ($E_R$), interception of diffusing particles ($E_{DR}$), impaction ($E_I$), and electrostatic attraction ($E_q$), and determined as:

$$E_T=1-(1-E_D)(1-E_R)(1-E_{DR})(1-E_I)(1-E_q) \tag{4}$$

The $E_D$, $E_R$, $E_{DR}$ and $E_I$ are calculated as (Wang et al., 2007; 2011):

$$E_D=0.84Pe^{-0.43} \tag{5}$$

$$E_R=\frac{1+R}{2Ku}\left[2\ln(1+R)-1+\alpha+\left(\frac{1}{1+R}\right)^2\left(1-\frac{\alpha}{2}\right)-\frac{\alpha}{2}(1+R)^2\right] \tag{6}$$

$$E_{DR}=\frac{1.24R^{2/3}}{(Ku\times Pe)^{1/2}} \tag{7}$$

$$E_I=\frac{1}{(2Ku)^2}\left[(29.6-28\alpha^{0.62})R^2-27.5R^{2.8}\right]Stk \tag{8}$$

where $Pe$ is the Peclet number, $Ku$ is the Kuwabara hydrodynamic parameter, $R$ is the ratio of particle to the fiber diameter, and $Stk$ is the Stokes number. The $Pe$, $Ku$, and $Stk$ are calculated as:

$$Pe=\frac{d_f U_0}{D} \tag{9}$$

$$Ku=\frac{-\ln\alpha}{2}+\alpha-\frac{\alpha^2}{4}-\frac{3}{4} \tag{10}$$

$$Stk=\frac{\rho_p d_x^2 C_c U_0}{18\mu d_f} \tag{11}$$

where $U_0$ is face velocity, $D$ is the diffusion coefficient, $\rho_p$ is NaCl density (2.2 g/$cm^3$), $d_x$ is particle diameter, $C_c$ is the Cunningham slip correction factor (Hinds, 1999) and $\mu$ is the air viscosity (N·s/$m^2$). In **Eqn. (4)**, $E_q$ can be further calculated according to the depositions by the Coulombic force $E_{qC}(n)$ and that by the dielectric polarization force $E_{qD}$, as:

$$E_q=1-[1-E_{qC}(n)](1-E_{qD}) \tag{12}$$

where $E_{qC}(n)$ is the function of the number of charges, and $n$, is the number of charges the particles carried. The $E_{qC}(n)$ and $E_{qD}$ can be calculated as (Chang et al., 2015):

$$E_{qC}(n)=\left(\frac{1-\alpha}{Ku}\right)^{1/8}\frac{\pi N_{CD}}{1+2\pi N_{CD}^{1/4}} \tag{13}$$

and

$$E_{qD}=\left(\frac{1-\alpha}{Ku}\right)^{2/5}\frac{\pi N_{DD}}{1+2\pi N_{DD}^{2/3}} \tag{14}$$

$N_{CD}$ and $N_{DD}$ are dimensionless parameters for charged and uncharged particles through bipolarly charged fibrous filter media, respectively, and defined as:

$$N_{CD}=\frac{C_c\sigma q(n)}{3\pi\mu\varepsilon_0(1+\varepsilon_f)d_x U_0} \tag{15}$$

and

$$N_{DD}=\frac{2C_c\sigma^2 d_x^2}{3\mu\varepsilon_0(1+\varepsilon_f)^2 d_f U_0}\left(\frac{\varepsilon_p-1}{\varepsilon_p+2}\right) \tag{16}$$

where $\sigma$ is the charging density of the fiber (C/$m^2$), $q(n)$ is the carried charges of the particle with $d_x$ (C), $\varepsilon_f$ is the fabric dielectric constant (1.5 for the polypropylene), $\varepsilon_0$ is the permittivity of the vacuum ($8.85\times10^{-12}$ $C^2/N\cdot m^2$) and $\varepsilon_p$ is the relative permittivity of the particle which is 4.86 for NaCl.

By considering the charge distributions of particles (size dependent) through charged filter media, the size dependent penetration, $P_{theo,dx}$, is calculated as:

$$P_{\text{theo},dx} = \sum_{n=-10}^{n=10} f(n) \times \exp\left(-\frac{4\alpha E_T(n)t}{\pi d_f(1-\alpha)}\right),$$

$n$ includes 0 (17)

where $f(n)$ is the fraction of the $d_x$ particles that carry number of $n$ charges and the total efficiency $E_T$ is rewritten to consider particle charges (up to 10 elementary charges) as:

$$E_T(n) = 1-(1-E_D)(1-E_R)(1-E_{DR})(1-E_I)\left[1-E_{qC}(n)\right]\left(1-E_{qD}\right) \quad (18)$$

To note, **Eqn. (17)** considers the polarization depositions for both neutral (zero charge) and charged particles, which resulted in an agreement between the model prediction and experimental data (Chang et al., 2016). Without considering the polarization deposition for charged particles, it would lead to errors. **Eqn. (17)** considers particle charges up to with 10 elementary charges, but normally the particle concentration fractions reduce to negligible (<1 %) for more than 6 charges for submicron particles (<1 μm).

From **Eqns. (3)** to **(18)**, the theoretical EF is size dependent, $\eta_{\text{theo},dx}$ and calculated as:

$$\eta_{\text{theo},dx} = 1 - P_{\text{theo},dx} \quad (19)$$

The result of **Eqn. (19)** will be compared with the size fractioned efficiency determined by the SMPS (detailed in **Section 2.7**).

As shown above, to predict the efficiency of charged filter media using the theoretical model involves many equations and cumbersome calculations, which can easily cause errors. The charge density in **Eqns. (15, 16)** was not easily and accurately measured. Thus, one can extrinsically determine it by fitting a value of the charging to match the size fractioned efficiency curve between the theoretical calculation and experimental measurement (Chang et al., 2016). However, an accurate charging density can be obtained only if accurate experimental data are obtained and all required parameters presented in these equations are correctly measured and determined. This study intended to determine the empirical charging density of each respirator investigated, so the calculations were inevitable. To conclude, given the complexity of obtaining the theoretical efficiency, charge density, and all filter specifications, it is necessary to find an easily accessible method to quickly screen the effectiveness and FE of respirators.

## 2.6 Surface potential measurement

A Trek model 244A electrostatic voltmeter equipped with a 1017AE probe (Advanced Energy Industries, Inc., Denver, CO) was used to measure the dipolar surface potential of the main filtration layer, as shown in **Fig. 1**. This voltmeter uses a technique that nullifies the field between the probe and the filter (Antoniu et al., 2011; Sachinidou et al., 2018). The potential $V_p$ of the voltmeter probe is driven by the electronic circuitry of the instrument at the potential $V$ of the monitored surface ($V_p = V$). Thus, the electric field in the air gap between the sample and probe is nullified. This measurement configuration is equivalent to that of a capacitor calculated as:

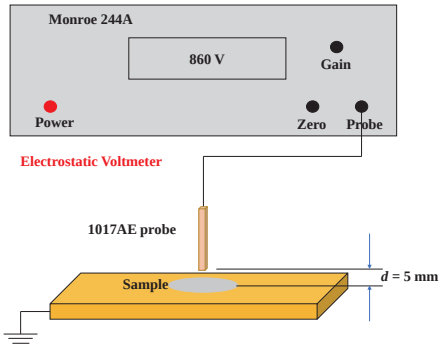


**Fig. 1** Schematic of surface potential measurement by electrostatic voltmeter.

$$C_p = \frac{Q}{V} = \frac{\varepsilon_d A}{t} \quad (20)$$

where $C_p$ is the capacitance of the capacitor, $Q$ is the charge carried by the surface area $A$ of the sample surface, $V$ is the measured surface potential (i.e., a potential difference between the sensor and the tested surface), $\varepsilon_d$ is the permittivity of the sample between the electrode and the tested surface, and $t$ is the thickness of the sample (Kachi et al., 2011). The surface electric charge density $\sigma$, assumed to be uniformly distributed, can be expressed as (Kachi et al., 2011):

$$\sigma = \frac{V\varepsilon_d}{t} \quad (21)$$

During the surface potential measurement, the major layer was positioned onto a grounded metal plate and a noncontact probe of the electrostatic voltmeter was placed 5 mm above the layer surface, according to Kachi et al. (2011). The environmental relative humidity (RH) was controlled between 30 % and 50 % to minimize the effect of RH on charge dissipation during the measurement (Kachi et al., 2011). The samples were in circular shape with a diameter of 4 cm. To obtain representative results, 20 different spots on the surface of the sample were measured and averaged. To be mentioned, dragging the sample and causing friction with the surface should be avoided during measurements, which can generate static charges. The measurements were repeated for 5 different pieces from different respirator samples in the same box to provide the average and standard deviation.

The measured surface potentials were correlated with the obtained charged density from theoretical calculations.

### 2.7 Filtration efficiency measurement

The standard GB 2626 method was applied to determine the performance of N95-EFs. Before the FE measurement, temperature and humidity conditioning were conducted. That is, 5 samples from a box were pretreated with temperature and RH at 38 ± 2.5 °C and 85 ± 5 %, respectively, for 24 ± 1 hours. Then, they were conditioned under 70 ± 3 °C and RH <30 % in a forced air oven for other 24 ± 1 hours. Finally, they were treated under –30 ± 3 °C in the freezer for other 24 ± 1 hours. We randomly picked 10 samples to conduct the conditioning test.

The mass-based FE, $\eta_m$, based on the upstream, $C_{m,up}$, and downstream mass concentrations, $C_{m,down}$, of NaCl particles of the respirator under 85 L/min flow rate, was determined as:

$$\eta_m = 1 - \frac{C_{m,down}}{C_{m,up}} \tag{22}$$

The mass concentrations were measured by a TSI DustTrak DRX (Model 8533, TSI Inc., Shoreview, MN) photometer. The challenging particles required a specific size distribution having a NMD of 0.075 ± 0.02 μm and a geometric standard deviation ($\sigma_g$) less than 1.86. **Fig. 2** shows an example of the size distribution of the generated particles in this study.

The TSI 8130 Automated Filter Tester (TSI Inc., Shoreview, MN) is a standard reference test rig. It uses a laser with a wavelength of 780 nm to illuminate challenging particles and to detect light scattering for the upstream and downstream particles of the filter by photometers. Lights scattered from particles whose diameters are much smaller than the wavelength of the incident laser would be very weak ($\propto d_x^6$), so the sensitivity is largely reduced for small particles. Therefore, photometric measurement is largely biased toward the detection of larger particles in the distribution, and it can significantly overestimate the FE of the filter media, typically against the small challenging particles (**Fig. 2**, by the SMPS) for charged media. Therefore, to provide the worst performance of respirator, the FE at MPPS, $\eta_{MPPS}$, which is the number-based minimum efficiency is measured. To find $\eta_{MPPS}$, the largest size dependent penetration, $P_{largest,dx}$, should be calculated by taking the ratio of upstream, $C_{n,up}$, to downstream number concentration, $C_{n,down}$, of the respirator as:

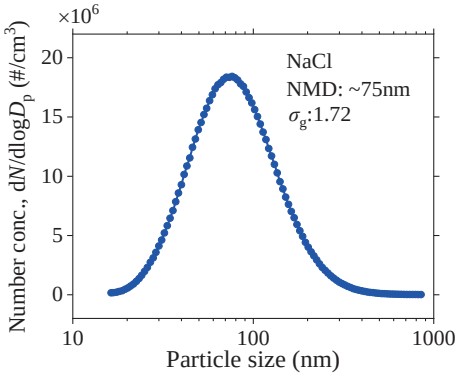


**Fig. 2** Size distribution of challenging particles.

$$\eta_{MPPS} = 1 - P_{largest,d_x} = 1 - \frac{C_{n,down}}{C_{n,up}} \tag{23}$$

The size distribution shown in **Fig. 3** is the denominator in **Eqn. (23)**. The experimental setup for mass-based and number-based FE measurements is shown in **Fig. 3**.

To measure the number-based filtration efficiency, the TSI SMPS (Model 3938, TSI Inc., Shoreview, MN) was applied, and the procedures are the same as that of the mass-based testing procedure by Dusttrak. Before introducing challenging particles into the respirator, they should be totally neutralized by a neutralizer, Po-210 here, which depends on the resident time (or flow rate) and ion concentration (Hinds, 1999). It is worth mentioning that since the efficiency testing was under a flow rate of 85 L/min, the upstream concentration of the particle source at smaller particle size may be low, which can lead to inaccuracy of EF of MPPS (usually in 20–50 nm for charged media). Thus, a suitable atomizer that has a sufficiently high flow rate (dilution rate can be reduced) and high particle concentration as well as the required size distribution is essential. In this study, a homemade atomizer with a maximum flow rate of 8 L/min was applied. The concentration of NaCl solution was 0.5–1.5 wt% in this study. To obtain representative results, measurements for the filtration efficiency by every type of FFRs were repeated at least five times using new samples.

## 3. Results and discussion

### 3.1 Specification of studied N95-EFs

#### 3.1.1 Mass- and Number-Based FE

This study found that pretreatment with temperature and humidity did not change the FE results of the tested respirators. **Table 1** summarizes the specifications and FE data measured for the first 30 tested respirators, including mass- and number-based efficiency, MPPS, pressure drop, filtration area, thickness, effective fiber diameter, solidity, empirical charging density, and surface potential. The order of these respirators shown in the table was based on their mass-based efficiency from high to low. It is seen 9 out of 30 did not pass 0.95 (or 95 %) mass-based efficiency. The pass rate shown here is reasonable because the half of them were purchased after January 2022, so only ~30 % failed. Due to the small size distribution of the NaCl challenging particles and more sensitivity of SMPS than the Dusttrak, as expected, the number-based efficiency was lower than that of mass-based ones except for samples 11, 16 and 21. These three respirators, in general, had a high pressure drop (150–225 Pa, oriented toward mechanical filter) and medium charging density (MPPS not small), causing a higher efficiency toward small sizes. A total of 11 out of 30 tested

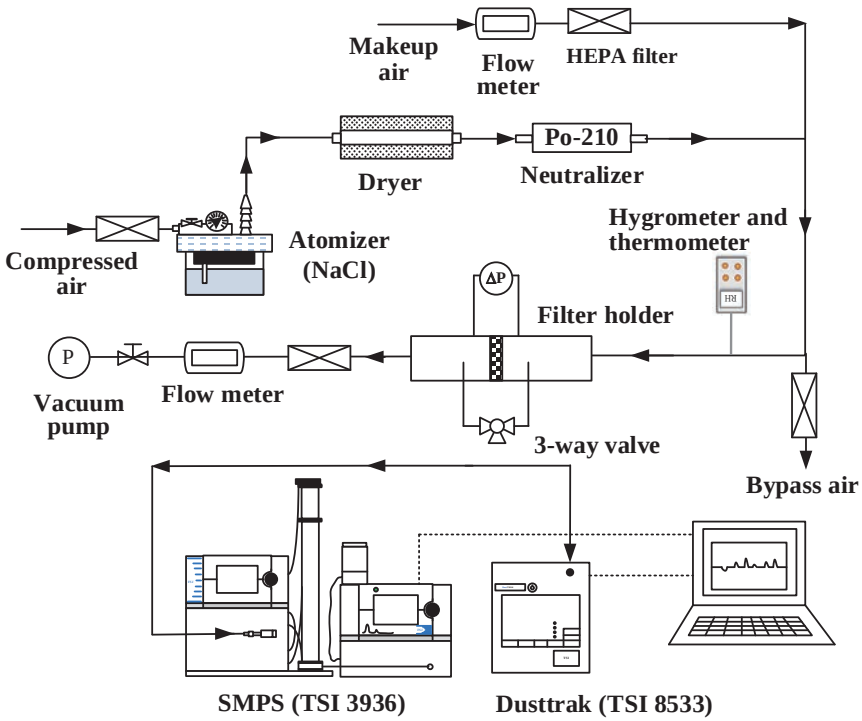


**Fig. 3** Test rig for measuring both mass- and number-based FEs of N95-FEs.

respirators did not pass the 95 % number-based efficiency. Samples 8, 17 and 20 passed mass-based FE while failed for number-based FE. Nevertheless, their number-based efficiencies were still acceptable (90.3 %, 86.3 % and 90.9 %, respectively).

### 3.1.2 Pressure Drop, Filtration Area, and Other Physical Properties

The pressure drops of the tested N95-EFs under 85 L/min flow rate varied largely from 25 to 185 Pa. As mentioned, pressure drop is very important and it depends on several physical properties including packing density, fiber diameter, thickness, and filtration area. As low as 50–65 Pa, samples 1, 4 and 5 passed both mass- and number-based 95 % efficiency, which was attributed to their high charging density (discussed later). Comparing samples 4 and 5, the latter had larger filtration area (23 % increase) and finer fiber diameter to compensate for its lower charging density. In general, the manufacturer intended to increase fiber charges to design their respirators with lower pressure drop for the comfort of the wearer. However, there is a high risk if the filter media is not properly charged when weighing and relying only on its low mechanical efficiency due to low pressure drop.

The filtration areas also varied largely from 143 to 235 $cm^2$. This means that the face velocity through the two extreme respirators had a 1.6 times difference, which can cause a nonnegligible filtration result. The differences in thickness, fiber diameter and solidity varied from 0.26 to 0.98 mm, 3.74 to 12.1 μm, and 0.091 to 0.195, respectively. The largest differences were 3.8, 3.2, and 2.1 times for these three parameters. Without considering their effectiveness, these randomly purchased N95-EFs had large differences in their physical design parameters. These unreasonably high differences were the potential reasons causing the failures of many respirators.

## 3.2 Empirical charging density

Once the required physical properties were obtained (**Table 1**), the charging density can be treated as the only variable in the theoretical FE calculation to match the experimental data. As expected, after applying favorable fiber charging density into the modeling, good agreements of whole size fractioned efficiency curve between theory (**Eqns. (3)–(19)** and **(22)–(23)**) and data were obtained for all samples. **Fig. 4** shows examples of the comparisons for 4 representative N95-EFs, including an N95 (#11), a KN95 (#17), a KF94 (#5), and an FFP2 (#9). It can be seen that the two curves almost collapsed together for all sizes, indicating that the applied charging density and the measured physical properties were very accurate.

### 3.2.1 MPPS and Charging Density

The charging density of the 30 samples varied from 2 to 122. The MPPS of filter media measured was closely related to the charging density and fiber diameter of the filter media (Chang et al., 2016; Tang et al., 2018a, b, c). When the media carried a relatively high charge, e.g., ≥50 μC/$m^2$, the MPPS would obviously move to small sizes, e.g., <50 nm. Our measurement results agreed with this trend.

**Table 1** Specifications and test results of 30 commercial N95-EFs.

| Label | Mass $\eta$ | Number $\eta$ at MPPS | MPPS (nm) | $\Delta P$ of whole mask (Pa) | $\Delta P$ of 4 cm flat sheet @10 cm/s (Pa) | Mask area ($cm^2$) | Thickness (mm) | The fiber diameter (μm) | Solidity | Charge density ($\mu C/m^2$) | Surface potential (V) | Std. ± (V) |
|---|---|---|---|---|---|---|---|---|---|---|---|---|
| 1 | 0.998 | 0.985 | 29.4 | 50.0 | 75.0 | 212 | 0.98 | 10.2 | 0.135 | 122 | 1393.1 | 203.7 |
| 2 | 0.996 | 0.987 | 39.2 | 107.5 | 127.5 | 168 | 0.4 | 5.6 | 0.158 | 85 | 824.3 | 125.4 |
| 3 | 0.993 | 0.977 | 45.3 | 130.0 | 137.5 | 149 | 0.31 | 3.7 | 0.131 | 75 | 594.0 | 39.6 |
| 4 | 0.989 | 0.978 | 33.0 | 62.5 | 77.5 | 175 | 0.38 | 4.7 | 0.099 | 95 | 760.3 | 137.2 |
| 5 | 0.989 | 0.966 | 34.0 | 63.5 | 95.0 | 215 | 0.34 | 4.1 | 0.091 | 55 | 575.3 | 101.2 |
| 6 | 0.985 | 0.951 | 45.3 | 120.0 | 150.0 | 177 | 0.35 | 5.7 | 0.180 | 45 | 577.5 | 166.4 |
| 7 | 0.985 | 0.961 | 52.3 | 115.0 | 137.5 | 169 | 0.49 | 4.9 | 0.128 | 48 | 586.1 | 216.5 |
| 8 | 0.983 | 0.903 | 125.0 | 185.0 | 237.5 | 181 | 0.32 | 4.4 | 0.180 | 15 | 203.6 | 40.4 |
| 9 | 0.981 | 0.955 | 60.4 | 157.5 | 172.5 | 155 | 0.36 | 5.2 | 0.184 | 35 | 475.5 | 225.2 |
| 10 | 0.979 | 0.957 | 50.5 | 150.0 | 200.0 | 188 | 0.34 | 5.4 | 0.189 | 35 | 331.3 | 130.2 |
| 11 | 0.979 | 0.989 | 45.3 | 170.0 | 172.5 | 143 | 0.44 | 5.2 | 0.175 | 58 | 663.3 | 95.6 |
| 12 | 0.979 | 0.958 | 52.3 | 110.0 | 155.0 | 199 | 0.36 | 5.3 | 0.159 | 45 | 477.8 | 86.1 |
| 13 | 0.975 | 0.957 | 39.2 | 70.0 | 107.5 | 217 | 0.31 | 4.7 | 0.120 | 65 | 428.4 | 83.5 |
| 14 | 0.972 | 0.962 | 62.6 | 142.5 | 237.5 | 235 | 0.35 | 5.8 | 0.195 | 33 | 343.6 | 108.7 |
| 15 | 0.969 | 0.954 | 58.3 | 110.0 | 150.0 | 193 | 0.55 | 7.5 | 0.181 | 40 | 468.1 | 97.8 |
| 16 | 0.966 | 0.970 | 52.3 | 135.0 | 150.0 | 157 | 0.48 | 4.9 | 0.142 | 52 | 567.7 | 72.6 |
| 17 | 0.964 | 0.863 | 54.2 | 82.5 | 120.0 | 205 | 0.26 | 6.1 | 0.184 | 21 | 136.1 | 59.5 |
| 18 | 0.963 | 0.952 | 50.5 | 110.0 | 137.5 | 177 | 0.36 | 6.1 | 0.181 | 48 | 572.6 | 81.2 |
| 19 | 0.963 | 0.953 | 58.3 | 115.0 | 155.0 | 190 | 0.4 | 5.8 | 0.168 | 28 | 529.2 | 93.3 |
| 20 | 0.956 | 0.909 | 39.2 | 77.5 | 100.0 | 182 | 0.55 | 5.6 | 0.111 | 40 | 376.9 | 233.4 |
| 21 | 0.953 | 0.955 | 47.9 | 140.0 | 225.0 | 227 | 0.32 | 5.0 | 0.178 | 45 | 606.6 | 85.2 |
| 22 | 0.936 | 0.873 | 45.3 | 72.5 | 100.0 | 195 | 0.35 | 7.6 | 0.186 | 25 | 204.6 | 86.3 |
| 23 | 0.914 | 0.866 | 52.3 | 68.8 | 87.5 | 180 | 0.36 | 7.7 | 0.180 | 15 | 169.6 | 34.8 |
| 24 | 0.905 | 0.873 | 93.1 | 75.0 | 102.5 | 193 | 0.49 | 7.1 | 0.151 | 15 | 174.0 | 11.3 |
| 25 | 0.904 | 0.846 | 69.8 | 66.5 | 95.0 | 199 | 0.41 | 8.9 | 0.194 | 15 | 145.7 | 56.3 |
| 26 | 0.875 | 0.832 | 143.0 | 67.5 | 97.5 | 204 | 0.56 | 6.6 | 0.122 | 8.5 | 128.2 | 20.4 |
| 27 | 0.866 | 0.808 | 160.4 | 72.5 | 100.0 | 195 | 0.46 | 6.8 | 0.145 | 10 | 96.5 | 10.7 |
| 28 | 0.848 | 0.805 | 254.0 | 92.5 | 130.0 | 199 | 0.47 | 5.6 | 0.135 | 12 | 103.2 | 12.4 |
| 29 | 0.464 | 0.360 | 294.3 | 45.0 | 62.5 | 196 | 0.43 | 9.9 | 0.173 | 2 | 45.7 | 5.3 |
| 30 | 0.395 | 0.201 | 450.0 | 25.0 | 37.5 | 212 | 0.39 | 12.1 | 0.166 | 3 | 56.5 | 8.31 |

For example, the MPPSs were smaller than 40 nm for media with charges higher than 85 $\mu C/m^2$. The shifting of MPPS to small sizes is due to relatively large enhancement of deposition by fiber charge for larger particles than smaller ones. Both Coulombic and polarization attractions were almost negligible for particles smaller than ~50 nm due to relatively low carried and induced charges for small particles. On the contrary, when charging density smaller than ~10 $\mu C/m^2$, they could be treated as a mechanical filter. For example, samples 26–30 had relatively large MPPSs ranging 143–450 nm. It was speculated that the media were not successfully charged as expected or the rate of charge decay was too fast. As mentioned earlier, this is risky as these respirators relied mostly only on mechanical filtration, such as samples 29 and 30 had a relatively low efficiency of ~40 %.

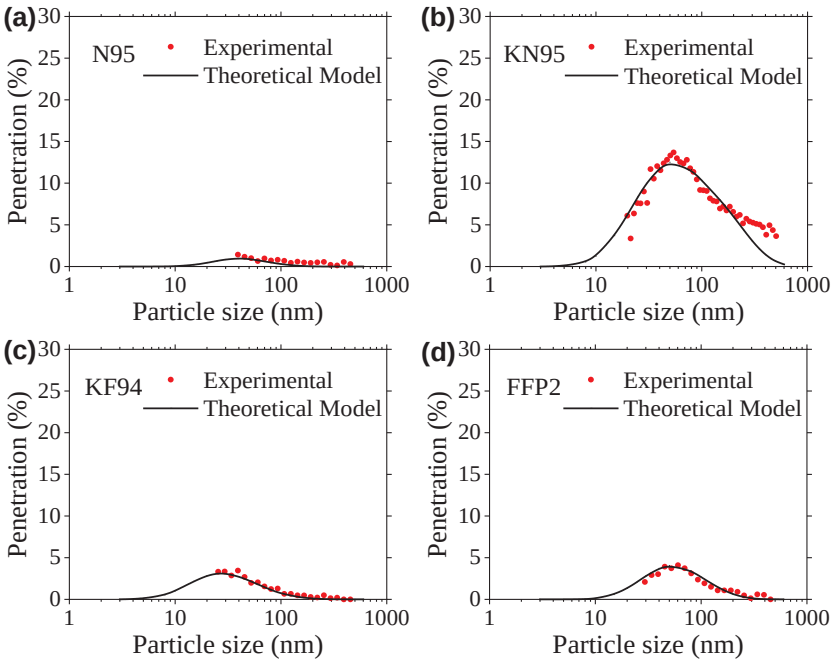


**Fig. 4** Comparison of theoretical and experimental efficiency curve of sample 11 **(a)**, sample 17 **(b)**, sample 5 **(c)** and sample 9 **(d)** respirators.

### 3.2.2 Charging Density and Surface Potential

**Table 1** also shows the measured surface potentials and standard deviations for the 30 samples. The surface potentials varied largely from 45.7 to 1393 and the deviations were not small, which majorly ranged ~10–40 % of the average potential. The surface potential is valid to be applied to the empirical equation only when it linearly correlates with the charging density. **Fig. 5** shows the comparison between the charge density and surface potential. A fairly good linear correlation with *R*-squared value of 0.906 was obtained. Therefore, this allowed us to substitute the charge density by the easily accessible surface potential to describe the charging property of filter media. This is a very important finding first reported, which was strictly based on rigorous experiments and theoretical calculations.

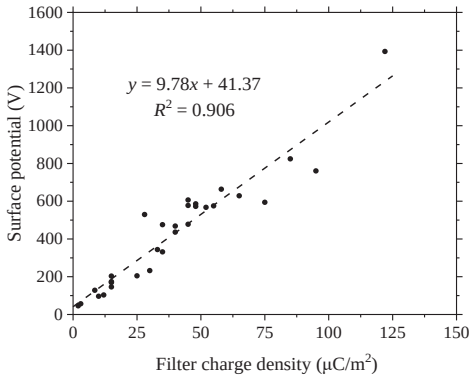


**Fig. 5** Correlation of surface potential and charge density of tested respirators.

## 3.3 Empirical equation for the FE of MPPS

Now the final step toward the applicability of the empirical equation involving only pressure drop, filtration area and surface potential to predict the efficiency of MPPS is to compare the prediction to the experimental data. Again, the three parameters are relatively easy to obtain as described earlier. Preferably, penetration may be used in the empirical equation as it was the first calculation result (**Eqn. (17)**) in the modeling. However, to have an intuitive relation with the 95 % FE of N95-EFs, we chose to use efficiency in the equation. There are many commercially available fitting programs, and we used TableCurve 3D software (Systat Software Inc., San Jose, CA) to find the equation.

When all three parameters are applied, there will be 3 independent and 1 dependent variables, which are one dimension over what the software can do. So, we combined the pressure drop and surface area by multiplying them together. This is reasonable as the FE increases with both parameters. Further, to make each term of the variable in the equation dimensionless, the reference pressure drop, respirator area, and surface potential should be determined. Ideally, the parameters from a standard filter media should be used. However, it is not available for now and has to be developed in the near future. We thus tried using a NIOSH certified N95, i.e. sample 11, as the reference.

The developed equation was a curved surface having a format of:

$$\eta_{\mathrm{MPPS,p}} = a + b\ln x + c(\ln x)^2 + d(\ln x)^3 + e\ln y \qquad (24)$$

where $a = 1.0036$, $b = -0.01725$, $c = 0.09753$, $d = 0.18983$, $e = -0.03338$, $R^2 = 0.966$, $\eta_{\mathrm{MPPS,p}}$ is the predicted FE of MPPS, $x$ is the normalized product of the pressure drop and respirator area ($x = (\Delta P{\cdot}S)_{\mathrm{sample}}/(\Delta P{\cdot}S)_{\mathrm{N95}}$), and $y$ is the

normalized surface potential ($y = V_{sample}/V_{N95}$). The comparison between measured and predicted FE at MPPS for the 30 samples is shown in **Table 2**. With a good *R*-squared value of 0.966, it can be seen that the predicted FEs ($\eta$ predicted) by the empirical equation are less than 8 % (majorly less than ~3 %) difference from the experimental FEs ($\eta$ data). The equation is very reliable because its prediction is accurate in distinguishing whether the samples pass or fail 95 % FE. For example, the equation would not predict a pass if the data showed fail and vice versa. The only exceptions were sample 10 and 20. The empirical equation underestimated the FE of sample 10 for about 2 %, and overestimated that of sample 20 for about 5 %. Therefore, we believe that the accuracy of the equation can be further improved by adding more data. Typically, we should have more mechanical respirators and those respirators that have FE around 95 % to comprehend the equation.

### 3.4 Validation and application of the developed empirical equation

It is very meaningful to validate the accuracy and

**Table 2** Comparison of the predicted efficiency by the empirical equation model with the experimental efficiency.

| Label | *x* | *y* | $\eta$, data | $\eta$, predicted | Residual |
|---|---|---|---|---|---|
| 1 | 0.435 | 2.100 | 0.9849 | 0.9601 | –0.0248 |
| 2 | 0.739 | 1.243 | 0.9867 | 0.9857 | –0.0010 |
| 3 | 0.797 | 0.896 | 0.9766 | 0.9731 | –0.0035 |
| 4 | 0.449 | 1.146 | 0.9781 | 0.9535 | –0.0246 |
| 5 | 0.551 | 0.867 | 0.9655 | 0.9699 | 0.0044 |
| 6 | 0.870 | 0.871 | 0.9513 | 0.9691 | 0.0178 |
| 7 | 0.797 | 0.884 | 0.9605 | 0.9726 | 0.0121 |
| 8 | 1.377 | 0.307 | 0.9033 | 0.9056 | 0.0023 |
| 9 | 1.000 | 0.717 | 0.9546 | 0.9571 | 0.0025 |
| 10 | 1.160 | 0.500 | 0.9569 | 0.9370 | –0.0199 |
| 11 | 1.000 | 1.000 | 0.9893 | 0.9703 | –0.0190 |
| 12 | 0.899 | 0.720 | 0.9575 | 0.9600 | 0.0025 |
| 13 | 0.623 | 0.646 | 0.9570 | 0.9619 | 0.0049 |
| 14 | 1.377 | 0.518 | 0.9624 | 0.9500 | –0.0125 |
| 15 | 0.870 | 0.706 | 0.9540 | 0.9601 | 0.0061 |
| 16 | 0.870 | 0.856 | 0.9704 | 0.9684 | –0.0020 |
| 17 | 0.696 | 0.205 | 0.8631 | 0.8510 | 0.0103 |
| 18 | 0.797 | 0.863 | 0.9516 | 0.9717 | 0.0201 |
| 19 | 0.899 | 0.798 | 0.9533 | 0.9645 | 0.0112 |
| 20 | 0.580 | 0.568 | 0.9087 | 0.9525 | 0.0438 |
| 21 | 1.304 | 0.915 | 0.9549 | 0.9730 | 0.0181 |
| 22 | 0.580 | 0.308 | 0.8727 | 0.9030 | 0.0303 |
| 23 | 0.507 | 0.256 | 0.8663 | 0.8704 | 0.0041 |
| 24 | 0.594 | 0.262 | 0.8727 | 0.8851 | 0.0124 |
| 25 | 0.551 | 0.220 | 0.8458 | 0.8564 | 0.0106 |
| 26 | 0.565 | 0.193 | 0.8315 | 0.8373 | 0.0058 |
| 27 | 0.580 | 0.146 | 0.8078 | 0.7820 | –0.0258 |
| 28 | 0.754 | 0.156 | 0.8053 | 0.7976 | –0.0077 |
| 29 | 0.362 | 0.069 | 0.3600 | 0.4387 | 0.0787 |
| 30 | 0.217 | 0.085 | 0.2013 | 0.1905 | –0.0108 |

feasibility of the equation. So, we use extra 5 new samples to test the equation. **Table 3** summarizes the pressure drop, filtration area, surface potential, and measured and predicted MPPS FE. Results showed that the maximum difference between data and prediction was only 3.4 %. Therefore, it is to conclude that the empirical equation is easy to use and can be applied to predict the MPPS FE.

### 3.5 Application of the developed empirical equation

The developed empirical equation **Eqn. (24)** was applied to help redesign the mechanical filters that were examined and did not pass 95 % MPPS FEs. Samples 8, 26, 28, 29 and 30 (see **Table 1**) were selected as representative mechanical respirators. By keeping the filtration area and surface potential unchanged, the equation was able to find the pressure drop required to improve them to have an MPPS FE larger than 95 %. The pressure drop required to be increased (or adding, e.g., through adding thickness) are summarized in **Table 4**. Sample 8 only needed 52.1 Pa to increase its MPPS FE from 90.3 % to 95 %, but others needed more (~180–360 Pa) as their original FEs were lower (~0.2–0.83). Comparing the calculation results between samples 29 and 30, a lower adding of pressure drop was needed for Sample 30 even its original FE was lower. This was attributed to the larger size of MPPS for sample 30 (450 nm) than 29 (294 nm). This indicated that **Eqn. (24)** with the feeds of data from 30 respirators is smart enough to consider the size effect in the filtration mechanism. One can also use **Eqn. (24)** to find the required filtration area or surface potential (or charging density) for these mechanical respirators to pass 95 % MPPS FE. Ultimately, the equation also allows users to adjust all three main parameters at the same time to design a good N95-EF with low pressure drop or low quantity of filter media. However, to note, **Eqn. (24)** is applicable to predict the MPPS FE for the respirators with specifications falling inside the boundary of the 30 samples. That is, it is limited to pressure drop from 25 to 185 Pa, filtration area of 143–235 $cm^2$ and surface potential of 46–1393 V.

## 4. Conclusion

To determine whether an N95 Equivalent-Facepiece filtering respirator (N95-EF) has passed 95 % filtration efficiency (FE), either through experimental measurement or theoretical calculation, is complex and cumbersome. This complexity could be the major reason causing the high failure rate for N95-EF sold in the market at the beginning of the COVID-19 pandemic, as respirator manufacturers could not easily follow the standard protocols to control their quality. In this study, we proposed a simple method to qualify commercial N95-EFs. It was based on rigorous empirical evidence and theoretical calculations. Specifically, we utilized three important and easily accessible respirator parameters including pressure drop, filtration area, and surface potential to form an empirical equation to predict FE at the most penetrating particle size (MPPS). Notably, The surface potential well correlated with the charging density, so it was used as its substitute. To note, the equation is reliable only if these parameters are defined correctly.

In the development of the empirical equation, we first built a standard test rig based on Chinese Standard GB 2626 to perform both mass- and number-based efficiency

**Table 3** Validation of the developed empirical equation for 5 new masks.

| New Sample | $\Delta P$ (Pa) | Area ($cm^2$) | Average surface potential (V) | Measured $\eta$ at MPPS | Predicted $\eta$ at MPPS | Residual |
|---|---|---|---|---|---|---|
| A | 67.5 | 204 | 142.1 | 0.830 | 0.857 | –0.027 |
| B | 72.5 | 200 | 175.5 | 0.866 | 0.877 | –0.011 |
| C | 170 | 145 | 750.1 | 0.984 | 0.971 | –0.013 |
| D | 110 | 199 | 477.3 | 0.958 | 0.950 | –0.008 |
| E | 82.5 | 193 | 167.4 | 0.841 | 0.875 | 0.034 |

**Table 4** Empirical equation application for mechanical filters.

| Label | Mass $\eta$ | Number $\eta$ at MPPS | MPPS | $\Delta P$ (Pa) | Surface area ($cm^2$) | Surface potential (V) | Required $\eta$ at MPPS | Predicted $\Delta P$ (Pa) | $\Delta P$ adding (Pa) |
|---|---|---|---|---|---|---|---|---|---|
| 8 | 0.983 | 0.903 | 125 | 185 | 181 | 203.6 | 0.95 | 236.2 | 52.1 |
| 26 | 0.875 | 0.832 | 143 | 67.5 | 204 | 128.2 | 0.95 | 251.4 | 183.9 |
| 28 | 0.848 | 0.805 | 254 | 92.5 | 199 | 89.4 | 0.95 | 298.1 | 205.6 |
| 29 | 0.464 | 0.361 | 294 | 45.0 | 196 | 45.7 | 0.95 | 405.6 | 360.6 |
| 30 | 0.395 | 0.201 | 450 | 25.0 | 212 | 56.5 | 0.95 | 340.7 | 315.7 |

evaluation of 35 different commercial N95-EFs. In addition, all respirators were measured with their thickness, fiber size, packing density, surface potential, and filtration area. The surface potential was correlated with the charge density derived through the comparison between the experimental and theoretical efficiency. Findings demonstrated a good correlation between filter charge density and surface potential validating the substitution.

The prediction of MPPS FE by the equation was accurate and majorly (28 out of 30) with ≤3 % of efficiency difference from the data. The empirical equation was successfully validated by comparing it with data from additional 5 new samples. The empirical equation was also successfully applied to help redesign mechanical respirators. To conclude, this work provides a simple empirical equation for quickly qualifying FEs of respirators. The equation can also be applied to design N95-EFs.

In conclusion, this study presents a straightforward empirical equation for rapidly assessing the filtration efficiencies of respirators, which can also guide N95-EF design. The equation is powerful but for now it is applicable to the respirators with specifications falling inside the boundary of the 30 samples tested. It is limited to pressure drop from 25 to 185 Pa, filtration area of 143–235 $cm^2$ and surface potential of 46–1393 V. To further improve the accuracy of the equation, more respirators should be tested, and their data should be included in refining the empirical equation.

## Data Availability Statement

The data have been included in **Tables 1–4** and the row data are available upon request.

## Acknowledgments

This work was financially supported by the Center for Filtration Research (CFR) at the University of Minnesota. The authors thank the CFR members including 3M, Applied Materials, BASF, Boeing Company, China Yancheng Environmental Protection Science and Technology City, Cummins Filtration, Donaldson Company, Ford Motor Company, Freudenberg Group, Guangxi Wat Yuan Filtration System, Mann Hummel GmbH, Math2Market GmbH, Samsung Electronics, Parker-Hannifin, Shigematsu Works, TSI, W. L. Gore & Associates, Xinxiang Shengda Filtration Technique.

## Nomenclature

| | |
|---|---|
| FE | Filtration efficiency |
| FFR | Facepiece filtering respirator |
| GSD | Geometric standard deviation |
| MPPS | Most penetrating particle size |
| NMD | Number median diameter |
| NIOSH | National Institute for Occupational Safety and Health |
| GB | National Standards of the People's Republic of China |
| N95-EF | N95 equivalent facepiece filtering respirator |
| $A$ | Surface area |
| $C_c$ | Cunningham slip correction factor |
| $C_{m,up}$ | Upstream mass concentration |
| $C_{m,down}$ | Downstream mass concentration |
| $C_{n,up}$ | Upstream number concentration |
| $C_{n,down}$ | Downstream number concentration |
| $C_p$ | Capacitance of the capacitor |
| $D$ | Diffusion coefficient |
| $d_f$ | Fiber diameter in the filter media |
| $d_x$ | Particle diameter |
| $E_T$ | Total single fiber efficiency |
| $E_D$ | Partial diffusion efficiency |
| $E_R$ | Partial interception efficiency |
| $E_{DR}$ | Partial efficiency for interception of diffusing particles |
| $E_I$ | Partial impaction efficiency |
| $E_q$ | Partial electrostatic deposition efficiency |
| $E_{qC}$ | Depositions by the Coulomb force |
| $E_{qD}$ | Depositions by the dielectric polarization force |
| $Ku$ | Kuwabara hydrodynamic parameter |
| $N_{CD}$ | Dimensionless parameter for charged particles through bipolarly charged fibrous filter media |
| $N_{DD}$ | Dimensionless parameter for uncharged particles through bipolarly charged fibrous filter media |
| $Pe$ | Peclet number |
| $P_{largest,\ dx}$ | Largest size dependent penetration |
| $P_{theo,\ dx}$ | Theoretical particle penetration |
| $P1$ | Measured pressure drop of the whole respirator |
| $P2$ | Measured pressure drop of the 4 cm circular sheet |
| $q(n)$ | Carried charges of the particle (C) |
| $Q$ | Charge carried by the sample surface |
| $R$ | The ratio of particle diameter to fiber diameter |
| $Stk$ | Stokes number |
| $t$ | The thickness of sample |
| $U_0$ | Face velocity (cm/s) |
| $V$ | Measured surface potential |
| $V_p$ | The potential of the voltmeter probe |
| $W$ | Weight of the flat sheet (g) |
| $x$ | Normalized product of pressure drop and mask area |
| $y$ | Normalized surface potential |
| $\alpha$ | Solidity |
| $\varepsilon_d$ | The permittivity of the sample between the electrode and the tested surface |
| $\varepsilon_f$ | Fabric dielectric constant |
| $\varepsilon_p$ | The relative permittivity of the particle |
| $\varepsilon_0$ | The permittivity of the vacuum ($8.85 \times 10^{-12}$ $C^2/N{\cdot}m^2$) |
| $\eta_{theo,dx}$ | Theoretical filtration efficiency |
| $\eta_m$ | Mass-based filtration efficiency |
| $\eta_{MPPS}$ | Number-based minimum efficiency |
| $\eta_{MPPS,p}$ | Predicted number-based minimum efficiency |
| $\mu$ | Air viscosity ($N{\cdot}s/m^2$) |
| $\rho_f$ | The density of filter media ($g/cm^3$) |
| $\rho_p$ | Particle density (2.2 $g/cm^3$ here) |
| $\sigma$ | Charge density ($C/m^2$) |

## References

Antoniu A., Dascalescu L., Vacar I.-V., Plopeanu M.-C., Tabti B., Teodorescu H.-N.L., Surface potential versus electric field measurements used to characterize the charging state of nonwoven fabrics, IEEE Transactions on Industry Applications, 47 (2011) 1118–1125. https://doi.org/10.1109/TIA.2011.2127432

Bahk J.-H., Bian Z., Shakouri A., Electron energy filtering by a nonplanar potential to enhance the thermoelectric power factor in bulk materials, Physical Review B, 87 (2013) 075204. https://doi.org/10.1103/PhysRevB.87.075204

Balazy A., Toivola M., Reponen T., Podgorski A., Zimmer A., Grinshpun

S.A., Manikin-based performance evaluation of N95 filtering-facepiece respirators challenged with nanoparticles, The Annual Occupational Hygiene, 50 (2006) 259–269. https://doi.org/10.1093/annhyg/mei058

Cai C., Floyd E.L., Effects of sterilization with hydrogen peroxide and chlorine dioxide solution on the filtration efficiency of N95, KN95, and surgical face masks, JAMA Network Open, 3 (2020) e2012099. https://doi.org/10.1001/jamanetworkopen.2020.12099

Chang D.-Q., Chen S.-C., Fox A.R., Viner A.S., Pui D.Y.H., Penetration of sub-50 nm nanoparticles through electret HVAC filters used in residence, Aerosol Science and Technology, 49 (2015) 966–976. https://doi.org/10.1080/02786826.2015.1086723

Chang D.-Q., Chen S.-C., Pui D.Y.H., Capture of sub-500 nm particles using residential electret HVAC filter media-experiments and modeling, Aerosol and Air Quality Research, 16 (2016) 3349–3357. https://doi.org/10.4209/aaqr.2016.10.0437

Chang D.-Q., Liu J.-X., Chen S.-C., Factors affecting particle depositions on electret filters used in residential HVAC systems and indoor air cleaners, Aerosol And Air Quality Research, 18 (2018) 3211–3219. https://doi.org/10.4209/aaqr.2018.10.0373

Chen C., Zhao B., Zhou W., Jiang X., Tan Z., A methodology for predicting particle penetration factor through cracks of windows and doors for actual engineering application, Building and Environment, 47 (2012) 339–348. https://doi.org/10.1016/j.buildenv.2011.07.004

Chen S.-C., Wang J., Bahk Y.-K., Fissan H., Pui D.Y.H., Carbon nanotube penetration through fiberglass and electret respirator filter and Nuclepore filter media: experiments and models, Aerosol Science and Technology, 48 (2014) 997–1008. https://doi.org/10.1080/02786826.2014.954028

CDC (Centers for Disease Control and Prevention), 2020. Types of masks and respirators <www.cdc.gov/coronavirus/2019-ncov/prevent-getting-sick/types-of-masks.html> accessed 29.01.2022.

CDC (Centers for Disease Control and Prevention), 2021, Use of masks to control the spread (COVID-19) <www.cdc.gov/coronavirus/2019-ncov/science/science-briefs/masking-science-sars-cov2.html> accessed 29.01.2022.

Davies C.N., Diffusion and sedimentation of aerosol particles from Poiseuille flow in pipes, Journal of Aerosol Science, 4 (1973) 317–328. https://doi.org/10.1016/0021-8502(73)90092-X

Dhand R., Li J., Coughs and sneezes: their role in transmission of respiratory viral infections, including SARS-CoV-2, American Journal of Respiratory and Critical Care Medicine, 202 (2020) 651–659. https://doi.org/10.1164/rccm.202004-1263PP

Duncan S., Bodurtha P., Naqvi S., The protective performance of reusable cloth face masks, disposable procedure masks, KN95 masks and N95 respirators: filtration and total inward leakage, PLOS ONE, 16 (2021) e0258191. https://doi.org/10.1371/journal.pone.0258191

Forsyth B., Liu, B.Y.H., Romay, F.J., Particle charge distribution measurement for commonly generated laboratory aerosols, Aerosol Science and Technology, 28 (1998) 489–501. https://doi.org/10.1080/02786829808965540

GB 2626, Respiratory protective equipment—non-powered air-purifying particle respirator, National Standard of the People's Republic of China, 2006.

Hao J., Passos De Oliveira Santos R., Rutledge G.C., Examination of nanoparticle filtration by filtering facepiece respirators during the COVID-19 pandemic, ACS Applied Nano Materials, 4 (2021) 3675–3685. https://doi.org/10.1021/acsanm.1c00139

Hinds W.C., Aerosol Technology: Properties, Behavior, and Measurement of Airborne Particles, 2nd ed., J. Wiley, New York, 1999, ISBN: 0-471-19410-7.

Jayaweera M., Perera H., Gunawardana B., Manatunge J., Transmission of COVID-19 virus by droplets and aerosols: a critical review on the unresolved dichotomy, Environmental Research, 188 (2020) 109819. https://doi.org/10.1016/j.envres.2020.109819

Kachi M., Nemamcha M., Tabti B., Dascalescu L., Comparison between three measurement methods for characterizing the charge state of granular insulating materials, Journal of Electrostatics, 69 (2011) 394–400. https://doi.org/10.1016/j.elstat.2011.05.002

Liu Z., Chen D.-R., Niu Q., Mensah D.A., Ji Z., Particle collection of electret media under different filtration pressures, Aerosol and Air Quality Research, 23 (2023) 220405. https://doi.org/10.4209/aaqr.220405

Patra I., Huy D.T.N., Alsaikhan F., Opulencia M.J.C., Van Tuan P., Nurmatova K.C., Majdi A., Shoukat S., Yasin G., Margiana R., Walker T.R., Karbalaei S., Toxic effects on enzymatic activity, gene expression and histopathological biomarkers in organisms exposed to microplastics and nanoplastics: a review, Environmental Sciences Europe, 34 (2022) 80. https://doi.org/10.1186/s12302-022-00652-w

Plana D., Tian E., Cramer A.K., Yang H., Carmack M.M., Sinha M.S., Bourgeois F.T., Yu S.H., Masse P., Boyer J., Kim M., Mo J., LeBoeuf N.R., Li J., Sorger P.K., Assessing the filtration efficiency and regulatory status of N95s and nontraditional filtering face-piece respirators available during the COVID-19 pandemic, BMC Infectious Diseases, 21 (2021) 712. https://doi.org/10.1186/s12879-021-06008-8

Prather K.A., Wang C.C., Schooley R.T., Reducing transmission of SARS-CoV-2, Science, 368 (2020) 1422–1424. https://doi.org/10.1126/science.abc6197

Sachinidou P., Heuschling C., Schaniel J., Wang J., Investigation of surface potential discharge mechanism and kinetics in dielectrics exposed to different organic solvents, Polymer, 145 (2018) 447–453. https://doi.org/10.1016/j.polymer.2018.05.023

Schilling K., Gentner D.R., Wilen L., Medina A., Buehler C., Perez-Lorenzo L.J., Pollitt K.J.G., Bergemann R., Bernardo N., Peccia J., Wilczynski V., Lattanza L., An accessible method for screening aerosol filtration identifies poor-performing commercial masks and respirators, Journal of Exposure Science & Environmental Epidemiology, 31 (2021) 943–952. https://doi.org/10.1038/s41370-020-0258-7

Stahl C., Frederick K., Chaudhary S., Morton C.J., Loy D., Muralidharan K., Sorooshian A., Parthasarathy S., Comparison of the filtration efficiency of different face masks against aerosols, Frontiers in Medicine, 8 (2021) 654317. https://doi.org/10.3389/fmed.2021.654317

Tang M., Chen S.-C., Chang D.-Q., Xie X., Sun J., Pui D.Y.H., Filtration efficiency and loading characteristics of $PM_{2.5}$ through composite filter media consisting of commercial HVAC electret media and nanofiber layer, Separation and Purification Technology, 198 (2018a) 137–145. https://doi.org/10.1016/j.seppur.2017.03.040

Tang M., Thompson D., Chen S.-C., Chang D.-Q., Pui D.Y.H., Filtration efficiency and loading characteristics of $PM_{2.5}$ through commercial electret filter media, Separation and Purification Technology, 195 (2018b) 101–109. https://doi.org/10.1016/j.seppur.2017.11.067

Tang M., Thompson D., Chen S.-C., Liang Y., Pui D.Y.H., Evaluation of different discharging methods on HVAC electret filter media, Building Environment, 141 (2018c) 206–214. https://doi.org/10.1016/j.buildenv.2018.05.048

Tien C.Y., Chen J.P., Li S., Li Z., Zheng Y.M., Peng A.S., Zhou F., Tsai C.-J., Chen S.-C., Experimental and theoretical analysis of loading characteristics of different electret media with various properties toward the design of ideal depth filtration for nanoparticles and fine particles, Separation and Purification Technology, 233 (2020) 116002. https://doi.org/10.1016/j.seppur.2019.116002

Wang J., Chen D.R., Pui D.Y.H., Modeling of filtration efficiency of nanoparticles in standard filter media, Journal of Nanoparticle Research, 9 (2007) 109–115. https://doi.org/10.1007/s11051-006-9155-9

Wang J., Kim S.C., Pui D.Y.H., Measurement of multi-wall carbon nanotube penetration through a screen filter and single-fiber analysis, Journal of Nanoparticle Research, 13 (2011) 4565–4573. https://doi.org/10.1007/s11051-011-0415-y

Yan Y., Zhou X., Xu H., Melcher K., Structure and physiological regulation of AMPK, International Journal of Molecular Sciences, 19 (2018) 3534. https://doi.org/10.3390/ijms19113534

You R., Zhao B., Chen C., Developing an empirical equation for modeling particle deposition velocity onto inclined surfaces in indoor environments, Aerosol Science and Technology, 46 (2012) 1090–1099. https://doi.org/10.1080/02786826.2012.695096

## Authors' Short Biographies

**Dr. Sheng-Chieh Chen** is an Associate Professor in the Department of Mechanical and Nuclear Engineering at Virginia Commonwealth University. He has been working on research on aerosol science and technology for about 2 decades. Air filtration is his current focus, typically for charged filter media used in respirators, HVAC systems, and indoor air purifiers.

**Dr. Yu Zhang** was trained as a Mechanical Engineer. She received her PhD degree from the Department of Mechanical and Nuclear Engineering at Virginia Commonwealth University in April 2023. Her expertise is in indoor air pollutants control. She fabricated photocatalytic metal-organic framework (MOF) coated electret which can simultaneously remove particulate matters (PMs), volatile organic compounds (VOCs), and bioaerosol.

**Mr. Genhui Jing** is a PhD student in the Department of Mechanical and Nuclear Engineering at Virginia Commonwealth University. He received his master's degree from the College of Chemistry & Chemical Engineering, Xi'an Shiyou University. He is studying nanoparticle removal by air and liquid filtration.

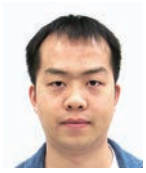

**Dr. Peng Wang** was trained as a Mechanical Engineer. He received his PhD degree from the Department of Mechanical and Nuclear Engineering at Virginia Commonwealth University in August 2021. His expertise is in experimental and numerical study of air filtration.

**Prof. Daren-Chen** is a Professor and Floyd D. Gottwald, Sr. Chair in the Department of Mechanical and Nuclear Engineering at Virginia Commonwealth University. He is the inventor of many aerosol generation and measurement instruments, including electrospray monodisperse particle generator, nanometer differential mobility analyzer, personal nanoparticle monitors, continuous gene transfection and many other particle processing tools. He was honored with the Sheldon K. Friedlander Award (1997), Smoluchowski Award (2002), Kenneth Whitby Award (2005) and Benjamin Liu Award (2012) for his significant contributions to nanoparticle instrumentation and experimental techniques.

KONA Powder and Particle Journal

KONA Powder and Particle Journal No. 42 (2025) 241–250/https://doi.org/10.14356/kona.2025009 Original Research Paper

# Rheological Characterization of Mineral Slurries Based on the Principle of Maximum Entropy†

**Jean C. G. Louzada[1], Elaine C. Andrade[2], Thiago C. Souza Pinto[3] and Laurindo S. Leal Filho[2*]**

[1] *Geosciences and Engineering Institute, Federal University of Southern and Southeastern Pará, Brazil*
[2] *Department of Mining and Petroleum Engineering, Polytechnic School, University of São Paulo, Brazil*
[3] *Mineral Development Center (CDM), Vale S.A., Brazil*

The rheological characterization of mineral slurries is a complex task, especially in the presence of coarse particles with high specific gravity, such as hematite. In laboratory rotational rheometers (LRRs), entrance effects, particle settling, and Taylor vortices can jeopardize the accuracy of the results. This paper presents a new methodology for the rheological characterization of mineral slurries in tubular devices and the Principle of Maximum Entropy (PME) supports this new approach. Iron ore slurries were prepared at mass concentrations of 36.8 % and 43.6 % solids and subjected to rheological characterization in LRR and a pumping loop tubular device (PLTD). The results from LRR revealed shear-thickening behavior for the slurries; whereas the results from PLTD, associated with entropic equations for the friction factor and shear rate, revealed shear-thinning behavior (at low shear rates) and shear-thickening behavior (at high rates). The results from LRR plus PLTD were plotted in a single rheogram, and curve fitting was accomplished by the power law model ($R^2 = 0.995$), indicating an overall shear-thickening behavior. PME proved to be capable of supporting the rheological characterization of mineral slurries at shear rates above 1500 $s^{-1}$ in PLTD, complementing the results obtained by LRR.

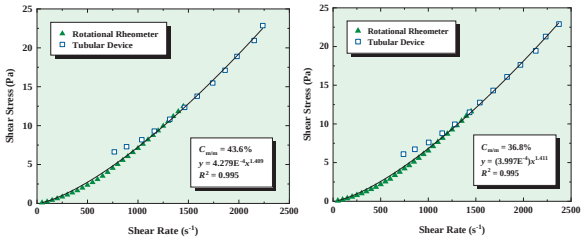


**Keywords:** rheometry, mineral slurries, the principle of maximum entropy

## 1. Introduction

Ores are often beneficiated in the form of slurries, which are subjected to different unit operations of mineral processing. Consequently, concentrates and tailings are also yielded as particulate suspensions, which are classified as pseudo-homogeneous fluids and exhibit complex rheological behavior (Kawatra and Bakshi, 1995). Thus, the rheology of mineral slurries is of vital importance for determining the operating conditions of flow (flow velocity and head loss), for the design and selection of pipelines and pumps, and for estimating energy consumption (Whiten et al., 1993).

The rheological characterization of mineral slurries presents many challenges, especially when performed in rotational rheometers and in the presence of coarse particles with high specific gravity. Under these conditions, wall slipping effects (Mooney, 1931; Senapati and Mishra, 2014), particle settling (Kawatra and Bakshi, 1996; Klein and Laskowski, 2000), centrifugal force (Mezger, 2020), and Taylor vortices (Pereira and Soares, 2012; Shi, 2016) recur. Such effects isolated or associated, can significantly jeopardize the accuracy of measurements. Therefore, an alternative to rotational and tube-capillary devices would be a tubular apparatus (test-loop experimental facility) that reproduces real flow conditions, i.e., turbulent flows, with high shear rates in rough pipes of larger diameters.

From an experimental perspective, previously existing challenges can be overcome with tubular devices of the pumping loop type. However, there is a gap in the literature regarding the determination of shear rate for turbulent flow of non-Newtonian fluids, since the established Rabinowitsch–Mooney model was developed for the laminar regime (Chilton and Stainsby, 1998; Chhabra and Richardson, 1999). Thus, the objective of this work is to present and propose a new methodology, based on the Principle of Maximum Entropy (PME), for shear rate and apparent viscosity determination of mineral slurries in pumping loop tubular devices (PLTD) because they can operate under experimental conditions that are closer to the reality of flow in pipes. The model used in this work for shear rate was obtained from the entropic velocity distribution maintained by Chiu et al. (1993) and developed for flow in tubes, which is applicable to Newtonian and

† Received 2 August 2023; Accepted 24 August 2023
J-STAGE Advance published online 13 April 2024
* Corresponding author: Laurindo S. Leal Filho;
Add: Av. Professor Melo Moraes, 2373–Cidade Universitária–CEP 05508-900, São Paulo-SP, Brazil
E-mail: lauleal@usp.br
TEL: +55-11-99981-1037

non-Newtonian fluids in laminar and turbulent regimes, regardless of tube roughness (Louzada et al., 2021).

## 1.2 Theoretical background

Rheology is classically defined as the science that studies the flow and deformation of matter under the action of external forces (Slatter, 2000). The rheological behavior of a fluid is described by the functional relationships between shear stress and shear rate or between viscosity and shear rate, which are governed by constitutive rheological equations (Peker and Helvaci, 2007).

Laboratory rotational rheometers (LRRs) were designed based on the dynamics of circular movements. In these devices, the torque is determined as a function of the angular velocity applied to the sensor in contact with the fluid. Stress and shear rate are calculated from the torque and angular velocity, respectively, through specific correlations for each sensor. LRR are classified according to sensor geometry into concentric cylinders, cone plates, parallel plates, vanes, and Mooney–Ewart (Barnes et al., 1989; Boger, 2009; Kelessidis and Maglione, 2008).

The most widely used rotational device is the concentric cylinder type, in which the fluid is confined in the annular space between the inner and outer cylinders. In the Searle system, the outer cylinder remains at rest, while the inner cylinder rotates. High rotational speeds can cause centrifugal force effects, secondary flows, and Taylor vortices, which can jeopardize the accuracy of the measurements (Mezger, 2020; Shi, 2016). **Eqns. (1)** and **(2)** allow the calculation of the shear rate ($\dot{\gamma}$) and shear stress ($\tau$) referring to the Mooney–Ewart sensor used in this work (Mezger, 2020).

$$\dot{\gamma} = \omega \frac{1+\delta^2}{\delta^2 - 1} \tag{1}$$

$$\tau = \frac{1+\delta^2}{2\delta^2} \frac{T}{2\pi L R_i^2 C_L} \tag{2}$$

The flow conditions in a concentric cylinder-type device operating in the Searle system can be determined from the Taylor number *(Ta)*, defined according to **Eqn. (3)** (Shi, 2016). Therefore, according to the magnitude of the Taylor number, the following flow regimes are defined (Shi, 2016): i) laminar if $Ta < 41.3$; ii) laminar as vortices begin to appear when $41.3 < Ta < 400$; iii) Turbulent for $Ta > 400$.

$$Ta = \frac{(R_e - R_i) u_{ci} \rho}{\eta} \sqrt{\frac{R_e - R_i}{R_i}} \tag{3}$$

Tubular rheometers are devices of simple design, essentially built with circular tubes and equipped with a pumping system, flow, and pressure meters (Fangary et al., 1997; Giguère et al., 2009). The rheological characterization performed in these devices is called an inverse problem in rheology, in which the shear stress ($\tau_w$) and shear rate ($\dot{\gamma}_w$) are determined from the pressure gradient ($\Delta P/L$) and mean velocity of fluid flow ($\bar{u}$), according to **Eqns. (4)** and **(5)**, respectively (Boger, 2009; Ma et al., 2012).

$$\tau_w = \left(-\frac{\Delta P}{L}\right).\left(\frac{D}{4}\right) \tag{4}$$

$$\dot{\gamma}_w = \frac{8\bar{u}}{D} \tag{5}$$

**Eqn. (4)** is used for any type of fluid regardless of the flow regime. On the other hand, **Eqn. (5)** is applied only to fluids with Newtonian behavior and laminar flow regime. For fluids with non-Newtonian behavior and laminar flows, the shear rate can be determined from the Rabinowitsch–Mooney model, as expressed by **Eqn. (6)**. In this model, the correction factor *n'* is determined from the shear stress, mean velocity flow, and pipe diameter, according to **Eqn. (7)** (Chhabra and Richardson, 1999; Kitanovski et al., 2005; Lu and Zhang, 2002; Metzner and Reed, 1955).

$$\dot{\gamma}_w = \left(\frac{8\bar{u}}{D}\right)\left(\frac{3n'+1}{4n'}\right) \tag{6}$$

$$n' = \frac{d(\ln \tau_w)}{d\left[\ln\left(\frac{8\bar{u}}{D}\right)\right]} \tag{7}$$

### 1.2.1 The principle of maximum entropy (PME)

The term entropy is not restricted to the thermodynamic state function. In the context of information theory, entropy is a measure of information or uncertainty about a given variable (Singh et al., 2017). For continuous random variables, Claude Shannon defined the entropy of a variable ($u$) according to **Eqn. (8)** (Chiu, 1989), where $f(u)$ is the probability density function of $u$.

$$H(u) = -\int_0^{u_{max}} f(u) \ln f(u) \, du \tag{8}$$

In his work, Chiu (1987) applied PME to hydraulic engineering, developing physically consistent models for velocity distributions, shear stress, and sediment concentration in open channels. The application of PME to fluid flow essentially consists of determining velocity entropy from **Eqn. (8)** and maximizing it based on Lagrange multipliers (Singh, 2014). PME and the maximization technique were applied by Chiu et al. (1993) to obtain velocity distributions for flows in tubes, defined by **Eqn. (9)** and applicable to fluids with Newtonian and non-Newtonian behaviors, regardless of the flow regime and roughness of the tube.

$$u_E(r) = \left(\frac{u_{max}}{M}\right) \ln\left\{1 + \left[e^M - 1\right]\left[1 - \left(\frac{r}{R}\right)^2\right]\right\} \tag{9}$$

**Eqn. (10)** correlates the entropic shear rate, $\dot{\gamma}_{w(E)}$ defined as the velocity gradient in the wall, with the entropic parameter ($M$), mean flow velocity ($\bar{u}$), and tube internal diameter ($D$) (Louzada et al., 2021).

$$\dot{\gamma}_{w(E)}=\left(-\frac{du_E}{dr}\right)\Big|_{r=R}=\left(\frac{8\bar{u}}{D}\right)\left[\frac{(e^M-1)^2}{2(Me^M-e^M+1)}\right] \quad (10)$$

Once obtained from a universal velocity distribution, **Eqn. (10)** allows the determination of the shear rate for any type of fluid, in the laminar or turbulent regime, and regardless of tube roughness. The literature also reports a model for the friction factor expressed as a function of the apparent Reynolds number ($Re_a$) and the entropy parameter ($M$), as shown in **Eqn. (11)** (Souza and Moraes, 2017).

$$f_E=\left(\frac{32}{Re_a}\right)\left[\frac{(e^M-1)^2}{(Me^M-e^M+1)}\right] \quad (11)$$

In a more recent contribution, Louzada et al. (2021) proposed a model for the entropic friction factor, defined only as a function of the entropy parameter, according to **Eqn. (12)**.

$$f_E=\frac{32}{[416.667(e^M-1)]^{\frac{1}{1.0028}}}\left[\frac{(e^M-1)^2}{(Me^M-e^M+1)}\right] \quad (12)$$

In the present work, **Eqn. (12)** is used to determine parameter $M$, using friction factor values obtained previously from the experimental data of the pressure gradient ($\Delta P/L$) and mean flow velocity ($\bar{u}$) resorting to the Darcy–Weissbach equation (**Eqn. (13)**).

$$\frac{\Delta P}{\rho g}=f\frac{L}{D}\frac{\bar{u}^2}{2g} \quad (13)$$

The apparent viscosity ($\eta$) is calculated from the well-known **Eqn. (14)**.

$$Re_a=\frac{\bar{u}D\rho}{\eta} \quad (14)$$

## 2. Materials and methods

### 2.1 Technological characterization of iron ore

The mining company Vale SA provided the iron ore sample used in this work. It comes from Carajás, Pará, Brazil. The technological characterization of the ore consisted of determining its mineralogical composition, chemical composition, particle size distribution, and specific gravity. The mineralogy was determined by X-ray diffraction (X'Pert Diffractometer, Philips 1997), in which the following minerals were identified: hematite, goethite, quartz, and magnetite. The chemical composition of the ore by X-ray fluorescence (Malvern Panalytical–Zetium Model) is shown in **Table 1**. Results on particle size distribution by laser diffraction (Mastersizer 2000–Malvern Instruments Ltd) are reported in **Table 2**. The specific gravity (4805 kg/m$^3$) of the iron ore was determined by gas pycnometry (Quantachrome pycnometer) using a cell with a volume of 150.87 cm$^3$. The measurement was performed at 21.8 °C by using nitrogen.

**Table 1** Chemical analysis of the iron ore.

| Elements | Grade (%) |
|---|---|
| Fe | 64.3 |
| $SiO_2$ | 2.50 |
| $Al_2O_3$ | 1.50 |
| P | 0.077 |
| Mn | 0.22 |
| $TiO_2$ | 0.13 |
| CaO | <0.10 |
| MgO | <0.10 |
| LOI | 3.44 |

**Table 2** Size analysis of the iron ore.

| $d_{3,2}$ (μm) | $d_{10}$ (μm) | $d_{50}$ (μm) | $d_{90}$ (μm) |
|---|---|---|---|
| 4.37 | 1.55 | 21.54 | 76.25 |

### 2.2 Rotational rheometry

Rotational rheometry experiments were conducted in an Anton Paar MCR 92 rheometer equipped with the RheoCompassTM software and operating on the Searle system. In this study, a Mooney–Ewart-type sensor (CC39) was used. The diameters of the inner and outer cylinders are 38.716 mm and 42.010 mm, respectively. The height of the inner cylinder corresponds to 60.014 mm, and the angle of the conical surface is 120°.

The experiments were carried out with slurries prepared at concentrations of 36.8 % and 43.6 % of solids (mass basis), and the shear rate values were kept in the range of 50 s$^{-1}$ and 1450 s$^{-1}$. The specific gravities of the slurries were: 1363.2 kg/m$^3$ and 1483.7 kg/m$^3$ for solid concentrations of 36.8 % and 43.6 %, respectively. The experiments were carried out after a previous stirring step for 120 seconds, at a shear rate of 1450 s$^{-1}$, in order to keep the particles suspended and mitigate the sedimentation effect. Once the 120 second stirring time elapsed, the shear rate was gradually reduced from 1450 s$^{-1}$ to the final value of 50 s$^{-1}$. The experimental results were submitted to curve fitting using the Power Law and Tscheuschner rheological models (Tozzi and Hartt, 2021).

### 2.3 Tubular rheometry

A tubular device constructed with a pipe with an internal diameter of 76.2 mm was used in the tubular rheometry tests (**Fig. 1**). Horizontal sections of the pipeline were constructed in perspex sections to allow flow visualization. The experimental apparatus consists of a tank, a pump, and a pipeline endowed with flow and pressure sensors. The tank has a usable volume of 1 m$^3$, and is equipped with a stirrer driven by a 6 HP WEG electric motor controlled by

a frequency inverter (WEG–CFW 500). The slurry was transported by a Warman centrifugal pump, model 4/3C-AH, driven by a 22 kW WEG W22 electric motor at a nominal speed of 1765 rpm, and controlled by a WEG frequency inverter, model CFW700. Pressure transducers (Siemens) and flow meters (Krohne Connaut) provided data regarding pressure drop and volumetric flow. The process variables were monitored and stored using a data acquisition system equipped with a digital indicator (DMY-2015 model) and VR2000 software version 3.3, both manufactured by Presys.

The experimental procedure consisted of hydraulic transport, in a closed circuit, of the slurries prepared at the same solid concentrations as in the rotational rheometry tests. The pressure differences ($\Delta P$) corresponding to the operating volumetric flows *(Q)* were measured.

From these experimental data, the friction factor was calculated from the Darcy–Weisbach equation. Shear stress ($\tau_w$), entropic shear rate ($\dot{\gamma}_{w(E)}$), apparent Reynolds number ($Re_a$), parameter $M$, and apparent viscosity ($\eta$), were determined using **Eqns. (4)**, **(10)**, **(11)**, **(12)**, and **(14)**, respectively.

## 3. Results and discussion

### 3.1 Rotational rheometry

The results of the shear stress as a function of shear rate, obtained by rotational rheometry, are shown in **Fig. 2**.

All suspensions behaved as shear-thickening fluids, with viscosity increasing with the increase in the shear rate, as observed in **Fig. 3**.

Furthermore, for the same shear rate, the slurry viscosity increases with increasing solids concentration. The behavior indices ($n$) referring to the suspensions with 36.8 % and 43.6 % solids showed values of 1.532 and 1.493, respectively, as shown in **Table 3**, corroborating the shear-thickening behavior. According to Brown and Jaeger (2014), when the behavior index ($n$) reveals values between 1 and 2, the fluid is classified as continuous shear thickening.

The experimental data were also adjusted using the Tscheuschner model, as shown in **Table 4**. The Bingham model was not used because it is inadequate to fit experimental data that follow nonlinear behavior at lower shear rates (Boger, 2009; Slatter, 2000).

Inertial effects and the possible occurrence of Taylor vortices were also investigated in rotational rheometry experiments. The peripheral velocity of the sensor was

**Fig. 1** Test-loop experimental facility.

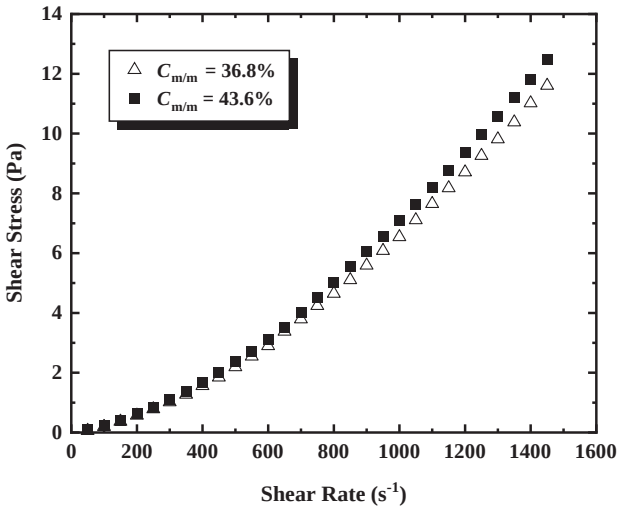


**Fig. 2** Shear stress as a function of the shear rate, obtained by rotational rheometry.

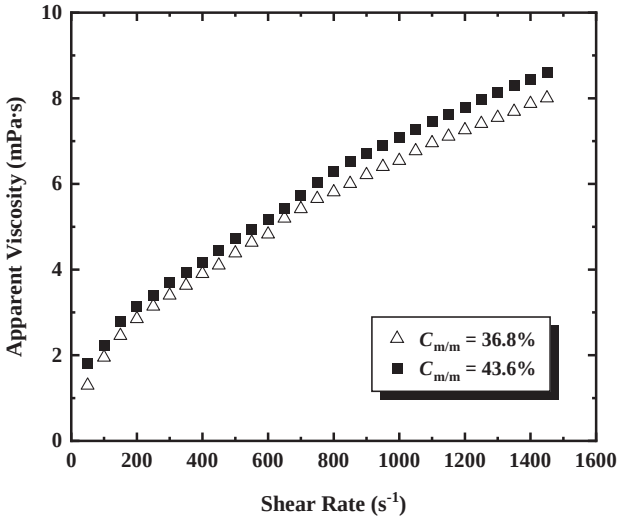


**Fig. 3** Apparent viscosity as a function of shear rate, obtained by rotational rheometry.

**Table 3** Power Law rheological model for iron ore slurries.

| $C_{m/m}$ (%) | Power Law model | $R^2$ |
|---|---|---|
| 36.8 | $\tau = 1.62\times10^{-4}\dot{\gamma}^{1.532}$ | 0.99 |
| 43.6 | $\tau = 2.30\times10^{-4}\dot{\gamma}^{1.493}$ | 0.99 |

calculated from the rotation values provided by the RheoCompass software. **Fig. 4** presents the Taylor number values as a function of the shear rate for the studied iron ore suspensions. The results depicted in **Fig. 4** show that the values of the Taylor number (*Ta*) for the two suspensions (36.8 % solids versus 43.6 % solids) are very close due to the fact that they were obtained at the same speeds and with the same sensors. Furthermore, the specific gravities of the suspensions were not so distinct: 1363.25 kg/m$^3$ versus 1483.71 kg/m$^3$. The results also reveal that the magnitude of *Ta* exhibited values between 41 and 400, except for a shear rate lower than 100 s$^{-1}$. For this reason, in the experimental conditions investigated, the flow regime was laminar in the presence of Taylor vortices, according to the criterion presented by Shi (2016). Regarding **Fig. 4**, it is observed that the magnitude of *Ta* decreases sharply for shear rates lower than 500 s$^{-1}$, where particle settling may occur. Therefore, the values of *Ta* obtained in this range may be inaccurate. Therefore, to prove the possible occurrence of flow instabilities and vortices, the conditions defined for the beginning of the vortex formation were applied. These results demonstrate the challenge of characterizing the rheology of mineral slurries consisting of coarse or "dense" particles in rotational devices. High shear rates allow the suspension of particles but favor the occurrence of centrifugal force, secondary flows, Taylor vortices, and turbulence. Conversely, lower shear rates guarantee laminar flows but do not prevent particle sedimentation.

**Table 4** Rheological model of Tscheuschner for iron ore slurries.

| $C_{m/m}$ (%) | Tscheuschner model | $R^2$ |
|---|---|---|
| 36.8 | $\tau = 0.16+0.27\dot{\gamma} - 0.28\dot{\gamma}^{0.99}$ | 0.99 |
| 43.6 | $\tau = 0.20+0.30\dot{\gamma} - 0.31\dot{\gamma}^{0.99}$ | 0.99 |

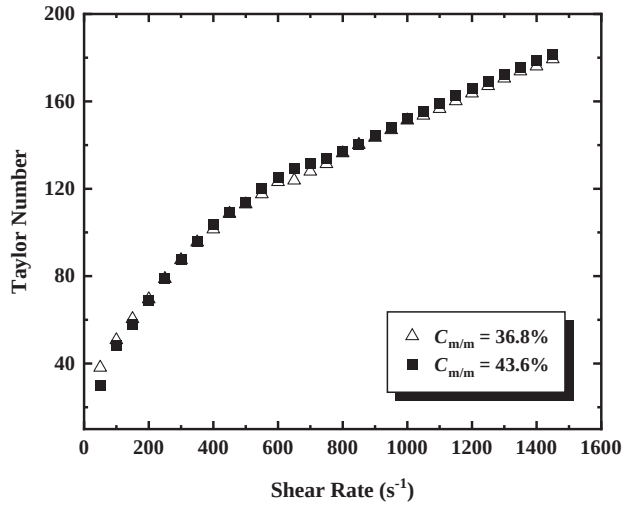


**Fig. 4** Taylor number as a function of the shear rate (rotational rheometer).

## 3.2 Tubular rheometry

### 3.2.1 Flow curves

The results of the pressure gradient as a function of the mean flow velocity for iron ore slurries are presented in **Fig. 5** and show that the pressure gradient decreases as the mean flow velocity is reduced.

The characteristic behavior of the curves shown in **Fig. 5** indicates that the particles remained suspended throughout the experiment. If there were sedimentation and formation of a bed of particles on the lower parts of the tube (bottom), there would be an increase in the pressure gradient due to the reduction of the sectional area of the tube available for fluid flow.

### 3.2.2 Friction factor, entropy parameter (*M*) and Reynolds number

**Fig. 6** presents the values of the friction factor as a

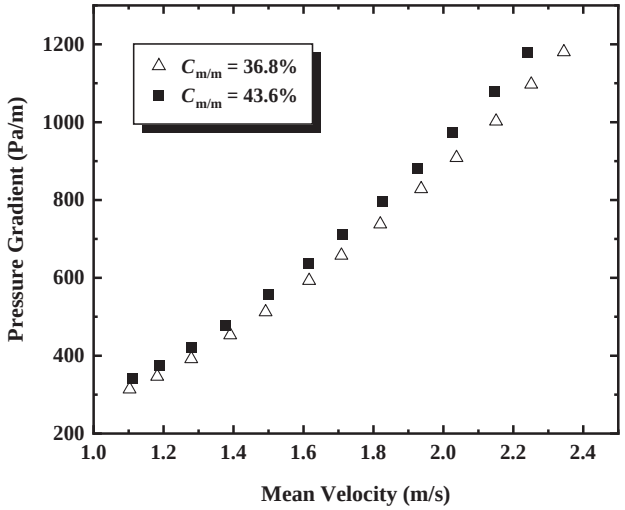


**Fig. 5** Pressure gradient as a function of mean flow velocity for iron ore suspensions (tubular rheometer).

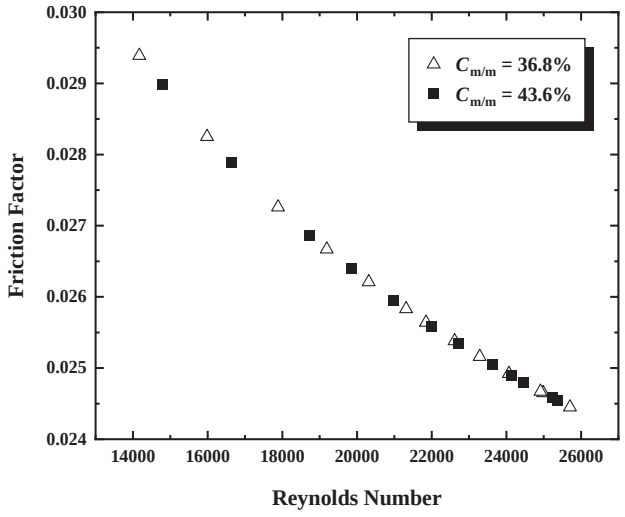


**Fig. 6** Friction factor as a function of Reynolds number (tubular rheometer).

function of the Reynolds number for the flow of iron ore suspensions. The results show that the lowest Reynolds numbers for suspensions at 36.8 % and 43.6 % of solids were 14,170.2 and 14,780.9, respectively, indicating turbulent flow.

In addition to being a modeling parameter of the velocity profile, the entropy parameter ($M$), like the Reynolds number, also indicates the degree of turbulence experienced by a flow. As such, for laminar regime $M = 0$ and for turbulent regime $M > 0$ (Chiu et al., 1993; Souza and Moraes, 2017). Therefore, the friction factor is also presented as a function of the entropy parameter in **Fig. 7**.

The lowest values of $M$ were 3.58 and 3.62, corresponding to slurries with 36.8 % and 43.6 % of solids, respectively, corroborating the state of turbulence indicated by the magnitude of the Reynolds numbers (**Fig. 6**). A realistic rheological characterization of particulate systems requires that the particles be homogeneously suspended in the carrier fluid. Flows with beds of sedimented particles reveal the co-existence of "different fluids" because of the different concentrations of solids along the cross-section of the tube.

### 3.2.3 Rheograms

The results of shear stress as a function of shear rate for the iron ore slurries are shown in **Fig. 8**. For the slurry at 36.8 % solids (mass basis), the lowest and highest shear rates were 739.86 $s^{-1}$ and 2373.24 $s^{-1}$, respectively. In relation to the suspension prepared at a solids concentration of 43.6 %, the lowest and highest rates were 766.05 $s^{-1}$ and 2236.68 $s^{-1}$, respectively. In this way, it is verified that the tubular device allows for much higher shear rates than those obtained from the laboratory Anton Paar rotational rheometer.

The Power Law model was fitted to the rheological curves presented in **Fig. 8**, and the consistency ($K$) and behavior ($n$) indices are reported in **Table 5**. The magnitudes of ($n$) revealed that the iron ore slurries behaved as shear-thinning fluids in the intervals that included the lowest shear rates ($n < 1.0$) and shear-thickening in the intervals that comprised the highest rates ($n > 1.0$), in the two solid concentrations investigated. Shear-thickening behavior is classified as continuous because the viscosity increases smoothly with increasing shear rate and the magnitude of $n$ is between 1 and 2 (Brown and Jaeger, 2014).

**Fig. 9** presents the results of the apparent viscosity as a function of shear rate, in which a reduction of the apparent viscosity is verified in the three lowest rates (shear-thinning behavior) and an increase in the others (shear-thickening behavior). For particulate suspensions (slurries), both shear-thinning and shear-thickening behavior observed at low and high shear rates have been reported (Brown and Jaeger, 2014; Stickel and Powell, 2005).

Shear-thinning behavior at lower rates may have been caused by the stratification of particles arranged in layers oriented in the direction of flow (Gürgen et al., 2017). This flow condition was identified in the work of Souza Pinto et al. (2014), who performed pumping experiments with slurries of hematite, quartz, and apatite in devices with internal diameters of 25.4 mm and 50.8 mm. Sampling the flows in three sections of the pipe concluded that, for the three

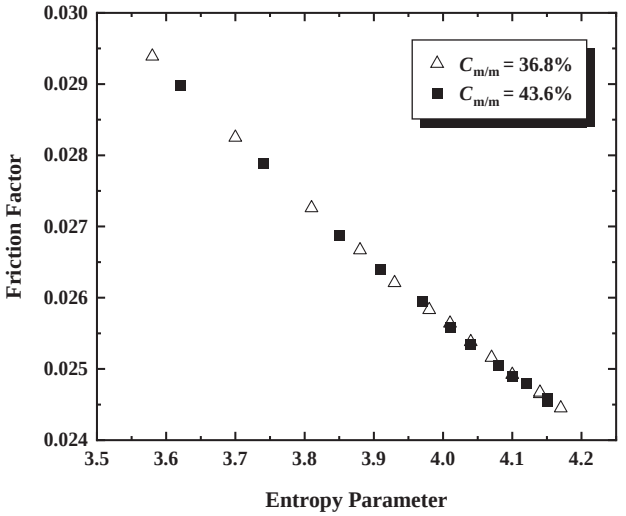


**Fig. 7** Friction factor as a function of the entropy parameter.

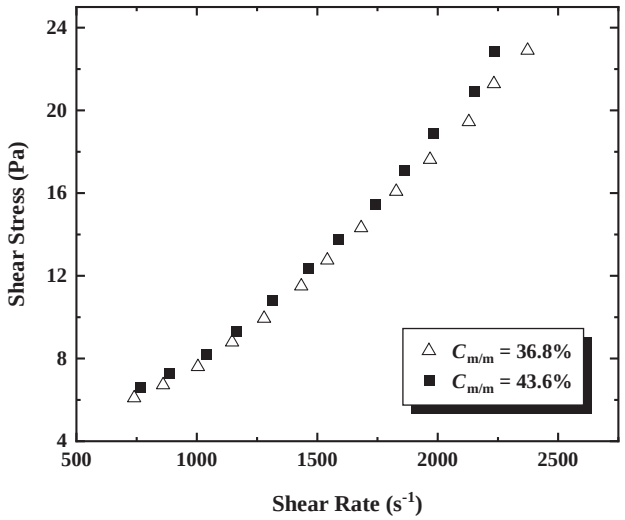


**Fig. 8** Shear stress as a function of the shear rate for iron ore slurries.

**Table 5** Fitting parameters of the Power Law rheological model ($R^2 = 0.99$) applied to the rheograms obtained from tubular rheometry.

| $C_{m/m}$ (%) | Shear rate ($s^{-1}$) | $K$ (Pa·$s^n$) | $n$ |
|---|---|---|---|
| 43.6 | 766.05–1038.54 | 0.065 | 0.69 |
| 43.6 | 1038.54–2236.68 | $5.76 \times 10^{-4}$ | 1.36 |
| 36.8 | 739.86–1004.65 | 0.049 | 0.78 |
| 36.8 | 1004.65–2373.24 | $7.43 \times 10^{-4}$ | 1.32 |

minerals studied, more than 60 % of the mass of solids was contained in the lower section of the pipes. On the other hand, the shear-thickening behavior may be due to the formation of particle agglomerates, called hydro clusters, and the hydrodynamic lubrication effects between particles at high shear rates (Salunkhe et al., 2018).

Hydroclusters are particle agglomerates that exhibit greater resistance to flow. Regarding the formation of hydroclusters, Seto et al. (2013) argued that in pipe flow, particles are "pushed" along a "compression axis". This effect is intensified when high shear rates are applied, thus decreasing the distance between particles. The particles agglomerates that may form as they approach will offer greater resistance to flow. In addition to the lubrication effect, friction between the rough surfaces of the particles may occur, which promotes an increase in viscosity (Seto et al., 2013).

In addition to the aforementioned effects, turbulence influences the rheological behavior of suspensions. Fox et al. (2006) defined turbulence as a phenomenon that is almost always undesirable because it creates greater resistance to flow, thus contributing to an increase in the apparent viscosity of the fluid. In this type of flow, random fluctuations in velocity are responsible for Reynolds stresses, which are associated with the high kinetic energy of the flow (Groisman and Steinberg, 2000) and act in the transfer of momentum between adjacent layers of fluid (Fox et al., 2006). Vortices in turbulent flows increase energy dissipation and the local shear rate in the fluid (Brown and Jaeger, 2014). Turbulence can also contribute to shear-thickening behavior because of the disorderly and chaotic movement of fluid elements, which obviously increases the probability of contact and friction between particles. Therefore, in the present study, the shear-thickening behavior of the suspensions may have been caused by the concomitant action of interactions between particles (collision, friction and lubrication) and turbulence.

### 3.3 Tubular rheometry versus rotational rheometry

The results of rotational and tubular rheometry for the iron ore slurries were presented concomitantly in a single curve, called in this study as "universal rheograms", which comprise a very wide range of shear rates. The rheological curves corresponding to the slurry at 36.8 % solids (**Figs. 10** and **11**) were based on shear rate values between 50.01 $s^{-1}$ and 2,373.24 $s^{-1}$. For the slurry bearing 43.6 % solids, the shear rate values ranged from 50.01 $s^{-1}$ to 2,236.68 $s^{-1}$, as shown in **Figs. 12** and **13**.

Satisfactory adjustment of all results by the Power Law model ($R^2$ = 0.995) indicates shear-thickening behavior. In all the results presented in **Figs. 10**, **11**, **12**, and **13**, there is

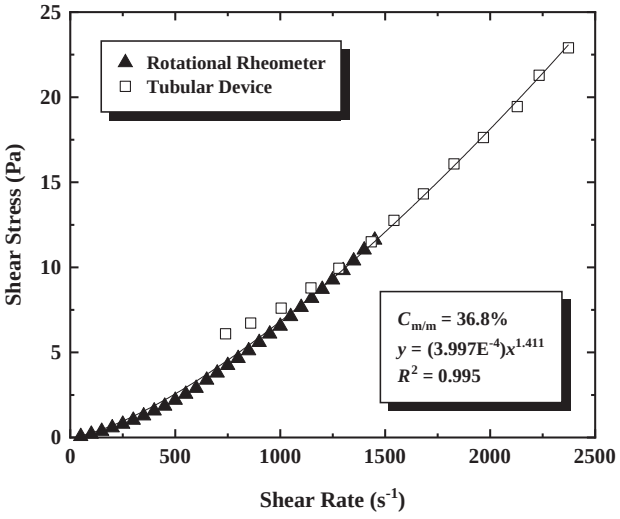


**Fig. 10** Shear stress as a function of shear rate obtained by rotational and tubular rheometry for iron ore suspension at 36.8 % solids.

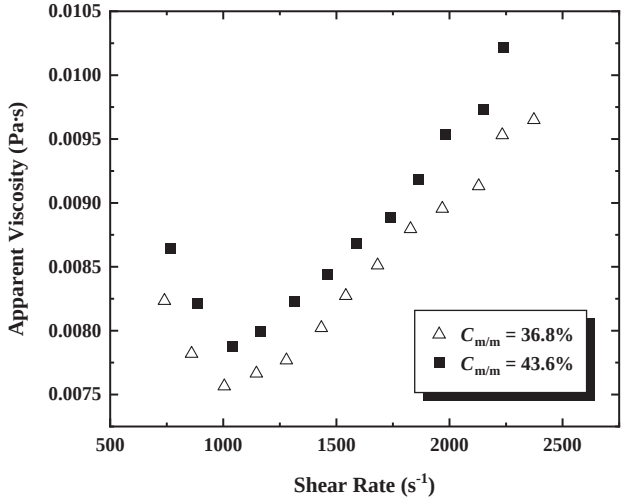


**Fig. 9** Apparent viscosity as a function of the shear rate for iron ore slurries.

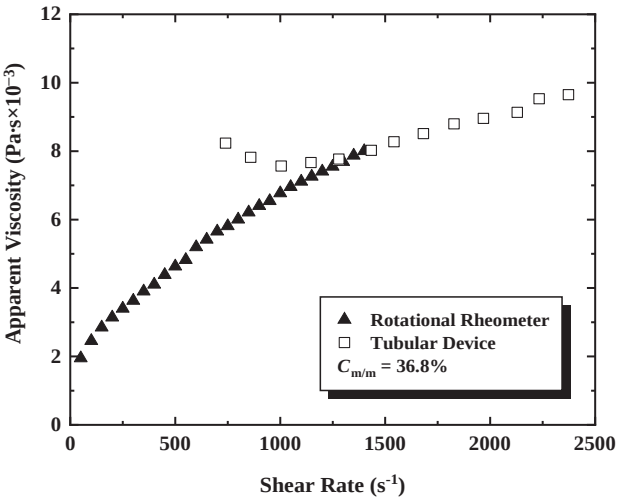


**Fig. 11** Apparent viscosity as a function of the shear rate, measured by rotational and tubular rheometry.

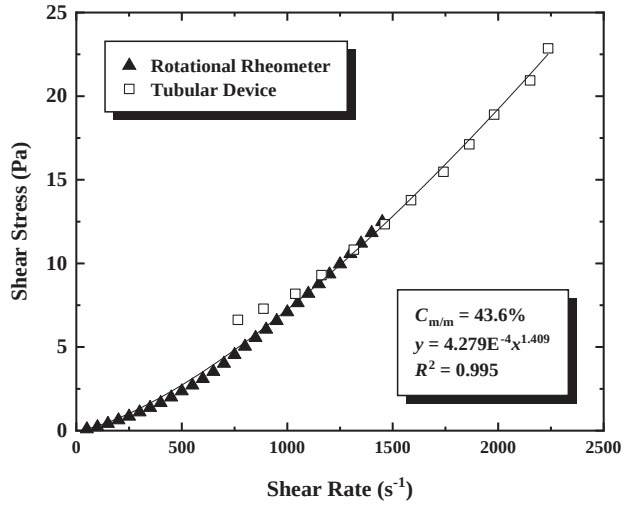


**Fig. 12** Shear stress as a function of the shear rate, measured by rotational and tubular rheometry.

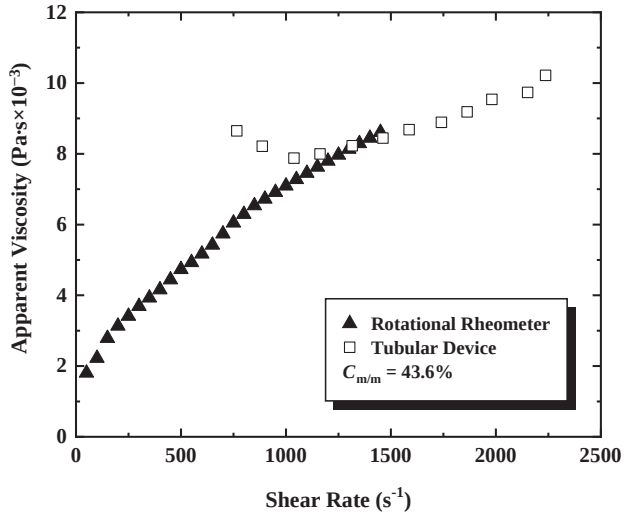


**Fig. 13** Apparent viscosity as a function of the shear rate, measured by rotational and tubular rheometry.

a divergence between the rotational and tubular rheometry data within a narrow range of shear rates: from 750 $s^{-1}$ to 1000 $s^{-1}$.

The characteristics of the flow curves shown in **Fig. 5** do not indicate sedimentation or the formation of a bed of particles in the tube.

However, stratification of particles in the flow may have occurred, which may have caused shear-thinning behavior for values of $\dot{\gamma}_w$ within the narrow range of 750 $s^{-1}$ and 1000 $s^{-1}$.

## 4. Conclusions

This work presents and proposes a novel methodology to investigate the rheology of iron ore slurries at two solid concentrations (36.8 % and 43.6 %) via tubular rheometry using the Principle of Maximum Entropy, which provides physically consistent mathematical models that meet the actual features of flow conditions in pipes, such as: typical turbulence levels, high shear rates, and pipe roughness. The results of mean flow velocity and pressure gradient obtained from simple pumping loop tests allowed the calculation of the friction factor, entropy parameter, apparent viscosity of the slurries, and Reynolds number by applying a previously developed model (Louzada et al., 2021). In this way, it was possible to obtain rheograms under shear rates closer to industrial reality ($\dot{\gamma} > 1000$ $s^{-1}$). In addition, the results obtained from experiments conducted in a laboratory rotational rheometer, under shear rates lower than 1450 $s^{-1}$, were complemented by those yielded by tubular rheometry at higher shear rates ($\dot{\gamma} \geq 766$ $s^{-1}$), since both sets of points were satisfactorily adjusted by the Power Law model in a single curve ($R^2 = 0.995$). The rheogram obtained from both complementary techniques was named "universal rheogram" and indicated that the iron ore slurries behaved as shear-thickening fluids ($n > 1$). However, within a narrow range of shear rate (750 $s^{-1} < \dot{\gamma} < 1000$ $s^{-1}$), three points ($\dot{\gamma}$, $\tau$) obtained from tubular rheometry deviated from the "universal rheogram", showing shear-thinning behavior for the slurry flow. Because the stratification of particles in the pipes may promote fluid shear-thinning behavior, a lack of turbulence in the piping system operating at its lowest shear rates ($\dot{\gamma} < 1000$ $s^{-1}$) could explain the deviating results. Thus, the range of 750 $s^{-1} < \dot{\gamma} < 1000$ $s^{-1}$ is too high to be applied in laboratory rotational rheometers, due to the occurrence of Taylor vortices, and too low to create enough turbulence to promote adequate particle suspension in pumping loop tubular devices. This is a limitation posed by the novel methodology proposed in this paper.

## Acknowledgements

The authors thank CAPES and the Instituto Tecnológico Vale (ITV) for financial support and the Graduate Program in Mineral Engineering at the University of São Paulo.

## Nomenclature

| | |
|---|---|
| PME | Principle of Maximum Entropy |
| $C_L$ | Correction factor (-) |
| $D$ | Internal diameter of the tube (m) |
| $f_E$ | Entropic friction factor (-) |
| $f(u)$ | The probability density function of the velocity |
| $H(u)$ | Entropy of the velocity |
| $K$ | The consistency of Power Law model (Pa·$s^n$) |
| $L$ | Length (m) |
| $M$ | Entropy parameter, defined as the product of the maximum flow velocity by the second Lagrange multiplier (-) |
| $n'$ | Correction factor of the Rabinowitsch–Mooney model (-) |
| $\Delta P$ | Pressure drop (Pa) |
| $r$ | Radial distance (m) |
| $R$ | Inner radius of the tube (m) |
| $R_e$ | Radius of the outer cylinder (m) |

| | |
|---|---|
| $Re_a$ | Apparent Reynolds number (-) |
| $R_i$ | Radius of the inner cylinder (m) |
| $T$ | Torque (N m) |
| $Ta$ | Taylor number (-) |
| $u$ | Velocity (m/s) |
| $\bar{u}$ | Mean flow velocity (m/s) |
| $u_E(r)$ | Entropic velocity distribution (m/s) |
| $u_{ci}$ | Peripheral velocity of the inner cylinder (m/s) |
| $u_{max}$ | Maximum flow velocity at the tube center (m/s) |
| $\dot{\gamma}$ | Entropic shear rate (-) |
| $\delta$ | Ratio between the radii of the outer and inner cylinders (-) |
| $\eta$ | Apparent viscosity (Pa·s) |
| $\rho$ | Density (kg m$^{-3}$) |
| $\tau$ | Shear stress (Pa) |
| $\tau_0$ | Yield stress (Pa) |
| $\tau_w$ | Wall shear stress (Pa) |
| $\omega$ | Angular velocity (s$^{-1}$) |

## Data Availability Statement

Rheology and flow data for iron ore slurries (depicted in **Figs. 2–13**) are available publicly in J-STAGE Data (https://doi.org/10.50931/data.kona.25532392).

## References


Barnes H.A., Hutton J.F., Walters K., An Introduction to Rheology, 1st ed., Elsevier, Amsterdam; New York, 1989, ISBN: 9780444871404.

Boger D.V., Rheology and the resource industries, Chemical Engineering Science, 64 (2009) 4525–4536. https://doi.org/10.1016/j.ces.2009.03.007

Brown E., Jaeger H.M., Shear thickening in concentrated suspensions: phenomenology, mechanisms and relations to jamming, Reports on Progress in Physics, 77 (2014) 1–23. https://doi.org/10.1088/0034-4885/77/4/046602

Chhabra R.P., Richardson J.F., Non-Newtonian Flow in the Process Industries, Elsevier, 1999, ISBN: 978-0-7506-3770-1. https://doi.org/10.1016/b978-0-7506-3770-1.x5000-3

Chilton R.A., Stainsby R., Pressure loss equations for laminar and turbulent non-Newtonian pipe flow, Journal of Hydraulic Engineering, 124 (1998) 522–529. https://doi.org/10.1061/(asce)0733-9429(1998)124:5(522)

Chiu C., Entropy and probability concepts in hydraulics, Journal of Hydraulic Engineering, 113 (1987) 583–599. https://doi.org/10.1061/(asce)0733-9429(1987)113:5(583)

Chiu C., Velocity distribution in open channel flow, Journal of Hydraulic Engineering, 115 (1989) 576–594. https://doi.org/10.1061/(asce)0733-9429(1989)115:5(576)

Chiu C., Lin G., Lu J., Application of probability and entropy concepts in pipe-flow study, Journal of Hydraulic Engineering, 119 (1993) 742–756. https://doi.org/10.1061/(asce)0733-9429(1993)119:6(742)

Fangary Y.S., Ghani A.S.A., El Haggar S.M., Williams R.A., The effect of fine particles on slurry transport processes, Minerals Engineering, 10 (1997) 427–439. https://doi.org/10.1016/s0892-6875(97)00019-8

Fox R.W., McDonald A.T., Pritchard P.J., Introdução À Mecânica Dos Fluidos, 6. ed., LTC, Rio de Janeiro (RJ), 2006, ISBN: 9788521614685.

Giguère R., Fradette L., Mignon D., Tanguy P.A., Analysis of slurry flow regimes downstream of a pipe bend, Chemical Engineering Research and Design, 87 (2009) 943–950. https://doi.org/10.1016/j.cherd.2009.01.005

Groisman A., Steinberg V., Elastic turbulence in a polymer solution flow, Nature, 405 (2000) 53–55. https://doi.org/10.1038/35011019

Gürgen S., Kuşhan M.C., Li W., Shear thickening fluids in protective applications: a review, Progress in Polymer Science, 75 (2017) 48–72. https://doi.org/10.1016/j.progpolymsci.2017.07.003

Kawatra S.K., Bakshi A.K., On-line viscometry in particulate processing, Mineral Processing and Extractive Metallurgy Review, 14 (1995) 249–273. https://doi.org/10.1080/08827509508914126

Kawatra S.K., Bakshi A.K., On-line measurement of viscosity and determination of flow types for mineral suspensions, International Journal of Mineral Processing, 47 (1996) 275–283. https://doi.org/10.1016/0301-7516(96)00009-9

Kelessidis V.C., Maglione R., Yield stress of water–bentonite dispersions, Colloids and Surfaces A: Physicochemical and Engineering Aspects, 318 (2008) 217–226. https://doi.org/10.1016/j.colsurfa.2007.12.050

Kitanovski A., Vuarnoz D., Ata-Caesar D., Egolf P.W., Hansen T.M., Doetsch C., The fluid dynamics of ice slurry, International Journal of Refrigeration, 28 (2005) 37–50. https://doi.org/10.1016/j.ijrefrig.2004.07.010

Klein B., Laskowski J.S., Rheological measurements on settling suspensions: characterization of a cyanide leach pulp, Mineral Processing and Extractive Metallurgy Review, 20 (2000) 41–55. https://doi.org/10.1080/08827509908962462

Louzada J.C.G., Souza Pinto T.C., Meier R.G., Souza P.A., Leal Filho L.S., Entropic friction factor modeling for mineral slurry flow in pressurized pipes, Journal of Hydraulic Engineering, 147 (2021) 1–6. https://doi.org/10.1061/(asce)hy.1943-7900.0001934

Lu P., Zhang M., Resistance properties of coal–water paste flowing in pipes, Fuel, 81 (2002) 877–881. https://doi.org/10.1016/s0016-2361(01)00217-4

Ma X., Duan Y., Li H., Wall slip and rheological behavior of petroleum-coke sludge slurries flowing in pipelines, Powder Technology, 230 (2012) 127–133. https://doi.org/10.1016/j.powtec.2012.07.019

Metzner A.B., Reed J.C., Flow of non-Newtonian fluids—correlation of the laminar, transition, and turbulent-flow regions, AIChE Journal, 1 (1955) 434–440. https://doi.org/10.1002/aic.690010409

Mezger T., The Rheology Handbook: For Users of Rotational and Oscillatory Rheometers, 5th revised ed., Vincentz, Hannover, 2020, ISBN: 9783748603702. https://doi.org/10.1515/9783748603702

Mooney M., Explicit formulas for slip and fluidity, Journal of Rheology, 2 (1931) 210–222. https://doi.org/10.1122/1.2116364

Peker S.M., Helvaci S.S., Solid-Liquid Two Phase Flow, 1st ed., Elsevier, Amsterdam; Boston, 2007, ISBN: 9780444522375.

Pereira A.S., Soares E.J., Polymer degradation of dilute solutions in turbulent drag reducing flows in a cylindrical double gap rheometer device, Journal of Non-Newtonian Fluid Mechanics, 179–180 (2012) 9–22. https://doi.org/10.1016/j.jnnfm.2012.05.001

Salunkhe A.A., Overney R.M., Berg J.C., The use of boundary lubricants for the reduction of shear thickening and jamming in abrasive particle slurries, Colloids and Surfaces A: Physicochemical and Engineering Aspects, 537 (2018) 13–19. https://doi.org/10.1016/j.colsurfa.2017.09.029

Senapati P.K., Mishra B.K., Rheological characterization of concentrated jarosite waste suspensions using Couette & tube rheometry techniques, Powder Technology, 263 (2014) 58–65. https://doi.org/10.1016/j.powtec.2014.04.092

Seto R., Mari R., Morris J.F., Denn M.M., Discontinuous shear thickening of frictional hard-sphere suspensions, Physical Review Letters, 111 (2013) 218301-1-218301–218305. https://doi.org/10.1103/PhysRevLett.111.218301

Shi F., Determination of ferrosilicon medium rheology and stability, Minerals Engineering, 98 (2016) 60–70. https://doi.org/10.1016/j.mineng.2016.07.016

Singh V., Sivakumar B., Cui H., Tsallis entropy theory for modeling in water engineering: a review, Entropy, 19 (2017) 1–25. https://doi.org/10.3390/e19120641

Singh V.P., Entropy Theory in Hydraulic Engineering: An Introduction, American Society of Civil Engineers, Reston, Virginia, 2014, ISBN: 9780784412725.

Slatter P., The role of rheology in the pipelining of mineral slurries, Mineral Processing and Extractive Metallurgy Review, 20 (2000) 281–300. https://doi.org/10.1080/08827509908962478

Souza P.A., Moraes E.L., The flow resistance factor treated by the maximum entropy principle, International Journal of Hydraulic Engineering, 6 (2017) 1–8. https://doi.org/10.5923/j.ijhe.20170601.01

Souza Pinto T.C., Moraes Junior D., Slatter P.T., Leal Filho L.S., Modelling the critical velocity for heterogeneous flow of mineral slurries, International Journal of Multiphase Flow, 65 (2014) 31–37. https://doi.org/10.1016/j.ijmultiphaseflow.2014.05.013

Stickel J.J., Powell R.L., Fluid mechanics and rheology of dense suspensions, Annual Review of Fluid Mechanics, 37 (2005) 129–149. https://doi.org/10.1146/annurev.fluid.36.050802.122132

Tozzi E., Hartt W., Non-Newtonian laminar flow in pipes using radius, stress, shear rate or velocity as the independent variable, Physics of Fluids, 33 (2021) 103–104. https://doi.org/10.1063/5.0067993

Whiten W., Steffens P., Hitchins J., An examination of pulp viscosity in tubes at higher shear rates, Minerals Engineering, 6 (1993) 397–404. https://doi.org/10.1016/0892-6875(93)90018-I

## Authors' Short Biographies

**Prof. Jean Carlo Grijó Louzada** is a chemical engineer from the Fluminense Federal University (2006), having obtained a Master of Science degree in metallurgical and materials engineering from the Federal University of Rio de Janeiro (2008) and a Doctor of Science from the Graduate Program Degree in Mineral Engineering (PPGEMin) from the University of São Paulo (2022). He is an associate professor at the Institute of Geosciences and Engineering at the Federal University of South and Southeast Pará.

**Elaine Cristina Andrade, MSc,** is a materials engineer from the Federal University of Pará (2010), having obtained a master's degree in science from the Technological Institute of Aeronautics (2013). She is currently a doctoral student at the Graduate Program in Mineral Engineering (PPGEMin) at the University of São Paulo.

**Dr. Thiago Cesar de Souza Pinto** is a chemical engineer from Universidade Santa Cecília (Unisanta), having obtained his master's and doctor's degrees in sciences from the Graduate Program in Mineral Engineering (PPGEMin) at the University of São Paulo. He was a researcher at the Instituto Tecnologico Vale and is currently a researcher at the Mineral Development Center (CDM) of the company Vale S.A.

**Prof. Laurindo de Salles Leal Filho** obtained a degree in mining engineering from the Federal University of Minas Gerais (1984), a master's degree in metallurgical and mining engineering from the Federal University of Minas Gerais (1988), a doctorate in mineral engineering from the University of São Paulo (1991) and postdoctoral fellow at the Imperial College of Sciences and Technology (1994). Lecturer in the Department of Mining and Petroleum Engineering at the Polytechnic School of the University of São Paulo since 1990, obtaining the associate professorship in 1999 and the position of full professor in 2001. Professor Leal Filho served as scientific director of the Instituto Tecnológico Vale from November 2013 to January 2019.

KONA Powder and Particle Journal

KONA Powder and Particle Journal No. 42 (2025) 251–260/https://doi.org/10.14356/kona.2025012 Original Research Paper

# Antibacterial Properties of Soft Solids (Chitosan and Polyacrylic Acid Gel Particles) in Solution and on a Bio-Surface (VITRO-SKIN)†

**Vasanthakumar Balasubramanian and Brij M. Moudgil***

*Center for Particulate and Surfactant Systems (CPaSS), Department of Materials Science and Engineering, University of Florida, USA*

Antimicrobial resistance presents a critical challenge to public health, driving the exploration of innovative strategies against microbial threats. Soft solids, notably polyelectrolyte gel complexes, offer promising antimicrobial alternatives with tailored physiochemical properties and biocompatibility. Primarily, soft solids incorporating chitosan and polyacrylic acid (PAA) complexes have gained importance for their antimicrobial efficacy, stemming from electrostatic interactions between oppositely charged components. This paper evaluates non-covalent interactions within chitosan and polyacrylic acid complexes to reduce *Escherichia coli* (*E. coli*) contaminants. Chitosan, derived from chitin, is valued for its biodegradability and low toxicity, and is currently used in drug delivery and wound healing systems. Conversely, PAA is an anionic polymer with carboxylic groups, widely used in pH-sensitive hydrogel-based drug delivery systems. In the present study, the antimicrobial effectiveness of chitosan and polyacrylic acid complexes was examined both in solution and on the bio-surface. Distinct patterns of antimicrobial activity were observed at the surface when applied individually and in combination. A synergistic antimicrobial effect of the chitosan and polyacrylic acid complex (gel particles), resulted in a remarkable reduction in viable cells both in solution and on the surface. This understanding enhances the potential use of soft solids in addressing the challenge of deactivating antimicrobial resistance pathogens.

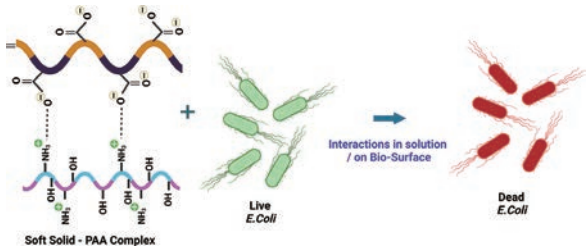


**Keywords:** chitosan, polyacrylic acid, gel particles, *E. coli*, VITRO-SKIN

## 1. Introduction

Contaminated environmental surfaces function as reservoirs for the transmission of many healthcare-associated pathogens. All these pathogens have been demonstrated to persist in the environment for hours to months and can pose a significant hazard due to touch-based transmission (Chemaly et al., 2014). The current surface disinfection treatments are inefficient for decontamination as some of the nosocomial pathogens may survive and give rise to substantial problems in terms of public health (Dancer, 2014). As per the 2023 report from the World Health Organization, antimicrobial resistance (AMR) poses a major threat to global public health and development. In 2019, bacterial AMR alone caused 1.27 million deaths worldwide (WHO, 2023). Polyelectrolyte complexes have remained one of the most exciting subjects of scientific research, in recent decades, due to desirable physicochemical and biological properties (non-toxicity, biocompatibility, softness, hydrophilicity, biodegradability) having high drug encapsulation efficiency with quick response to stimuli (light, pH, temperature, antigens, ionic strength, etc.). These complexes found potential applications in pharmacy, the food industry, wastewater treatment, pulp, and paper production (Meka et al., 2017). Polyelectrolyte complexes are formed as ionically crosslinked networks between polyelectrolytes with opposite charges in solution without any chemical covalent cross-linker. The significant interactions between two polyelectrolyte polymers may include reversible electrostatic and dipole-dipole associations and hydrogen and hydrophobic bonds (Luo and Wang, 2014). Polyelectrolyte complexes consist of a neutralized polyelectrolyte core surrounded by excess polyelectrolyte, stabilizing the colloids against aggregation (Dautzenberg and Karibyants, 1999).

Chitosan is a derivative product obtained by the deacetylation of chitin, which is biodegradable and possesses low toxicity, and can be used in drug delivery, bioadhesion, wound healing, etc. (Singla and Chawla, 2010). Polyacrylic acid is an anionic polymer having anionic/acidic (–COOH) pendant groups on the polymer chains and is widely used for biomedical applications, especially for pH-sensitive hydrogel-based drug delivery systems (Rizwan et al., 2017). This study aimed to investigate (I) the antimicrobial efficacy of chitosan and polyacrylic acid separately and as a mixture in solution and at a bio-substrate (VITRO-SKIN) surface and (II) the effect of the ratio of chitosan and

† Received 23 April 2024; Accepted 7 May 2024
J-STAGE Advance published online 29 June 2024
* Corresponding author: Brij M. Moudgil;
Add: Gainesville, FL 32611, USA
E-mail: moudgil@ufl.edu
TEL:+1-352-328-7292 (M) FAX: +1-352-392-7219

polyacrylic acid within the mixture against *Escherichia coli* (*E. coli*).

## 2. Materials and methods

### 2.1 Materials

Polyacrylic acid (PAA) (purity of 99.0 %, molecular weight 450 kDa) was obtained from Polysciences Inc. (Warrington, PA, USA). Medium molecular weight chitosan (molecular weight 190–310 kDa) with a degree of deacetylation 75 %–85 % was purchased from Sigma-Aldrich®. Trypticase soy broth (TSB), trypticase soy agar (TSA), ampicillin sodium salt, and neutralizer broth (D/E broth) were obtained from Thermo Fisher Scientific Inc. Artificial skin substrate (VITRO-SKIN®) was purchased from IMS Inc. (Portland, ME, USA).

### 2.2 Bacterial strain

*E. coli* (ATCC 25922GFP) was obtained from ATCC. The culture was cultured by growing *E. coli* in trypticase soy broth (TSB) supplemented with 100 µg/ml ampicillin at 37 °C and harvested in the log phase at an OD600 of 0.3–0.4 by centrifugation at 3200× *g* (RCF: relative centrifugal force) for 15 min. The cell concentration was adjusted to $10^9$ CFU/ml (OD600 0.5) and further diluted with sterilized water to obtain a bacterial concentration of $10^6$ CFU/ml.

### 2.3 In vitro antimicrobial activity assay

Viability assays and microbial removal from the substrate were conducted as described previously (Nandakumar, 2018). Viability assay was performed in solution without the artificial skin substrate. For this purpose, a bacterial suspension of $10^6$ CFU/ml was directly added to the suspensions of the desired polyelectrolytes/polyelectrolyte mixtures, vortexed for 30 s at 1500 rpm (37 × *g*) and neutralized with D/E broth. The cell viability in the suspension was determined via the agar plate count method after incubating at 37 °C overnight before counting colony-forming units (CFU). Centrifugation speed (1500 rpm (37 × *g*)) chosen for this experiment was verified not to affect concentrations of free bacteria in the suspension. Results were expressed in terms of the total number of bacteria recovered (CFU) on the logarithmic scale.

Bacterial removal test protocol was as follows: (i) spreading the polyelectrolytes over 1 $cm^2$ area of pre-hydrated skin substrate and air-drying at room temperature for 30 min, (ii) polyelectrolytes coated skin substrate was exposed to the bacterial suspension of $10^6$ CFU/ml followed by further drying for 20 min, (iii) skin substrates were neutralized using D/E broth and vortexed at 3000 rpm (150 × *g*) for 30 s continuously to recover the remaining bacteria bound to the substrate. For solution studies, the interaction time for the polyelectrolytes and *E. coli* was 30 s, and the solution was vortexed at 1500 rpm (37 × *g*) continuously. Enumeration of bacteria using the agar plate count method was achieved as described above.

Removal efficacy following treatment was expressed as $\log_{10}$ bacterial removal using **Eqn. (1)**:

$$\log_{10}\text{ bacterial removal} = \log_{10}(\text{Initial bacterial inoculum on skin}) - \log_{10}(\text{bacteria remaining on skin}) \quad (1)$$

### 2.4 Synthesis of chitosan–polyacrylic acid polyelectrolyte complexes (soft solid)

The polyelectrolyte complex was prepared as follows: chitosan was dissolved in a 1.0 % w/v lactic acid solution for 12 h under mechanical stirring in order to form a 1.0 % w/v chitosan solution. The polyelectrolyte complexes were prepared by free mixing the specific ratios of polyacrylic acid and chitosan and the volume was adjusted to 5 mL. The polyelectrolyte complex was cast onto a petri dish plate, followed by keeping the plates at 60 °C on a hot plate overnight. The polyelectrolyte film formed was removed and sterilized in UV for 20 min in a laminar bio-hood and stored at room temperature for further testing.

### 2.5 Measurement of swelling behavior

The swelling behavior of the polyelectrolyte complex was estimated using mass balance at room temperature. The dry polyelectrolyte films were weighed and immersed in 25 ml of distilled water in a petri dish at room temperature. After 24 h, the swollen films were removed from the water, wiped off, and weighed. The swelling ratio was calculated using **Eqn. (2)**:

$$\text{DSW}\ (\%) = [(W_s - W_d)/W_d] \times 100 \quad (2)$$

where $W_s$ and $W_d$ denote the weight of the swollen and dry samples, respectively.

### 2.6 Measurement of the hydrophobicity of cell surface

The hydrophobicity of the bacterial cell surface was determined by microbial adherence to solvents (MATS) according to Bellon-Fontaine et al. (1996). Briefly, 2.4 ml of bacterial cells (washed thrice) suspended in 100 mM $KNO_3$ were vortexed at 1500 rpm (0.3 × *g*) for 90 s with 0.4 ml of chloroform and hexadecane and left undisturbed for 20 min. The extent of bacterial partitioning and adhesion to the solvents enabled comparisons between the electron donor properties and the hydrophobic nature of bacterial cell surfaces and was quantified using the following **Eqn. (3)**:

$$\text{Hydrophobicity}\ (\%) = (1 - A/A_0) \times 100 \quad (3)$$

where $A_0$ is the optical density of the aqueous suspension at 600 nm before mixing and $A$ is the optical density of the aqueous suspension after mixing with the solvent pair.

### 2.7 Substrate preparation and characterization

VITRO-SKIN® is a commercially available artificial skin substrate coated with collagen, gelatin, and silica particles to mimic the physicochemical properties of natural human skin, including pH, topography, and ionic strength. As per the manufacturer's manual, the substrate was prepared by hydrating a 1.0 cm × 1.0 cm patch overnight using a glycerol: water (15:85) binary mixture in a humidity chamber. The zeta potential of the substrate was measured using Paar Physica Electro Kinetic Analyzer at 10 mM KCl and pH 6.7. In addition, contact angle measurements were conducted using the sessile drop method within 60 s of deposition and were used to estimate the critical surface energy of the artificial skin substrate using the Owens–Wendt model (Owens and Wendt, 1969).

### 2.8 Characterization of bacteria

The *E. coli* strain employed in this study (ATCC 25922GFP) was characterized by surface energy using a light scattering technique described elsewhere (Zhang et al., 2015). Briefly, *E. coli* cells at set concentration were suspended in ethanol: water binary mixture of varying surface tensions, and vortexed for 30 s at 1500 rpm (37 × *g*) before leaving them undisturbed for 20 min. The samples were then centrifuged at 43 *g* (RCF) for 45 s and measured for optical density at 600 nm. Suspension with the highest optical density (OD 600 nm) was determined as closest to the surface energy values of the bacterial cell. Zeta potential measurements of *E. coli* were conducted using Brookhaven ZetaPlus at 10 mM KCl and pH 8.0.

## 3. Results and discussion

### 3.1 Characterization of the bacteria and substrate

This study used the MATS assay to investigate the surface hydrophobicity, hydrophilicity, and Lewis acid-base properties of the *E. coli* strain. The chosen bacteria showed strong interactions with a weak acidic polar solvent (chloroform: 12.5 ± 2.5 % adhesion) compared with interactions with a nonpolar solvent with a similar Lifshitz-van der Waals component (hexadecane: 2.8 ± 0.5 %). The low percentage of bacteria adhering to a nonpolar solvent such as hexadecane indicated that the strain evaluated had low hydrophobicity with base-like (electron donor) behavior. The quantitatively important existence of chemical groups such as $–COO^-$ and $–HSO_3^-$ on the surface of microorganisms could explain their strong electron donor character (Pelletier et al., 1997). Comparable results were obtained from the measured surface energy values of 47.5 ± 1.5 mJ/m$^2$, which are consistent with the findings of Oh et al. (2018) (57.2 ± 1.5 mJ/m$^2$). Additionally, a zeta potential of –25.33 ± 1.46 mV (pH 4.0, 10 mM KCl) and an IEP at pH 2.0 were observed, as reported by Ammam (2012).

VITRO-SKIN substrate was characterized for surface energy from contact angle measurements and was estimated to be 40.2 ± 2.3 mJ/m$^2$ using the Owens–Wendt model (Nandakumar, 2018). Streaming potential measurements of the artificial skin substrate indicated a zeta potential of +22.5 ± 0.7 at 10 mM KCl and pH 6.7, in agreement with the reported zeta potential of +23 mV for human skin at pH 6 (Morykwas et al., 1987).

### 3.2 Intermolecular interactions in polyelectrolytes in solution

The interaction between chitosan and polyacrylic acid at pH 4, and thus the subsequent formation of the soft solid in water, is schematically illustrated in **Fig. 1**. At low pH values, e.g., pH 4 (typically below the pKa of around pH 6.5), chitosan carries a net positive charge due to the protonation of its amino groups. This positive charge enables chitosan to readily interact with negatively charged species in its surroundings, such as proteins or anionic polymer molecules. The electrostatic attraction between the positively charged chitosan and the oppositely charged species can form complexes or aggregates (Yilmaz Atay et al., 2019). In contrast, polyacrylic acid (PAA) contains carboxylic acid (–COOH) groups, which can undergo ionization and form charged species based on the pH of the solution. As the pH increases and approaches the pKa value of PAA, typically around 4–5, the carboxylic acid groups begin to deprotonate.

The polymer is partially ionized at this pH range, with a balance between protonated (–COOH) and deprotonated ($–COO^-$) carboxylic acid groups. This state allows for interactions with water molecules, leading to increased

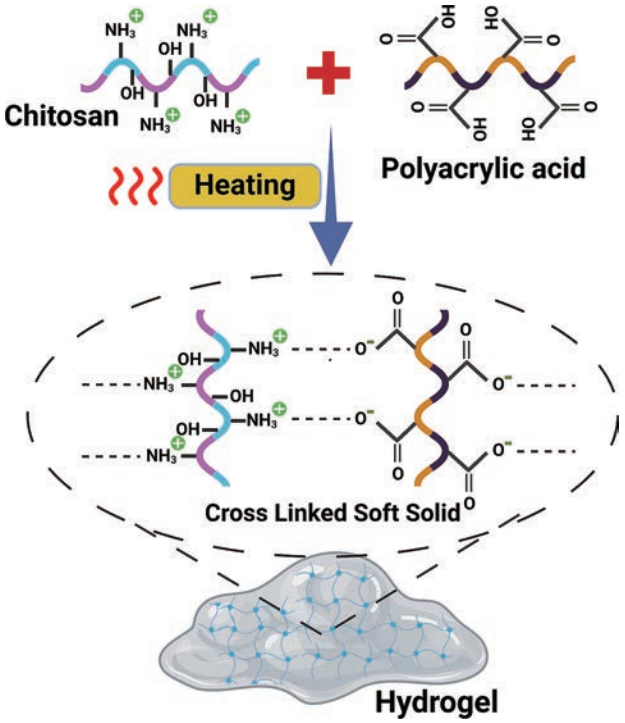


**Fig. 1** Formation of soft solid particles.

hydrophilicity and solubility of PAA resulting in maximum swelling behavior and high solubility in water.

At the experimental pH values (pH 4.0 ± 0.2), beyond the pKa, PAA is in its deprotonated form, with the carboxylic acid groups carrying a negative charge ($–COO^-$). The negatively charged electrostatic repulsion among PAA molecules leads to the expansion of the polymer chain and an increase in its hydrodynamic volume. In addition, hydrogen bonds can form between the hydroxyl and amino groups of chitosan and the carboxyl groups of polyacrylic acid. These interactions can contribute to the stability of the chitosan–polyacrylic acid complex. The coulomb repulsion between chain segments, on the one hand, and a non-monotonic change in the hydrogen bonding between chain segments between the negatively charged segments can prevent the polymer chains from collapsing or aggregating, maintaining their solubility in water (Katiyar and Jha, 2017).

The interactions between the charged functional groups present in both polymers primarily determine the pH-dependent behavior of the soft solids resulting from complexation between chitosan and PAA. It is important to note that the specific interactions between chitosan and polyacrylic acid at the experimental pH can be influenced by experimental conditions, such as polymer concentration, mixing ratio, interaction time, and reaction temperature. Complexation can occur due to hydrogen bonding and ionic interactions between oppositely charged functional groups. The resultant complex soft solids can undergo changes in structure, swelling, and other properties due to the balance between electrostatic attraction and repulsion between the partially charged functional groups (De la Torre et al., 2003). Chavasit et al. (1988) observed that the maximum complex formation between chitosan and polyacrylic aid occurred at different mole ratios within 3 to 6 pH range, due to the degree of ionization of the functional groups. At pH 4, the degree of ionization of chitosan and polyacrylic acid was approximately 0.95 and 0.2, respectively. The following complex formation mechanism occurs at pH 4:

$$NH_3^+ + HOOC \rightarrow NH_3^+ {}^-OOC + H^+$$

Swelling characteristics of the soft solid can be used to assess the antimicrobial efficacy by cell attachment and subsequent cell membrane disruption. It is a vital characteristic of the polyelectrolyte complex to determine hydrophilicity. The water absorption in the polyelectrolyte complex is due to interactions between water and hydrophilic groups, such as hydroxyl groups (OH), and carboxylic groups ($–COO^-$), which produce electrostatic and hydrogen-bonding interactions. It thus indicates the successful formation of crosslinked networks (Hatakeyama H. and Hatakeyama T., 1998). Since the formation of polyelectrolyte complex is based on electrostatic interactions, it suggests that the greater the number of protonated cationic groups, the higher the antimicrobial activity. Chitosan forms polyelectrolyte complex with higher swelling ability in aqueous media, where the C = O and N–H groups of chitosan in the complex could be protonated, consequently resulting in a higher net positive charge, thus leading to better antibacterial activity (Mohamed and Fahmy, 2012).

The swelling experimental results indicate an increase in water uptake after 24 h in the tested polyelectrolyte complexes. An inverse correlation was noticed between the water uptake and the degree of polyelectrolyte complex formation, as the water uptake changes from 300 % to 800 %. Under the tested conditions, the polyelectrolyte complex containing 100 µg/ml of chitosan has the highest water uptake (781 %). It is noteworthy that a comparable equilibrium swelling ratio of 850 % was documented at pH 5 in a study conducted by Jozaghkar et al. (2022). This equilibrium swelling ratio was achieved at a specific ratio of chitosan to polyacrylic acid, namely 0.01:1. This finding underscores the importance of pH and the ratio of chitosan to polyacrylic acid in influencing the swelling behavior of the soft solids. This performance may be due to the large pore size of the polyelectrolyte complex formed due to the imbalance of the concentration of cations and anions present in the polyelectrolyte complex (Tsao et al., 2010). As the chitosan concentration increases in the polyelectrolyte complex, the polymer chains may be connected into higher polymer density networks through more ionic crosslinks resulting in less water uptake.

Maximum log reduction (one million to one thousand) of *E. coli* cells was accomplished in the presence of a polyelectrolyte complex containing >100 µg/ml of chitosan 30 s of interaction. Complete degradation of the polyelectrolyte complex was observed after (~10 h) when the chitosan concentration was less than 100 ug/ml in the complex, contributing to 0.5–1.0 log reduction of *E. coli* cells. This response can be attributed to a natural release of polymer chains from this hydrated network because of its few ionic and high porosity crosslinks, as demonstrated for other polymers (Chellat et al., 2000).

### 3.3 Antimicrobial efficacy of chitosan, polyacrylic acid, and their complexes (soft solid) in solution

The antimicrobial efficacy of chitosan, polyacrylic acid, and their complex (soft solids) at different ratios of polyelectrolytes in the solution is shown in **Fig. 2**. There is no significant reduction of *E. coli* up to 1000 µg/ml of chitosan; however, 1 log and 6 log reduction (complete kill) are observed at 1000 and 10,000 µg/ml concentrations of chitosan, respectively. Jeon et al. (2014) showed a concentration-dependent bactericidal activity of 76 nm spherical chitosan against *E. coli*. Of all concentrations examined by them, 2000 µg/ml of chitosan showed the

most antimicrobial activity resulting in complete inhibition of *E. coli* during 6 h of incubation. All *E. coli* were killed in 120 min in the presence of 5000 ppm of chitosan in solution from initial 1E+05 (100,000) cells. Liu et al. (2004) reported a similar result using a bacterial strain similar to the one used in the present study. Under the present test conditions, the enhanced antimicrobial activity of chitosan is primarily due to the protonation of amino groups in the chitosan molecule. The most commonly hypothesized antibacterial effect of chitosan is to interact with the negatively charged bacterial cell wall, thereby altering membrane permeability. Several studies have shown that chitosan molecules in a solution can bind to DNA in the cell nucleus, where they can inhibit mRNA synthesis, thereby preventing its replication, leading to the cell death (Ardean et al., 2021). Another suggested mechanism is that chitosan serves as a chelating agent, binding to essential metal ions and thus limiting microbial growth (Yilmaz Atay, 2019). Kong et al. (2010) reported that the antimicrobial mechanism of chitosan at acidic pH (pH < 6) can be attributed to the electrostatic interactions between a positively charged amino group in chitosan and negatively charged bacterial surface molecules such as lipopolysaccharides and outer membrane proteins, resulting in the alteration of cell membrane permeability. The change in membrane permeability leads to the leakage of intracellular substances, eventually resulting in cell death.

On the contrary, there is no loss in viability of *E. coli* cells in the presence of polyacrylic acid. Polyacrylic acid is a negatively charged polymer, and its interaction with *E. coli* cells is repulsive.

The antimicrobial efficacy of chitosan and polyelectrolyte mixtures (soft solids) of varying ratios of chitosan and polyacrylic acid in solutions is plotted in **Fig. 2**. The tested polyelectrolyte complexes with the ratio of 1000 µg/ml chitosan and 9000 µg/ml polyacrylic acid, resulted in ~ 5E+03 (5,000) viable cells (out of 1 million initial cell count) after the 30 s exposure. According to Hu et al. (2002), the soft solid's zeta potential increases as the chitosan to polyacrylic acid ratio increases. When the content of chitosan (aminoglycoside units) exceeds that of polyacrylic acid, some of the excess chitosan is adsorbed onto the surface of the chitosan–polyacrylic acid complex (soft solid), increasing the surface charges of the soft solid and resulting in an increase in zeta potential. The antimicrobial mechanism of this complex is speculated to be the complex acting like a molecular ionic sponge, attracting the anionic microbial membrane into the three-dimensional porous structure of the polyelectrolyte complex, leading to membrane disruption and microbial death (Tsao et al., 2010).

### 3.4 Antimicrobial efficacy of chitosan and polyacrylic acid mixtures on the VITRO-SKIN surface

The removal of *E. coli* from VITRO-SKIN in the presence of different concentrations of chitosan and polyacrylic acid is shown in **Fig. 3**. The viable *E. coli* cells are reduced on the VITRO-SKIN as a function of the increase in the chitosan concentration alone. In contrast, no change was observed when exposed to polyacrylic acid alone. From the streaming potential studies, the surface charge of the VITRO-SKIN is found to be +22 mV due to the presence of collagen (Brohem et al., 2011; Li et al., 2009). Due to electrostatic repulsion between the amino group of chitosan and the VITRO-SKIN, the functional group may be oriented away from the VITRO-SKIN (i.e., exposed to the air). Elemental analysis of VITRO-SKIN reveals the

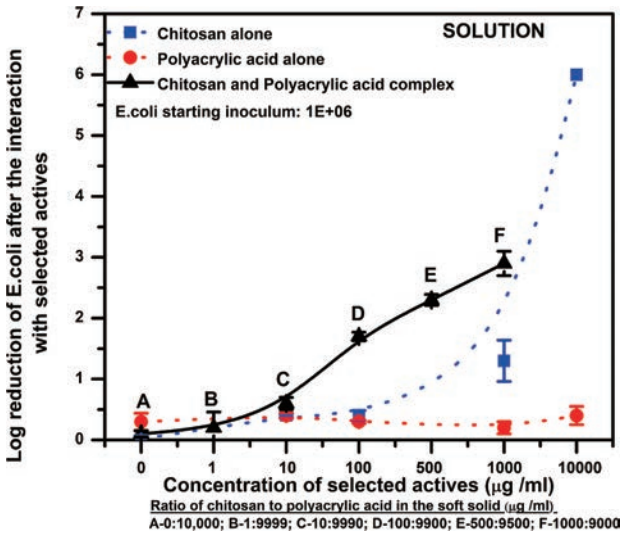


**Fig. 2** Reduction of *E. coli* cells in the presence of chitosan, polyacrylic acid, and soft solids in solution. The raw data are publicly available at J-STAGE Data (https://doi.org/10.50931/data.kona.25965100).

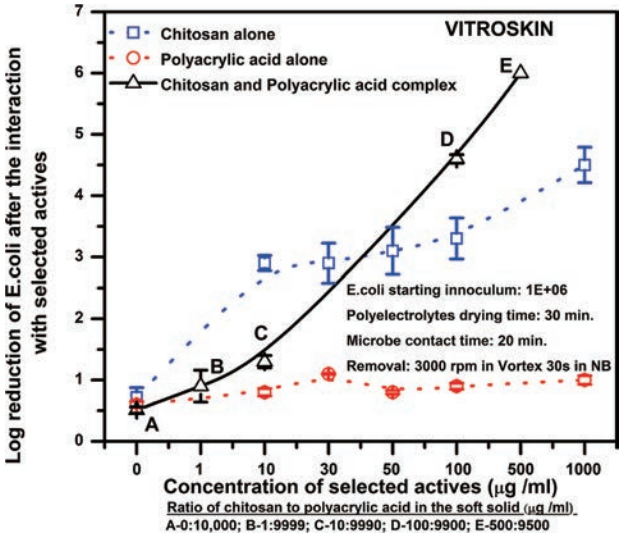


**Fig. 3** Reduction of *E. coli* cells in the presence of chitosan, polyacrylic acid, and the soft solid at the bio-surface. The raw data are publicly available at J-STAGE Data (https://doi.org/10.50931/data.kona.25970965).

presence of 1.7 mg of nitrogen per $cm^2$ (data not shown) that originates from the collagen in the VITRO-SKIN. The zeta potential measurement indicates that the IEP of collagen is about 9.3, which carries a net positive charge (Li et al., 2009).

As described earlier, chitosan includes amino groups that are protonated at lower pH levels, such as pH 4, producing a positively charged polymer. Electrostatic repulsion between the amine functional groups in chitosan and collagen can occur when it comes into touch with a positively charged surface (VITRO-SKIN). On the other hand, chitosan has hydroxyl groups in addition to amino groups. These hydroxyl groups can form hydrogen bonds with positively charged surface functional groups. These interactions can result in chitosan adsorption on the VITRO-SKIN surface, contributing to the overall stability of the chitosan–VITRO-SKIN surface complex. It is reported that the functional group –COOH and $NH_2$ in collagen may interact through hydrogen bonds with –OH and $–NH_2$ groups from chitosan, as chitosan possesses large numbers of –OH groups, and thus alters the collagen triple helix structure (Sionkowska et al., 2004). This conformational change facilitates an adequate interaction of amino groups in chitosan with the approaching microbe, thus increasing the permeability of the cell membrane. *E. coli* cell outer membrane acts as a permeability barrier and inhibits the transport of macromolecules and hydrophobic compounds entering or leaving bacteria cell membranes. The fluorescence intensity studies reported an increase in the *E. coli* cell membrane permeability observed after interaction with chitosan in 10 minutes (Tang et al., 2010). This behavior is ascertained from the removal studies that log reduction of *E. coli* on the VITRO-SKIN increases proportionally to the tested chitosan concentration.

On the contrary, no significant cell removal from VITRO-SKIN was observed in the presence of polyacrylic acid. Polyacrylic acid is a polyelectrolyte with negatively charged carboxylate groups, especially at lower pH values where carboxyl groups remain protonated. A positively charged VITRO-SKIN surface can attract and facilitate the adsorption of PAA through electrostatic interactions and hydrogen bonding. The adsorbed PAA layer may create a charged or steric barrier that hinders the approach and attachment of *E. coli* cells to the surface. PAA's ability to absorb water and swell may contribute to the creation of a hydrated layer that hampers bacterial adhesion. The electrostatic repulsion between negatively charged PAA and the negatively charged bacterial surface may prevent direct contact and adhesion. The interactions between collagen and polyacrylic acid result in the formation of polyelectrolyte complex through electrostatic interactions involving the $NH_3^+$ group of the collagen in the VITRO-SKIN and the $–COO^–$ groups of polyacrylic acid (Barbani et al., 1999). Besides, due to their similar surface charges, electrostatic repulsion is anticipated between polyacrylic acid and the approaching *E. coli* cells. Also, collagen has no antimicrobial activity, hence no reduction in cell number on the VITRO-SKIN is observed in the presence of polyacrylic acid.

The complete reduction of *E. coli* cells (total kill) is observed in the presence of a polyelectrolyte mixture (500 μg/ml of chitosan and 9500 μg/ml of polyacrylic acid). In the polyelectrolyte complex, swelling and porosity of the mixture are governed by the percentage of the ionic components in the complex. The pKa values for polyacrylic acid and chitosan have been reported to be 4.0 and 6.5 at pH 4, with ionization levels of 0.2 and 0.95, respectively (Choi and Rubner, 2005). In the present experimental conditions (pH 4.0), more carboxyl groups than amino groups are undissociated. As the chitosan concentration increases from 1 μg/ml to 500 μg/ml, a more stable porous structure in the mixture is anticipated. Under the tested conditions, the available dissociated carboxyl groups in polyacrylic acid interact via non-covalent forces with the groups present in the chitosan. Our research findings suggest that in order to achieve the antimicrobial effect of the soft solids, it is necessary to have direct contact with bacterial suspension. It is worth noting that the reduction in pH alone cannot account for this effect (Gratzl et al., 2015).

### 3.5 Antimicrobial mechanism of soft solid on a positively charged bio-surface

When the chitosan–PAA complex interacts with a positively charged bio-surface (VITRO-SKIN), the interactions are influenced by the charge distribution on the complex and the bio-surface, as shown in **Fig. 4**.

The electrostatic repulsion between the positive charges of chitosan and the positive charges on the bio-surface can facilitate the repulsion of chitosan molecules away from the bio-surface. The positively charged chitosan molecules in the soft solid align and orient themselves away from the VITRO-SKIN and towards the negatively charged bacterial cells, promoting electrostatic interactions and adhesion. However, the carboxylic acid groups in PAA can undergo ionization on the positively charged bio-surface, leading to the formation of negatively charged carboxylate groups ($–COO^–$) on PAA. The negatively charged carboxylate groups can lead to electrostatic interactions with the positively charged bio-surface, enabling the adhesion of the complex on the surface. The adsorbed chitosan layer can physically encapsulate the *E. coli* cells due to its three-dimensional structure, leading to physical entrapment and hindered mobility of *E. coli* cells. Chitosan contains hydrophobic groups (such as acetyl groups in the case of partially deacetylated chitosan) along with its positively charged amino groups. Furthermore, the hydrophobic regions of chitosan can interact with hydrophobic regions on the bacterial cell surface, including lipids and other

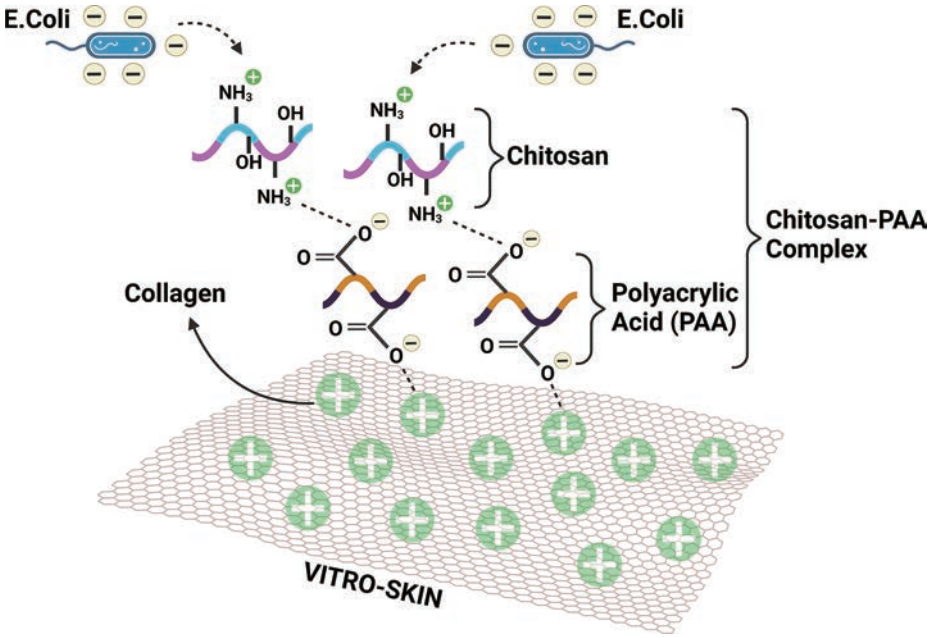


**Fig. 4** Interaction of soft solids with *E. coli* at VITRO-SKIN.

hydrophobic molecules present in the cell membrane. Chitosan's hydroxyl and amino groups can also form hydrogen bonds with various functional groups on the bacterial cell surface, such as hydroxyl, carbonyl, and amine groups. The combination of electrostatic interactions, hydrophobic interactions, and hydrogen bonding creates a multifaceted interaction between chitosan and bacterial cells. Chitosan's interaction with the *E. coli* cell membrane could potentially lead to leakage of intracellular components. A previous study has confirmed the leakage of proteins and other intracellular constituents caused by chitosan (Kong et al., 2008). In Gram-negative bacteria, high negative charges given by lipopolysaccharide (LPS) can be neutralized by positive charges from chitosan, resulting in disruption of the bacterial outer membrane, enabling chitosan to penetrate the cell membrane resulting in cell death (Feng et al., 2021). The 20-minute interaction time allows for prolonged exposure of the bacteria to the antimicrobial properties of the hydrogel. Additionally, an acidic environment due to the carboxylic acid groups in PAA can hinder bacterial growth and reproduction, further inhibiting the viability of *E. coli*. Topuzoğullari (2020) observed that positively charged poly electrolyte complexes, generated at greater [quaternized 4-vinylpyridine]/[PAA] ratios, resulted in higher antibacterial activity of these compounds is dependent on these free quaternized 4-vinylpyridine groups. The free quaternized 4VP groups that do not interact with PAA due to insufficient acrylic acid groups and the polyelectrolyte complex characteristics become similar to free polycation, which causes a similar antibacterial activity. In the present study, a similar trend was observed as more protonated chitosan was observed over PAA due to the higher degree of ionization of chitosan over PAA at pH 4.0.

### 3.6 Antimicrobial mechanism of soft solid in water

In water, the chitosan–PAA complex can exhibit antimicrobial properties against gram-negative bacteria, as shown schematically in **Fig. 5**. The electrostatic attraction between the positively charged chitosan and the negatively charged bacteria promotes the adsorption of the complex onto the bacterial cell membrane. This interaction can disrupt the integrity of the cell membrane, leading to leakage of cellular contents and eventually bacterial death.

Additionally, the carboxylic acid groups (–COOH) in PAA can release hydrogen ions ($H^+$) in the solution, leading to a decrease in the pH locally around the complex. The acidic environment generated by the release of $H^+$ ions can further disrupt the bacterial cell membrane, destabilizing the bacterial cells and inhibiting their growth. Both the soft solid and the bacteria are in constant motion in water due to induced shear force. The diffusion of the complex and the bacteria increases the chances of their encounter and subsequent collision. The number of chitosan–PAA complex molecules available in the solution also influences the interaction with *E. coli*. The greater the number of complex molecules, the higher the probability of interactions occurring with bacterial cells. The chitosan content in the gel is critical to its antibacterial efficacy against gram-positive and gram-negative bacteria in the solution. The creation of hydrogen and covalent connections among the functional groups of the chitosan chains is enhanced as the concentration increases, minimizing dispersion, and causing the structure to acquire a densely overlapping coiled conformation. The extensive intra- and intermolecular bonding at higher molecular densities is related to the random-coil structure of chitosan in solution, which is often recognized

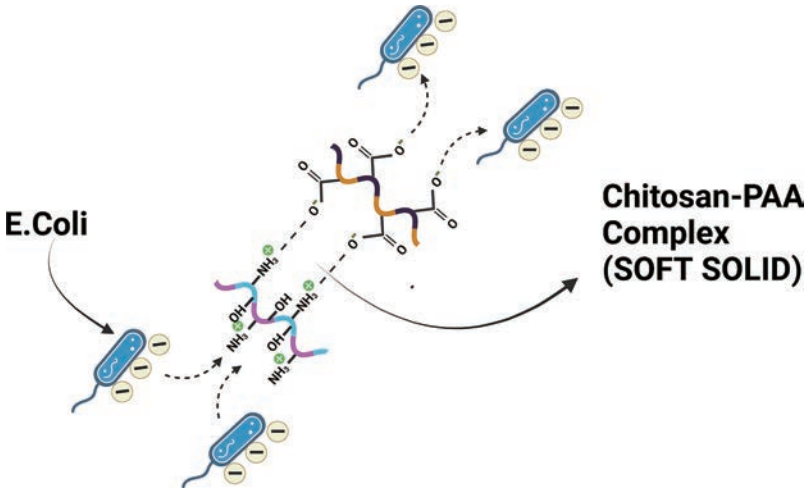


**Fig. 5** Interaction of soft solid with *E. coli* in the solution.

in the literature. This, in turn, places geographical constraints on functional groups. As a result, fewer charged sites are accessible for interaction, limiting binding to bacterial cell walls (Goy et al., 2016). The soft solid allows for a larger surface area available for contact with bacteria, increasing the likelihood of collision between the soft solid complex and *E. coli* cells. Increased availability of complex molecules enhances the chance of multiple binding events and can lead to stronger adhesion and antimicrobial effects.

## 4. Summary and conclusions

This present study showed the antimicrobial efficacy of soft solid containing chitosan and polyacrylic acid emerges as an additional methodology for combating microbial challenges, both in solution and at bio substrate surfaces. In solution, the remarkable efficacy of chitosan at a concentration of 10,000 μg/ml in achieving a 6-log reduction (complete eradication) of microbial populations highlights its unparalleled potential as a potent antimicrobial agent. This level of microbial reduction surpasses that of many commercial antimicrobial agents, which typically achieve a 99.9 % (3 log) reduction in microbial populations. Simultaneously, the introduction of polyacrylic acid reveals its inherent compatibility, as it exhibits no detrimental effect on *E. coli* viability. The strategic blending of chitosan and polyacrylic acid at a ratio of 1000 μg/ml and 9000 μg/ml, respectively, provides a balanced compromise, resulting in a controlled reduction to approximately 5E+03 (5,000) viable cells—a noteworthy accomplishment from an initial population of one million. On the surface, a decrease in viable *E. coli* cells with increasing chitosan concentration on the VITRO-SKIN indicates that chitosan alone has an antibacterial action.

Conversely, the unaltered state in the presence of polyacrylic acid underscores its selective approach. However, the true marvel lies in the combination of chitosan and polyacrylic acid, as demonstrated by the total reduction of *E. coli* cells in the presence of a polyelectrolyte mixture containing 500 μg/ml of chitosan and 9500 μg/ml of polyacrylic acid. The interplay of intramolecular forces between chitosan and polyacrylic acid, encompassing electrostatic attractions, hydrogen bonding, and potentially hydrophobic interactions, appears to result in their synergistic efficacy. This study underlines the synergistic potential of these soft solids and emphasizes the importance of careful formulation to achieve the best antibacterial results. By exploiting the precise interplay of intramolecular forces within soft solids, it is possible to engineer advanced wound dressings, implant coatings, and biomedical textiles that inherently possess antimicrobial properties. These materials could prevent the initial adhesion of pathogens, minimize infection risk, and mitigate the formation of virulent biofilms, which are critical challenges in modern healthcare settings.

## Acknowledgments

The authors would like to thank the National Science Foundation of the United States for Grant No. 1362060 and the Centre for Particulate and Surfactant Systems (CPaSS) industry members for their financial assistance. Unilever is acknowledged for providing enhancement funding for the project, as well as their active involvement, assistance, and commitment to this initiative. We extend our sincere gratitude to Dr. Dinesh O. Shah for his thought-provoking discussions, which have enriched our research endeavors. Additionally, we express our appreciation to Rohan Bhargava and Dr. Vijayakumar Govindaraj for their dedicated assistance in experimental work and figure preparation, respectively.

## Data Availability Statement

Data on log reduction measurements of soft solids (chitosan and polyacrylic acid gel particles) in solution are

available publicly in J-STAGE Data (https://doi.org/10.50931/data.kona.25965100).

Data on log reduction measurements of soft solids on a bio-surface (VITRO-SKIN) are available publicly in J-STAGE Data (https://doi.org/10.50931/data.kona.25970965).

## References


Ammam M., Electrophoretic deposition under modulated electric fields: a review, Royal Society of Chemistry Advances, 2 (2012) 7633–7646. https://doi.org/10.1039/C2RA01342H

Ardean C., Davidescu C.M., Nemeş N.S., Negrea A., Ciopec M., Duteanu N., Negrea P., Duda-Seiman D., Musta V., Factors influencing the antibacterial activity of chitosan and chitosan modified by functionalization, International Journal of Molecular Sciences, 22(14) (2021) 7449. https://doi.org/10.3390/ijms22147449

Barbani N., Lazzeri L., Cristallini C., Cascone M.G., Polacco G., Pizzirani G., Bioartificial materials based on blends of collagen and poly (acrylic acid), Journal of Applied Polymer Science, 72(7) (1999) 971–976. https://doi.org/10.1002/(SICI)1097-4628(19990516)72:7<971::AID-APP13>3.0.CO;2-N

Bellon-Fontaine M., Rault J., Van Oss C., Microbial adhesion to solvents: a novel method to determine the electron-donor/electron-acceptor or Lewis acid-base properties of microbial cells, Colloids and Surfaces B: Biointerfaces, 7(1-2) (1996) 47–53. https://doi.org/10.1016/0927-7765(96)01272-6

Brohem C.A., Cardeal S., Tiago M., Soengas M.S., Barros M., Maria-Engler S.S., Artificial skin in perspective: concepts and applications, Pigment Cell & Melanoma Research, 24(1) (2011) 35–50. https://doi.org/10.1111/j.1755-148X.2010.00786.x

Chavasit V., Kienzle-Sterzer C., Torres J.A., Formation and characterization of an insoluble polyelectrolyte complex: chitosan-polyacrylic acid, Polymer Bulletin 19 (1988) 223–230. https://doi.org/10.1007/BF00255376

Chellat F., Tabrizian M., Dumitriu S., Chornet E., Magny P., Rivard H., Yahia H., In vitro and in vivo biocompatibility of chitosan-xanthan polyionic complex, Journal of Biomedical Materials Research, 51(1) (2000) 107–116. https://doi.org/10.1002/(SICI)1097-4636(200007)51:1<107::AID-JBM14>3.0.CO;2-F

Chemaly R.F., Simmons S., Dale C., Ghantoji S.S., Rodriguez M., Gubb J., Stachowiak J., Stibich M., The role of the healthcare environment in the spread of multidrug-resistant organisms: update on current best practices for containment, Therapeutic Advances in Infectious Disease,2(3-4)(2014)79–90.https://doi.org/10.1177/2049936114543287

Choi J., Rubner M.F., Influence of the degree of ionization on weak polyelectrolyte multilayer assembly, Macromolecules, 38 (1) (2005) 116–124. https://doi.org/10.1021/ma048596o

Dancer S.J., Controlling hospital-acquired infection: focus on the role of the environment and new technologies for decontamination, Clinical Microbiology Reviews, 27(4) (2014) 665–690. https://doi.org/10.1128/CMR.00020-14

Dautzenberg H., Karibyants N., Polyelectrolyte complex formation in highly aggregating systems. Effect of salt: response to subsequent addition of NaCl, Macromolecular Chemistry and Physics, 200(1) (1999) 118–125. https://doi.org/10.1002/(SICI)1521-3935(19990101)200:1<118::AID-MACP118>3.0.CO;2-K

De la Torre P.M., Torrado S., Torrado S., Interpolymer complexes of poly (acrylic acid) and chitosan: influence of the ionic hydrogel-forming medium, Biomaterials, 24(8) (2003) 1459–1468. https://doi.org/10.1016/S0142-9612(02)00541-0

Feng P., Luo Y., Ke C., Qiu H., Wang W., Zhu Y., Hou R., Xu L., Wu S., Chitosan-based functional materials for skin wound repair: mechanisms and applications, Frontiers in Bioengineering and Biotechnology, 9 (2021) 650598. https://doi.org/10.3389/fbioe.2021.650598

Goy R.C., Morais S.T., Assis O.B., Evaluation of the antimicrobial activity of chitosan and its quaternized derivative on *E. Coli* and *S. Aureus* growth, Revista Brasileira de Farmacognosia, 26(1) (2016) 122–127. https://doi.org/10.1016/j.bjp.2015.09.010

Gratzl G., Walkner S., Hild S., Hassel A.W., Weber H.K., Paulik C., Mechanistic approaches on the antibacterial activity of poly (acrylic acid) copolymers, Colloids and Surfaces B: Biointerfaces, 126 (2015) 98–105. https://doi.org/10.1016/j.colsurfb.2014.12.016

Hatakeyama H., Hatakeyama T., Interaction between water and hydrophilic polymers, Thermochimica Acta, 308(1–2) (1998) 3–22. https://doi.org/10.1016/S0040-6031(97)00325-0

Hu Y., Jiang X., Ding Y., Ge H., Yuan Y., Yang C., Synthesis and characterization of chitosan–poly (acrylic acid) nanoparticles, Biomaterials, 23(15) (2002) 3193–3201. https://doi.org/10.1016/S0142-9612(02)00071-6

Jeon S.J., Oh M., Yeo S., Galvão K.N., Jeong K.C., Underlying mechanism of antimicrobial activity of chitosan microparticles and implications for the treatment of infectious diseases, PLOS ONE, 9(3) (2014) e92723. https://doi.org/10.1371/journal.pone.0092723

Jozaghkar M.R., Azar A.S., Ziaee F., Mirtaleb F., Preparation, assessment, and swelling study of amphiphilic acrylic acid/chitosan-based semi-interpenetrating hydrogels, Turkish Journal of Chemistry, 46(2) (2022) 499–505. https://doi.org/10.3906/kim-2109-50

Katiyar R.S., Jha P.K., Phase behavior of aqueous polyacrylic acid solutions using atomistic molecular dynamics simulations of model oligomers, Polymer, 114 (2017) 266–276. https://doi.org/10.1016/j.polymer.2017.03.007

Kong M., Chen X.G., Liu C.S., Liu C.G., Meng X.H., Yu L.J., Antibacterial mechanism of chitosan microspheres in a solid dispersing system against *E. Coli*, Colloids and Surfaces B: Biointerfaces, 65(2) (2008) 197–202. https://doi.org/10.1016/j.colsurfb.2008.04.003

Kong M., Chen X.G., Xing K., Park H.J., Antimicrobial properties of chitosan and mode of action: a state of the art review, International Journal of Food Microbiology, 144(1) (2010) 51–63. https://doi.org/10.1016/j.ijfoodmicro.2010.09.012

Li Y., Asadi A., Monroe M.R., Douglas E.P., PH effects on collagen fibrillogenesis in vitro: electrostatic interactions and phosphate binding, Materials Science and Engineering: C, 29(5) (2009) 1643–1649. https://doi.org/10.1016/j.msec.2009.01.001

Liu H., Du Y., Wang X., Sun L., Chitosan kills bacteria through cell membrane damage, International Journal of Food Microbiology, 95(2) (2004) 147–155. https://doi.org/10.1016/j.ijfoodmicro.2004.01.022

Luo Y., Wang, Q., Recent development of chitosan-based polyelectrolyte complexes with natural polysaccharides for drug delivery, International Journal of Biological Macromolecules, 64 (2014) 353–367. https://doi.org/10.1016/j.ijbiomac.2013.12.017

Meka V.S., Sing M.K., Pichika M.R., Nali S.R., Kolapalli V.R., Kesharwani P., A comprehensive review on polyelectrolyte complexes, Drug Discovery Today, 22(11) (2017) 1697–1706. https://doi.org/10.1016/j.drudis.2017.06.008

Mohamed N.A., Fahmy M.M., Synthesis and antimicrobial activity of some novel cross-linked chitosan hydrogels, International Journal of Molecular Sciences, 13(9) (2012) 11194–11209. https://doi.org/10.3390/ijms130911194

Morykwas M.J., Thornton J.W., Bartlett R.H., Zeta potential of synthetic and biological skin substitutes: effects on initial adherence, Plastic and Reconstructive Surgery, 79(5) (1987) 732–739. https://doi.org/10.1097/00006534-198705000-00009

Nandakumar V., Physicochemical aspects of bacterial adhesion on surfaces and strategies to remove adhered bacteria from surfaces, PhD. Thesis, University of Florida 2018. <https://ufdcimages.uflib.ufl.edu/UF/E0/05/20/40/00001/NANDAKUMAR_V.pdf> accessed 07052024.

Oh J.K., Yegin Y., Yang F., Zhang M., Li J., Huang S., Verkhoturov S.V., Schweikert E.A., Perez-Lewis K., Scholar E.A., Taylor T.M., Castillo A., Cisneros-Zevallos L., Min Y., Akbulut M., The influence of surface chemistry on the kinetics and thermodynamics of bacterial adhesion, Scientific Reports, 8(1) (2018) 17247. https://doi.org/10.1038/s41598-018-35343-1

Owens D.K., Wendt R.C., Estimation of the surface free energy of polymers, Journal of Applied Polymer Science, 13 (1969) 1741–1747. https://doi.org/10.1002/app.1969.070130815

Pelletier C., Bouley C., Cayuela C., Bouttier S., Bourlioux P., Bellon-

Fontaine M.N., Cell surface characteristics of Lactobacillus casei subsp. Casei, Lactobacillus paracasei subsp. Paracasei, and Lactobacillus rhamnosus strains, Applied and Environmental Microbiology, 63(5) (1997) 1725–1731. https://doi.org/10.1128/aem.63.5.1725-1731.1997

Rizwan M., Yahya R., Hassan A., Yar M., Azzahari A.D., Selvanathan V., Sonsudin F., Abouloula C.N., PH sensitive hydrogels in drug delivery: brief history, properties, swelling, and release mechanism, material selection and applications, Polymers, 9(4) (2017) 137. https://doi.org/10.3390/polym9040137

Singla A.K., Chawla M., Chitosan: some pharmaceutical and biological aspects—an update, Journal of Pharmacy and Pharmacology, 53 (2010) 1047–1067. https://doi.org/10.1211/0022357011776441

Sionkowska A., Wisniewski M., Skopinska J., Kennedy C., Wess T., Molecular interactions in collagen and chitosan blends, Biomaterials, 25(5) (2004) 795–801. https://doi.org/10.1016/S0142-9612(03)00595-7

Tang H., Zhang P., Kieft T.L., Ryan S.J., Baker S.M., Wiesmann W.P., Rogelj S., Antibacterial action of a novel functionalized chitosan-arginine against Gram-negative bacteria, Acta Biomaterialia, 6(7) (2010) 2562–2571. https://doi.org/10.1016/j.actbio.2010.01.002

Topuzoğullari M., Effect of polyelectrolyte complex formation on the antibacterial activity of copolymer of alkylated 4-vinylpyridine, Turkish Journal of Chemistry, 44(3) (2020) 634–646. https://doi.org/10.3906/kim-1909-95

Tsao C.T., Chang C.H., Lin Y.Y., Wu M.F., Wang J., Han J.L., Hsieh K.H., Antibacterial activity and biocompatibility of a chitosan–γ-poly (glutamic acid) polyelectrolyte complex hydrogel, Carbohydrate Research, 345(12) (2010) 1774–1780. https://doi.org/10.1016/j.carres.2010.06.002

WHO (World Health Organization), Antimicrobial resistance, (2023). <https://www.who.int/news-room/fact-sheets/detail/antimicrobial-resistance> accessed07052024.

Yilmaz Atay H., Antibacterial activity of chitosan-based systems, in: Jana S., Jana S. (Eds.), Functional Chitosan: Drug Delivery and Biomedical Applications, Springer Singapore, Singapore, 2019, pp. 457–489, ISBN: 978-981-15-0263-7. https://doi.org/10.1007/978-981-15-0263-7_15

Zhang X., Zhang Q., Yan T., Jiang Z., Zhang X., Zuo Y.Y., Quantitatively predicting bacterial adhesion using surface free energy determined with a spectrophotometric method, Environmental Science & Technology, 49(10) (2015) 6164–71. https://doi.org/10.1021/es5050425

## Authors' Short Biographies

**Dr. Vasanthakumar Balasubramanian** works as a Research Assistant Scientist in Materials Science and Engineering at the University of Florida. He has a B.Tech. degree in Chemical Engineering from Bharathidasan University, an M.Tech degree in Biotechnology from Anna University, and a Ph.D. degree in Materials Engineering from the Indian Institute of Science (IISc), Bangalore, India. His research interests include biomaterials, biomineral separation, biofilms, nanotechnology, and interfacial engineering. One of his research interests is using nanoparticles and biopolymers to remove microbes from substrates.

**Prof. Brij M. Moudgil** is a Distinguished Professor of Materials Science and Engineering (Emeritus) at the University of Florida. He received his B.E from the Indian Institute of Science, Bangalore, India and his M.S and Eng.Sc.D degrees from Columbia University, New York. His research interests include surfactant and polymer adsorption, dispersion and aggregation of fine particles, adhesion and removal of microbes from surfaces, synthesis of functionalized nanoparticles, antiscaling and surfactant-mediated corrosion inhibitors, photocatalytic degradation of hazardous microbes, and nanotoxicity. He has published more than 400 technical papers and has been awarded over 33 patents. He is a member of the U.S. National Academy of Engineering.

KONA Powder and Particle Journal

KONA Powder and Particle Journal No. 42 (2025) 261–267/https://doi.org/10.14356/kona.2025015 Original Research Paper

# Compression of an Assembly of Bi-Dispersed Particles†

**Ching S. Chang[1]*, Jason Chao[1] and Yibing Deng[2]**

[1] *Department of Civil and Environmental Engineering, University of Massachusetts, USA*
[2] *Shanghai Urban Construction Vocational College, China*

A compression model that elucidates the compressibility of a granular soil assembly is useful for engineering and mechanical applications. While the literature offers numerous compressibility models for granular soils, a significant limitation arises because these models overlook the impact of soil composition. Typically, soils consist of a blend of sand and silt as a result of geological processes. Moreover, empirical observations indicate a substantial influence of silt content on the compressional behavior of bi-dispersed granular soils. This study introduces an approach grounded in a more rigorous theoretical foundation for predicting the compression of bi-dispersed packings. The analytical method is based on Edwards thermodynamics, which is a realm of physics. Within this framework, the analytical method incorporates the excess free volume resulting from the dispersity of the bi-dispersed particle packing. An evaluation was conducted to validate the model's applicability by comparing the predictions with the experimental results for Hokksund sand-silt mixtures.

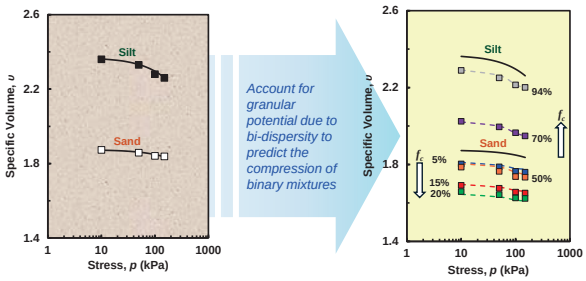


**Keywords:** compression, powder, particle, thermodynamics, bi-dispersed packing

## 1. Introduction

The soil compressibility is a vital engineering property that critically influences optimizing design protocols and comprehensive assessments. A compression model that elucidates the relationship between stress and void ratio is very useful for analyzing soil foundations or earth structures (Lehane and Fahey, 2002) and is also an essential component of critical state soil mechanics.

Numerous compressibility models for granular soils have been proposed (Chong and Santamarina, 2016; Hardin, 1987; Meidani et al., 2017; Pestana and Whittle, 1995; Schofield and Wroth, 1968; Vesić and Clough, 1968). These models typically use empirical methodologies that incorporate initial density, soil type, and applied stress. However, a notable drawback exists in these models, as they neglect the impact of soil composition. This oversight is significant because natural soils or man-made fills typically comprise a combination of sand and silt due to geological processes such as erosion, breakage, and weathering. Furthermore, it has been observed that the fractional content of silt (fines content $f_c$) has a substantial influence on the compressional behavior of granular soils in experiments (Carrera et al., 2011; Konishi et al., 2007; Lipiński et al., 2017; Lupogo, 2009; Xu et al., 2009; Yang et al., 2006; Zuo and Baudet, 2020) and in discrete element simulations (Minh et al., 2014; Wiącek et al., 2017). Thus, a comprehensive understanding of the effects of fines content is essential for engineers when assessing the deformation characteristics of granular soils. It is highly desirable to have a model that explicitly accounts for the effect of fines content on compressibility.

The current literature offers only a limited number of approaches for examining how the fines content influences the compressional behavior of sand-silt mixtures. Thevanayagam et al. (2002) introduced the concept of the intergranular void ratio for a sand silt mixture, while Cabalar and Hasan (2013) and Monkul and Ozden (2007) empirically correlated the intergranular void ratio with compressibility. Chang et al. (2017) proposed a compression model for sand-silt mixtures, in which a parameter is empirically determined as a function of fines content.

In this study, we propose an approach with a more rigorous theoretical foundation for predicting the compression of a sand-silt mixture. The analytical method was based on Edwards thermodynamics for granular materials. Within this framework, we hypothesized that the presence of excess free-volume potential in bi-dispersed particle packing (Chang, 2022a) is similar to the excess free energy observed in chemical solutions containing two species of molecules. Using this concept, we modeled the compressibility of binary mixtures of granular soil with varying fines content, considering the potential of excess free volume to cause additional volume reduction during compression.

† Received 7 May 2024; Accepted 3 July 2024
J-STAGE Advance published online 10 August 2024
* Corresponding author: Ching S. Chang;
Add: 130 Natural Resources Road, Marston Hall, Amherst, MA 01003, USA
E-mail: chang@ecs.umass.edu
TEL: +1-413-545-5401

In the subsequent sections, we first briefly describe the concept of excess free volume and define a granular potential related to the volume change in a bi-dispersed packing. Then, the compression model framework was formulated considering the granular potential of a bi-dispersed packing. To validate our proposed model, we compared the predicted outcomes with the experimental results for Hokksund sand-silt mixtures. The effect of the fines content on the compressibility is discussed, and the applicability of the model is highlighted.

## 2. Modeling concept

The decrease in volume due to packing compression typically involves two main aspects: (1) the elastic deformation of solid particles, and (2) the reduction of void volume resulting from particle rearrangement, which is treated as plastic deformation in an elastic-plasticity framework. As the magnitude of elastic deformation is typically minimal, this investigation disregards it, and compressibility is only considered due to the rearrangement of particles under stress. This rearrangement reduces the number of voids among particles, thereby decreasing the void ratio.

Here, we focus solely on bi-dispersed packings. The void ratio is assumed to be influenced by two main variables: $e(p, y_2)$, where $y_2$ is the solid fraction of fine particles (note: the solid fraction of coarse particles $y_1 = 1 - y_2$ in a bi-dispersed mixture).

### 2.1 Compression of bi-dispersed packing

For a mono-dispersed packing assembly comprising N particles, the total assembly volume $V$ is given by $V = v^o N$. Here, $v^o$ is termed particle volume, representing the average volume of a solid particle and its surrounding void space. The magnitude of $v^o$ is dependent on the density and the applied pressure of the packing.

In the case of bi-dispersed packing, the total granular system volume $V = v_1N_1 + v_2N_2$. Here, $N_1$ and $N_2$ are number of particles in species 1 and 2, respectively; $v_1$ and $v_2$ are the partial particle volumes associated with species 1 and 2, respectively.

We note that under the same applied pressure and relative density, the particle volume $v_i^0$ in a mono-dispersed packing differs from the partial particle volume $v_i$ in a bi-dispersed packing. The change in volume from $v_i^0$ to $v_i$ arises from particle interactions due to the mixing of two species.

This phenomenon resembles the change in mole energy observed in mixed chemical solutions, which results from the interaction between two species of molecules. Analogous to free energy in thermodynamics, we consider the concept of "free volume," representing the available void volume in a packing that can be changed during particle rearrangement.

Thus, we adopt an approach akin to the "Gibbs excess free energy" concept in classic thermodynamics (Silbey et al., 2004). In this context, we define the *excess free volume* $\Delta v_i$ of each species as

$$v_i = v_i^0 - \Delta v_i \tag{1}$$

In conventional usage, "excess free energy" typically denotes the additional energy available for performing work resulting from chemical reactions among multiple species (Silbey et al., 2004). However, in this case, the *excess free volume* $\Delta v_i$ represents the extra volume available for reduction due to the size difference between the two particle species.

From **Eqn. (1)**, we observe that the difference between the monoparticle volume and partial particle volume (i.e., $v_i^0 - v_i$) signifies the volume reduction potential of each species. In a mixture of two species, the excess free volume of both species is diminished, resulting in a reduction in the overall volume of the packing mixture.

### 2.2 Excess free volume

To quantify the excess free volume in each species, we determined the partial particle volumes $v_1$ and $v_2$. For a bi-dispersed packing, the total granular system volume $V$ is an extensive variable and is homogeneous of degree 1 (Silbey et al., 2004); thus, according to Euler's homogeneous function theorem, the total volume of a mixture is given by

$$V(N_1, N_2) = \frac{\partial V}{\partial N_1} N_1 + \frac{\partial V}{\partial N_2} N_2 = v_1 N_1 + v_2 N_2 \tag{2}$$

This relationship is critical because it reveals how the partial particle volumes are related to the partial derivative with respect to the number of particles in each species, providing a central understanding for estimating their values.

Using a statistical mechanics approach, we represent the global packing configuration as a set of microstates. Each microstate is a local configuration of a single particle and its nearest neighbors. Using this model, we analyze the values of partial particle volumes $v_1$ and $v_2$.

**Eqn. (2)** provides a method for measuring the partial particle volume of a species. The partial particle volume $v_1$ can be defined as $\partial V/\partial N_1$, where the change in assembly volume d$V$ is caused by adding a small number (d$N_1$) of large particles to the mixture while keeping the total number $N_2$ of small particles constant. The partial particle volume $v_2$ can be determined similarly.

To consider the local configuration, we deliberately considered a single particle added to the mixture at a random location. By repeating the process $M$ times, we obtain $M$ different local configurations for the added particle and its neighboring particles. Then, this statistical mechanics approach can be employed to obtain the value of $\partial V/\partial N_1$ from this set of local configurations.

However, directly determining $v_1$ and $v_2$ through statistical mechanics is challenging due to the lack of detailed knowledge about the complete packing structure, which makes it impractical to generate all possible microstates of the system. Nevertheless, this concept can help us estimate the possible ranges of $v_1$ and $v_2$ by analyzing the following extreme scenarios of microstates.

### (1) Inserting a large particle:

a) If the surrounding particles are all large, as shown in **Fig. 1(a)**, the added particle displaces them, increasing the packing volume. This scenario is akin to a uniformly sized packing; thus, the volume change $\Delta V$ is comparable to the baseline particle volume $v_1^0$. Thus, $v_1 = v_1^0$ and the excess free volume is zero.

b) Conversely, if the surrounding particles are all small (**Fig. 1(b)**, the void volume around the added large particle varies with the sizes of the neighboring particles. When the large particle is surrounded by tiny particles, the void volume is minimized. In this case, $\Delta V$ is similar to the volume of the solid particle $v_1^g$, hence $v_1 = v_1^g$, and the excess free volume is $\left(v_1^0 - v_1^g\right)$.

Considering both extreme scenarios, the possible range of excess free volume for the large-particle species was determined to range from 0 to $\left(v_1^0 - v_1^g\right)$.

### (2) Inserting a small particle:

a) When all surrounding particles are small, as shown in **Fig. 1(c)**, the local configuration resembles uniform packing. The volume change $\Delta V$ due to inserting the small particle is similar to the baseline particle volume $v_2^0$, thus $v_2 = v_2^0$, and the excess free volume is zero.

b) Conversely, if the surrounding particles are all large, as shown in **Fig. 1(d)**, and the inserted particle is significantly smaller than the available void space, it remains mobile despite the surrounding particles being jammed (mechanically stable). This particle is called a rattler particle. In this scenario, the change in system volume $\Delta V$ is negligible, so $v_2 = 0$, and the excess free volume is $v_2^0$.

Considering both extreme scenarios, the possible excess free volume for the small-particle species was determined to range from 0 to $v_2^0$.

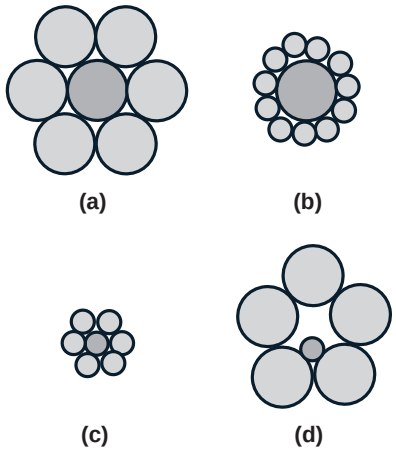


**Fig. 1** Four extreme scenarios: **(a)** a large particle surrounded by large particles, **(b)** a large particle surrounded by small particles, **(c)** a small particle surrounded by small particles, and **(d)** a small particle surrounded by large particles.

## 2.3 Determination of granular potential

For convenience, we express the excess free volume as a dimensionless variable. The granular potential $\mu_i$ of the $i$th species was defined as excess free volume per unit solid volume, i.e., $\mu_i = \Delta v_i / v_i^g$ .

In this context, all volumes are replaced by specific volumes. **Eqn. (1)** becomes $\upsilon_i = \upsilon_i^0 - \mu_i$, where $\upsilon_i^0$ is the specific volume of the $i$th mono-dispersed packing, and $\mu_i$ is the granular potential. And **Eqn. (2)** can be written as

$$\upsilon = \upsilon_1 y_1 + \upsilon_2 y_2 \tag{3}$$

Here, $y_1$ and $y_2$ are the solid fractions of the large and small particles, respectively.

By using **Eqn. (3)** and $\upsilon_i = \upsilon_i^0 - \mu_i$, it can be expressed as

$$\upsilon = \sum_{i=1}^{2} \upsilon_i^0 y_i - \sum_{i=1}^{2} \mu_i y_i \tag{4}$$

Note that, **Eqn. (4)** delineates the free volume into two components: the first term represents the volume average of the two components, representing the volume without particle interactions between the two species, and the second term represents the volume reduction due to the release of granular potential from the interaction between the two species. The second term is also defined as the Gibbs volume potential given by

$$G = \mu_1 y_1 + \mu_2 y_2 \tag{5}$$

Based on the previous analysis, the range of the granular potential $\mu_1$ extends from 0 to $(\upsilon_1^0 - 1)$, while the range of $\mu_2$ spans from 0 to $\upsilon_2^0$. This can be expressed as follows:

$$\mu_1 = \alpha_1(\upsilon_1^0 - 1); \quad \mu_2 = \alpha_2 \upsilon_2^0 \tag{6}$$

Here both $0 < \alpha_1 < 1$ and $0 < \alpha_2 < 1$. The specific values of $\alpha_1$ and $\alpha_2$ are dependent on the nature of the interactions between species, which are influenced by the overall structure and composition of the assembly.

To determine the values of $\alpha_1$ and $\alpha_2$, we assume variables $\alpha_1$ and $\alpha_2$ are functions of the characteristic length $\lambda$ introduced for the bi-dispersed packing, falling within the range $d_1 \geq \lambda \geq d_2$. The variable $\lambda$ is an internal variable whose value depends on the overall structure and composition of the assembly.

As elucidated by Chang (2022a), in the context of particle filling and embedment mechanisms, the expressions of granular potential for the two species are given as follows:

$$\mu_1 = (v_1^0 - 1)\left(1 - \frac{\lambda}{d_1}\right)^{\eta}; \quad \mu_2 = v_2^0\left(1 - \frac{d_2}{\lambda}\right)^{\eta} \tag{7}$$

It is important to note that, in **Eqn. (4)**, when the second term (granular potential) is zero, for the example of the size ratio between the two species equaling 1 (i.e., $\lambda = d_1 = d_2$, see **Eqn. (7)**), the specific volume versus fines content $f_c$ forms a line identical to the line $v_1^0 y_1 + v_2^0 y_2$ shown in **Fig. 2**, which represents the upper bound for the granular mixture with zero interactions between species.

Conversely, when the size ratio approaches infinity ($d_2 \ll d_1$), the predicted relationship is illustrated in **Fig. 2** by two lines AB and BC, which respectively represent the lower bounds of the granular mixture. For the range AB, $\lambda = d_1 \gg d_2$, **Eqn. (7)** shows that $\mu_1 = 0$, and $\mu_2 = v_2^0$. The equation of AB is $(v_1^0 y_1 + v_2^0 y_2) - v_2^0 y_2$. For the range BC, $\lambda = d_2 \ll d_1$, **Eqn. (7)** shows that $\mu_2 = 0$, and $\mu_1 = v_1^0 - 1$. The equation of BC is given by $(v_1^0 y_1 + v_2^0 y_2) - (v_1^0 - 1) y_2$.

The curve with symbols in **Fig. 2** represents measured specific volumes for the Hokksund sand-silt mixture. At $f_c$ = 20 %, the granular potential $G$ calculated from **Eqn. (5)** is the distance from the upper bound line to the measured curve. In general, considering the overall structure and composition of the assembly, the granular potential of a packing lies between the upper bound and the lower bound, as calculated from **Eqn. (7)** using the values of $\lambda$ and $\eta$. The exponents $\eta$ is a material constant that depends on the shape and surface friction of particles and can be calibrated from the measured volume of one specimen with a particular fines content $f_c$ (Chang, 2022a,b).

The characteristic length $\lambda$ can be determined by the second law of thermodynamics. In the case of Edwards thermodynamic theory, the second law of thermodynamics stipulates that the Gibbs volume potential must be minimized for a closed system to reach equilibrium at constant compactivity (Chang, 2022b). Since the parameters $e_1^0$, $d_i$, $y_i$, $\eta$ are constant, the following condition holds.

$$\frac{dG}{d\lambda} = \frac{d}{d\lambda}\left(\mu_1(v_1^0, \lambda) y_1 + \mu_2(v_2^0, \lambda) y_2\right) = 0 \tag{8}$$

The two terms in this equation can be regarded as the volume transfers between the two species, and their zero-sum ensures the condition of steady-state volume at equilibrium. This characteristic allows us to determine the value of $\lambda$, thus to calculate the granular potentials $\mu_i$ for each species. Consequently, this principle provides a straightforward method for predicting the specific volume of a mixture based on the specific volumes of its individual components.

This theory's validity has been confirmed by verifying the maximum and minimum void ratios through ASTM compacted procedures for soil mixtures of various types (Chang, 2022b).

To illustrate the prediction process, an example of a Hooksund sand-silt mixture is used, where the silt volume fraction $y_2$ = 0.2. The sand particles were 0.45 mm in size, while the silt particles were 0.032 mm. At a pressure of 10 kPa, the specific volume for sand is $v_i^0$ = 1.873, and for silt, it's $v_2^0$ = 2.36.

We initially assumed a trial value of $\eta$ = 3.6. The Gibbs volume potential $G$ of the packing (see **Eqns. (5)** and **(7)**) was calculated for the range $0.45 \geq \lambda \geq 0.032$ as shown in **Fig. 3**. The minimum of $G$ corresponds to $\lambda$ = 0.2637. At this value of $\lambda$, $\mu_1 y_1$ = 0.029 for sand particles and $\mu_2 y_2$ = 0.296 for silt particles. The volume reduction potential was $G$ = 0.325.

The specific volume of the mixture can then be obtained in **Eqn. (4)**. With $v_1^0 y_1 + v_2^0 y_2 = 1.9704$ and $G$ = 0.325, the calculated specific volume for the bi-dispersed packing at fines content $f_c$ = 0.2 is 1.6504 (i.e., 1.9704 − 0.325).

If the predicted value does not match the measured value, the value of $\eta$ can be calibrated. Once the correct value of $\eta$ is determined, it can be used to predict specific volumes for any other fines content. The calculated curve is plotted as a solid line in **Fig. 2** and compared with the measured results represented by symbols.

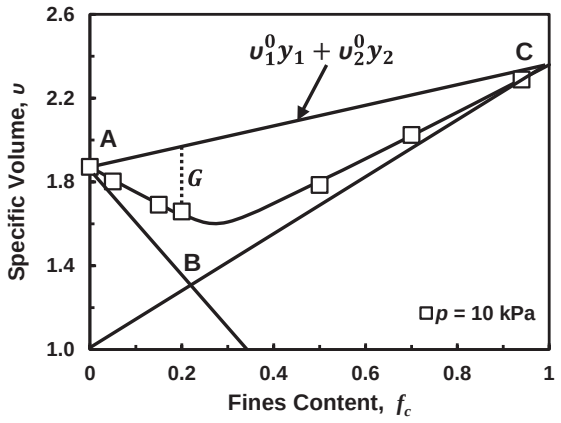


**Fig. 2** The specific volume versus fines content. The line of AC is the upper bound, and the line of ABC is the lower bound of granular potential. Adapted with permission from Ref.(Yang et al., 2006). Copyright: (2006) ASTM International.

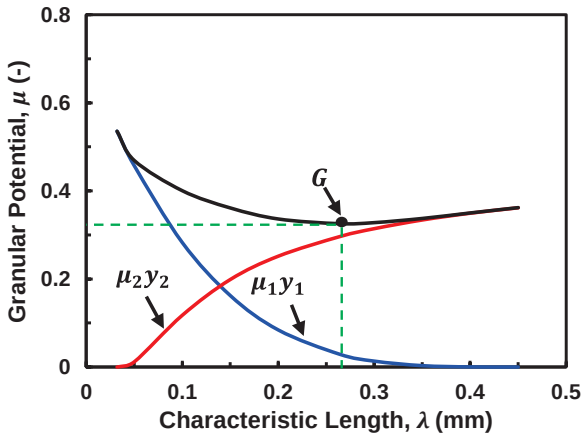


**Fig. 3** Calculated granular potential of each species and Gibbs volume potential for the bi-dispersed packing.

## 3. Experimental data

To verify the proposed model for soil mixtures under static load compression, we selected experiments on the sand-silt mixtures reported by Yang et al. (2006). These experiments involve various particle size combinations. For the mixtures, the mean sizes ($d_{50}$) of the sand and silt particles were 0.45 mm and 0.032 mm, respectively, resulting in a particle size ratio of 14. The soil mixtures were composed of Hokksund sand and nonplastic Chenbei silt. Samples were prepared with fines contents ranging from 5 % to 94 %. All samples were prepared using moisture tamping to achieve a relative density ($D_r$) of 20 %. This ensured that the observed difference in compressibility of the samples was due to the fines content of the soil mixture and not the relative density.

During compression testing, samples were subjected to isotropic loading up to 200 kPa. At this stress level, no evidence of particle crushing was observed in the compression experiments, ensuring that the fines content remained constant throughout each test.

## 4. Results

To understand how static compression affects bi-dispersed packing, we modify **Eqn. (4)** to accommodate pressure-dependent functions for both $v_i^0$ and $\mu_i$. The modified equation is expressed as follows:

$$v = \sum_{i=1}^{2} v_i^0(p)\, y_i + \sum_{i=1}^{2} \mu_i\left(v_i^0(p), f_c\right) y_i \tag{9}$$

In this equation, $v_i^0(p)$ represents the individual compression behavior of the two components of the mixture. $\mu_i\left(v_i^0(p), f_c\right)$ represents the volume reduction due to the impact of the granular potential resulting from the bi-dispersity of the assembly.

In **Eqn. (9)**, the granular potential $\mu_i$ is a function of $v_i^0(p)$ dependent on applied stress $p$. Once $v_i^0(p)$ is known, the evolution of granular potential $\mu_i$ can be obtained from **Eqns. (7)** and **(8)** following the previously described process.

The expression of $v_i^0(p)$ can be obtained from the individual compression curves of the sand and silt using any phenomenologically based analytical model.

### 4.1 Compression of monodispersed packing

In **Fig. 4**, the two compression curves of sand and silt, which are the components of the Hokksund sand-silt mixture, are displayed as symbols. The sand and silt particle assemblies were compacted to the same relative density ($D_r$ = 20 %). We adopted the compression model proposed by Meidani et al. (2017) to obtain the expressions for the two compression curves.

In this model, the total volume of voids is conceptually divided into two fractions: (1) active void volume, which is subject to reduction and eventual elimination through particle rearrangement, and (2) inactive void volume within interlocked particles, which cannot be further reduced by particle rearrangement.

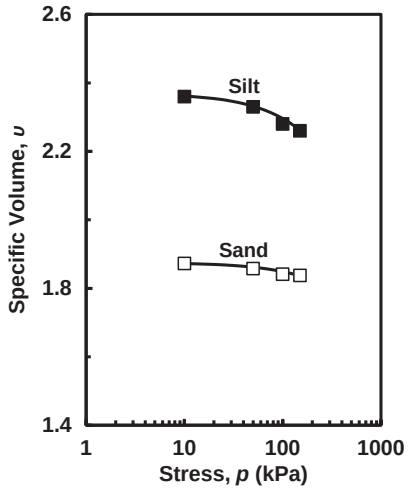


**Fig. 4** Comparison of predicted and measured compression curves for sand and silt of the Hokksund sand-silt mixture. Adapted with permission from Ref.(Yang et al., 2006). Copyright: (2006) ASTM International.

Meidani et al. (2017) observed that the variation of ($\mathrm{d}v$/$\mathrm{d}p$) versus $v$ exhibits linear relationship for several types of sand and silt. The linear relationship can be expressed as follows:

$$\frac{\mathrm{d}v}{\mathrm{d}p} = \alpha\left(v - v_r\right) \tag{10}$$

The parameter $v_r$ represents the inactive part of the specific volume. Let a dimensionless parameter $a = \alpha p_a$, and the integral of this equation becomes

$$v(p, v_0) = \left[v_0 - v_r\right]\exp\left(-\frac{a}{p_a}p\right) + v_r \tag{11}$$

Here $v_0$ is the initial specific volume, $p$ is the applied pressure, and $p_a$ is the atmospheric pressure (101.325 kPa). The model relies on two parameters $a$ and $v_r$, with $v_r$ being the inactive specific volume of the packing and $a$ is a material constant.

In **Fig. 4**, **Eqn. (11)** is used to model the compression curves of the sand and silt. For the sand compression curve, the parameters $v_0 = 1.873$, $v_r = 1.48$, and $a = 0.0611$ are employed, while for the silt compression curve, the parameters $v_0 = 2.360$, $v_r = 1.55$, and $a = 0.0611$ are used. The modeled curves are represented by solid lines, and the measured results are plotted as symbols.

### 4.2 Compression of bi-dispersed packing

In **Fig. 5**, the measured compression data for Hokksund sand-silt mixtures with fines contents ranging from 5 % to 94 % ($f_c$ = 5, 15, 20, 50, 70, and 94 %) are presented as symbols. The influence of the fines content on the

compression curves can be observed from two perspectives: the initial specific volumes and the shape of the compression curves.

At an initial confining pressure of 10 kPa, significant variations were observed in the initial specific volumes for bi-dispersed specimens with different fines contents.

The trend shows that the initial specific volume decreases as the fines content increases up to 20 %, which is caused by the filling of voids between sand particles by silt particles. At a 20 % fines content, the voids between sand particles were nearly filled. Consequently, further increases in fines content beyond 20 % caused the additional silt particles to separate and lose contact, reversing the volume decrease trend and leading to an increase in volume.

These initial specific volumes for all fines contents are shown in **Fig. 5**, which were previously predicted and plotted in **Fig. 2**. The parameter $\eta = 3.6$ was calibrated from the data point at $p = 10$ kPa and $f_c = 0.2$.

The shape of the compression curve can be computed using **Eqn. (9)**. The analytical expressions of the compression curves of sand ($v_i^0(p)$) and silt ($v_2^0(p)$) serve as input information for predicting the compression curves of sand-silt mixtures. With these two functions, the granular potential $\mu_i$ can be obtained from **Eqns. (7)** and **(8)**. The required parameters for predicting the compression curves are summarized as follows:

- To simulate $v_i^0(p)$ for sand: $v_r = 1.48$, $a = 0.0611$.
- To simulate $v_2^0(p)$ for silt: $v_r = 1.55$, $a = 0.0611$.
- To calculate granular potential $\mu_i$: $\eta = 3.6$.

The methods for determining $v_r$ and $a$ are described in **Section 4.1**, and the method for determining $\eta$ is described in **Section 2.3**.

In **Fig. 5**, the two solid lines represent the predicted compression curves of the sand and silt (replotted from **Fig. 4**). The predicted curves for mixtures with different fines content are depicted by dashed lines and are compared with the measured data points represented by symbols. The fines content for each compression curve is indicated on the left or right side of the curve. Initially, the compressibility of the mixture decreases with increasing fines content. However, after reaching 20 % fines content, the trend reversed, and the compressibility increased with further increasing fines content.

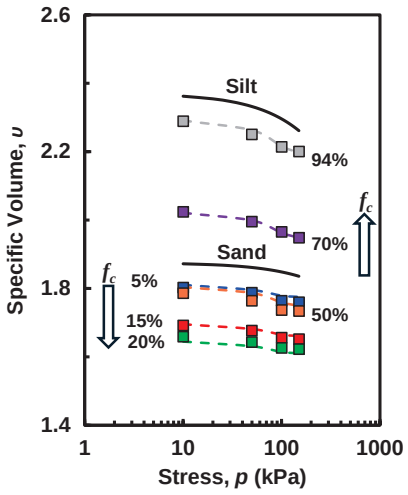


**Fig. 5** Comparison of predicted and measured compression curves for the Hokksund sand-silt mixtures with various fines contents. Adapted with permission from Ref. (Yang et al., 2006). Copyright: (2006) ASTM International.

## 5. Conclusion

The fines content significantly influences the compressibility of bi-dispersed packing. To address this influence, we developed an analytical model grounded in a physics-based methodology for predicting the compression of such mixtures. The proposed model effectively explains the significant variation in the initial specific volume of specimens after compression. Furthermore, it accurately captures the compressibility patterns under various compression loads in soil mixtures with diverse fines contents. Consequently, the notion of granular potential stemming from bi-dispersity emerges as a credible framework for modeling the assembly of bi-dispersed particles. It is worth noting that this model is applicable only to mixtures of dry particles with particle sizes greater than 2 μm. The effects of hydration, capillary, and cohesive forces exhibit in wet particles are not considered.

## Acknowledgments

This work was supported by the National Science Foundation of US under the research grant CMMI-1917238.

## Data Availability Statement

Data on compression curves for sand and silt of the Hokksund sand-silt mixture are available publicly in J-STAGE Data (https://doi.org/10.50931/data.kona.27139746).

## Nomenclature

| | |
|---|---|
| $d_i$ | particle size (mm) |
| $d_{50}$ | the mean particle size (mm) |
| $D_r$ | relative density (-) |
| $e$ | void ratio (-) |
| $e_i^0$ | void ratio of mono-dispersed species (-) |
| $f_c$ | fines content (solid fraction of small particles) |
| $G$ | Gibbs volume potential (-) |
| $N_i$ | number of particles in the $i$th species (-) |
| $p$ | applied pressure (Pa) |
| $v_i$ | partial particle volume of *the* $i$th species (mm$^3$) |
| $v_i^0$ | particle volume of the *the* $i$th species (mm$^3$) |
| $v_i^g$ | volume of a solid particle of the $i$th species (mm$^3$) |
| $\Delta v_i$ | the excess free volume of *the* $i$th species (mm$^3$) |
| $V$ | total assembly volume (mm$^3$) |
| $V_s$ | solid volume (mm$^3$) |
| $y_i$ | solid volume fraction of the $i$th species (-) |
| $\lambda$ | characteristic length (mm) |
| $\mu_i$ | granular potential of the $i$th species (-) |

$\upsilon$ specific volume (-)
$\upsilon_0$ initial specific volume (-)
$\upsilon_i$ partial specific volume of the *i*th species (-)
$\upsilon_i^0$ specific volume of *the i*th species (-)
$\upsilon_r$ inactive specific volume (-)
$\eta$ material constant (-)

## References


Cabalar A.F., Hasan R.A., Compressional behaviour of various size/shape sand-clay mixtures with different pore fluids, Engineering Geology, 164 (2013) 36–49. https://doi.org/10.1016/j.enggeo.2013.06.011

Carrera A., Coop M., Lancellotta R., Influence of grading on the mechanical behaviour of Stava tailings, Géotechnique, 61 (2011) 935–946. https://doi.org/10.1680/geot.9.P.009

Chang C.S., Jamming density and volume-potential of a bi-dispersed granular system, Geophysical Research Letters, 49 (2022a) e2022GL098678. https://doi.org/10.1029/2022GL098678

Chang C.S., Deng Y., Compaction of bi-dispersed granular packing: analogy with chemical thermodynamics, Granular Matter, 24 (2022b) 58. https://doi.org/10.1007/s10035-022-01219-5

Chang C.S., Meidani M., Deng Y., A compression model for sand–silt mixtures based on the concept of active and inactive voids, Acta Geotechnica, 12 (2017) 1301–1317. https://doi.org/10.1007/s11440-017-0598-1

Chong S.-H., Santamarina J.C., Soil compressibility models for a wide stress range, Journal of Geotechnical and Geoenvironmental Engineering, 142 (2016) 06016003. https://doi.org/10.1061/(ASCE)GT.1943-5606.0001482

Hardin B.O., 1-D Strain in normally consolidated cohesionless soils, Journal of Geotechnical Engineering, 113 (1987) 1449–1467. https://doi.org/10.1061/(ASCE)0733-9410(1987)113:12(1449)

Konishi Y., Hyodo M., Ito S., Compression and undrained shear characteristics of sand-fines mixtures with various plasticity, Doboku Gakkai Ronbunshuu C, 63 (2007) 1142–1152. https://doi.org/10.2208/jscejc.63.1142

Lehane B., Fahey M., A simplified nonlinear settlement prediction model for foundations on sand, Canadian Geotechnical Journal, 39 (2002) 293–303. https://doi.org/10.1139/T01-091

Lipiński M.J., Wdowska M.K., Jaroń Ł., Influence of fines content on consolidation and compressibility characteristics of granular materials, IOP Conference Series: Materials Science and Engineering, 245 (2017) 032062. https://doi.org/10.1088/1757-899X/245/3/032062

Lupogo K., Effects of fines on mechanical behaviour of sandy soils, master thesis, Delft University of Technology, (2009). <https://repository.tudelft.nl/record/uuid:f4b5b6d0-8b00-44da-8011-cd664bfa96bd>accessed05072024.

Meidani M., Chang C.S., Deng Y., On active and inactive voids and a compression model for granular soils, Engineering Geology, 222 (2017) 156–167. https://doi.org/10.1016/j.enggeo.2017.03.006

Minh N.H., Cheng Y.P., Thornton C., Strong force networks in granular mixtures, Granular Matter, 16 (2014) 69–78. https://doi.org/10.1007/s10035-013-0455-3

Monkul M.M., Ozden G., Compressional behavior of clayey sand and transition fines content, Engineering Geology, 89 (2007) 195–205. https://doi.org/10.1016/j.enggeo.2006.10.001

Pestana J.M., Whittle A.J., Compression model for cohesionless soils, Geotechnique, 45 (1995) 611–631. https://doi.org/10.1680/geot.1995.45.4.611

Schofield A.N., Wroth C.P., Critical State Soil Mechanics, McGraw-Hill, Maidenhead, England, 1968, ISBN: 978-0070940482.

Silbey R.J., Alberty R.A., Bawendi M.G., Physical Chemistry, 4th edition, Wiley, 2004, ISBN: 978-0471215042.

Thevanayagam S., Shenthan T., Mohan S., Liang J., Undrained fragility of clean sands, silty sands, and sandy silts, Journal of Geotechnical and Geoenvironmental Engineering, 128 (2002) 849–859. https://doi.org/10.1061/(ASCE)1090-0241(2002)128:10(849)

Vesić A.S., Clough G.W., Behavior of granular materials under high stresses, Journal of the Soil Mechanics and Foundations Division, 94 (1968) 661–688. https://doi.org/10.1061/JSFEAQ.0001134

Wiącek J., Parafiniuk P., Stasiak M., Effect of particle size ratio and contribution of particle size fractions on micromechanics of uniaxially compressed binary sphere mixtures, Granular Matter, 19 (2017) 34. https://doi.org/10.1007/s10035-017-0719-4

Xu M., Song E.X., Cao G., Compressibility of broken rock-fine grain soil mixture, Geomechanics and Engineering, 1 (2009) 169–178. https://doi.org/10.12989/gae.2009.1.2.169

Yang S.L., Lacasse S., Sandven R., Determination of the transitional fines content of mixtures of sand and non-plastic fines, Geotechnical Testing Journal, 29 (2006) 102–107. https://doi.org/10.1520/GTJ14010

Zuo L., Baudet B.A., Normalised behaviour of a non-plastic silt–pumice sand mixture, Géotechnique, 70 (2020) 822–832. https://doi.org/10.1680/jgeot.19.P.012


## Authors' Short Biographies

**Prof. Ching S. Chang** is a Professor of Civil and Environmental Engineering at the University of Massachusetts, Amherst. With over 30 years of experience, he specializes in multi-scale modeling and the constitutive behavior of granular soils, clay, asphalt concretes, rocks, and mixed soils. He is a pioneer in modeling granular micromechanics and has authored more than 300 papers in journals, edited books, and conference proceedings. He also serves as a reviewer for multiple journals, extramural funding agencies, and provides consulting services to the industry.

**Jason Chao** is a Ph.D. candidate in Geotechnical Engineering at the University of Massachusetts, Amherst, starting his program in 2021. Jason is committed to advancing geotechnical engineering knowledge through both experimental and theoretical approaches.

**Prof. Yibing Deng** is a Professor at Shanghai Urban Construction Vocational College. He earned his doctoral degree in geotechnical engineering from the University of Massachusetts Amherst in 2021. His research focuses on the effects of particle size distribution on the density state and shear behavior of granular soils, and he has developed several theoretical models to account for the influence of density state on mechanical behaviors. He has published over 40 articles in peer-reviewed journals.

KONA Powder and Particle Journal

KONA Powder and Particle Journal No. 42 (2025) 268–284/https://doi.org/10.14356/kona.2025018 Original Research Paper

# Decoding Attractive Interactions in Granular Materials through Vibration-Induced Densification †

**Maria-Graciela Cares-Pacheco * and Véronique Falk**

*Reactions and Chemical Engineering Laboratory (LRGP-CNRS), Université de Lorraine, France*

Within the intricate world of granular materials, the behavior of grain assemblies presents complexities characterized by nonlinear and inelastic phenomena, which seamlessly link the microscopic grain scale to the macroscopic bulk scale. A key challenge in understanding the mechanics of granular materials lies in establishing connections between these microscopic grain properties and their macroscopic flow behavior. This study delves into vibration-induced densification, a phenomenon relevant across various technological domains in powder processing and manufacturing. Specifically, we explore the vibrational conditions that induce compaction and decompaction under vertical vibration, employing a particle damper across industrial powders, including glass beads, joint filler, wheat flour, and pharmaceutical excipients. The experiments involve controlling the vibration wave by adjusting parameters such as frequency and amplitude while measuring and recording the acceleration and force signals. Our findings reveal a significant correlation between the force required to decompact the powder bed and the attractive forces between grains. This correlation facilitates the determination of a dimensionless granular number $A_d$, offering insights into the contact force network at a macroscopic level and its relation to flow indices. By proposing this experimental approach, we provide a straightforward method to unveil the intricate relationship between local particle interactions and the overarching mechanical behavior of granular materials, contributing to advancements in understanding and predicting powder flow behavior.

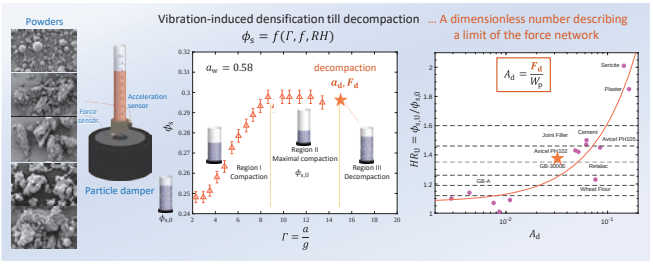


**Keywords:** densification, compaction, vibration, adhesion, force network

## 1. Introduction

Throughout history, granular materials such as sand, wheat, and wood have played fundamental roles in human civilization. From ancient times to this day, these materials have been integral to various aspects of daily life and industrial processes. Since the advent of the industrial revolution in the eighteenth century, engineers have grappled with the intricate challenges posed by the handling and processing of grains, many of which revolve around flow-related issues (Bérut et al., 2019; Carson et al., 2019; Ghadiri et al., 2020). Poor flow properties can trigger a cascade of complications, from segregation and feeder blockages to the formation of ratholes, necessitating manual interventions such as hammering and scraping to silos collapsing during storage (Carson et al., 2019; Schulze, 2021).

The behavior of granular assemblies is inherently complex, marked by nonlinear, inelastic effects and highly dissipative interactions that occur across scales—from microscopic grain interactions to macroscopic flow dynamics (Andreotti et al., 2011; Herrmann et al., 1998; Jaeger et al., 1996). This intricate interplay between local particle interactions and global mechanical behavior highlights the necessity for comprehensive, multi-scale research to fully understand granular materials.

The macroscopic mechanical properties of granular materials are intricately linked to the microscale, specifically the particle scale. Unlike elastic solids, which support external forces under loading, granular materials transmit these forces through a percolating network of particles, forming chain-like structures that act as preferential pathways for force transmission (Majmudar and Behringer, 2005; Radjai et al., 2010). The distribution of forces within granular materials is broad and highly heterogeneous. Extensive experimental and numerical research has been conducted to investigate the evolution, properties, and statistical behavior of these force distributions within highly idealized granular assemblies (Kollmer and Daniels, 2019; Papadopoulos et al., 2018; Wu and Wang, 2022). Although force transmission in idealized granular materials presents relatively straightforward dynamics, the force transmission encountered in industrial processing is far more complex. Irregular particle shapes and adhesive interactions complicate the establishment of a direct correspondence between macroscopic and microscopic features, as commonly observed in non-cohesive, circular-shaped granular

† Received 17 May 2024; Accepted 28 August 2024
J-STAGE Advance published online 19 October 2024
* Corresponding author: Maria-Graciela Cares-Pacheco;
Add: Nancy F-54000, France
E-mail: maria-graciela.cares@univ-lorraine.fr
TEL: +33-372-74-7237-49

assemblies (Gilabert et al., 2007; Marteau and Andrade, 2021; Saint-Cyr et al., 2013).

This work aims to address some of these issues by experimentally extracting force network information. The challenge lies in describing an infinite number of packing configurations that seem to statistically retain consistent macroscopic properties. Given this challenge, dynamic densification experiments emerge as a promising approach. The compaction of fine granular materials is a common unit operation across various industries, including pharmaceuticals, cosmetics, metallurgy, agro-food, nuclear, and automotive. It is employed to create products such as agglomerates, capsules, tablets, pellets, and battery electrodes, all of which are designed with specific compositions, porosities, shapes, and strengths. Additionally, compaction can occur as a result of discrete taps or vibrations during transportation or handling. These actions can significantly alter the volume and may lead to the segregation of granular materials. The resulting contact network and force transmission are essential aspects that evolve throughout the compaction process.

When a powder is shaken, the grains reorganize themselves into a denser structure. Several empirical or heuristic models have described the dynamics of compaction under gentle tapping, mainly using glass beads (Knight et al., 1995; Ribière et al., 2005, 2007; Suaza-Montalvo et al., 2023a). The density, or packing fraction, plots depend on the amplitude of the taps and the geometry and are usually described as logarithmically slow. However, the densification of complex (or heterogeneous) granular materials, such as powders, often fails to describe many phenomena encountered during vibration. Whether particles reorganize during densification depends on the energy or force supplied to the powder—the confinement strategy—and is therefore device-related (Saker et al., 2019). The force-wave signal transmitted to the powder bed significantly affects force transmission and densification dynamics (Suaza-Montalvo et al., 2023a).

For instance, in uniaxial compression devices, a step-like force signal is applied to the powder (**Fig. 1A**). At low compression forces, where little to no particle deformation occurs, densification takes place through particle rearrangement as particles roll into void spaces (Cares-Pacheco et al., 2021). In vibration-induced densification, such as in tapping devices like the Densitap, the shock wave generated by rotating a snail cam (**Fig. 1B**) facilitates particle separation and lift-off, creating new pathways for rearrangement (Cares-Pacheco et al., 2021). When utilizing particle dampers (**Fig. 1C**), the transmitted signal to the powder (frequency, amplitude, and period) can be precisely controlled. This control allows for varying porosity levels to be achieved through particle rolling or lift-off, with the latter exhibiting different fluidization regimes (Suaza-Montalvo et al., 2023a). At a fixed frequency, increasing the acceleration is akin to increasing the superficial gas velocity in fluidized beds, leading to different flow regimes ranging from bubbling to slugging to turbulent.

By employing an experimental methodology centered around vibration-induced densification across a spectrum of industrial powders, we aim to explore the mechanics governing force transmission, particle interactions, and densification dynamics. Specifically, our methodology focuses on tracking the evolution of the packing fraction until the powder bed undergoes decompaction or fluidization. This investigation examines the effects of signal frequency and amplitude, powder-column height, and air humidity conditioning.

Our study marks a significant step forward in our ongoing efforts to gain deeper insights into the complexities inherent in granular materials. Of particular interest is the extraction of a dimensionless parameter representing force chains and its correlation with flow indicators.

## 2. Materials and methods

### 2.1 Powders

In this study, six powders were selected to represent a wide range of industries and physical characteristics, based on their industrial applications. Two pharmaceutical excipients were chosen: RetaLac®, a binder produced by Meggle for direct compression and dry granulation of modified release formulations, and Avicel® PH-102, a microcrystalline cellulose from FMC Biopolymer®. Avicel® PH-102 is

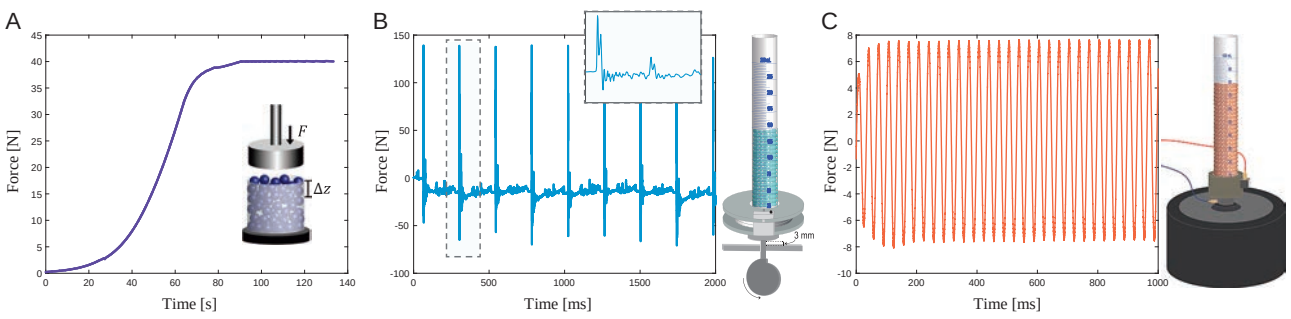


**Fig. 1** Schematic representation of various devices used for compacting granular materials, along with the force signal transmitted to the sample. **A)** Uniaxial compression; **B)** Tapping; and **C)** Particle damper.

widely used across various industries as a texturizer, anti-caking agent, fat substitute, emulsifier, extender, and bulking agent in food production. To investigate the effects of highly uniform water-inert materials, two types of glass beads (GB) were selected. Glass beads are often used as "model materials" in granular physics due to their spherical, smooth, and hard particle properties. The first type, GB-A, is monodisperse, while GB 3000E from Potters® Industries LLC (Spheriglass® 135 3000-E), a polydisperse material, is specifically used in highway safety marking. Both types of glass beads were carefully washed prior to use. From the food industry, artisan-made T45 wheat flour from the Poinsignon flour mill in France was selected. Finally, joint filler from MAPEI®, used for grouting tiles and finishing walls, was chosen to represent the construction industry.

The behaviors of these powders in relation to water is presented in **Fig. 2**. The sorption isotherms indicated that the wheat flour (B) absorbed the most water, followed by Avicel PH102 (A) and RetaLac (E). Joint filler (C) exhibited minimal water absorption, while both types of glass beads, 3000E and GB-A (D), remained chemically inert to water. All powders were conditioned and stored at room temperature in sealed containers, with relative humidity maintained at approximately 20 % (using lithium chloride - LiCl) and 60 % (using sodium chloride - NaCl) through saturated salt/water solutions. The samples were allowed to equilibrate until they either matched the environmental conditions or exhibited stable behavior over a week, as confirmed by daily measurements of water activity ($a_w$) using an Aqualab 4TE from METER.

Details on the microstructural attributes of the powders are illustrated in **Fig. 3**, and their physical properties are summarized in **Table 1**. These properties include the characteristic diameters of the particle size distribution, pycnometric density ($\rho_p$), fluidization classifications according to Geldart (Geldart, 1973), and minimum fluidization velocities ($v_{mf}$) calculated using Grace's correlations (Grace, 1986). These correlations, which compile extensive experimental data, provide valuable insights into fluidization behavior. Geldart's correlation, introduced approximately 50 years ago, describes fluidization behavior based on the density difference and particle size (using $d_{3,2}$ here). Grace's correlation further elucidates the fluidization regime by considering the superficial gas velocity, air in this case, and the mean particle diameter ($d_{50}$).

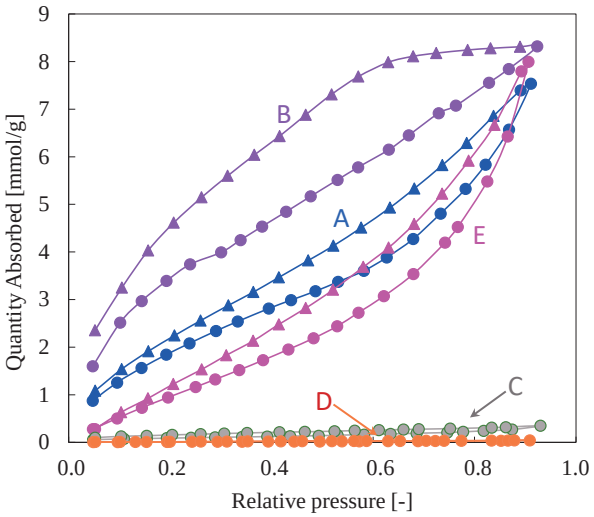


**Fig. 2** Water sorption isotherms of powders at 25 °C: **A)** Avicel PH102, **B)** Wheat flour T45, **C)** Joint Filler, **D)** Glass beads (GB 3000E and GB-A), and **E)** RetaLac. Sorption curves are indicated by circular data points (○) and desorption curves by triangular data points (△).

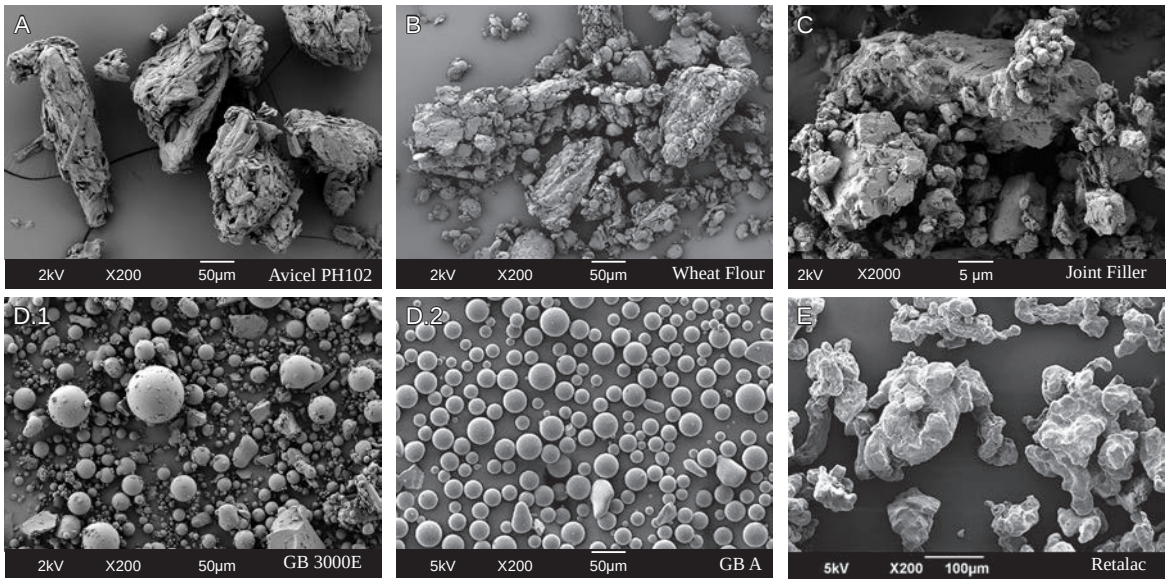


**Fig. 3** Scanning electron microscopy (SEM) micrographs at different magnifications of the principal powders used in the study **A)** Avicel PH102, **B)** Wheat flour T45, **C)** Joint Filler, **D)** Glass beads, **D.1** GB 3000E and **D.2** GBA and **E)** RetaLac.

**Table 1** Physical properties of samples.

| Powder | Particle size distribution [μm] | | | | | $\rho_p$ [a] [kg m$^{-3}$] | Geldart type | $v_{mf}$ [$10^{-3}$ m s$^{-1}$] |
|---|---|---|---|---|---|---|---|---|
| | $d_{10}$ | $d_{50}$ | $d_{90}$ | $d_{4,3}$ | $d_{3,2}$ | | | |
| Avicel PH-102 | 35 | 111 | 225 | 122 | 69 | 1550 | A | 3.10 |
| Wheat flour | 17 | 83 | 177 | 91 | 25 | 1460 | C-A | 0.38 |
| Joint filler | 2 | 18 | 72 | 29 | 6 | 2810 | C | 0.04 |
| GB 3000E | 4 | 24 | 60 | 29 | 8 | 2660 | A | 0.07 |
| GB-A | 24 | 34 | 49 | 36 | 33 | 2490 | A | 1.14 |
| RetaLac | 47 | 191 | 415 | 222 | 132 | 1420 | B | 10.4 |

[a] Envelope density of the particles (equal to the pycnometric density for non-porous particles).

The particle size distribution was determined by laser diffraction (PSD-LD) in a liquid medium (ethanol) using a Mastersizer 3000 (Malvern Instruments). Morphological characterization was performed using scanning electron microscopy (SEM) with a Gemini 3 from Zeiss, equipped with a field-emission gun operating at 2 kV. The PSD-LD results indicate that RetaLac, Avicel PH102, and wheat flour consist of larger particles, while joint filler and glass beads exhibit a similar PSD with smaller particle sizes. The SEM micrographs in **Fig. 3** reveal the morphology of the samples. With the exception of GB-A, most samples display heterogeneity in size, shape, and surface roughness. Avicel PH102 particles have an isometric rod shape with a rough surface. RetaLac appears to be composed of agglomerates of amorphous-like particles. Wheat flour consists of irregularly shaped gluten and starch, with starch partially covering the gluten particles in a globule-like structure. The joint filler exhibits an uneven shape with flat surfaces, while GB-3000E is mostly spherical, though with some surface irregularities.

According to Geldart's classification, RetaLac is categorized as a Class B powder, characterized by smooth and homogeneous fluidization with minimal bubbling. Wheat flour falls between cohesive (Class C) and aeratable (Class A) powders. Joint filler is classified as a cohesive powder (Class C). Avicel PH102 and glass beads are both classified as Class A powders, which are associated with more pronounced bubbling during fluidization. Notably, GB 3000E exhibits greater cohesiveness compared to GB-A.

## 2.2 Experimental setup

To investigate the conditions that facilitate the compaction and decompaction of the powder bed, harmonic signals were generated with variations in amplitude and frequency. The experimental setup includes an electromagnetic shaker (BK vibration exciter 4809) connected to a cylindrical borosilicate glass vessel (26 mm in diameter and 240 mm in height), as shown in **Fig. 4**. The container weighs 72 g. The excitation system comprises a custom-made signal generator and a power amplifier (B&K 2718).

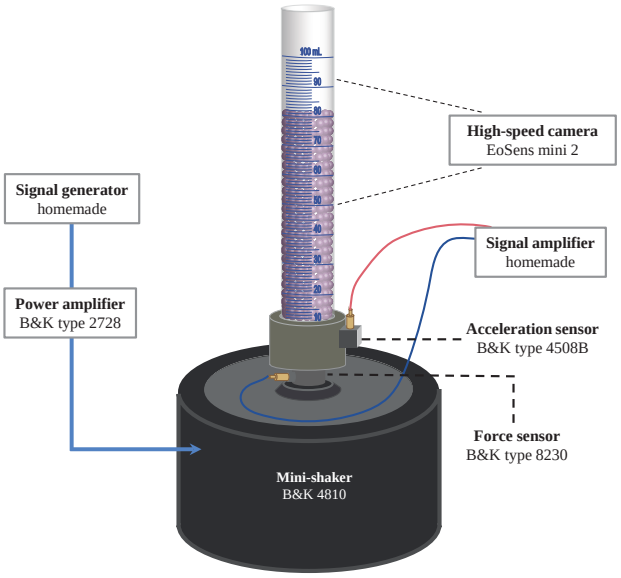


**Fig. 4** Schematic representation of harmonically driven vibration experiments, including a particle damper, its excitation system, and data acquisition sensors.

Acceleration is measured using a DeltaTron® accelerometer (B&K 4508B) attached to the bottom of the vessel (**Fig. 4**). Force measurements are conducted using a force transducer (B&K 8230) mounted at the base of the container. Both excitation and data acquisition are controlled via LabVIEW. The height of the powder bed is captured via a high-speed camera (MotionBLITZ EoSens® mini 2), and the images are subsequently analyzed to determine the powder bed height, enabling the assessment of compactness dynamics and the Hausner ratio $HR(t)$ under various experimental conditions.

The compactness of the granular system can be quantified using various metrics, including the packing fraction $\phi$, porosity $1-\phi$, and the void ratio $e = 1/\phi - 1$. While $\phi$ is more commonly used in granular physics (Suaza-Montalvo et al., 2023a), $e$ is more commonly used in soil mechanics (Sonzogni et al., 2024). In dynamic systems, $\phi$ relates the volume of the particles $V_p$ to the volume of the pile $V(t)$ at a given time, quantifying the available space for particle

reorganization within the bulk:

$$\phi(t) = \frac{V_p}{V(t)} = \frac{m_p}{V(t) \cdot \rho_p} \quad (1)$$

where $\rho_p$ is the envelope density of the particles (equal to the pycnometric density for non-porous particles) and $m_p$ is the powder mass.

*HR*, based on the pioneering work of Hausner (1967), is a measure commonly used in powder technology to assess flowability (Saker et al., 2019), though it mathematically reflects the compactness of the powder. It is defined as the ratio of the initial (loose) volume $V_i$ to the tapped volume $V(t)$:

$$HR(t) = \frac{V_i}{V(t)} \quad (2)$$

Higher *HR* values indicate poorer flowability and greater cohesion among particles, which often correlates with increased compactness.

The densification dynamics are influenced by two primary factors: system geometry and vibration. System geometry encompasses variables such as grain size, vessel dimensions, and powder bed height. Vibration is governed by two dimensionless parameters: the relative acceleration, $\Gamma$, compares the imposed acceleration, $a$, to gravity, $g$:

$$\Gamma = \frac{a}{g} \quad (3)$$

and the relative frequency, Ω, compares the period, $2\pi/\omega$, to the time it takes for a grain to fall under gravity over a distance equal to its size, $d$:

$$\Omega = \frac{\omega}{\sqrt{g/d}} \quad (4)$$

The continuous densification methodology involves pouring the powder into a container using a funnel. Densification is then initiated by gradually increasing the acceleration of the imposed motion in steps at a fixed frequency. Each acceleration level is maintained until the powder bed stabilizes for at least 5 minutes. This stabilized state is considered quasi-static and is referred to as "stable compactness," denoted as $\phi_{s,i}(\Gamma_i)$. An entire experiment involves studying the relationship $\phi_{s,i} = f(\Gamma_i)$, until the powder bed undergoes decompaction. Since this is a continuous process, only the first acceleration step begins with the powder in an aerated state. Force and acceleration signals are depicted using peak-to-peak values of smoothed signals. The total error associated with each experimental data point was determined as described in previous works, accounting for both experimental and instrumental errors (Suaza-Montalvo et al., 2023a).

## 3. Results and discussions

The results section is structured as follows. We begin by demonstrating the high sensitivity of the force and acceleration signals to the dynamic behavior of the powders. Next, we delve into the densification dynamics. Finally, we aimed to characterize the force contact network at the mesoscale by drawing insights from the macroscopic results obtained through vibration-induced densification tests performed on different powders. It is important to note that our discussion of the results does not primarily focus on providing a detailed description or physical characterization of the powders used in this study. Instead, our powder selection effectively illustrates key phenomena and highlights significant findings. This approach was chosen to enhance the clarity and address the broad scope of the study.

In all figures where applicable, the results are presented in the following order: A: Avicel PH102, B: Wheat Flour, C: Joint Filler, D: Glass Beads (either 3000E or A type), and E: RetaLac.

### 3.1 Force and acceleration signals

In this study, dynamic densification experiments involving $\phi_s$ with $\Gamma$ are conducted, during which all grains move in phase with the container, resembling macroscopically rigid inertial bodies. Nonetheless, a notable observation is that both force and acceleration signals are highly sensitive to particle movements. For example, during the initial seconds of excitation, depending on $\Gamma$, both force and acceleration signals can exhibit significant fluctuations (**Fig. 5A**), coinciding with the onset of fluidization phenomena (see Suaza-Montalvo et al., 2023b, Videos 06, 07, 08, and 09 in the DOREL repository for details). The fluidization of particles in these early moments of vibration can be attributed to the release of trapped air within the powder bed as it densifies (**Figs. 5B, C**). A key determinant of fluidization is the air velocity within the bed, $v_{air}$, which describes the rate of volume reduction over time:

$$v_{air} = \frac{1}{S}\frac{\Delta V}{\Delta t} \quad (5)$$

The determination and analysis of the average air velocity showed that when $v_{air}$ surpasses the minimum fluidization velocity of particles, the bulk undergoes fluidization, as evidenced by the observations (**Fig. 5C**). As the $v_{air}$ decreases, signaling reduced air availability, the densification of the bulk continues, resembling behavior more akin to solids on a macroscopic scale, and both the force and acceleration signals become stable. This phenomenon, consistent across various powders and vibration conditions, exemplifies the sensitivity of the force and acceleration signals in describing the dynamic response of the powder bed.

The differences in the signals can be attributed to the mass experienced by the system. As fluidization phenomena increase, the duration of particle flight between collisions with the container also increases. This trend continues

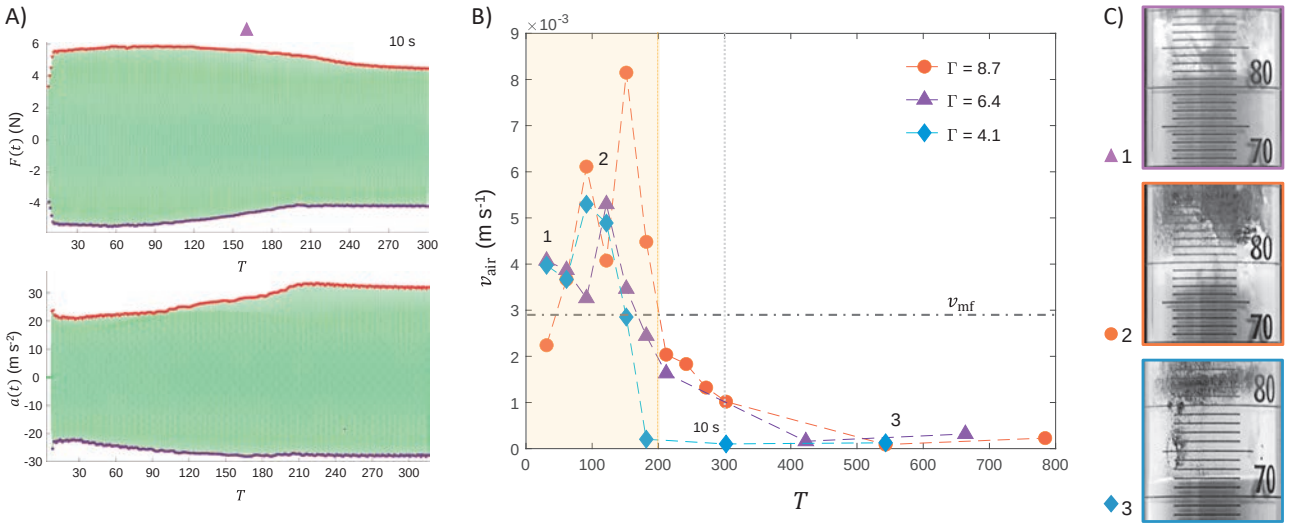


**Fig. 5** **A)** Evolution of force and acceleration signals for Avicel PH 102 with the period $T$. **B)** Accompanied by an average estimation of air velocity evolution with $T$ at various $\Gamma$ values. **C)** Snapshots illustrating the observed behaviors of the powder bed.

until the air velocity decreases. Consequently, during fluidization, the average contribution of the grain mass felt by the container decreases. This mass is generally referred to as the dynamic mass of the granular sample, representing the portion of the grain mass that is effectively perceived by the container (Masmoudi et al., 2016; Meyer and Seifried, 2023).

The sensitivity of force and acceleration signals to packing density states and grain characteristics suggests that these signals can serve as structural descriptors, which may be more relevant to rheology than purely geometrical descriptors such as radial pair distributions.

## 3.2 Packing dynamics

Dynamic densification tests were conducted to investigate how vibration affects both force transmission and particle-scale interactions, focusing on macroscopic measurements. It is interesting to note that when decompaction conditions ($\Gamma_d$ and $F_d$) are applied to an aerated powder, the powder may initially compact slightly, displaying either liquid-like, gas-like, or combined behaviors. It then reaches a convective state, after which it can decompact. This convective state can be sustained through several perturbations until suddenly the movement of the grains leads to the reintroduction of air into the bed, facilitating the decompaction process (see Suaza-Montalvo et al., 2023b, Video 16 in the DOREL repository for details).

The subsequent subsections present results from a series of experiments exploring the impact of frequency, sample conditioning (free-water), the shape of the force signal, and powder height.

### 3.2.1 The effect of relative frequency Ω on packing dynamics

The evolution of packing fraction $\phi_s$ with respect to $\Gamma$ and Ω for Avicel PH102 and wheat flour is depicted in **Fig. 6**. The compaction dynamics vary depending on the powder type but follow a similar trend. At a constant Ω, an increase in $\Gamma$ leads to an initial rise in the packing fraction until it reaches its maximum compaction state. Subsequently, further increases in vibration amplitude result in the decompaction of the powder bed, as illustrated by the star data points in **Fig. 6**. Decompaction may occur either gradually, with a convection-like motion inducing the aspiration of air into the powder bed, or abruptly, creating a powder cloud that impedes volume measurement. Specifically, lower frequency signals, as observed in samples such as RetaLac, wheat flour, and sericite, resulted in an explosive decompaction of the bed at lower acceleration levels compared to the 100 Hz driven signal.

Two general observations emerge from these experiments. Firstly, for low-cohesive samples such as GB A (**Fig. 6D**) and RetaLac (**Fig. 6E**), the densification dynamics are independent of the vibration frequency, as typically reported in the literature for glass bead-based studies (Ribière et al., 2007; Suaza-Montalvo et al., 2023a). Secondly, an increase in Ω induces powder bed decompaction at higher $\Gamma$ values. Two possible explanations can be drawn from this last statement.

First, the kinetic vibration energy $E_v$ for a harmonically driven system can be expressed as

$$E_v = \frac{m_p\, d\, g}{2}\left(\frac{\Gamma}{\Omega}\right)^2 \tag{6}$$

From this equation, it can be inferred that increasing $\Gamma$ results in an increase in the kinetic vibration energy supplied to the powder bed. Conversely, increasing Ω reduces the kinetic vibration energy. Additionally, this phenomenon is closely related to energy dissipation. Notably, even under steady-state conditions, the dissipated energy can vary

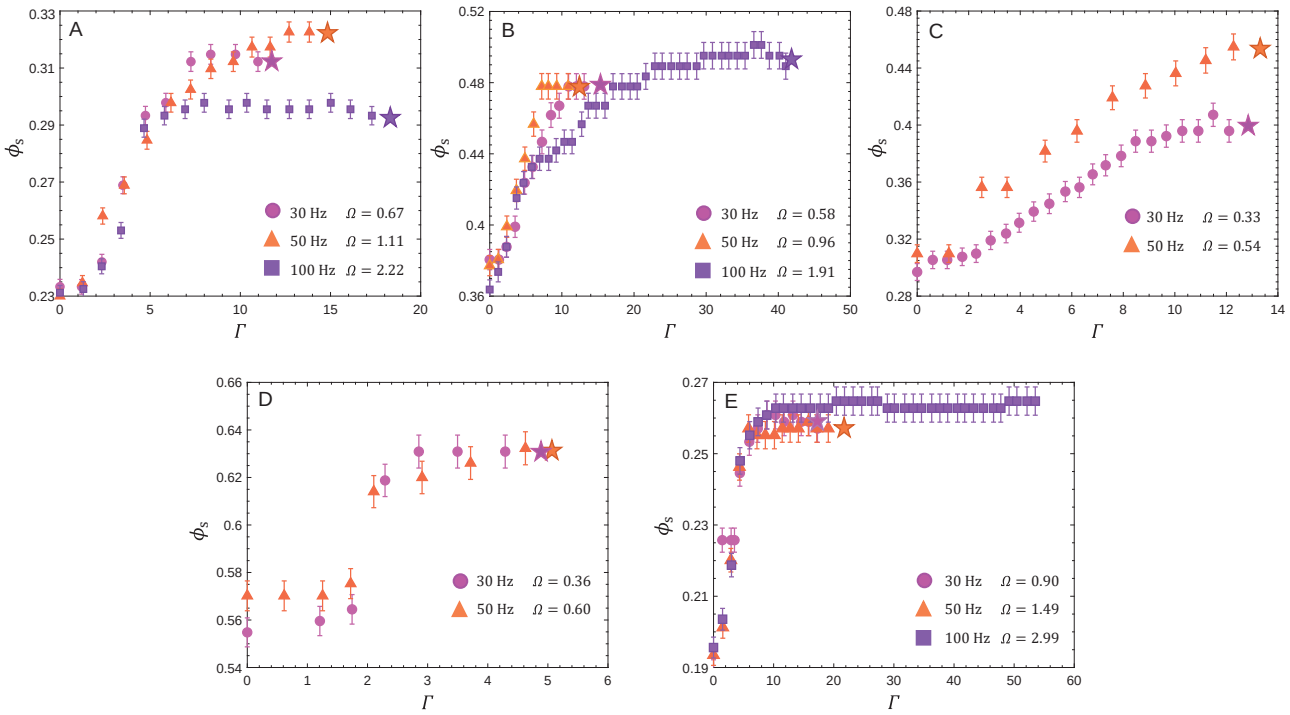


**Fig. 6** The evolution of $\phi_s$ as a function of frequency and relative frequency $\Gamma$ for **A)** Avicel PH102 at 20 % RH, **B)** Wheat Flour T45 at 60 % RH, **C)** Joint Filler at 60 % RH, **D)** GB-A at 20 % RH, and **E)** RetaLac at 20 % RH. The star denotes the relative frequency at which powder bed decompaction occurs.

from one period to another due to the complex nonlinearities in granular damping. This complexity is further amplified in cohesive powders, which exhibit cluster-like behaviors, making the analysis more demanding. Therefore, considering a more general expression to average behaviors can be prudent for analysis. Several expressions have been proposed to determine the maximum achievable energy dissipated in vibrated granular materials such as glass beads (Marhadi and Kinra, 2005; Masmoudi et al., 2016; Sack et al., 2013; Terzioglu et al., 2023), differing by scaling terms. In the solid-like state, observed just before decompaction, the particles do not lift off the container bottom (Suaza-Montalvo et al., 2023b, Video 04). Consequently, very little relative motion occurs between the particles. Recently, Meyer and Seifried (2023) described the energy dissipated per cycle during solid-like behavior, denoted as $\tilde{E}_{\text{diss}}$, as approximately 0.1 % of the particles' kinetic energy. The formula is given by

$$\tilde{E}_{\text{diss}} = \frac{\pi}{1000} m_p \left(\frac{\Gamma g}{\omega}\right)^2 \tag{7}$$

**Eqn. (7)** does not account for cohesion, which is typically observed in powders. However, calculating $\tilde{E}_{\text{diss}}$ at each decompaction point shows that higher dissipation energies are obtained for samples decompacting at larger $\Gamma$ values. This indicates that as the vibrational amplitude increases, more energy is dissipated within the system, potentially influencing the overall behavior and stability of the powder bed.

### 3.2.2 The effect of conditioning (air-humidity) on packing dynamics

In this section, the influence of air humidity on $\phi_s$ concerning $\Gamma$ was investigated by conditioning the samples at 20 % and 60 % RH. It's noteworthy that each powder possesses unique adsorption/absorption kinetics (**Fig. 2**) and reaches equilibrium at different rates. Consequently, after one week of conditioning, samples may exhibit varying water activities ($a_w$)—free or non-chemically bound water—despite following the same conditioning protocol. For instance, powders such as Avicel PH102 and RetaLac quickly reach equilibrium, with their $a_w$ values aligning well with the relative humidity of the conditioning environment. However, other samples, such as Joint Filler, require longer conditioning periods.

The evolution of the packing fraction, $\phi_s$, with respect to $\Gamma$ and RH for all samples is shown in **Fig. 7**. The figure illustrates how conditioning at higher relative humidity can impact compaction dynamics, potentially increasing or decreasing the energy required to decompact the bed depending on the nature of the powder. Interestingly, the compaction dynamics appear to be independent of, or non-linearly related to, the powder's behavior towards water. For instance, low-adsorption samples such as GB 3000E (**Fig. 7D**) and Joint filler (**Fig. 7C**) show no statistical differences in compaction dynamics with increasing RH. A similar trend was observed for water-absorbing samples like wheat flour (**Fig. 7B**). Notably, air humidity does not affect the decompaction of GB 3000E.

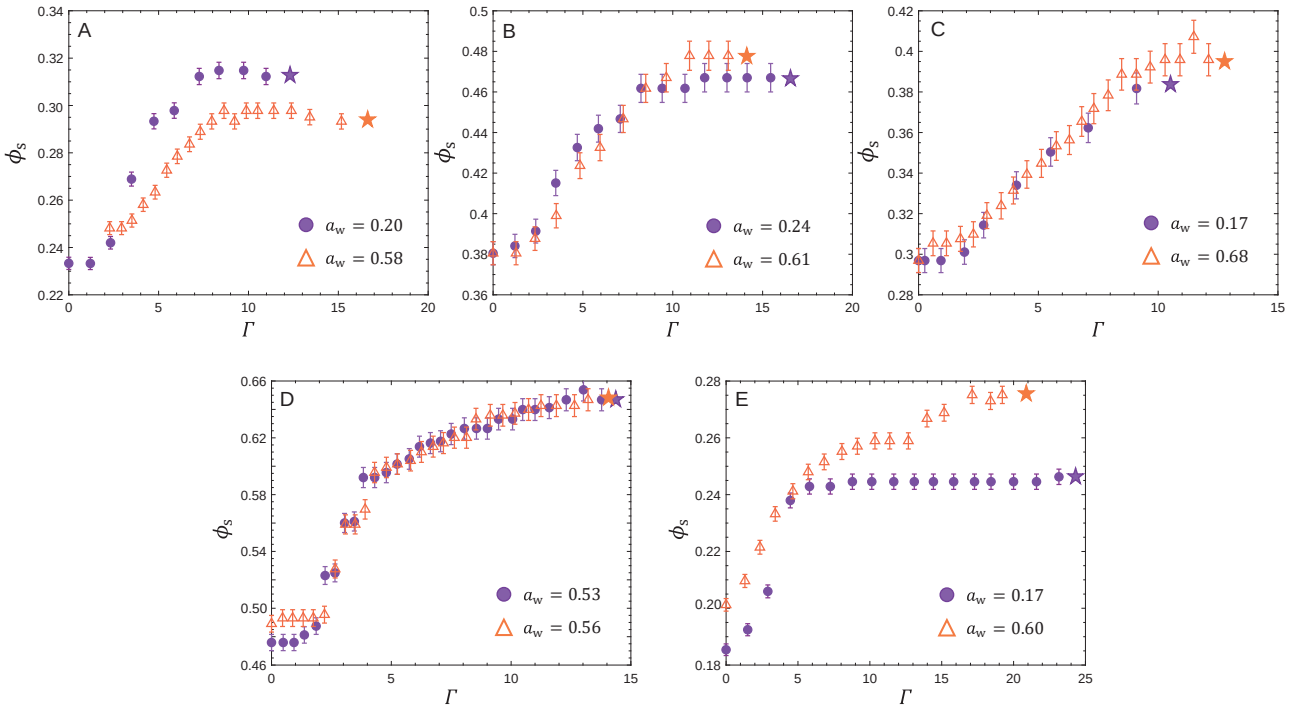


**Fig. 7** The evolution of $\phi_s$ as a function of $\Gamma$ at a fixed vibration frequency of 30 Hz for samples conditioned at different relative humidities (RH): ○ 20 % RH and △ 60 % RH, is shown for **A)** Avicel PH102, **B)** Wheat flour T45, **C)** Joint Filler, **D)** GB 3000E, and **E)** RetaLac. The star denotes the relative frequency $\Gamma_d$ at which powder bed decompaction occurs.

The effect of RH on fine glass beads has been previously studied by Landi et al. (2011), who demonstrated that cohesion increases with air humidity. However, they concluded that only a small portion of the total condensed water on a single sphere forms capillary bridges. Furthermore, the strength of the interaction is weak because glass beads are chemically inert to water. This might explain why no changes in decompaction are observed for GB 3000E when exposed to different RH. Indeed, the $a_w$ values obtained for glass beads are more reflective of environmental conditions. Therefore, GB 3000E exhibits statistically similar dynamics and serves as a good example of the excellent repeatability of the experiments.

For Avicel PH 102 and RetaLac, increased air humidity can either decrease or increase the packing fraction, respectively. Both powders are hydrophilic and absorb water at low moisture content (**Fig. 2**), with Avicel PH-102 being more hydrophilic and having smaller particles than RetaLac. These results highlight the challenges in drawing general conclusions based on physical properties such as particle size distribution, shape, and behavior towards water. A common trend observed among the samples is that, at a fixed frequency, lower packing fractions correspond to larger $\Gamma_d$ (**Fig. 7**). This indicates that less compacted samples require more energy for decompaction. This phenomenon can be attributed to force transmission through the powder bed. Assuming that the contact network, or force network, formed by chain-like structures serves as preferential pathways for force transmission, it must be closely related to the geometric arrangement of the particles. The average number of contacts per particle, $Z$, is expected to be smaller for loosely packed fractions compared to more compacted ones. A smaller $Z$ implies that fewer paths are available for force propagation, which ultimately influences the distribution of forces and promotes energy dissipation. Additionally, the strength of the contact can be influenced by the formation of liquid bridges.

In summary, individual particle properties alone cannot be linearly or easily related to packing dynamics, making straightforward conclusions challenging. However, the combination of these properties—such as size, shape, chemical nature of the surface, and condition—plays a significant role in mesoscale phenomena. From a mesoscale perspective, the overall behavior is influenced by the joint effects of multiple particle properties. For instance, size and shape affect the coordination number $Z$, which in turn influences packing dynamics. Therefore, the interplay between these properties at the mesoscale is crucial for understanding packing and compaction behavior. These experimental findings suggest that the dynamic parameters governing powder bed decompaction offer insights into mesoscale behavior, describing the contact force network from a macroscopic perspective.

### 3.2.3 The effect of force wave shape on packing dynamics

To better understand the influence of force wave shape on densification dynamics, damping experiments are

compared with uniaxial compaction experiments conducted under zero shear conditions. This experimental approach is based on the forces exerted on the system. Due to differences between devices, such as vessel geometry and powder content—fixed at 10 mL for FT4, while the powder mass is constant at 30 g for PD—the comparison is conducted using the specific energy $E_m$, determined from the force signal applied to the powder bed as follows:

$$E_m = \frac{F\Delta z}{m_p} \tag{8}$$

where Δz is the change in bed height.

For the compaction experiments with the FT4 compression cell, $F$ is the force applied to the bed by the vented piston (**Fig. 1A**), as thoroughly described in a previous work (Cares-Pacheco et al., 2021). In summary, the piston compresses the sample in increments of force from 2 to 40 N at a rate of 0.4 N/s. For each increment, the piston maintains the force for 60 seconds to reach a steady state, after which the volume change with respect to the applied load is measured.

From **Fig. 8**, it can be observed that uniaxial compression and vibration-induced densification (step-like dynamics) methods exhibit similarities for cohesive powders. For easily flowing powders such as Avicel PH102 (**Fig. 8A**), particles tend to separate, move, and perform free parabolic flights during damping experiments, potentially leading to higher probabilities of reorganization. This capacity allows them to form denser organizational structures through vibration, as the restrictions imposed by the piston are reduced under similar energy provided to the system (see Suaza-Montalvo et al., 2023b, Videos 06 and 07 in the DOREL repository for details). Conversely, for more cohesive powders like wheat flour (**Fig. 8B**; see Suaza-Montalvo et al., 2023b, Video 08) and joint filler (**Fig. 8C**), particle separation into individual entities is more challenging. Compaction in these cases appears to occur through the movement of agglomerates, resulting in cluster-like behavior and reduced particle rearrangement. Zhao et al. (2021) explored the influence of vibration on wheat flour, highlighting that densification primarily involves smaller particles occupying interparticle voids, resulting in a denser bulk material with reduced permeability. Such behavior is also expected in uniaxial compression tests at low stress and may explain the similarities in the dynamics of densification observed between the two methods.

The significant difference between the FT4 and PD packing fractions for joint filler at 30 % RH may stem from its lower elastic modulus (**Table 2**), potentially influencing particle deformation.

### 3.2.4 The effect of volume fraction on packing dynamics

The effect of bed height on compactness is illustrated in **Fig. 9**. Experiments were carried out at three vessel filling fractions. The first filling fraction corresponded to a volume of 15 mL, resulting in a column height of 2.9 cm; the second to 50 mL, approximately half of the container, resulting in a height of 9.6 cm; and the third to the maximum filling of the measurable volume, which was 100 mL, resulting in a column height of 19.2 cm.

Several general observations arise from these experiments, as shown in **Fig. 9**. Firstly, $\phi_s$ increases with powder height, indicating that higher fillings lead to higher compactness. Secondly, low-volume fillings tend to have problems achieving high compaction levels. Notably, wheat flour shows intriguing behavior, as it does not exhibit clear densification at low or medium filling volumes (**Fig. 9B**). Similarly, glass beads 3000E do not densify at low volumes; instead, they maintain a convective, fluid-like behavior within the bulk while maintaining a relatively constant bulk height (**Fig. 9D**). This behavior is consistently observed with glass beads and can be visually observed at a macroscopic level, especially with larger particles, as depicted in **Fig. 10**, where some GB A particles were colored to follow their path.

As shown in **Eqn. (7)**, common trends closely relate the dissipated energy to the number of grains, as the loss factor monotonically increases with the mass of the powder (Masmoudi et al., 2016). This aligns with our findings, which demonstrate the challenges in compacting powder at low volumes.

The relationship between the force required to decompact the powder bed and the powder volume is surprisingly non-monotonic (**Fig. 9**). Medium-volume powder columns consistently decompact at lower $\Gamma$ values, indicating that the force does not follow a simple, consistent trend with increasing or decreasing volume. Instead, the required force exhibits complex and fluctuating behavior as the volume changes, suggesting that other factors or interactions are influencing the decompaction force in a non-linear manner. While dissipation initially appears to be a major contributing factor, it does not fully explain why medium volumes decompact at lower accelerations.

When the powder bed is mechanically excited, compression waves or shear waves propagate from the point of excitation. As the grains interact with this external field through scattering and absorption, the field can also exert forces on them. This elastic longitudinal wave moves through the material at a velocity, $c$, that can be determined as

$$c = \sqrt{\frac{E_{el}(1-\nu)}{\rho(1-2\nu)(1+\nu)}} \tag{9}$$

where $E_{el}$ is the Young's modulus, $\nu$ is the Poisson's ratio and $\rho$ the density of the material, here represented by the pycnometric density, $\rho_p$.

The elastic modulus of the powders has been determined

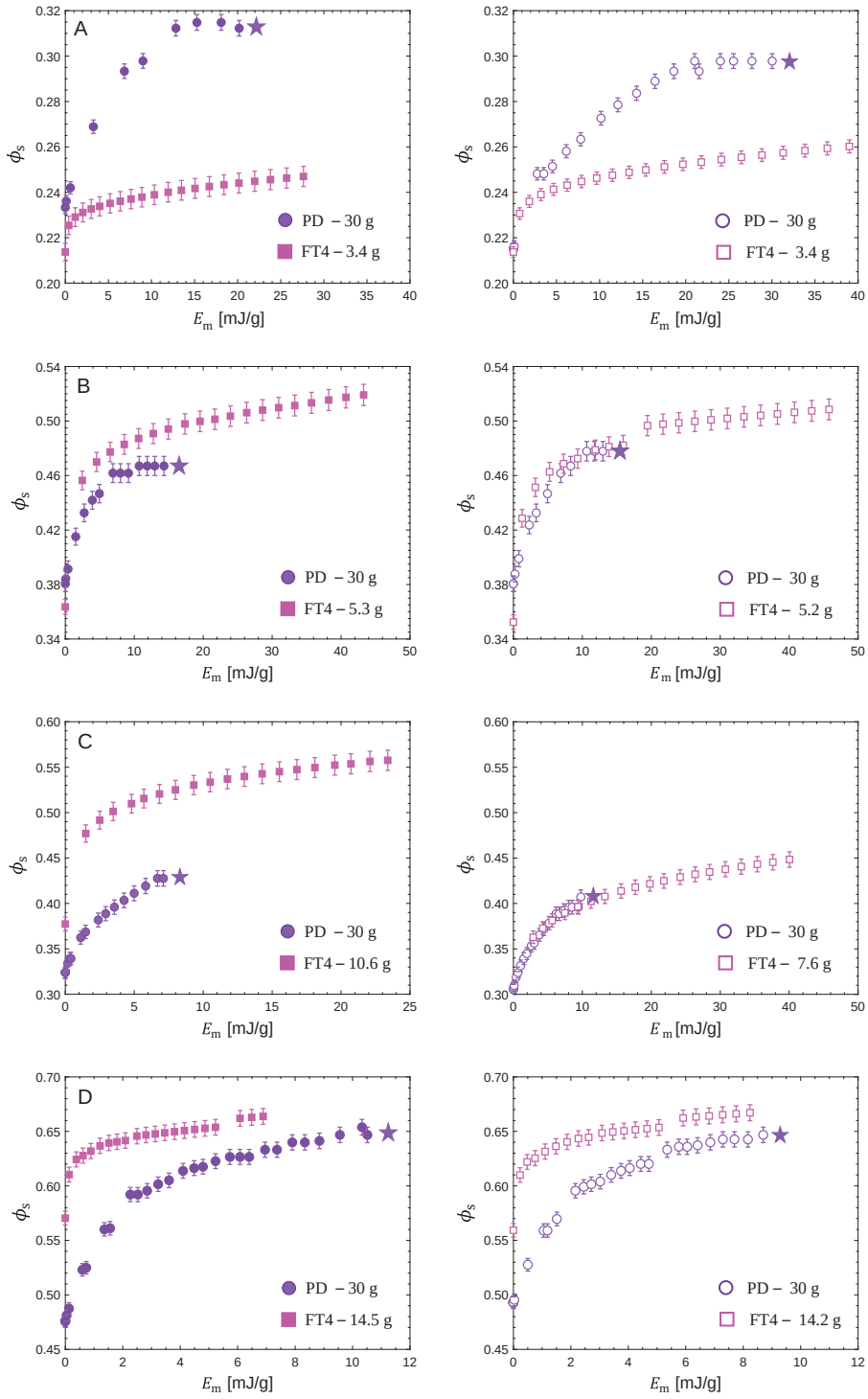


**Fig. 8** Dynamic densification $\phi_s$ as a function of $E_m$. Compaction is generated using a particle damper (PD) at $f$ = 30 Hz (○) and uniaxial compression with the FT4 (□). Filled symbols represent samples conditioned at 20 % RH **(left)**, and empty symbols represent samples conditioned at 60 % RH **(right)**. The star indicates the $E_m$ at which powder bed decompaction occurs. The data are shown for **A)** Avicel PH 102, **B)** Wheat flour, **C)** Joint filler, and **D)** GB 3000E.

in previous works using the apparent mass vibration method, as described in Cares-Pacheco et al. (2024). This methodology evaluates the elastic properties of the powders under aerated conditions, and under these conditions, $v$ is neglected. As a result, the velocity $c$ of the elastic longitudinal wave is simplified to $c = \sqrt{E_{el} / \rho_p}$ . The wavelength $\lambda$ of the wave propagating through the powder can be determined using the relationship $\lambda = c/f$, where $f$ is the driven frequency.

The results are presented in **Table 2**. It is important to note that **Eqn. (9)** assumes the material is isotropic and homogeneous, meaning its properties are consistent in all

directions. This assumption may not hold true for all materials, and deviations from isotropy or homogeneity could affect the accuracy of the calculated wave velocity and wavelength. However, this approach still provides a reasonable approximation for the interpretation of the experimental data.

Since only the first mode of propagation is expected within the vessel (Gaete-Garretón et al., 2007), the theoretical longitudinal wave transmitted to the powder, as described in **Table 2**, is depicted in **Fig. 11**, along with the filling volumes used during the experiments. It is observed that higher compression—wave crest—is expected for medium and maximum fillings. However, dissipation increases with the number of particles (Marhadi and Kinra, 2005). Therefore, particles at medium fillings, experiencing higher compression but lower dissipation, might

**Table 2** Calculations of the velocity $c$, and wavelength $\lambda$, of the vibration propagating within the powder bed, determined from the powder's elastic modulus $E_{el}$[b].

| Powder | $E_{el}$ [MPa] | $c$ [m/s] | $\lambda$ [m] |
|---|---|---|---|
| Av. PH102 | 0.20 | 12.5 | 0.32 |
| GB-3000E | 0.57 | 13.8 | 0.65 |
| Wheat flour | 0.24 | 15.4 | 0.46 |
| Joint filler | 0.17 | 20.7 | 0.27 |

[b] Cares-Pacheco et al. (2024)

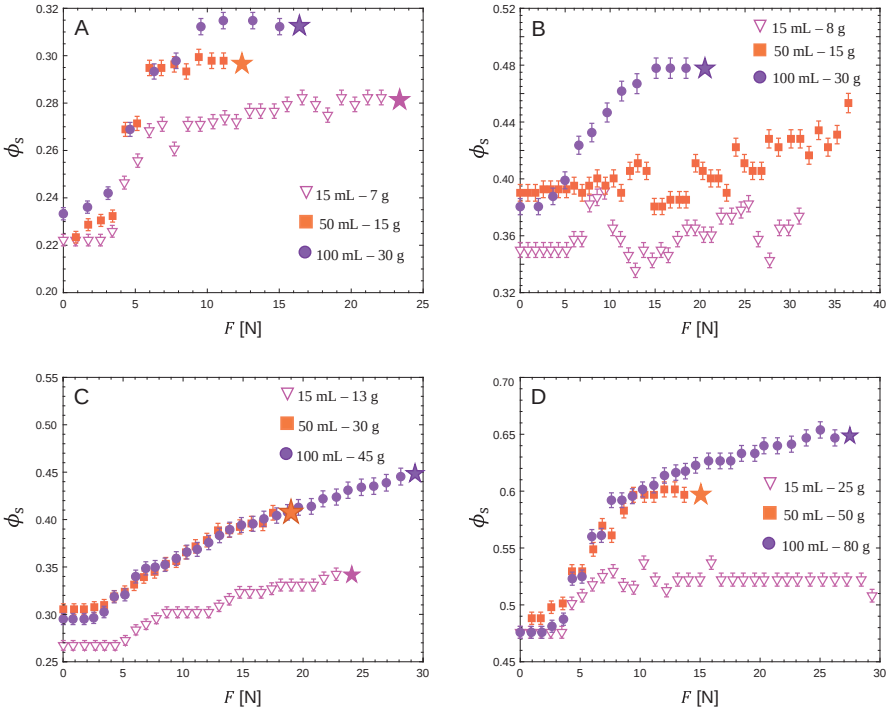


**Fig. 9** The densification dynamics of $\phi_s$ as a function of $F$, where $\phi_s$ is investigated at a fixed $f = 30$ Hz for different volumes: low volume, ▽ 15 mL; medium volume, □ 50 mL; and full volume, ○ 100 mL. Samples include **A)** Avicel PH102 conditioned at 30 % RH, **B)** wheat flour conditioned at 30 % RH, **C)** joint filler conditioned at 60 % RH, and **D)** GB 3000E conditioned at 30 % RH. The star indicates the force at which powder bed decompaction occurs.

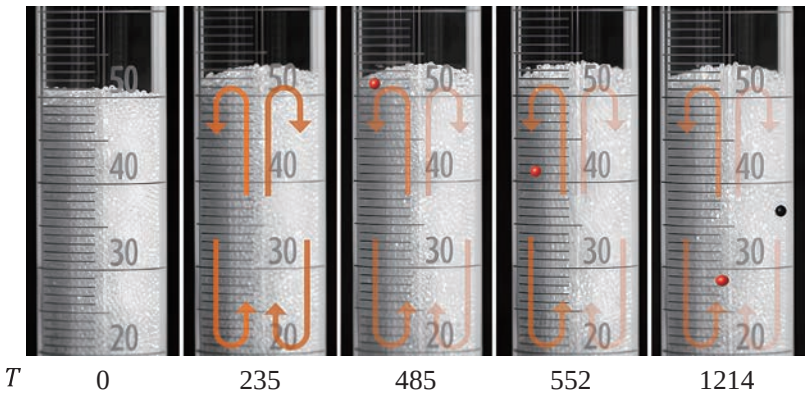


**Fig. 10** Convective movement observed with GB-A. Some particles were colored red and black to track their path.

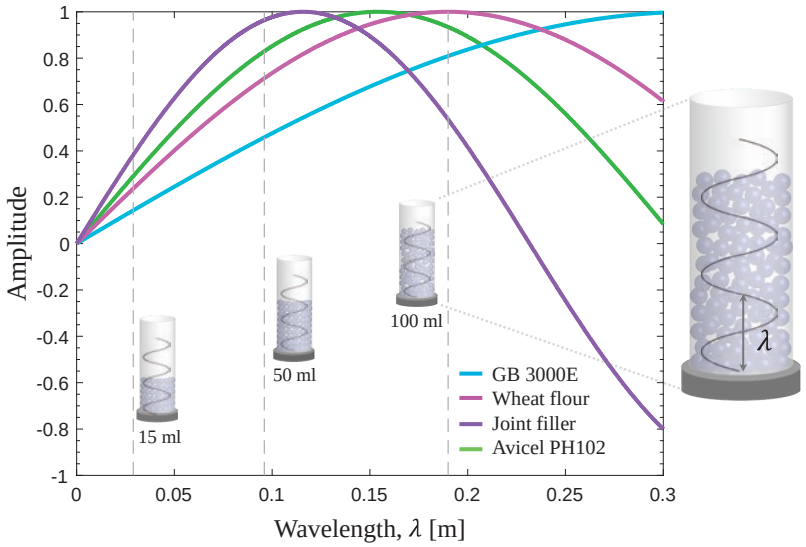


**Fig. 11** Theoretical longitudinal wave (LW) propagating within the powder column from **Table 2**, with vertical dashed lines delineating the powder volume in the vessel. The diagram shows the direction of LW propagation through the powder.

decompact more easily at lower accelerations.

This simplified analysis of the transmission of vibration waves from the experiments (**Fig. 11**) shows potential. Indeed, the length and shape of the vibration propagating within the material can be correlated with the acoustic impedance of the system (transducer + container + media) (Hueter and Bolt, 1955). It has been demonstrated that the acoustic impedance response of the system varies with column height, leading to completely different dynamic behaviors. For instance, for wood particles immersed in water, at low acoustic impedance, the particles exhibited agglomeration with a large cluster-like structure at the center of the suspension, while a highly dispersive granular suspension was observed at the maximum impedance regime (Cares-Pacheco et al., 2010; Gaete-Garretón et al., 2011).

Recently, Sonzogni et al. (2024), using particle dynamic simulations, concluded that the void ratio $e$, in isotropic compaction depends in a nonlinear and nonmonotonic way on the degree of adhesion of monodisperse hard particles. Our experiments appear to validate this statement; however, it is important to note that the degree of cohesion in real samples cannot be isolated from other particle properties, such as elastic modulus, size, and shape. The combined effects of these factors may also contribute to the observed behaviors, making it challenging to attribute the dynamics solely to cohesion.

## 3.3 Decoding attractive interactions

Despite conditioning the powder and implementing strict pouring protocols to achieve a highly reproducible initial packing fraction and constant powder height, the authors acknowledge the extremely low probability of reproducing the same contact network after pouring the

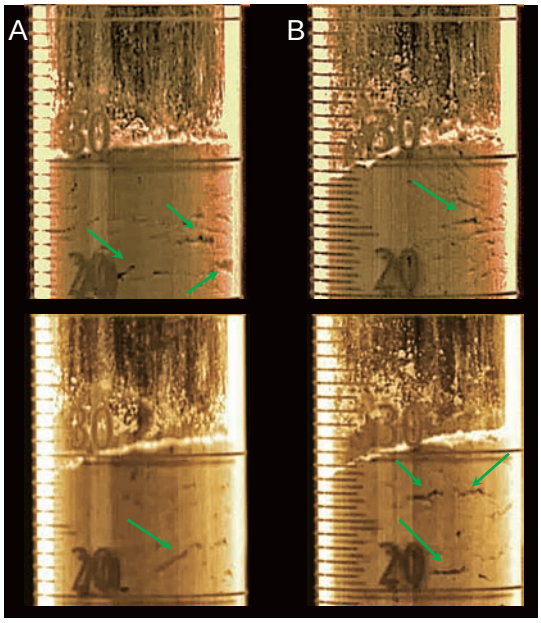


**Fig. 12** Snapshots from two separate compaction dynamics experiments, **A** and **B**, on different samples of the same powder under identical vibration conditions. The images, captured at synchronized intervals, compare the dynamics at two different moments (**top** and **bottom** sets). Green arrows highlight differences in particle rearrangement within the bulk.

powder. For instance, **Fig. 12** shows two distinct experiments for the same sample under identical excitation conditions (see Suaza-Montalvo et al., 2023b, Video 03 in the DOREL repository for details). Although both samples achieved a reproducible packing evolution $\phi(t)$, with less than 2 % variability, image analysis revealed that particles within the bulk follow different trends, indicating that the contact network itself, and its evolution during vibration are not identical but statistically retain a consistent packing

fraction. This underscores the challenges in describing force contact networks in 3D configurations and highlights the difficulties, or even the irrationality, of comparing experiments with theoretical modeling at the grain scale for such configurations. The particles can assume virtually infinite packing configurations while statistically retaining consistent macroscopic properties.

The anisotropy in the contact network prompts us to focus on identifying indicators that offer meaningful insights into the system dynamics. In this regard, the decompaction conditions ($\Gamma_d$ and $F_d$) are applied to the granular material, irrespective of its packing state, the powder bed will not be able to compact. Instead, a fluid-like behavior, either liquid-like or gas-like, or both, will be observed, indicating an unstable state. Such experimental findings allow us to infer that the parameters facilitating the decompaction of a powder bulk provide insights into the mesoscale, macroscopically describing a limit of stability in the contact network. In this context, $\Gamma_d$ serves as a descriptor of bulk cohesion. A dimensionless number can be defined from it as the ratio of cohesive forces to non-cohesive forces:

$$A_d = \frac{F_d}{W_p} \tag{10}$$

**Eqn. (10)** is akin to a Bond number of the mesoscale, quantifying bulk adhesion as the ratio of decompaction force to the gravitational weight of the powder, $W_p$. A strong force network is characterized by $A_d > 1$, while $A_d < 1$ values will denote a weak contact network.

The decompaction force relies on both the vibration wave (its shape and intensity—Ω, $\Gamma$, but also the period between cycles) and the system geometry (container dimensions, grain size, and powder height). This implies that various configurations can be explored, each corresponding to specific conditions under study. Nevertheless, the *maximum packing fraction* $\phi_U$, can be identified for a fixed system geometry, representing the highest achievable reorganization state of the powder in a vessel. This fraction is intrinsic to the powder and appears to correlate more closely with the powder's flowability assessment when using the *HR* (Saker et al., 2019). This maximum consolidation state is referred to as the "Ultimate" state, and all parameters describing it are denoted by the subscript *U* (e.g., $F_{d,U}$ and $HR_U$). This ultimate consolidation state $\phi_U$, can be determined either through continuous experiments, like those conducted in this study, or through stationary studies, as elaborated in Suaza-Montalvo et al. (2023a).

The relationship between the ultimate Hausner ratio $HR_U$ as a flow indicator and cohesive interactions from $F_{d,U}$ values, for our fixed geometry and various powders (30 g of powder and 20 % RH) is depicted in **Fig. 13**. Here, the $HR_U$ values show a linear increase with $A_d$ (plotted on a semi-logarithmic scale). This observation supports our hypothesis, indicating that lower $A_d$ values are associated with a weak force network, where $W_p$ outweighs cohesive interactions, as typically seen in gravitational flows. Conversely, higher $A_d$ values are linked with strong networks that hinder flow.

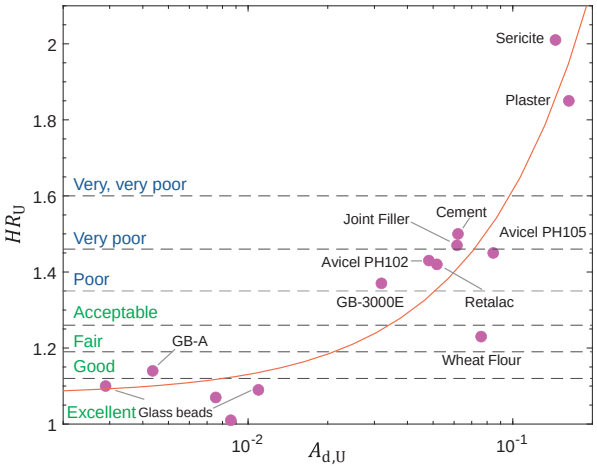


**Fig. 13** Evolution of $HR_U$ with $A_{d,U}$, both determined from the experiments where the highest packing fraction was obtained. The *y*-axis shows the Hausner classification of flowability.

It can be observed that wheat flour deviates from the expected trend, and Avicel PH102 is described as having poor flowability. For wheat flour, which consists mainly of gluten and starch, fair flowability can be attributed to its bi-modal particle size distribution and elastic properties, with gluten particles being larger and harder than starch particles (Cares-Pacheco et al., 2024). In the case of Avicel PH102, a powder formulated for compaction, its aptitude for compaction does not directly correlate with its ability to flow. However, this may explain the presence of a medium-strength force network; despite the low cohesion between particles (with a Bond number of 14), particle deformation during compaction increases the number of contact points.

In an effort to delve deeper into our potential contact network descriptor $A_{d,U}$, **Table 3** compiles dimensionless cohesion descriptors derived from previous studies. These descriptors were obtained using techniques such as Inverse Gas Chromatography (IGC) (Jiménez-Garavito et al., 2023) and shear test experiments (Cares-Pacheco and Falk, 2023). Notably, the dispersive surface energy $\gamma_s^d$ is highlighted as a powerful descriptor of the surface properties of divided solids, indicating cohesion at the particle scale. This is represented by the granular Bond number $Bo_g$, which relates interparticle cohesion $F_c$ to the particle weight $W_g$ as follows, based on the multi-asperity model by Chen et al. (2008):

$$F_c = \frac{H}{12 z_0^2}\left(\frac{d}{2(L_0 / z_0)^2} + \frac{3 d_a d}{d_a + d}\right) \tag{11}$$

where $L_0$ is the separation distance, set at 0.1 μm; $d_a$ is the

**Table 3** Summary of attractive interparticle forces descriptors at different scales, with the dispersive surface energy ($\gamma_s^d$) used to determine the granular Bond number ($Bo_g$[c]) as a particle-scale descriptor, the parameter $C$[d] from shear testing as a bulk-scale descriptor, the flow factor ($f_c$), and $A_{d,U}$ as a mesoscale descriptor of the contact network, with the ultimate Hausner ratio ($HR_U$) serving as its flow index.

| Powder | IGC[c] | | FT4[d] | | PD decompaction | |
|---|---|---|---|---|---|---|
| | $\gamma_s^d$ | $Bo_g$ | $C$ | $f_c$ | $A_{d,U}$ | $HR_U$ |
| Avicel PH-102 | 57.8 | 14 | 0.027 | 17 | 48 | 1.43 |
| Wheat flour | 42.8 | 109 | 0.073 | 7 | 76 | 1.23 |
| Joint filler | 39.9 | 5681 | 0.064 | 7 | 62 | 1.47 |
| GB-3000E | 47.2 | 170 | 0.021 | 22 | 32 | 1.37 |

[c] Jiménez et al., 2023; [d] Cares-Pacheco and Falk, 2023.

asperities diameter, set at 0.2 μm; $z_0$ is the equilibrium separation distance equal to 0.4 nm; and $H$ is the Hamaker constant, determined using Frenkel's relation:

$$H = 24\pi D_0^2 \gamma_s^d \tag{12}$$

with $D_0$ being the cut-off distance, equal to 0.165 nm.

The parameter $C$, which compares the adhesive interactions between grains as determined from the yield locus and the confining normal stress or preconsolidation stress in shear testing, serves as a critical bulk-scale descriptor (Cares-Pacheco and Falk, 2023). To ensure a comprehensive comparison under consistent consolidation conditions, the $C$ and $f_c$ values listed in **Table 3** were obtained at the same preconsolidation force at which powder decompaction occurs in our damping tests. This consistency ensures that the comparison across different descriptors is meaningful and reliable, particularly when assessing the mesoscale descriptor $A_{d,U}$ and the $HR_U$ as a flow index.

The comparative analysis of the samples reveals distinct characteristics in their cohesion properties and contact networks. For Avicel PH-102, the moderate $A_{d,U}$ value indicates a well-established contact network. The relatively low $C$ and $Bo_g$ values suggest moderate bulk cohesion and interparticle forces, respectively. Wheat flour, on the other hand, exhibits higher $Bo_g$ and $C$ values, indicating strong interparticle forces and bulk cohesion. The high $A_{d,U}$ value indicates a robust contact network, likely contributing to the overall cohesion.

Joint filler displays an extremely high $Bo_g$ signifying very strong interparticle cohesion, consistent with its high $C$. The high $A_{d,U}$ value further indicates a well-developed contact network, supporting the strong bulk properties. In contrast, GB-3000E had the lowest $A_{d,U}$, suggesting a less developed contact network compared to the other samples. The low $C$ and moderate $Bo_g$ values indicate weaker cohesion at both the particle and bulk scales. It's important to note that the analysis seems biased by the $Bo_g$ values, particularly for GB-3000E and Joint filler. In these cases, the higher $Bo_g$ values are more influenced by particle size distribution rather than accurately reflecting cohesive behavior, as observed with GB-3000E. This indicates that $Bo_g$ may not always be a reliable indicator of cohesion, particularly when particle size distribution significantly affects the results.

From a broader perspective, a higher $Bo_g$ generally corresponds to a higher $C$, indicating that stronger interparticle forces contribute to greater bulk cohesion. However, despite extensive research (Capece et al., 2015; Cares-Pacheco and Falk, 2023; Giraud et al., 2020), establishing a direct correlation between particle-scale properties and bulk properties from shear testing has been challenging, primarily due to the extreme sensitivity of $Bo_g$ to particle size. Nevertheless, while bulk cohesion from the yield locus in shear testing is often categorized as a bulk property, it actually represents a fracture plane, providing a two-dimensional view of plastic failure phenomena. As a result, this parameter may not fully capture the essence of bulk cohesion, which is inherently a three-dimensional characteristic. The challenge lies in accurately linking these scales without relying solely on one specific physical property of the grains.

There is a notable correlation between $C$ and $A_{d,U}$; a more robust contact network, indicated by higher $A_{d,U}$ often supports higher bulk cohesion, indicated by higher $C$. The $A_{d,U}$ parameter provides insight into the limitations of the contact network, offering a view into the mesoscale and reflecting how particles rearrange and interact beyond simple pairwise contacts. The discovery of a macroscale descriptor for the contact force network, which can be determined independently of particle size or any specific particle properties, holds significant promise for better modeling and understanding granular materials on a broader scale.

## 4. Conclusions

This study delved into the intricate dynamics of vibration-induced densification across a broad spectrum of industrial powders, including wheat flour, joint filler, glass beads, and pharmaceutical excipients. By utilizing a particle damper, we conducted an extensive series of

experiments to investigate the effects of frequency, air humidity conditioning, and powder height on densification dynamics. We consistently analyzed the evolution of packing fraction with acceleration to explore the conditions leading to compaction and decompaction.

Our findings illuminate the pivotal role of transmitted vibration waves in shaping the densification dynamics of granular materials, underscoring the significance of particle dampers. Notably, the sensitivity of force and acceleration signals to changes in packing density highlights their potential as structural descriptors of bulk material.

The results demonstrate that under decompaction conditions, the granular assembly does not reach a steady state but instead exhibits liquid-like, gas-like, or combined behaviors. The decompaction force appears to counteract interparticle forces, preventing particle cohesion. These experimental findings suggest that the dynamic parameters controlling the decompaction of the powder bed provide insights into the mesoscale, revealing limitations within the contact force network.

The comparison between adhesive interaction descriptors such as $Bo_g$ and bulk cohesion $C$ highlights that the $A_{d,U}$ parameter shows a notable correlation with $C$ and can be similar to $Bo_g$. This indicates that a more robust contact network, as reflected in higher $A_{d,U}$ values, often corresponds to greater bulk and interparticle cohesion. The bulk cohesion parameter $C$, typically derived from the yield locus in shear testing, primarily represents a fracture plane, offering only a two-dimensional perspective on plastic failure and may not fully capture the three-dimensional nature of bulk cohesion. Unlike $Bo_g$, which is sensitive to particle size and reflects particle-scale properties, $A_{d,U}$ provides valuable insights into the mesoscale structure of the contact network, highlighting complex interactions beyond simple pairwise contacts. The potential of this macroscale descriptor for the contact force network, independent of particle size and specific particle properties, could significantly enhance the modeling and understanding of granular materials on a broader scale.

The results also highlight the importance of accurately quantifying the effects of air humidity on the samples. The water activity of the samples, representing free water, emerges as a suitable indicator that should be considered to ensure reproducible results and to better understand its role in particle interactions.

Consistent results, depending on particle nature and conditioning, highlight that simple, hard, cohesionless, round grains cannot adequately represent the intricate interactions between grains in real granular assemblies, which are often cohesive and possess arbitrary shapes. By extracting and comprehending realistic particle-scale and bulk-scale data, this research establishes a foundation for developing comprehensive, physics-based insights for effectively understanding the behavior of granular materials.

Future research should prioritize longitudinal wave propagation, acoustic impedance, and powder column height by using the experimental framework established here. Moreover, integrating theoretical data-driven models can complement experimental findings, providing a more nuanced understanding of the microscopic forces. This integration has the potential to enhance the predictive capabilities of existing models and provide valuable insights into the behavior of granular materials under diverse conditions.

## Acknowledgments

The authors acknowledge Andrea Suaza-Montalvo, Maria Camila Jiménez-Garavito, and Assia Saker for their valuable contributions to the experimental work. The combined data laid the groundwork for this study.

## Data Availability Statement

Some data supporting the findings of this study are openly available in the DOREL repository at the Université de Lorraine. The data can be accessed through the https://doi.org/10.12763/VKDBAS.

## Nomenclature

| | |
|---|---|
| $a$ | acceleration (m s$^{-2}$) |
| $a_w$ | water activity (-) |
| $A_d$ | ratio of cohesive to noncohesive forces (-) |
| $A_{d,U}$ | ultimate $A_d$ (-) |
| $Bo_g$ | granular Bond number (-) |
| $c$ | wave velocity (m s$^{-1}$) |
| $C$ | ratio of bulk cohesion to preconsolidation stress from shear testing experiments (-) |
| $d_a$ | asperity diameter (m) |
| $D_0$ | cut-off distance (m) |
| $d$ | particle diameter (μm) |
| $d_{3,2}$ | Sauter diameter (μm) |
| $d_{4,3}$ | De Brouckere mean diameter (μm) |
| $d_{10}$, $d_{50}$, $d_{90}$ | particles diameters corresponding to the 10$^{th}$, 50$^{th}$, and 90$^{th}$ percentiles (μm) |
| $E_{el}$ | elastic (Young's) modulus (MPa) |
| $E_m$ | specific energy (J kg$^{-1}$) |
| $E_v$ | kinetic vibration energy derived from harmonically driven systems (J) |
| $\tilde{E}_{diss}$ | dissipated energy (J) |
| $f$ | frequency (Hz) |
| $f_c$ | flow factor derived from the shear test |
| $F$ | force (N) |
| $F_c$ | cohesion force derived from the multi-asperity model (N) |
| $F_d$ | force at decompaction point (N) |
| $F_{d,U}$ | ultimate force at decompaction point (N) |
| $g$ | gravity (m s$^{-2}$) |
| $H$ | Hamaker constant (J) |
| $HR$ | Hausner ratio (-) |
| $HR_U$ | ultimate Hausner ratio (-) |
| $L_0$ | separation distance (m) |
| $m$ | mass (kg) |
| $m_p$ | mass of powder (kg) |
| $S$ | cross section of the vessel (m$^2$) |

| | |
|---|---|
| $V$ | volume of a vessel (L) |
| $W_p$ | powder weight (N) |
| $W_g$ | particle weight (N) |
| $v$ | velocity (m $s^{-1}$) |
| $v_{air}$ | average air velocity (m $s^{-1}$) |
| $v_{mf}$ | minimum fluidization velocity (m $s^{-1}$) |
| $Z$ | average number of contacts per particle (-) |
| $z_0$ | equilibrium separation distance (m) |
| $\gamma_s^d$ | dispersive surface energy (J $m^{-2}$) |
| $\Gamma$ | relative acceleration (-) |
| $\Gamma_d$ | relative acceleration at decompaction point (-) |
| $\Delta t$ | time duration (s) |
| $\Delta V$ | bed volume reduction ($m^3$) |
| $\Delta z$ | bed height reduction (m) |
| $\lambda$ | wavelength (m) |
| $\mu$ | gas viscosity (Pa s) |
| $\nu$ | Poisson's ratio (-) |
| $\rho$ | density (kg $m^{-3}$) |
| $\rho_p$ | pycnometric density (kg $m^{-3}$) |
| $\phi$ | packing fraction (-) |
| $\phi_s$ | stable packing fraction (-) |
| $\phi_U$ | ultimate packing fraction (-) |
| $\phi_{s,d}$ | packing fraction at decompaction point (-) |
| $\omega$ | angular frequency (rad $s^{-1}$) |
| $\Omega$ | relative frequency (-) |

## References


Andreotti B., Forterre Y., Pouliquen O., Les Milieux Granulaires—Entre Fluide et Solide, EDP Sciences, 2011. ISBN: 978-2759800971.

Bérut A., Pouliquen O., Forterre Y., Brownian granular flows down heaps, Physical Review Letters, 123 (2019) 248005. https://doi.org/10.1103/PhysRevLett.123.248005

Capece M., Ho R., Strong J., Gao P., Prediction of powder flow performance using a multi-component granular Bond number, Powder Technology, 286 (2015) 561–571. https://doi.org/10.1016/j.powtec.2015.08.031

Cares-Pacheco M.-G., Cordeiro E., Gérardin F., Falk V., Consistency in Young's modulus of powders: a review with experiments, Powders, 3(2) (2024) 280–304. https://doi.org/10.3390/powders3020017

Cares-Pacheco M.G., Falk V., A phenomenological law for complex granular materials from Mohr-Coulomb theory, Advanced Powder Technology, 34 (2023) 103888. https://doi.org/10.1016/j.apt.2022.103888

Cares-Pacheco M.-G., Jiménez Garavito M.-C., Ober A., Gerardin F., Silvente E., Falk V., Effects of humidity and glidants on the flowability of pharmaceutical excipients. An experimental energetical approach during granular compaction, International Journal of Pharmaceutics, 604 (2021) 120747. https://doi.org/10.1016/j.ijpharm.2021.120747

Cares-Pacheco M.G., Vargas Y., Gaete L., Sainz J., Alarcón J., Ultrasonically assisted extraction of bioactive principles from Quillaja Saponaria Molina, Physics Procedia, 3 (2010) 169–178. https://doi.org/10.1016/j.phpro.2010.01.024

Carson J.W., Wellwood G., Maynard E.P., How to reduce safety risks when storing and handling bulk solids, Informa Markets, (2019). <https://www.powderbulksolids.com/> accessed 16.05.2024.

Chen Y., Yang J., Dave R., Pfeffer R., Fluidization of coated group C powders, AIChE Journal, 54 (2008) 104–121. https://doi.org/10.1002/aic.11368

Gaete-Garretón L., Hernández Y., Cares M., Vega R., Influence of acoustic parameters in ultrasonic comminution of Zn powders in liquid phase, presented at the Internation Congress on Acoustics, ICA 19th, Madrid, 2007.

Gaete-Garretón L., Vargas-Hernández Y., Cares-Pacheco M.G., Sainz J., Alarcón J., Ultrasonically enhanced extraction of bioactive principles from Quillaja Saponaria Molina, Ultrasonics, 51 (2011) 581–585. https://doi.org/10.1016/j.ultras.2010.12.012

Geldart D., Types of gas fluidization, Powder Technology, 7 (1973) 285–292. https://doi.org/10.1016/0032-5910(73)80037-3

Ghadiri M., Pasha Mehrdad, Nan W., Hare C., Vivacqua V., Zafar U., Nezamabadi S., Lopez A., Pasha Massih, Nadimi S., Cohesive powder flow: trends and challenges in characterisation and analysis, KONA Powder and Particle Journal, 37 (2020) 3–18. https://doi.org/10.14356/kona.2020018

Gilabert F.A., Roux J.-N., Castellanos A., Computer simulation of model cohesive powders: influence of assembling procedure and contact laws on low consolidation states, Physical Review E, 75 (2007) 011303. https://doi.org/10.1103/PhysRevE.75.011303

Giraud M., Gatumel S., Vaudez S., Bernard-Granger G., Nos J., Gervais T., Berthiaux H., Investigation of a granular Bond number based rheological model for polydispersed particulate systems, Chemical Engineering Science, 228 (2020) 115971. https://doi.org/10.1016/j.ces.2020.115971

Grace J.R., Contacting modes and behaviour classification of gas—solid and other two-phase suspensions, The Canadian Journal of Chemical Engineering, 64 (1986) 353–363. https://doi.org/10.1002/cjce.5450640301

Hausner H., Friction conditions in a mass of metal powder, International Journal of Powder Metal, 3 (1967) 7–13.

Herrmann H.J., Hovi J.-P., Luding S., Eds., Physics of Dry Granular Media, Springer Netherlands, Dordrecht, 1998, ISBN: 978-0792351023. https://doi.org/10.1007/978-94-017-2653-5

Hueter T.F., Bolt R.H., Sonics: Techniques for the Use of Sound and Ultrasound in Engineering and Science, Wiley, 1955, ISBN: 9780471419761.

Jaeger H.M., Nagel S.R., Behringer R.P., Granular solids, liquids, and gases, Reviews of Modern Physics, 68 (1996) 1259–1273. https://doi.org/10.1103/RevModPhys.68.1259

Jiménez Garavito M.C., Cares Pacheco M.G., Witschger O., Bau S., Gerardin F., Falk V., The effect of silica nanoparticles on the dustiness of industrial powders, Advanced Powder Technology, 34 (2023) 104105. https://doi.org/10.1016/j.apt.2023.104105

Knight J.B., Fandrich C.G., Lau C.N., Jaeger H.M., Nagel S.R., Density relaxation in a vibrated granular material, Physical Review E, 51 (1995) 3957–3963. https://doi.org/10.1103/PhysRevE.51.3957

Kollmer J.E., Daniels K.E., Betweenness centrality as predictor for forces in granular packings, Soft Matter, 15 (2019) 1793–1798. https://doi.org/10.1039/C8SM01372A

Landi G., Barletta D., Poletto M., Modelling and experiments on the effect of air humidity on the flow properties of glass powders, Powder Technology, 207 (2011) 437–443. https://doi.org/10.1016/j.powtec.2010.11.033

Majmudar T.S., Behringer R.P., Contact force measurements and stress-induced anisotropy in granular materials, Nature, 435 (2005) 1079–1082. https://doi.org/10.1038/nature03805

Marhadi K.S., Kinra V.K., Particle impact damping: effect of mass ratio, material, and shape, Journal of Sound and Vibration, 283 (2005) 433–448. https://doi.org/10.1016/j.jsv.2004.04.013

Marteau E., Andrade J.E., An experimental study of the effect of particle shape on force transmission and mobilized strength of granular materials, Journal of Applied Mechanics, 88 (2021) 111009. https://doi.org/10.1115/1.4051818

Masmoudi M., Job S., Abbes M.S., Tawfiq I., Haddar M., Experimental and numerical investigations of dissipation mechanisms in particle dampers, Granular Matter, 18 (2016) 71. https://doi.org/10.1007/s10035-016-0667-4

Meyer N., Seifried R., Systematic design of particle dampers for transient vertical vibrations, Granular Matter, 25 (2023) 3. https://doi.org/10.1007/s10035-022-01290-y

Papadopoulos L., Porter M.A., Daniels K.E., Bassett D.S., Network analysis of particles and grains, Journal of Complex Networks, 6 (2018) 485–565. https://doi.org/10.1093/comnet/cny005

Radjai F., Topin V., Richefeu V., Voivret C., Delenne J.-Y., Azéma E., El Youssoufi M.S., Force transmission in cohesive granular media, in: J. D. Goddard J.T.J. et P.G. (Ed.), Mathematical Modeling and Physical Instances of Granular Flows, AIP Conference Proceedings Vol. 1227, 2010, pp. 240–260, ISBN: 978-0735407725.

Ribière P., Philippe P., Richard P., Delannay R., Bideau D., Slow compaction of granular systems, Journal of Physics: Condensed Matter, 17 (2005) S2743–S2754. https://doi.org/10.1088/0953-8984/17/24/024

Ribière Ph., Richard P., Philippe P., Bideau D., Delannay R., On the existence of stationary states during granular compaction, The European Physical Journal E, 22 (2007) 249–253. https://doi.org/10.1140/epje/e2007-00017-x

Sack A., Heckel M., Kollmer J.E., Zimber F., Pöschel T., Energy dissipation in driven granular matter in the absence of gravity, Physical Review Letters, 111 (2013) 018001. https://doi.org/10.1103/PhysRevLett.111.018001

Saint-Cyr B., Radjai F., Delenne J.-Y., Sornay P., Cohesive granular materials composed of nonconvex particles, Physical Review E, 87 (2013) 052207. https://doi.org/10.1103/PhysRevE.87.052207

Saker A., Cares-Pacheco M.-G., Marchal P., Falk V., Powders flowability assessment in granular compaction: What about the consistency of Hausner ratio?, Powder Technology, 354 (2019) 52–63. https://doi.org/10.1016/j.powtec.2019.05.032

Schulze D., Powders and Bulk Solids: Behavior, Characterization, Storage and Flow, Springer International Publishing, Cham, 2021, ISBN: 978-3030767198. https://doi.org/10.1007/978-3-030-76720-4

Sonzogni M. Vanson J.-M., Ioannidou K., Reynier Y., Martinet S., Radjai F., Dynamic compaction of cohesive granular materials: scaling behavior and bonding structures, Soft Matter, 20 (2024) 5296–5313. https://doi.org/10.1039/D3SM01116J

Suaza-Montalvo A., Cares-Pacheco M.G., Falk V., Time-dependent behaviour of industrial granular materials under vibration: modelling and phenomenology, Chemical Engineering Science, 271 (2023a) 118571. https://doi.org/10.1016/j.ces.2023.118571

Suaza-Montalvo A., Cares Pacheco M.-G., Falk V., Vidéos des phenomenes observés pendant la compaction de poudres. Partie de la thèse: étude expérimentale de la compaction par vibration des poudres industrielles: phénoménologie et intérêt, Université de Lorraine, Dorel data repository (2023b). https://doi.org/10.12763/VKDBAS

Terzioglu F., Rongong J.A., Lord C.E., Influence of particle sphericity on granular dampers operating in the bouncing bed motional phase, Journal of Sound and Vibration, 554 (2023) 117690. https://doi.org/10.1016/j.jsv.2023.117690

Wu M., Wang J., Prediction of 3D contact force chains using artificial neural networks, Engineering Geology, 296 (2022) 106444. https://doi.org/10.1016/j.enggeo.2021.106444

Zhao Y., Phalswal P., Shetty A., Ambrose R.P.K., Effects of powder vibration and time consolidation on soft and hard wheat flour properties, KONA Powder and Particle Journal, 38 (2021) 226–234. https://doi.org/10.14356/kona.2021007

## Authors' Short Biographies

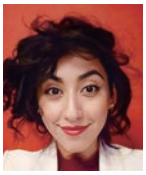

**Dr. Maria-Graciela Cares** is an Assistant Professor at the Université de Lorraine, affiliated with the Reactions and Chemical Engineering Laboratory (LRGP-CNRS), and teaches at the engineering school ENSIC in Nancy, France. She holds a degree in Physics Engineering from the University of Santiago de Chile, a Master's in Materials Science from the Université de Franche-Comté, and a Ph.D. from IMT Mines Albi. Her expertise spans Physics and Engineering, with a particular focus on granular physics and powder technologies, which has led to collaborations with the cosmetics, pharmaceutical, food, and automotive industries.

**Prof. Véronique Falk** graduated from École Nationale Supérieure des Industries Chimiques de Nancy (ENSIC), France, in 1991, earning degrees in Chemical Engineering and a Master's. She completed her PhD in 1995, focusing on catalytic cracking in collaboration with Total Raffinage. Since 2014, she has been a professor at Ecole Nationale Supérieure en Génie des Systèmes et de l'Innovation (Université de Lorraine), serving as deputy director since 2019. Her research at Laboratoire Réactions et Génie des Procédés (LRGP-CNRS) focuses on experimental powder technology, including rheology, mixing, granulation, compression, and product formulation, with extensive industry collaboration.

KONA Powder and Particle Journal No. 42 (2025) 285–287/https://doi.org/10.14356/kona.2025021 Information Article

# The 56th Symposium on Powder Technology

The 56th Symposium on Powder Technology organized by Hosokawa Powder Technology Foundation took place at Grand Cube Osaka (Osaka International Convention Center), in Japan on Tuesday, September 3, 2024. It was held by the planning of Council of Powder Technology, Japan and with the sponsorship of Hosokawa Micron Corporation. Nearly 250 people from the industries and universities attended this symposium. The theme of the symposium this year was "Powder Technology and its Applications for Advanced Manufacturing Processes". There were six lectures, including the KONA Award commemorative lecture, from basic and applied perspectives. This year's symposium was held in a hybrid format, with both in-person and online participation, for the third consecutive year.

The event began with an opening address by Mr. Yoshio Hosokawa, the president of the Foundation, who welcomed participants from a wide range of academic and industrial fields and introduced the background of the Symposium and the Foundation's activities in the field of powder technology in Japan and abroad.

Prior to the lectures, the KONA Award presentation ceremony was held, and the plaque of the KONA Award was handed from the president to the 2023 KONA Awardee; Emeritus Professor Wiwut Tanthapanichakoon, Chulalongkorn University, Thailand. The KONA Award is an international award given to researchers who have made outstanding achievements in the field of powder and particle science and technology. He is the 38th recipient of the award and the first Asian (excluding Japan) to receive the KONA Award. The contents of the symposium are shown below.

In the subsequent lecture session, the 2023 KONA Award commemorative lecture was delivered first, in which he gave an easy-to-understand explanation of his contributions to the development of powder and particle science and technology and the promotion of technological exchange between Thailand and Japan, particularly with regard to representative examples of research results applying submicron- and nano-sized particle technology, such as the development of HEPA filter technology.

Opening address by President Yoshio Hosokawa.

The 2023 KONA Award commemorative lecture by Emeritus Prof. Wiwut Tanthapanichakoon.

Following this, two keynote lectures were delivered by prominent figures in the field of powder technology: Professor Shoji Maruo of Yokohama National University and Research Director Yuji Hotta of AIST. Prof. Maruo presented the latest trends in ultra-precision 3D printing technology using various powder materials, while Dr. Hotta discussed the effectiveness of AI technology in material development, particularly for ceramics, and the contributions of Material DX.

Subsequently, three industry experts delivered presentations on the application of powder technology and nanoparticle synthesis and processing techniques in product developments that have been attracting much attention recently. Dr. Chie Kawamura from Taiyo Yuden Co., Ltd. discussed the development of energy devices using multilayer ceramic capacitors (MLCCs), Dr. Takahiro Morishita from Toyo Tanso Co., Ltd. presented on the development of high-performance carbon materials through powder control technology and their

Lectures by Prof. Shoji Maruo, Dr. Mikinori Hotta, Dr. Chie Kawamura, Dr. Takahiro Morishita, and Mr. Kenji. Shimizu.

applications, and Mr. Kenji Shimizu from Hosokawa Micron Corporation spoke about technological innovations in powder measurement equipment that meet the needs of cutting-edge powder production processes.

After the lectures, a general discussion session was held, chaired by Executive Director of the Foundation and Emeritus Professor Makio Naito of Osaka University. Questions and opinions were raised by attendees from various fields, leading to a lively exchange where the speakers directly responded to the inquiries.

At the conclusion of the symposium, President Kohei Hosokawa of Hosokawa Micron Corporation delivered a closing address, marking the successful end of the event. Following the symposium, in the reception hall, a social gathering was held, continuing from last year, allowing the lecturers and attendees to engage in meaningful exchanges in a relaxed atmosphere from beginning to end. This year, over 80 participants attended the venue, filling the room to capacity, with nearly 250 attendees in total, including online participants. The following 57th Symposium is scheduled to be held in Tokyo next year.

Lecture scene.

General discussion.

Closing remarks by HMC President Kohei Hosokawa.

Get-acquainted party.

**The 56th Symposium on Powder Technology**

**Theme:** "Powder Technology and its Applications for Advanced Manufacturing Processes"
**Date:** Tuesday, September 3, 2024
**Place:** Grand Cube Osaka (Osaka International Convention Center)

**Opening address** Mr. Yoshio Hosokawa (*President of Hosokawa Powder Technology Foundation, Chairman of Hosokawa Micron Corporation, Japan*)

・2023 KONA Award presentation ceremony

**Session 1** Chaired by Prof. Masayoshi Fuji (*Nagoya Institute of Technology, Japan*)

・Lecture 1 (Special lecture by the 2023 KONA Awardee)
**"Our Contributions to the Advancement of Powder/Particle Technology Including Thailand–Japan Collaborations"**
Emeritus Prof. Wiwut Tanthapanichakoon (*Chulalongkorn University, Thailand*)

・Lecture 2
**"Ultra-Precision 3D Printing Technology Using Various Powder Materials"**
Prof. Shoji Maruo (*Graduate School of Engineering, Yokohama National University, Japan*)

**Session 2** Chaired by Dr. Yoshio Sakka (Special Researcher, NIMS)

・Lecture 3
**"Data-Driven Materials Research and Development Contributing to Material Innovation and Enhanced Reliability for Ceramics and Other Materials"**
Dr. Mikinori Hotta (*Group Leader, National Institute of Advanced Industrial Science and Technology (AIST), Japan*)

・Lecture 4
**"Development of All-Solid-State Batteries and Fuel Cells Utilizing the Material Technology of Multilayer Ceramic Capacitors"**
Dr. Chie Kawamura (*Chief Researcher, Taiyo Yuden Co. Ltd., Japan*)

**Session 3** Chaired by Honorary Research Advisor, Dr. Hisao Makino (*CRIEPI, Japan*)

・Lecture 5
**"High-Performance Graphite Products Based on Powder Control Technology and the Latest Carbon Powder Materials"**
Dr. Takahiro Morishita (*Executive Fellow, Toyo Tanso Co. Ltd., Japan*)

・Lecture 6
**"The Latest Powder Property Measurement Technology"**
Mr. Kenji Shimizu (*Powder Technology Research Institute, Hosokawa Micron Corporation, Japan*)

**General discussion** Chaired by Emeritus Prof. Makio Naito (*Osaka University, Japan*)

**Closing remarks** Dr. Kohei Hosokawa (*President of Hosokawa Micron Corporation, Japan*)

# The KONA Award 2023

The KONA Award has been presented to the researchers who have greatly contributed to research and development as well as education in the field of Powder and Particle Science and Technology since 1990. Originally given by the Hosokawa Micron Corporation, it is now presented annually to researchers worldwide by the Hosokawa Powder Technology Foundation. The application for this award requires a specified recommendation form written in English to be submitted to the President of the Hosokawa Foundation. The award candidates are reviewed by the KONA Award Committee members, and the results are reported to the Selection Committee of the Foundation for nominating the awardee. It needs to be finally approved at the Board of Directors' meeting of the Foundation. The KONA Award is presented at a ceremony in or outside Japan with a plaque and a prize of one million yen. The KONA Award 2023 has been presented to Emeritus Prof. Wiwut Tanthapanichakoon from Thailand. The KONA Award plaque was presented to the awardee at the 56th Symposium on Powder Technology on September 3, 2024.

Dr. Wiwut Tanthapanichakoon (WT) has made great contributions to powder/particle and aerosol technology as well as chemical engineering from the viewpoints of not only academic research but also the promotion of collaboration in these fields, especially between Thailand and Japan, for nearly half a century. After studying chemical engineering at Kyoto University and obtaining his PhD degree at the University of Texas, he joined Chulalongkorn University (CU) in late 1978 and became a full professor in 1993, and an Emeritus Professor in 2004, and then took the post of the first Executive Director, National Nanotechnology Center (NANOTEC) in Thailand. After completing his term at NANOTEC, he became a TITech professor and in 2015 was appointed the first Thai Emeritus Professor in its century-long history.

During his long career, WT was a short-term JSPS visiting scientist for a total of 8 times at Kanazawa University (KZU), Kyoto Univ., and TITech. To initiate close research collaborations, WT went to KZU first as a 3-month JSPS visiting scientist in 1980. Starting from scratch, he could successfully manage to develop, create, and validate an innovative computer code that efficiently simulates the 3D convective diffusional deposition and dendritic growth of submicron aerosol particles on a single fiber using the Monte–Carlo method. In the 1980s, the filter performance and life expectancy of an entire HEPA and ULPA (fibrous air) filters, which are indispensable to clean rooms had to be determined experimentally because their theoretical investigations and simulations were impractical for submicron and nanosized particles that move by Brownian motion.

WT and KZU collaborators not only experimentally validated the methodology but also extended the simulation to the more realistic case of polydisperse particles and then used it to predict their performance and the filter life. They could quadruple the service life of a high-efficiency electret filter by gradually varying the packing density from lowest at the inlet to highest at the outlet, compared to the conventional case of equal, uniform packing density. WT has co-authored 21 papers on this important area since 1981.

In the area of nanoparticle synthesis (NPS), WT and his collaborators pioneered and extended the simple method of arc discharge in water to a variety of liquids (alcohols, alkanes, aromatics, etc.) and produced carbon and metal nanoparticles (NP) with higher yields and diverse morphologies (nanoballs, nanotubes, nano-onions, nano-whiskers, nano-horns, etc.) and novel characteristics. They further found that monoolein surfactant had an enhancing effect on carbon NP synthesis and the use of a metal-graphite electrode pair yielded metal-embedded CNP. They also investigated the synthesis of ZnS NP in microemulsion and of hydroxyapatite NP in an emulsion liquid membrane system as well as the effect of zinc precursors on the thermal and light emission properties of ZnO NP embedded in polyimide films. WT co-authored 24 papers on NPS since 2004.

While pursuing these opportunities, he introduced and established powder/particle technology as an integrated/comprehensive discipline in Thailand starting from the late 1980s with strong cooperation and support from Japan. WT was Deputy Dean for Research Affairs & Director of Engineering Institute for Research and Development (EIRD), and Chairman, ChE Dept. He played a key role in the initiation and establishment of the Thai Powder Technology Center (TPTC) in 1992 with strong support from APPIE (TPTCCC) and SPTJ, serving as Director. In 1996, he set up the Particle Technology and Material Processing Lab in the ChE Dept. He also set up and served as Director, Center of Excellence in Particle Technology (CEPT) with strong support from CU.


At the KONA Award presentation ceremony,
President Hosokawa (Right) and 2023 KONA Awardee Emeritus Prof. Wiwut Tanthapanichakoon (Chulalongkorn Univ., Thailand).

# General Information

**History of the Journal**

The KONA journal (currently called "KONA Powder and Particle Journal") was first published as an open-accessed scientific journal in 1983 by the Council of Powder Technology, Japan (CPT), which was established in 1969 by Hosokawa Micron Corporation as a nonprofit organization to promote powder technology, in order to introduce excellent Japanese papers to the world. From issue No.8, the CPT changed its editorial policy to internationalize the KONA journal and to incorporate papers by authors throughout the world. In response to this change, three editorial blocks have been organized worldwide: Asian–Oceanian, American and European–African. Issues from No.1 (1983) to No.12 (1994) of the KONA journal were published by the CPT, and issues from No.13 (1995) and onwards by the Hosokawa Powder Technology Foundation. The policy and system have not changed even after the Hosokawa Foundation took over the publication from the CPT. From issue No.38 (2021), the KONA journal primarily publishes review articles by leading researchers, including established and recently Ph.D.-awarded young researchers in the field.

**Aims and Scope**

KONA publishes review and original research papers in a broad field of powder and particle science and technology, ranging from fundamental principles to practical applications. Papers on critical reviews of existing knowledge in special areas are particularly welcome.

The submitted papers are published only when they are judged by the Editor to contribute to the progress of powder science and technology, and approved by any of the three Editorial Committees.

The paper submitted to the Editorial Secretariat should not have been previously published.

**Category of Papers**

- Invited articles
  Review papers and feature articles invited by the KONA Editorial Committees.
- Contributed papers
  Original review papers and some limited number of original research papers of high quality submitted to the KONA Editorial Committees, and refereed by the reviewers and editors.

**Submission of Papers**

To submit your paper, please use the online Editorial Manager® for KONA Online Paper Submission and Peer Review System. For further information, please visit the journal's website at https://www.kona.or.jp/jp/journal/info.html

*Publication in KONA is free of charge.*

**Publication Schedule**

*KONA will cease publication with its issue, No. 43, around January 10, 2026.*

**Subscription**

KONA is distributed for free to senior researchers at universities and laboratories, as well as to institutions and libraries in the field throughout the world.

**Instructions to Authors**

(1) **Language**

All submissions should be written in good English. Authors may choose either British or American English, provided that the chosen style is used consistently. Authors from non-English-speaking countries are encouraged to use professional English editing services to proofread their manuscripts.

(2) **Data Repository Information**

In order to promote open data discoverability and use of research outputs, this journal encourages authors to submit data files supporting their manuscript work, which can be deposited in the journal's J-STAGE Data site <https://jstagedata.jst.go.jp/kona> after acceptance of the paper through the peer-review process.

These data may describe observations, experiments, modeling or analyses, and may take the form of databases, simulations, movies, large figures, or as otherwise appropriate.

For questions or more information, please contact the KONA Editorial Office (contact_zainq@hmc.hosokawa.com).

(3) **Manuscript format**

- Electric files should be submitted to the Editorial Secretariat via Online Submission System. Author's short biography with less than 100 words per person should be attached to the final version.
- The structure of manuscripts should follow the following order; title, authors, affiliations, abstract, graphical abstract, keywords, main text, (data availability statement), (acknowledgement), (nomenclature), references. The items with parentheses are not mandatory.
- Full postal addresses must be given for all the authors. Indicate the corresponding author by the asterisk mark"*" after the name. Telephone and fax numbers and e-mail address should be provided for the corresponding author.
- Abstract should not exceed 200 words.
- Graphical abstract should be a concise, visual summary of the article which will be displayed in the contents list both online and print.
- The appropriate number of keywords is 5 or 6.
- The maximum pages printed in KONA are supposed to be: 15 for an original research paper and 25 for a review paper.
- Symbols and units should be listed in alphabetical order with their definition and dimensions in SI units.
- The color figures will appear in color both on the KONA Website (https://www.kona.or.jp) and also in the paper version.
- Concerning references, the alphabetical system should be adopted. Please use reference management software such as Endnote to manage references as far as possible.

  **List**: References should be arranged first alphabetically and then further sorted chronologically if necessary. More than one reference from the same author(s) in the same year must be identified by the letters "a", "b", "c", etc., placed after the year of publication.

  Examples:

  - Reference to a book:
    Strunk Jr. W., White E.B., The Elements of Style, fourth ed., Longman, New York, 2000, ISBN: 9780205309023.
  - Reference to a chapter in an edited book:
    Mettam G.R., Adams L.B., How to prepare an electronic version of your article, in: Jones B.S., Smith R.Z. (Eds.), Introduction to the Electronic Age, E-Publishing Inc., New York, 2009, pp.281–304.
  - Reference to a journal publication:
    Tsuji Y., Tanaka T., Ishida T., Lagrangian numerical simulation of plug flow of cohesionless particles in a horizontal pipe, Powder Technology, 71 (1992) 239–250. DOI: 10.1016/0032-5910(92)88030-L

  **Text**: All citations in the text should refer to:

  1. Single author: the author's name (without initials, unless there is ambiguity) and the year of publication;
  2. Two authors: both authors' names and the year of publication;
  3. Three or more authors: first author's name followed by "et al." and the year of publication.

  Citations may be made directly (or parenthetically). Groups of references should be listed first alphabetically, then chronologically.

  Examples:

  "as demonstrated (Hidaka et al., 1995; Tsuji, 1992a, 1992b, 1993). Mori and Fukumoto (2002) have recently shown ...."

(4) **Copyright and permission**

- The original paper to be submitted to KONA has not been published before in any language or in any journals or media; it is not submitted and not under consideration for publication in whole or in part elsewhere.
- Authors are responsible for obtaining permission from the copyright holders to reproduce any figures, tables and photos for which copyright exists.
- The KONA Journal applies the Creative Commons Attribution License to all works published by the Journal. Copyright stays with the agreed copyright owner, and the Hosokawa Powder Technology Foundation is granted the exclusive right to publish and distribute the work, and to provide the work in all forms and media.
- Users of the journal will be able to reuse the contents in any way they like, provided they are accurately attributed. No permission is required from either the authors or the publisher.

# HOSOKAWA MICRON GROUP

## GLOBAL NETWORK

The Hosokawa Micron Group, headquartered in Japan, has various locations around the world. Our competence centers have combined their know-how to offer you customized process technologies for optimal solutions. With more than 120 years of experience, we are a market leader in the development, design, and manufacture of powder and particle processing machines and systems. With its wide range of processing technologies, the Hosokawa Micron Group continues to set standards in particle processing.


# From lab to production scale

*Picoline multi-processing device*

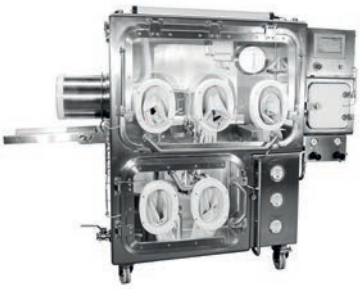

*Isolator housing an Alpine Spiral Jet Mill*

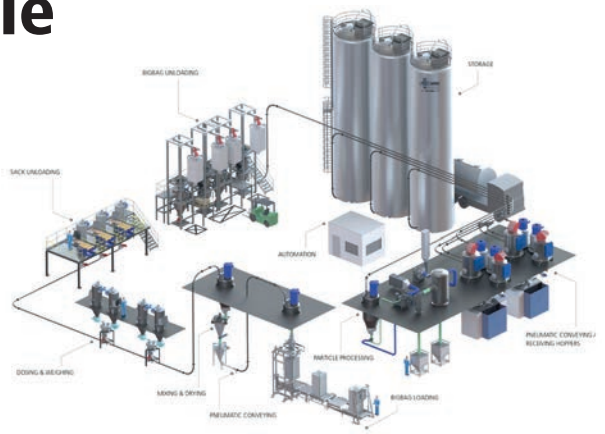

*Comprehensive processing system*

### LAB AND R&D

We offer integrated powder processing systems including containment solutions, designed to offer maximum flexibility and optimal solutions for product development in laboratory and pilot plant settings.

### PRODUCTION EQUIPMENT

Obtain cutting-edge technology for powder processing from the world market leader. Coordinated components and scalable processes for almost all types of dry powder processing.

### COMPLETE PROCESSING SYSTEMS

We specialize in designing and manufacturing innovative powder processing technologies for industries like chemicals, minerals, food, and pharma, with extensive expertise we proudly share with our customers.

# Process technologies for tomorrow

- AGGLOMERATION
- DRYING
- MIXING
- CONVEYING
- DOSING & WEIGHING
- STORAGE
- CONTAINMENT
- CLASSIFYING
- CRYOGENIC GRINDING
- COARSE MILLING
- COMPACTING
- FINE GRINDING
- CRUSHING & CUTTING
- COATING

## INNOVATIVE TEST CENTERS

Our global research and testing facilities offer a wide range of machines and complete processing systems, adaptable to various plant configurations.

## TOLL PROCESSING FACILITIES

As a professional and reliable partner in toll processing, we help you manage capacity needs without investment risks, whether for one-time or recurring projects.

## OVER A CENTURY OF EXPERIENCE

Profit from our many years of expertise in providing advanced solutions. Renowned customers worldwide trust the technology and know-how of the Hosokawa Micron Group.

## GLOBAL REPAIR & MAINTENANCE SERVICE

Our responsive service teams handle repairs and maintenance quickly and efficiently, whether on-site or in our advanced workshops around the world.

# Let our experts help you

Our seasoned experts are ready to help you develop the perfect solution for your powder and bulk solids processing needs. Whether you require innovative design, state-of-the-art equipment, or streamlined processes, we ensure that your operations achieve peak performance and optimal efficiency.
Together, we can transform your operations and achieve unparalleled success.

**www.hosokawa.com**

# HOSOKAWA MICRON GROUP

The Hosokawa Micron Group will always be the leading global company covering the mountain range of Powder Technologies. The Group has been a pioneer in the filed of powder and particle processing and blown film processing. We provide R&D, engineering, manufacturing and services in various fields of the world's major industrial markets.

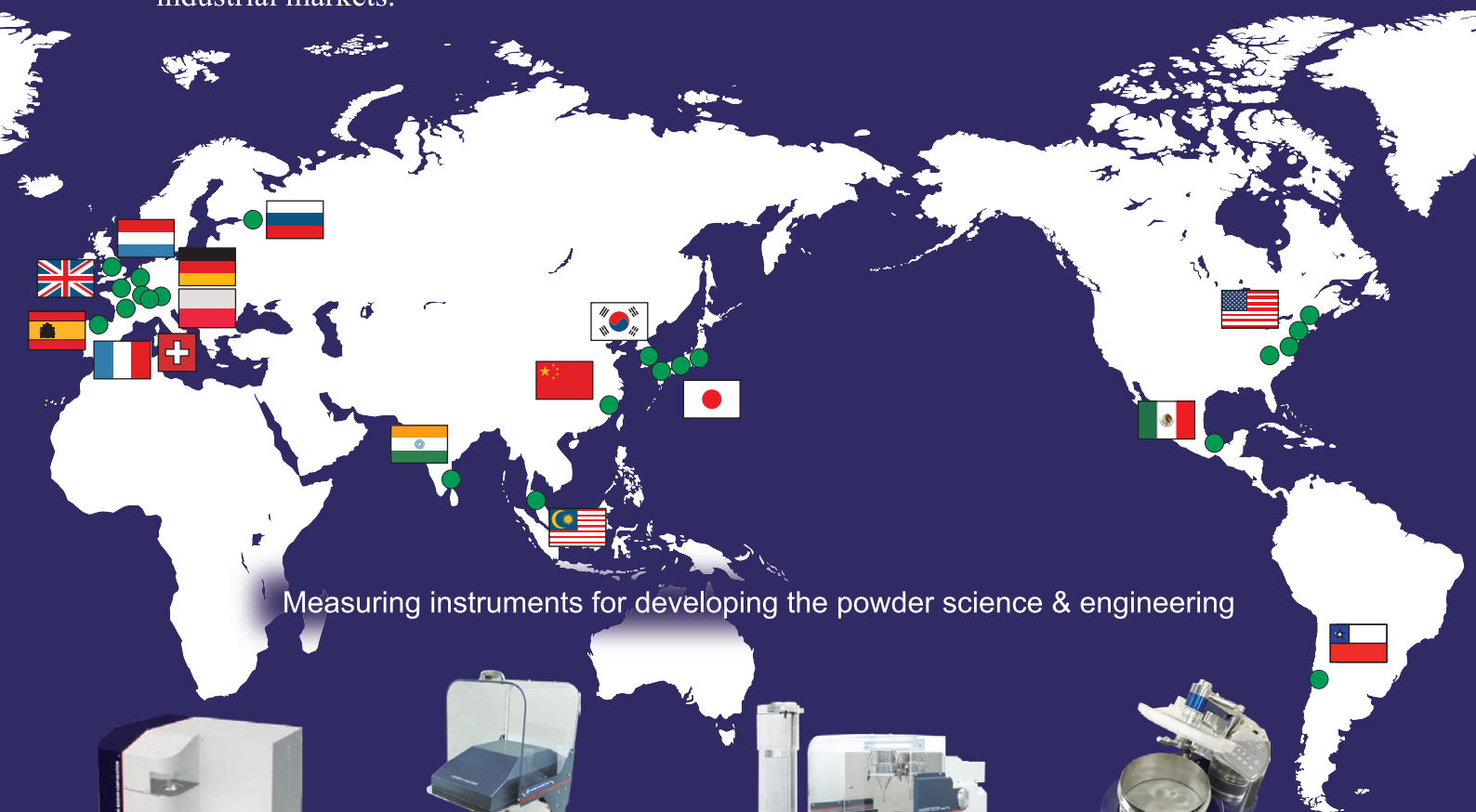

Measuring instruments for developing the powder science & engineering

Dynamic Particle Image Analyzer
Parshe Analyzer

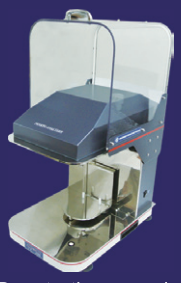

Penetration speed
Peneto Analyzer, PNT-N

Carr's indicies
Powder characteristics tester, PT-X

Wet sieving
Viblette, VBL-F

Process Technologies for Tomorrow

## HOSOKAWA MICRON CORPORATION


**Headquaters Location :**

**HOSOKAWA MICRON CORPORATION**

**URL : www.hosokawamicron.com**